

AD-A150 774

FLUID MECHANICS AND HEAT TRANSFER SPIRALLY FLUTED

1/8

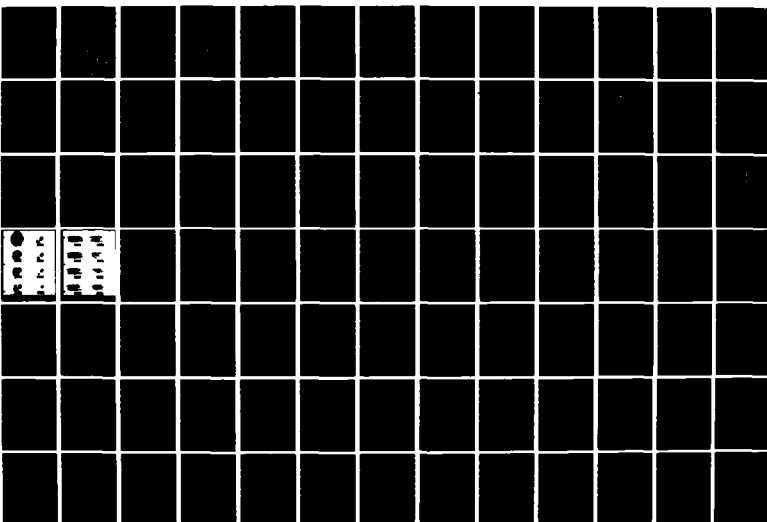
TUBING(U) GA TECHNOLOGIES INC SAN DIEGO CA

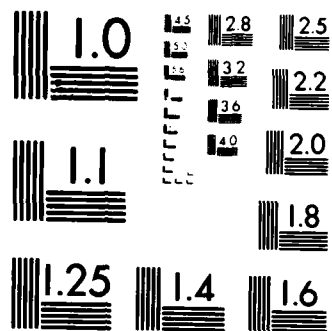
J S YANPOLSKY ET AL. DEC 84 GA-A17833 N00014-82-C-0721

UNCLASSIFIED

F/G 20/4

NL





MICROCOPY RESOLUTION TEST CHART  
NATIONAL BUREAU OF STANDARDS-1963-A

4

# GA Technologies

AD-A150 774

GA-A17833

## FLUID MECHANICS AND HEAT TRANSFER SPIRAL FLUTED TUBING

FINAL REPORT

by  
J. S. YAMPOLSKY, P. A. LIBBY, B. E. LAUNDER,  
and J. C. LaRUE

Prepared under  
Contract N0014-82-C-0721  
for the Office of Naval Research

"Original contains color  
plates: All DTIC reproduct-  
ions will be in black and  
white"

DTIC  
ELECTE  
MAR 1 1985  
S B D

DECEMBER 1984

DISTRIBUTION STATEMENT A

Approved for public release  
Distribution Unlimited

85 02 01 112

DTIC FILE COPY

## DISCLAIMER

This report was prepared as an account of work sponsored by an agency of the United States Government. Neither the United States Government nor any agency thereof, nor any of their employees, makes any warranty, express or implied, or assumes any legal liability or responsibility for the accuracy, completeness, or usefulness of any information, apparatus, product, or process disclosed, or represents that its use would not infringe privately owned rights. Reference herein to any specific commercial product, process, or service by trade name, trademark, manufacturer, or otherwise, does not necessarily constitute or imply its endorsement, recommendation, or favoring by the United States Government or any agency thereof. The views and opinions of authors expressed herein do not necessarily state or reflect those of the United States Government or any agency thereof.



# GA Technologies

**GA-A17833**

## **FLUID MECHANICS AND HEAT TRANSFER SPIRAL FLUTED TUBING**

**FINAL REPORT**

by

**J. S. YAMPOLSKY, P. A. LIBBY,\* B. E. LAUNDER,\*\*  
and J. C. LaRUE\*\*\***

**Prepared under  
Contract N0014-82-C-0721  
for the Office of Naval Research**

\* University of California, San Diego, California

\*\* University of Manchester, Institute of Science and Technology, Manchester, England

\*\*\* University of California, Irvine, California

**GA PROJECT 3783  
DECEMBER 1984**

## CONTENTS

INTRODUCTION . . . . .	1
OVERALL PERFORMANCE OF SPIRAL FLUTED TUBING . . . . .	3
Single-Phase Flow . . . . .	3
Boiling . . . . .	11
Condensing . . . . .	11
Research Program . . . . .	14
References . . . . .	14
PROGRAM RESULTS . . . . .	17
Theoretical Program . . . . .	17
Experimental Program . . . . .	26
Conclusions . . . . .	30
Recommendations for Further Work . . . . .	32
SECTION A: Flow Visualization Studies	
SECTION B: Measurements of Turbulent Flow in a Spirally Fluted Tube	
SECTION C: Preliminary Studies of the Turbulent Flow in Rotating Tubes	
SECTION D: The Prediction of Convective Heat Transfer in Spirally Fluted Tubes	

## FIGURES

1. Shell side NU-REY correlation . . . . .	5
2. Tube side NU-REY correlation . . . . .	6
3. Shell side NU-REY correlation . . . . .	7
4. Tube side NU-REY correlation . . . . .	8
5. Enhancement of 30° helix for varied heat flux . . . . .	10
6. Spirally fluted tube friction factor comparisons . . . . .	12
7. Spirally fluted tube evaporator test . . . . .	13
8. Spirally fluted tube freon 113 condenser . . . . .	15
9. Curvilinear/polar grid . . . . .	18

10.	Regions of application of the turbulence models . . . . .	19
11(a).	$(\vec{U} + \vec{V})$ . . . . .	20
11(b).	$(\vec{U} + \vec{V}) - \vec{\omega}R$ . . . . .	22
11(c).	$(V_{\theta} \cos\phi - W \sin\phi) \cos\phi + V_r$ . . . . .	23
12.	Comparison of predicted and experimental data for Nusselt modulus $n=30$ , $\phi=30^\circ$ . . . . .	24
13.	Comparison of predicted and experimental data $n=30$ , $\phi=30$ . .	25
14.	Mean axial velocity as a function of radius for air . . . .	27
15.	Mean axial velocity as a function of radius for water . . .	28
16.	Turbulent kinetic energy as a function of radius in air . .	29
17.	Azimuthal velocity as a function of radius in air . . . . .	31

# TABLE

1.	Nomenclature . . . . .	4
----	------------------------	---

Accession For	
NTIS GRA&I	<input checked="" type="checkbox"/>
DTIC TAB	<input type="checkbox"/>
Unannounced	<input type="checkbox"/>
Justification	
PER LETTER	
Availability Codes	
Dist	Special
A-1	



## INTRODUCTION

The objective of this program is to develop an understanding of the fluid mechanics and heat transfer mechanisms that result in the demonstrated performance of the spiral fluted tubing under development at GA Technologies Inc. (GA). Particularly emphasized are the processes that result in the augmentation of the heat transfer coefficient without an increase in friction coefficient in the single-phase flow. Quantitative delineation of these processes would allow for their application to the optimal solution of heat transfer problems in general as well as to tubular heat exchanges using spiral fluted tubes.

GA has been developing spiral fluted tubing since 1978 to improve the performance of heat exchanger equipment by enhancing the heat transfer coefficient and extending both the inner and the outer heat transfer surfaces of the tube. The fabrication technique of rolling flutes on a flat strip and subsequently welding the corrugated strip to form spiral fluted tubing results in a low fabrication cost approximately equal to that of commercially welded plain tubing.

Measurements of the heat transfer performance in single-phase liquid flow show an improvement over a plain tube by a factor of 3 on the outside and a factor of 2.56 on the inside of a spiral fluted tube when the area extension is included. The improvement in evaporation on the inside of the tube is shown by measurement in a single tube to be a factor between 2.4 and 3.2 relative to a plain tube, and the improvement in condensation on the outside of a spiral fluted tube is shown by measurement to be a factor between 2.8 and 5.6 relative to a plain tube. In both evaporation and condensation, the area extension is included and the heat transfer enhancement varies with heat flux.

This investigation was a collaborative effort of J. C. LaRue of the University of California at Irvine (UCI), B. E. Launder of the University of Manchester Institute of Science and Technology (UMIST), P. A. Libby of the University of California at San Diego (UCSD), and J. S. Yampolsky of GA. The experimental phase of the program consisted of the following:

1. Flow visualization studies using high-speed photography of dye injected into water flowing in a cast acrylic spiral fluted tube.
2. Time-resolved axial velocity measurements as a function of radius at the exit plane of a spiral fluted tube with water flowing through the tube.
3. Simultaneous time-resolved measurement of the axial and radial velocity components and temperature with heated air flowing through the tube cooled by a water jacket.

There were two approaches pursued in the theoretical phase: The study done at UCSD employed a Reynolds stress/flux description of the turbulent flow with heat transfer in a smooth tube rotating about its axis, while the study at UMIST developed the methodology for performing numerical studies of the laminar and turbulent flow in the spiral fluted tube. The effect of the geometric parameters were also investigated. Sections A through D of this report each cover one of the individual studies separately.

## OVERALL PERFORMANCE OF SPIRAL FLUTED TUBING

The heat transfer performance of spiral fluted tubing was measured in a series of programs sponsored by the United States Department of Energy (Refs. 1 through 3). These are summarized below. (Table 1 identifies the nomenclature used in the discussion.)

### SINGLE-PHASE FLOW

Three sets of data were developed on single-phase water flow on the inside of spiral fluted tubing with some geometric differences in the tubes used and the testing methods. The details of both are given in the cited references. The heat transfer performance on both the shell side and tube side of spiral fluted tubing as measured in a seven-tube heat exchanger with water (Ref. 2) is shown in Figs. 1 through 4. The Nusselt Modulus,

$$\frac{hd_{hyd}}{k} \bigg/ \frac{c\mu^{0.4}}{k},$$

is the ordinate and the Reynolds Number,

$$\frac{vd_{hyd}}{v},$$

is the abscissa. The Dittus-Boelter smooth tube correlation is shown for comparison. The heat flow is radially inward in Figs. 1 and 2 and radially outward in Figs. 3 and 4. These data indicate that the direction of heat flow has no effect on the amount of enhancement within the accuracy of the data, and that the enhancement on the outside of the tube is greater than that on the inside of the tube by a factor of 2.28 compared with a factor of 1.59 as compared with a plain tube for heat flowing radially inward and a factor of 2.35 compared to a factor of 1.63 as

TABLE 1  
NOMENCLATURE

Nusselt modulus	$Nu/Pr^{0.4}$
Nusselt number	$Nu = hd_{hyd}/k$
Conductance coefficient	$h$ (Btu/hr-ft <sup>2</sup> -°F)
Hydraulic diameter	$d_{hyd} = \frac{4 \times \text{cross section area (ft)}}{\text{wetted perimeter}}$
Thermal conductivity	$k$ (Btu/hr-°F-ft)
Reynolds number	$Re = vd_{hyd}/\nu$
Mean axial fluid velocity	$v$ (ft/sec)
Kinematic viscosity	$\nu$ (ft <sup>2</sup> /sec)
Flux parameter	$\psi^*$
Flux	$\Psi$ (Btu/hr-ft <sup>2</sup> )
Mechanical equivalent of heat	$J$ (ft-lb/Btu)
Flute height	$\epsilon$ (ft)
Prandtl number	$Pr = c_p \mu / k$
Specific heat at constant pressure	$c_p$ Btu/lb-°F
Absolute viscosity	$\mu$ (lb/ft-sec)
Dittus-Boelter correlation	$Nu/Pr^{0.4} = 0.022 Re^{0.8}$
Friction factor (Moody)	$\lambda = \frac{\Delta p}{1/d_{hyd} \rho v^2 / 2g}$
Pressure drop	$\Delta p$ (lb/ft <sup>2</sup> )
Density	$\rho$ (lb/ft <sup>3</sup> )
Gravitational constant	$g$ (ft/sec <sup>2</sup> )
Tube length	$l$ (ft)

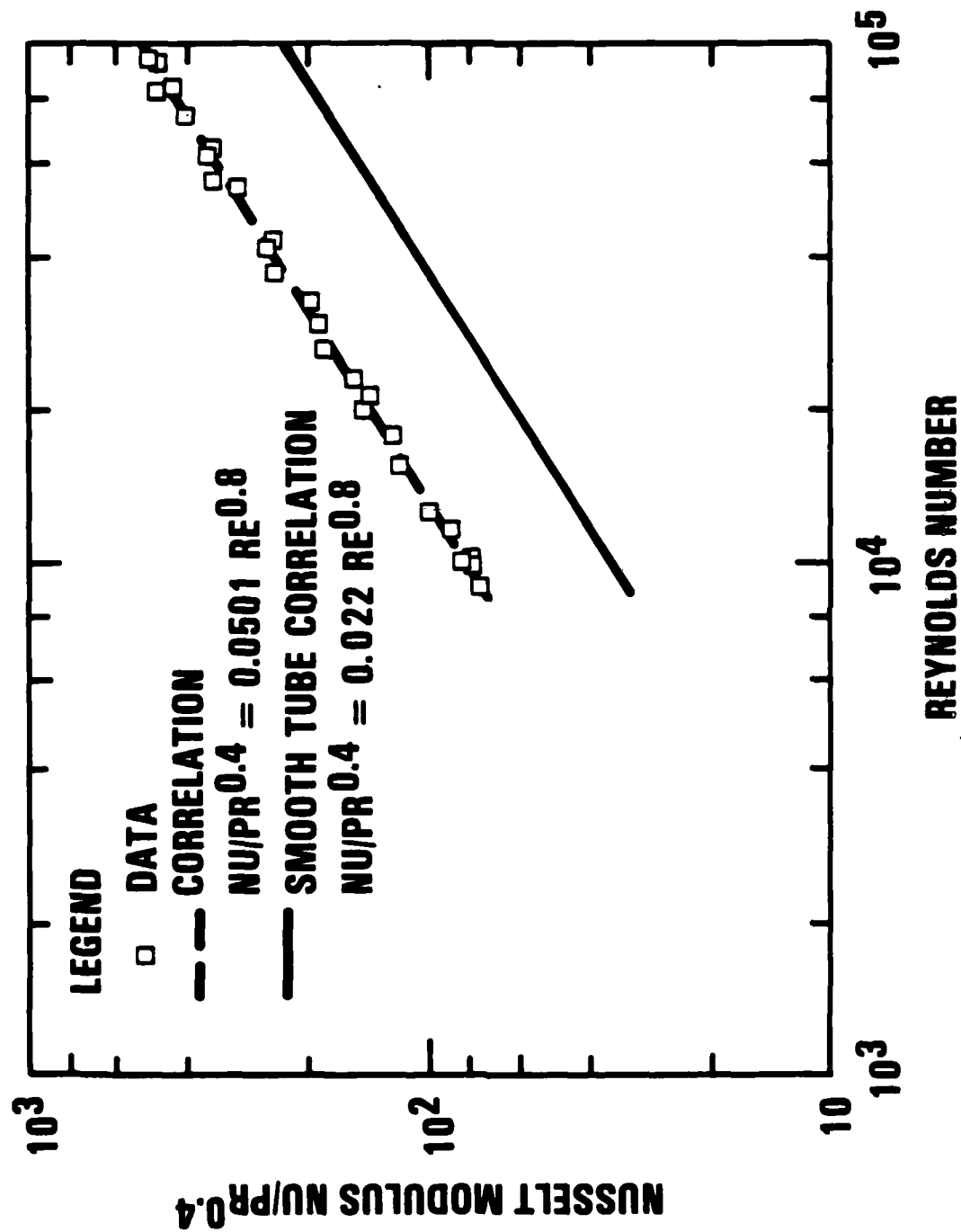
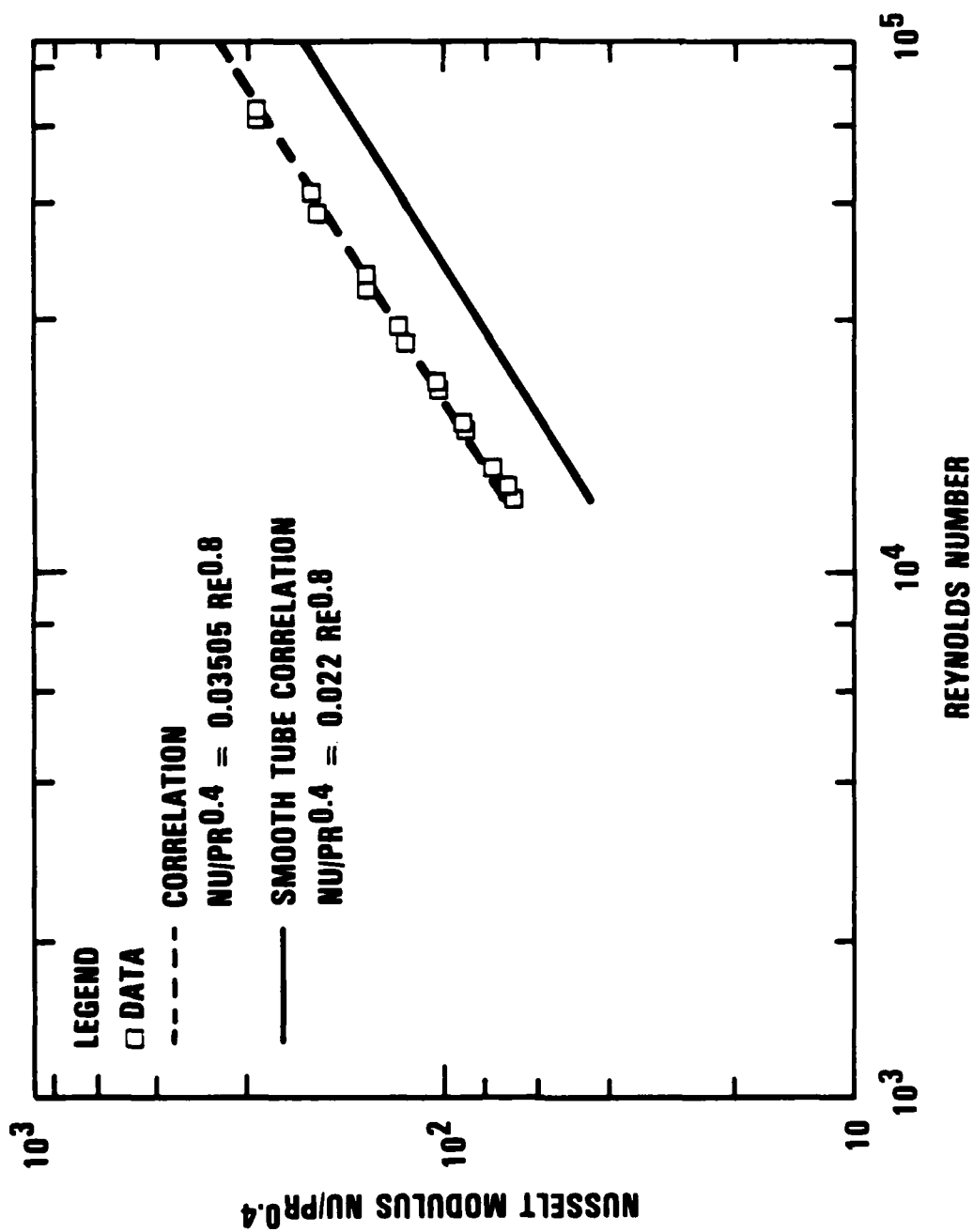


Fig. 1. Shell side NU-REY correlation

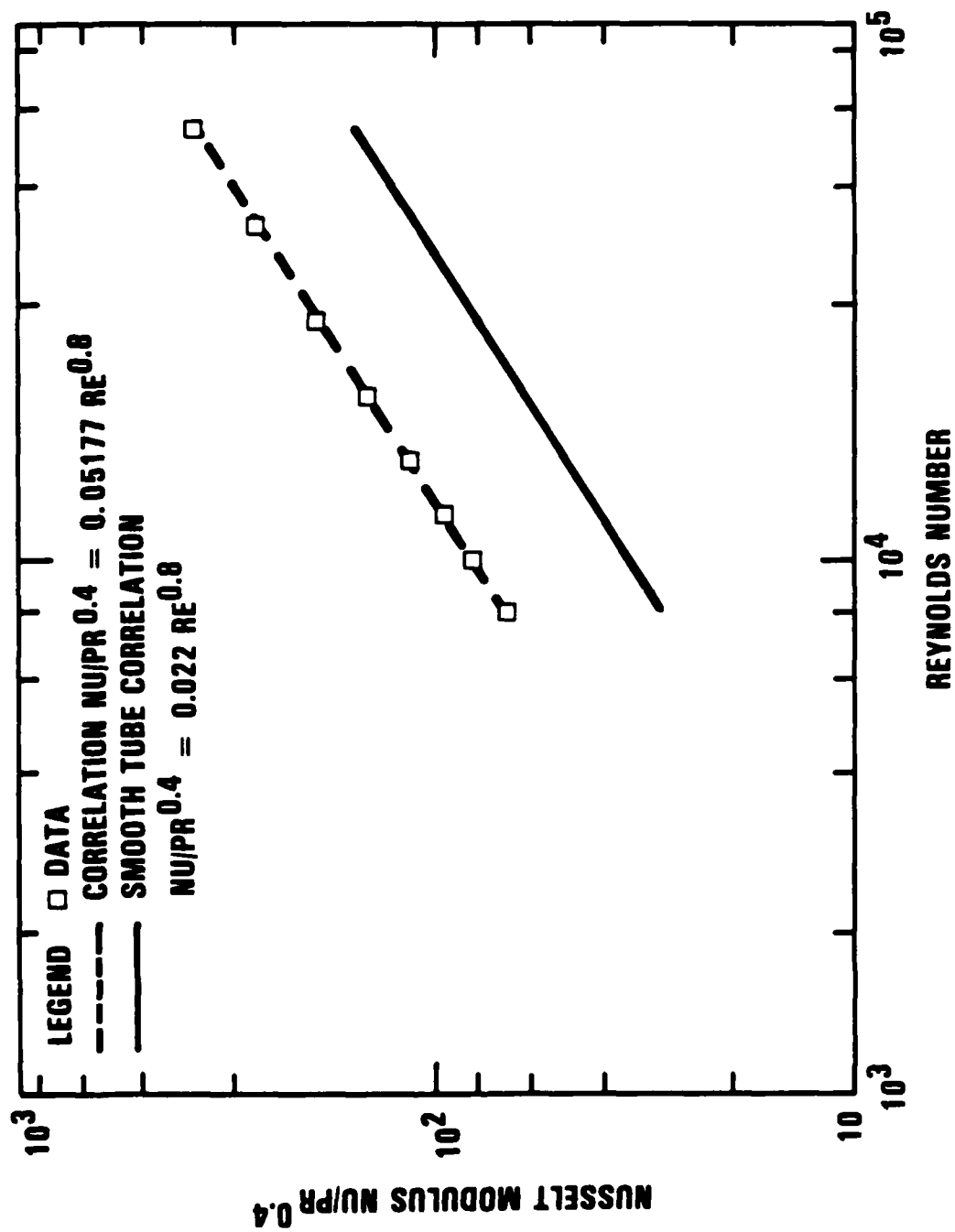
A17833





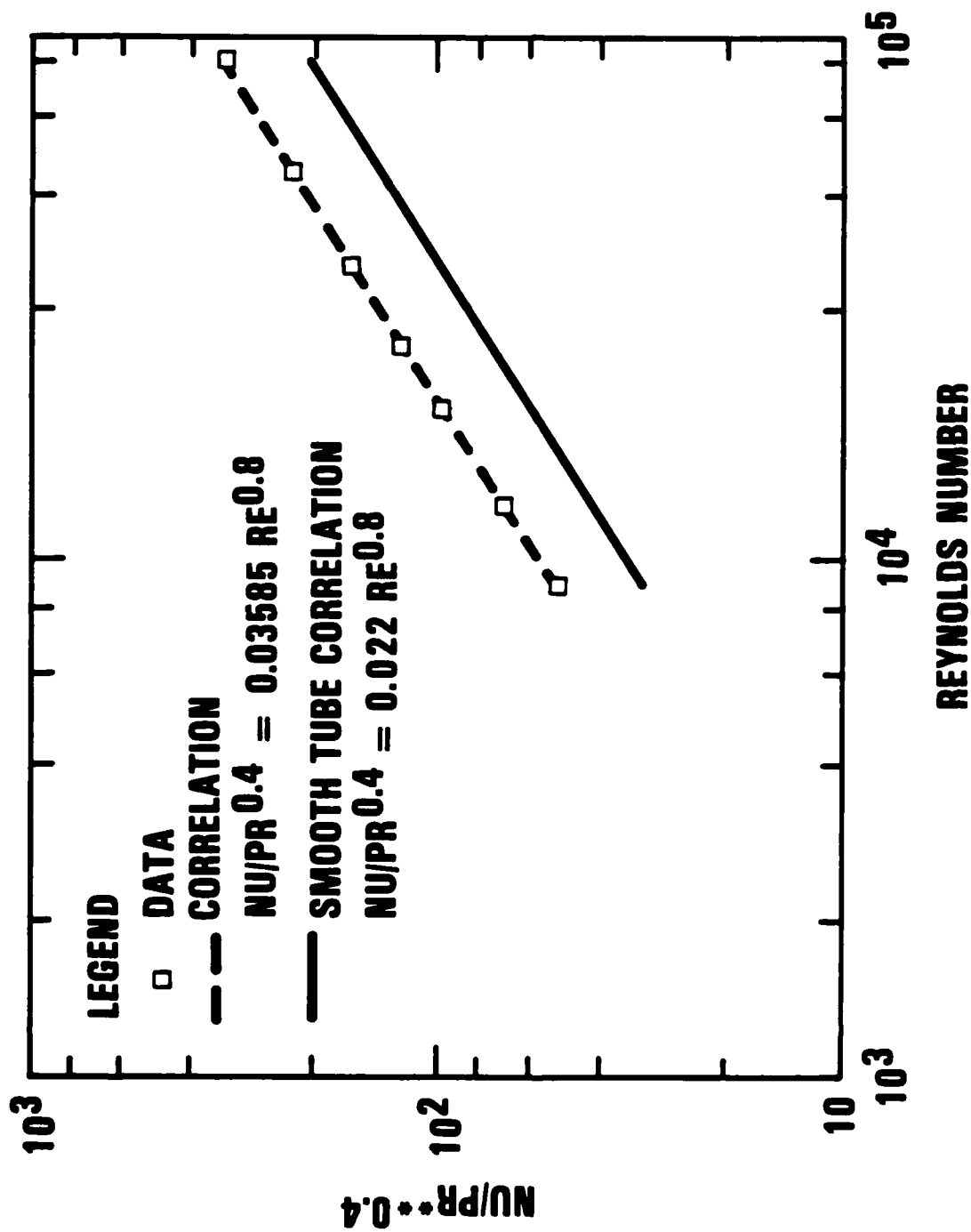
A17833

Fig. 2. Tube side NU-REY correlation



A17833

Fig. 3. Shell side NU-REY correlation



A17833

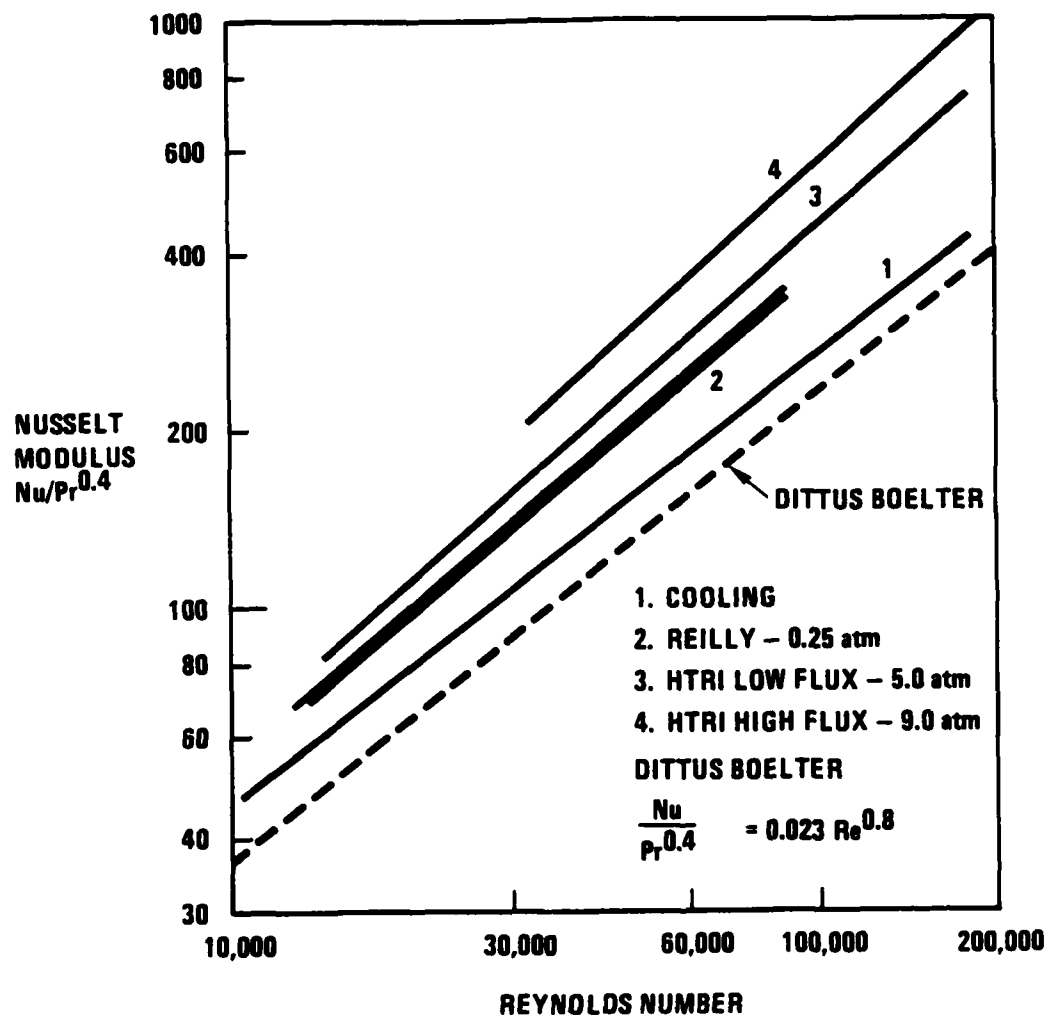
Fig. 4. Tube side NU-REY correlation

compared with a plain tube for heat flowing radially outward. These enhancement factors do not include the area extension by a factor of 1.4 on the outside and a factor of 1.6 on the inside that the flutes provide over that of a plain tube with the same cross-sectional area. Since the enhancement factor is essentially the same when the direction of heat is reversed (Refs. 1 and 3) (Figs. 2 and 4) the enhancement is not flux dependent.

Previous measurements (Refs. 1 and 4) of spiral fluted tubing showed a dependency of the enhancement factor for large values of heat flux. These data are shown in Fig. 5. The present results are in agreement with curve 2 of Fig. 5, the Reilly tests in which the enhancement ratio was 1.59 to 1.64. Curves 3 and 4, the HTRI low-flux and high-flux tests, indicate enhancement factors of 1.86 and 2.34 respectively. The minimum enhancement factor, the HTRI tests with the heat flux reversed, is shown by curve 1 to be 1.22, which is less than the 1.63 factor shown in Fig. 4. The geometric difference between the tubes' geometry might provide an explanation for the improved minimum enhancement of Fig. 4 as compared with curve 1 of Fig. 5. The ratio of flute height to a diameter equivalent to the cross-sectional area was 0.0465 in. for the tube used in the HTRI tests and 0.0566 in. for the tubes in the seven-tube heat exchanger tests. This increase of the flute height ratio in excess of 20% would increase the secondary flow within the flute. As will be seen later from the UMIST work, this secondary flow is the mechanism that accounts for the enhancement observed in spiral fluted tubing by transporting the laminar sublayer away from the wall.

A purely empirical approach to a heat flux parameter is proposed to compare the data. As there were variations in the tube dimensions, heat flux, and Reynolds number for each of the data sets, the nondimensional heat flux parameter suggested is

$$\psi^* = \frac{\psi J}{\mu \text{Re}^{1/5}} \frac{\epsilon}{d_{\text{hyd}}} .$$



A17833

Fig. 5. Enhancement of 30° helix for varied heat flux (does not include area extension)

$\psi^*$  has a mean value of  $4 \times 10^8$  for the high-flux HTRI test data (curve 4 of Fig. 5),  $1.91 \times 10^8$  for the low-flux HTRI test data (curve 3 of Fig. 5),  $0.416 \times 10^8$  for the Reilly test data (curve 2 of Fig. 5),  $0.403 \times 10^8$  for one of the data sets in the seven-tube bundle (Fig. 2), and  $0.393 \times 10^8$  for another of the seven-tube data sets (Fig. 2). The heat flux parameter  $\psi^*$  has essentially the same value for the Reilly test data as for the seven-tube test data, as does the enhancement factor in both of these cases. The increase of the enhancement factor with increasing values of this flux parameter indicates that a threshold of heat flux exists below which the enhancement factor is constant. This is seen in the same value for the enhancement factor when the heat flow is reversed.

A separate series of measurements was made to determine the friction coefficient for the same tube as that used in the seven-tube tests (Ref. 2). The results shown in Fig. 6 indicate that the isothermal friction coefficient for both air and water are the same as for a smooth tube within the error band of the measurements.

#### BOILING

The boiling performance of a fluorocarbon on the inside of a vertical spiral fluted tube as a function of boiling heat flux is shown in Fig. 7. The spiral fluted tube shows a boiling coefficient enhancement factor range of 1.5 to 2.0 as compared with that calculated for a plain tube exclusive of area extension. The boiling coefficient per foot of the spiral fluted tube is increased by a factor of 2.4 to 3.2 relative to a plain tube if the area extension of 1.6 is included. These data are for the overall boiling coefficient. Subcooled liquid entered the tube, and saturated or almost saturated vapor exited.

#### CONDENSING

The measured condensing heat transfer coefficient on the outside of a vertical spiral fluted tube is compared with that of a smooth tube in

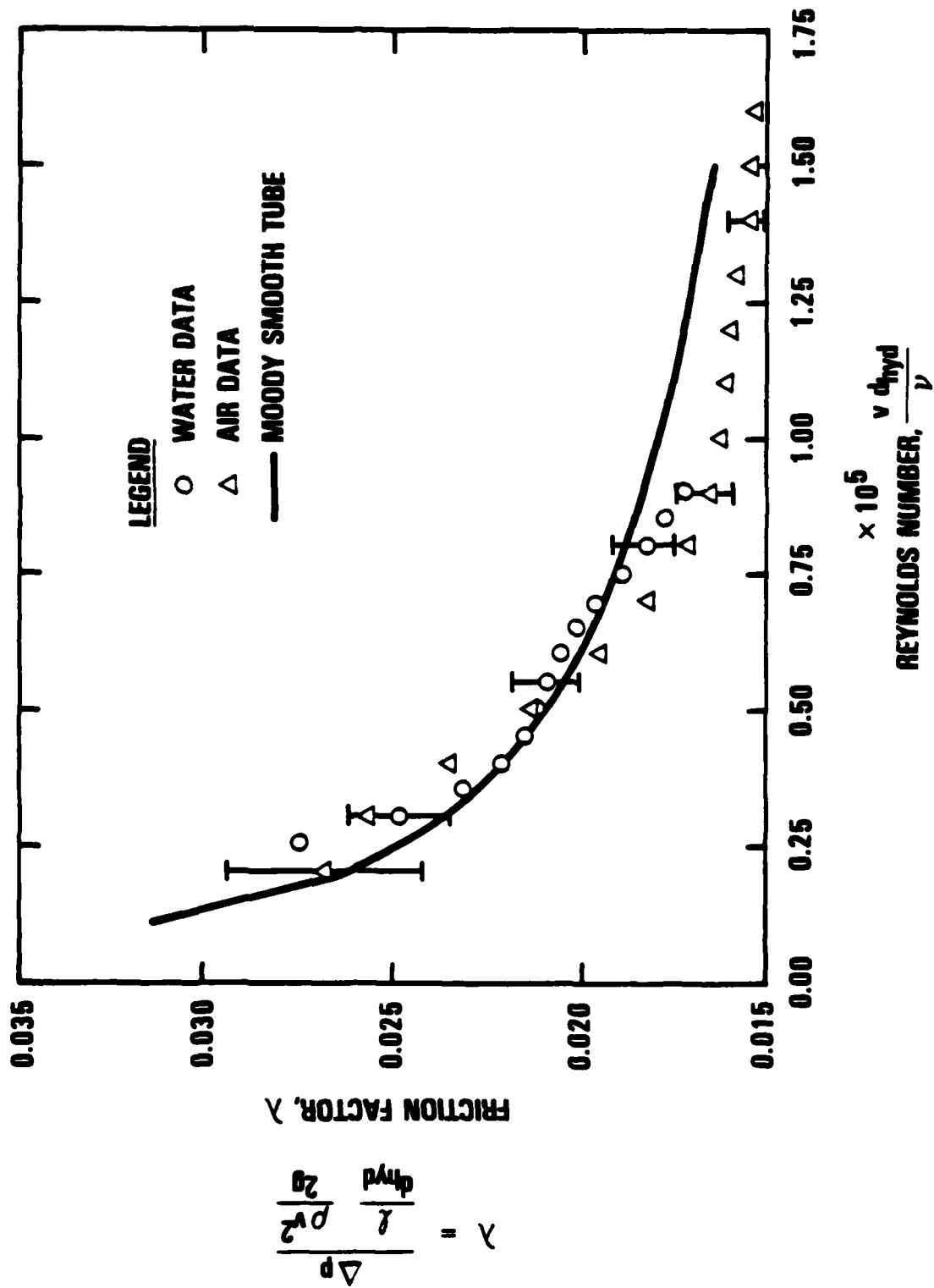
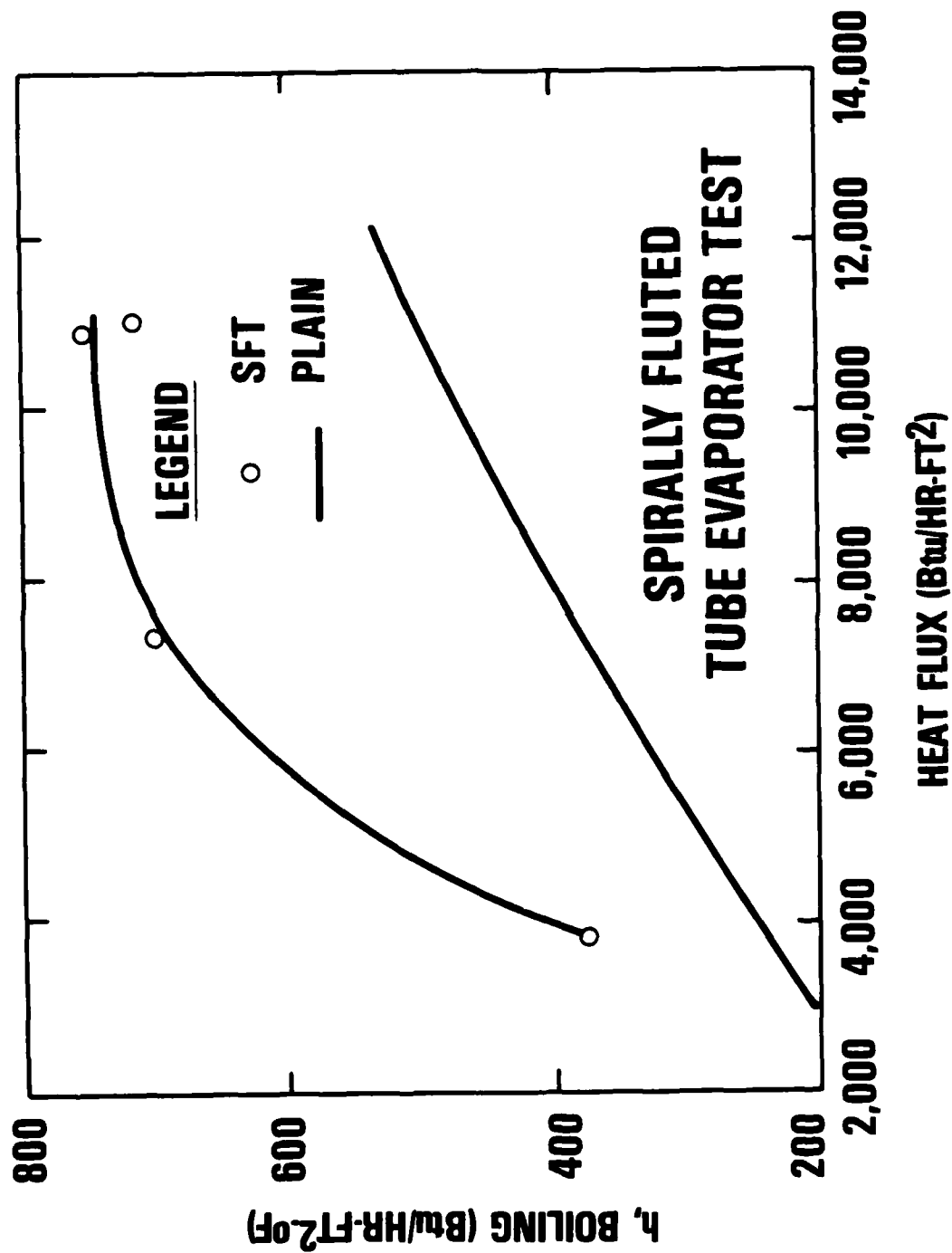


Fig. 6. Spirally fluted tube friction factor comparisons

A17833



A17833

Fig. 7. Spirally fluted tube evaporator test



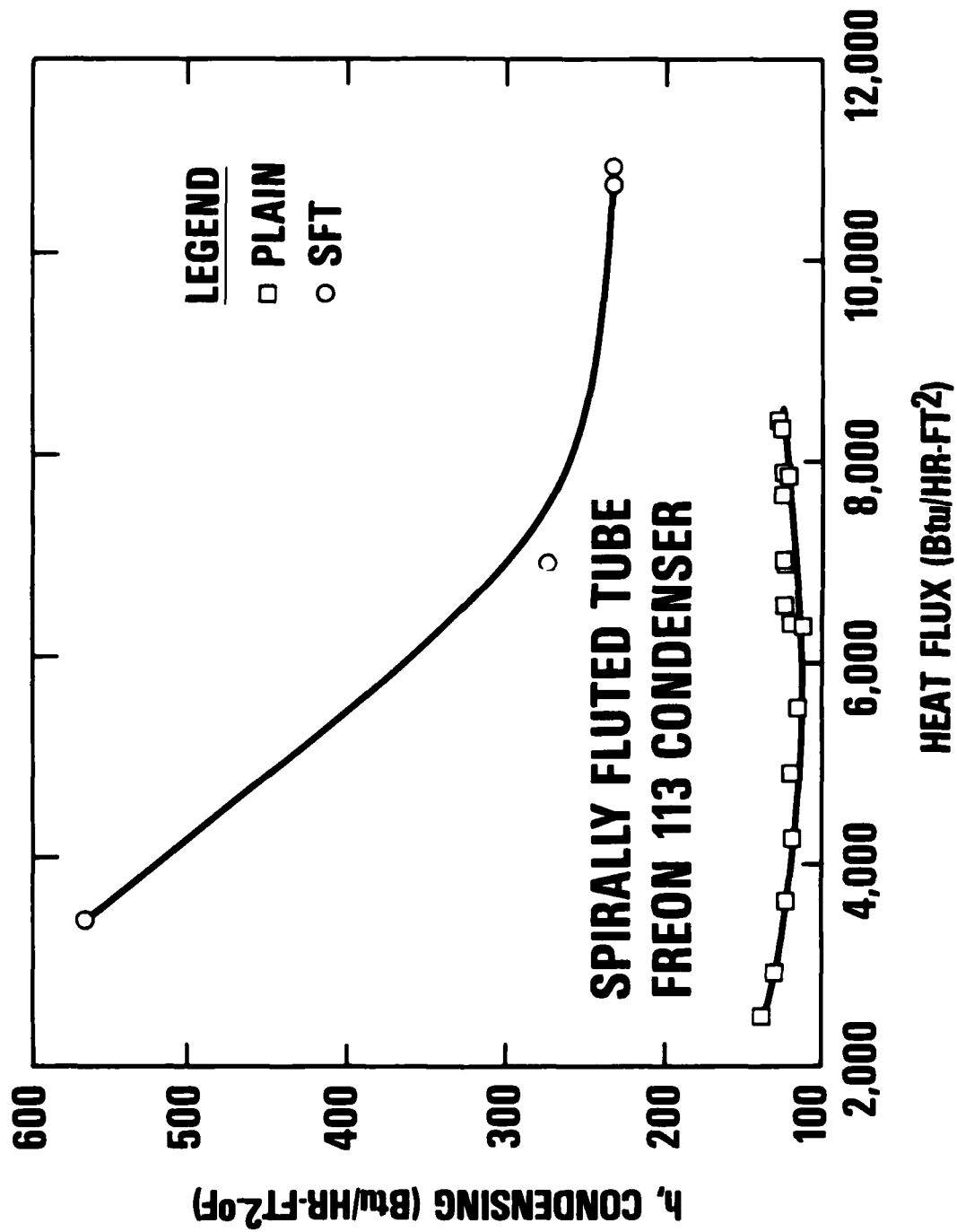
Fig. 8 for a fluorocarbon. The spiral fluted tube shows a condensing coefficient enhancement factor range of 2 to 3.8 as compared with a plain tube, exclusive of area extension. The condensing coefficient per foot of tube is increased by a factor of 2.8 to 5.6 relative to a smooth tube if the area extension of 1.4 is included.

#### RESEARCH PROGRAM

The objective of this research program is to determine the fluid mechanics of the flow in spiral fluted tubes that results in the enhancement of the heat transfer coefficient without an accompanying increase in the frictional coefficient. Overall heat transfer measurements, discussed earlier in this report, show that the heat transfer coefficient in single-phase liquid flow is increased by a factor of 1.6 on the inside of the spiral fluted tube compared with a plain tube, while the friction coefficient is essentially the same as that of a plain tube. Measurements have also shown that beyond a high threshold value of heat flux, the degree of enhancement increases with further increases of heat flux when the direction of the heat flow is radially inward. The work was a collaborative effort among four institutions. Each effort is reported separately in individual sections of this report. The principal findings as they pertain to the objectives are reviewed and discussed in the next section, Program Results.

#### REFERENCES

1. Yampolsky, J. S., "Spirally Fluted Tubing for Augmented Heat Transfer," DOE Report GA-A15442, June 1979.
2. Yampolsky, J. S., and P. Pavlics, "Tubing For Augmented Heat Transfer," DOE Report GA-A17109, August 1, 1983.
3. Yampolsky, J. S., and P. Pavlics, "Spiral Fluted Tubing For Augmented Heat Transfer In Process Industries," DOE Report GA-A17334, October 1983.



A17833

Fig. 8. Spirally fluted tube freon 113 condenser

4. Reilly, D. J., "An Experimental Investigation of Enhanced Heat Transfer on Horizontal Condenser Tubes," M. S. Thesis, Naval Postgraduate School, 1978.

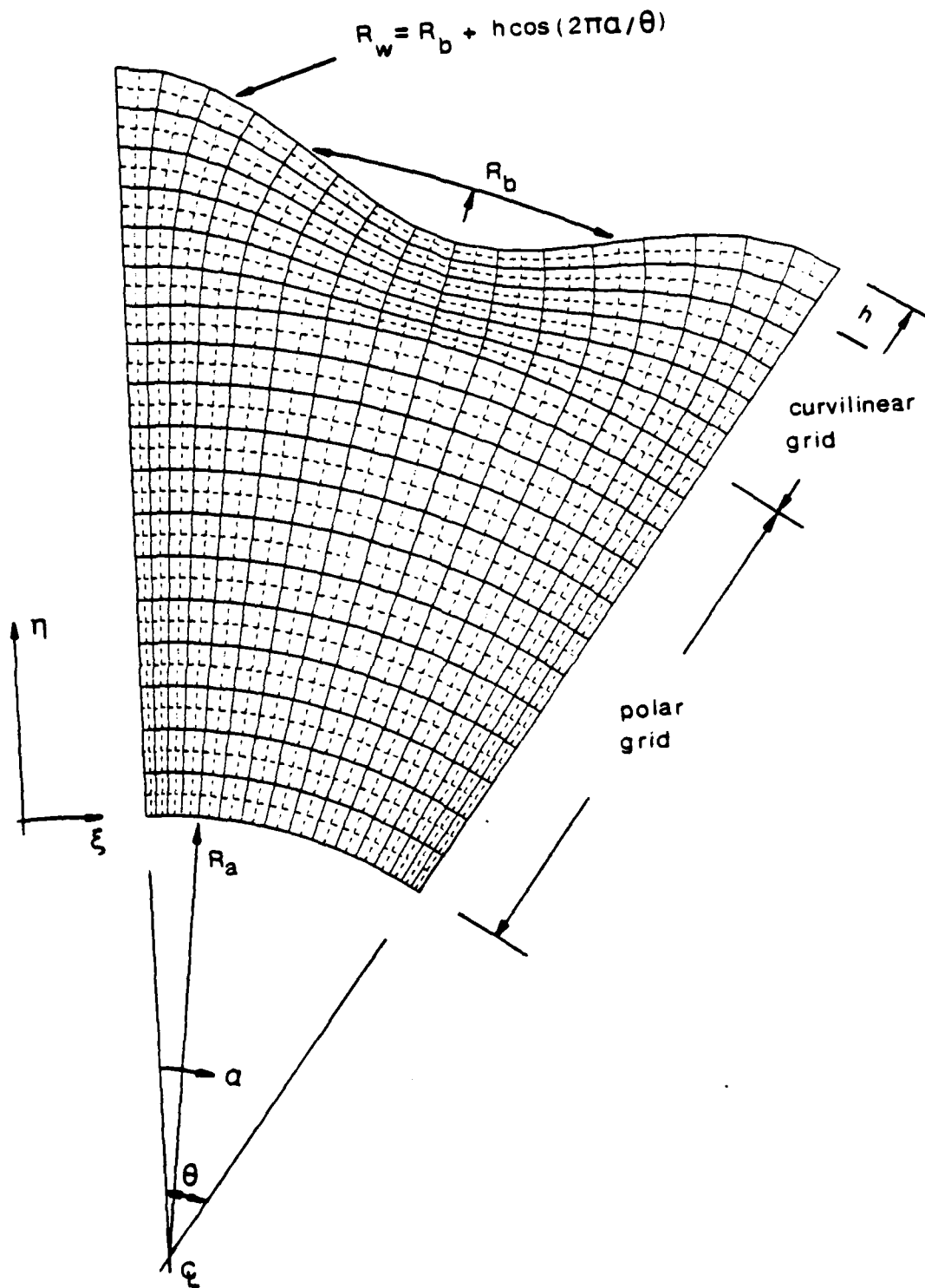
## PROGRAM RESULTS

### THEORETICAL PROGRAM

The program at UMIST under the direction of B. E. Launder is documented in the Ph.D. thesis of Anna Barba, and is reproduced in Section D of this report. A brief summary of the results follows, using figures from that work.

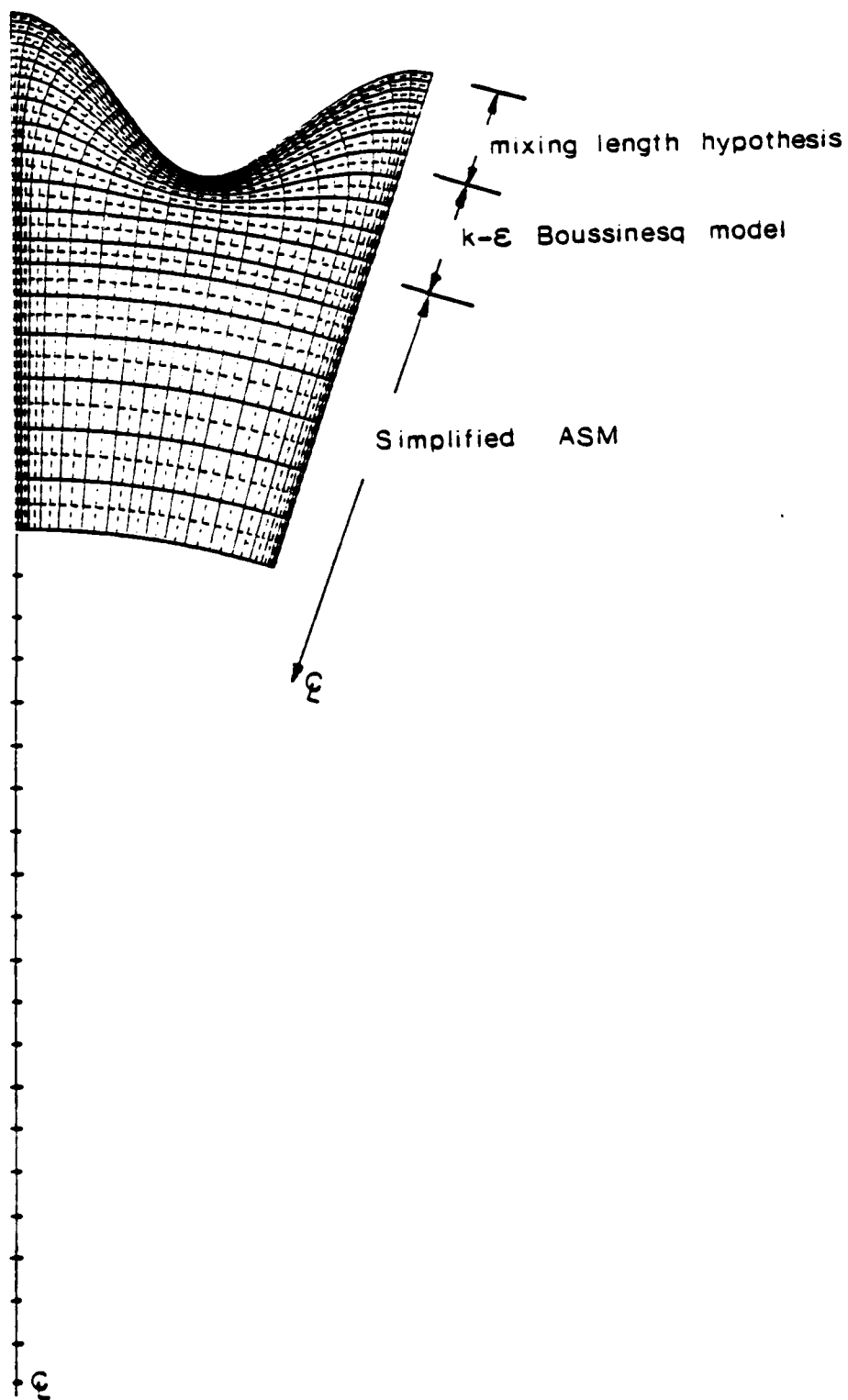
The flow is analyzed over a sector of the tube cross section having as boundaries a single flute at the outer surface (the tube wall) and an arc at a finite radius at the inner surface, with radii forming the side surfaces. The orthogonal coordinate lines  $\xi$  and  $\eta$  map the solution domain shown in Fig. 9. The tube wall coincides with a line of constant  $\eta$  but the undulation of the constant- $\eta$  lines decreases with radius until the lines become cylindrical. The constant- $\xi$  lines are orthogonal to the constant- $\eta$  lines and are radial at the crest and through positions. A third coordinate,  $\zeta$ , is in the axial direction and follows the spiralling of the flutes. The turbulence models and the domain of their application are shown in Fig. 10. Near the wall, in the vicinity of the flutes, a mixing length hypothesis including established viscous-damping effects was used. A  $k \sim \epsilon$  Boussinesq turbulence model was used between the flutes and the cylindrical polar grid where a simplified algebraic stress model was employed.

The calculated velocity field ( $\vec{u} + \vec{v}$ ) is shown in Fig. 11(a) for the spiral fluted tube geometry used in the seven-tube bundle tests, except that in the actual flutes the flute helix is counterclockwise while it is clockwise in the calculated flutes. A secondary flow can be seen in the flute region. This results from the flow through the tube encountering the flute spiralling clockwise around the tube. This flow creates a region of high pressure on the leading face of the flute, which forces



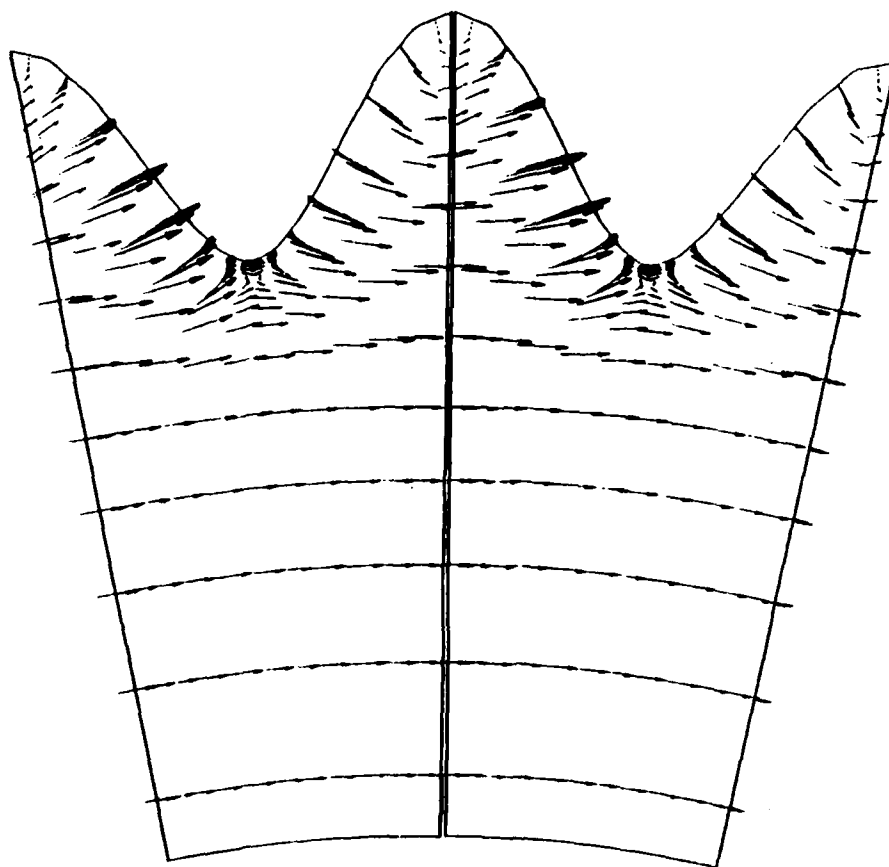
A17833

Fig. 9. Curvilinear/polar grid



A17833

Fig. 10. Regions of application of the turbulence models



$$n=30 ; \varphi=30 ; h=0.06R_b$$

A17833

Fig. 11(a).  $(\vec{U}+\vec{V})$

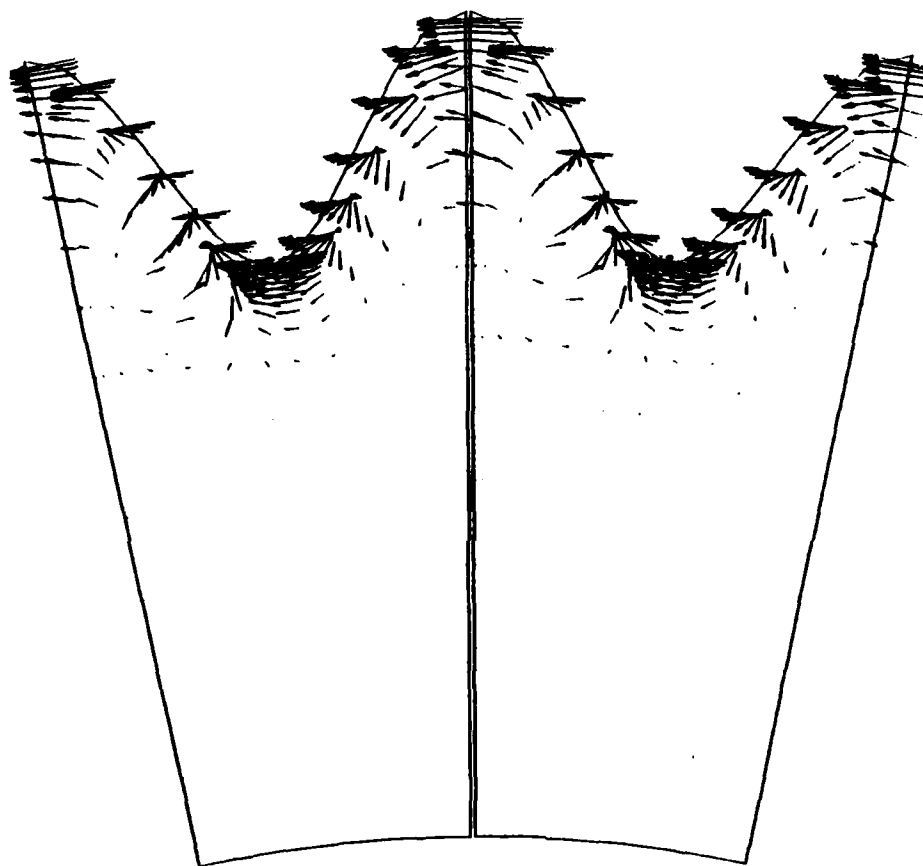
adjacent fluid clockwise and away from the wall and creates a low-pressure region on the trailing face of the flute. The angular momentum of the secondary flow in the flutes induces the rotation of the core flow. The rotation of the core flow was observed in the flow visualization.

The secondary flow can be directly seen in Fig. 11(b), which shows the velocity field in the flutes relative to the rotating core flow. The solid body rotation is subtracted from the vector field  $a(\vec{u} + \vec{v}) - \vec{\omega}R$ . This shows the flow seen by an observer rotating with the core flow. The velocity field relative to the flute spiral is given by  $(V_{n\theta} + V_r)$ , which is shown in Fig. 11(c). This is what is seen by an observer on the flute spiralling around the tube. The counterclockwise vectors indicate that the fluid in the tube lags the rotation rate of the flutes. This view demonstrates how the spiral fluted tube promotes a flow in the fluid adjacent to the wall and offers an explanation for the observed enhancement of heat transfer coefficient, since the principal resistance to heat transfer is in the various sublayers at the wall.

The comparison of the measured with predicted mean velocity, the mean axial fluctuation, the turbulent kinetic energy, and the azimuthal velocity as a function of radius in the spiral fluted tube will be discussed in the next section. Figure 12 shows the predicted Nusselt number as a function of Reynolds number on the data set of the heat transfer measurements previously used to show the effect of heat flux. The calculated values should be compared with the data of curve 2 (previously pointed out to be essentially the same as the seven-tube data which are free from the effect of heat flux). The predicted values are too high by a factor of 2. The friction coefficient prediction shown in Fig. 13 is also too high by about the same factor.

Calculations were also made with a simplified algebraic stress model closure in the core region to investigate the effect of flux on the heat transfer enhancement. This showed no buoyancy effect.

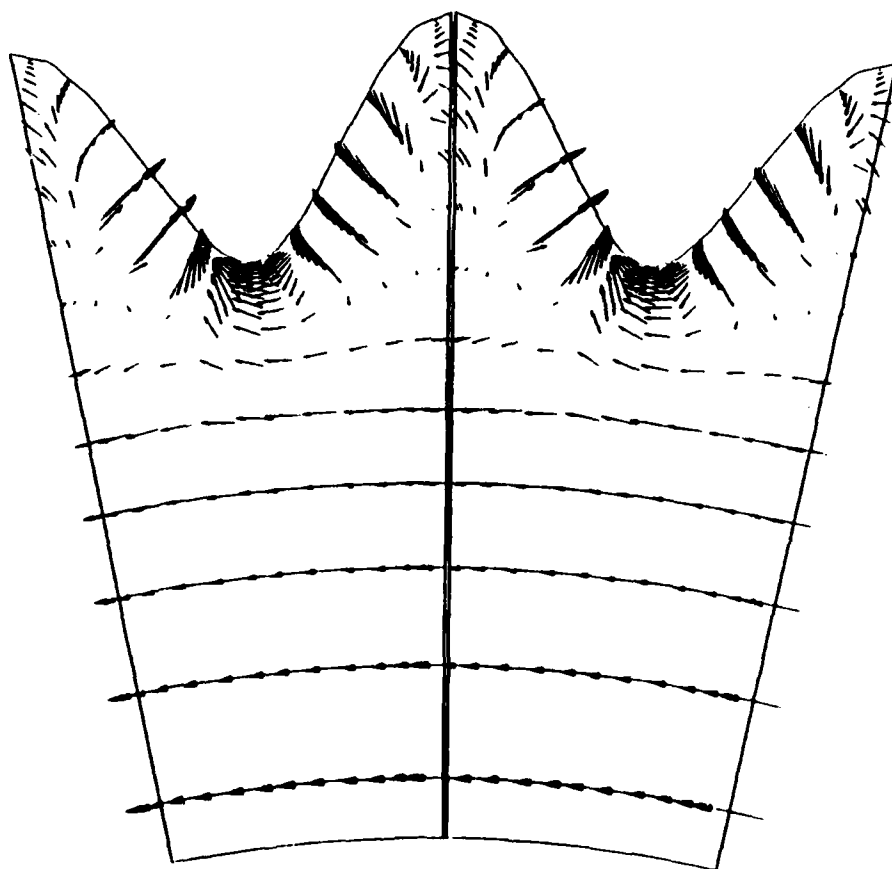




$n=30 ; \varphi=30 ; h=0.6 R_b$

A17833

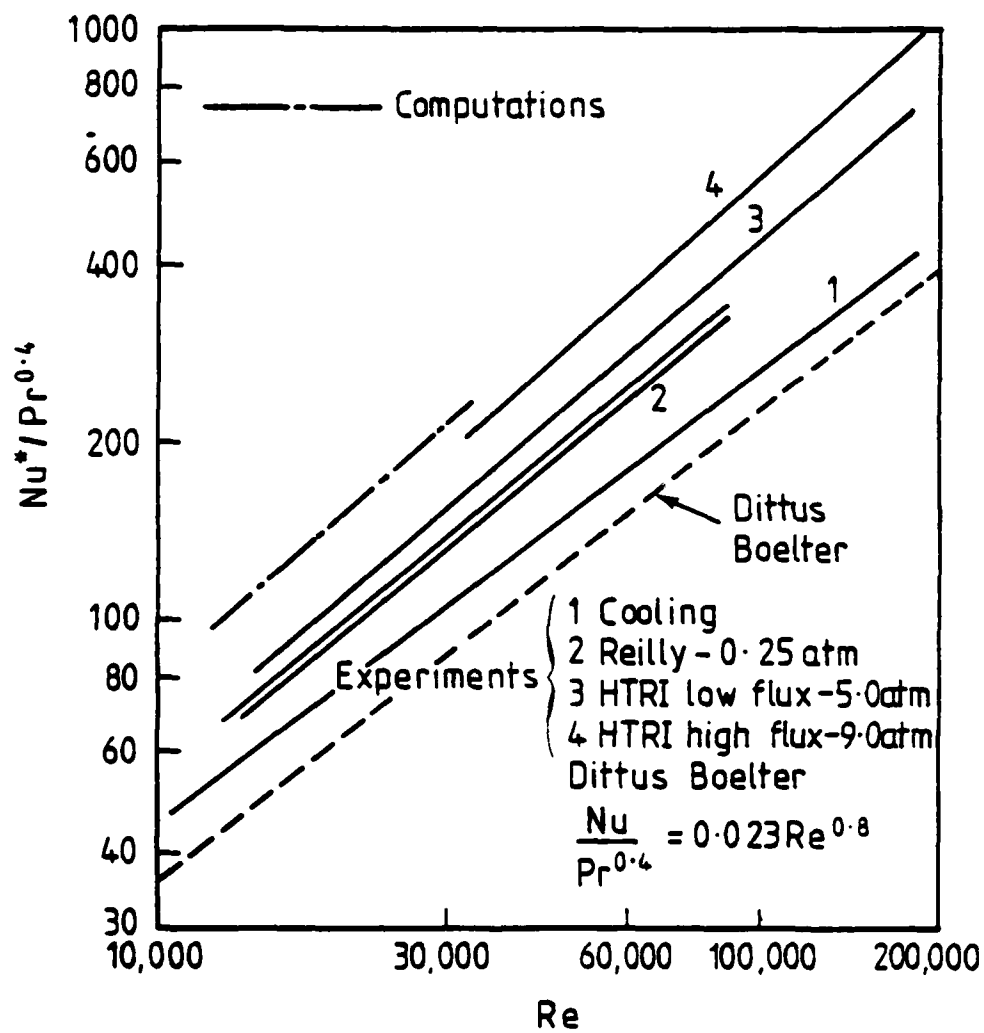
Fig. 11(b).  $\vec{U} + \vec{V} - \vec{\omega R}$



$n=30 ; \varphi=30 ; h=.06R_b$

A17833

Fig. 11(c).  $(V_{\theta} \cos \phi - W \sin) \cos \phi + V_r$



A17833

Fig. 12. Comparison of predicted and experimental data for Nusselt modulus  $n=30$ ,  $\phi=30^\circ$

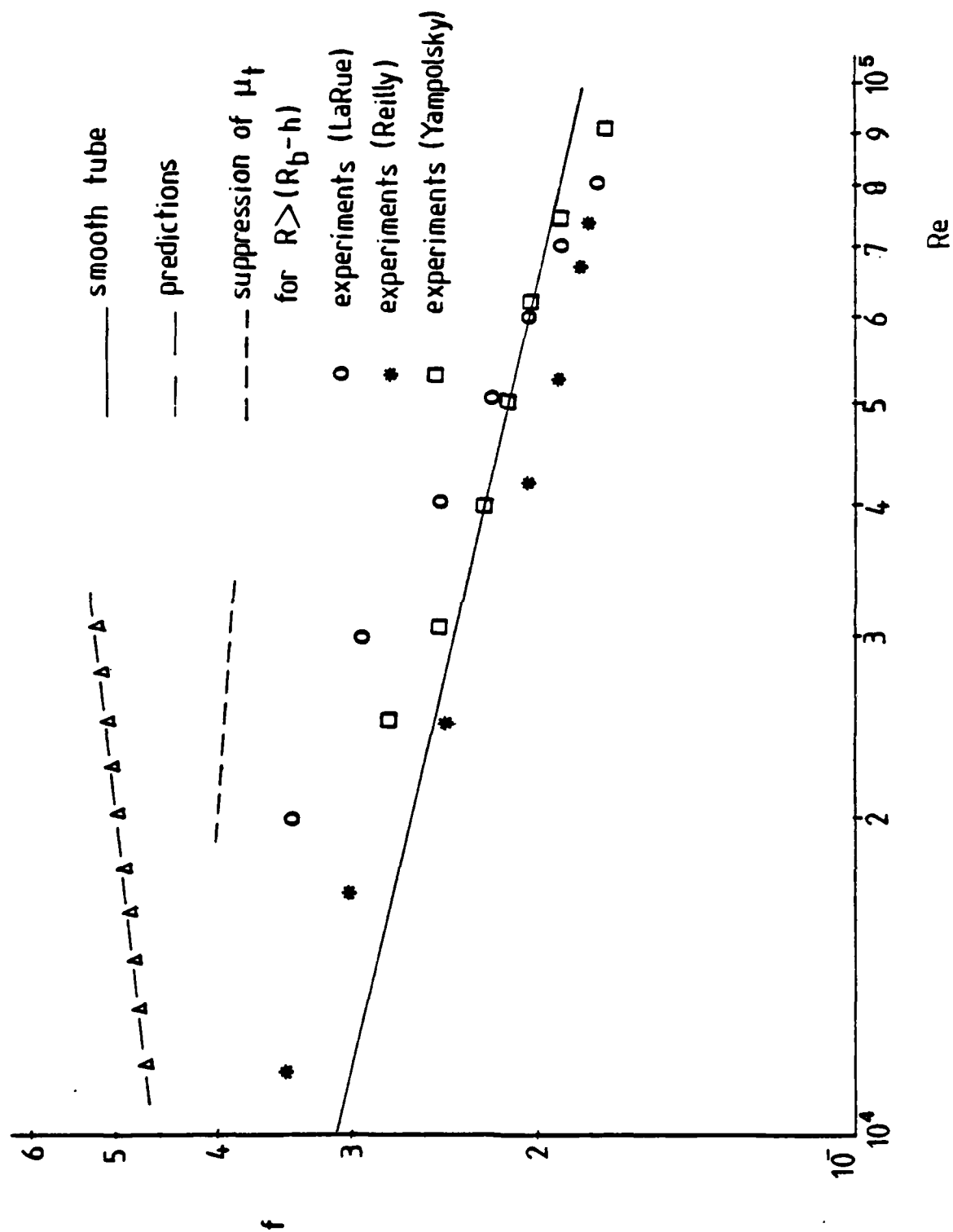


Fig. 13. Comparison of predicted and experimental data  $n=30$ ,  $\phi=30$

A17833

## EXPERIMENTAL PROGRAM

The experimental program was under the direction of J. C. La Rue with the collaboration of J. S. Yampolsky. The work was started at UCSD but was shifted to UCI. The flow visualization studies were part of this work. Two experimental test rigs were constructed, one for water and one for air. Hot wires were used for measurements in air and hot films for the water measurements. Considerable difficulty was encountered with the durability of the hot film probes in the water measurements. The measurements were made in the exit plane from a spirally fluted tube, 8 ft long in the case of water and 12 ft long for air, with the last 4 ft cooled by a water jacket. A two-element x-probe with a resistance temperature cold wire was used for the air flow experiment, which gave both vector velocity and temperature data. A single element probe was used to develop axial velocity data in the water experiment. The details of the work and the data developed are given in the final report from UCI, included in this report, which was the masters thesis of D. S. Babikian. A comparison of some of these results with the results of the theoretical work at UMIST follow.

The comparison of the mean axial velocity relative to the centerline velocity as a function of radius is shown in Fig. 14 for air and Fig. 15 for water as measured in these experiments, predicted in the theoretical calculations, and measured in a smooth tube by other experimenters. The predictions are in close agreement with the experiment, but the velocity gradient is less severe when compared with experiments in plain tubes by the others. This indicates that the flow in a spiral fluted tube has less shear, as would occur at a reduced Reynolds number (laminarization). Probably this is the effect of the rotational nature of the flow.

The turbulent kinetic energy as a function of radius is shown in Fig. 16. The agreement is extremely good when the turbulent transport near the wall in the flutes was suppressed, but the predictions were high without this arbitrary correction.

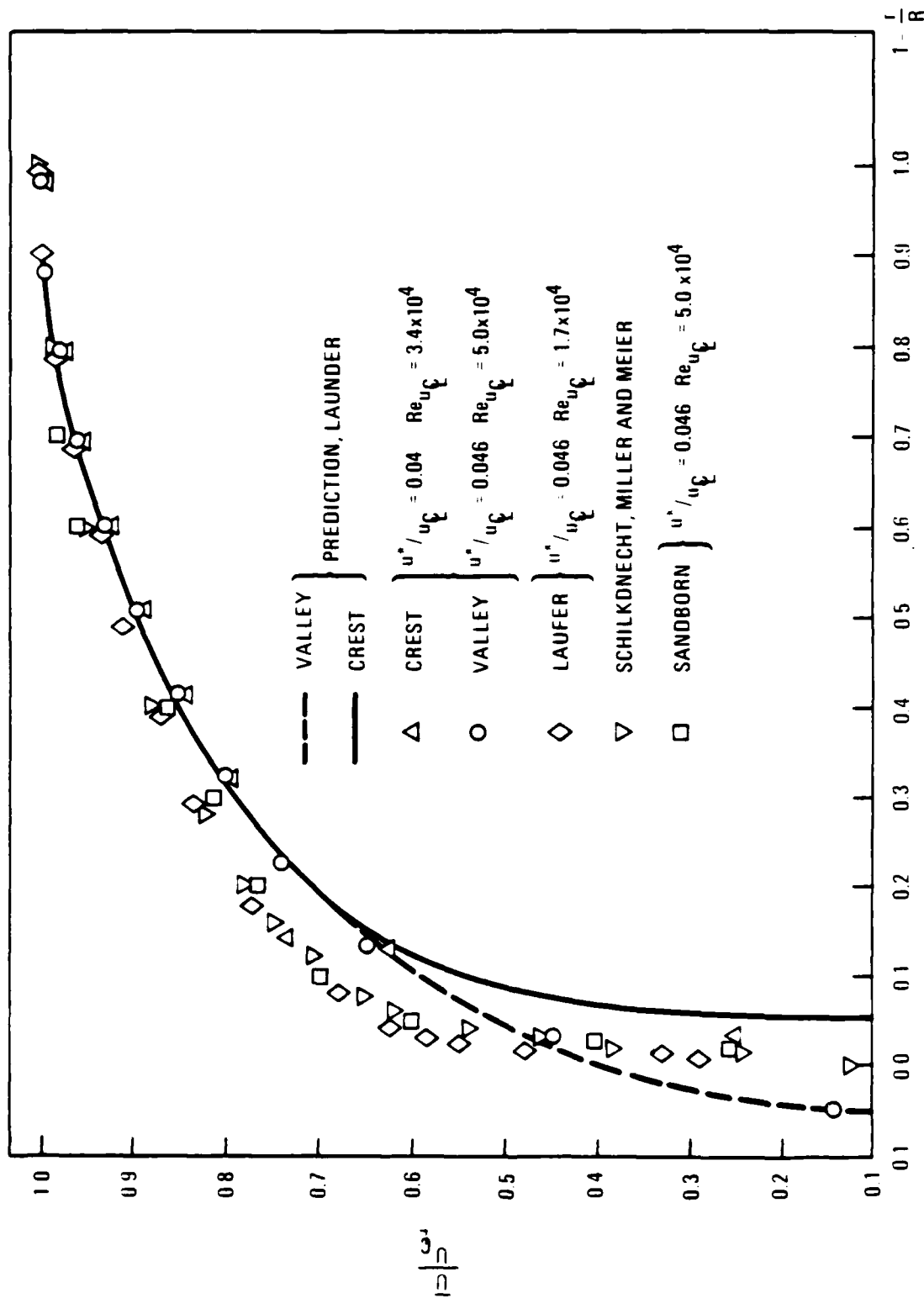


Fig. 14. Mean axial velocity as a function of radius for air

A17833

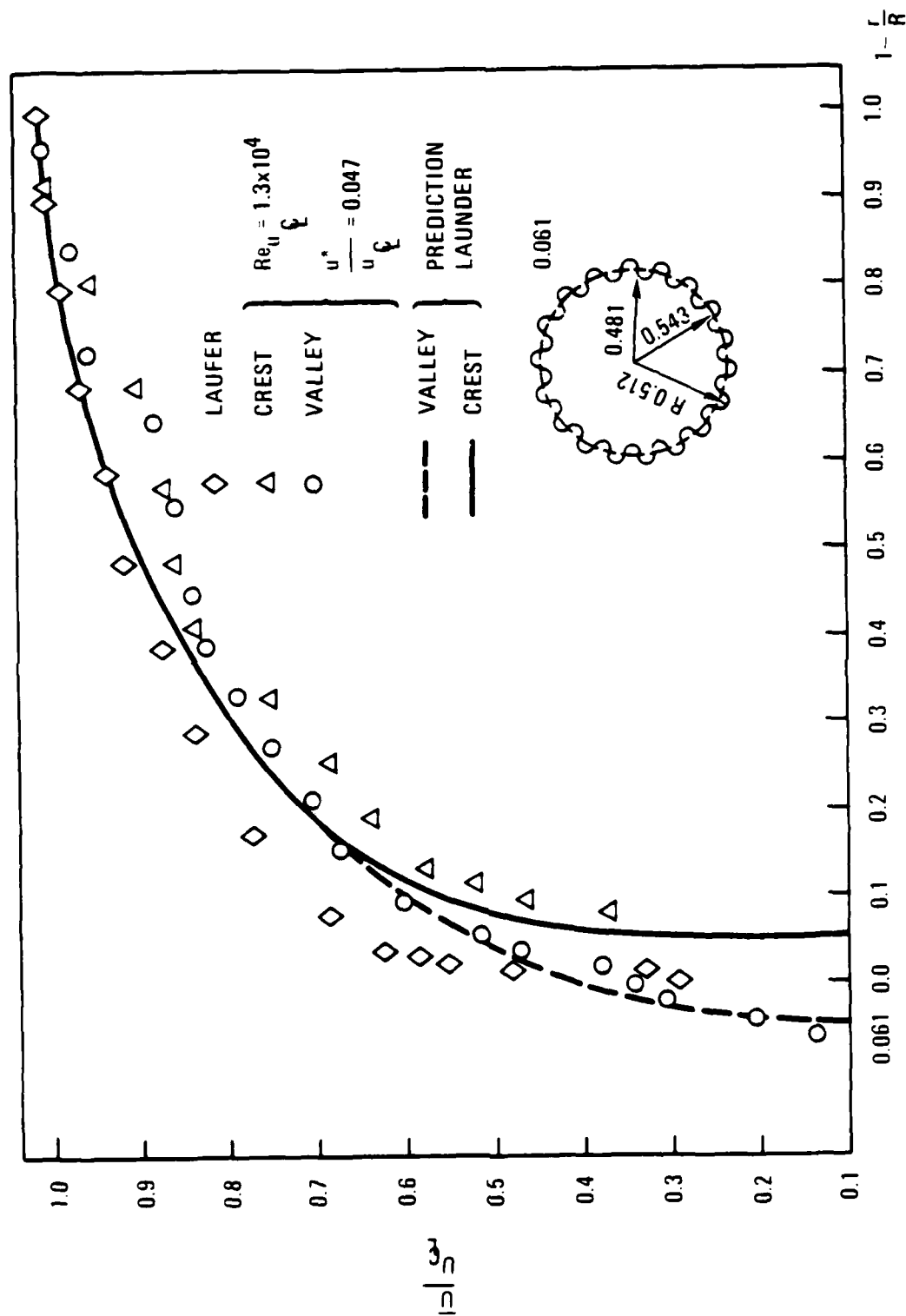
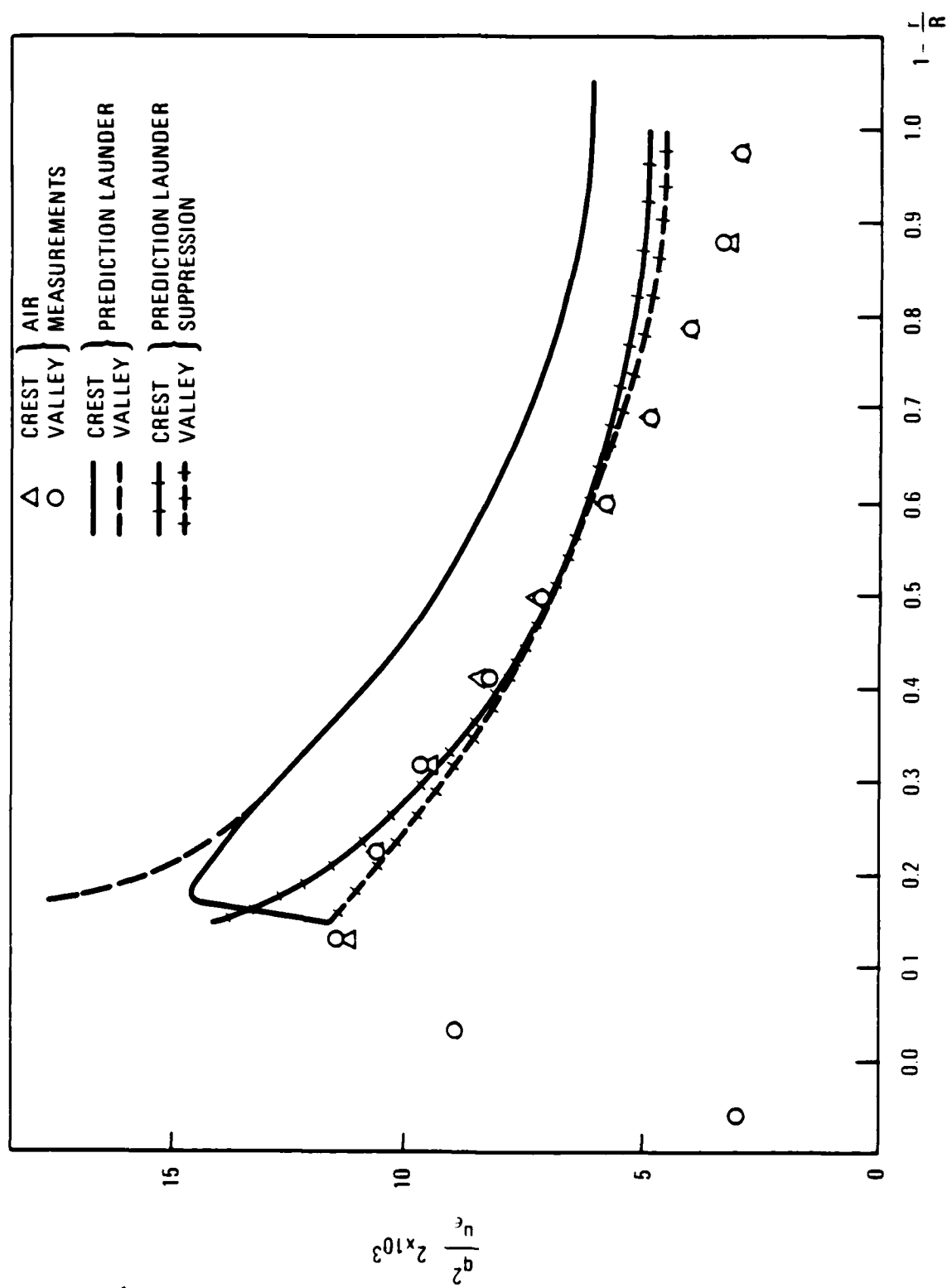


Fig. 15. Mean axial velocity as a function of radius for water

A17833



**A17833**

Fig. 16. Turbulent kinetic energy as a function of radius in air



Figure 17 shows that the prediction of the rotational flow was considerably higher than that measured. Since these measurements were done in air where the heat transfer enhancement of spiral fluted tubes is minimal, caution should be exercised as to any conclusions drawn. However, it does appear that the calculations overpredict the flow rotation. Moreover, the measurements do not show any rotation in the center of the tube, which may indicate that the core flow is not in the solid body rotation that was assumed in the calculation.

## CONCLUSIONS

The physical mechanism that results in the enhancement of heat transfer without an increase of friction appears to be the secondary flow induced in the flutes by their helical curvature. This secondary flow efficiently transports the low momentum fluid at the wall into the flow stream, where turbulent transport is very high relative to the molecular transport at the wall. As the principal resistance to heat transfer is the laminar sublayer at the wall, its transport into the stream, where turbulent processes prevail, without an increase in the rate of shear results in the enhancement of heat transfer without an accompanying increase in friction. The evidence for the secondary flow is inductive on the basis of the physical measurements and flow visualization and direct on the basis of the theoretical calculations. The flow visualization and hot wire measurements show that the flow internal to the flutes in the core is rotating, which implies the presence of angular momentum, the source of which can only be within the flutes. Hence there is rotation in the flutes, a secondary flow. The theoretical calculations directly show and identify this secondary flow. However, these calculations overpredict both the heat transfer enhancement and the friction in the spiral fluted tube. This result may be attributed to the simplicity of the turbulence models used, which was necessitated by the numerical difficulties imposed by the geometry of the spiral fluted tube.

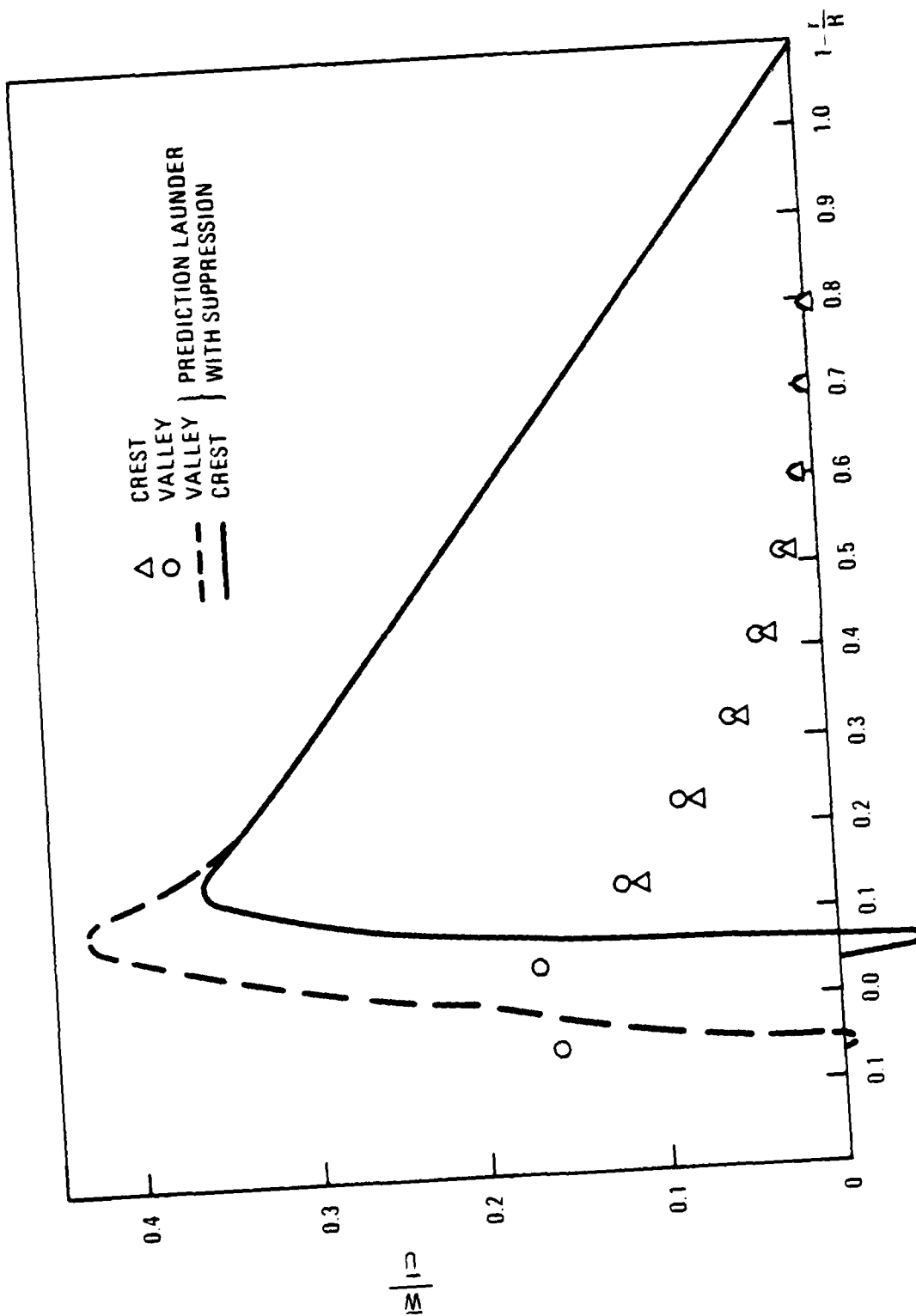


Fig. 17. Azimuthal velocity as a function of radius in air

A17833

#### RECOMMENDATION FOR FURTHER WORK

There are three areas that might be considered fruitful for additional investigation. These are the experimental, theoretical, and overall heat transfer categories. In the experimental area, it would be useful to make detailed vector velocity and pressure drop measurements in the laminar flow regime, as well as in the turbulent regime, for liquids with different Prandtl numbers. This investigation should (1) determine the details of the flow within the flutes (secondary flow), (2) investigate the question of the length required for fully developed flow within the tube or if fully developed flow is not established, and (3) measure the velocity and temperature field with heat transfer. Improvement of the theoretical calculation requires the development of more complex models, particularly in the flute area. This in turn will require considerable improvement in the numerical methodology. In fact, the latter is necessary for any progress in improving the modeling. The last area to investigate is the overall heat transfer coefficient dependency on heat flux to empirically determine the correlation.

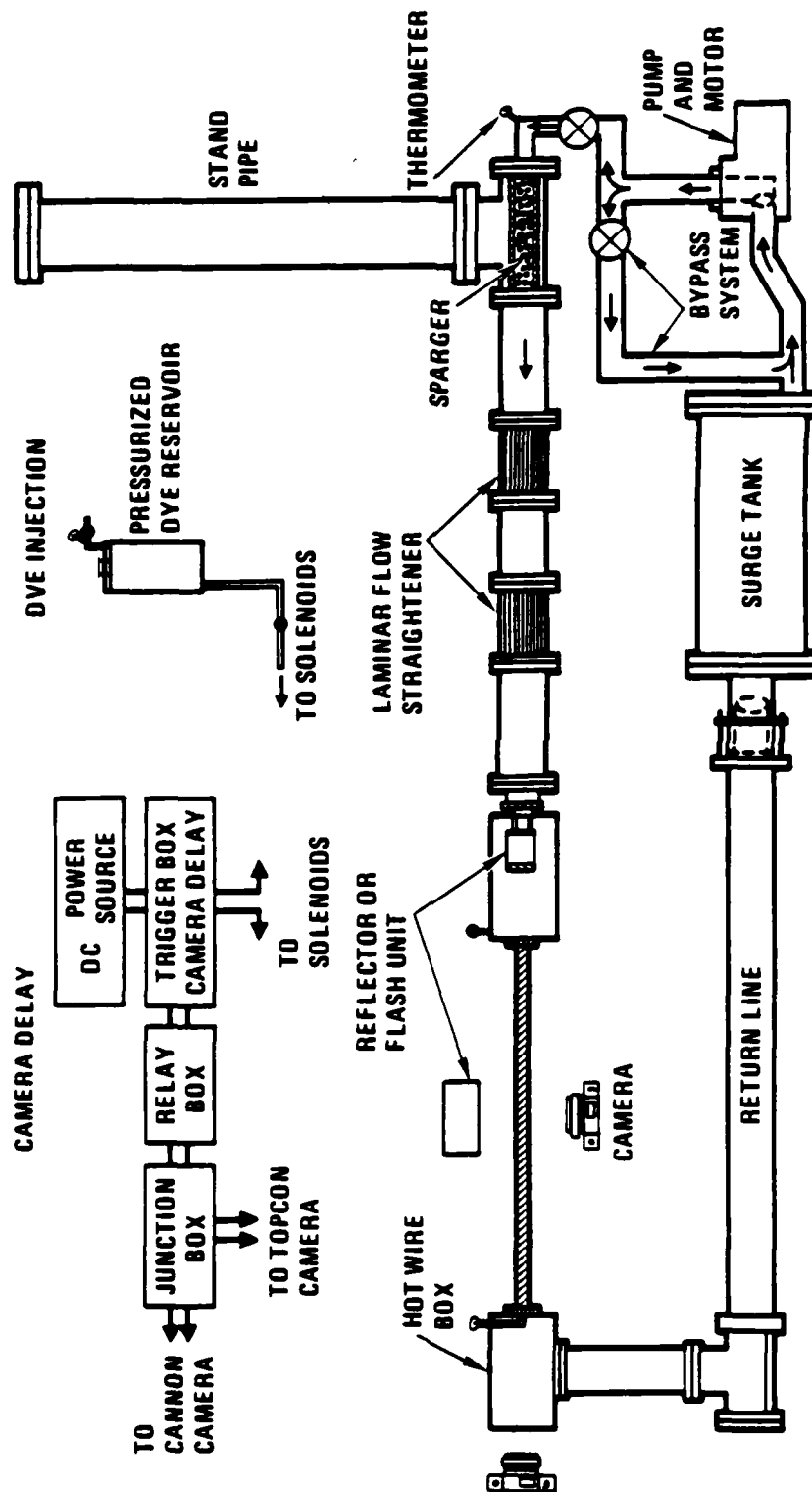
**SECTION A**  
**FLOW VISUALIZATION STUDIES**

## SECTION A FLOW VISUALIZATION STUDIES

The flow visualization studies that were initiated in Ref. 1 were continued until satisfactory high-speed motion pictures were obtained. This required the use of a high-speed xenon flash for individual frame flash synchronization. The equipment was supplied and set up by Professor A. Ellis of UCSD.

The water tunnel shown in Fig. 1 was used for the flow visualization studies with an 8-ft-long transparent test section. The test section is an acrylic casting with a square outer cross section and a spiral fluted internal cross section forming the flow passage. Its construction was described previously (Ref. 1). The photographs were taken from the side of the test section and through a transparent plate at the end of the water tunnel with illumination from the upstream plenum section and transversely across the test section. Colored dye (red and green) was injected at opposite sides of the test section 2 ft upstream from the discharge. The motion pictures, taken at 2000 frames/sec with observation by projection at 24 frames/sec, allowed viewing the flow slowed down by a factor of 80. Study of the movies clearly showed the rotational nature of the flow; a complete revolution was completed in approximately two pitch lengths. However, the resolution was insufficient to reveal details of the flow within the flutes.

Figure 2 is a sequence of frames enlarged from the 16-mm motion picture of the end view. Frame 1 was taken prior to the dye injection. At the right can be seen the injection needle, which also indicates the parallax. The second frame 20 ms later shows the emergence at the right of the red dye, which lags the green dye injected at the left, showing almost 30 deg of rotation. The flow is seen progressively in each of the frames to continue to rotate to frame 8, taken 0.180 sec after dye

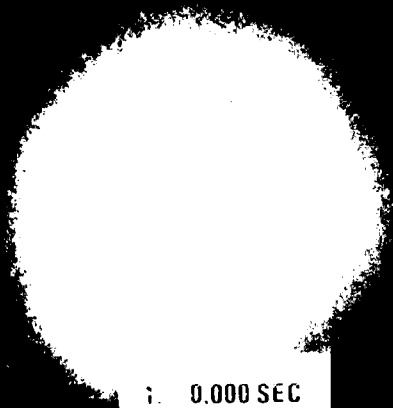


A17833

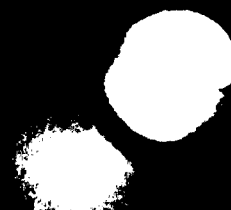
Fig. 1. Water tunnel

injection began. The diffusion of the flow radially inward is seen by the reduction of the diameter of the circle from the upstream light. As the flow progresses downstream toward the camera, the image of the dye is out of focus. As was mentioned earlier, the tube is 8 ft long, the dye was injected 6 ft from the entrance to the tube, and the camera was positioned 5 ft from the injection point. The parallax should be noted in the earlier sequences (frames 1-4). The parallax and the opacity of the dye and the flutes limit the information that can be derived from the flow close to the wall.

Figure 3 is a sequence of frames enlarged from the 16-mm motion pictures taken from the side of the tube with the light from the far side of the test section. The flutes on the near side are visible as a result of the refraction of the light. The red dye is injected on the viewer's side and the green dye 180 deg opposite. Frame 1 was taken at the instant of injection and frame 2 was taken 20 msec later, and the dark spot in the center is the red dye. Both the red and green dye are visible in frame 3, and the rotation can be inferred by the green dye being displaced upward and the red dye downward, which is consistent with the left-handed spiral of the flutes. The green dye marks the far-side flutes, which can be observed as lines orthogonal with the near-side flutes. The progression of the flow around the tube can be seen in the succeeding frames, and in frames six and seven the orthogonal lines on the red dye are observed, indicating that the red dye is now on the far side of the tube. The time when the flow has turned 90 deg can be seen from frame 6 in Fig. 2 to be approximately 60 ms and 180 deg from Fig. 3, frame 7. The Reynolds number was approximately 20,000. These flow visualization photographs and the motion pictures clearly show that the flow in the spiral fluted tube is rotational, close to solid body rotation but at a rate less than the helix angle of the flutes.



1. 0.000 SEC



5. 0.050 SEC



2. 0.020 SEC



6. 0.060 SEC



3. 0.030 SEC



7. 0.080 SEC

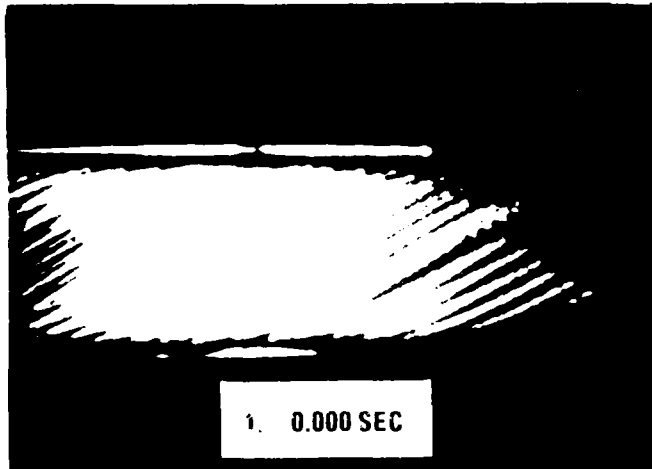


4. 0.040 SEC

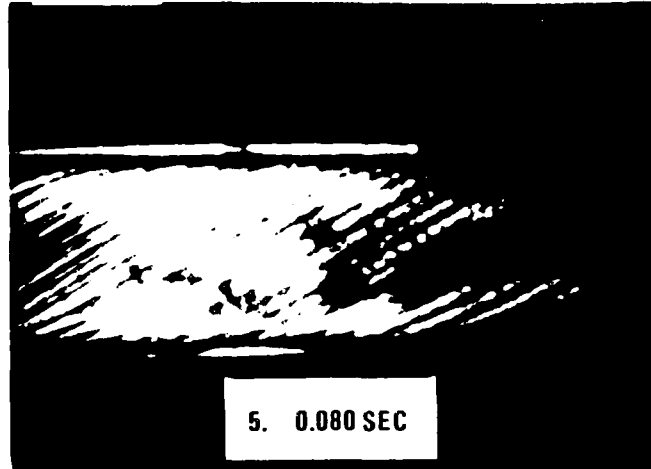


8. 0.180 SEC

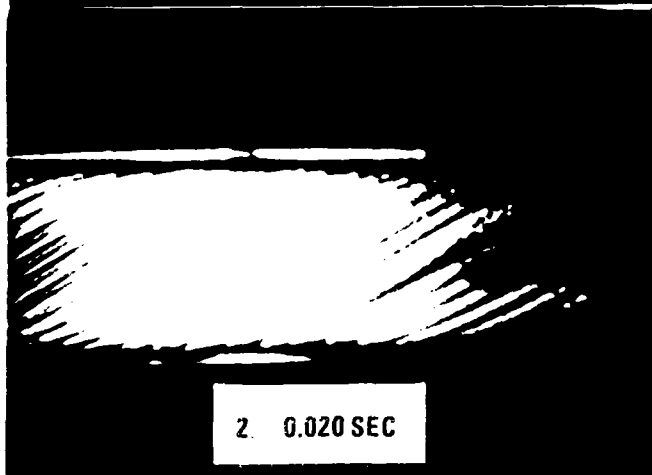




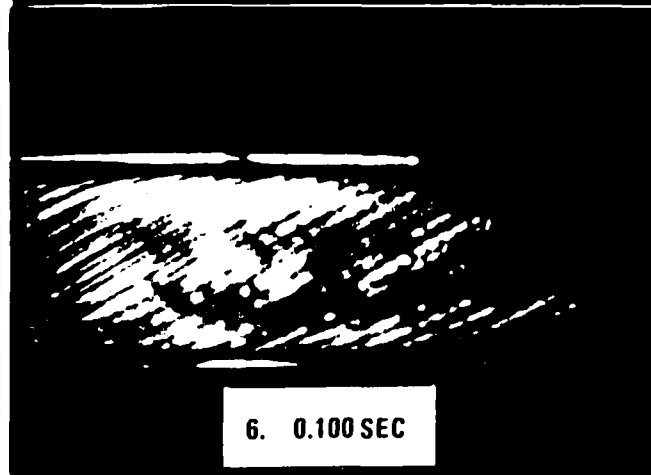
1. 0.000 SEC



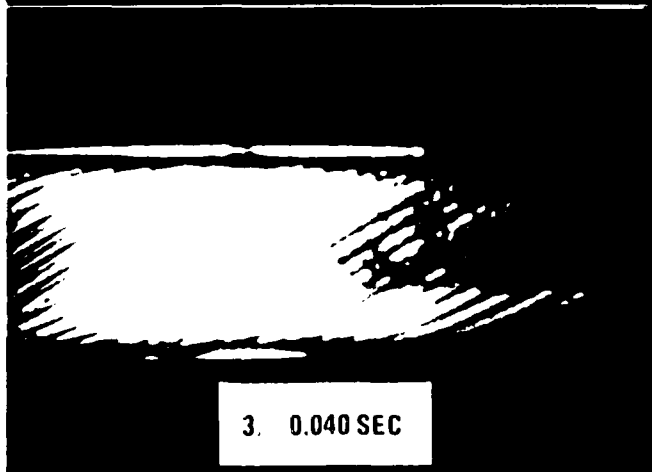
5. 0.080 SEC



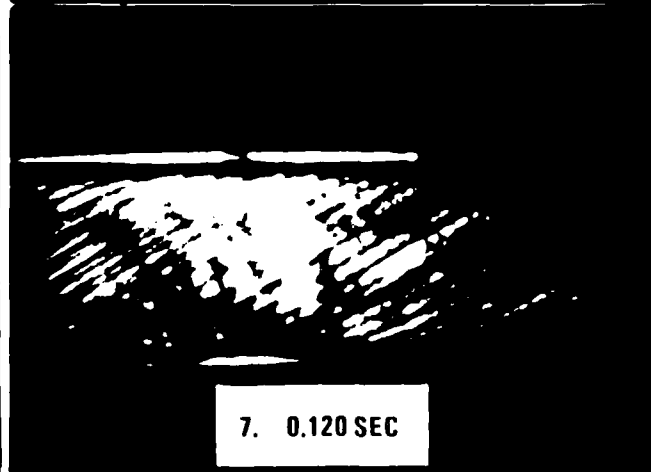
2. 0.020 SEC



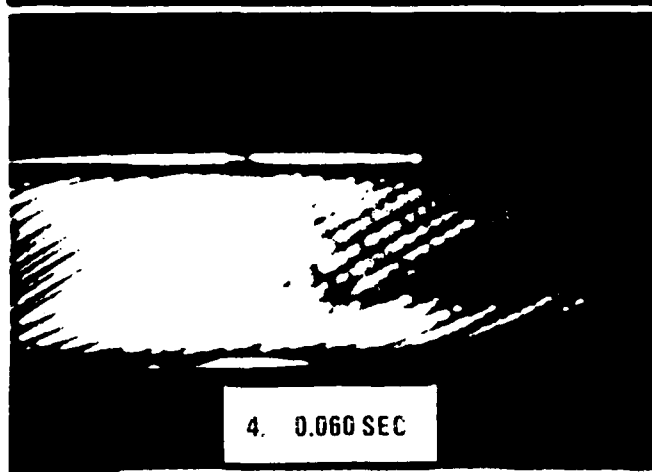
6. 0.100 SEC



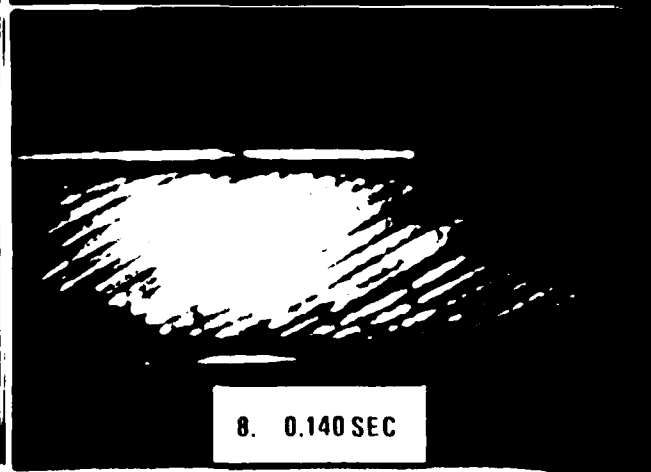
3. 0.040 SEC



7. 0.120 SEC



4. 0.060 SEC



8. 0.140 SEC

Fig. 6. Side view sequence with dye injection

#### REFERENCE

1. LaRue, J. C., P. A. Libby, and J. S. Yampolsky, "Fluid Mechanics and Heat Transfer Spirally Fluted Tubing," Office of Naval Research, GA-A16541, August 1981.

**SECTION B**  
**MEASUREMENTS OF TURBULENT FLOW**  
**IN A SPIRALLY FLUTED TUBE**

**UNIVERSITY OF CALIFORNIA, IRVINE  
FLUID DYNAMICS  
AND  
HEAT TRANSFER LABORATORY**

**MEASUREMENTS OF  
TURBULENT FLOW IN A  
SPIRALLY FLUTED TUBE**

**FINAL REPORT**

**by  
D.S. BABIKIAN and J.C. LARUE**

**PREPARED UNDER  
CONTRACT No. 787113  
for  
GA TECHNOLOGIES  
and  
OFFICE OF NAVAL RESEARCH**

**OCTOBER 1984**

## TABLE OF CONTENTS

LIST OF SYMBOLS.....	i
LIST OF TABLES.....	iv
LIST OF FIGURES.....	v
ABSTRACT.....	xi
1. INTRODUCTION AND BACKGROUND.....	1
2. ARRANGEMENTS AND TECHNIQUES OF THE EXPERIMENT.....	7
2.1 Water Flow Facility.....	7
2.2 Test Section and Coordinate System.....	8
2.3 Water Calibration Facility.....	9
2.4 Water Sensor.....	10
2.5 Signal Processing for Water Data.....	12
2.6 Air Flow Facility.....	12
2.7 Sensors and Calibration for Air Experiment.....	13
2.8 Signal Processing for Air Experiment.....	16
2.9 Experimental Conditions.....	17
3. RESULTS AND DISCUSSION.....	19
3.1 Mean Velocity for Water Flow.....	20
3.2 Turbulence Intensity for Water Flow.....	24
3.3 Mean Axial Velocity for Air Flow.....	25
3.4 Mean Azimuthal Velocity and Flow Angle.....	27
3.5 Turbulence Intensity.....	28
3.6 Correlation Coefficients.....	29
3.7 Temperature Field.....	30

3.8	Mixing Length.....	33
3.9	Eddy Diffusivities and Turbulent Prandtl Number.....	35
4.	SUMMARY AND CONCLUSIONS.....	37
5.	RECOMMENDATIONS.....	39
	ACKNOWLEDGMENTS.....	39a
	REFERENCES.....	40
APPENDICES		
A.	Physical Background for Operation of Hot Film Sensor.....	43
B.	Calibration Technique for Film Temperature Determination.....	46
C.	Computation of Flow Angle and Mean Velocity.....	48
D.	Computation of Wall Friction Velocity.....	52
E.	Computation of Wall Friction Factor by Means of Axial Velocity Gradient at the Wall.....	53
F.	Computation of Mixing Length and Turbulent Prandtl Number....	57
G.	Tabulation of Experimental Data.....	61

# LIST OF SYMBOLS

$A_c$	flow area
$A, B$	calibration constants
$D$	mean diameter of the fluted tube [m]
$d_s$	diameter of the sensor [mm], [ $\mu$ m]
$D_h$	hydraulic diameter of the fluted tube [m]
$E_b$	voltage [V]
$f$	wall friction factor
$h_f$	flute height [mm]
$h$	heat transfer coefficient [ $W/m^2K$ ]
$I$	electrical current
$J$	quantity defined by Eq. 9
$K$	thermal conductivity [ $W/mK$ ]
$k$	tangential cooling coefficient
$L_f$	length of the fluted tube [m]
$L$	length of the sensor [mm]
$\ell_f$	lead of flute $\ell_f = NP_f$ [m]
$\ell$	mixing length [m]
$\ell_o$	mixing length of rectilinear flow [m]
$N$	number of flutes
$n$	exponent
$Nu$	Nusselt number $Nu = hd_s/K$
$P_f$	Pitch of flute $P_f = (2\pi R/N)/\tan \phi_f$ [m]
$P$	pressure [ $N/m^2$ ]
$p$	perimeter of the fluted tube [m]

$q$	heat transfer rate [w]
$R$	mean radius of the fluted tube [m]
$R_H$	operating (hot) resistance of sensor
$R_C$	operating (cold) resistance of sensor
$Re_{U_m}$	Reynolds number based on hydraulic diameter and bulk mean velocity, $Re_{U_m} = \frac{U_o D_h}{\nu}$
$Re_{U_o}$	Reynolds number based on hydraulic diameter and centerline velocity, $Re_{U_m} = \frac{U_m D_h}{\nu}$
$r$	radial distance from centerline [m]
$R_L$	Richardson number defined by Eq. 11
$S$	spacing of flute $S = (2\pi R/N) \cos \phi_f$
$T_{max}$	max temperature of air flow [C°]
$\bar{T}$	mean temperature [C°]
$T_a$	air temperature [C°]
$T_w$	water temperature [C°]
$T_f$	film temperature [C°]
$U_o$	centerline velocity [m/s]
$U_m$	bulk mean axial velocity [m/s]
$\bar{U}, \bar{V}, \bar{W}$	mean velocities components in axial, radial and azimuthal directions [m/s]
$u'v'w'$	turbulence velocity components in axial radial and azimuthal directions [m/s]
$u^*$	wall friction velocity in axial direction [m/s]
$y$	distance from the wall [m]
$\bar{\phi}$	mean flow angle [degrees]
$\phi_f$	angle of flute [degrees]



$\phi'$	root mean flow angle [degrees]
$\tau_c, \tau_v$	shear stress at crest and valley respectively [ $\text{N/m}^2$ ]
$\mu$	dynamic viscosity [ $\text{kg/ms}$ ]
$\nu$	kinematic viscosity [ $\text{m}^2/\text{s}$ ]
$\rho$	density [ $\text{kg/m}^3$ ]
$\beta$	constant in Eq. 12
$\epsilon$	eddy diffusivity for momentum [ $\text{m}^2/\text{s}$ ]
$\epsilon_\theta$	eddy diffusivity for heat [ $\text{m}^2/\text{s}$ ]
$\sigma_t$	turbulent Prandtl number
$\theta$	temperature fluctuation [ $^\circ\text{C}$ ]
$\alpha_c$	temperature coefficient of resistance

## List of Tables

Table 1	Geometrical Parameters of Fluted Tubes
Table 2	Fluid Dynamic Properties
Table 3	Coefficients in Universal Velocity Distribution for Water Flow and Comparison Studies

### List of Figures

- Figure 1 Schematic of water flow Facility
- Figure 2 Side and end view of a portion of the test section
- Figure 3 Sketch of spiral fluted tube
- Figure 4 Water calibration facility
- Figure 5 Block diagram of signal processing electronics
- Figure 6 Schematic of air flow facility
- Figure 7 Mean axial velocity normalized by the centerline velocity for the water flow: crest to centerline, ; valley to centerline, ; smooth tube data of Laufer (1953), ; smooth tube data of Schildknecht, Miller, Meier (1979), ; smooth tube data of Sandborn (1955), ; fluted tube data of Silberman (1980), .
- Figure 8 Mean axial velocity normalized by the friction velocity for the water flow. (Same symbols as Figure 7).
- Figure 9 Power law dependence of normalized mean axial velocity for the water flow: crest to centerline with  $n=3.1$ , ; valley to centerline with  $n=4.1$ , ; smooth tube data of Nikuradse at  $Re = 4 \times 10^3$  with  $n=6.0$  (from Schlichting (1979)), .
- Figure 10 Universal logarithmic velocity distribution for the water flow. (Same symbols as Figure 7).

- Figure 11 Normalized mean velocity distribution as a function of distance from the nearest solid surface for the water flow. (Same symbols as Figure 7).
- Figure 12 Root mean square axial velocity normalized by the mean centerline velocity for the water flow. (Same symbols as Figure 7).
- Figure 13 Root mean square axial velocity normalized by the friction velocity for the water flow. (Same symbols as Figure 7).
- Figure 14 Root mean square axial velocity normalized by the local mean velocity for the water flow. (Same symbols as Figure 7).
- Figure 15 Mean axial velocity normalized by the centerline velocity for the air flow. (Same symbols as Figure 7).
- Figure 16 Mean axial velocity normalized by the friction velocity for the air flow. (Same symbols as Figure 7).
- Figure 17 Power law dependence of normalized mean axial velocity for the air flow: crest to centerline with  $n=4.10$ ; valley to centerline with  $n=4.08$ , ; smooth tube data of Nikuradse at  $Re = 2.3 \times 10^4$  with  $n=6.6$  (from Schlicking (1979)). (Same symbols as Figure 9).
- Figure 18 Universal logarithmic velocity distribution for the air flow. (Same symbols as Figure 7).
- Figure 19 Normalized mean velocity distribution as a function of distance from the nearest solid surface for the air flow. (Same symbols as Figure 7).

Figure 20 Mean azimuthal velocity normalized by the centerline velocity for the air flow: crest to centerline, ; valley to centerline, .

Figure 21 Mean azimuthal velocity normalized by the friction velocity for the air flow. (Same symbols as Figure 20).

Figure 22 Mean flow angle normalized by the flute angle: crest data, ; valley data, ; fluted tube data of Silberman (1980): crest data at top of pipe, ; valley data at top of pipe, ; crest data at bottom of pipe, ; valley data at bottom of pipe, .

Figure 23 Relative rotation rate: crest data, ; valley data, .

Figure 24 Root mean square axial velocity normalized by the mean centerline velocity for the air flow. (Same symbols as Figure 7).

Figure 25 Root mean square radial velocity normalized by the mean centerline velocity for the air flow. (Same symbols as Figure 7).

Figure 26 Root mean square azimuthal velocity normalized by the mean centerline velocity for the air flow. (Same symbols as Figure 7).

Figure 27 Root mean square axial velocity normalized by the local mean velocity for the air flow. (Same symbols as Figure 7).

- Figure 28 Root mean square radial velocity normalized by the local mean velocity for the air flow. (Same symbols as Figure 7).
- Figure 29 Root mean square azimuthal velocity normalized by the local mean velocity for the air flow. (Same symbols as Figure 7).
- Figure 30 Turbulent kinetic energy normalized by the friction velocity for the air flow. (Same symbols as Figure 7).
- Figure 31 Correlation coefficients for the air flow. Top set of data corresponds to  $R_{uv}$  while the lower set of data corresponds to  $R_{uw}$ . (Same symbols as Figure 7 but with the addition of Bremhorst and Bullock, (1973), ).
- Figure 32 Correlation of axial and radial velocity normalized by the friction velocity squared for the air flow. (Same symbols as Figure 7).
- Figure 33 Correlation of axial and azimuthal velocity normalized by the friction velocity squared for the air flow. (Same symbols as Figure 7).
- Figure 34 Correlation of axial and radial velocity normalized by the turbulent kinetic energy for the air flow. (Same symbols as Figure 7).
- Figure 35 Mean temperature profile for the air flow. Valley, top half of tube, ; valley, lower half of tube, ; crest, top half of tube, ; crest, lower half of tube, ; Bremhorst and Bullock, (1973), top half of tube, ; Bremhorst and Bullock, (1973), lower half of tube, .

- Figure 36 Root mean square temperature normalized by the difference between mean centerline and wall temperature for the air flow. (Same symbols as Figure 36).
- Figure 37 Correlation coefficients for velocity and temperature for the air flow:  $R_{u\theta}$ , crest, ;  $R_{u\theta}$ , valley, ;  
 $R_{v\theta}$ , crest, ;  $R_{v\theta}$ , valley, ;  $R_{w\theta}$ , crest ;  
 $R_{w\theta}$ , valley, ;  $R_{v\theta}$ , Bremhorst and Bullock (1973), .
- Figure 38 Correlation of radial velocity and temperature normalized by the difference between mean centerline and wall temperatures for the air flow. (Same symbols as Figure 36).
- Figure 39 Mean velocity gradient for the air flow. (Same symbols as Figure 7).
- Figure 40 Mean temperature gradient for the air flow. (Same symbols as Figure 7).
- Figure 41 Mixing length for the air flow. (Same symbols as Figure 7).
- Figure 42 Richardson number for the air flow. (Same symbols as Figure 7).
- Figure 43 "Constant",  $\beta$ , required for mixing length correction. (Same symbols as Figure 7).
- Figure 44 Eddy diffusivity for momentum for the air flow. (Same symbols as Figure 7).
- Figure 45 Eddy diffusivity for heat for the air flow. (Same symbols as Figure 7).

Figure 46 Turbulent Prandtl number for the air flow. (Same symbols as Figure 7).

Figure D1 Spirally fluted tube friction factor comparisons.



## Turbulent Flow in a Spirally Fluted Tube

### ABSTRACT

Tubes with spiral flutes at the wall have been shown to lead to augmentation of the heat transfer rate relative to smooth tubes at the same Reynolds numbers. Clearly it is of both fundamental and applied interest to determine the characteristics of the flow field that lead to the augmentation of the heat transfer rate. The statistical characteristics of the velocity field of air and water flows and in addition the characteristics of the temperature field in the air flow in a spiral fluted tube are determined. These results show for the air flow that the radial transport of heat is increased throughout the flow field by about 30% relative to the corresponding quantity in a smooth tube. This increase in the radial component of the heat flux is not accompanied by an increase in the turbulence level. For example, the intensity of the axial velocity fluctuations for both the water and air flows in the fluted tube are nearly the same as that in the smooth tube. Near the wall, for both the water and air flows, the mean velocity and its gradient are reduced relative to the corresponding smooth tube values. The reduced velocity gradient is consistent with a reduced shear stress. This reduction in shear stress is offset by the increased surface area of the spiral fluted

tube so that the pressure gradient and friction factor are nearly equal to the corresponding smooth tube values. For the water flow, measurements at the wall of the intensity of the axial velocity indicate the presence of a secondary flow with a characteristic length corresponding to the flute spacing. This secondary flow increases the transfer of fluid from the wall and thus is in large part responsible for the augmentation in heat transfer.

## 1. INTRODUCTION

A fundamental goal of heat exchanger design is the reduction in size of the heat exchanger so as to accomplish a desired amount of energy transfer with a minimum capital cost in as small volume as possible. One method used to meet this goal (cf. Kays and London 1964) has been to increase both the turbulence level and the area for heat transfer per unit length by the addition of fins. Associated with this method is an increase in the power used to pump the fluid through the heat exchanger due to increased fluid friction and pressure drop.

Tubes with swirling flows produced by tangential injection, twisted tape, wall slots and spiral flutes have also been found to lead to increased heat transfer rates (cf. Carnavos, (1974), and Webb, (1981), for recent comprehensive reviews). For most of the tubes with swirling flows, there is also an increase in pressure drop. However, one tube developed by Yampolsky (1979) which uses a relatively large number of spiral flutes (30) on the surface of the tube to produce the swirling motion has been shown by Reilly (1978) and Yampolsky (1979) to lead to an augmentation of the heat transfer ratio by a factor of two or three without an increase in the pressure drop (cf. Yampolsky and Pavlics (1983)). It is the goal of the research reported herein to determine experimentally the statistical properties of air and water flows in the spiral fluted tube developed by Yampolsky (1979) so as to gain a physical insight into the properties of the flow field that lead to the augmentation in heat transfer with no increase in

pressure drop relative to that in a smooth tube at the same Reynolds number we next review some related studies of the swirling flows.

Since there are extensive reviews of heat transfer in swirling flows presented by Carnavos (1974) and Webb (1981), a brief review of only the previous studies that are directly related to the present study is discussed. Swirling flows in tubes for the augmentation of heat transfer rates have been produced using a number of different generating mechanisms. For example, Hay and West (1975) produce a swirling or spiral motion by tangentially injecting heated air into a tube through a single slot at an angle of 90, 60, or 30°. A disadvantage associated with tangential injection is that the tangential velocity decays with distance. Iqumentsev and Nuzmееv (1978) overcome this difficulty through the use of a spirally coiled wire placed at the wall of a smooth tube. Palen, Chan, and Taborek (1971) present one among a number of studies of heat transfer in swirling flows produced by flutes on the tube wall. In that particular study, there are only four flutes equally spaced around the circumference of a tube which has a mean radius of 1.23 cm. The relative flute height is about 0.4 of the mean radius while the pitch to diameter ratio is about 2.25.

Carnavos also reports heat transfer studies of Blumenkrantz and Taborek (1970) who studied the heat transfer augmentation associated with multi-fluted tubes similar to that used in the studies of Palen, Chan and Taborek and reports that the maximum heat transfer augmentation (along with the highest pressure drop relative to a smooth tube at the same flow conditions) occurs for a tube with three

flutes which each have a height to radius ratio of 0.2 and a lead to diameter ratio of 4.25.

In all the studies cited above, heat transfer rates are increased by factors of at least 2 or 3 relative to the heat transfer rates in smooth tubes at corresponding Reynolds numbers. However, concomitant with the increased heat transfer rates obtained in those studies is an increase in the pressure drop and friction factor. This increase in heat transfer rate and pressure drop in spiral-fluted tubes that are reviewed by Carnavos lead him to speculate that the increase in heat transfer rate and pressure drop must be due to an increase in the turbulence level.

The increase in the pressure drop for the multi-fluted tube studies reviewed by Carnavos is perplexing since a reduction in pressure drop has been found in tube flows with swirl where the swirling motion is produced by rotation of the tube about its longitudinal axis (cf. White, (1964), Cannon and Kays (1969), Murakami et al. (1970) and Singh et al. (1980)). In addition Silberman (1970), (1972) and (1980), reports that swirling flows produced by means of spiral flutes on the tube surface also show a reduction in pressure drop relative to that corresponding to the flow in a smooth tube at the same Reynolds number. The flute spacing for the tube used by Silberman is much less than that for the tubes studied by Palen, Chan, and Taborek (1974)

More recently a tube with spiral flutes on the inner and outer surface has been developed by Yampolsky (1979) which leads to an augmentation in the heat transfer rate of a factor of two or three without a concomitant increase in the pressure drop (cf. Reilley (1978), Yampolsky (1979) and Yampolsky and Pavlics (1983). One possible reason for the difference in the relative pressure drop is related to the number and geometry of the flutes which differ significantly from the type discussed by Palen, Chan and Taborek (1971) and Carnavos (1974). For example, Yampolsky's tube has 30 flutes compared to the 3 or 4 of the aforementioned studies with a lead to diameter ratio of 5.43 compared to 2.25. In contrast to the speculation of Carnavos, it would seem that the increase in heat transfer rates in the Yampolsky tube may not be due to increased levels of turbulence but may be due to the production of a secondary flow near the tube wall.

It is interesting to note that no detailed studies of the flow field have been performed for flows in spiral multi-fluted tubes which exhibit increased heat transfer rates. This dearth of data provided the motivation for the present study which has as its principal focus the determination of the statistical properties of the flow of water and air in the Yampolsky tube. The goal of the work is to gain a better understanding of the properties of the flow field that lead to the augmentation of heat transfer rate without an increase in pressure drop and friction factor. For the water flow which is isothermal, results are based on single hot film measurements of the time resolved axial velocity. For the air flow, which is heated, measurements are

based on the simultaneous measurement of the time resolved axial and azimuthal velocity and temperature and the simultaneous time resolved axial and radial velocity and temperature.

For the water flow, statistical quantities such as the mean and intensity of the axial velocity are presented as a function of distance from both the valley and crest of the spiral flutes for a Reynolds number of 8720 based on the mean velocity and hydraulic diameter. For the air flow, the mean and intensities of the axial, azimuthal and radial velocities, the Reynolds stress and the axial, azimuthal and radial heat fluxes are presented for a Reynolds number of  $2.64 \times 10^4$  based on the mean velocity and the hydraulic diameter. Again measurements are made as a function of distance from the flute valley and flute crest.

Statistical quantities of interest obtained in the spiral fluted tube are compared to corresponding quantities obtained in turbulent, non-swirling flows in the smooth tube studies of Laufer (1953), Sandborn (1955), and Schildknecht et al. (1979). Comparisons are also made to the corresponding statistical properties of the flow field reported by Silberman (1980) in a spiral multi-fluted tube. The tube studied by Silberman is not used in processes involving heat transfer but is used in the transport of sand-water slurries and thus the heat transfer properties associated with the tube are not known.

The flute geometry of the Silberman tube is similar to the Yampolsky tube only in that the number of flutes is relatively large (10 as compared to 30) and that the pitch to diameter ratio is identical and equal to 0.181. Other geometrical properties as

indicated in Table 1 are significantly different and thus differences in the results are expected though qualitative features of the flow are expected to be similar. We next consider the details of the experiment and of the flows.



## 2. ARRANGEMENTS AND TECHNIQUES OF THE EXPERIMENT

Turbulence measurements are obtained in both a water and an air flow facility. In this section we describe the two flow facilities, the test section, the associated calibration facilities, the sensors, instrumentation, and the data processing and analysis facilities.

### 2.1 Water Flow Facility

The water flow facility is a closed system and is operated in an isothermal mode. The facility is shown schematically in Figure 1 and consists basically of a 1 HP Gould pump with a plastic impeller, a filter to remove particles in the flow that might lead to surface contamination of the sensor, a damping tank, two sets of honeycomb flow straighteners, the test section, probe traverse and holder, a receiving tank and a return line. The flow rate was varied by means of the by-pass and the main flow valves.

In order to obtain a reasonably stable calibration of the hot film sensor used to measure the time resolved velocity, the water in the water flow facility is first passed through a mixed bed deionizer to reduce the quantity of dissolved minerals in the water to less than 10 ppm of total dissolved solids. A pH of seven for the water is generally maintained for all the experiments to prevent rapid dissolution of the quartz coating on the sensor.

The velocity and mean temperature sensors are mounted on a manual probe traverse that controls the radial motion of the sensor. The traverse has a resolution of  $\pm 0.125$  mm and consists of a scale and vernier which are mounted on the outside of the receiving tank. A round support shaft 1.2 cm in diameter, attached to a slider on the

fixed part of the traverse which also holds the vernier passes through a water tight fitting into the receiving tank. A small air foil shaped probe holder which holds the temperature and velocity sensors is attached to the end of the probe support shaft on the inside of the receiving tank. The velocity and temperature sensors are mounted on probe shafts of respectively 0.5 and 0.625 cm diameter, which are held horizontally in the airfoil shaped probe holder. The temperature and velocity sensors are both placed about 20 cm upstream of the support shaft and 0.5 mm downstream of the exit plane of the test section. Radial profiles starting from either the valley or crest of the spiral fluted tube are accomplished by rotating the fluted tube which formed the test section so that either a flute valley or a flute crest is aligned with the radius along which the probe is traversed.

## 2.2 Test Section and Coordinate System

A portion of the 2.4 m long test section showing end and side views of the spiral multi-fluted aluminum tube is shown in Figure 2. As indicated on Figure 3, the mean radius of the tube,  $R$ , is measured from the centerline to a position midway between the crest and valley. The radial coordinate,  $r$  has its origin at the centerline. The flute height is 1.5 mm and the flute spacing is 2.53 mm. There are 30 flutes equally spaced around the tube circumference each at an angle of  $30^\circ$  relative to the tube axis which corresponds to a lead to diameter ratio,  $\ell_f/D$ , of 5.43 where the lead,  $\ell_f$ , is the distance in the downstream direction that corresponds to one complete rotation of a flute. Other details of the fluted tube used in the present study are presented in Table 1. Also, since comparisons are made to the

corresponding results of Silberman (1980) the geometrical properties of the tube used by Silberman are also presented.

The inlet to the test section consists of an abrupt contraction while the exit of the test section, which extends 7.5 cm into the receiving tank, consists of an abrupt expansion.

Table 1  
Geometrical Parameters of Fluted Tubes

Parameter	Yampolsky (water flow)	Yampolsky (air flow)	Silberman Tube
mean diameter (cm)	2.80	2.80	30.48
hydraulic diameter (cm)	1.59	1.59	25.67
number of flutes	30	30	10
flow area (cm <sup>2</sup> )	5.52	5.52	---
flute height/radius	0.120	0.120	0.073
flute spacing/radius	0.181	0.181	0.314
pitch/diameter	0.181	0.181	0.181
lead/diameter	5.43	5.43	01.81
helix angle	30°	30°	60°
length/diameter	85.71	142.86	63
length/hydraulic diameter	151	251.57	74.80
length/lead	15.78	26.32	34.81

### 2.3 Water Calibration Facility

Figure 4 shows the calibration tunnel which consists basically of a pump, a filter to remove solids, a flow rate adjusting valve, a by-

pass valve, a honeycomb flow straightener, a reservoir tank, a constant head tank, a receiving tank and an axisymmetric nozzle with a smooth transition from an upstream diameter of 7.6 cm to a downstream diameter of 2.54 cm. The velocity at the exit plane of the nozzle is laminar and is controlled by means of the by-pass and flow-rate adjusting valves through the range of 0.2 to 1.7 m/sec. The velocity at the exit plane of the nozzle is obtained by means of a water manometer and two pressure taps - one mounted at the nozzle throat and the other mounted in the plenum. The water used in the calibration facility is deionized water with a PH of around seven.

#### 2.4 Water Sensors

The time resolved velocity is measured by means of a TSI 1210-10AW hot film sensor and associated constant temperature anemometer. The sensor which has a diameter of 0.025 mm, a length of 0.254 mm and is operated at an overheat ratio of 1.055, is calibrated in the range of velocity from 0.24 to 1.50 m/sec and over a temperature range of about 22 to 26°C. The calibration is performed in the laminar jet of the water calibration facility both before and after data collection. A modified form of the Kings law correlation is found to describe the relationship between bridge voltage squared and velocity and temperature where the modification is to the exponent,  $n$ , of the velocity term as given in the following equation (see Appendix A for more details of the calibration procedure):

$$\frac{E_b^2}{T_f - T_w} = A + BU^n \quad (1)$$

where  $E_b$  is the bridge voltage

$T_f$  is the temperature of the hot film

$T_w$  is the temperature of the water

$U$  is the velocity

$n$  is the exponent

and  $A$  and  $B$  are the calibration constants which are determined by the method of least squares.

Values of the exponent,  $n$ , in Eqn. 1 for hot film sensors are found to be in the range of 0.35 to 0.55 (cf., Jorgenson (1970), Andreas (1978), Gourdon et al. (1980), Glovonangeli (1980), and Adrian et al. (1984)). For the work reported herein, a value for the exponent of 0.38 is found to minimize the standard deviation of the difference between the measured velocity and that calculated using Eqn. 1.

Low overheats and hence low values of  $(T_f - T_w)$  in Eqn. 1 are necessary to prevent the formation of bubbles on the surface of the sensor. This small temperature difference leads to relatively large sensitivity changes in the mean water temperature which naturally arise from frictional effects during the course of data collection. For example, for the present experiment a change in the water temperature of about  $1.2^\circ\text{C/hr}$  is not uncommon. At a true velocity of 70 cm/sec this temperature change, if not accounted for, would lead to an error of about 15% in the mean velocity. Thus, a temperature calibration is required. (Details of the temperature calibration procedure can be found in Appendix B). Since the temperature variation of the water during data collection at a particular position

0.01°C, a constant correction for the mean temperature is applied to all the data collected at a particular position. The mean temperature is determined by means of a MINCO platinum resistance thermometer which is mounted near the hot film sensor.

## 2.5 Signal Processing for Water Data

A block diagram of the signal-processing electronics is shown in Figure 5. The voltage from the constant temperature anemometer is passed through a buck and gain amplifier where the mean voltage is subtracted and the fluctuations are amplified so as to correspond to the dynamic range of the analog FM instrumentation tape recorder. The signal corresponding to the time resolved velocity is recorded at a tape speed of 19.05 cm/sec which corresponds to a frequency response of 2.5 KHz. After data collection is completed, the signals are played back at a tape speed of 19.05 cm/sec, low passed filtered at 2 KHz, digitized at a sample rate of 4096 samples/sec using a Tustin analog to digital converter with 14 bit resolution and then stored on digital magnetic tape for later processing. The data are analyzed by means of a LSI 11/23 and Sky MNK array processor using standard software.

## 2.6 Air Flow Facility

The air flow test facility is shown in Figure 6. Filtered laboratory air is used as the test fluid and supplied at a steady flow rate by means of a centrifugal air compressor which is equipped with a by-pass valve. The air, which is heated to about 30°C above ambient by the air compressor, next passes through a set of flow straighteners located in a 5.1 cm diameter pipe that is just upstream of the 4 m

long test section. The test section used in the air experiments is from the same batch of tubing as used in the water experiment and a description of the geometrical properties of the tube is presented in Table 1. The downstream 2.4 m of the test section is surrounded by a second tube of 7 cm diameter through which water flows so as to provide a constant wall temperature of approximately 38.4°C along the downstream 2.4 m of the test section. The velocity and temperature sensors are placed 0.5 mm downstream of the exit plane of the test section and are mounted on a traverse which has a position resolution of  $\pm 0.254$  mm.

## 2.7 Sensors and Calibration for Air Experiment

The probe used for the air measurements consists of three sensors - two hot wires which form an "x" configuration and one cold wire which is mounted normal to the plane of the "x" array and placed 0.6 mm upstream of the center of "x" array. This configuration, with a suitable calibration, permits the simultaneous time resolved measurement of the temperature and the axial velocity and, depending on the orientation of the "x" array (either vertical or horizontal) in addition, either the radial or the azimuthal velocity respectively.

The two hot wires which are operated in the constant temperature mode and which are spaced 0.5 mm apart consist of platinum plated tungsten wire, 1.25 mm in length and 3.8  $\mu$  in diameter. The cold wire consists of a 1.0 mm long 0.625  $\mu$  diameter platinum wire which is operated in an A.C. Wheatstone bridge at a current of 180  $\mu$ A. Thus, the probe has a spatial resolution of about 1.25 mm. Based on the work of LaRue et al. (1981), at the centerline velocity of about 40

m/s, the cold wire should have a frequency response of around 8 KHz and the velocity sensitivity should be negligible. The frequency response of the hot wire sensors, based on the square wave test, is greater than 30 KHz.

The triple sensor probe is directly calibrated both before and after the experiment as a function of temperature, velocity and flow angle in a laminar, temperature-controlled calibration jet. Calibration ranges for velocity, temperature, and flow angle are respectively 2 to 55 m/sec, 20 to 70°C and -30° to +30°.

The calibration equation for the cold wire is linear and is given by the following equation

$$E_{cw} = A_{cw} + B_{cw} T_a \quad (2)$$

where  $E_{cw}$  is the cold wire bridge voltage

$T_a$  is the air temperature and

$A_{cw}$  and  $B_{cw}$  are the calibration constants.

The calibration data are determined by measuring the cold wire bridge voltage,  $E_{cw}$ , at various air temperatures and applying the method of least squares to the calibration pairs to determine the calibration constants,  $A_{cw}$  and  $B_{cw}$ .

An appropriate equation relating the hot wire bridge voltage to the velocity, flow angle and temperature is

$$\frac{E_{b,i}^2}{T_{w,i} - T_a} = A_1 + B_1 U^n [\cos^2(\phi_{o,i} \pm \phi) \pm k^2 \sin^2(\phi_{o,i} \pm \phi)]^{n/2} \quad (3)$$



where

$E_{b,i}$  is the bridge voltage

$T_{w,i}$  is the temperature of the hot wire

$T_a$  is the temperature of the air

$U$  is the velocity

$n$  is the exponent

$k$  is the tangential cooling coefficient

$\phi$  is the angle between the velocity and the probe axis

$\phi_{o,i}$  is the angle between the normal to the wire and the hot wire sensor

$(\phi_{o,i} \pm \phi)$  is the angle between the flow vector and the hot wire,

$A_i$  and  $B_i$  are the calibration constants for sensor  $i$ .

and the subscript  $i$  refers to a particular sensor.

The exponent  $n$  is chosen to be 0.5 and the calibration constants  $A_i$  and  $B_i$  are determined by the method of least squares. The temperature of the hot wire,  $T_{w,i}$  is determined directly by holding the angle and velocity fixed and varying the temperature of the calibration air supply. Under these conditions, as discussed in more detail in Appendix B, the bridge voltage is a linear function of the air temperature and the wire temperature can be determined in a straight-forward manner. Once the two sets of calibration constants have been determined, the calibration equation corresponding to each sensor can be inverted so that the flow angle,  $\phi$ , and velocity,  $U$ , can be determined. Details of the inversion can be found in Appendix C, while the inversion equations are shown in Eqns. 4 and 5. (The

subscripts 1, and 2 refer to each of the sensors.)

$$\phi = \frac{1}{2} \sin^{-1} \left( \frac{D(k_2^2 + 1) - (k_1^2 + 1)}{D(k_2^2 - 1) + (k_1^2 - 1)} \right) \quad (4)$$

where

$$D = \left[ \frac{\left( \frac{E^2}{T_w - T_a} \right)_1 - A_1}{\left( \frac{E^2}{T_w - T_a} \right)_2 - A_2} \right] B_2 \quad (5)$$

$$U = \left\{ \frac{\left( \frac{E^2}{T_w - T_a} \right)_2 - A_2}{B_2} \cdot \left[ \frac{1}{\frac{(k_2^2 + 1) - (k_2^2 - 1) \sin 2\phi}{2}} \right]^{.25} \right\}^2$$

## 2.8 Signal Processing for Air Experiments

A block diagram of the signal processing used during data collection for the air flow studies is similar to that shown in Figure 5 for the water experiments. The voltages from the sensor electronics (the two constant temperature anemometers and the A.C. Wheatstone bridge) are passed through calibrated buck and gain amplifier which removes the mean voltage and amplifies the fluctuating portion of the signal so as to correspond to the dynamic range of the FM instrumentation tape recorder. The tape speed is 96.2 cm/sec which corresponds to a frequency response of 10 KHz. The recorded signals are played back at the same tape speed, low pass filtered at 5 kHz and digitized at a sample rate of 10240 samples/sec by means of a 14 bit Tustin analogue to digital converter which is equipped with simultaneous sample and hold circuits. The data triplets corresponding to 30 sec of data (307200 digitized data triplets) are stored on

digital magnetic tape and analyzed using an LSI 11/23 computer equipped with a Sky MNK array processor and standard software.

## 2.9 Data Collection Procedure

Data are collected along a line starting at either a flute valley or crest. In the case of the water experiments, that line corresponds to a radius and passes through the centerline of the tube. In the water experiments, due to the flute spacing the traverse will start at a flute valley and end at a flute crest. The spacing between data collection positions is  $r/R = 0.04$  for  $0 < r/R < 0.48$  and is reduced to  $r/R = 0.02$  for  $r/R > 0.48$ .

For the air experiments, data are collected at positions starting at either the top of a flute crest or bottom of a flute valley and extending to the flute valley or crest on the opposite side of the tube that is most nearly diametrically opposite the starting position. This type of traverse permits an assessment of the flow symmetry but because of the flute spacing the line along which data are collected does not pass through the centerline of the tube but instead is displaced from the centerline by  $r/R = 0.025$ . Data are collected for 45 sec at each position and collection positions are separated by  $r/R = 0.1$ .

The fluid dynamic parameters of the present study along with the corresponding parameters for the comparison experiments are presented in Table 2.

Table 2  
Fluid Dynamic Parameters

Parameter/ Source	Water Flow	Air Flow	Laufer (1953)	Sandborn (1955)	Schildknecht et al (1979)	Silberman (1980)
Diameter, d (cm)	2.80	2.80	2.94	10.16	5.00	30.48
Hydraulic Diameter, d <sub>h</sub> (cm)	1.59	1.59	2.94	10.1	5.0	25.67
Centerline Velocity, U <sub>0</sub> (m/s)	0.669	38.82	30.48	8.81	6.32	40.47
Mean or Bulk Velocity U <sub>m</sub> (m/sec)	0.495	29.76	27.33	7.90	6.18	30.41
Reynolds number Based on Mean Velocity, Re <sub>U<sub>0</sub></sub>	1.18x10 <sup>4</sup>	3.44x10 <sup>4</sup>	5.0x10 <sup>4</sup>	5.0x10 <sup>4</sup>	1.77x10 <sup>4</sup>	5.8x10 <sup>5</sup>
Reynolds number Based on Mean Velocity, Re <sub>U<sub>m</sub></sub>	8.72x10 <sup>3</sup>	2.64x10 <sup>4</sup>	4.49x10 <sup>4</sup>	4.48x10 <sup>4</sup>	1.72x10 <sup>4</sup>	4.36x10 <sup>5</sup>
Friction Factor, f <sub>l</sub>	0.0315	0.0247	0.021	0.021	0.018	0.05
Wall Frictional Velocity, u* (m/sec)	3.14	1.654	1.40	0.40	0.29	1.70

1. For the water and air flow for the present experiment, cf. Yampolsky and Pavlics (1983). (Appendix D).

### 3. RESULTS AND DISCUSSION

The velocity characteristics for the flow of water and air in the spiral multi-fluted tube are presented in this section. The temperature characteristic and heat fluxes are also presented for the air flow case. In general for both flows data are collected on two radii - one starting at a flute crest (called hereafter crest data) and extending past the center of the tube with the other starting at a flute valley (called hereafter valley data) and extending past the center of the tube.

Data obtained in the present experiment are compared to the corresponding data obtained in the smooth tube studies of Laufer, Sandborn, and Schildknecht et al. and to the corresponding quantities obtained by Silberman (1980) in a spiral fluted tube. However, it should be recalled that the geometrical characteristics of the tube used in the Silberman experiments are different from those of the tube used in the present experiment and the length to diameter ratio at the measuring station is considerably less in the Silberman study than in the present one though the lead to diameter ratio is about twice that of the present study. Thus, differences are to be expected, for example in the Silberman tube, the axial velocity profile may not be fully developed though the azimuthal profile may be more nearly fully developed than in the present study.

The temperature and heat flux characteristics, for the air flow, are compared to the corresponding smooth tube results of Bremhorst and Bullock, (1970) and (1973). Apparently, no corresponding measurements

of temperature and turbulent heat flux have been made in a fluted tube.

We begin by first considering the results for the water flow and subsequently consider the results for the air flow. The first results considered pertain to the mean velocity components and intensities. For the air flow, the Reynolds stresses are next presented. This is followed by a discussion of the mean temperature, temperature intensity and heat flux for the air flow, and then by a discussion of the mixing length, eddy diffusivities and turbulent Prandtl number.

### 3.1 Mean Velocity for Water Flow

The mean axial velocity for the water experiments which correspond to a Reynolds number of  $1.18 \times 10^4$  (based on centerline velocity) are presented in Figures 7 and 8 along with the smooth tube data of Laufer, Sandborn, and Schildknecht et al. which correspond to Reynolds numbers of 50,000 for the first two references and 17,700 for the latter. In the spiral fluted tube, the normalized mean axial velocity is reduced relative to that in the smooth tube. For example, for the crest and valley data, the reduction near the wall at  $(1-r/R) < 0.2$  is in excess of 10 and 20% respectively. It should be noted that for the smooth tube, the variation in Reynolds number from the 17,700 of Schildknecht et al. to the 50,000 of Laufer has a negligible effect on the normalized mean axial velocity. Therefore, it seems reasonable to conclude that the relative reduction in normalized mean axial velocity is not due to a Reynolds number effect but is due to the swirl induced by the flutes.

An alternate way of quantifying the effect of swirl on the normalized mean velocity is by comparison of the value of the exponent in the power law description of the mean velocity profile which is given as:

$$\left(\frac{\bar{U}}{\bar{U}_0}\right)^n = \left(1 - \frac{r}{R}\right) \quad (6)$$

Figure 9 shows that the assumption of a power law variation is supported by the data. With respect to the value of the exponent for flow in a smooth tube, Schlichting (1979) reports that, based on the work of Nikuradse, report a value of  $n = 6.0$  for  $Re = 4 \times 10^3$ . Also, the exponent is found to increase with increasing Reynolds number. The exponent for the crest data is found to be 3.1 while that for the valley data is found to be 4.1. These results are consistent with the observation that the effect of swirl is to lead to a mean velocity profile, which appears to correspond to a flow Reynolds number lower than the actual one.

At very high Reynolds numbers, as discussed by Schlichting, the mean velocity distribution should be described by a universal functional form which must contain the logarithm of the independent variable. The universal velocity distribution law for large Reynolds numbers has the form

$$\frac{\bar{U}_0 - \bar{U}}{u_*} = A \ln \left(1 - \frac{r}{R}\right) + B \quad (7)$$

Consistent with that velocity distribution law, the velocity defect when plotted versus  $(1 - r/R)$  on semi-logarithmic paper should correspond to a straight line. Data plotted in this manner are presented on Figure 10 for the present data, the smooth tube of Laufer, and the fluted tube of Silberman (1980). The straight line on that figure corresponds to the universal logarithmic distribution where the coefficients, A and B in Eqn. 7 which are determined by the method of least squares are listed in Table 3.

The coefficients differ, but the form of the curves are similar with the exception of the Silberman data which exhibits an abrupt change in slope at  $(1 - \frac{r}{R}) \sim 0.24$ . It should be remembered that the length to diameter ratio for the Silberman experiments is only about 75 while that for the Laufer and present experiments is greater than 100. Thus, the flow studied by Silberman may not be fully developed with respect to the axial mean velocity profile.

Table 3  
Coefficients in Universal Velocity Distribution for  
Water Flow and Comparison Studies

Data Set/Coefficient	A	B
Crest Data (water)	- 5.00	- 0.20
Valley Data (water)	- 3.14	+ 1.19
Smooth Tube (Laufer)	- 2.86	- 0.08
Fluted Tube (Silberman)	- 2.21	+ 3.88



We next consider the mean velocity profile near the solid surface and in particular, the slope there which is used to compute the wall shear stress. The normalized mean velocity plotted as a function of distance from the nearest solid surface is shown in Figure 11. The origin for the horizontal axis corresponds to the solid surface in contrast to the origin of Figures 7-10 which corresponds for the fluted tube to the radius midway between the crest and the valley. It is clear in this figure as it is in Figures 7 and 8 that the normalized mean velocity is much less than the corresponding mean velocity in the smooth tube. For example at  $y/R = 0.1$ , where  $y$  is the distance from the nearest solid surface, the mean velocity corresponding to the crest and the valley data are reduced respectively 14% and 28% relative to the mean velocity in the smooth tube. The velocity gradient near the wall is also less than in the smooth tube case. The mean gradient at the wall, which is determined by fitting a third order polynomial to the profile near the wall (and including the zero velocity point at the wall), can be used to estimate the friction factor (cf. Appendix E). The major assumptions used in this computation are that the viscosity at the wall is the molecular viscosity and that the shear stress calculated at the crest and at the valley are each representative of the shear stress over half the surface area. This is clearly an ad hoc assumption since the shear stress may not vary in a linear manner along the surface from the crest to the valley. The shear stress at the crest is computed to be  $1.58 \text{ N/m}^2$  while that at the valley is computed to be  $0.40 \text{ N/m}^2$ . Thus agreement of the friction factor value of 0.0318 computed by

associating each of these values of the shear stress with half the area with the value of 0.0315 computed using the pressure drop data of Yampolsky and Palvics (1983) must be viewed as fortuitous. It is interesting to note that the average of the valley and crest shear stresses are about 60% of the smooth tube value at the same Reynolds number but the wetted area of the fluted tube is about 170% that of a smooth tube which results in a computed friction factor about equal to that of the smooth tube at the same Reynolds number.

### 3.2 Turbulence Intensity for Water Flow

The root mean square axial velocity normalized by the centerline velocity, the friction velocity and the local mean velocity are shown respectively in Figures 12-14. The distribution is qualitatively similar to the smooth tube data in that the minimum intensity is at the centerline with a generally monotonic rise to a maximum which occurs near the wall. This behavior is considerably different from that in the fluted tube study of Silberman where there is a broad maximum in the intensity which occurs in the range of  $0.15 < (1-r/R) < 0.4$ . For the present data for  $(1-r/R) < 0.45$  the relative intensity for the crest and valley data are about the same as the smooth tube data however, for  $(1-r/R) > 0.45$  the relative intensity for the crest data increases relative to that of the valley data which remains nearly equal to the smooth tube data to  $(1-r/R) \approx 0.6$  which corresponds to the circumference which is tangent to the crest. The relative intensity decreases at positions further from the centerline until a point about midway between the crest and the valley when there is a relative increase as the solid surface of

the valley is approached. The presence of a secondary vortical motion, with center midway between the valley and crest could account for the reduction in turbulent kinetic energy at that position.

### 3.3 Mean Axial Velocity for Air Flow

The mean velocity normalized by the centerline velocity and the friction velocity is shown respectively in Figures 15 and 16. Qualitatively similar to the water flow data, the mean velocities are reduced relative to the corresponding smooth tube data. However, the relative reduction is less than that of the water flow. For example, at  $(1-r/R) = 0.2$  the reduction for the crest and valley data is respectively about 5% and 7% which is about one-half the reduction found for the water flow. Some of this difference may be due to the fact that the Reynolds number for the air experiment is about three times that of the water experiment.

The relative reduction in mean velocity can also be seen in the reduced value of the exponent in the power law relationship given by Eqn. 6. The exponent corresponding to the crest data is 4.1 while that corresponding to the valley data is 4.08. Schlichting, referring to the results of Nikuradse states that the exponent,  $n$ , should be about 6.6. It is interesting to recall that for the water flow there is a 25% difference between the exponents for the crest and valley data. This difference corresponds to the fact that in the water flow the mean velocity for the valley data is less than that of the crest data for  $(1-r/R) < 0.5$  in contrast to the corresponding data for the air flow which differ significantly only for  $(1-r/R) < 0.2$ .

The velocity defect normalized by the friction velocity plotted versus  $(1-r/R)$  is shown in Figure 18 where the horizontal axis is logarithmic. Both the valley and crest data are nearly linear when plotted in this manner which suggests that the universal velocity defect law, given by Eqn. 7 is valid for the air flow data. The value of the coefficients for the crest and the valley data for the coefficient multiplying the logarithmic term are -4.798 and -3.952 respectively and for the intercept are -0.411 and -0.126 respectively. The magnitude of the coefficient multiplying the logarithmic term for the crest data is larger than that corresponding to the valley data. This corresponds to the larger weighting given to the portion of the profile nearest the solid boundary.

The mean velocity profiles as a function of distance from the nearest solid surface for the crest and valley data, the smooth tube data, and fluted tube data of Silberman are shown in Figure 19 which corresponds to Figure 11 for the water data. Again it is clear that the mean velocity is reduced relative to that in the smooth tube. For example, at  $y/R = 0.1$ , the mean velocity corresponding to the crest and the valley data are reduced respectively 5% and 13% relative to that in the smooth tube. These reductions are about one-half those found in the water flow. The shear stress computed using the gradient of the mean velocity, obtained in a manner similar to that used to determine the shear stress for the water flow is found to be  $1.691 \text{ N/m}^2$  at the valley and  $4.157 \text{ N/m}^2$  at the crest. The ratio of crest to valley shear stress is about 2.5 while the corresponding ratio for the water data is about 4.0. The friction factor of 0.024

is computed using the preceding values for the shear stress and assuming that the shear stress at the crest corresponds to half the surface area and that the shear stress at the valley corresponds to the other half of the surface area. This value is only about 10% higher than the value of 0.0217 obtained using the pressure drop data of Yampolsky and Pavlics (1983).

### 3.4 Mean Azimuthal Velocity and Flow Angle

The normalized mean axial velocity is presented in Figures 20 and 21. The azimuthal velocity is nearly zero on the centerline and rises to a maximum at a circumference corresponding to the crest. There is a gradient in the mean azimuthal velocity in the azimuthal direction as the mean azimuthal velocity for the valley data is 10 to 15% higher than that of the valley data in the range  $0.2 < (1-r/R) < 0.6$ .

The mean flow angle normalized by the flute angle is shown in Figure 22 along with the corresponding data from the fluted tube study of Silberman. (The mean flow angle is defined as the angle between the mean azimuthal and axial velocity component.) The present data reaches a maximum flow angle of about 35% of the flute angle near the circumference corresponding to the level of the crest.

The mean flow angle presented in Figure 22 does not indicate whether a fluid particle at a particular flute angle has a rotation rate,  $\bar{W}/r$ , that will correspond to a complete revolution in the time that it takes a fluid particle to move an axial distance equal to the lead length,  $l_f$ , of the flute. This time is given by the ratio of the lead length divided by the local axial velocity,  $\frac{l_f}{\bar{U}}$ . Thus the rotation rate required for a fluid particle to make one complete

revolution in the time it takes that fluid particle to move a distance equal to the lead length is  $2\pi\bar{U}/\lambda_f$ . Figure 23 shows the ratio of the local rotation rate to that required for a complete revolution in one lead length. It is obvious that the fluid is not in solid body rotation. The relative rotation rate is nearly zero at the centerline and increases to a maximum of about 60% near the flute crest and then falls to about 30% in the flute valley. However, it should be noted that this last data point has a large uncertainty associated with it due to the relatively large size of the sensing volume compared to the scale of the flute valley. The maximum relative rotation rate is less than that found in the Silberman study and may be due to the relatively small ratio of length to lead of 26 which suggests that the azimuthal velocity profile may not be fully developed.

### 3.5 Turbulence Intensity

The intensities of the axial, radial and azimuthal velocities normalized by the centerline velocity are shown in Figures 24-26 and the corresponding quantities normalized by the local mean velocity are shown in Figures 27-29. For both the crest and valley data, the distributions of the root mean square (rms) axial velocity normalized by the centerline and by the local mean velocity are similar to the corresponding data of Schildknecht et al., but for the mid-radius positions is about 12% higher than the corresponding smooth tube data of Laufer and Sandborn. These results are in contrast with the corresponding ones for water where the relative axial velocity intensity for  $(1-r/R) > 0.5$  was about the same as for the smooth tube data of Laufer and where  $(1-r/R) < 0.5$ , the relative intensity for the

crest data became larger than even the corresponding results of Schildknecht et al. while the corresponding valley data reached values intermediate between those of Laufer and Schildknecht et al.

The normalized rms radial velocity for  $(1-r/R) > 0.9$  for both the crest and valley data is about 14% less than the corresponding smooth tube data and for  $(1-r/R) > 0.1$  is about 50 to 60% less. The normalized rms azimuthal velocity for  $(1-r/R) > 0.1$  is about 25% less than that of the corresponding smooth tube data and about 60% of the rms axial velocity.

The turbulence kinetic energy,  $q^2$ , normalized by the friction velocity is shown on Figure 30 and is nearly equal to the corresponding values of Schildknecht et al. and about 11% higher than the corresponding results of Laufer.

### 3.6 Correlation Coefficients

The correlation coefficients are shown in Figure 31. The correlation coefficient for the axial and radial velocity, for both the crest and valley data is similar to the smooth tube data of Laufer and generally about 30% higher than the data of Schildknecht et al. For  $(1-r/R) > 0.3$ , the data is generally similar to that of Bremhorst and Bullock (1973) but does not show the gradual decrease near the wall that the latter data set does. The correlation coefficient between the axial and azimuthal velocity is negligible in the central region of the flow ( $1-r/R > 0.5$ ) but shows an increase for both the crest and valley data as the tube wall is approached.

The two Reynolds stresses normalized by the square of the friction velocity correlation is only slightly greater than the smooth

tube data of Laufer but about 25% greater than the corresponding data of Schildknecht et al. for  $1-r/R > 0.1$ . Near the wall the present correlations are somewhat lower than the smooth tube correlations - a result that is due to the relative displacement of the solid surface from the position corresponding to  $r/R = 0$  and of course to the geometry of the flutes. The correlation of the axial and azimuthal velocity show, for both the crest and valley data, that there is little or no correlation for  $1-r/R > 0.5$  but that a positive correlation exists for  $1-r/R < 0.5$ . This suggests that the influence of the flutes on the flow extends to only about the half radius position with the most significant influences as expected near the fluted surface. The axial and radial velocities normalized by the turbulent kinetic energy are shown in Figure 34. The results so normalized are similar to the smooth tube data of Laufer.

### 3.7 Temperature Field

The difference between the mean temperature at the wall  $T_w$ , and at that particular radial location normalized by the difference between the wall temperature and the centerline temperature,  $T_{max}$ , is shown on Figure 35. The profiles about the centerline are nearly symmetric, though the valley data in the lower half of the tube are about 3% higher than the corresponding crest data in the lower half of the tube. In the upper half of the tube, the mean temperature for the valley and crest data are nearly identical. In the spiral fluted tube, the normalized mean temperature is less than that in the smooth tube and the gradient near the wall is less than that in the smooth tube. This latter observation is consistent with an augmentation of



the heat transfer rate in the spiral fluted tube relative to that in the smooth tube.

The root mean square temperature normalized by the difference between the wall and centerline temperature is shown in Figure 36. The root mean square temperature for the crest and valley data are within 3% of each other and both are about 35% higher than the corresponding data of Bremhorst and Bullock.

The correlation coefficient for the temperature with each of the three velocity coefficients is shown in Figure 37 along with the corresponding data of Bremhorst and Bullock for a smooth heated tube. For each of the three correlations the crest and valley data are similar. The axial velocity-temperature correlation coefficient is a factor of two or more larger than the radial velocity temperature correlation and peaks in the outer region of the flow at  $1-r/R \sim 0.3$ . The radial velocity temperature correlation coefficient reaches a maximum at  $1-r/R \sim 0.4$ . At the centerline, the correlation coefficient is about equal in magnitude to that found by Bremhorst and Bullock for the smooth tube though the correlation coefficient for the present data is positive while that of Bremhorst and Bullock is negative. The reason that the correlation coefficient is not zero on the centerline as expected from symmetry considerations is that the line along which data are collected does not pass through the exact fluid dynamic centerline of the tube. At  $1-r/R \sim 0.9$  the correlation coefficients for the smooth and spiral fluted tubes are about equal but for  $1-r/R < 0.9$  the correlation coefficient for the smooth tube becomes and remains larger than the corresponding value in the smooth

tube. At  $1-r/R = 0.5$  for example, the correlation coefficient for the smooth tube is about 30% larger than the corresponding value in the spiral fluted tube. It should be remembered at  $1-r/R \sim 0.5$  that the rms temperature in the smooth tube is about 30% less than that in the spiral fluted tube while in the spiral fluted tube at  $1-r/R \sim 0.5$  the rms radial velocity is about 14% less than in the smooth tube. Thus in the spiral tube flow at  $r/R \sim 0.5$  the unnormalized value of the correlation coefficient should be only about 15% less than that in the smooth tube.

The correlation coefficient of the temperature and azimuthal velocity is essentially zero from the centerline to  $1-r/R \sim 0.9$  with an indication of a positive correlation near the flute crest and a negative correlation near the valley. These different signs of the correlation coefficient at positions corresponding to  $1-r/R < 0.1$  may correspond to a small secondary though intermittent vortex motion with center on a radius passing through a valley at about the crest height that preferentially transports hot fluid from the region of the flow where  $1-r/R > 0.1$  to the region of the flute valley and subsequently transports cool fluid from the flute valley to the region of the crest.

The radial velocity-temperature coefficient normalized by the difference between the wall temperature and local mean temperature is shown in Figure 38. The minimum occurs at the centerline and increases monotonically as the wall of the tube is approached. In addition there is little difference between the values corresponding to the valley and crest data. Clearly, throughout the tube, the

radial transport of heat is significantly larger than in the smooth tube as the values of the radial heat flux are at all radial positions about 30% higher than the corresponding smooth tube values of Bremhorst and Bullock.

### 3.8 Mixing Length

The computation of both the mixing length and the eddy diffusivities for heat and momentum requires numerical values for the gradient of the mean axial velocity and temperature. These gradients are obtained by first using the method of least squares to fit a third order polynomial through the mean axial velocity and temperature profiles in various ranges. The gradients in the mean temperature and velocity are determined by differentiation of the third order polynomials and are shown for reference in Figures 39 and 40, respectively.

The mixing length is important in models used for the prediction of turbulent flows. The measurements of the three mean and rms velocity components and the velocity correlation coefficients permits an examination of the mixing length. For a complex three dimensional flow, as discussed by Kosliness, Launder, and Sharma (1974) and Shook and Sagar (1976), the correlation of the axial and radial velocities are given by expressions of the form:

$$\overline{u'v'} = \ell^2 J \frac{\partial \bar{U}}{\partial r} \quad (8)$$

where

$$\begin{aligned}
J^2 = & 2\left(\frac{\partial \bar{U}}{\partial x}\right)^2 + 2\left(\frac{1}{r} \frac{\partial \bar{W}}{\partial \phi}\right)^2 + \left(\frac{\partial \bar{U}}{\partial r}\right)^2 \\
& + \left(\frac{\partial \bar{W}}{\partial x}\right)^2 + \frac{2}{r} \left(\frac{\partial \bar{W}}{\partial x}\right) \left(\frac{\partial \bar{U}}{\partial \phi}\right) + \frac{1}{r^2} \left(\frac{\partial \bar{U}}{\partial \phi}\right)^2 \\
& + \left[r \frac{\partial}{\partial r} \left(\frac{\bar{W}}{r}\right)\right]^2
\end{aligned} \tag{9}$$

for a flow with a mean radial velocity,  $\bar{V} \approx 0$ .

For a smooth tube, the mixing length,  $l_0$ , is given by the expression presented by Schlichting (1973) where

$$l_0 = R \left[ 0.14 - 0.08 \left(1 - \frac{r}{R}\right)^2 - 0.06 \left(1 - \frac{r}{R}\right)^4 \right] \tag{10}$$

For the present flow, we assume that the terms involving gradients in the radial direction such as  $\frac{\partial \bar{U}}{\partial r}$  and  $\frac{\partial}{\partial r} \left(\frac{\bar{W}}{r}\right)$  are dominant. It is clear however that, while terms such as  $\frac{\partial \bar{W}}{\partial \phi}$  should be zero for fully developed smooth tube flows, that, based on the mean velocity data shown on Figures 7, 15, and 20, gradients in the azimuthal direction though considerably smaller than the gradients in the radial direction are not identically equal to zero. The mixing length calculated using Eqn. (8) and the simplified form of Eqn. (9) is shown in Figure 41 where it is normalized by the mixing length for a smooth tube with no swirl as given by Eqn. (10). The mixing length for the swirling flow is smaller than that for the smooth tube for  $1-r/R < 0.3$ . For  $1-r/R > 0.3$ , the mixing length for the swirling flow becomes relatively larger. It should be recalled that the mean velocity gradient becomes very small in the central region of the tube and that

therefore the relatively large values may be due to errors associated with the differentiation of the experimental data.

The reduction in the mixing length is not unexpected. Bradshaw (1973) has discussed the effect of swirl on the mixing length and suggests that the Richardson number

$$R_i = \frac{\frac{2\bar{W}}{2} \frac{\partial}{\partial r} (r\bar{W})}{\left(\frac{\partial \bar{W}}{\partial r}\right)^2 + \left[r \frac{\partial}{\partial r} \left(\frac{\bar{W}}{r}\right)\right]^2} \quad (11)$$

affects the mixing length as indicated in the following expression where

$$\ell = \ell_0 (1 + \beta R_i) \quad (12)$$

where  $\beta$  is a negative constant equal to about -5.0. The value of the computed  $R_i$  number obtained using Eqn. 11 is shown in Figure 42 where negative values correspond to flows that are stabilized, i.e., to flows where  $\bar{W}$  increased with  $r$ . The value of the "constant",  $\beta$  is shown in Figure 43. The "constant" varies between -2.3 and 0 for  $0.1 \leq 1 - r/R \leq 0.7$ . The magnitude is less than that suggested by Bradshaw though the sign is as suggested. The large values of  $\beta$  near the centerline may be due to numerical errors introduced during the process of differentiation.

### 3.9 Eddy Diffusivities and Turbulent Prandtl Number

The eddy diffusivity for momentum,  $\epsilon$ , is defined as

$$\epsilon = \frac{\overline{u'v'}}{\partial \bar{U} / \partial r} \quad (13)$$

and the eddy diffusivity for heat,  $\epsilon_\theta$ , is defined as

$$\epsilon_\theta = \frac{\overline{v'\theta'}}{\partial \bar{T} / \partial r} \quad (14)$$

The eddy diffusivities for heat and momentum are shown respectively on Figures 44 and 45.

The eddy diffusivity for both the crest and valley data are similar in shape with a peak at about  $1-r/R \sim 0.4$  with a reasonably constant value in the central region of the flow (for  $1-r/R > 0.8$ ) and, as expected, a value of zero at the wall.

As shown in Figure 45 the eddy diffusivity for heat for the crest and valley data differs more than does the eddy diffusivity for momentum. For  $0.4 < 1-r/R < 0.8$  the eddy diffusivities for the crest data are about 10% higher than the valley data. The peak in the eddy diffusivity for heat also occurs at  $1-r/R \sim 0.4$ . The eddy diffusivity for heat is zero at the wall of the tube but is not constant valued in the central portion of the tube.

The turbulent Prandtl number,  $\sigma_t$ , which is the ratio of the eddy diffusivity for momentum divided by the eddy diffusivity for heat is shown in Figure 46. The values for both the valley and crest data in the range  $0.2 < 1-r/R < 0.8$  show that the turbulent Prandtl number is about two. Typical values of about 0.7 are found for flows far from a solid surface. Near a solid surface, values up to 0.9 are typically found, but in this flow values as high as 5 are found.

AD-A150 774

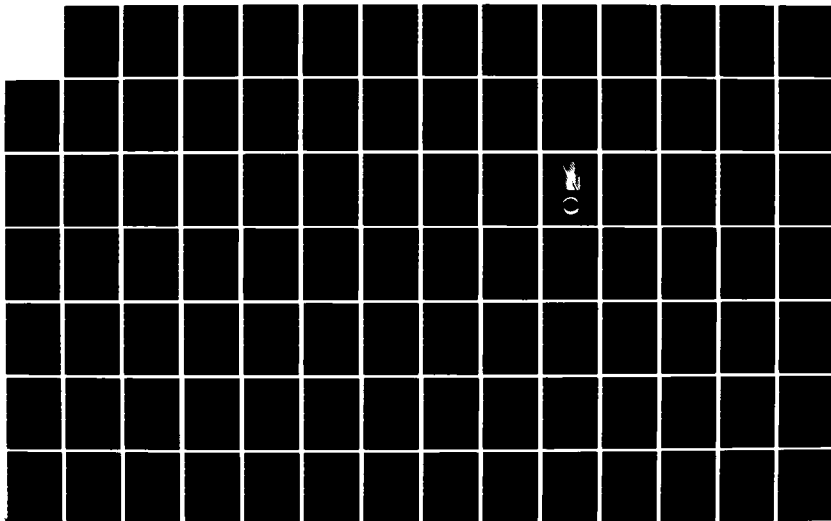
FLUID MECHANICS AND HEAT TRANSFER SPIRALLY FLUTED  
TUBING(U) GA TECHNOLOGIES INC SAN DIEGO CA  
J S YAMPOLSKY ET AL. DEC 84 GA-A17833 N00014-82-C-0721

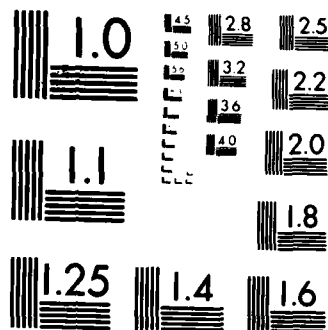
2/8

UNCLASSIFIED

F/G 20/4

NL





MICROCOPY RESOLUTION TEST CHART  
NATIONAL BUREAU OF STANDARDS 1963-A



#### 4. SUMMARY AND CONCLUSIONS

The mean velocity and temperature as well as the corresponding gradients are relatively less for the spiral fluted tube flow as compared to the corresponding quantities in the smooth tube flow. Corresponding to the relatively low mean velocity gradients at the wall, the shear stress is lower than in a smooth tube at the same Reynolds numbers. The reduction in shear stress is offset by the increased surface area so that the pressure drops for the smooth and fluted tube are nearly the same.

The turbulent intensity for the axial velocity in the fluted tube, except near the wall, is about the same as that in the smooth tube. This result indicates that the flutes do not lead to an increase in the turbulence level, and that the augmentation in the heat transfer rate for the fluted tube must be due to some other flow effect such as a secondary vortex type flow in the vicinity of the flutes. Measurements in the water flow of the axial velocity intensity support this point of view.

The fluid is not, in a mean sense, in solid body rotation. Near the crest, the rotation rate is reduced by about 40% of that corresponding to the flute angle. At the same radial location, but directly above a valley, the rotation rate is reduced about 70% relative to that corresponding to the flute angle. These results suggest that the azimuthal velocity profile is not fully developed in contrast to the axial velocity profile which appears to be.

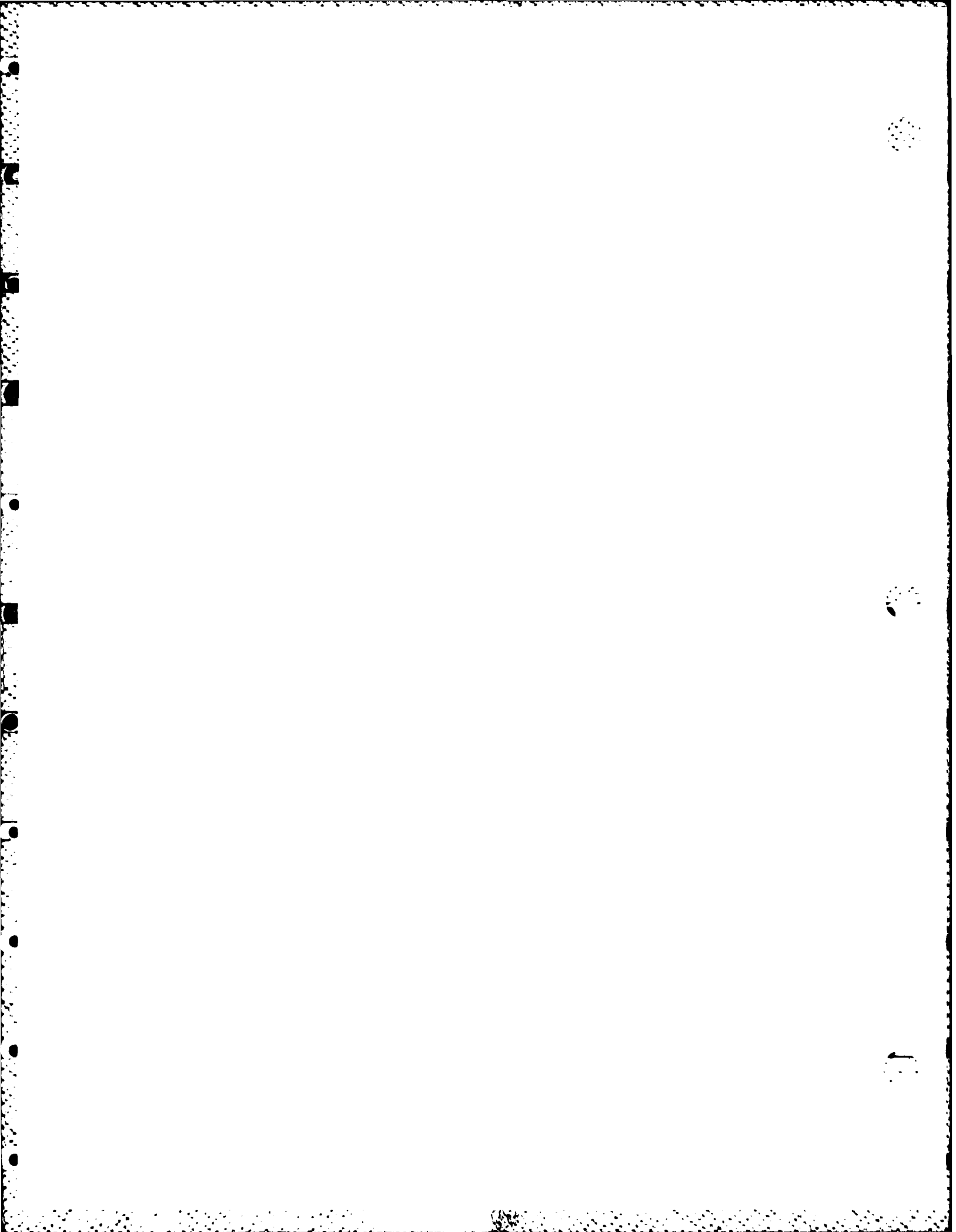
As expected, the effect of increasing rotation rate with radius is to lead to a reduction in the Prandtl mixing length. Also of

interest is that the turbulent Prandtl number reaches a value of approximately two at the mid-radius positions.

## 5. RECOMMENDATIONS

Further measurements, especially detailed measurements, near the flutes are clearly required in order to better determine flow features that are responsible for the augmentation in heat transfer. In order to accomplish these measurements, a tube with larger flutes and flute separation will have to be constructed in order to reduce the relative spatial averaging effects due to finite probe size. Alternatively laser anemometry techniques can be employed using the present tube. The effect of spatial averaging will be reduced since the relative length scale for the laser sampling volume is about 10% of that of the hot wire probe. However, seed particle migration may lead to some difficulties with the use of the laser system.

Also, measurements should be made in fluted tubes of various lengths to assess whether both the axial and azimuthal velocity fields are fully developed. Finally, since significant augmentation in water has been found at high heat flux levels, measurement of the time resolved velocity and temperature fields should be made at different flux levels to determine the effect of heat flux on the fluid motion.



## ACKNOWLEDGEMENTS

The work reported herein represents a joint effort between the University of California at Irvine, the University of California at San Diego and GA Technologies. In particular we wish to acknowledge J.S. Yampolsky of GA who took an active part in the direction of the work. We also wish to acknowledge helpful discussions with B.E. Launder of the University of Manchester and P.A. Libby of USCD.

The experimental program was accomplished with the direct aid of the following students in the phases of research as noted:

M. Petach (UCSD) Construction of air test rig, data collection of simultaneous time resolved velocity and temperature

P.B. Byers (UCSD) Construction of air test rig, preliminary measurements of axial velocity.

R. Hummer (UCSD) Manufacture and construction of air test rig.

E. Seiler, A. Flowers C. Mangol, D. Melving (UCI) Design and construction of water calibration tunnel.

S. Montgomery (UCI) Design construction of water calibration tunnel, data collection in water flow facility.

V. Allienello (UCI) Manufacture of components for the water tunnel.

We also wish to acknowledge Dr. K.N. Helland for his help during the development of data analysis software and to Ms. Verna Bruce for her expert wordprocessing.

The experimental program received support from GA Technologies under Contract Number 787113.

## References

- Adrian, R.J., Johnson R.E., Jones, B.G., Merati, P., and Tung, T.C., "Aerodynamic Disturbances of Hot Wire Probes and Directional Sensitivity", J. Phys. E. Sci. Instrum., Vol. 17, 1984, pp. 62-71.
- Andreas, Edgar L., "Analysis of Crossed Hot Film Velocity Data", DISA Information, No. 24, May 1979, pp. 15-23.
- Blumenkarantz, A., and Taborek, J., "Heat Transfer and Pressure Drop Characteristics of Turbotic Spirally Deep Grooved Tubes in the Turbulent Regime", December 1970. (referred to in Carnavos, T.C.)
- Bradshaw, P., AGARDograph No. 169, N.A.T.O. (1973).
- Bremhorst, K., and Bullock, K.J., "Spectral Measurements of Turbulent Heat and Momentum Transfer in Fully Developed Pipe Flow," Int. J. Heat Mass Transfer, Vol. 16, 1973, pp. 2141-2154.
- Bremhorst, K., and Bullock, K.J., "Spectral Measurements of Temperature and Longitudinal Velocity Fluctuations in Fully Developed Pipe Flow", Int. J. Heat Mass Transfer, Vol. 13, 1970, pp. 1313-1329.
- Cannon, J.N., and Kays, W.M., "Heat Transfer to a Fluid Flowing Inside a Pipe Rotating About Its Longitudinal Axis", Journal of Heat Transfer, American Society of Mechanical Engineers, Vol. 91, Series C., No. 1, Feb. 1969, pp. 135-141.
- Carnavos, T.C., "Some Recent Developments in Augmented Heat Exchange Elements," Heat Exchangers Design and Theory Sourcebook, ed. by N. Afgan and F.U. Schlunde, Chapter 17, Scripta Book Co., W.D. McGraw-Hill Company, 1974, pp. 442-489.
- Glovanangeli, J.R., "A Non-Dimensional Heat Transfer Law for a Slanted Hot-Film in Water Flow", DISA Information, No. 25, Feb. 1980, pp. 6-9.
- Gourdon, C., Costes, J., and Domench, S., "Triple Hot-Film Probe Calibration in Water", DISA Information, No. 26, Feb. 1981, pp. 19-22.
- Hay, N., and West, P.D., "Heat Transfer in Free Swirling Flow in a Pipe", J. of Heat Transfer, Transaction of ASME, Vol. 97, Sec. C, No. 3, Aug. 1975, pp. 411-416.
- Hinze, J.O. "Turbulence", 2nd Ed, McGraw-Hill Book Co., Inc., New York, NY 1975.
- Huang, F., and Tsou, F.K., "Friction and Heat Transfer in Laminar Free Swirling Flow in Pipes", ASME Paper 79-HT for meeting Aug. 6-8, 1979.
- HTRI Reboiler Program RTF-2, Design or Rating of Axial Flow Boiling Equipment, unpublished data.

- Igumenstev, T.I., and Nazmeev, Yu G., "Intensification of Convective Heat Exchange by Spiral Swirlers in the Flow of Anomalously Viscous Liquid in Pipes", Journal of Engineering Physics, Vol. 35, No. 2, Aug. 1978, pp. 890-894.
- Jorgenson, F.E., "Directional Sensitivity of Wire and Fiber-Film Probes", DISA Information, No. 11, May 1971, pp. 31-37.
- Kays, W.M., and London, A.L., "Compact Heat Exchangers", 2nd Ed., McGraw-Hill Book Company, New York, NY, 1964.
- Kooslinen, M.L., Launder, B.E. and Sharma, B.I., "Prediction of Momentum, Heat and Mass Transfer in Swirling Turbulent-Boundary Layers", Journal of Heat Transfer, American Society of Mechanical Engineering, Vol. 96, Series C, No. 2, 1974, pp. 204-209.
- Laufer, J., "The Structure of Turbulence in Fully Developed Pipe Flow", N.A.C.A., Technical Note 2954, 1953.
- LaRue, J.C., Deaton, T.S., and Gibson, C.H., "Measurement of High-Frequency Turbulent Temperature," Review of Scientific Inst., Vol. 46, No. 6, 1975, pp. 757-764.
- LaRue, J.C., Libby, P.A., and Yampolsky, J.S., "Fluid Mechanics and Heat Transfer in Spirally Fluted Tubing", General Atomic Report GA-A16541, Aug. 1981.
- Murakami, M., Kito, O., Katayama, Y., Iida, Y., "An Experimental Study of Swirling Flow in Pipes", Bulletin of the Japan Soc. Mech. Engrs., Vol. 19, No. 128, Feb. 1970, pp. 118-126.
- Palen, J., Cham. B., Taburek, J., "Comparison of Condensation of Steam on Plain and Turbotec Spiral Grooved Tubes in a Baffle Shell-and-Tube Condenser," HTRI Report 2439-3001, January 1971.
- Reilly, D.J., "An Experimental Investigation of Enhanced Heat Transfer on Horizontal Condenser Tubes", M.S. thesis, Naval Postgraduate School (1978).
- Sandborn, V.A., "Experimental Evaluation of Momentum Terms in Turbulent Pipe Flow", N.A.C.A. Technical Note 3266, 1955.
- Schildknecht, M., Miller, J.A., and Meier, G.E.A., "The Influence of Suction on the Structure of Turbulence in Fully Developed Pipe Flow," J. Fluid Mech., Vol. 90, Part 1, 1979, pp. 67-107.
- Schlichting, H., "Boundary-Layer Theory", 7th Ed., McGraw-Hill Book Company, New York, NY, 1979.
- Shook, C.A., and Sagar, S.K., "Turbulent Flow in Helically Ribbed Pipes", The Canadian Journal of Chemical Engineering, Vol. 54, Dec. 1976, pp. 489-496.

- Silberman, E., "Effect of Helix Angle on Flow in Corrugated Pipes", Journal of the Hydraulic Division, ASCE, Vol. 96, No. HY11, Proc. Paper 7685, Nov. 1970, pp. 2253-2263.
- Silberman, E., Closure to "Effect of Helix Angle on Flow in Corrugated Pipes", Journal of the Hydraulics Division, ASCE, Vol. 98, No. HY8, Aug. 1972, pp. 1449-1450.
- Silberman, E., "Effect of Helix Angle on Flow in Corrugated Pipe Flow," Journal of the Engineering Mechanics Division, EM4, Aug. 1980, pp. 699-717.
- Singh, M.P., Sinha, P.C., and Aggarwal, M., "Swirling Flow in a Straight Circular Pipe", Zeitschrift fuer Angewandte Mathematik und Mechanik, Vol. 60, N 9, Sep. 1980, pp. 429-436.
- Webb, R.L., "The Use of Enhanced Surface Geometrics in Condensers: An Overview", Power Condenser Heat Transfer Technology, ed. by Marto, P.J., and Nunn, R.H., McGraw-Hill Book Company, 1981, pp. 287-324.
- White, A., "Flow of a Fluid in an Axially Rotating Pipe", Journal of Mechanical Engineering Science, Vol. 6, No. 1, Mar. 1964, pp. 47-52.
- Yampolsky, J.S., "Spirally Fluted Tubing for Augmented Heat Transfer", General Atomic Report GA-A15442.
- Yampolsky, J.S., and Pavlics, P., "Spirally Fluted Tubing for Augmented Heat Transfer in Process Industries", General Atomic Report GA-A17334, Oct. 1984.



## APPENDIX A

### PHYSICAL BACKGROUND FOR OPERATION OF HOT FILM SENSOR

A complete understanding of the operation of a hot film sensor requires a thorough understanding of the concept of forced convection heat transfer from the surface of heated cylinder in cross flow, (cf. Hinze (1975)). The rate of heat transfer from the film depends upon the following:

- o Velocity of the cross flow;
- o Difference in temperature between the film and the fluid;
- o Dimensions and physical properties of the film;
- o Properties of the fluid.

The heat transferred per unit time to the ambient fluid from a film is described by

$$q = h\pi d_s \ell_s (T_f - T_w) \quad (A1)$$

where

$h$  is the heat transfer coefficient

$d_s$  is the diameter of the sensor

$\ell_s$  is the length of the sensor

$T_f, T_w$  are the temperature of the film and the ambient fluid respectively

For thermal equilibrium conditions, this heat loss must be equal to the heat generated per unit time by the electric current through the film

$$q = I^2 R_H \quad (A2)$$

where

$I$  is the current

$R_H$  is the operating resistance of the film

With the introduction of the dimensionless Nusselt number

$$Nu = \frac{hd}{K} \quad (A3)$$

where

$K$  is the heat conductivity of the water  
equation (A1) becomes

$$q = \pi K l_s (T_f - T_w) Nu$$

Thus, at thermal equilibrium

$$I^2 R_H = \pi K l_s (T_f - T_w) Nu \quad (A4)$$

The equation (A4) can be written

$$Nu = \frac{I^2 R_H}{\pi K l_s} \cdot \frac{1}{(T_f - T_w)}$$

or

$$Nu \sim \frac{E^2}{(T_f - T_w)} \quad (A5)$$

Introducing King's law for basic heat transfer relation for flow over cylinder

$$Nu = \tilde{A} + \tilde{B} Re^n \quad (A6)$$

where  $Re$  is the Reynolds number,  $Re = \frac{\bar{U}_d s}{\nu}$

assuming constant fluid properties, and from equations (A5) and (A6), we obtain

$$Nu = A + BU^n \quad (A7)$$

This equation relates between anemometer voltage and effective cooling velocity around the film. The final form of the calibration equation was found to be

$$\frac{E^2}{T_f - T_w} = 0.0432 + 0.0236U^{.38}$$

In order to prevent the formation of gas bubbles on the surface of the sensor an overheat ratio of 1.055 is selected which corresponds to a film temperature of 56.099°C. The method used to determine the film temperature is described in Appendix B.

## APPENDIX B

### CALIBRATION TECHNIQUE FOR FILM TEMPERATURE DETERMINATION

Since the temperature sensitivity is dependent on the difference between the film and water temperature,  $T_f - T_w$ , (which is small in water because of the possibility of gas bubbles forming on the sensor at higher values of  $T_f$ ) inaccuracies in the value of the film temperature will effect the calculated response to ambient temperature variations. The temperature of each film must be determined in order to reduce the uncertainty of the computed velocity.

The relation between the operating temperature of the film,  $T_f$ , and the overheat ratio  $\frac{R_H}{R_C} = 1.055$  (ratio of operating resistance at  $T_f$ , and the resistance at ambient temperature,  $T_w$ ) is as follows

$$\frac{R_H}{R_C} = 1 + \alpha_c (T_f - T_w) \quad (B1)$$

where  $\alpha_c$  is the temperature coefficient of resistivity of the film and is provided by the probe manufacturer. In principle the above equation can be used to obtain an accurate value for  $T_f$  but in practice due to resistances not associated directly with the film,  $R_H$  may not be accurately known. Thus for most accuracy,  $T_f$  should be determined by means of a direct calibration technique.

One such calibration technique involves holding the calibration velocity fixed and then varying the water temperature and recording the corresponding bridge voltage. A least square fit of the temperature - voltage squared calibration pairs can be shown to

provide a means of determining the film temperature. We develop this relationship by first considering the King's law relationship where

$$\frac{E^2}{T_f - T_w} = A + BU^n \quad (B2)$$

For a constant velocity Eqn (B2) can be rewritten as

$$E^2 = CT_f - CT_w \quad (B3)$$

where  $T_f$  is the temperature of the film and is constant.

$T_w$  is the ambient temperature

From the least square fit of temperature versus bridge voltage squared, we would obtain an equation of the form

$$E^2 = \tilde{A} + \tilde{B} T_w \quad (B4)$$

where  $\tilde{A}$  and  $\tilde{B}$  are the coefficients obtained from the least squares fit. From a comparison of the terms in Eqns. (B3) and (B4) it is easy to see that

$$\tilde{A} = CT_f \quad \text{and} \quad \tilde{B} = -C \quad (B5)$$

which implies that

$$T_f = -\frac{\tilde{A}}{\tilde{B}} \quad (B6)$$

## APPENDIX C

### COMPUTATION OF FLOW ANGLE AND MEAN VELOCITY

The calibration and development of an inversion equation relating the flow angle and total velocity to the bridge voltage squared obtained from two sensors in an x-wire sensor requires some discussion - especially since the expected flow angles are large (greater than  $\pm 30^\circ$ ). We begin this development with King's law type relationship between the bridge voltage squared and the effective cooling velocity:

$$\frac{E^2}{\Delta T} = A + BU_{\text{eff}}^{0.5} \quad (C1)$$

where

$$\Delta T = T_f - T_a \quad (C2)$$

$$U_{\text{eff}} = U_0 [\cos^2 \phi + k^2 \sin^2 \phi]^{0.5} \quad (C3)$$

where

$U_{\text{eff}}$  is the effective cooling velocity

$U$  is the velocity

$\phi$  is the angle between  $U$  and the sensor

$k$  is the tangential cooling coefficient of the sensor

$T_f$  is the temperature of the film

$T_a$  is the temperature of the air

Applying the above equation for both sensors of an "x" wire probe we obtain

$$\frac{E^2}{\Delta T} \Big|_1 = A_1 + B_1 U_{o_1}^{0.5} [\cos^2(\phi_{o_2} + \phi) + k_1^2 \sin^2(\phi_{o_1} + \phi)]^{0.25} \quad (C4)$$

$$\frac{E^2}{\Delta T} \Big|_2 = A_2 + B_2 U_{o_2}^{0.5} [\cos^2(\phi_{o_2} - \phi) + k_2^2 \sin^2(\phi_{o_2} - \phi)]^{0.25} \quad (C5)$$

Let

$$\phi_o + \phi = \alpha \quad (C6)$$

$$\phi_o - \phi = \beta \quad (C7)$$

We assume that

$$\phi_{o_1} = \phi_{o_2} = 45^\circ$$

such that

$$\alpha + \beta = 90^\circ$$

Also

$$U_{o_1} = U_{o_2}$$

Substituting for  $U_o$  in Eq. (C4) from Eq. (C5) leads to

$$\left[ \frac{\left( \frac{E}{\Delta T} \right)_1 - A_1}{\left( \frac{E}{\Delta T} \right)_2 - A_2} \frac{B_2}{B_1} \right]^4 = \frac{\cos^2 \alpha + k_1^2 \sin^2 \alpha}{\cos^2 \beta + k_2^2 \sin^2 \beta} \quad (C8)$$

but use of the following trigonometric identities

$$\cos^2 \alpha = 1 - \sin^2 \alpha$$

$$\cos^2 \beta = 1 - \sin^2 \beta$$

$$\sin^2 \beta = \sin^2(90 - \alpha) = \frac{1 - \cos(180 - 2\alpha)}{2} = \frac{1 + \cos 2\alpha}{2}$$

$$\sin^2 \alpha = \frac{1 - \cos 2\alpha}{2}$$

upon substituting into equation (C8)

$$\frac{\cos^2 \alpha + k_1^2 \sin^2 \alpha}{\cos^2 \beta + k_2^2 \sin^2 \beta} = \frac{(k_1^2 + 1) - (k_1^2 - 1) \cos 2\alpha}{(k_2^2 + 1) + (k_2^2 - 1) \cos 2\alpha} \quad (C9)$$

Recall that  $\alpha = 45 + \phi$

$$\cos 2\alpha = \cos(90 + 2\phi) = -\sin 2\phi$$

Thus the right hand side of equation (C9) becomes

$$\frac{(k_1^2 + 1) + (k_1^2 - 1) \sin 2\phi}{(k_2^2 + 1) - (k_2^2 - 1) \sin 2\phi} \quad (C10)$$



Substituting (C10) into equation (C8) and solving for  $\phi$  leads to

$$\sin 2\phi = \frac{\left[ \frac{\left( \frac{E^2}{\Delta T} \right)_1 - A_1}{B_2} \right]^4 (k_2^2 + 1) - (k_1^2 + 1)}{\left[ \frac{\left( \frac{E^2}{\Delta T} \right)_1 - A_1}{B_2} \right]^4 (k_2^2 - 1) + (k_1^2 - 1)} \quad (C11)$$

and solving equation C5 for U leads to

$$U_o = \left\{ \frac{\left( \frac{E^2}{\Delta T} \right)_2 - A_2}{B_2} \cdot \frac{1}{\left[ \frac{(k_2^2 + 1) - (k_2^2 - 1)\sin 2\phi}{2} \right]^{.25}} \right\}^2 \quad (C12)$$

The calibration equations for a hot wire one and two were found to be respectively

$$\frac{E^2}{T_{w1} - T_a} = 0.003508 + 0.0007565U^{.5} [\cos^2(45+\phi) + (0.125)^2 \sin^2(45+\phi)]^{.25}$$

$$\frac{E^2}{T_{w1} - T_a} = 0.0038337 + 0.0007320U^{.5} [\cos^2(45-\phi) + (0.125)^2 \sin^2(45-\phi)]^{.25}$$

where by direct calibration

$$T_{w1} = 256.262^\circ\text{C} \quad \text{and} \quad T_{w2} = 256.167^\circ\text{C}$$

# APPENDIX D COMPUTATION OF WALL FRICTION VELOCITY

The wall friction velocity can be calculated from

$$u^* = \sqrt{\frac{\Delta P}{L} \frac{D_h}{4\rho}} \quad (D1)$$

where

$$\frac{\Delta P}{L} = f \frac{\rho \bar{U}_m^2}{2D_h} \quad (D2)$$

Combining Equations (D1) and (D2) yield

$$u^* = \sqrt{\frac{f}{8} \bar{U}_m^2}$$

where

$f$  is the friction factor

$\bar{U}_m$  is the bulk mean velocity

The friction factor as a function of Reynolds number as obtained from Yampolsky and Pavlics (1983) is shown in Figure D1.

As can be seen below a Reynolds number of 80,000 the friction factor for a spiral fluted tube is the same as that for smooth tube within the uncertainty of the measurements. At higher values of Reynolds number the friction factor is approximately 5-10% less than that of a smooth tube.

## APPENDIX E

### CALCULATION OF WALL FRICTION FACTOR BY MEANS OF AXIAL VELOCITY GRADIENT AT THE WALL

In fully developed flow in a horizontal pipe the pressure drop is balanced by shear forces at the tube wall. The force balance equation for a unit length of tubing is as follows

$$\frac{dP}{dx} A_c = \int \tau \, ds \quad (E1)$$

where  $\tau$  is the shear stress at a particular location on the tube surface

$S$  is the coordinate along the tube surface

$A_c$  is the cross sectional area

$\frac{dP}{dx}$  is the pressure drop

If we assume that the shear stress at the valley and the shear stress at the crest each act on equal amount of the perimeter

$$p_v = p_c = \frac{p}{2} \quad (E2)$$

when:  $p$  is the perimeter of the tube

$p_v$  and  $p_c$  are the perimeters of valley and crest respectively

then equation (E1) becomes

$$\frac{dP}{dx} A_c = \frac{p}{2} (\tau_v + \tau_c) \quad (E3)$$

where  $\tau_v$  and  $\tau_c$  are the shear stress at a valley and a crest respectively.

Assuming that the shear stress at the wall can be evaluated as

$$\tau_v = \mu \left. \frac{d\bar{U}}{dr} \right|_v$$

$$\tau_c = \mu \left. \frac{d\bar{U}}{dr} \right|_c$$

then

$$\frac{dP}{dx} = \frac{\mu}{A_c} \frac{p}{2} \left[ \left. \frac{d\bar{U}}{dr} \right|_v + \left. \frac{d\bar{U}}{dr} \right|_c \right] \quad (E4)$$

For fully developed pipe flow

$$\frac{dP}{dx} = f \frac{\rho \bar{U}_m^2}{2D_h} \quad (E5)$$

where  $f$  is the friction factor

$\bar{U}_m$  is the Bulk velocity

$D_h$  is the hydraulic diameter

$\rho$  is the fluid density

Substituting eq. (E5) into eq. (E4) we find that

$$f = \frac{v D_h p}{\bar{U}_m^2 A_c} \left[ \left. \frac{d\bar{U}}{dr} \right|_v + \left. \frac{d\bar{U}}{dr} \right|_c \right] \quad (E6)$$

Note that

$$D_h = \frac{4A_c}{p}$$

Equation (E6) becomes

$$f = \frac{4v}{\bar{U}_m} \left[ \left. \frac{d\bar{U}}{dr} \right|_v + \left. \frac{d\bar{U}}{dr} \right|_c \right] \quad (E7)$$

where  $\nu$  is the kinematic viscosity,  $\nu = \frac{\mu}{\rho}$ .

The mean axial velocity gradient at the wall can be determined by fitting a third order polynomial to the experimental data points near the wall.

$$\frac{\bar{U}}{\bar{U}_0} = a + b\left(1 - \frac{r}{R}\right) + c\left(1 - \frac{r}{R}\right)^2 + d\left(1 - \frac{r}{R}\right)^3 \quad (E8)$$

and then differentiating with respect to  $r$  to obtain

$$\frac{d\bar{U}}{dr} = -\frac{\bar{U}_0}{R} [b + 2c\left(1 - \frac{r}{R}\right) + 3d\left(1 - \frac{r}{R}\right)^2] \quad (E9)$$

The constants  $b$ ,  $c$ , and  $d$  are the second, third, and fourth coefficients of the third order polynomial. Evaluating equation (E9) at the valley and crest,  $\frac{dU}{dr} \big|_v$  and  $\frac{dU}{dr} \big|_c$  can be determined and the friction factor  $f$  can be calculated by means of equation (E7).

A third order polynomial fit for our experimental data leads to the following equations:

a - for water flow

valley data

$$\frac{d\bar{U}}{dr} = -\frac{\bar{U}_0}{R} [2.452 - 30.702\left(1 - \frac{r}{R}\right) + 1144.755\left(1 - \frac{r}{R}\right)^2]$$

crest data

$$\frac{d\bar{U}}{dr} = -\frac{\bar{U}_0}{R} [220.33 - 4391.86\left(1 - \frac{r}{R}\right)^2 + 21961.23\left(1 - \frac{r}{R}\right)^3]$$

b - for air flow

valley data

$$\frac{d\bar{U}}{dr} = \frac{\bar{U}_o}{R} [- 1.98 - 286.52(1 - \frac{r}{R}) + 3539.22(1 - \frac{r}{R})^2]$$

crest data

$$\frac{d\bar{U}}{dr} = \frac{\bar{U}_o}{R} [+ 220.21 - 3020.26(1 - \frac{r}{R}) + 9275.04(1 - \frac{r}{R})^2]$$

## APPENDIX F

### CALCULATION OF MIXING LENGTH AND TURBULENT PRANDTL NUMBER

#### a. The mixing Length $\ell$

The mixing length is computed using the equations derived by Kooslinen et al (1974) and Shook and Sagar (1976). Using the mixing length hypotheses in a complex flow the Reynolds stress can be expressed by

$$\overline{u'v'} = \ell^2 J \frac{\partial \bar{U}}{\partial r} \quad (F1)$$

where

$\ell$  is the mixing length

and the quantity  $J$  is defined by the following equation:

$$\begin{aligned} J^2 = & 2 \left( \frac{\partial \bar{U}}{\partial x} \right)^2 + 2 \left( \frac{1}{r} \frac{\partial \bar{W}}{\partial \phi} \right)^2 + \left( \frac{\partial \bar{U}}{\partial r} \right)^2 \\ & + \left( \frac{\partial \bar{W}}{\partial x} \right)^2 + \frac{2}{r} \left( \frac{\partial \bar{W}}{\partial x} \right) \left( \frac{\partial \bar{U}}{\partial \phi} \right) \\ & + \frac{1}{r^2} \left( \frac{\partial \bar{U}}{\partial \phi} \right)^2 + \left[ r \frac{\partial}{\partial r} \left( \frac{\bar{W}}{r} \right) \right]^2 \end{aligned} \quad (F2)$$

for a flow where  $\bar{V} = 0$

In case of fully developed flow, eqn. (F2) reduces to

$$J^2 = \left( \frac{\partial \bar{U}}{\partial r} \right)^2 + \left( \frac{\partial \bar{W}}{\partial r} + \frac{\bar{W}}{r} \right)^2 \quad (F3)$$

Substituting eqn. (F3) into eqn. (F1) and solving for the mixing length  $\ell$

$$l^2 = \frac{\overline{u'v'}}{\frac{\partial \bar{U}}{\partial r} [(\frac{\partial \bar{U}}{\partial r})^2 + (\frac{\partial \bar{W}}{\partial r} + \frac{\bar{W}}{r})^2]^{0.5}} \quad (F4)$$

b) The Turbulent Prandtl Number  $\sigma_t$

The turbulent Prandtl number is defined as

$$\sigma_t = \frac{\epsilon}{\epsilon_\theta} \quad (F5)$$

where  $\epsilon$  is the eddy diffusivity for momentum  $\epsilon = \frac{\overline{u'v'}}{\partial \bar{U} / \partial r}$

$\epsilon_\theta$  is the eddy diffusivity for heat  $\epsilon_\theta = \frac{\overline{v'\theta'}}{\partial \bar{T} / \partial r}$

Equation (F5) will take the following final form

$$\sigma_t = \frac{\frac{\overline{u'v'}}{\partial \bar{U} / \partial r}}{\frac{\overline{v'\theta'}}{\partial \bar{T} / \partial r}} \quad (F6)$$

A third order polynomial obtained using the method of least squares is used to the measured data  $\bar{U}$ ,  $\bar{W}$ ,  $\bar{T}$  at values of  $(1 - \frac{r}{R})$ , for the region  $r = 0$  to  $r = R$ . To obtain an accurate fit the entire region was divided into smaller regions based on the minimum standard deviation of the measured data and that calculated using the third order polynomial fit.

The following are the equations obtained for  $\frac{\partial \bar{U}}{\partial r}$ ,  $\frac{\partial \bar{W}}{\partial r}$ , and  $\frac{\partial \bar{T}}{\partial r}$  for the air flow. For crest data

$$\frac{d\bar{U}}{dr} = \frac{\bar{U}_0}{R} [8.871 - (2)(35.529)(1 - \frac{r}{R}) + (3)(49.850)(1 - \frac{r}{R})^2] \quad 0.061 < 1 - \frac{r}{R} < .150$$



$$\frac{d\bar{U}}{dr} = \frac{\bar{U}_0}{R} [2.100 - (2)(3.678)(1 - \frac{r}{R}) + (3)(2.765)(1 - \frac{r}{R})^2] \quad 0.150 < 1 - \frac{r}{R} < 0.507$$

$$\frac{d\bar{U}}{dr} = \frac{\bar{U}_0}{R} [0.794 - (2)(0.333)(1 - \frac{r}{R}) + (3)(0.033)(1 - \frac{r}{R})^2] \quad 0.507 < 1 - \frac{r}{R} < 1.000$$

$$\frac{d\bar{W}}{dr} = \frac{\bar{U}_0}{R} [0.079 - (2)(0.930)(1 - \frac{r}{R}) + (3)(1.054)(1 - \frac{r}{R})^2] \quad 0.061 < 1 - \frac{r}{R} < 0.413$$

$$\frac{d\bar{W}}{dr} = \frac{\bar{U}_0}{R} [-0.987 + (2)(1.441)(1 - \frac{r}{R}) - (3)(0.722)(1 - \frac{r}{R})^2] \quad 0.413 < 1 - \frac{r}{R} < 0.601$$

$$\frac{d\bar{W}}{dr} = \frac{\bar{U}_0}{R} [0.290 - (2)(0.469)(1 - \frac{r}{R}) + (3)(0.223)(1 - \frac{r}{R})^2] \quad 0.601 < 1 - \frac{r}{R} < 1.000$$

$$\frac{d\bar{T}}{dr} = \frac{1}{R} [183.797 - (2)(618.570)(1 - \frac{r}{R}) + (3)(710.650)(1 - \frac{r}{R})^2] \quad 0.061 < 1 - \frac{r}{R} < 0.300$$

$$\frac{d\bar{T}}{dr} = \frac{1}{R} [23.165 - (2)(13.780)(1 - \frac{r}{R}) + (3)(1.950)(1 - \frac{r}{R})^2] \quad 0.300 < 1 - \frac{r}{R} < 1.000$$

For valley data

$$\frac{d\bar{U}}{dr} = \frac{U_0}{R} [3.776 - (2)(16.938)(1 - \frac{r}{R}) + (3)(33.998)(1 - \frac{r}{R})^2] \quad -0.061 < 1 - \frac{r}{R} < 0.100$$

$$\frac{d\bar{U}}{dr} = \frac{U_0}{R} [1.878 - (2)(3.049)(1 - \frac{r}{R}) + (3)(2.159)(1 - \frac{r}{R})^2] \quad 0.100 < 1 - \frac{r}{R} < 0.600$$

$$\frac{d\bar{U}}{dr} = \frac{U_0}{R} [0.595 - (2)(0.045)(1 - \frac{r}{R}) - (3)(0.167)(1 - \frac{r}{R})^2] \quad 0.600 < 1 - \frac{r}{R} < 1.000$$

$$\frac{d\bar{W}}{dr} = \frac{U_0}{R} [0.198 + (2)(19.939)(1 - \frac{r}{R}) + (3)(628.348)(1 - \frac{r}{R})^2] \quad -0.061 < 1 - \frac{r}{R} < 0.000$$

$$\frac{d\bar{W}}{dr} = \frac{U_0}{R} [+0.053 - (2)(.777)(1 - \frac{r}{R}) + (3)(0.881)(1 - \frac{r}{R})^2] \quad 0.000 < 1 - \frac{r}{R} < .413$$

$$\frac{d\bar{W}}{dr} = \frac{U_0}{R} [0.036 - (2)(0.490)(1 - \frac{r}{R}) + (3)(0.442)(1 - \frac{r}{R})^2] \quad 0.413 < 1 - \frac{r}{R} < 0.601$$

$$\frac{d\bar{W}}{dr} = \frac{U_0}{R} [-0.564 + (2)(0.603)(1 - \frac{r}{R}) - (3)(0.219)(1 - \frac{r}{R})^2] \quad 0.601 < 1 - \frac{r}{R} < 1.000$$

$$\frac{d\bar{T}}{dr} = \frac{1}{R} [71.23 - (2)(258.8)(1 - \frac{r}{R})^2 + (3)(386)(1 - \frac{r}{R})^2] \quad -0.061 < 1 - \frac{r}{R} < 0.226$$

$$\frac{d\bar{T}}{dr} = \frac{1}{R} [19 - (2)(8)(1 - \frac{r}{R})^2 - (3)(0.797)(1 - \frac{r}{R})^2] \quad 0.226 < 1 - \frac{r}{R} < 1.000$$

These equations are obtained by using minimum of five fit points.

## APPENDIX G

### TABULATION OF EXPERIMENTAL DATA

The following tables are the data for both water and air experiments. The mean velocities, turbulent intensities, correlations, kinetic energy and temperature field that are directly measured quantities are presented in tables G1, G2 and G3 evaluated at values of  $r/R$ . The mixing length, eddy diffusivity, and turbulent Prandtl number with values of velocity and temperature gradients evaluated at  $r/R$  are presented in Table G4. Values in Table G4 are obtained after fitting third order polynomials that are shown in Appendix F.

TABLE G1a  
WATER FLOW, CREST DATA

$\frac{r}{R}$	$\bar{U}$	$u'^2 \times 10^2$
0.000	0.670	2.457
0.078	0.664	2.564
0.196	0.634	2.779
0.314	0.600	3.221
0.431	0.580	3.716
0.510	0.572	4.205
0.588	0.558	4.888
0.667	0.503	5.189
0.745	0.457	5.711
0.804	0.428	6.073
0.863	0.385	6.220
0.882	0.348	6.622
0.902	0.309	7.050
0.922	0.247	6.977

TABLE G1b  
WATER FLOW, VALLEY DATA

$\frac{r}{R}$	$\bar{U}$	$u'^2 \times 10^2$
0.000	0.670	2.457
0.039	0.666	2.477
0.157	0.650	2.651
0.275	0.636	3.033
0.353	0.588	3.274
0.451	0.570	3.783
0.549	0.559	4.466
0.608	0.550	4.660
0.667	0.527	4.647
0.725	0.502	4.901
0.784	0.473	5.243
0.843	0.451	5.524
0.902	0.402	5.959
0.941	0.343	6.274
0.961	0.313	5.745
0.980	0.255	4.399
1.000	0.228	4.807
1.020	0.205	5.035
1.039	0.133	5.591
1.059	0.092	4.848

TABLE G2a  
AIR FLOW, CREST DATA  
MEAN AND RMS VALUES AND CORRELATIONS

r/R	$\bar{u}$	$\bar{w}$	$\bar{\phi}$	$u'$	$v'$	$w'$	$\phi'$	$q^2$	$\overline{u'v'}$	$\overline{u'w'}$	$R_{uv}$	$R_{uw}$
0.023	36.570	0.013	0.023	1.571	.997	1.009	1.502	4.481	0.148	0.175	0.096	0.113
0.117	36.314	0.010	0.025	1.674	1.027	1.044	1.586	4.749	0.390	0.104	0.236	0.0611
0.211	35.692	0.078	0.129	1.895	1.102	1.126	1.724	6.076	0.660	0.098	0.326	0.0473
0.305	34.850	0.220	0.348	2.125	1.184	1.227	1.923	7.430	0.960	0.123	0.394	0.0486
0.399	33.753	0.321	0.819	2.350	1.259	1.338	2.193	8.899	1.199	0.167	0.419	0.0545
0.493	32.438	0.491	0.957	2.613	1.341	1.456	2.424	10.754	1.561	.274	0.460	0.0737
0.587	30.791	0.885	1.795	2.860	1.406	1.563	2.817	12.595	1.891	0.402	0.478	0.0923
0.681	29.000	1.379	2.948	3.093	1.451	1.642	3.175	14.365	2.134	0.498	0.490	0.1007
0.774	26.550	1.970	4.645	3.293	1.507	1.722	3.674	16.078	2.445	0.725	0.507	0.1313
0.868	22.928	2.536	6.973	3.343	1.525	1.846	4.628	16.901	2.452	0.892	0.506	0.1482

TABLE G2b  
AIR FLOW, VALLEY DATA  
MEAN AND RMS VALUES AND CORRELATIONS

$\tau/R$	$\bar{U}$	$\bar{W}$	$\bar{\phi}$	$u'$	$v'$	$w'$	$\phi'$	$q^2$	$\overline{u'v'}$	$\overline{u'w'}$	$R_{uv}$	$R_{uw}$
0.023	39.134	0.000	0.015	1.570	1.007	1.011	1.495	4.495	0.175	0.148	0.110	0.0943
0.117	38.861	0.012	0.025	1.672	1.055	1.050	1.552	5.017	0.410	0.052	0.231	0.0308
0.211	38.234	0.086	0.133	1.87	1.116	1.118	1.688	5.997	0.681	0.038	0.326	0.0175
0.305	37.294	0.241	0.395	2.099	1.197	1.219	1.902	7.329	0.960	0.063	0.387	0.0248
0.399	36.122	0.370	0.583	2.345	1.269	1.330	2.139	8.869	1.226	0.140	0.414	0.0477
0.493	34.673	0.787	1.297	2.595	1.341	1.439	2.440	10.595	1.535	0.186	0.445	0.0501
0.587	33.030	1.229	2.142	2.850	1.401	1.542	2.751	12.458	1.882	0.208	0.471	0.0475
0.681	31.112	1.785	3.344	3.119	1.530	1.634	3.122	14.737	2.052	0.380	0.433	0.0752
0.774	28.568	2.461	4.898	3.275	1.512	1.722	3.617	15.971	2.479	0.596	0.506	0.106
0.868	24.889	2.976	10.227	3.377	1.571	1.826	4.407	17.210	2.656	0.643	0.517	0.115
0.962	18.120	3.123	8.955	2.393	1.704	2.215	7.236	13.542	2.295	1.989	0.580	0.376
1.056	5.243	0.845	0.1563	1.381	1.204	1.113	11.155	4.599	-0.194	-0.260	-0.133	-0.170

TABLE G3a  
AIR FLOW, CREST DATA  
TEMPERATURE FIELD

$r/R$	$T_w - \bar{T}$	$\theta'$	$\overline{v' \theta'}$	$\overline{u' \theta'}$	$R_{v\theta}$	$R_{u\theta}$
0.023	18.345	0.789	0.051	0.688	0.0635	0.547
0.117	18.196	0.837	0.149	0.797	0.169	0.563
0.211	17.808	0.926	0.243	1.040	0.234	0.593
0.305	17.119	1.010	0.345	1.347	0.279	0.617
0.399	16.433	1.101	0.424	1.686	0.295	0.637
0.493	15.538	1.212	0.539	2.121	0.324	0.672
0.582	14.311	1.288	0.625	2.672	0.331	0.693
0.681	13.069	1.333	0.647	3.008	0.320	0.710
0.774	11.565	1.330	0.609	3.188	0.290	0.709
0.868	9.484	1.195	0.389	2.649	0.205	0.668

TABLE G3b  
AIR FLOW, VALLEY DATA  
TEMPERATURE FIELD

$r/R$	$T_w - \bar{T}$	$\theta'$	$\overline{v' \theta'}$	$\overline{u' \theta'}$	$R_{v\theta}$	$R_{u\theta}$
0.023	17.156	0.772	0.063	0.656	0.0803	0.273
0.117	17.083	0.820	0.156	0.762	0.179	0.510
0.211	16.981	0.900	0.233	0.984	0.233	0.670
0.305	16.295	0.994	0.327	1.263	0.274	0.708
0.399	15.686	1.098	0.393	1.643	0.286	0.718
0.493	14.000	1.120	0.486	1.944	0.307	0.696
0.589	13.817	1.285	0.569	2.545	0.318	0.670
0.681	12.810	1.345	0.599	3.010	0.297	0.639
0.774	11.169	1.318	0.556	3.053	0.279	0.606
0.868	9.532	1.201	0.364	2.470	0.197	0.585
0.962	5.556	0.700	0.207	0.853	0.186	0.557
1.056	-----	0.699	-0.246	0.263	-0.030	0.542



TABLE G4a  
AIR FLOW, CREST DATA  
MIXING LENGTH, EDDY DIFFUSIVITY AND TURBULENT PRANDTL NUMBER

$r/R$	$\frac{d\bar{u}}{dr}$	$\frac{\partial \bar{w}}{\partial r}$	$\frac{dT}{dr}$	$l$	$R_t$	$\beta$	$\epsilon$	$\epsilon_\theta$	$\sigma_T$
0.023	142.26	-331.95	$1.21 \times 10^2$	$3.162 \times 10^{-3}$	0.966	21.200	$1.038 \times 10^{-3}$	$4.21 \times 10^{-4}$	2.465
0.117	379.37	-533.49	$2.42 \times 10^2$	$1.641 \times 10^3$	-0.129	16.062	$1.028 \times 10^{-3}$	$6.157 \times 10^{-4}$	1.670
0.211	610.55	-572.02	$3.72 \times 10^2$	$1.326 \times 10^{-3}$	-0.286	1.836	$1.081 \times 10^{-3}$	$6.532 \times 10^{04}$	1.653
0.305	838.77	-492.00	$5.09 \times 10^2$	$1.167 \times 10^{-3}$	-0.407	0.066	$1.145 \times 10^{-3}$	$6.778 \times 10^{-4}$	1.689
0.399	1061.06	-246.00	$6.54 \times 10^2$	$1.032 \times 10^{-3}$	-0.414	-0.560	$1.130 \times 10^{-3}$	$6.483 \times 10^{-4}$	1.743
0.493	1283.35	-112.63	$8.08 \times 10^2$	$9.697 \times 10^{-4}$	-0.313	-1.131	$1.216 \times 10^{-3}$	$6.671 \times 10^{-4}$	1.823
0.582	1410.79	-115.59	$9.69 \times 10^2$	$9.590 \times 10^{-4}$	-0.246	-1.654	$1.340 \times 10^{-3}$	$6.450 \times 10^{-4}$	2.078
0.681	1769.42	-100.77	$1.14 \times 10^3$	$8.153 \times 10^{-4}$	-0.280	-1.864	$1.206 \times 10^{-3}$	$5.675 \times 10^{-4}$	2.125
0.774	2551.87	-47.42	$1.31 \times 10^3$	$6.103 \times 10^{-4}$	-0.353	-1.853	$9.581 \times 10^{-4}$	$4.649 \times 10^{-4}$	2.061
0.868	6212.22	+35.57	$4.45 \times 10^3$	$2.521 \times 10^{-4}$	-0.362	-2.376	$3.947 \times 10^{-4}$	$8.742 \times 10^{-5}$	4.515

TABLE G4b  
AIR FLOW, VALLEY DATA  
MIXING LENGTH, EDDY DIFFUSIVITY AND TURBULENT PRANDTL NUMBER

$r/R$	$\frac{dU}{dr}$	$\frac{\partial \bar{w}}{\partial r}$	$\frac{d\bar{T}}{dr}$	$z$	$R_1$	$\beta$	$\epsilon$	$\epsilon_\theta$	$\sigma_\tau$
0.023	87.38	-35.58	$8.36 \times 10^1$	$4.693 \times 10^{-3}$	-0.243	161.18	$2.003 \times 10^{-3}$	$7.536 \times 10^{-4}$	2.639
0.117	376.63	-31.57	$2.31 \times 10^2$	$1.699 \times 10^{-3}$	-0.251	8.70	$1.089 \times 10^{-3}$	$6.753 \times 10^{-4}$	1.615
0.211	638.77	-62.49	$3.76 \times 10^2$	$1.291 \times 10^{-3}$	-0.394	1.26	$1.066 \times 10^{-3}$	$4.507 \times 10^{-4}$	1.726
0.305	873.79	-128.34	$5.17 \times 10^2$	$1.126 \times 10^{-3}$	-0.386	-0.08	$1.099 \times 10^{-3}$	$6.325 \times 10^{-4}$	1.756
0.399	1084.71	-229.12	$6.55 \times 10^2$	$9.165 \times 10^{-4}$	-0.284	-1.16	$1.130 \times 10^{-3}$	$6.000 \times 10^{-4}$	1.883
0.493	1358.90	-362.06	$7.90 \times 10^2$	$9.041 \times 10^{-4}$	-0.303	-1.32	$1.130 \times 10^{-3}$	$6.152 \times 10^{-4}$	1.837
0.587	1398.07	-430.04	$9.22 \times 10^2$	$9.716 \times 10^{-4}$	-0.328	-1.17	$1.346 \times 10^{-3}$	$6.17 \times 10^{-4}$	2.188
0.681	1783.74	-524.25	$1.05 \times 10^3$	$7.964 \times 10^{-4}$	-0.334	-1.59	$1.150 \times 10^{-3}$	$5.705 \times 10^{-4}$	2.018
0.774	2503.87	-492.14	$1.13 \times 10^3$	$6.274 \times 10^{-4}$	-0.392	-1.68	$9.901 \times 10^{-4}$	$4.92 \times 10^{-4}$	2.012
0.868	3573.51	-319.713	$1.28 \times 10^3$	$4.561 \times 10^{-4}$	-0.319	-2.34	$7.432 \times 10^{-4}$	$2.045 \times 10^{-4}$	3.642
0.962	8629.45	-6.549	$4.09 \times 10^3$	$1.907 \times 10^{-4}$	2.050	0.44	$2.659 \times 10^{-4}$	$5.061 \times 10^{-5}$	5.257
1.056	17044.98	-----	$7.99 \times 10^3$	-----	0.0051	-----	$-1.138 \times 10^{-5}$	$-3.079 \times 10^{-5}$	3.701

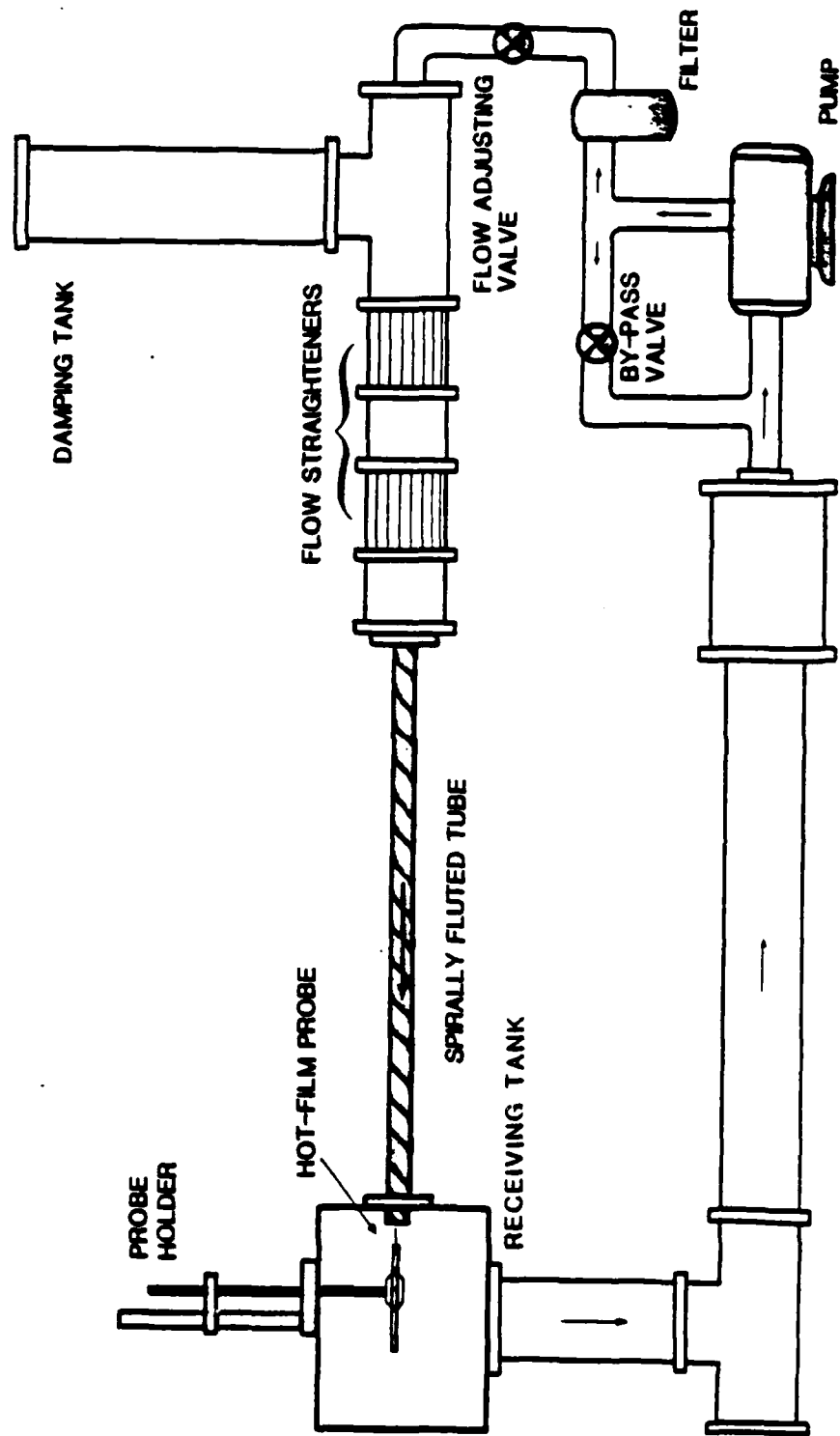


Figure 1 Schematic of water flow Facility

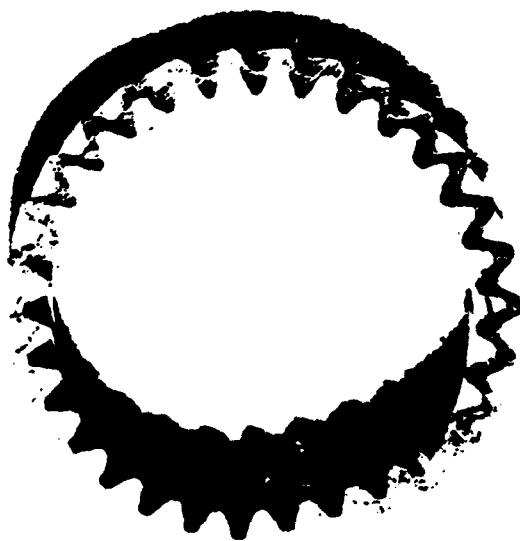


Figure 2 Side and end view of a portion of the test section

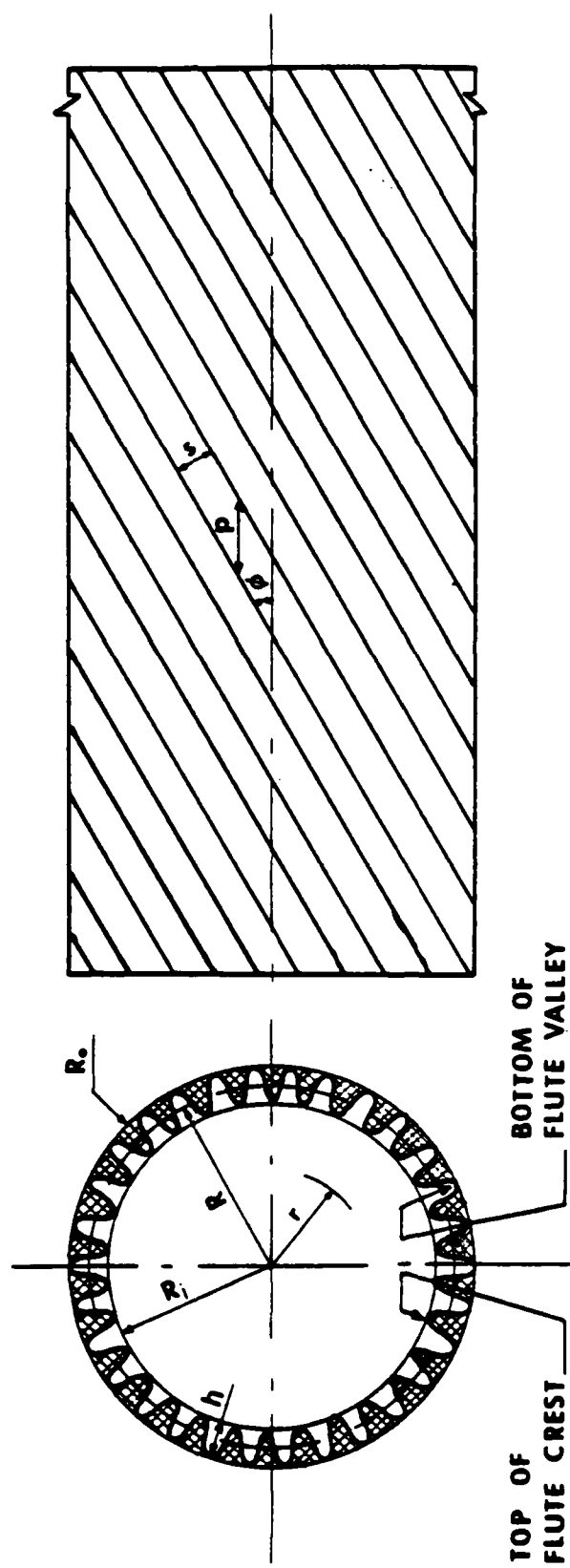


Figure 3 Sketch of spiral fluted tube

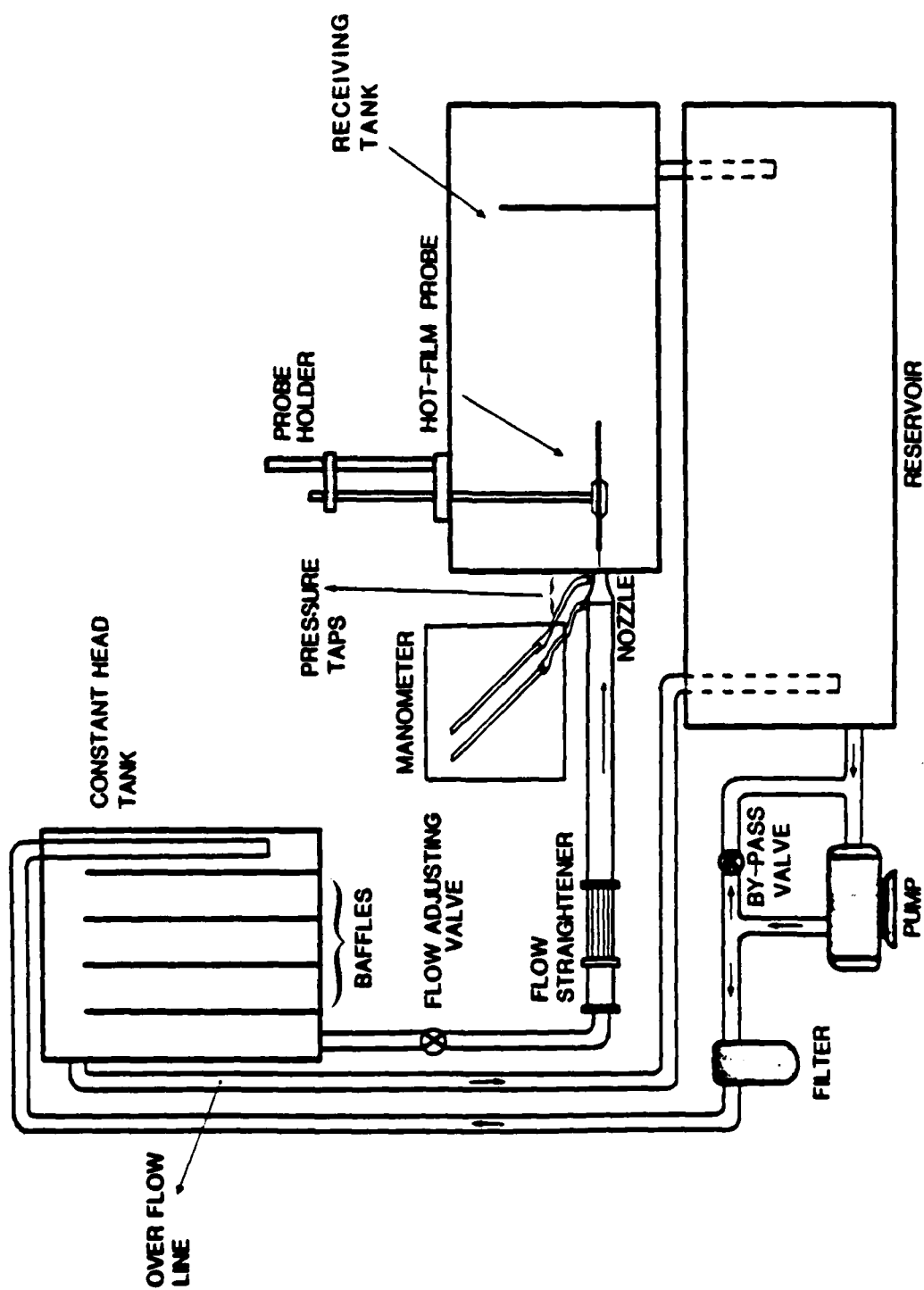


Figure 4 Water calibration facility

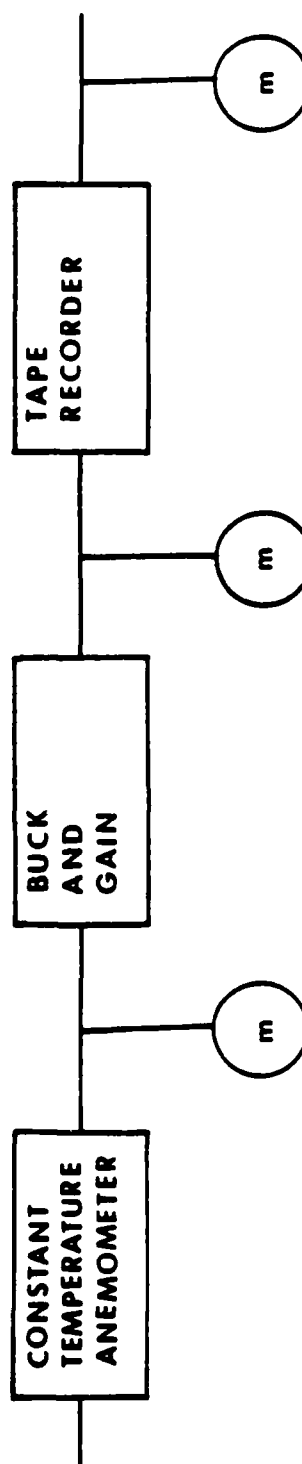


Figure 5 Block diagram of signal processing electronics

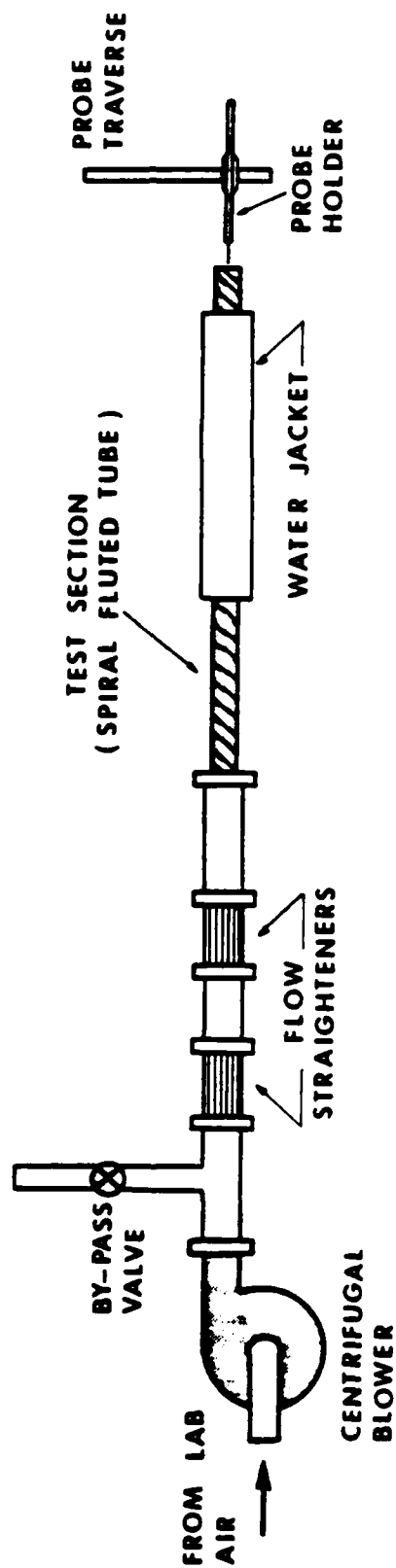


Figure 6 Schematic of air flow facility



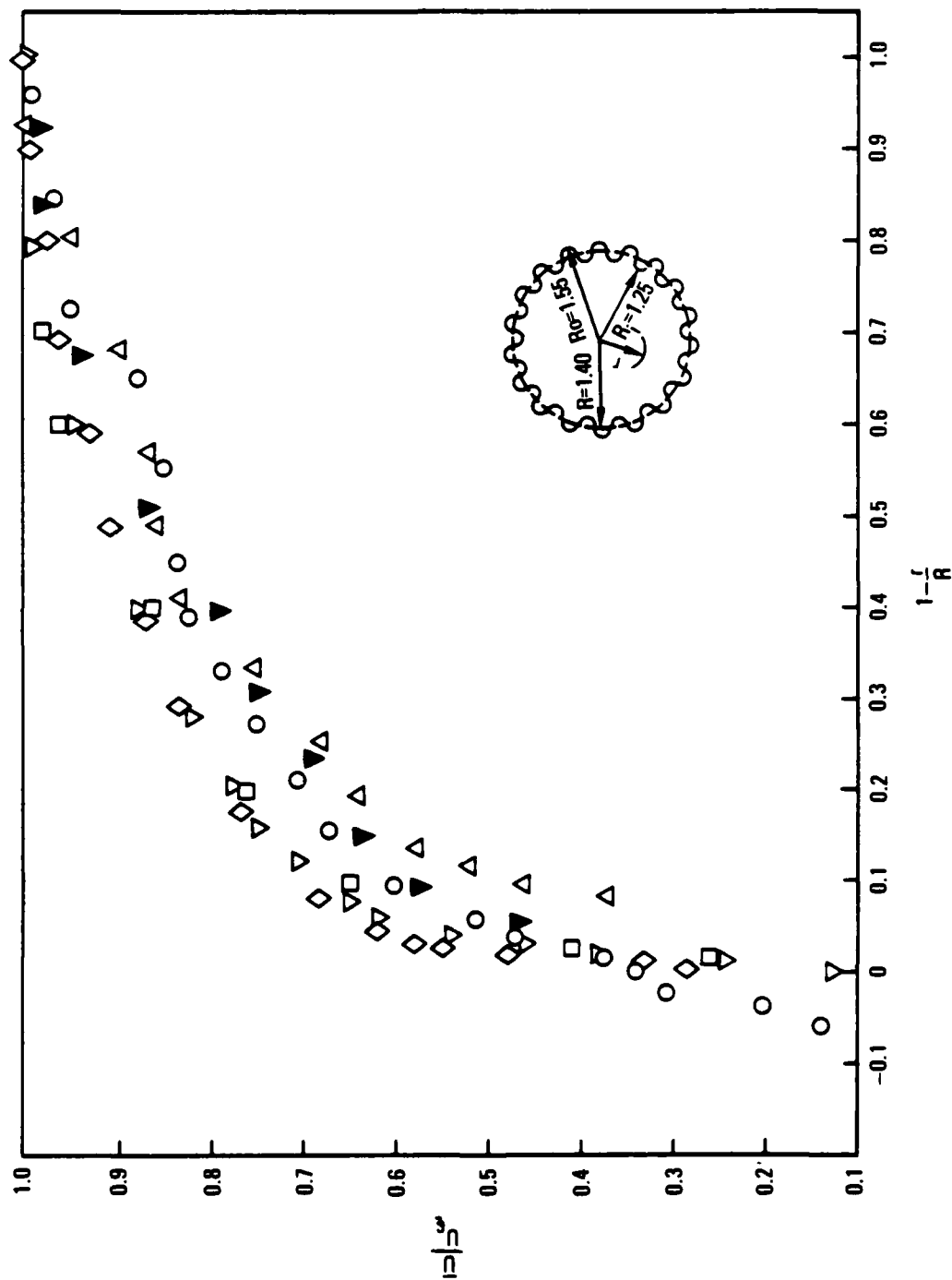


Figure 7 Mean axial velocity normalized by the centerline velocity for the water flow: crest to centerline,  $\Delta$ ; valley to centerline,  $\circ$ ; smooth tube data of Laufer (1953),  $\diamond$ ; smooth tube data of Schildknecht, Miller, Meier (1979),  $\nabla$ ; smooth tube data of Sandborn (1955),  $\square$ ; fluted tube data of Silberman (1980),  $\blacktriangledown$ .

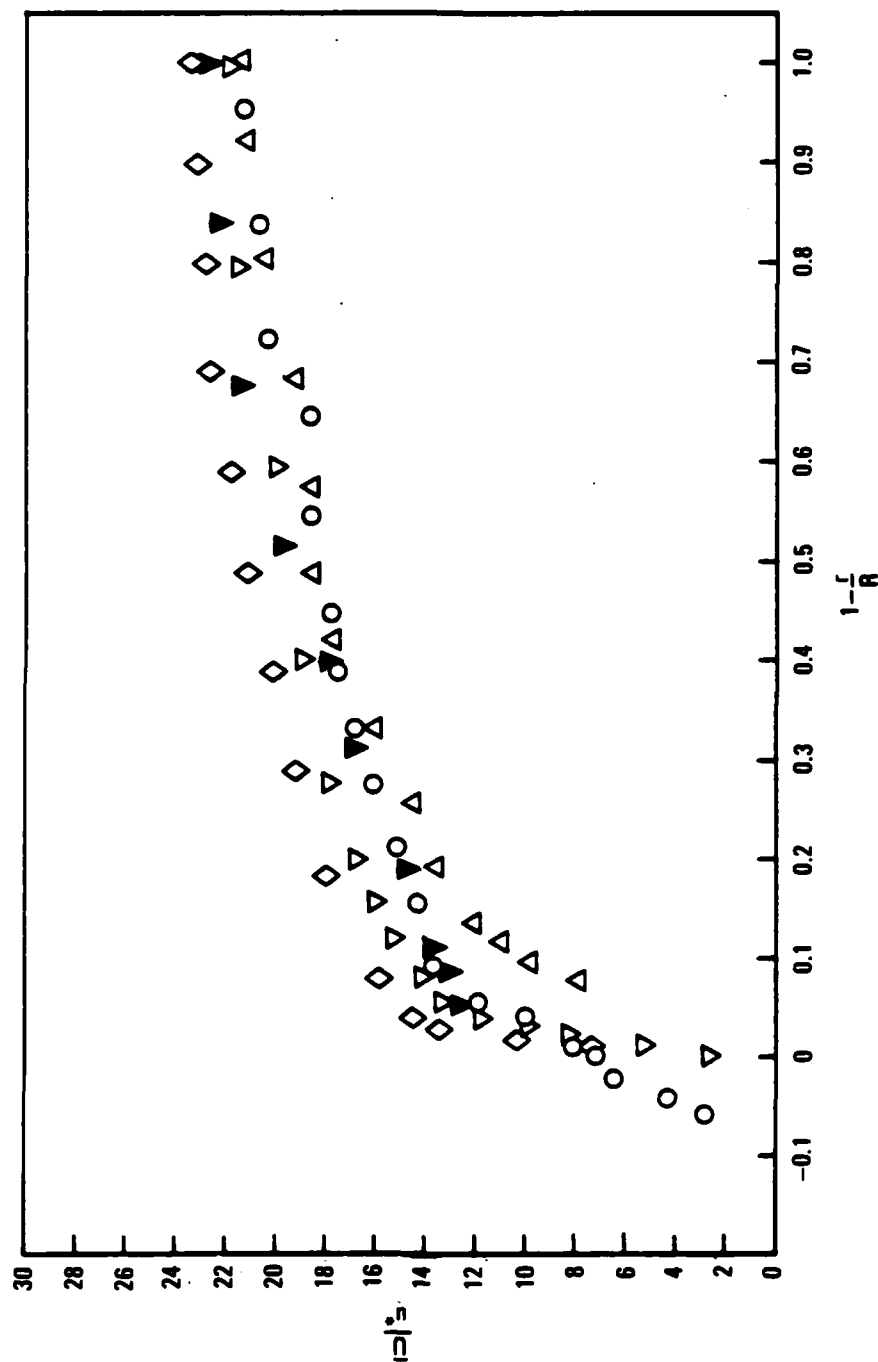


Figure 8 Mean axial velocity normalized by the friction velocity for the water flow. (Same symbols as Figure 7).

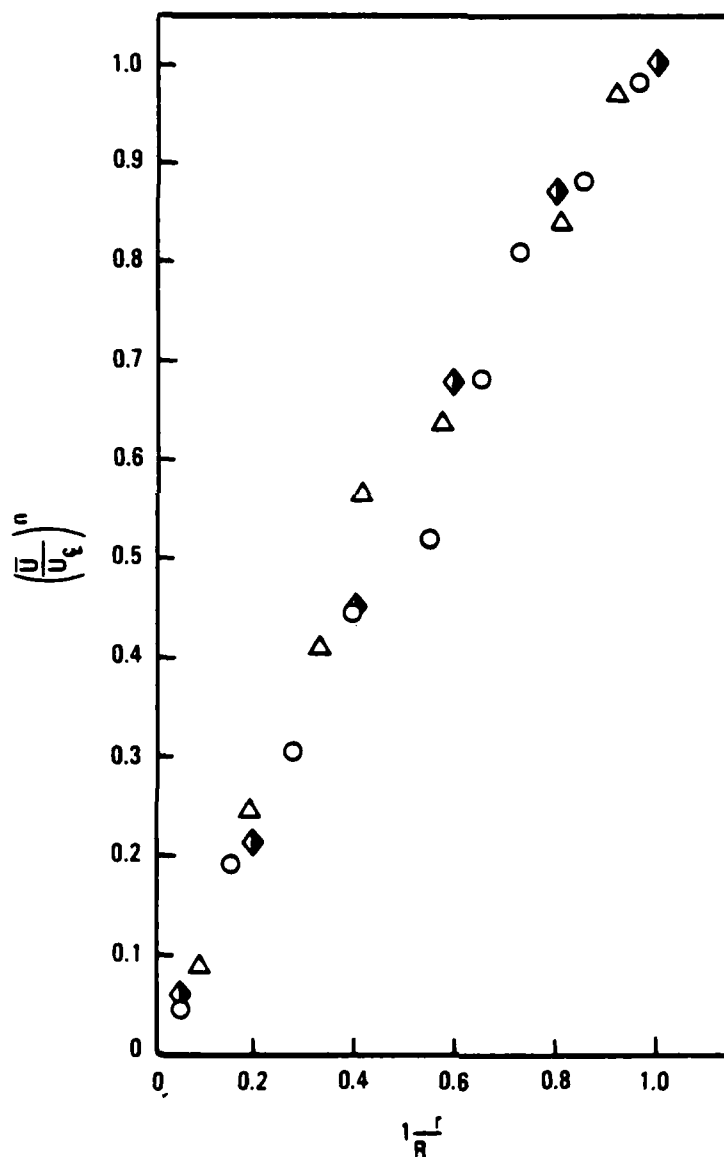


Figure 9 Power law dependence of normalized mean axial velocity for the water flow: crest to centerline with  $n=3.1$ ,  $\Delta$  ; valley to centerline with  $n=4.1$ ,  $\circ$  ; smooth tube data of Nikuradse at  $Re = 4 \times 10^3$  with  $n=6.0$  (from Schlichting (1979)),  $\blacklozenge$  .

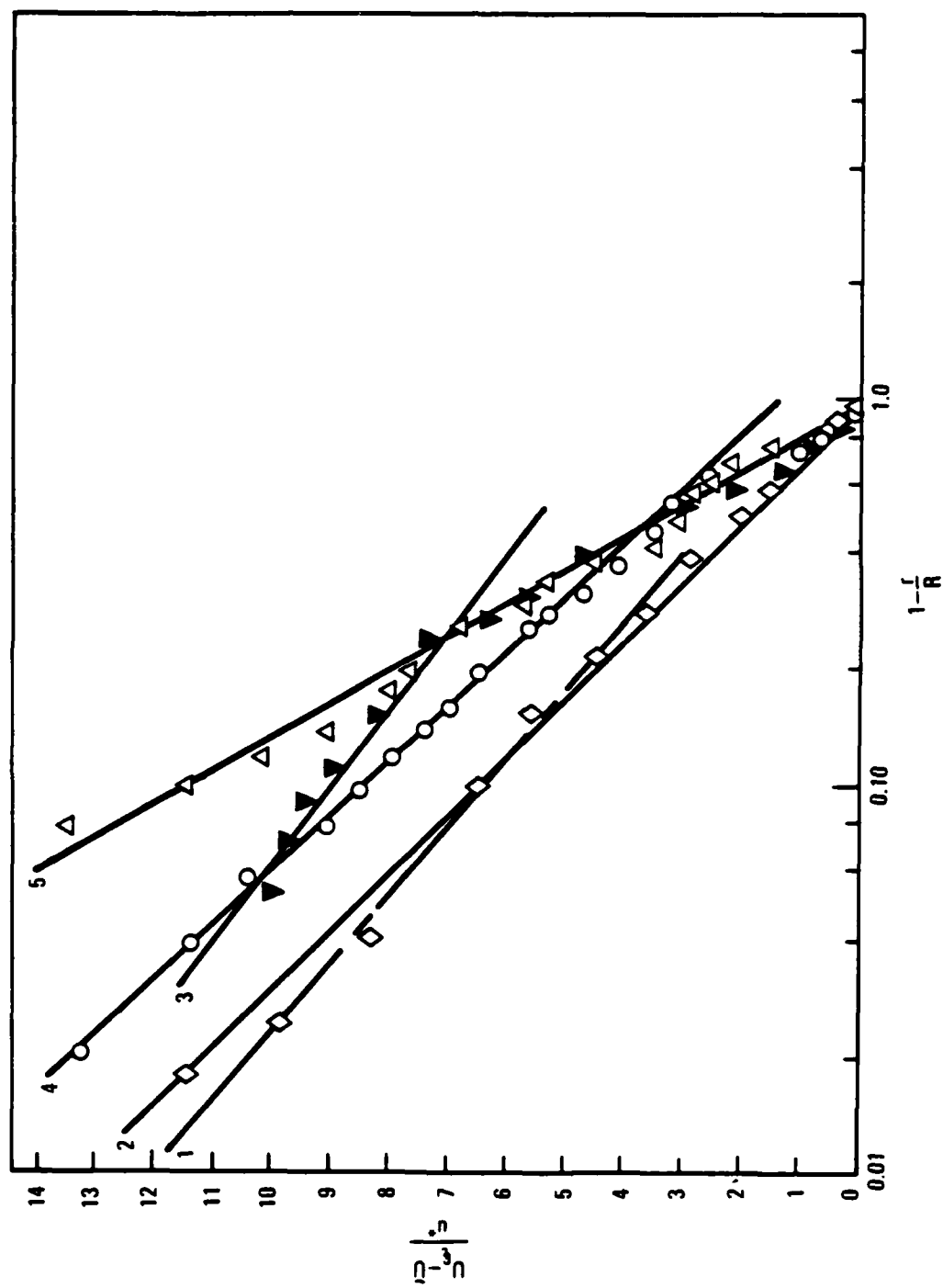


Figure 10 Universal logarithmic velocity distribution for the water flow.  
(Same symbols as Figure 7).

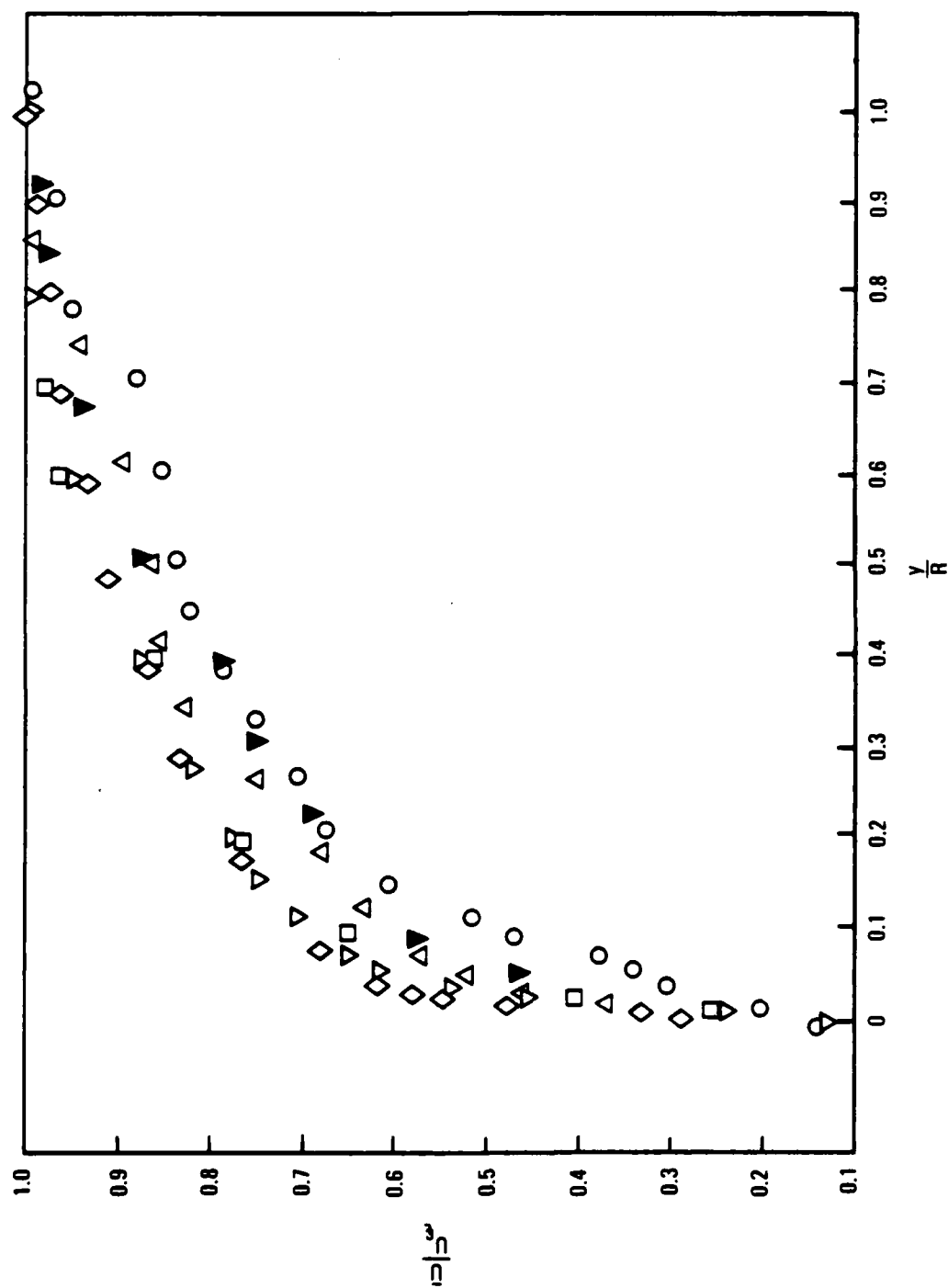


Figure 11 Normalized mean velocity distribution as a function of distance from the nearest solid surface for the water flow. (Same symbols as Figure 7).

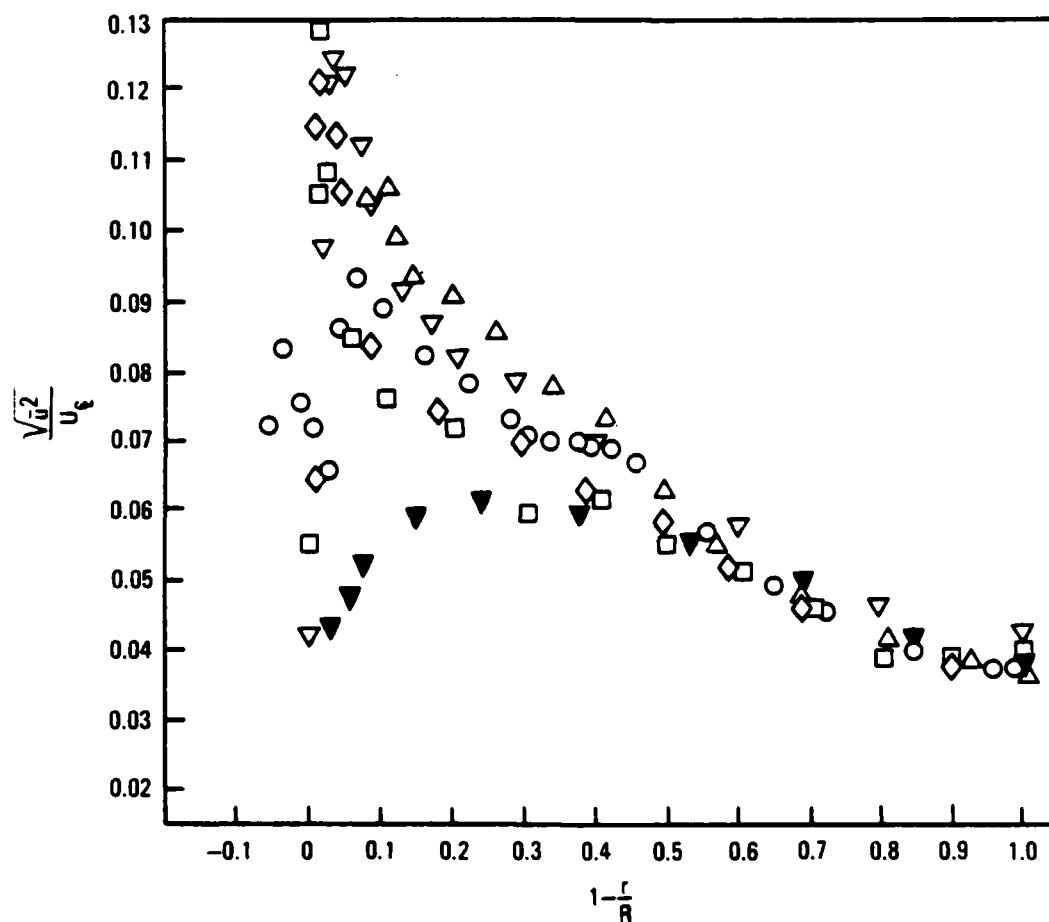


Figure 12 Root mean square axial velocity normalized by the mean centerline velocity for the water flow. (Same symbols as Figure 7).

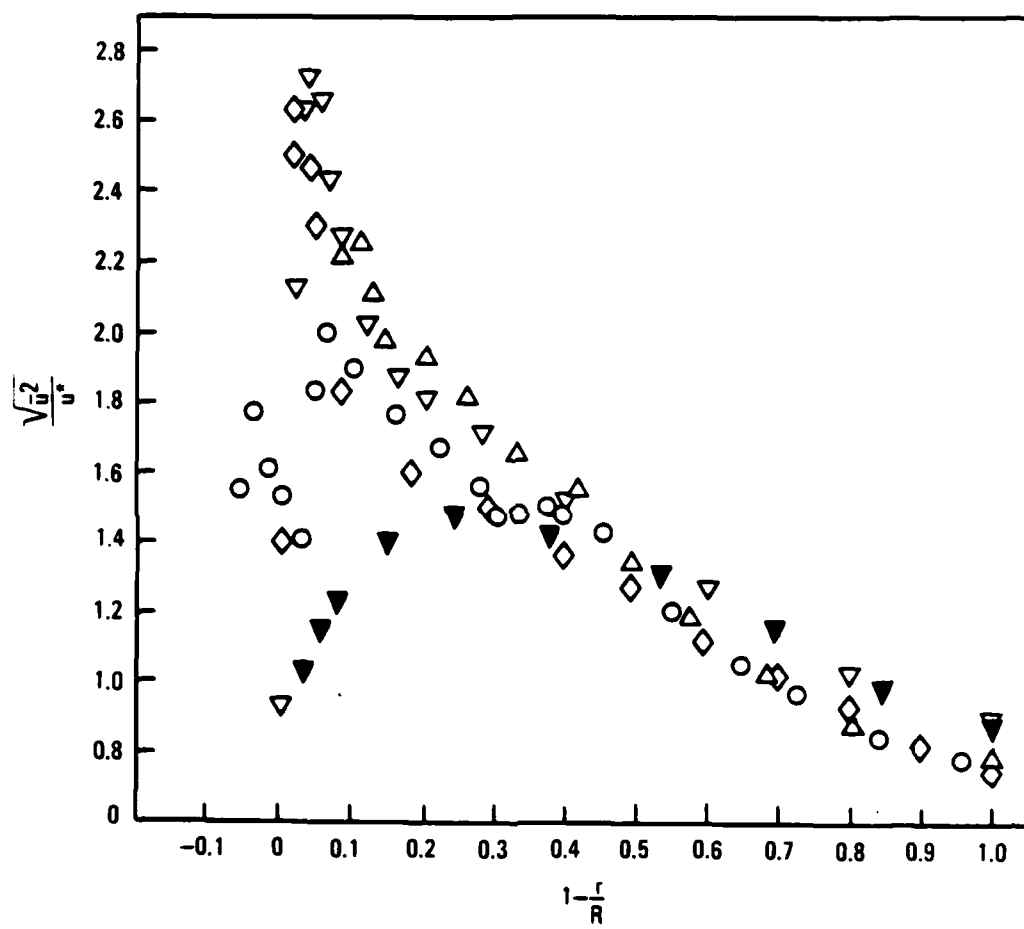


Figure 13 Root mean square axial velocity normalized by the friction velocity for the water flow. (Same symbols as Figure 7).

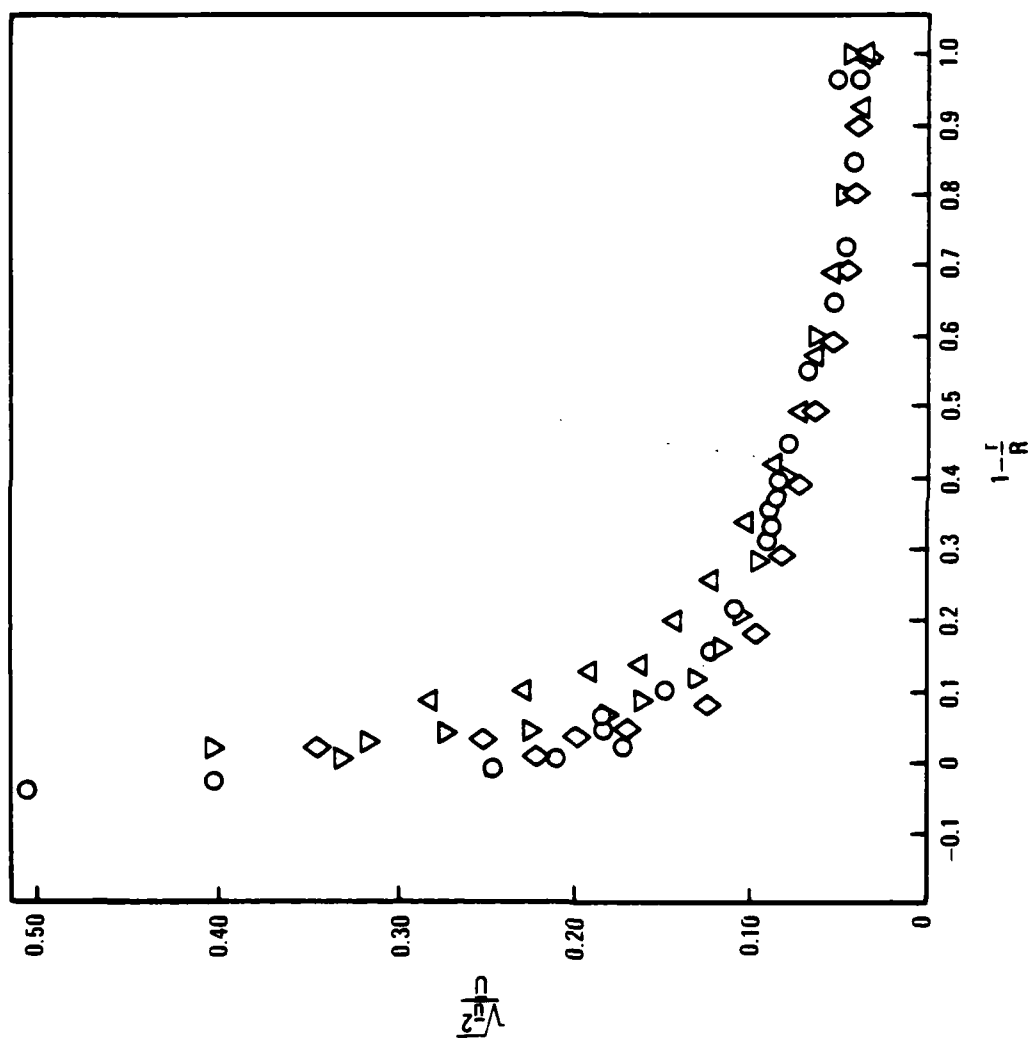


Figure 14 Root mean square axial velocity normalized by the local mean velocity for the water flow. (Same symbols as Figure 7).



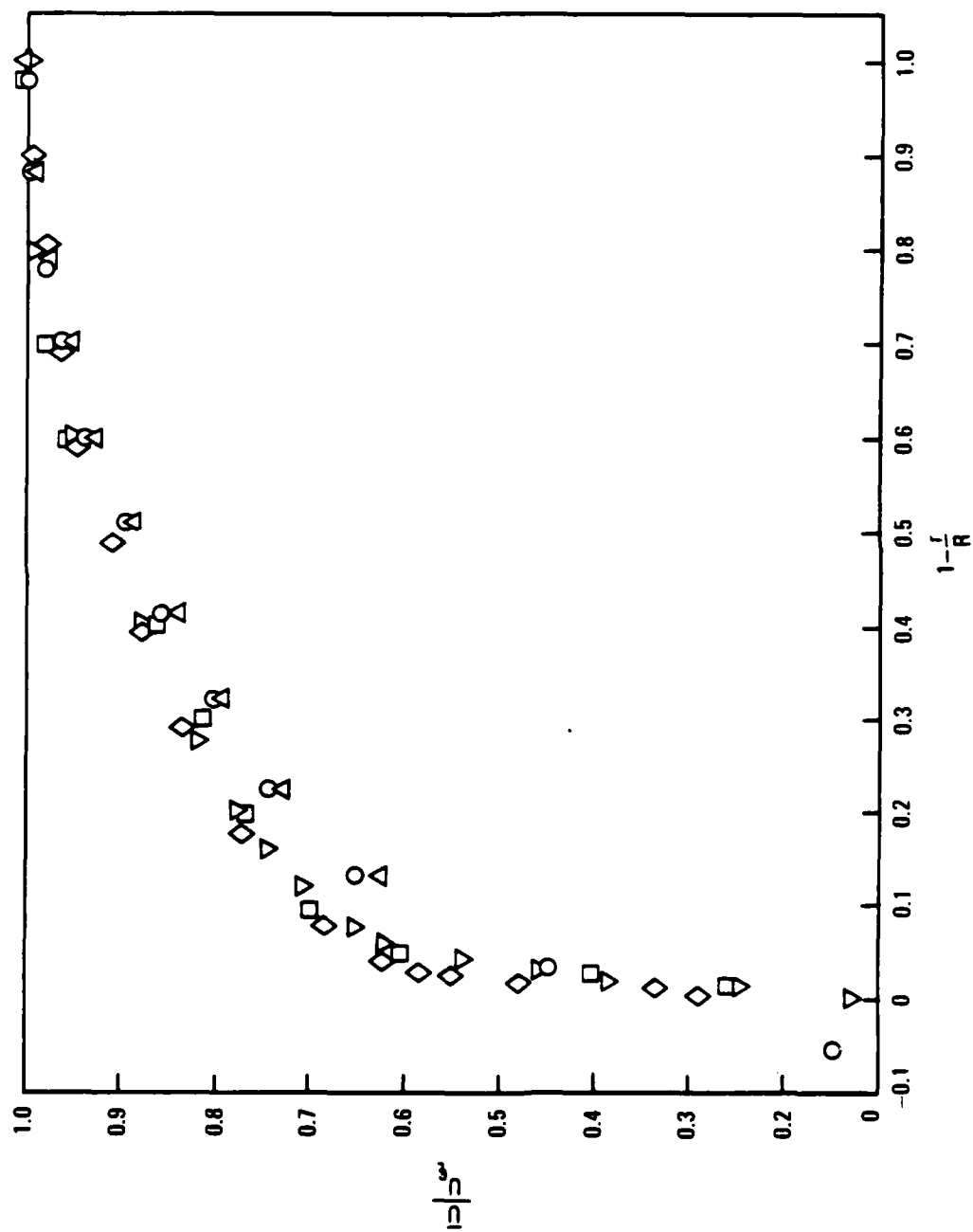


Figure 15 Mean axial velocity normalized by the centerline velocity for the air flow. (Same symbols as Figure 7).

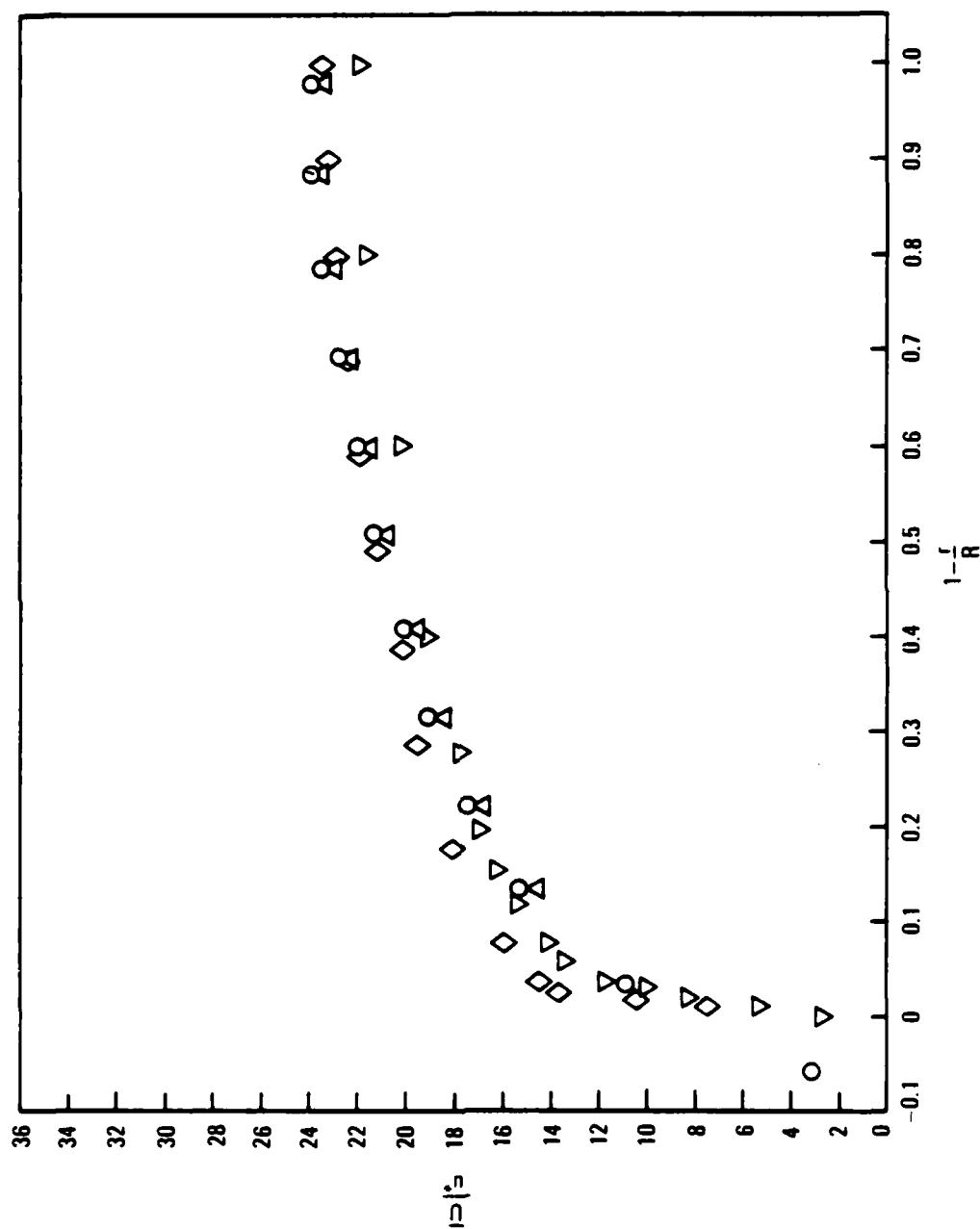


Figure 16 Mean axial velocity normalized by the friction velocity for the air flow. (Same symbols as Figure 7.)

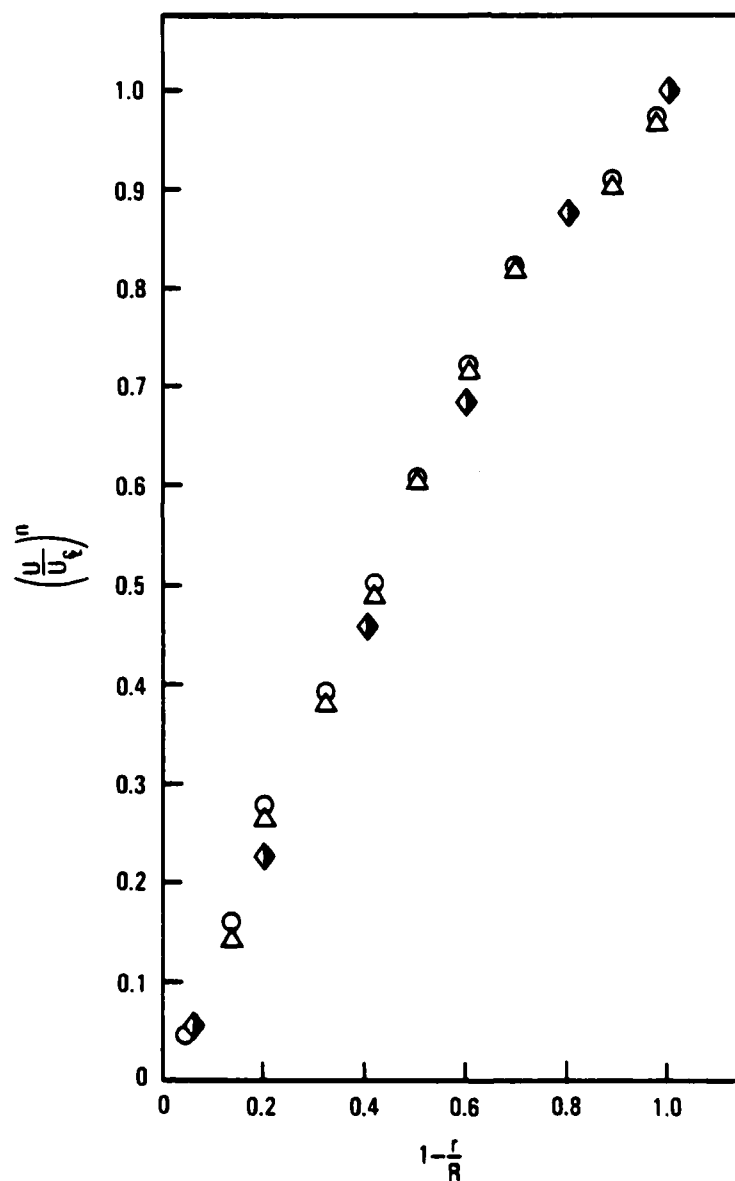


Figure 17 Power law dependence of normalized mean axial velocity for the air flow: crest to centerline with  $n=4.10$ ; valley to centerline with  $n=4.08$ , ; smooth tube data of Nikuradse at  $Re = 2.3 \times 10^4$  with  $n=6.6$  (from Schlicking (1979)). (Same symbols as Figure 9).

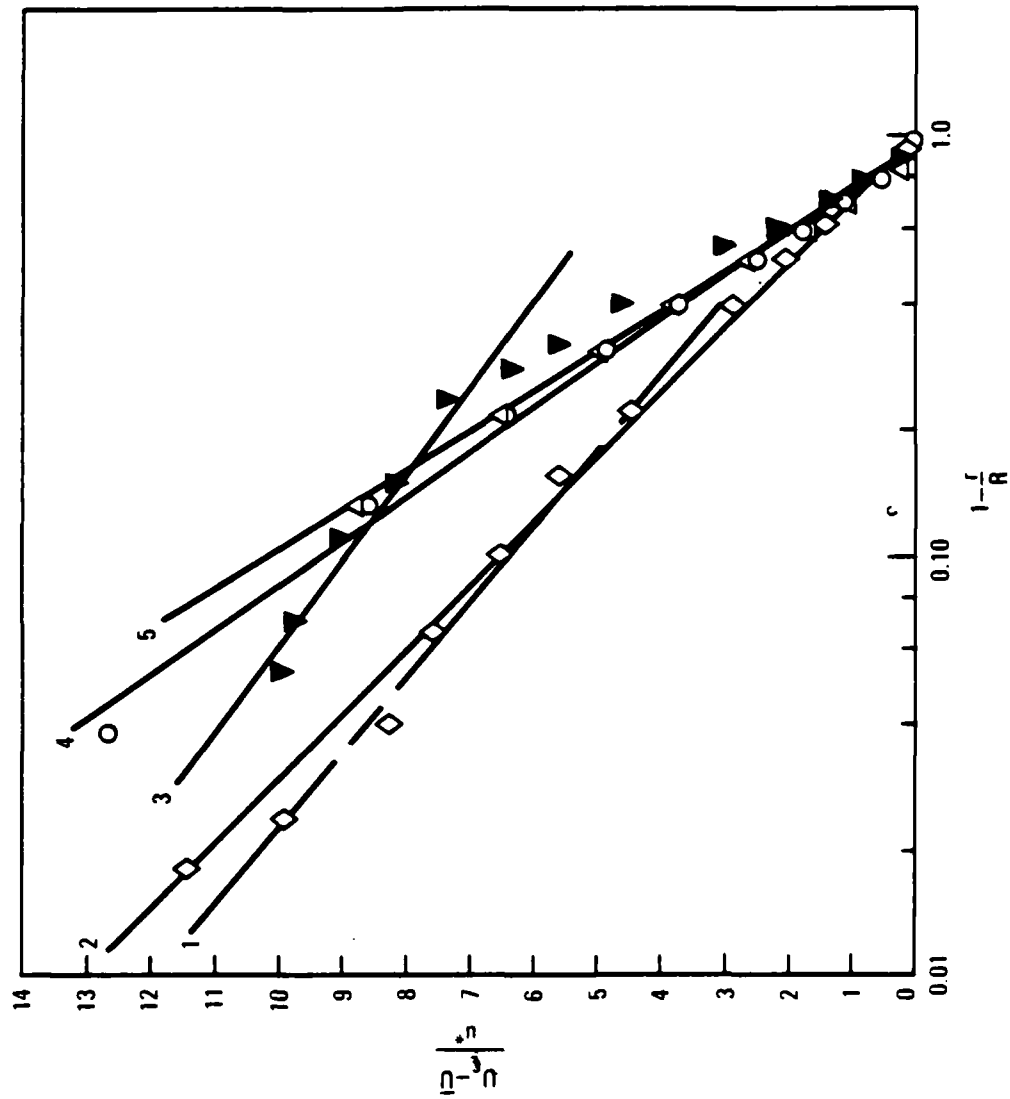


Figure 18 Universal logarithmic velocity distribution for the air flow.  
(Same symbols as Figure 7).

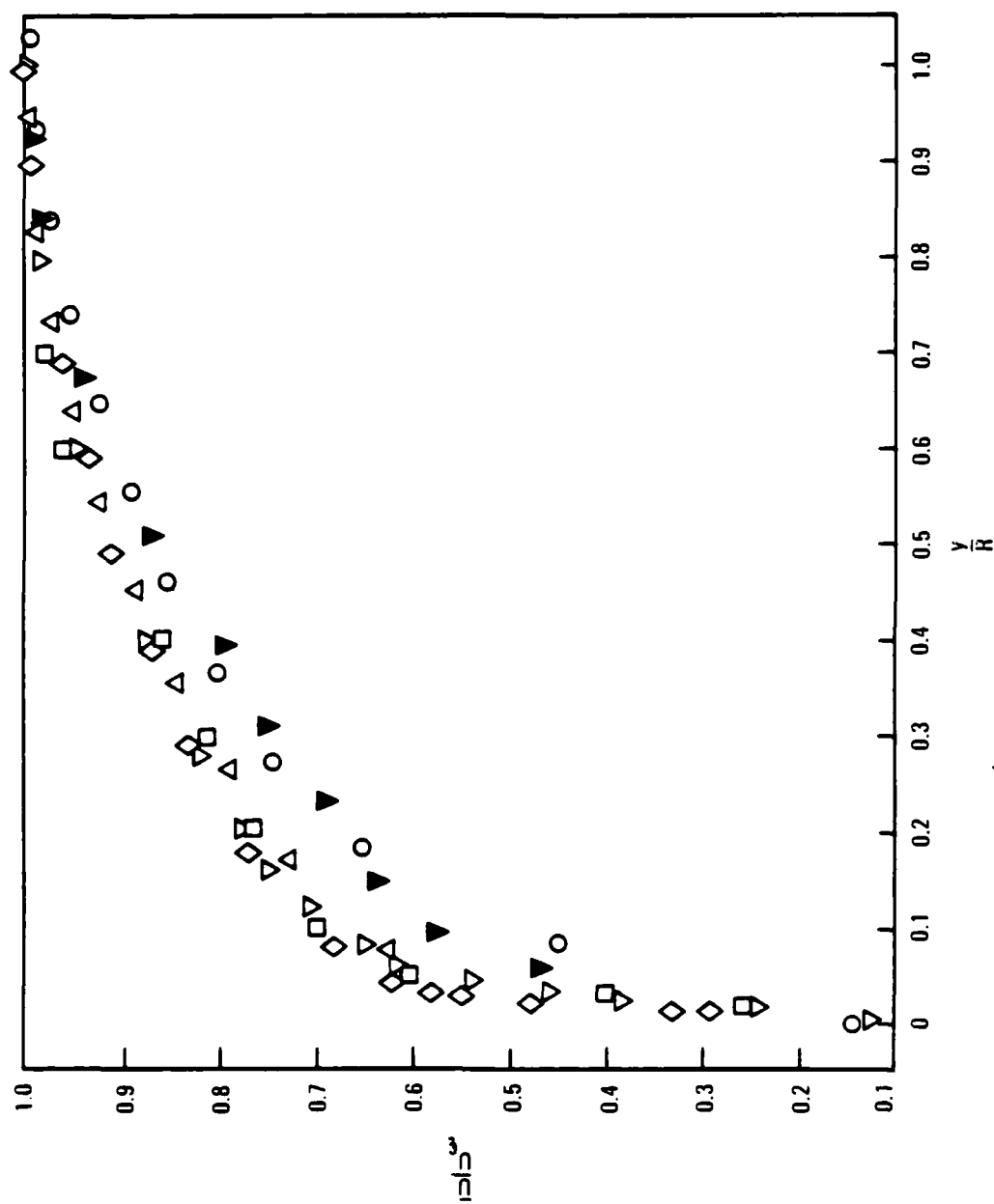


Figure 19 Normalized mean velocity distribution as a function of distance from the nearest solid surface for the air flow. (Same symbols as Figure 7).

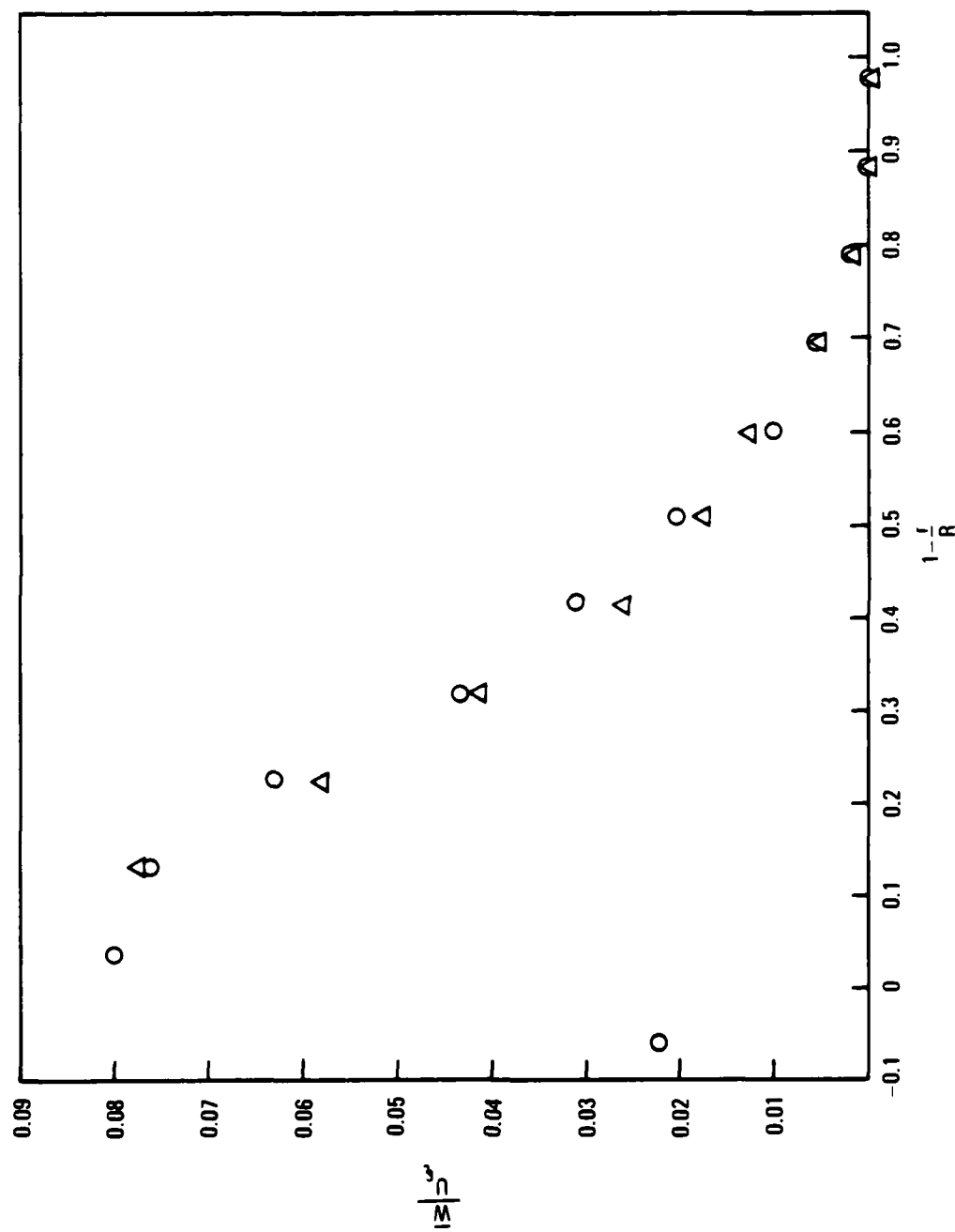


Figure 20 Mean azimuthal velocity normalized by the centerline velocity for the air flow: crest to centerline,  $\Delta$ ; valley to centerline,  $\circ$ .

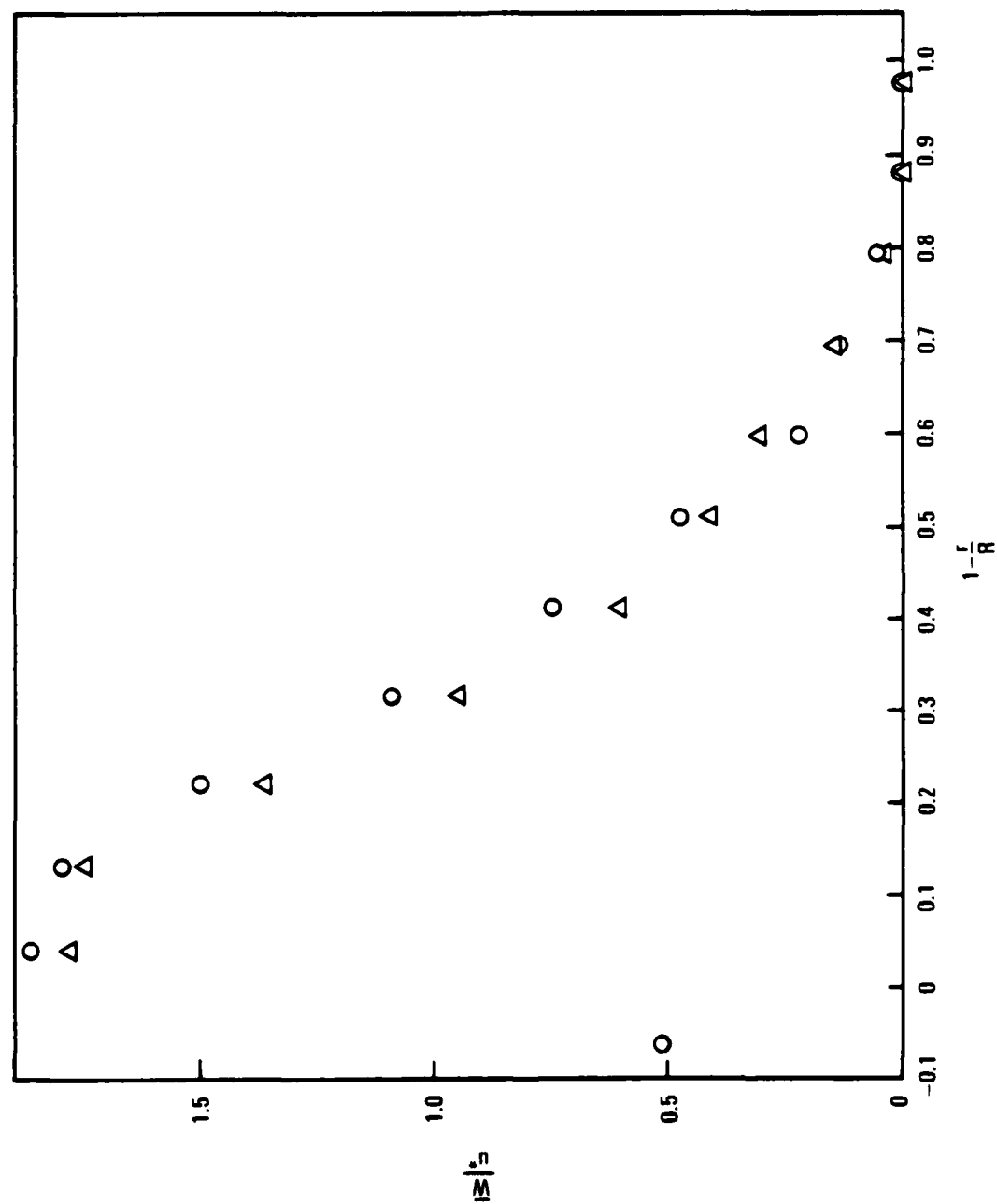


Figure 21 Mean azimuthal velocity normalized by the friction velocity for the air flow. (Same symbols as Figure 20).

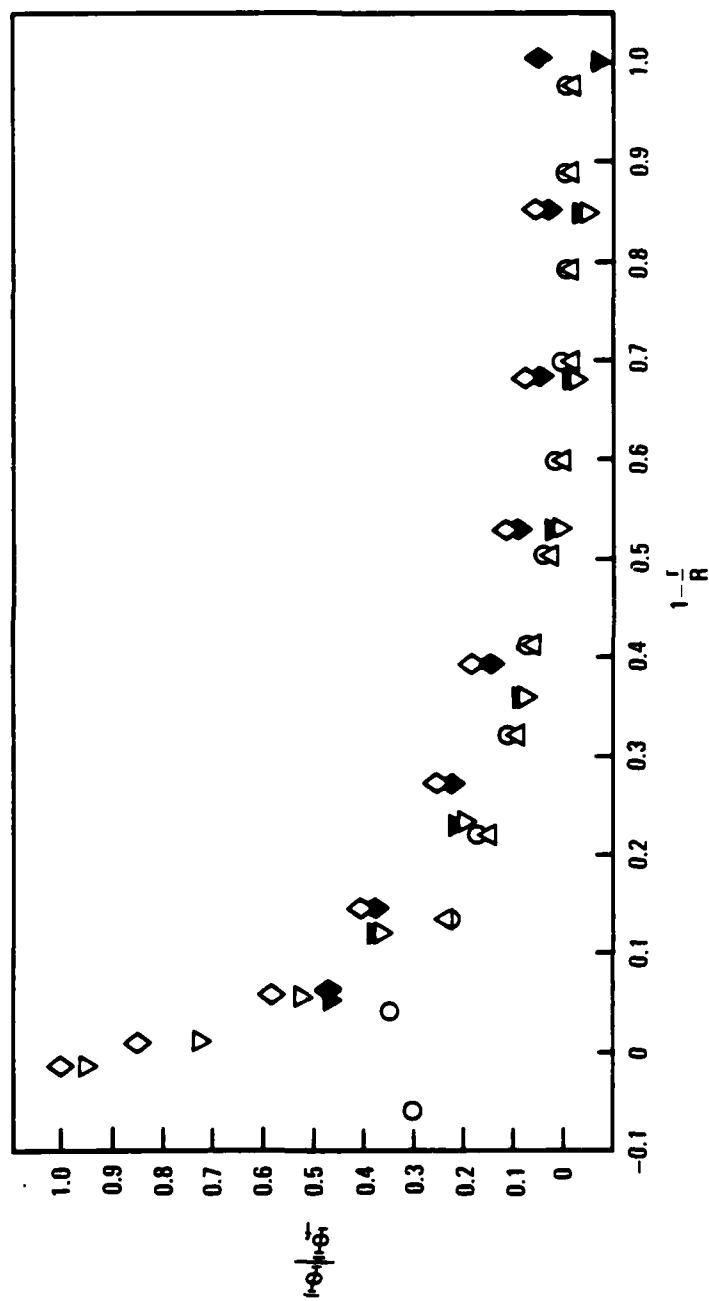


Figure 22 Mean flow angle normalized by the flute angle: crest data,  $\Delta$ ; valley data,  $\circ$ ; fluted tube data of Silberman (1980): crest data at top of pipe,  $\diamond$ ; valley data at top of pipe,  $\diamond$ ; crest data at bottom of pipe,  $\nabla$ ; valley data at bottom of pipe,  $\nabla$ .



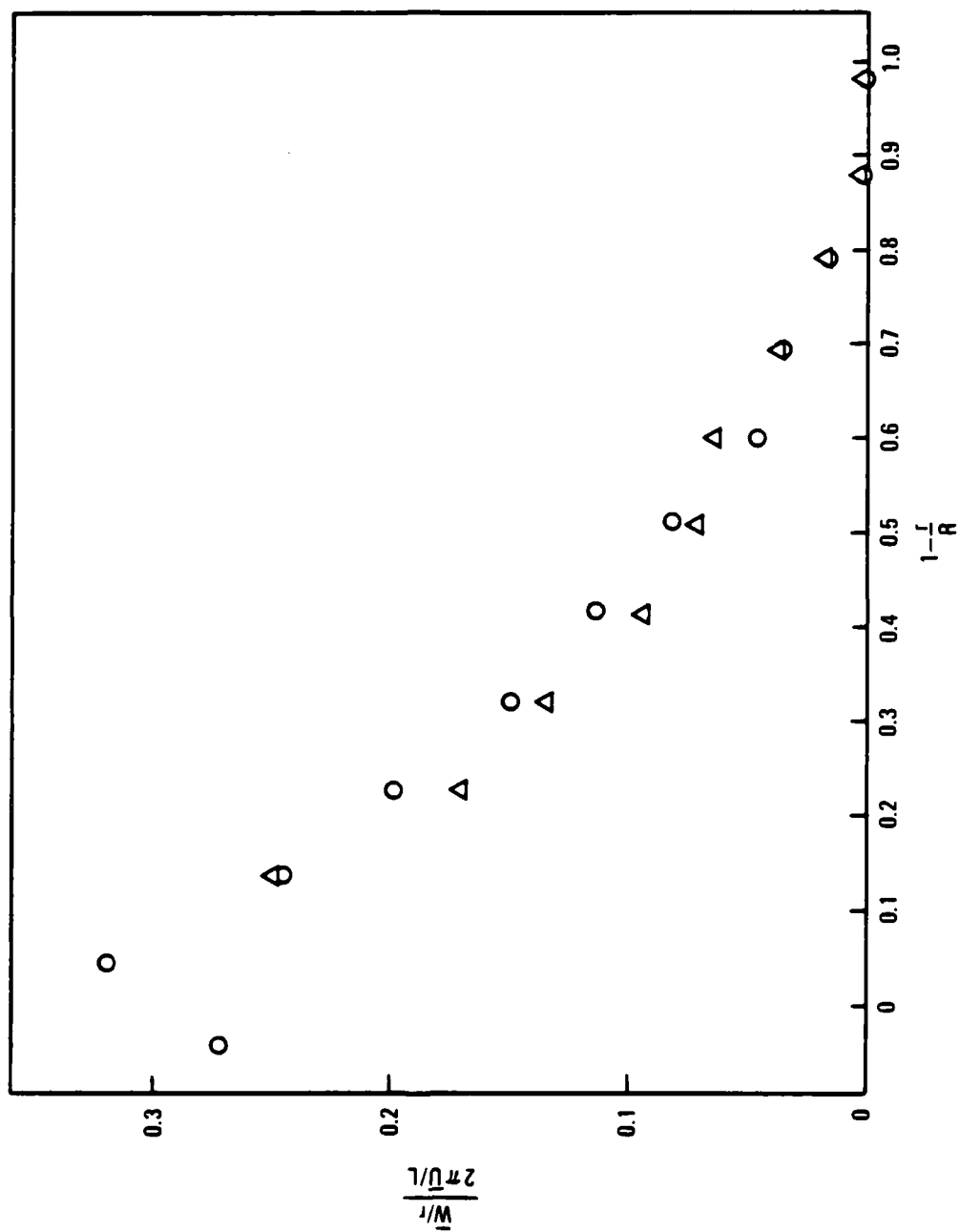


Figure 23 Relative rotation rate: crest data,  $\Delta$ ; valley data,  $\circ$ .

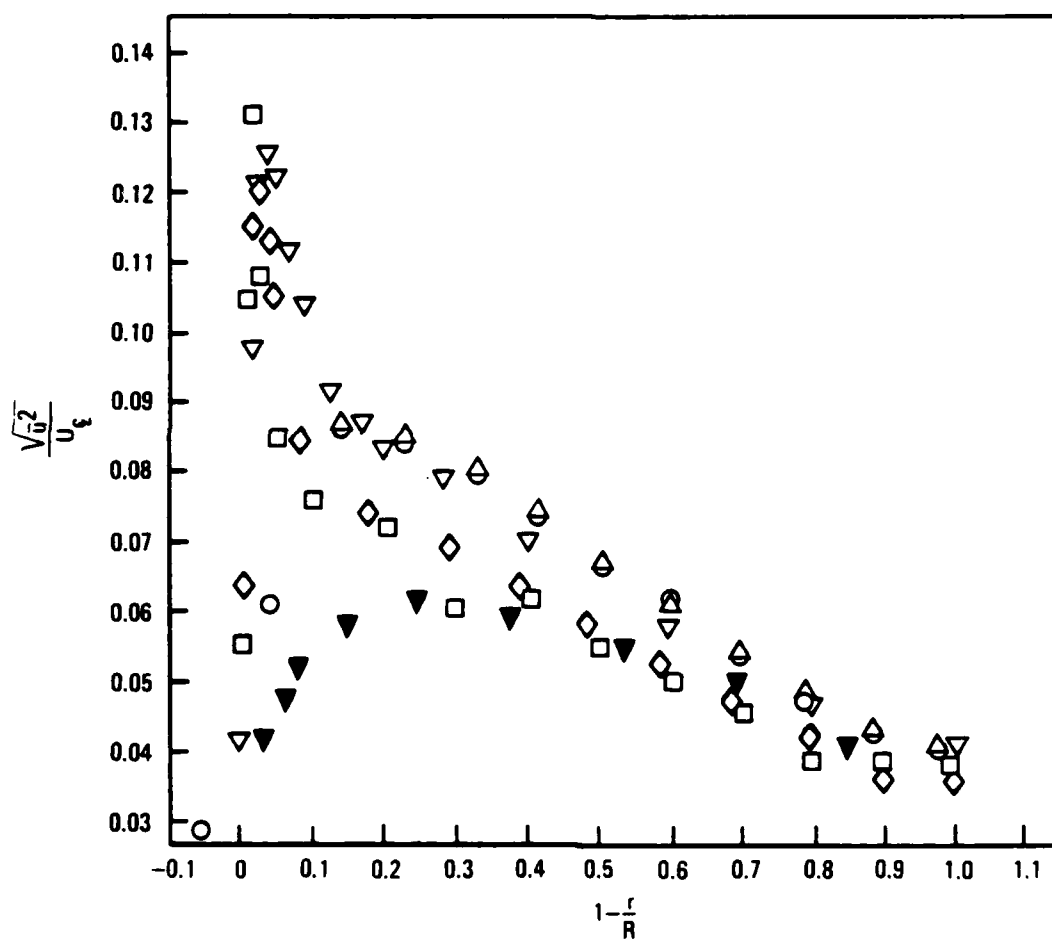


Figure 24 Root mean square axial velocity normalized by the mean centerline velocity for the air flow. (Same symbols as Figure 7).

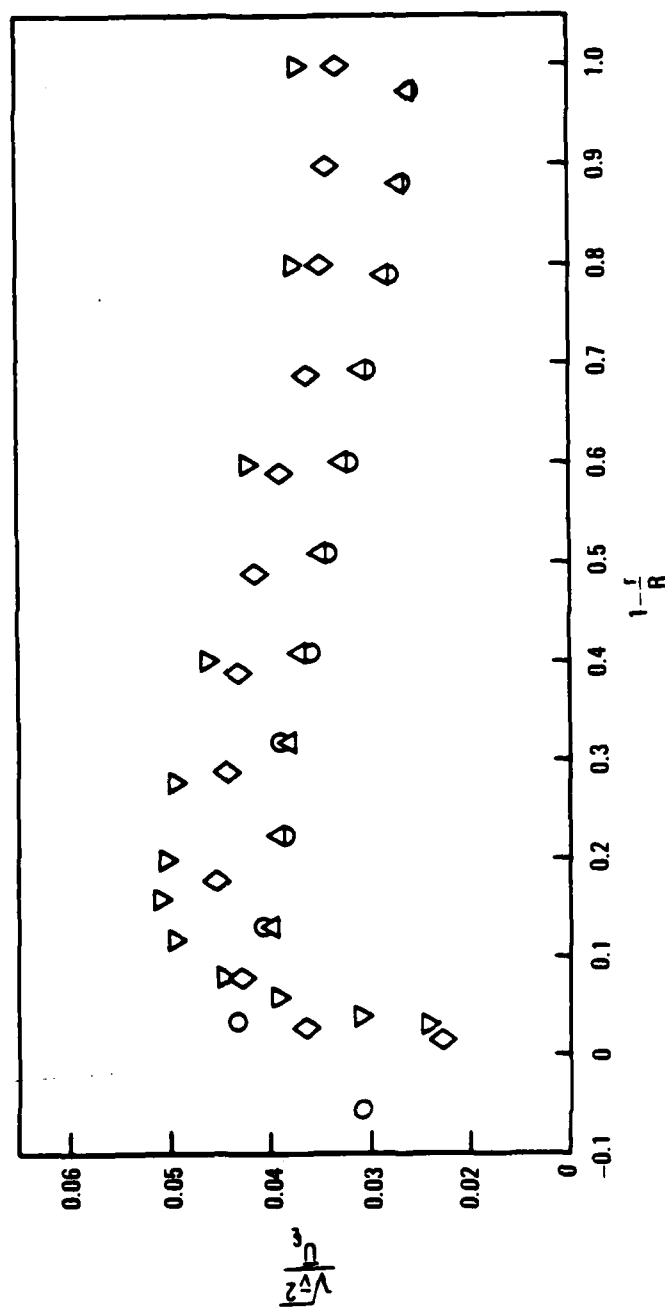


Figure 25 Root mean square radial velocity normalized by the mean centerline velocity for the air flow. (Same symbols as Figure 7).

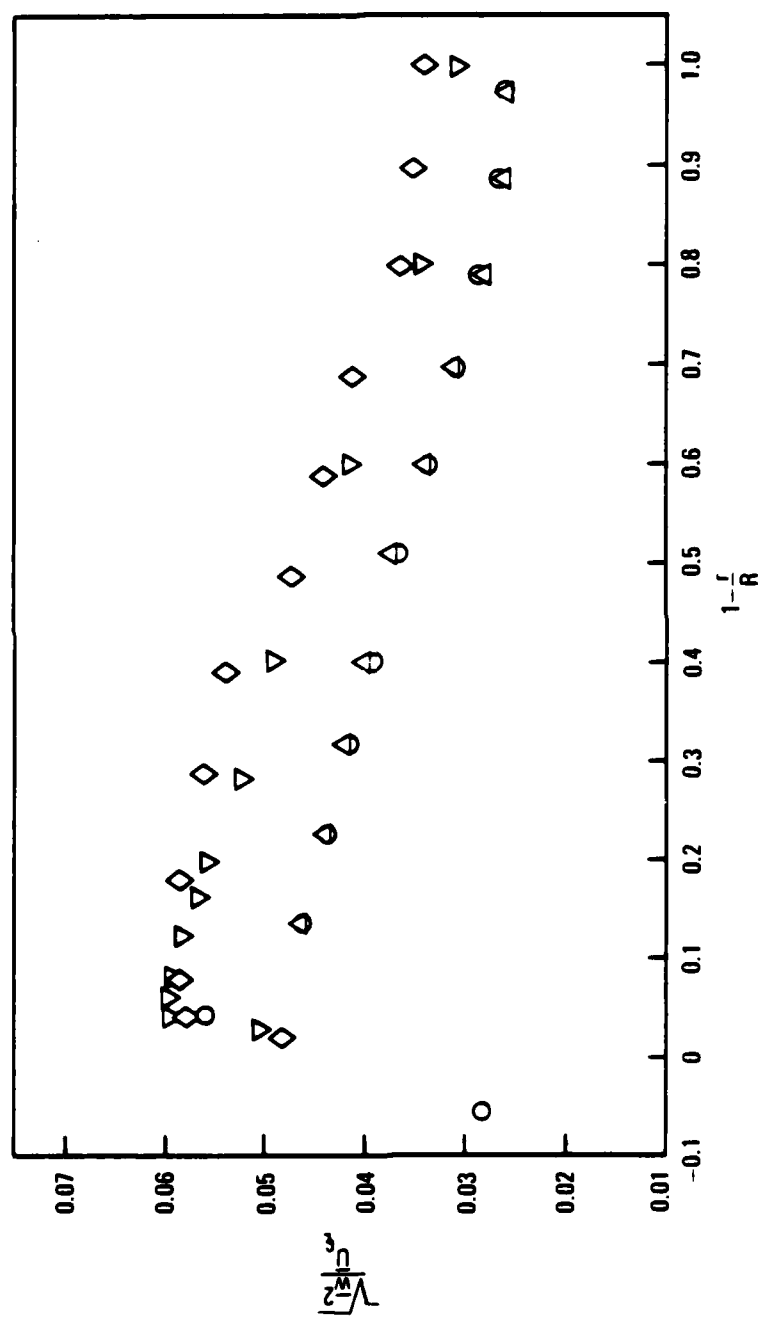


Figure 26 Root mean square azimuthal velocity normalized by the mean centerline velocity for the air flow. (Same symbols as Figure 7).

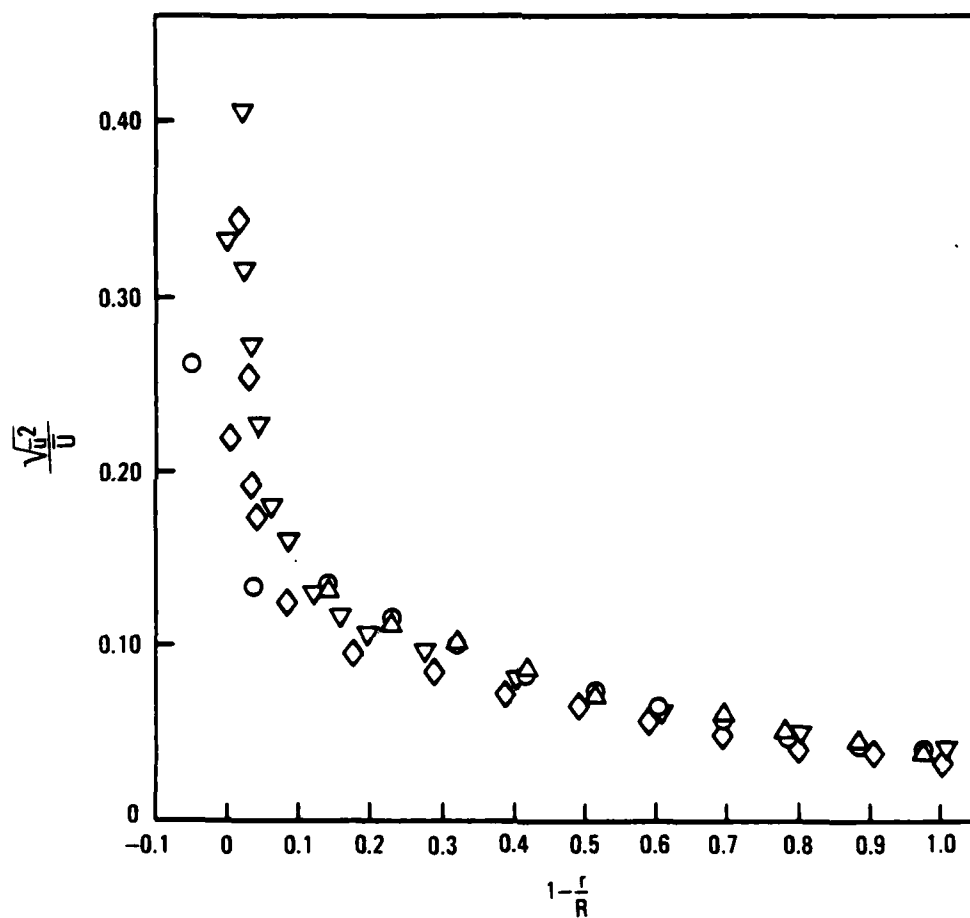


Figure 27 Root mean square axial velocity normalized by the local mean velocity for the air flow. (Same symbols as Figure 7).

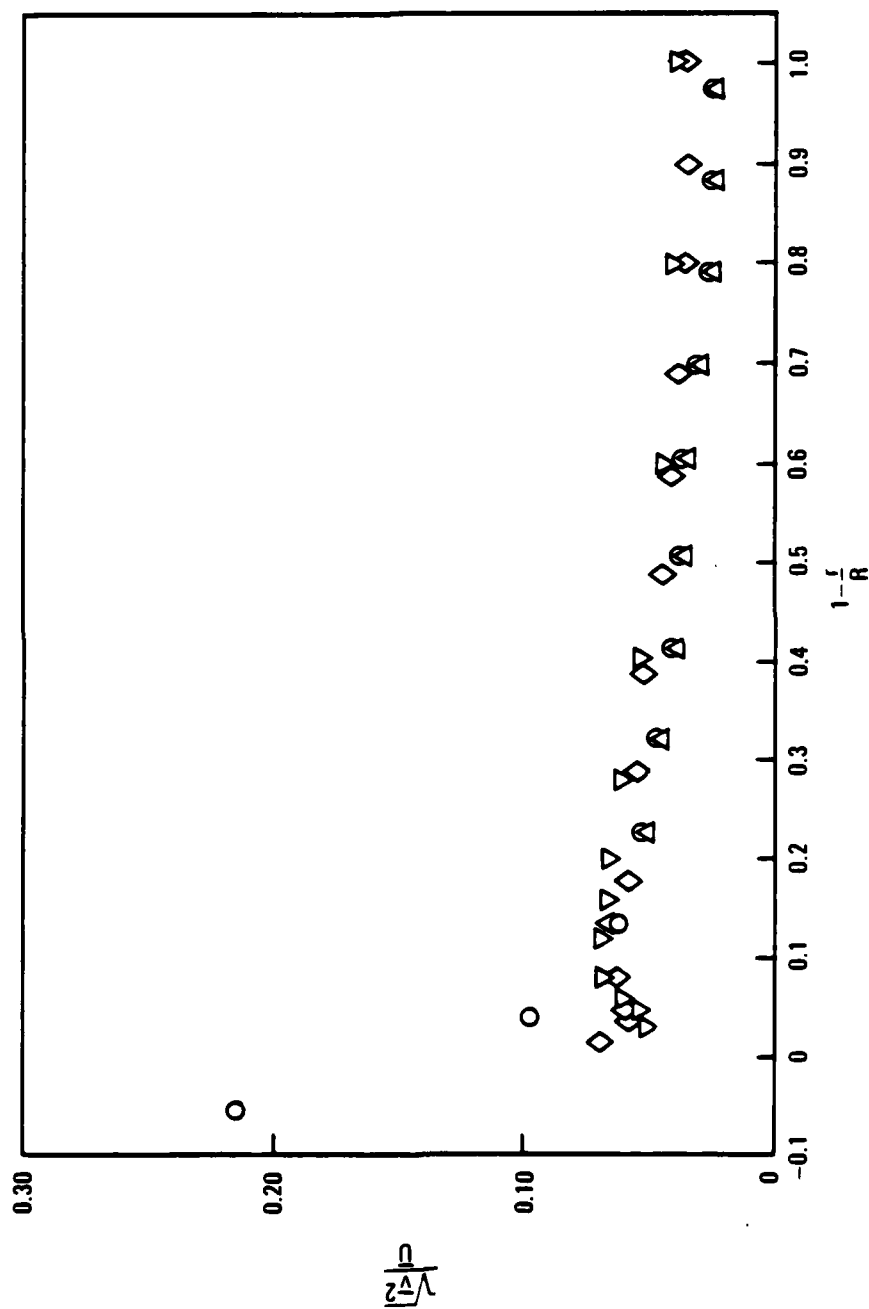


Figure 28 Root mean square radial velocity normalized by the local mean velocity for the air flow. (Same symbols as Figure 7).

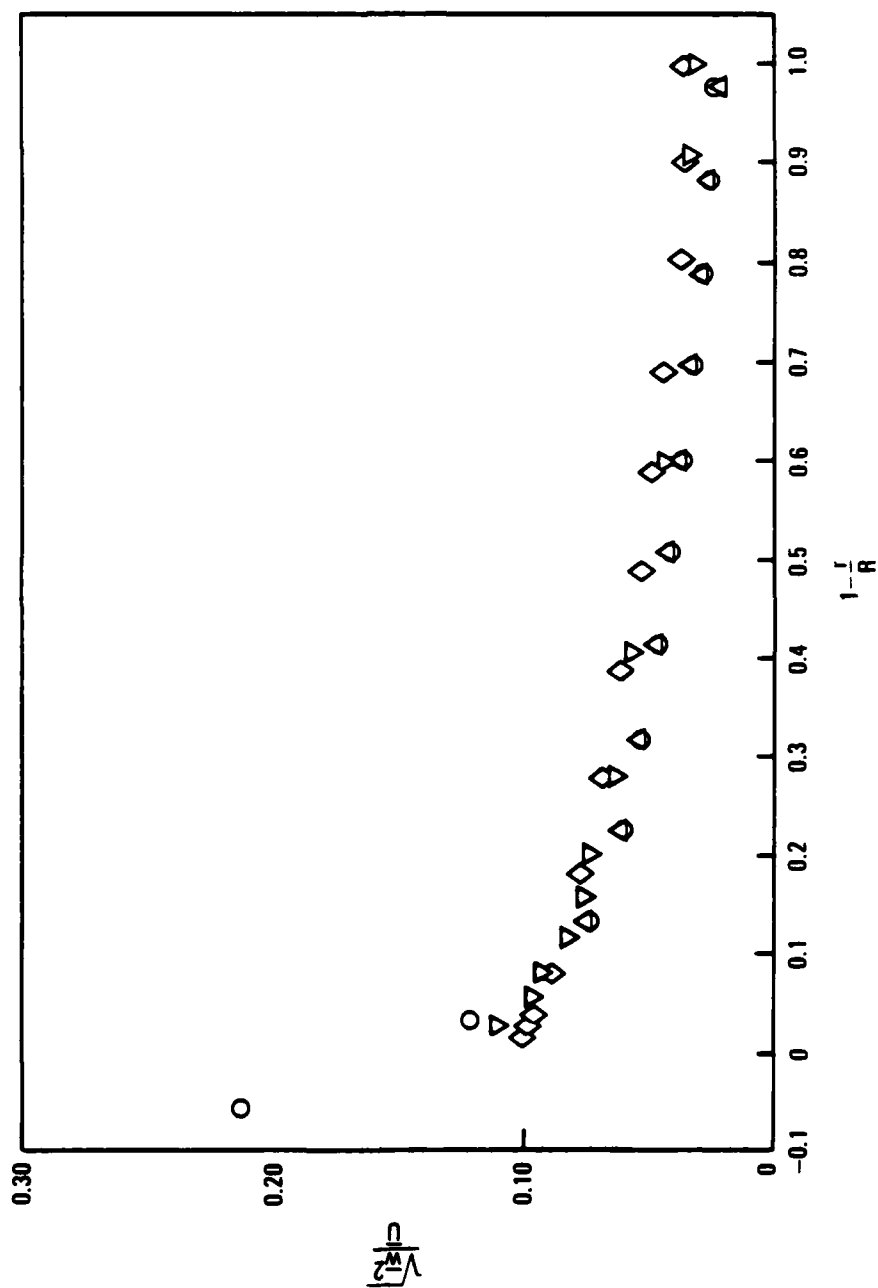


Figure 29 Root mean square azimuthal velocity normalized by the local mean velocity for the air flow. (Same symbols as Figure 7).

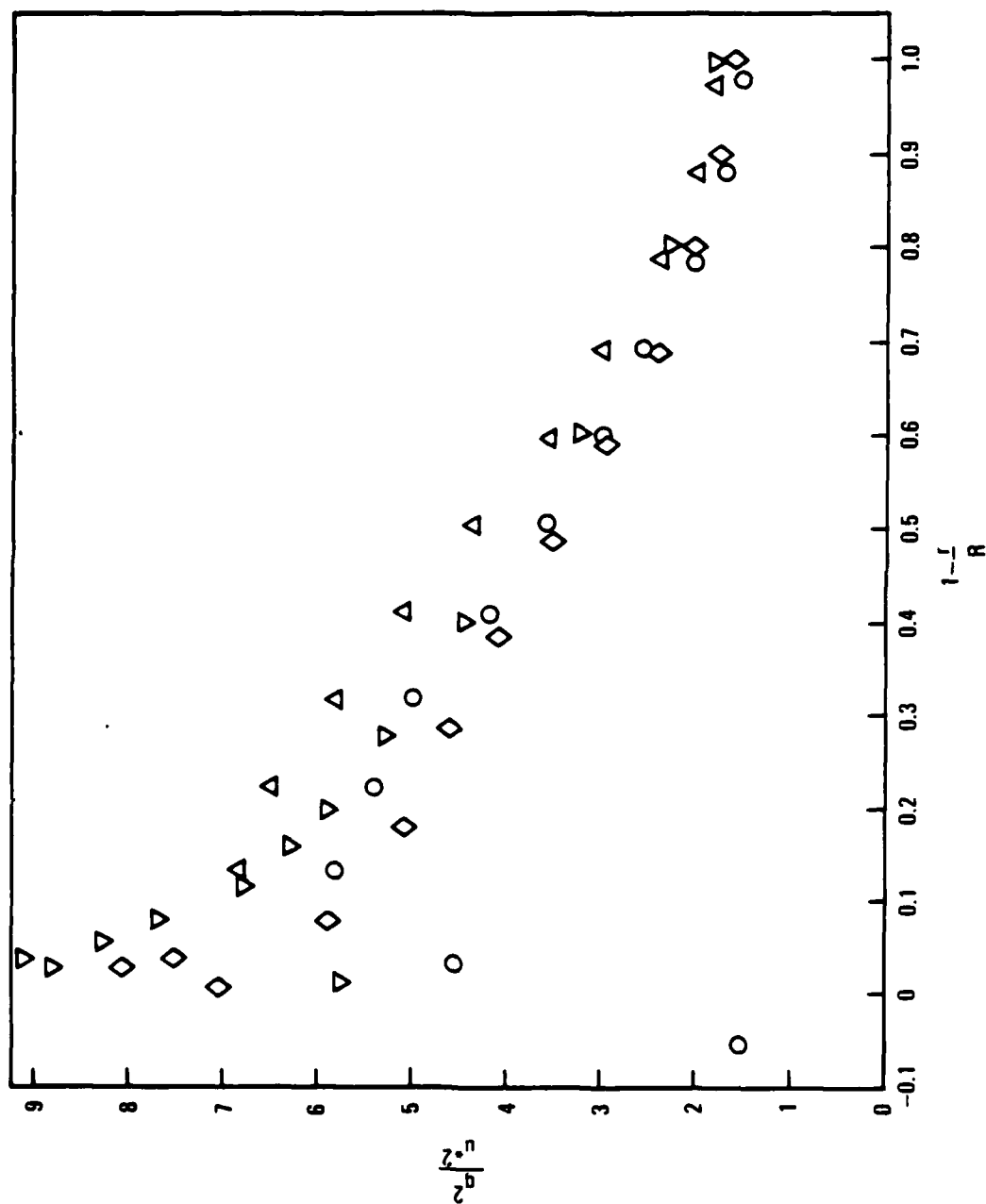


Figure 30 Turbulent kinetic energy normalized by the friction velocity for the air flow. (Same symbols as Figure 7).



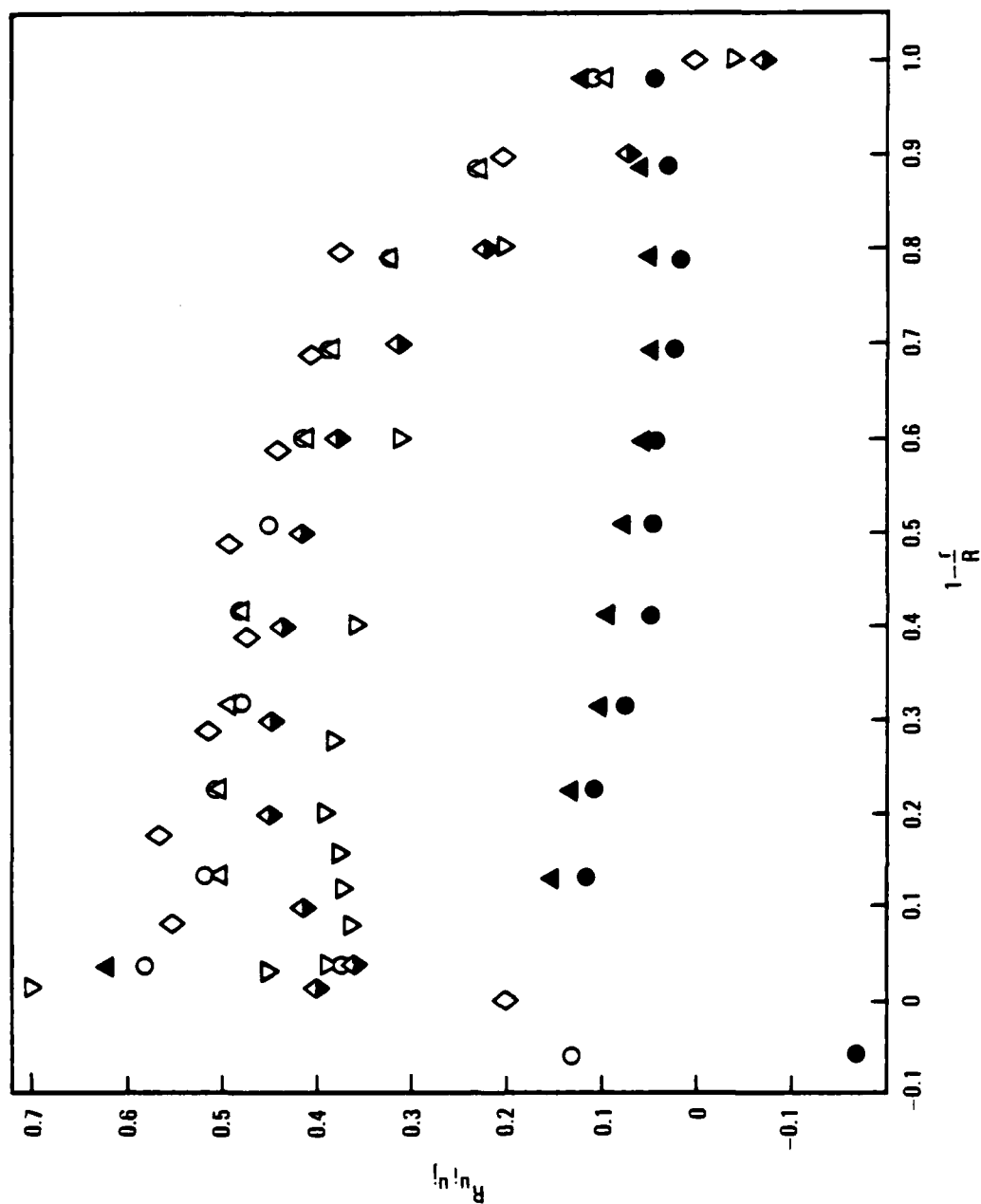


Figure 31 Correlation coefficients for the air flow. Top set of data corresponds to  $R_{uy}$ , while the lower set of data corresponds to  $R_{uw}$ . (Same symbols as Figure 7 but with the addition of Bremhorst and Bullock, (1973),  $\blacklozenge$ ).

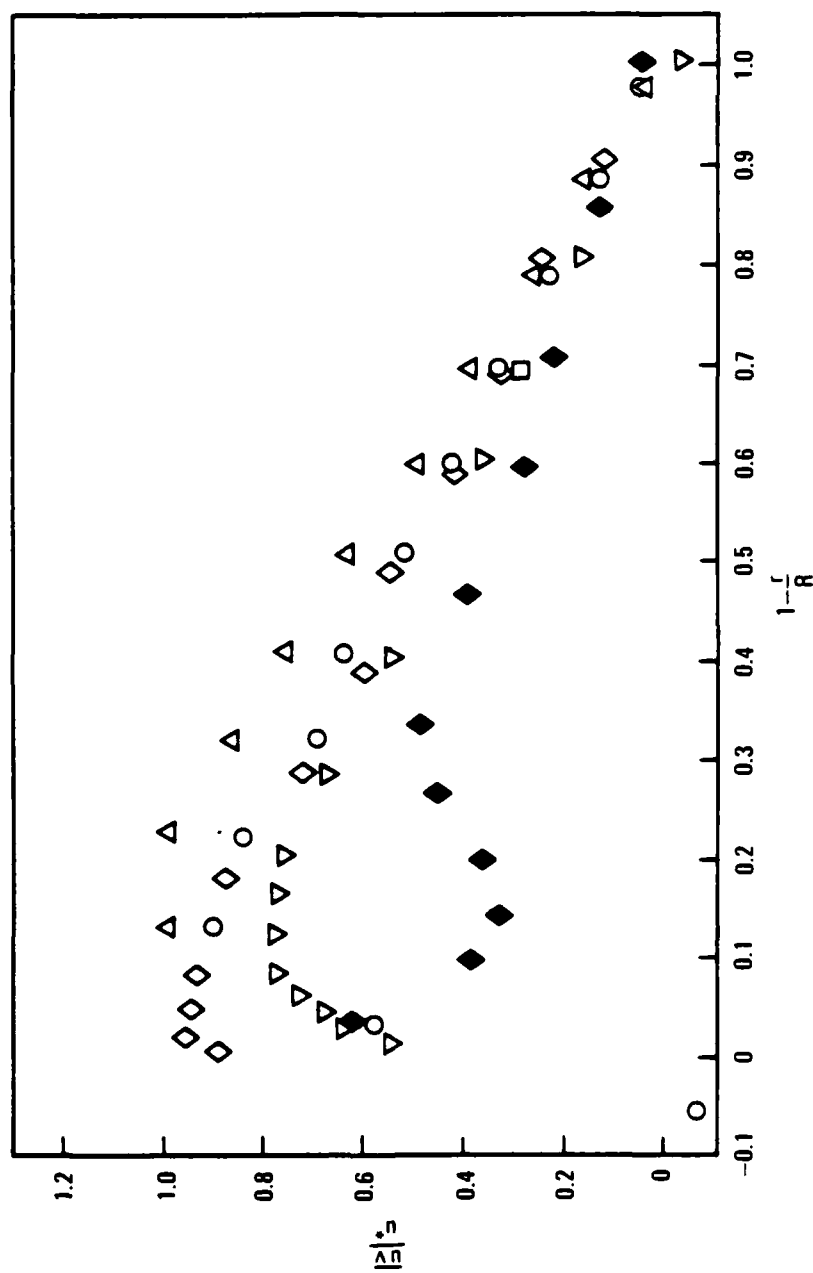


Figure 32 Correlation of axial and radial velocity normalized by the friction velocity squared for the air flow. (Same symbols as Figure 7).

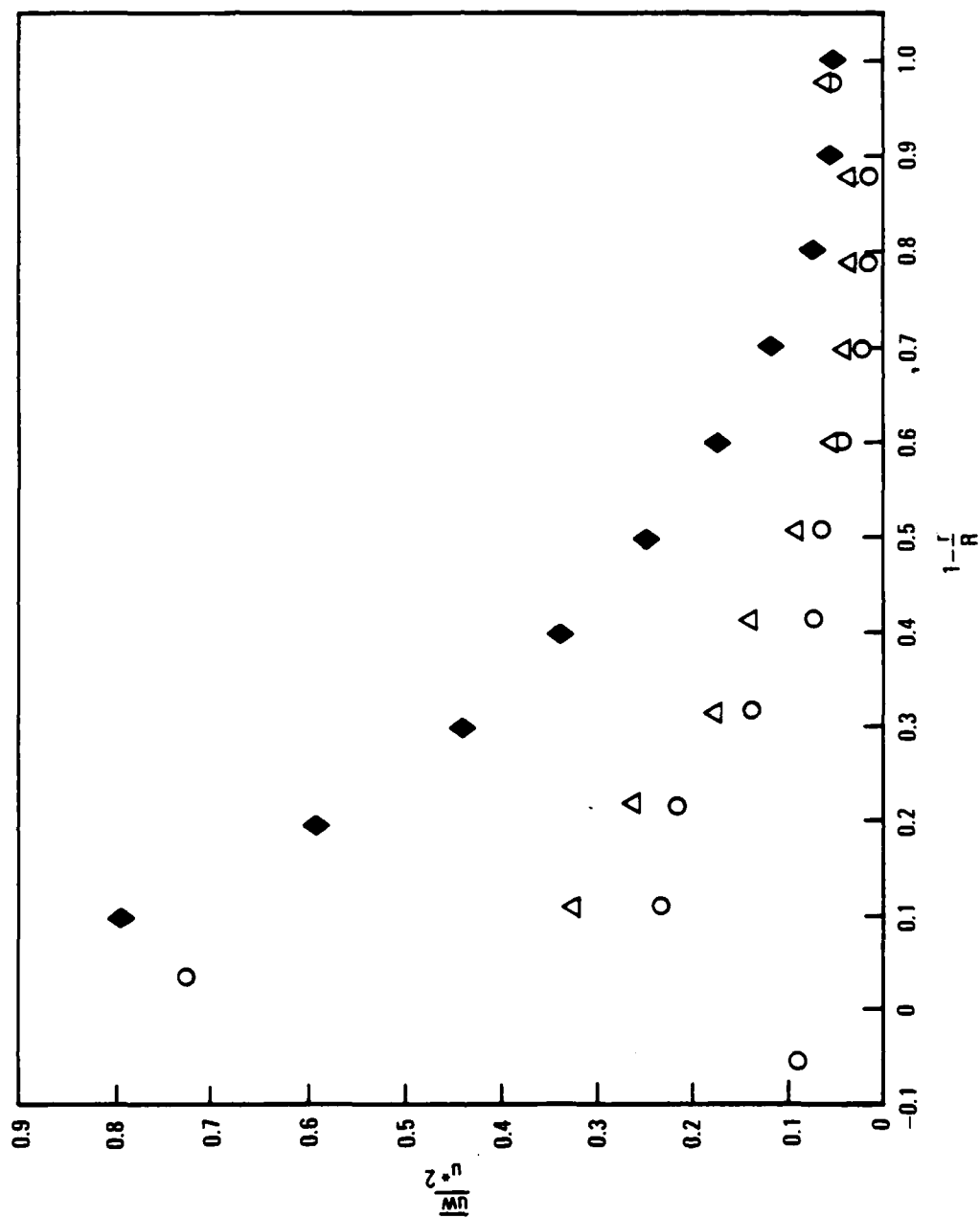


Figure 33 Correlation of axial and azimuthal velocity normalized by the friction velocity squared for the air flow. (Same symbols as Figure 7).

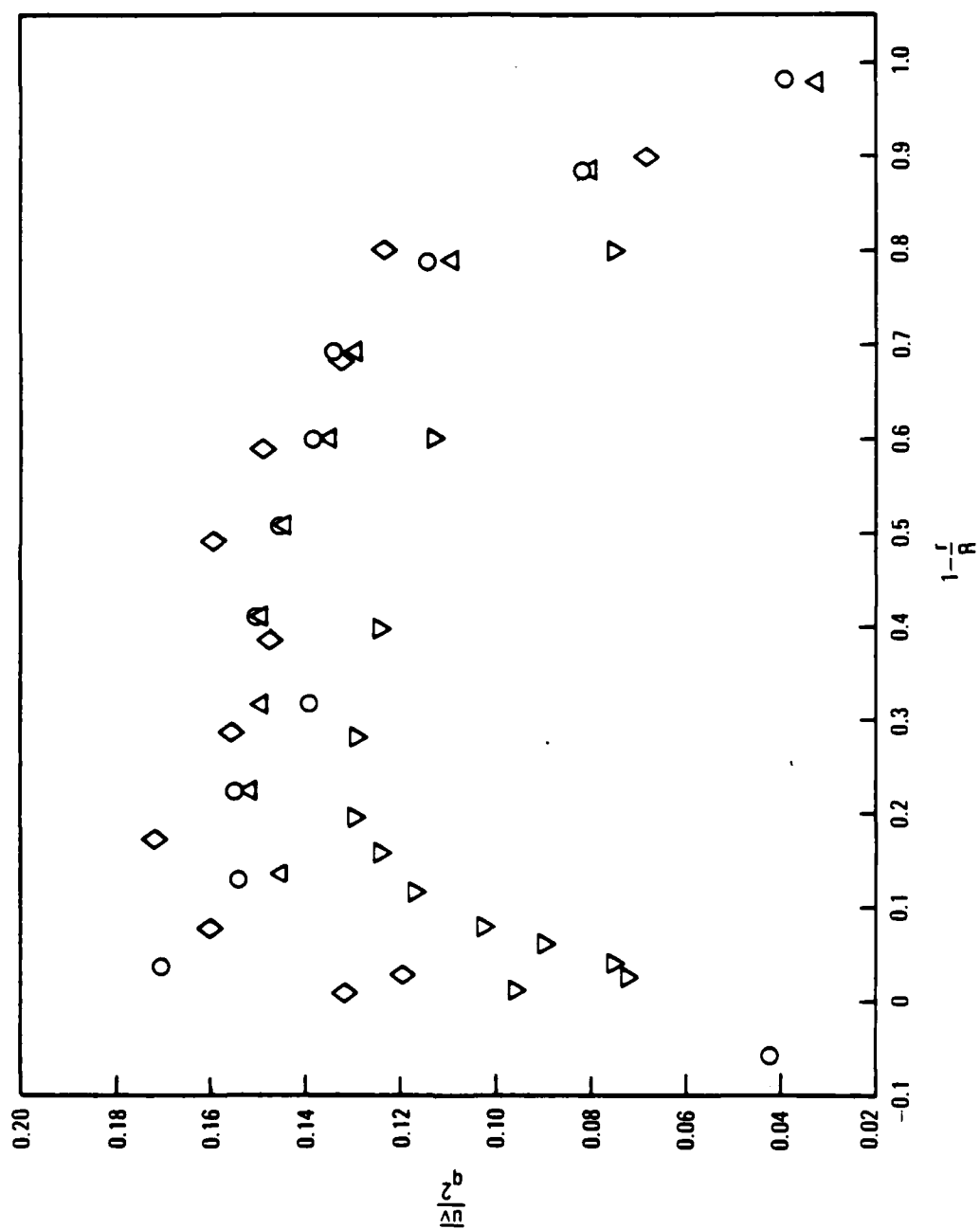


Figure 34 Correlation of axial and radial velocity normalized by the turbulent kinetic energy for the air flow. (Same symbols as Figure 7).

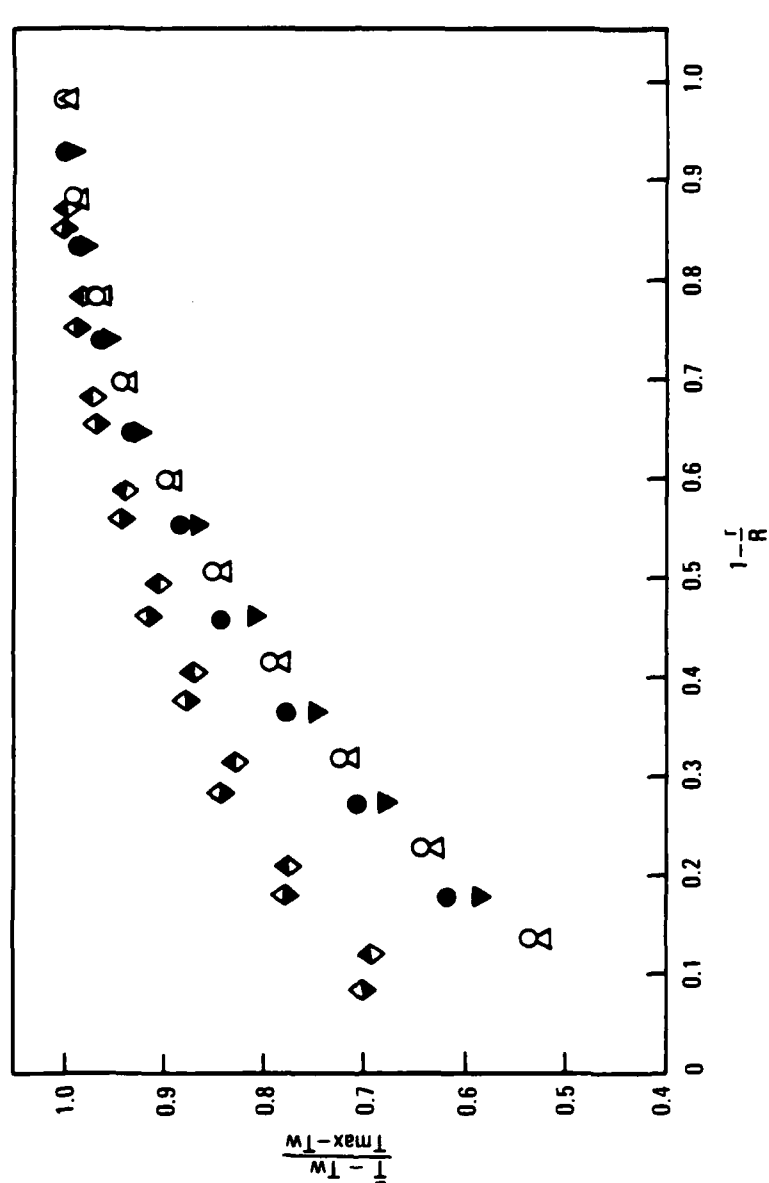


Figure 35 Mean temperature profile for the air flow. Valley, top half of tube, O; valley, lower half of tube, ●; crest, top half of tube, △; crest, lower half of tube, ▽; Bremhorst and Bullock, (1973), top half of tube, ◇; Bremhorst and Bullock, (1973), lower half of tube, ◆.

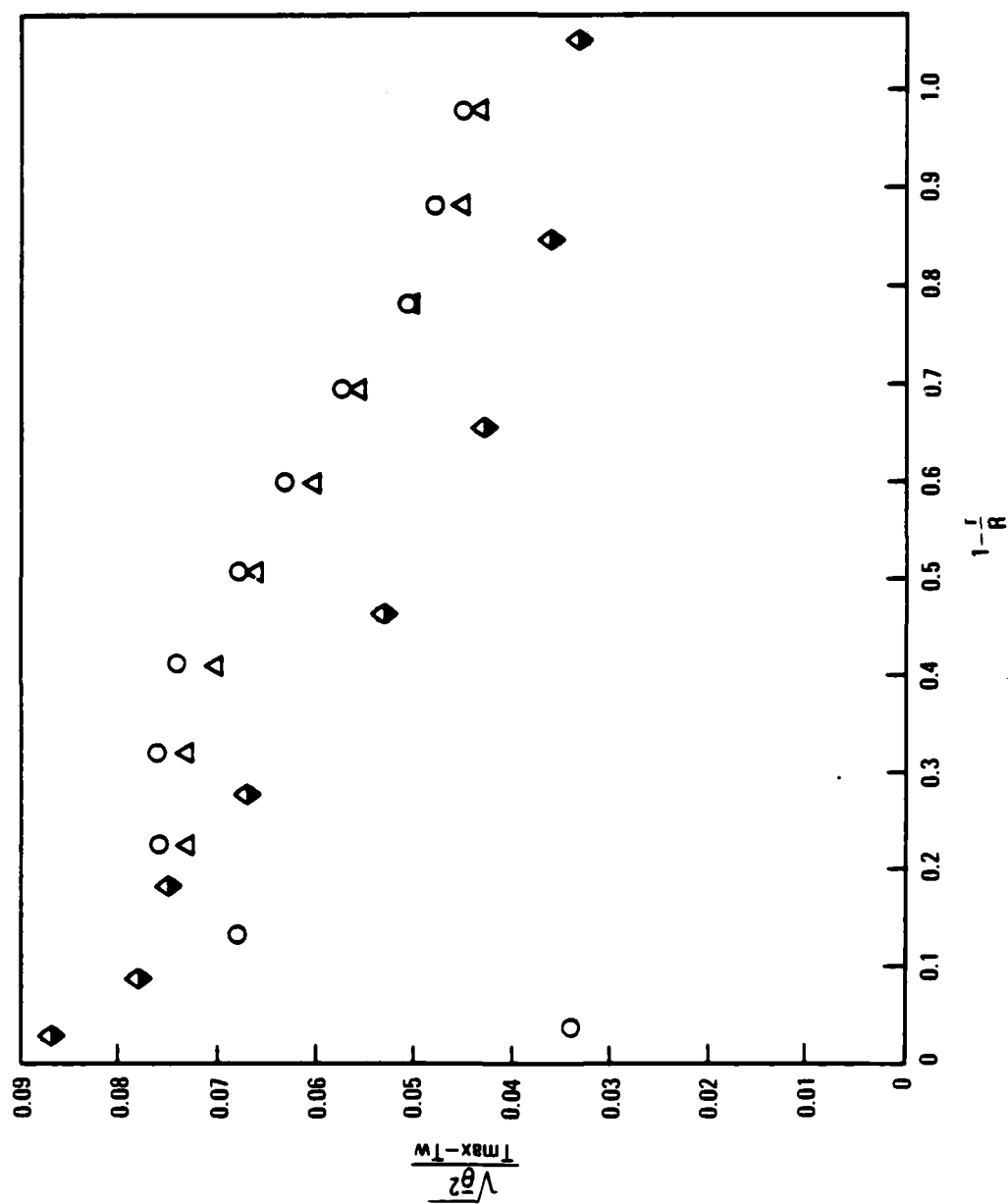


Figure 36 Root mean square temperature normalized by the difference between mean centerline and wall temperature for the air flow. (Same symbols as Figure 3f).



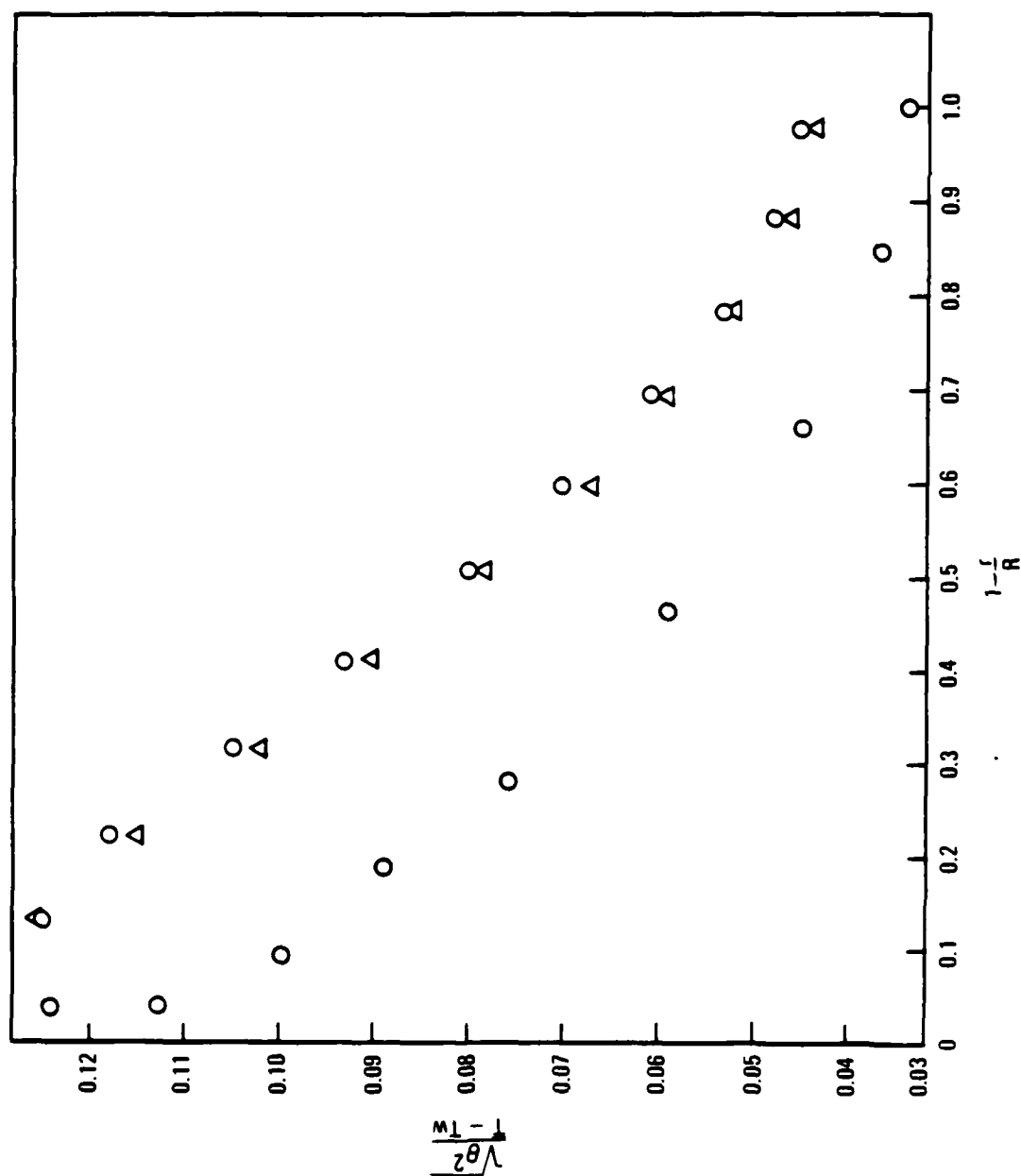


Figure 38 Correlation of radial velocity and temperature normalized by the difference between mean centerline and wall temperatures for the air flow. (Same symbols as Figure 36).



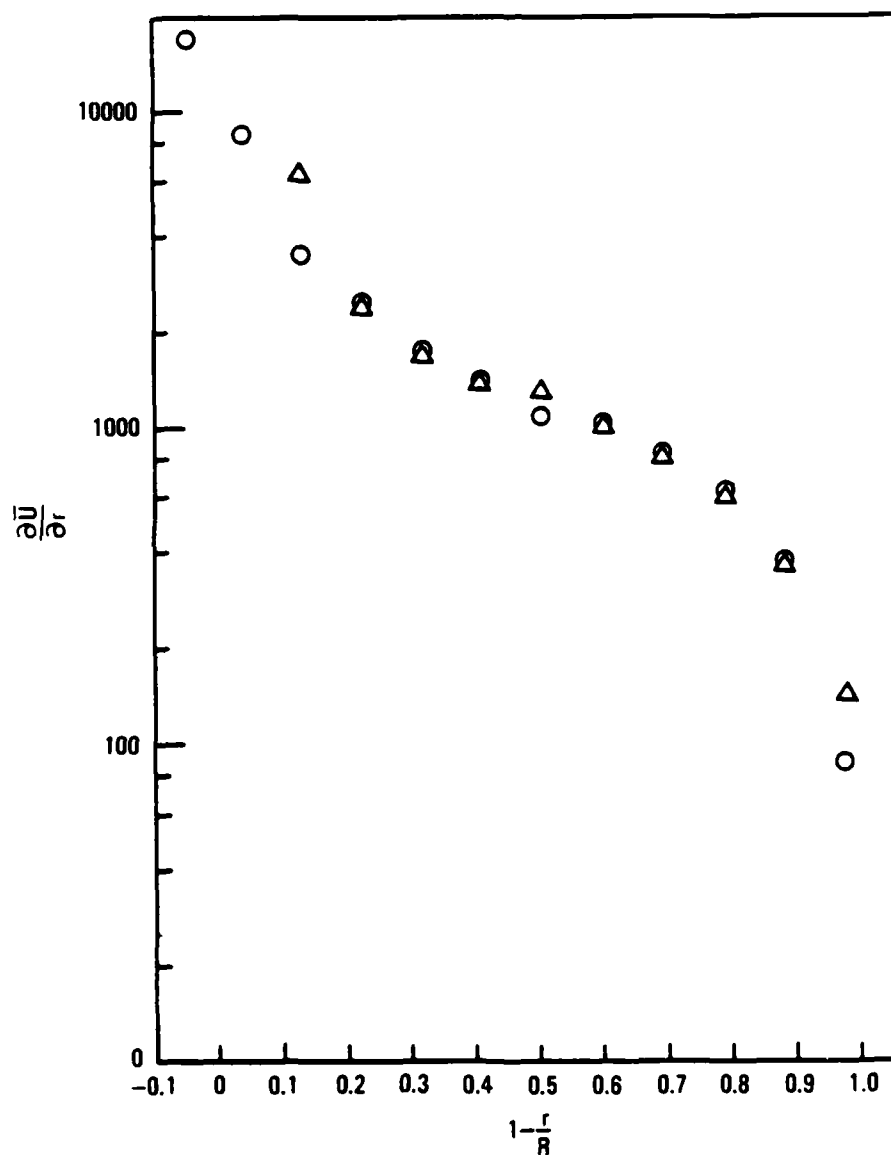


Figure 39 Mean velocity gradient for the air flow. (Same symbols as Figure 7).

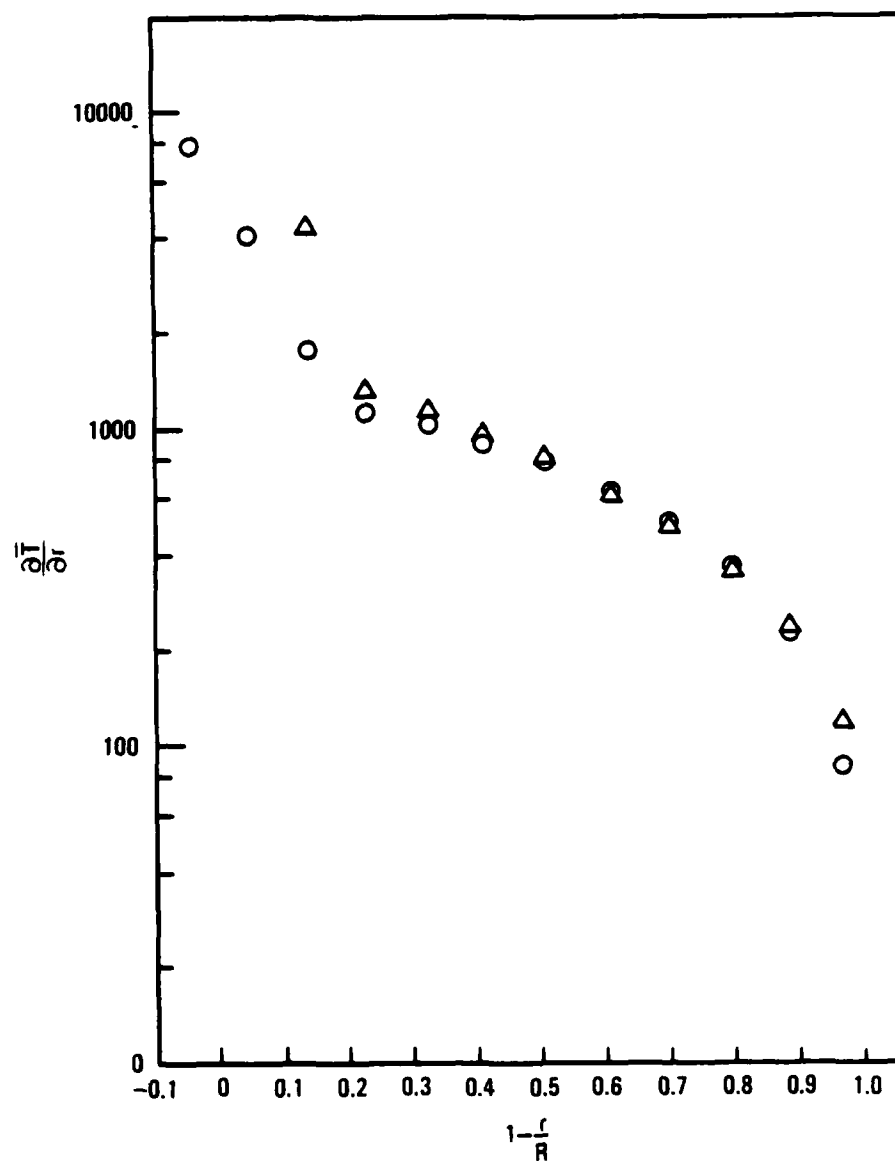


Figure 40 Mean temperature gradient for the air flow. (Same symbols as Figure 7).

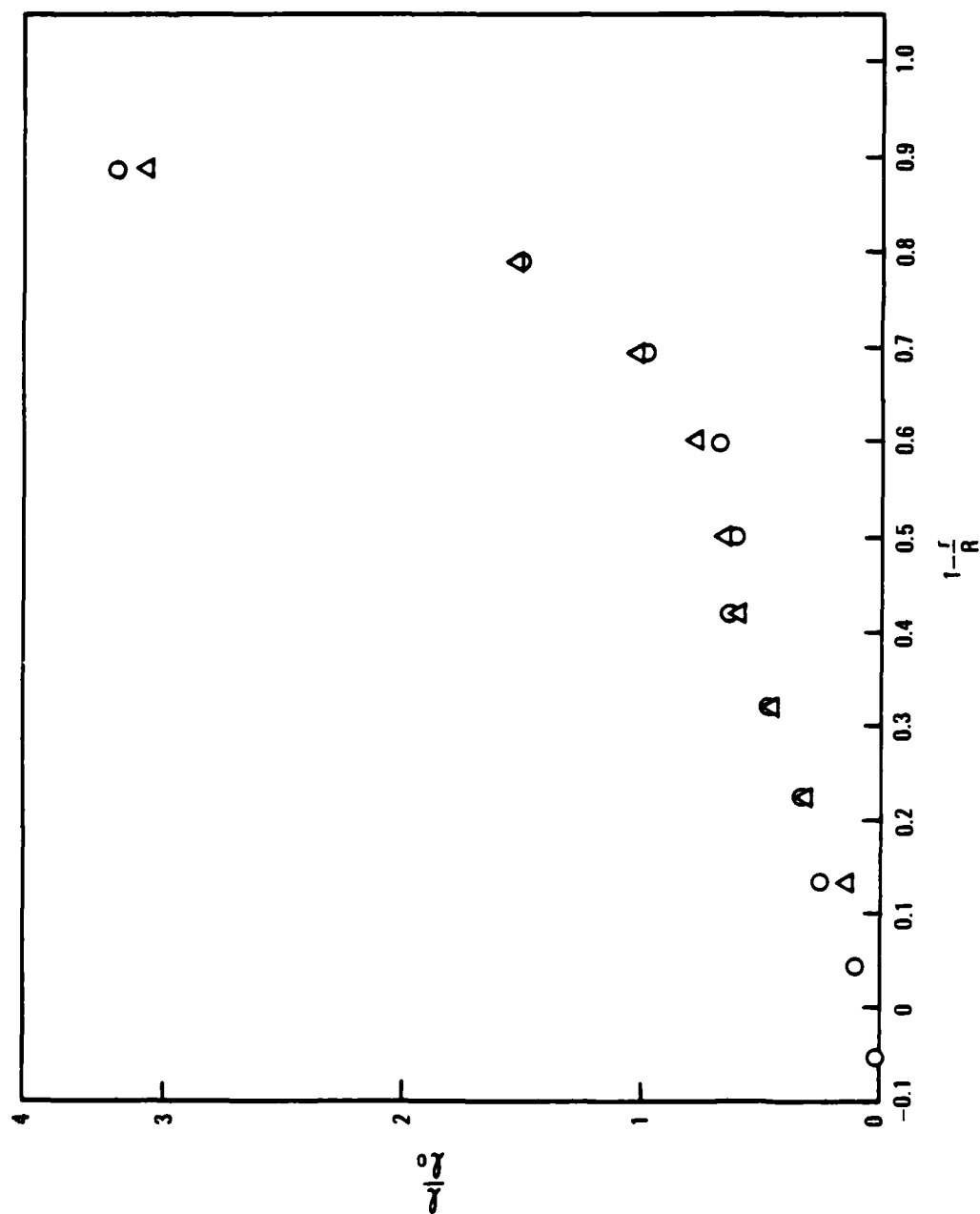


Figure 41 Mixing length for the air flow. (Same symbols as Figure 7).

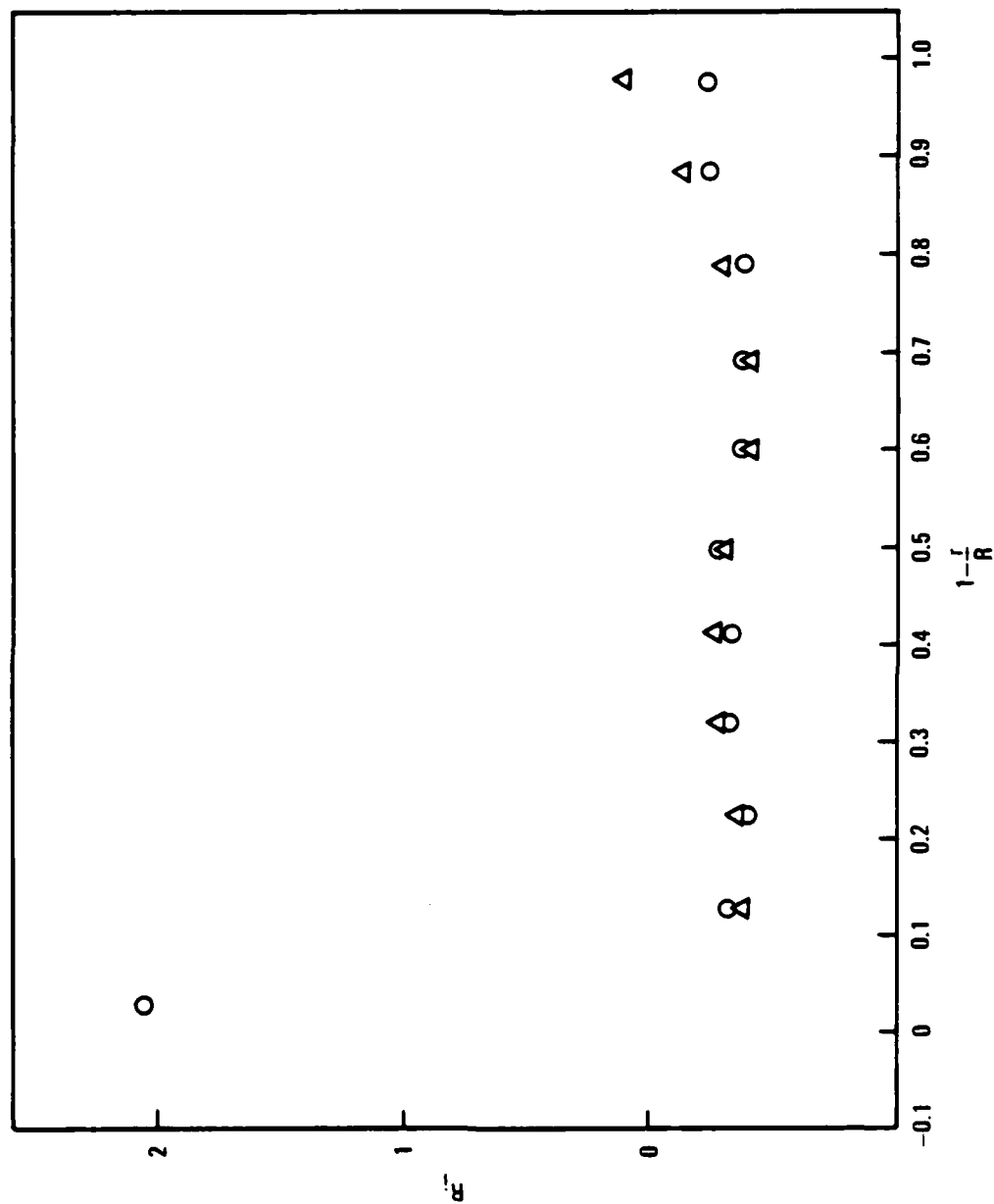


Figure 42 Richardson number for the air flow. (Same symbols as Figure 7).

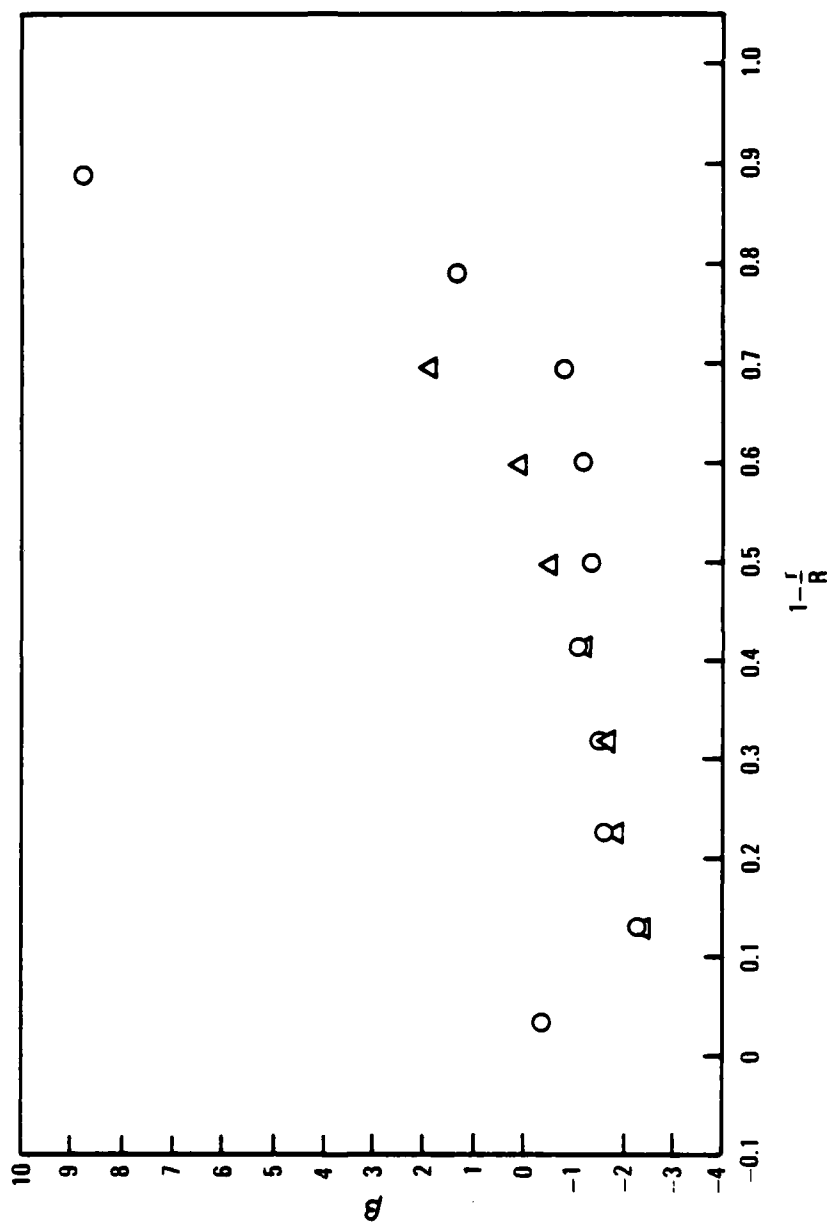


Figure 43 "Constant",  $\beta$ , required for mixing length correction. (Same symbols as Figure 7).

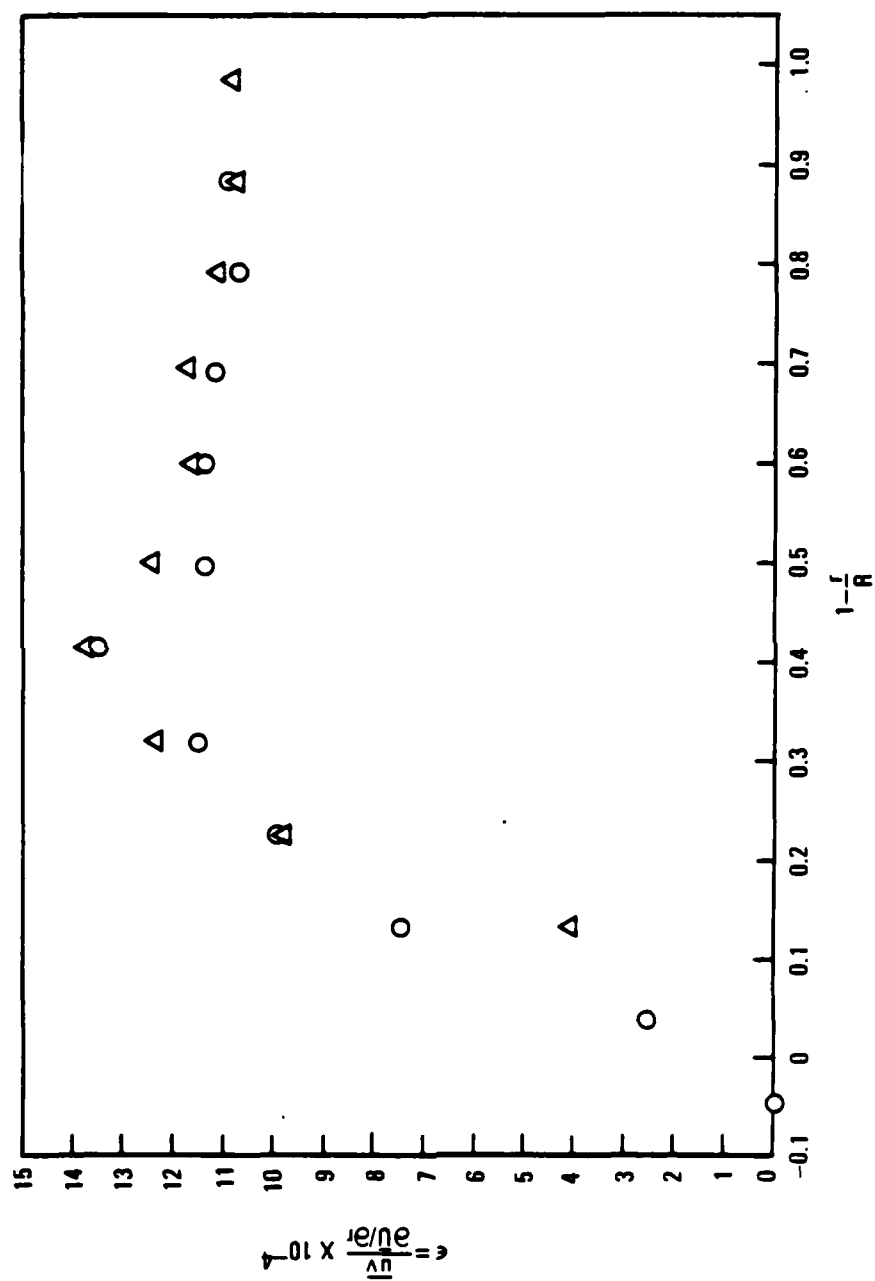


Figure 44 Eddy diffusivity for momentum for the air flow. (Same symbols as Figure 7).

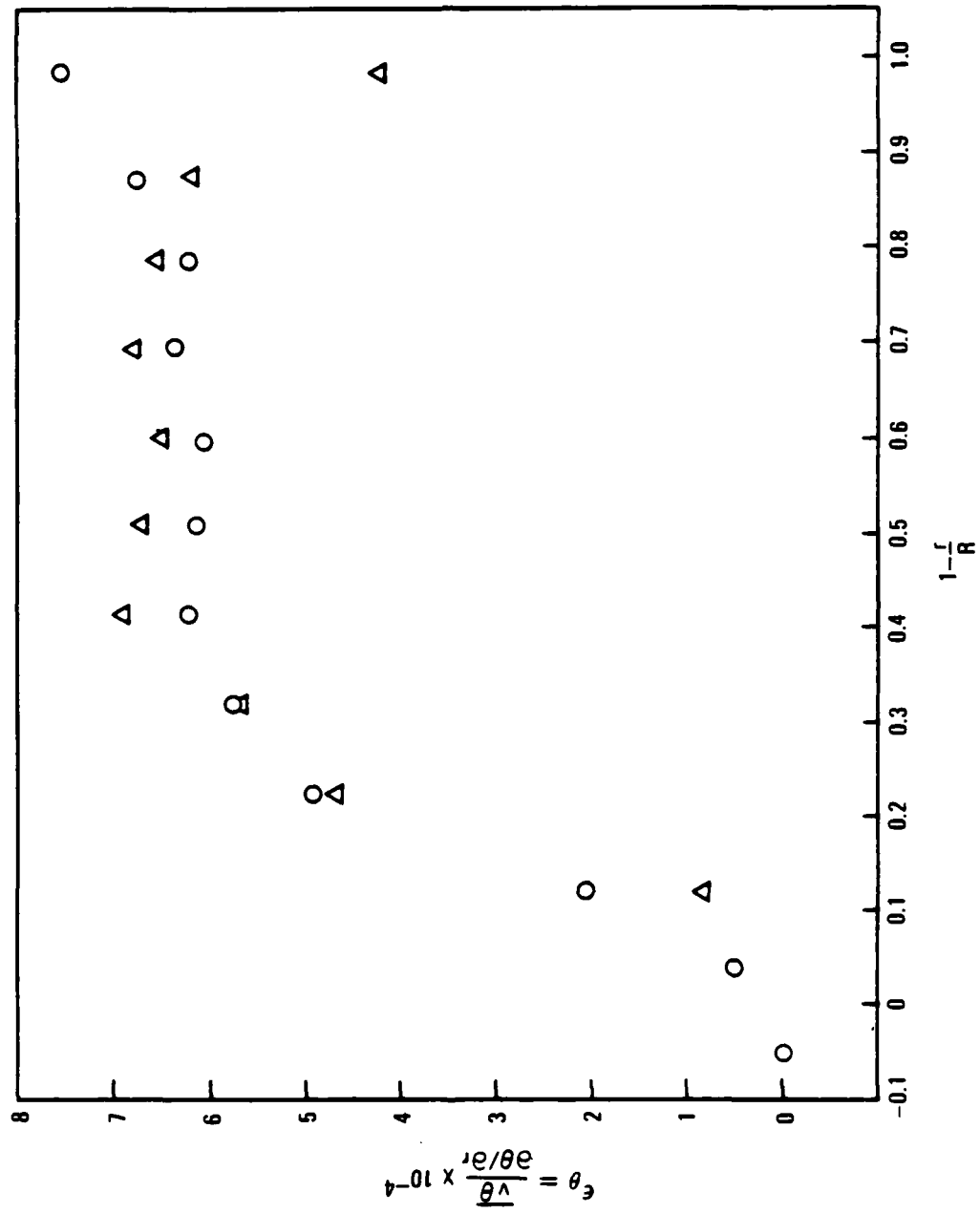


Figure 45 Eddy diffusivity for heat for the air flow. (Same symbols as Figure 7).

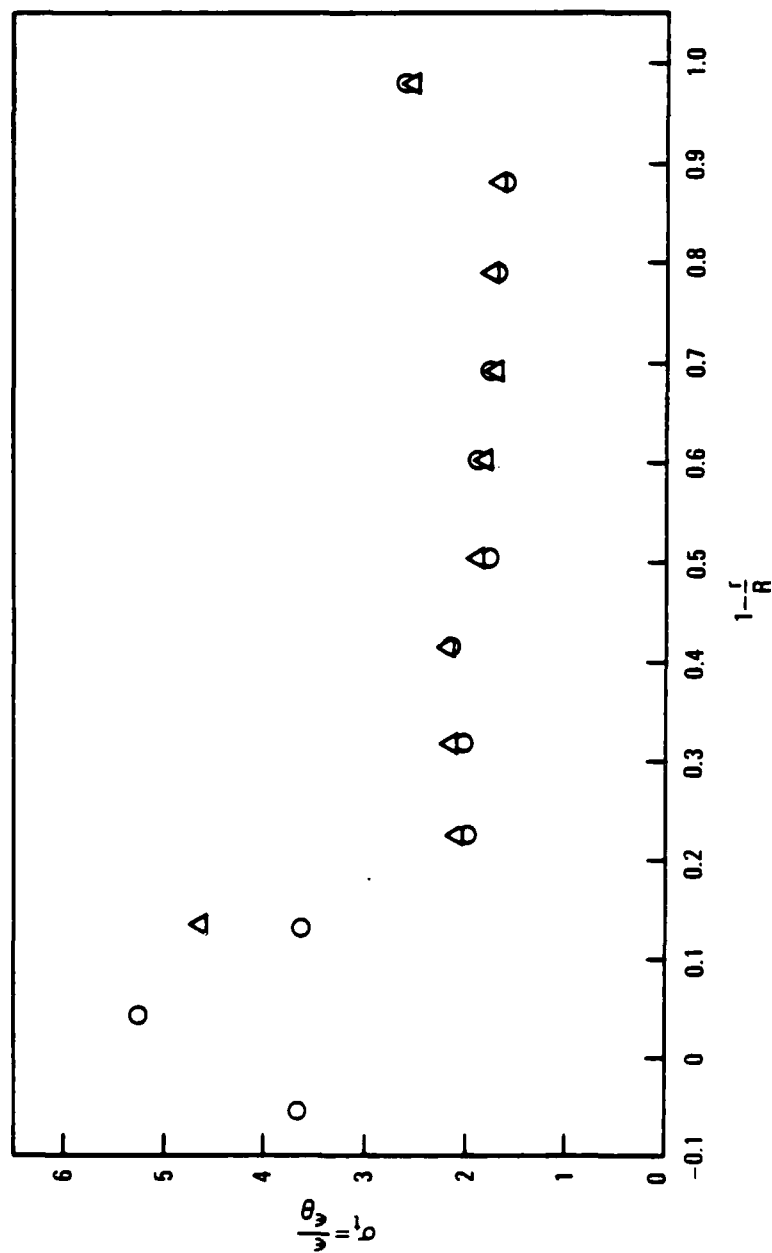


Figure 46 Turbulent Prandtl number for the air flow. (Same symbols as Figure 7).



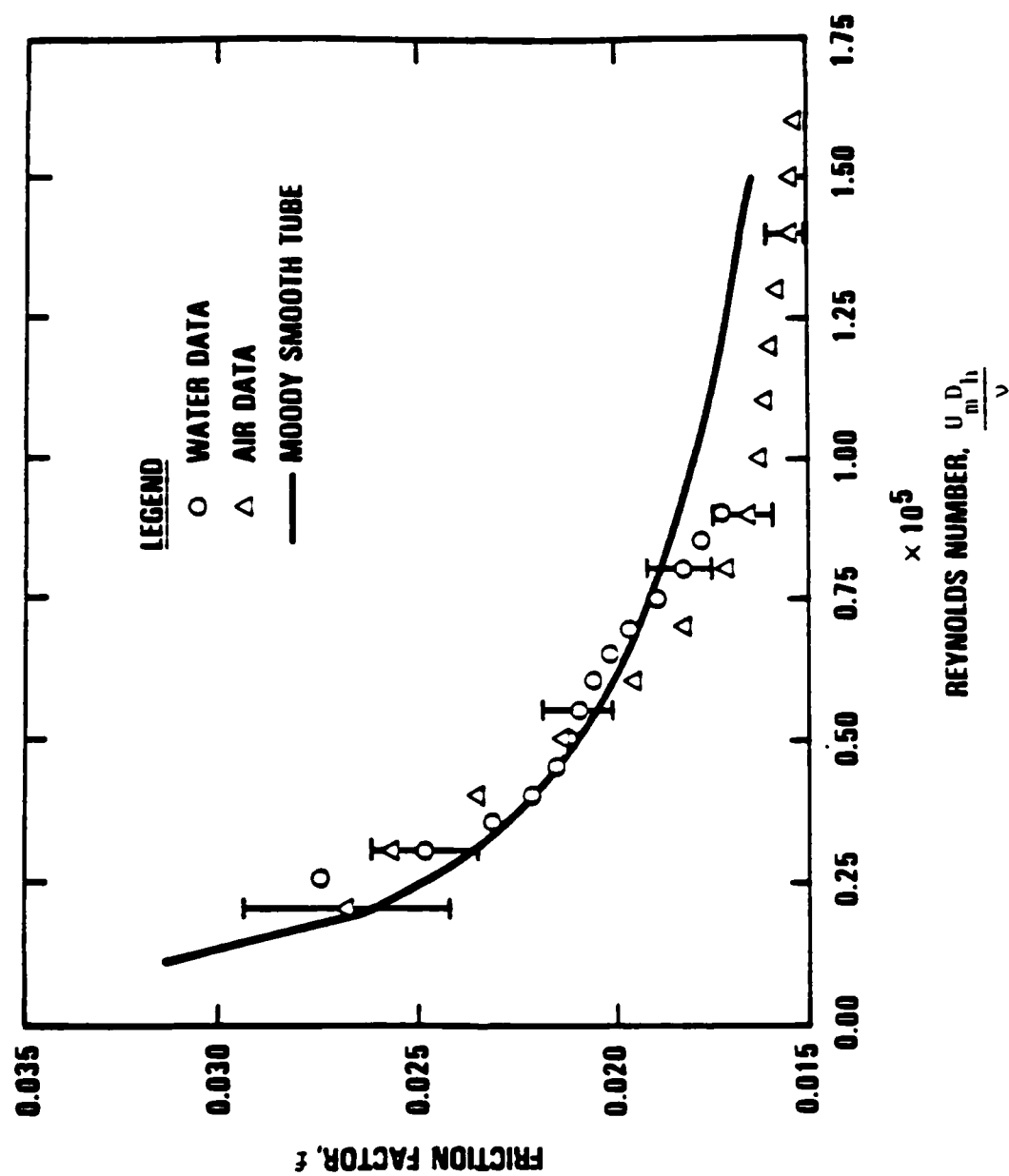


Figure D1 Spirally fluted tube friction factor comparisons



**SECTION C**  
**PRELIMINARY STUDIES OF THE TURBULENT FLOW**  
**IN ROTATING TUBES**

# PRELIMINARY STUDIES OF THE TURBULENT FLOW IN ROTATING TUBES

by

Paul A. Libby

Department of Applied Mechanics and Engineering Sciences  
University of California, San Diego  
La Jolla, California 92093

**Abstract:** The equations for a Reynolds stress/flux description of the turbulent flow with heat transfer in a smooth tube rotating about its axis of rotation are developed. Numerical solutions using the Keller box method are obtained only for the isothermal, nonrotating case. Future work will involve extensions of the numerical method to include rotation and heat transfer.

## INTRODUCTION

The requirement of enhanced heat transfer arises in a variety of industrial processes with the consequence that tubes with various inserts, fins, etc. are used to increase their heat transfer characteristics. Generally the enhanced heat transfer involves augmented momentum transfer so that increased pressure drop and increased heat transfer accompany one another. However, the spirally-fluted tube of Yampolsky [1] appears to possess the attractive feature of favorable heat transfer characteristics with either no penalty in pressure drop or with a reduction in that drop. From a fundamental point of view this feature calls for an explanation of the turbulent mechanism by which the heat transfer at the wall is facilitated while the momentum transfer leading to pressure drop is not similarly increased. It is our purpose to apply a second-moment method to the swirling flow with heat transfer in tubing rotating about its axis of symmetry in order to examine one of the fundamental aspects of the flow in tubes with spiral fluting.

We show schematically in Fig. 1 the flow in a spirally-fluted tube. A circular tube with inside radius  $R$  has a perimeter consisting of flutes of height  $h$  which spiral so as to form an angle with the axis of rotation denoted  $\phi$  ( $\phi = 0$  for straight flutes). At stations sufficiently far from the tube entrance the flow is fully developed. An idealization is adopted such that the influence of the flutes on the flow is described by suitable boundary conditions at the outer radius of the core which we denote as  $R$ . From this perspective it is appropriate to consider the fully developed flow in a circular tube which is rotated about its axis of rotation. Experiments in this case are reported by White [2] and Murakami and Kikuyama [3]. As might be expected the effect of rotation is stabilizing, so that the intensity of the turbulence and the pressure drop are diminished by rotation. This same situation prevails in the core region of spirally fluted tubes but the distribution of azimuthal velocity in the vicinity of the flutes is destabilizing; the interaction of these two regions determines the fluid dynamics of such tubes. Despite the absence of this interaction the cleanness of the flow situation in a rotating tube makes this case

attractive for initial study although it does leave open the connection between the geometry of the flutes and the effective rate of rotation of the pipe.

For the analysis of the turbulent flow in rotating tubes an appropriate method for describing the turbulence must be selected. In spirally-fluted tubes Launder and coworkers treat three-dimensional laminar flow [4] and three-dimensional turbulent flow by the  $k-\epsilon$ -method [5]. We view our analysis as complementary to that in [5] in that we consider the axisymmetric portion of the flow but with a full Reynolds stress/flux closure. It is widely accepted that descriptions utilizing this closure represent the most complete formulation of turbulent shear flows currently available since anisotropy of the velocity fluctuations is taken into account. However, in flows with complex geometry, e.g., in three-dimensional flows, the resulting equations are frequently too complicated with the consequence that methods incorporating less fluid mechanical detail, e.g., the well-known  $k-\epsilon$ -method, are employed. Here we deal with a flow which is sufficiently simple from a geometric point of view to be amenable to treatment by the full Reynolds stress/flux closure.

The basis for such a treatment is provided by Launder and Morse [6] who apply Reynolds stress closure to axisymmetric shear flows without and with swirl. It should be noted at the outset that reference [6] is in the nature of a progress report; it indicates that in its present stage of development the theory of axisymmetric shear flows is not adequate. Launder and Morse show that the spreading rate for nonswirling jets is predicted to be 50% too high. In addition with swirl the shear stress "...  $\overline{uw}$  has the wrong sign and thus the numerical solutions display a reduced rate of spread in contrast to the strong augmentation found in practice." These shortcomings suggest the difficulties of predicting swirling turbulent flows and the importance of close coordination between experimental and predictive efforts.

As a further justification for our adopted approach we note that second-moment closure exposes in a clear fashion the mechanism whereby swirl affects the heat transfer characteristics of the tube. We find that in the balance equations involving the radial velocity fluctuations

additional terms proportional to the radial pressure gradient,  $\partial \bar{p} / \partial r$ , enter; e.g., in the equation for the mean radial flux of temperature the additional term is  $\bar{r}^2 \partial \bar{p} / \partial r$ . It is interesting to observe that this term is the counterpart of the gravity term in the atmospheric boundary layer (cf., e.g., Meroney [7]), a term which appears to lead in some circumstances to large heat flux without accompanying increases in momentum flux.

The velocity characteristics are studied first under the assumption that the rates of heat transfer are sufficiently small so that the density may be considered constant. As a second step in the analysis the characteristics of the temperature field in the tube with heat transfer are treated.

We encounter considerable difficulties with the numerical treatment of the resultant equations and in fact these studies are preliminary because of the limited results we provide. Clearly the classical case of the turbulent isothermal flow in a smooth nonrotating tube must be solved first before the more complex rotating and nonisothermal cases are taken up. After considerable effort our numerical technique did yield solutions for this initial case and we present the comparison between prediction and experiment. In some respects the comparison is satisfactory but in others the agreement does not engender confidence in the ability of the theory to yield accurate results for more complex flows. In addition we are unable to achieve convergence of our numerical technique for the next case we consider, namely that for rotating isothermal flow.

The numerical technique we apply to the system of describing equations is the Keller box method. In this method the equations are reduced to a system of first order ordinary differential equations which are linearized according to the method of quasilinearization and then put in algebraic form by the use of central differences. Explicit statements of the boundary conditions at one end of the integration range displace the algebraic equations in such a fashion as to yield a block tridiagonal matrix which may be solved by a standard algorithm. An error measure is defined as the square root of the sum of the squares of the differences of each variable at each

grid point in the mesh between the  $k$ -th and the  $(k + 1)$ -th iterate. Convergence is achieved when this error is suitably small. The converged solutions we obtain involve a heavily graded mesh so as to place a large number of points close to the wall. Despite considerable effort the calculations are not robust; thus, for example, when we attempt to extend the theory to the case of a rotating tube, we are unable to achieve convergence. Clearly either alternative numerical techniques or further study of the application of the Keller box method to the system of equations involved here is required.

## ANALYSIS

Figure 1 shows schematically the flow and coordinate system considered. Since we assume the flow is of constant density and fully-developed, in considering the velocity field only the mean pressure  $\bar{p}$  varies in the streamwise direction. We follow the practice in [6] and denote the mean velocity components by capital letters and the related fluctuations by lower case letters. Thus the mean velocity components of interest are  $U(r)$  and  $W(r)$  with fluctuations  $u$  and  $w$ . Although the mean radial velocity is zero, its fluctuation  $v$  plays an important role in the theory.

### Describing Equations for the Velocity Field

With these assumptions preliminary work indicates that we must consider the following equations resulting directly from [6] but with a wall correction to the pressure-strain model added:



Conservation of  $\bar{u}^2$ :

$$0 = -\frac{2}{3} \epsilon - (c_1 - c_{1u} f) \frac{\epsilon}{k} \left( \bar{u}^2 - \frac{2}{3} k \right) - 2 \left( 1 - \frac{1}{3} (2\alpha - \beta) + c_{2u} f \right) \bar{u} \bar{v} \frac{dU}{dr} + \frac{c_s}{r} \frac{d}{dr} \left( \frac{r k \bar{v}^2}{\epsilon} \frac{d}{dr} \bar{u}^2 \right) \quad (1)$$

Conservation of  $\bar{v}^2$ :

$$0 = -\frac{2}{3} \epsilon - (c_1 - c_{1u} f) \frac{\epsilon}{k} \left( \bar{v}^2 - \frac{2}{3} k \right) - 2 \left( \frac{1}{3} (\alpha - 2\beta) - c_{2u} f \right) \bar{u} \bar{v} \frac{dU}{dr} + \frac{c_s}{r} \frac{d}{dr} \left( \frac{r k \bar{v}^2}{\epsilon} \frac{d \bar{v}^2}{dr} \right) - \frac{2 c_s k}{r^2 \epsilon} \bar{u}^2 (\bar{v}^2 - \bar{u}^2) \quad (2)$$

Conservation of  $\bar{u}^2$ :

$$0 = -\frac{2}{3} \epsilon - (c_1 - c_{1u} f) \frac{\epsilon}{k} \left( \bar{u}^2 - \frac{2}{3} k \right) - \frac{2}{3} (\alpha + \beta) \bar{u} \bar{v} \frac{dU}{dr} - \frac{c_s}{r} \frac{d}{dr} \left( \frac{r k \bar{v}^2}{\epsilon} \frac{d}{dr} \bar{u}^2 \right) - \frac{2 c_s k}{r^2 \epsilon} \bar{u}^2 (\bar{v}^2 - \bar{u}^2) \quad (3)$$

Conservation of  $\bar{u} \bar{v}$ :

$$-\frac{\bar{u} \bar{v}}{r} \frac{dW}{dr} = - (c_1 - c_{1u} f) \frac{\bar{u} \bar{v}}{k} \epsilon - (1 - \alpha) \bar{v}^2 \frac{dU}{dr} + \left( \beta (\bar{u}^2 + c_{2u} f (\bar{u}^2 - \bar{v}^2)) - \gamma k \right) \frac{dU}{dr} + \beta \bar{u} \bar{v} \frac{dW}{dr} + \frac{c_s}{r} \frac{d}{dr} \left( \frac{r k \bar{v}^2}{\epsilon} \frac{d}{dr} \bar{u} \bar{v} \right) - \frac{c_s k}{r \epsilon} \bar{u}^2 \frac{\bar{u} \bar{v}}{r} - (1 + \alpha) \bar{u} \bar{v} \frac{dW}{dr} \quad (4)$$

Conservation of  $\epsilon$ :

$$0 = -c_{\epsilon 2} \frac{\epsilon^2}{k} - c_{\epsilon 1} \frac{\epsilon}{k} \overline{uv} \frac{dU}{dr} + \frac{c_{\epsilon}}{r} \frac{d}{dr} \left( \frac{r k \overline{v^2}}{\epsilon} \frac{d\epsilon}{dr} \right) \quad (5)$$

In these equations the notation is standard but several comments are indicated. The quantity  $k$  is the turbulent kinetic energy  $1/2 \overline{u_k u_k}$  while  $\epsilon$  is the velocity dissipation. The units of  $k/\epsilon$  are  $(L/U)$  so that the coefficients in the diffusion terms have the units of  $(UL)$  as required. The function  $f$  is the so-called wall function which corrects the pressure-strain model for the effect of the wall; it is proportional to  $k^{3/2}/(\epsilon y)$  where  $y$  is the distance from the wall. We discuss this matter in more detail later.

We need additional equations to complete the formulation but it is convenient to discuss Eqs. (1)-(5) before proceeding. In these equations the following empirical constants appear:  $c_1$ ;  $c_2$  with the related constants  $\alpha = (8 - c_2)/11$ ,  $\beta = (8c_2 - 2)/11$  and  $\gamma = (30c_2 - 2)/55$ ;  $c_{\epsilon}$ ;  $c_{\epsilon 1}$ ;  $c_{\epsilon 2}$ ; and the two constants arising from the wall function,  $c_{1w}$  and  $c_{2w}$ . Values of these constants are given in [6] and [8].

In the absence of swirl  $W \equiv 0$  and Eqs.(1)-(5) represent five equations for the three velocity intensities,  $\overline{u^2}$ ,  $\overline{v^2}$ ,  $\overline{w^2}$ , the mean velocity  $U$  and the dissipation  $\epsilon$ . Solutions to these equations subject to regularity conditions at the axis ( $r = 0$ ) and boundary conditions at the wall describe the turbulent flow in nonrotating circular tubes.

The continuity and three mean momentum equations do not enter explicitly in our formulation; the first of these equations leads to  $V \equiv 0$  while the x-wise momentum equation becomes

$$\frac{1}{r} \frac{d}{dr} (r \overline{uv}) = -\frac{1}{\rho} \frac{\partial \bar{p}}{\partial x} = \frac{\lambda U^2}{4R}$$

where  $\lambda = 8 \overline{uv} (r = R) / U^2 = 8 (U/u_r)^2$  is the friction factor  $u_r$  is the shearing velocity and  $U$  is the mean velocity defined by

$$U = \frac{2}{R^2} \int_0^R U r \, dr. \quad (6)$$

We thus obtain the radial distribution of Reynolds shear stress

$$\overline{uv} = \frac{1}{8} \lambda U^2 \frac{r}{R} = u_r^2 \frac{r}{R} \quad (7)$$

so that  $\overline{uv}$  is not a dependent variable in Eqs.(1)-(5). The radial momentum equation determines the radial pressure gradient after the characteristics of the velocity are known; we have

$$\frac{1}{r} \frac{d}{dr} \left( r \overline{v^2} \right) - \frac{W^2 + \overline{u^2}}{r} = - \frac{1}{\rho} \frac{\partial \bar{p}}{\partial r} \quad (8)$$

As suggested earlier Eq.(8) will enter significantly in the analysis of the coupled velocity and temperature fields but for the present may be set aside.

Finally, the azimuthal momentum equation leads to the important result that the Reynolds shear stress  $\overline{wv} \equiv 0$ . We thus find that only two of the possible three shear stresses are operative in the flow under consideration.

With rotation and thus swirl two additional equations are required, namely, those for:

Conservation of  $\overline{uw}$ :

$$\begin{aligned} \frac{\overline{uv}}{r} \frac{W'}{r} = & - (c_1 - c_{1w} f) \frac{\overline{uu}}{k} \epsilon - (1 - \alpha) \overline{uv} \frac{dW}{dr} \\ & - \beta \overline{uv} \frac{W'}{r} + \frac{c_s}{r} \frac{d}{dr} \left( \frac{r k \overline{v^2}}{\epsilon} \frac{d}{dr} \overline{uw} \right) - \frac{c_s k}{r^2 \epsilon} \overline{w^2} \overline{uw} \end{aligned} \quad (9)$$

Conservation of  $\overline{vw}$ :

$$\begin{aligned} (\overline{v^2} - \overline{w^2}) \frac{W}{r} = & - (1 - \alpha) \left( \overline{v^2} \frac{dW}{dr} - \overline{w^2} \frac{W}{r} \right) - \\ & \beta \left( \frac{\overline{v^2}}{r} \frac{W}{r} - \overline{uv} \frac{dU}{dr} - \overline{w^2} \frac{dW}{dr} \right) - \gamma k \left( \frac{dW}{dr} - \frac{W}{r} \right) - c_{2w} f \overline{uv} \frac{dW}{dr} \end{aligned} \quad (10)$$

These additional equations determine  $\overline{uw}$  and  $W$  so that with swirl we have seven equations in seven unknowns.

### Boundary Conditions

Equations (1)-(5), (9) and (10) contain three intensities, the dissipation and the  $\overline{uw}$ -stress, each involving second derivatives, and the  $U$ - and  $W$ -velocity components involving first derivatives for a total order of twelve. In nonswirling flow  $\overline{uw} \equiv W \equiv 0$  and the total order is reduced to nine.

Consider in detail the boundary conditions for the case of nonrotating flow. We take the boundary conditions on axis to be those arising from regularity considerations, namely

$$\frac{d}{dr} \overline{u^2} = \frac{d}{dr} \overline{v^2} = \frac{d}{dr} \epsilon = 0 \quad (11)$$

and from the physical requirement that  $\overline{v^2} = \overline{u^2}$ . Although alternative strategies can be followed, we find it convenient to specify  $U = U_0$  at  $r = R$ .<sup>\*</sup> Now if these five conditions on the axis are imposed, the equations imply that  $d\overline{u^2}/dr = dU/dr = 0$  are automatically satisfied so that for this case we have five conditions on the axis and four at  $r = R$ .

The starting point of our considerations of the boundary conditions at the surface of the tube in the nonrotating case is the observation that our equations do not apply at the wall, i.e., within the viscous sublayer, and thus that the conditions we seek relate to the outer edge of that layer taken to be sufficiently thin so that without introducing significant spatial ambiguity we can consider that edge to be at  $r = R$ . In deriving these conditions it is convenient to introduce a coordinate  $y$  measured from the wall. The next observation is that the dissipation, based as it is on notions of isotropic turbulence which fail as the wall is approached, must be expected to have a special character as  $y \rightarrow 0$ . Accordingly, we require that  $\epsilon$  behave in a fashion consistent with experimental observations in the wall region of turbulent flows, e.g., as given by mixing length theory. Thus as  $y \rightarrow 0$  we require that  $c, k \overline{v^2}/\epsilon = \nu_T = \kappa^2 y^2 \partial U/\partial y$  and that the logarithmic law applies, namely that

<sup>\*</sup> It is worth noting that when the Keller box method is used, the boundary conditions must be treated with more care than in more conventional numerical techniques.

$$\frac{U}{u_r} = \frac{1}{\kappa} \ln \left( \frac{y u_r}{\nu} \right) + B \quad (12)$$

where  $u_r^2 = \overline{uv}(r = R)$ ;  $\kappa$  is the Karman constant and  $B$  is a second empirical constant. Equation (12) provides a means for eliminating  $y$  since  $dU/dy = u_r/\kappa y$ . Thus

$$\epsilon = \frac{c_s k \overline{v^2}}{\kappa^2 y^2 (dU/dy)} = \frac{c_s k \overline{v^2}}{u_r^2} \left( - \frac{\partial U}{\partial r} \right) \quad (13)$$

In addition to providing one boundary condition to be applied at  $r = R$  Eq. (13) implies that as  $y \rightarrow 0$ ,  $r \rightarrow R$ ,  $\epsilon y \rightarrow$  constant and that as a consequence Eqs. (1)-(5) take on special forms. Before discussing these in details we note that the variable  $y$  can also be eliminated from Eq. (12); although we use the resulting equation only *a posteriori*, we set it forth at this juncture; we have\*

$$\frac{U}{u_r} = \frac{1}{\kappa} \ln \left( \frac{u_r R}{\nu} \frac{u_r}{\kappa R (-dU/dr)} \right) + B \quad (14)$$

where  $U$  and  $dU/dr$  are evaluated at  $r = R$ .

While Eq. (13) is a synthetically imposed condition reflecting the inapplicability of the dissipation equation in the vicinity of the tube wall, the remaining boundary conditions at  $r = R$  are determined by the differential equations specialized to reflect the special character of  $\epsilon$  as  $r \rightarrow R$ . In particular  $\overline{u^2}$ ,  $\overline{v^2}$  and  $\overline{w^2}$ , each divided by  $u_r^2$ , are found from Eqs. (1)-(3) to take on constant values given by algebraic combinations of the various empirical constants arising in the equations. This feature implies that values of the three intensities at the outer edge of the viscous sublayer, taken to be at  $r = R$ , can be specified; indeed such a specification is standard in predictive methods involving Reynolds stress closure (cf. reference 8). Thus for nonrotating tube flow we have five boundary conditions at  $r = 0$  and four at  $r = R$ .

\* An alternative approach would involve satisfaction of Eq. (14) for specific values of  $(u_r R/\nu)$  and determination of  $U_0$  as part of the solution. The indirect procedure we follow appears more convenient.

If the tube is rotating about its axis of symmetry, we have two additional conditions at the axis,  $\overline{u\omega} = \overline{W} = 0$ . Since  $\overline{v\omega} \equiv 0$ , the only mean shear stress at the outer edge of the viscous sublayer is  $\overline{u\omega} = u_\tau^2$ . Thus, if we again consider mixing length theory to apply close to the wall, we readily conclude that

$$\frac{dW}{dr} (r = R) = 0$$

This completes specification of the boundary conditions for the case of a rotating tube.

### Nondimensionalization and Reduction to First Order Equations - Nonrotating Case

We use the shearing velocity  $u_\tau$  and the radius  $R$  as the two nondimensionalizing quantities.

Accordingly, we define the following dependent variables:

$$M_u = U/u_\tau, \quad I_u = \overline{u^2}/u_\tau^2, \quad I_v = \overline{v^2}/u_\tau^2, \quad I_w = \overline{w^2}/u_\tau^2$$

$$E = \epsilon R/u_\tau^3, \quad K = \frac{1}{2} (I_u + I_v + I_w)$$

In order to reduce the differential equations to first order we introduce the following additional dependent variables:

$$G_u = I'_u/T_\nu, \quad G_v = I'_v/T_\nu, \quad G_w = I'_w/T_\nu, \quad G_\epsilon = E'/T_\nu$$

where  $T_\nu = E/K I_v \eta$  is a dimensionless transport parameter and where prime denotes differentiation with respect to  $\eta = r/R$ , the single independent variable.

When these new variables are substituted into Eqs. (1)-(5) and Eq. (7) used to eliminate  $\overline{u\omega}$ , two steps are needed to achieve a formulation convenient for numerical analysis. In the first step Eq. (4) is solved for  $M_u'$  to obtain

$$M_u' = -\frac{c_s}{\eta} \left( \frac{G_\epsilon}{E} - \frac{1}{\eta T_\nu} - \frac{G_u + G_v + G_w}{2K} - \frac{G_v}{I_v} - \frac{(c_1 - c_{1w}f) E \eta}{K} - \frac{c_s K I_u}{\eta E} \right)$$

$$\left[ (1 - \alpha) I_v - \beta I_u - \gamma K + c_{2u} (I_u - I_v) f \right]^{-1} \quad (15)$$

This equation permits the remaining equations to be solved explicitly for the derivatives of the other eight variables. We obtain from Eqs. (1)-(3) and (5) the following:

$$I'_u = T_v G_u \quad (16)$$

$$G'_u = \frac{\eta}{c_t} \left[ \frac{2}{3} E + (c_1 - c_{1u} f) \frac{E}{K} (I_u - \frac{2}{3} K) + 2 \eta (1 - \frac{1}{3} (2 \alpha - \beta) - c_{2u} f) M'_u \right] \quad (17)$$

$$I'_v = T_v G_v \quad (18)$$

$$G'_v = \frac{\eta}{c_t} \left[ \frac{2}{3} E + (c_1 - c_{1u} f) \frac{E}{K} (I_v - \frac{2}{3} K) + \frac{2 c_s K I_u}{E \eta^2} (I_v - I_u) - 2 \eta (\frac{1}{3} (\alpha - 2 \beta) - c_{2u} f) M'_u \right] \quad (19)$$

$$I'_w = T_v G_w \quad (20)$$

$$G'_w = \frac{\eta}{c_t} \left[ \frac{2}{3} E - (c_1 - c_{1u} f) \frac{E}{K} (I_u - \frac{2}{3} K) - \frac{2 c_s K I_w}{E \eta^2} (I_v - I_w) + \frac{2}{3} \eta (\alpha + \beta) M'_u \right] \quad (21)$$

$$E' = T_v G_t \quad (22)$$

$$G'_t = \frac{\eta}{c_t} \left[ c_{t2} \frac{E^2}{K} + c_{t1} \frac{E}{K} \eta M'_u \right] \quad (23)$$

In terms of the dimensionless variables the boundary conditions become:

At  $\eta = 0$ :

$$M_u = M_u(0), \text{ given}$$

$$G_u = G_v = G_t = 0, \quad I_v = I_w$$

At  $\eta = 1$ :

$$E = \kappa c, K I_v (-M_u')$$

$$I_u, I_v, I_w, \text{ given}$$

In these equations the wall function  $f(\eta)$  is expressed as

$$f = \frac{\phi k^{3/2}}{\epsilon y}$$

where  $\phi$  is selected so that  $f(r = R) = 1$ ; from the behavior of  $\epsilon$  as  $y \rightarrow 0$  either with or without swirl we have

$$\phi = \frac{c_s \bar{v}^2}{\kappa u_r k^{1/2}}$$

where all variables are evaluated at  $r = R$ . Thus we have in dimensionless form

$$f = \frac{c_s I_v(1)}{\kappa K^{1/2}(1)} \frac{K^{3/2}}{E(1-\eta)}, \quad \eta < 1$$

(24)

$$= 1, \quad \eta = 1$$

For the case of a rotating tube Eqs. (9) and (10) are similarly nondimensionalized and decomposed into three first order differential equations. The first of the two steps required to achieve a form convenient for numerical analysis is in this case somewhat more complicated in



AD-A150 774

FLUID MECHANICS AND HEAT TRANSFER SPIRALLY FLUTED

3/8

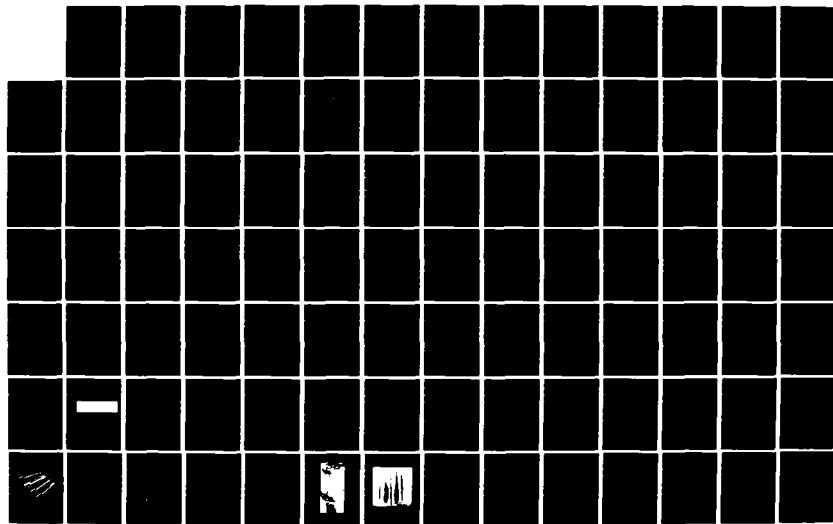
TUBING(U) GA TECHNOLOGIES INC SAN DIEGO CA

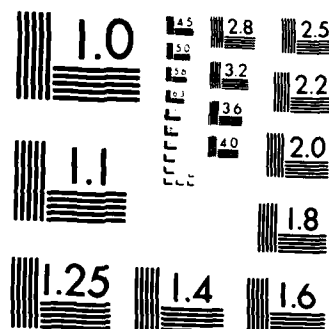
J S YAMPOLSKY ET AL. DEC 84 GA-A17833 N00014-82-C-0721

F/G 20/4

NL

UNCLASSIFIED





MICROCOPY RESOLUTION TEST CHART  
NATIONAL BUREAU OF STANDARDS 1963-A

that the derivatives of  $U$  and  $W$  must be found by solution of two algebraic equations. The remaining derivatives are then given explicitly as in Eqs. (16) -(23) but with additional terms arising from the rotation.

### Describing Equations for the Temperature Field

Our study to this point deals only with the prediction of the characteristics of the velocity within the tube and treats the density as constant. We now take up analysis of the situation when the temperature of the wall differs slightly from that of the fluid, "slightly" implying that the density can continue to be treated as constant.

This approximation calls for comment. If the radial pressure gradient is considered to be suitably "large" in the same sense that body forces due to gravity are treated in the Boussinesq approximation, then we find that with swirl coupling between the velocity and temperature characteristics arises in the balance equations involving the radial velocity fluctuation. In particular a term  $\overline{v} \partial \bar{p} / \partial r$  enters the  $\overline{v}^2$ -equation, a term  $\overline{u} \partial \bar{p} / \partial r$  the  $\overline{uv}$ -equation and as indicated earlier a term  $\overline{r} \partial \bar{p} / \partial r$  the  $\overline{vr}$ -equation. Here in the interests of simplicity and in the spirit of an preliminary investigation we provisionally neglect these coupling effects.

The temperature is decomposed into  $T + t$ , i.e., into mean and fluctuating components, so that the the equation for  $T(x,r)$  with axial conduction neglected becomes

$$U \frac{\partial T}{\partial x} = \frac{1}{r} \frac{\partial}{\partial r} (r \overline{v} t) \quad (25)$$

We denote the mean temperature on the axis of the tube as  $T_o = T_o(x)$  and the temperature at the wall as  $T_w$ , taken constant, and introduce as a principal dependent variable appropriate for a fully-developed flow the quantity

$$\Theta(\eta) = \frac{T(x,\eta) - T_w}{T_o(x) - T_w}$$

Note that  $0 \leq \Theta \leq 1$ . Implied by these considerations is a modification of the usual notion of fully-developed flow insofar as the temperature characteristics are concerned, a modification called for by the heat added or withdrawn along the length of the tube.

When the definitions of  $\Theta$  and of our earlier variables are introduced in Eq. (31), we find

$$M_s \Theta \Lambda + \frac{1}{\eta (T_s - T_w)} \left( \eta \frac{\overline{v} t}{u_r} \right)' = 0 \quad (26)$$

where

$$\Lambda = \frac{R}{T_s - T_w} \frac{dT_s}{dz}$$

is a dimensionless thermal loading parameter assumed here to be constant. The second term in Eq. (26) involves the mean radial flux of temperature.

As an aside it is worth noting the physical significance and characteristics of  $\Lambda$ . If Eq. (26) is integrated, we have

$$(-\Lambda) \int_0^1 M_s \Theta \eta d\eta = \frac{\overline{v} t}{u_r (T_s - T_w)} (\eta = 1) \quad (27)$$

The right side is a dimensionless heat flux and the integral is a dimensionless measure of the energy being convected within the tube, both positive definite quantities. Thus  $\Lambda < 0$  and we conclude, as must be the case on physical grounds, that if  $T_s < T_w$ , then  $dT_s/dz > 0$  while if  $T_s > T_w$ , then  $dT_s/dz < 0$ .

The definition of  $\Lambda$  and the assumption that it is constant imply that

$$T_s(z/R) = T_w + A \exp\left(\frac{\Lambda z}{R}\right)$$

where  $A$  is an integration constant which can be determined by specification of  $T_s$  at some streamwise station.

A second-moment closure consistent with our earlier treatment of the velocity field requires an equation for the radial flux  $\overline{vt}$ ; as indicated by the review due to Launder [9] there exist uncertainties regarding the second-moment equations for turbulent heat and mass transfer since considerably less attention has been devoted to them than to the corresponding equations for momentum transfer. Accordingly, we are justified in making simplifying assumptions. We find that if we neglect a wall correction associated with the correlation  $\overline{ut}$ , we need only one additional partial differential equation to close the set of equations for the temperature field, namely that for the mean radial flux  $\overline{vt}$

$$U \frac{\partial}{\partial z} \overline{vt} = (\overline{v^2} \frac{\partial T}{\partial r} + \overline{uv} \frac{\partial T}{\partial z}) - (c_{e1} + c_{e1w} f) \frac{\epsilon}{k} \overline{vt} + \frac{c_e}{r} \frac{\partial}{\partial r} \left[ \frac{rk}{\epsilon} (\overline{v^2} \frac{\partial}{\partial r} \overline{vt} + \overline{uv} \frac{\partial}{\partial z} \overline{vt}) \right] - \frac{\overline{w^2} k \overline{vt}}{\epsilon r^2} \quad (28)$$

The first two terms on the left side describe production, the third dissipation and the remainder turbulent diffusion. The additional empirical constants are  $c_e$ ,  $c_{e1}$  and  $c_{e1w}$ .

We now assume that the flux  $\overline{vt}$  can be represented in a form appropriate for a fully-developed flow, namely as

$$\overline{vt}(z, \eta) = (T_o(z) - T_w) \overline{v\theta}(\eta)$$

Furthermore, we introduce two additional dimensionless dependent variables

$$F_{v\theta} = \frac{\overline{v\theta}}{u_r}, \quad G_{v\theta} = \frac{F_{v\theta}'}{T_v}$$

where  $T_v$  is the dimensionless exchange parameter introduced earlier.

Equations (26) and (28) and the definition of  $G_{v\theta}$  lead to three additional equations for the temperature field within the tube, namely

$$F_{v\theta}' = T_v G_{v\theta} \quad (29)$$

$$F_{v\theta}' = \Lambda M_w \eta \Theta - F_{v\theta} \quad (30)$$

$$\frac{c_e}{\eta} G_{v\theta}' + I_v \Theta' = -\Lambda \left[ M_u F_{v\theta} + \eta \Theta - \frac{c_s G_{v\theta}}{I_v \eta} \left( 1 - \frac{\eta I_v'}{I_v} \right) \right] + c_e \left[ \frac{G_{v\theta}}{I_v} + \frac{F_{v\theta}}{\eta} \left( \frac{\eta^2 K}{E} \right)' \right] - \left[ (c_{e1} + c_{e1w} f) \frac{E}{K} + \frac{I_w K}{E \eta^2} \right] F_{v\theta} \quad (31)$$

These equations are to be solved subject to the obvious conditions at the axis,  $\Theta(0) = 1$ ,  $F_{v\theta}(0) = 0$ . We follow a procedure close to that used earlier for the velocity boundary conditions at the wall of the tube. The mean temperature distribution within the logarithmic portion of the wall layer when the mixing length varies as  $(\kappa/\sigma_t) y$  where  $\sigma_t$  is a turbulent Prandtl number, assumed given, is easily found to be

$$T = \frac{q_w \sigma_t}{\rho c_p u_r} \frac{U}{u_r} + T_w$$

where  $q_w$  is the rate of heat transfer taken to be positive when the fluid is heated by the tube.

Then some rearrangement leads to

$$\Theta(1) = \frac{q_w \sigma_t}{\rho c_p u_r (T_o - T_w)} M_u(1) = F_{v\theta} M_u(1) \quad (32)$$

which provides the desired boundary condition at  $\eta = 1$ .

## NUMERICAL ANALYSIS

Generally the equations for a Reynolds stress closure are solved by uncoupling the second order partial differential equations and by solving each difference representation by a scalar tridiagonal algorithm. This is the basis of many of the program originating with the group at the Imperial College of Science and Technology. Although never reported, it is likely that this procedure is slowly convergent and we therefore consider here the numerical treatment of Eqs. (15)

- (23) by the Keller box method. That we intend to use this method is suggested by our

formulation in terms of first order equations. We first consider the linearization of these equations as follows: If for notational convenience we replace the dependent variables  $M_u, I_u$ , etc. by their equivalent  $y_1, y_2, \dots, y_9$  we can formally write

$$y_i' = g_i(y_1, y_2, \dots, y_9, \eta), \quad i = 1, 2, \dots, 9 \quad (33)$$

and can use quasilinearization to obtain the equations for the  $k+1$ -iterate, given the  $k$ -th iterate, namely

$$\begin{aligned} {}^{k+1}y_i' &= {}^k \left( \frac{\partial g_i}{\partial y_l} \right) {}^{k+1}y_l + {}^k \left( g_i - \frac{\partial g_i}{\partial y_l} y_l \right) \\ & \quad {}^k \left( \frac{\partial g_i}{\partial y_l} \right) {}^{k+1}y_l + {}^k h_{i,l}, \quad i = 1, 2, \dots, 9 \end{aligned} \quad (34)$$

where summation with respect to  $l$  is indicated by the repeated index. Equations (34) constitute a set of linear ordinary differential equations.

Suppose we use the subscript  $n$  to denote a value corresponding to a grid point location  $\eta = \eta_n$  and let a spacing between such points be denoted as

$$\delta_n = \eta_n - \eta_{n-1}$$

Then a central difference representation of Eqs. (34) is

$${}^{k+1}y_{i,n} - {}^{k+1}y_{i,n-1} = \frac{\delta_n}{2} \left[ {}^k \left( \frac{\partial g_i}{\partial y_l} \right)_n {}^{k+1}y_{l,n} + {}^k \left( \frac{\partial g_i}{\partial y_l} \right)_{n-1} {}^{k+1}y_{l,n-1} + {}^k h_{i,n} + {}^k h_{i,n-1} \right] \quad (35)$$

Equations (35) replace Eqs. (33) by a set of algebraic equations subject to iteration.

If  $n = 1$  denotes values arbitrarily close to  $\eta = 0$ , a value denoted  $\delta_0$ , and  $n = N$  values at  $\eta = 1$  and if the first five equations in the system of equations are explicit statements of the five boundary conditions at  $\eta = 0$ , then the matrix given by Eqs. (35) takes the form shown schematically in Fig. (2). Thus despite the two point nature of the differencing scheme leading to Eqs. (35) we achieve a block tridiagonal matrix with  $N$  submatrices involving  $9 \times 9$  elements.

The last four equations in the matrix specify the four boundary conditions at  $\eta = 1$ .<sup>\*</sup> There is a standard, efficient algorithm for the solution of such a matrix.

One of the difficulties connected with implementing the solution of Eqs. (35) and the other approaches to the solution of the equations for a Reynolds stress closure is that estimates for all dependent variables at all grid points must be provided in order to initiate the integration cycle. Here we use the experimental results of Laufer as discussed by Hinze [10] to construct analytic representations of the nine dependent variables within the range  $\eta = \delta_c$  to  $\eta = 1$ .

A second difficulty relates to achieving convergence and the rate of such convergence when it occurs. If we define an error measure as

$$E_M = \left[ \sum_{i=1}^9 \sum_{n=1}^N ({}^{k+1}y_{i,n} - {}^k y_{i,n})^2 \right]^{1/2}$$

we require  $E_M$  to be suitably small. Since the nature of the flow to be described by the solution involves large changes in the dependent variables close to the wall, our experience with convergence of the iterations indicates it is essential to have a fine grid spacing close to  $\eta = 1$ . Unless a prohibitively large value for  $N$  is used, this requirement suggests the use of a graded mesh. Accordingly, we assume

$$\delta_n = \delta_o (1 + \epsilon_\delta)^n \quad (36)$$

where  $\epsilon_\delta$  is a grading parameter and where  $\delta_o$  is a spacing parameter selected so that

$$\sum_{n=1}^{N-1} \delta_n = \delta_o \sum_{n=1}^{N-1} (1 + \epsilon_\delta)^n = 1 - \delta_c \quad (37)$$

In our numerical examples we let  $N = 21$ ,  $\delta_c = 0.01$  and  $\epsilon_\delta = -0.2$ . These values locate the

---

<sup>\*</sup> Our earlier remark on the need for careful selection of the boundary conditions when the Keller box method is used is now reinforced.



first eleven grid points between  $\eta = 0.01$  and  $\eta \approx 0.9$  and the remaining ten between the latter value and  $\eta = 1$ .

Our experience with this numerical technique to the extent that we have been able to experiment with it suggests that it does not yield a robust computing scheme. Convergence is at best slow and heavy underrelaxation is required to achieve any convergence. For example, to reduce  $E_m$  from 560 to 0.05 requires 66 iterations with an underrelaxation factor of 0.15. How this performance compares with the conventional approach to equations of the sort encountered here is unknown.

The following are the values of the empirical constants used in our calculations:

$$\begin{aligned} c_1 &= 1.5 & c_2 &= 0.40 & c_s &= 0.22 & c_{s1} &= 1.45 \\ c_{s2} &= 1.90 & c_t &= 0.35 & c_{1u} &= 0.50 & c_{2u} &= 0.060 \\ \kappa &= 0.40 & B &= 5.4 \end{aligned}$$

These are all standard values (cf. [8]) with the exception of  $c_s$ ; we find it necessary to increase the standard value of 0.15 to that indicated here in order to achieve the correct Reynolds number in Eq. (14).

Experiment suggests and we therefore impose the following values of the intensities at  $\eta = 1$ , values:

$$I_v(1) = 5.06 \quad I_v = 0.810 \quad I_w = 2.89$$

## RESULTS AND CONCLUDING REMARKS

We compare our predictions for nonrotating, isothermal tube flow with the experimental results of Laufer (cf. [10]). We thus specify  $M_u(0) = 28.6$  which corresponds to a Reynolds number  $u, R/\nu = 8740$ . We find from Eq. (14) that the predicted value of  $u, R/\nu$  is 8130, reasonably

close to that corresponding to experiment and that the mean velocity profile is in excellent agreement with data both in terms of the logarithmic and velocity defect representations.

Figures 3a - c compare the measured and predicted intensities. Here we see that the predicted axis values and the distribution of the radial intensity as indicated by  $I_v$  are in reasonable agreement with the data but that near the wall the other two intensities decrease more rapidly than the data. Although we have explored a variety of alterations to the specification of the boundary conditions at the wall, we are unable to improve these results which may or may not be considered satisfactory.

Further studies are beyond the scope of the present investigation. Future research should be devoted to removing the discrepancy indicated by Figs. 3a and 3c and to achieving a more robust numerical procedure, first for nonrotating, isothermal flow and subsequently for the more general case of a rotating tube with heat transfer.

## ACKNOWLEDGEMENTS

The author gratefully acknowledges helpful discussions with Professors J. C. LaRue and B. E. Launder, Dr. W. P. Jones and Mr. J. Yampolsky and the contribution of Ms. Barbara Hanson in the preparation of this report.

## REFERENCES

1. Yampolsky, J., "Spirally-Fluted Tubing for Augmented Heat Transfer." General Atomic Report GA-A15442 (1979).
2. White, A., "Flow of a Fluid in an Axially Rotating Pipe," J. Mech. Eng. Sci. 6, 47-51 (1964).
3. Murakami, M. and Kikuyama, K., "Turbulent Flow in Axially Rotating Pipes." J. Fluid Eng. 102, 97-103 (1980).
4. Barba, A., Bergeles, G., Gosman, D. and Launder, B. E., "The Prediction of Convective Heat Transfer in Viscous Flow Through Spirally Fluted Tubes," ASME 83-WA HT-37. (1983).
5. Private communication. See section in this report by UMIST group.
6. Launder, B. E. and Morse, A., "Numerical Prediction of Axisymmetric Free Shear Flows with Reynolds Stress Closure," *Turbulent Shear Flows I*, Springer-Verlag, Berlin-Heidelberg-New York, 279-294 (1979).
7. Meroney, R. N., "An Algebraic Stress Model for Stratified Turbulent Shear Flows," *Computers and Fluids* 4, 93-107 (1976).

8. Launder, B. E., Reece, G. J. and Rodi. W., "Progress in the Development of a Reynolds-stress Turbulence Closure," J. Fluid Mech. 68, 537-566 (1975).
9. Launder, B. E., "Heat and Mass Transfer," in P. Bradshaw, Ed., Turbulence, Topics in Applied Physics, 12, 231-287 (1978).
10. Hinze, J. O., Turbulence, McGraw Hill, New York, 521 (1959).

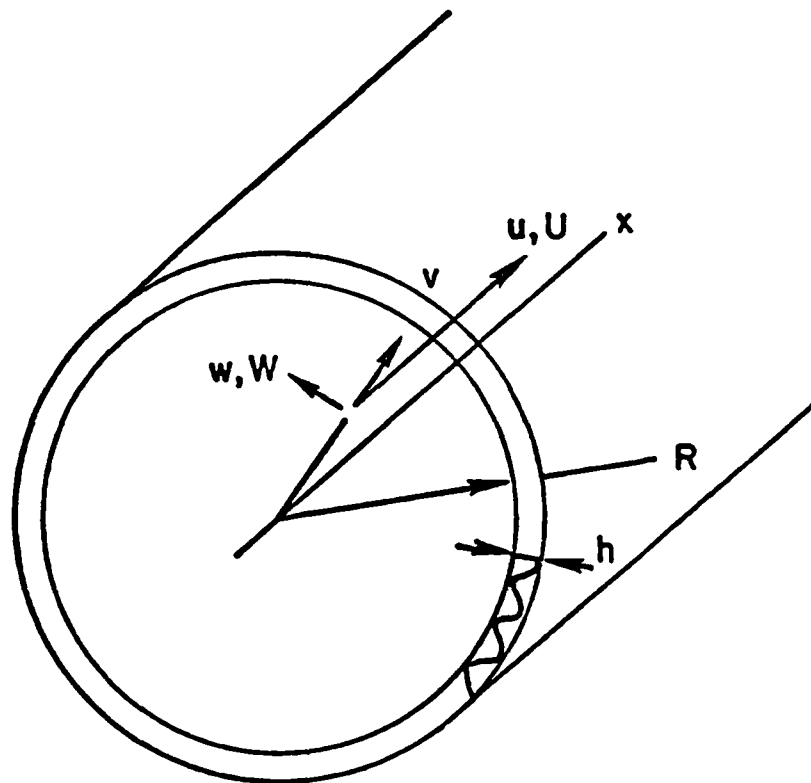
## FIGURE CAPTIONS

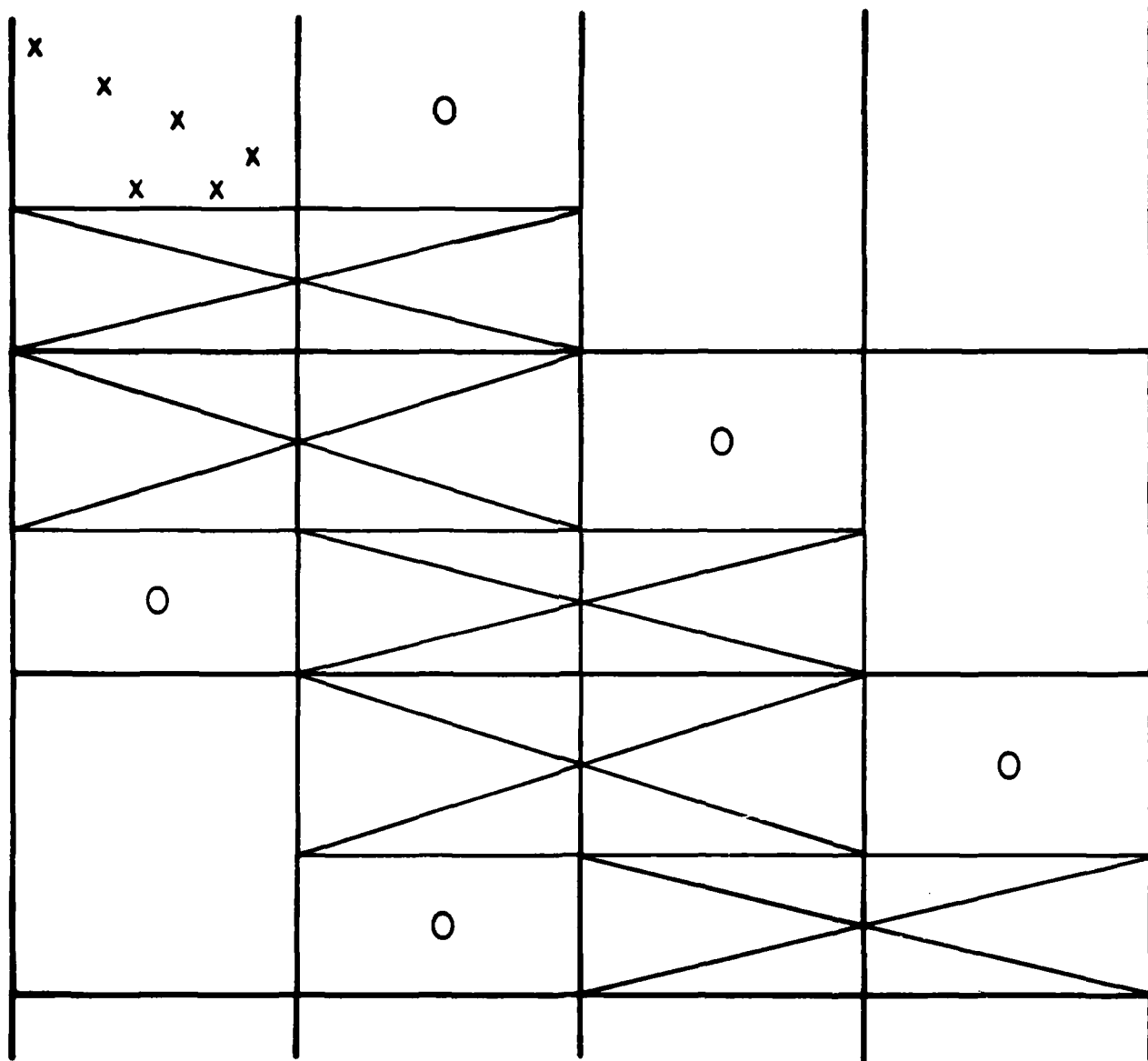
Figure 1. Schematic representation of the flow and coordinate system

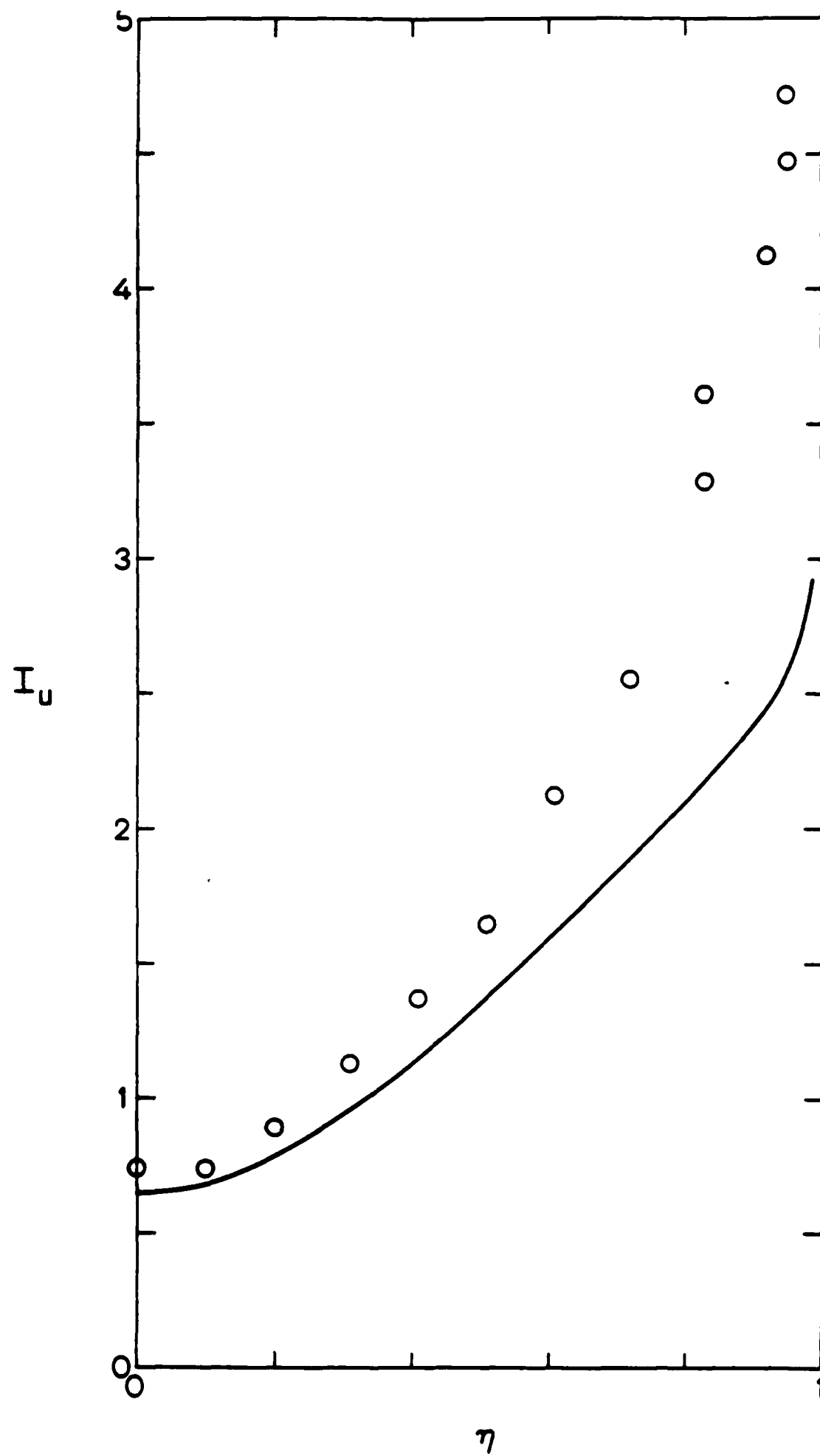
Figure 2. Schematic representation of the block tridiagonal matrix

Figure 3. Comparison of measured and predicted intensities

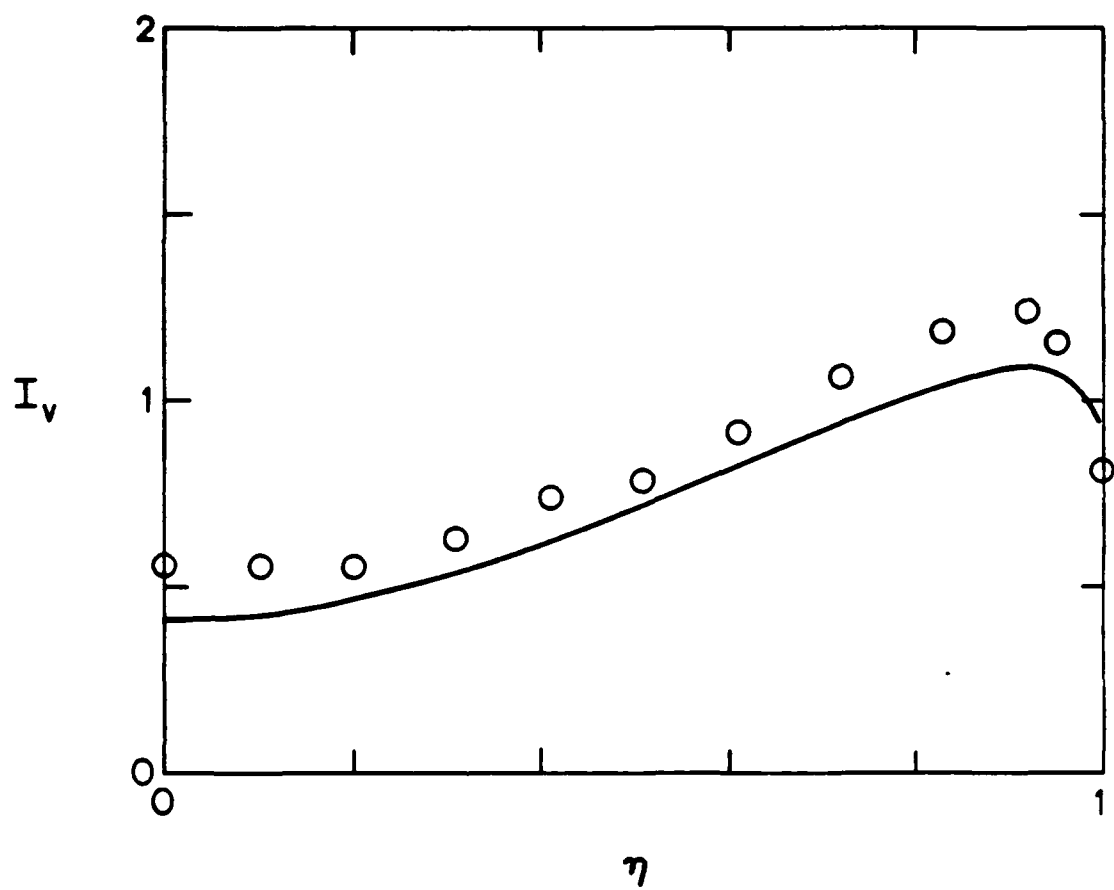
- a. The intensity of the axial velocity component  $I_u$
- b. The intensity of the radial velocity component  $I_v$
- c. The intensity of the azimuthal velocity component  $I_w$

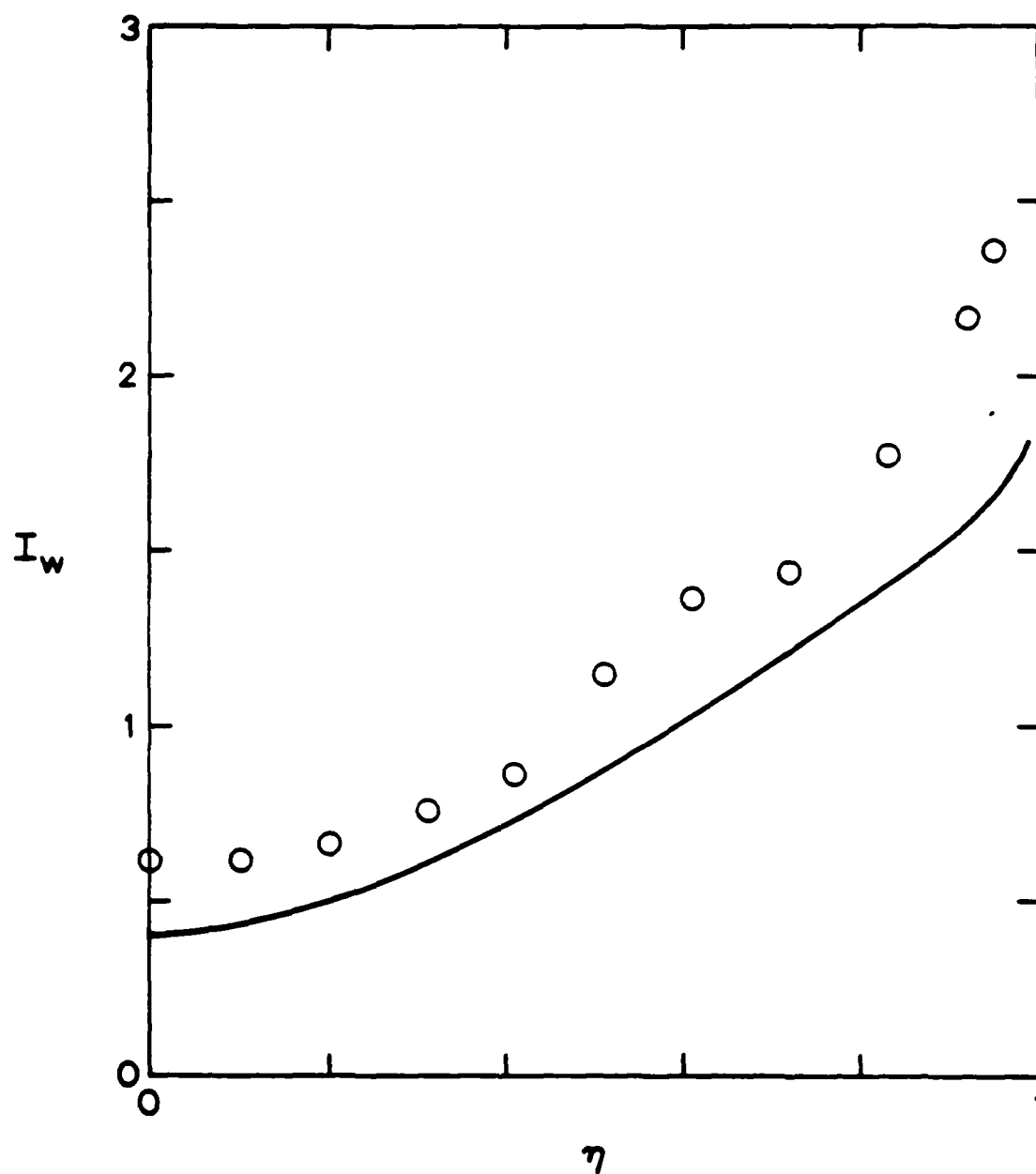












**SECTION D**  
**THE PREDICTION OF CONVECTIVE HEAT TRANSFER**  
**IN SPIRALLY FLUTED TUBES**

**SECTION D**  
**THE PREDICTION OF CONVECTIVE HEAT TRANSFER**  
**IN SPIRALLY FLUTED TUBES**

THE PREDICTION OF CONVECTIVE HEAT TRANSFER  
IN SPIRALLY FLUTED TUBES

by

ANNA BARBA

A thesis submitted for the degree of

DOCTOR OF PHILOSOPHY

to the Victoria University of Manchester  
Faculty of Technology

Department of Mechanical Engineering  
University of Manchester  
Institute of Science and Technology

Manchester

August, 1984

No portion of the work referred to in the thesis  
has been submitted in support of an application  
for another degree or qualification of this or  
any other university or other institution of  
learning.

## CONTENTS

	<u>Page</u>
Acknowledgements	i
Abstract	ii
Nomenclature	iv
<u>CHAPTER 1</u>	<u>INTRODUCTION AND LITERATURE SURVEY</u>
1.1	Introduction 1
1.2	Literature Survey 2
•	Introduction 5
1.2a	Experimental Studies 23
1.2b	Numerical Studies 30
•	Concluding Remarks 31
1.3	The Problem Considered, Present Contribution and Objectives 33
1.4	Organization of Thesis 35
1.5	Figures
<u>CHAPTER 2</u>	<u>THE LAMINAR FLOW PROCEDURE</u>
2.1	Introduction 61
2.2	The Co-ordinate System 62
2.3	The Describing Equations 64
2.4	The Boundary Conditions 67
2.5	Discretization and Solution of the Equations by the Computer Program 68
•	Introductory Remarks 69
2.5a	Formulation and Organization of the Finite-Difference Equations

	<u>Page</u>
2.5b The Special Treatment of Pressure	82
2.5c Solution of the Difference Equations	86
2.6 Outline of the Computer Program	92
• General Structure	
2.7 Experiences in Applying the Computer Program	96
2.8 Figures	101

### CHAPTER 3 THE LAMINAR FLOW CALCULATIONS

3.1 Introduction	113
3.1.1 Validation Tests	113
3.1.1a Velocity Field	113
3.1.1b Convective Heat Transfer	116
3.1.2 Parametric Study of the Results	116
3.1.2a Velocity Field	116
3.1.2b Convective Heat Transfer	123
3.2 Concluding Remarks	130
3.3 Figures	133

### CHAPTER 4 THE TURBULENT FLOW PROCEDURE

• Introduction	169
4.1 The Turbulence Models Adopted	169
4.1.1 General Considerations	169
4.1.2 Mixing-Length Hypothesis	170
4.1.3 The k- $\epsilon$ Boussinesq Viscosity Model	173
4.1.4 Simplified Algebraic-Stress Model	176
(a) Swirl Flow Treatment	180
(b) Buoyancy Effects due to Swirl	181
4.1.5 Matching the Near-Wall and Fully Turbulent Regions	182



	<u>Page</u>
4.2 Numerical Aspects of Treatment for Turbulent Flows	183
4.2.1 The Describing Equations and Boundary Conditions	183
4.2.2 Discretization of the Partial Differential Equations	188
4.2.2a Two-Dimensional Region	188
4.2.2b One-Dimensional Region	190
4.3 Experiences in Applying the Computer Program	193
4.3.1 Use of the Mixing-Length Hypothesis for the Whole Solution Domain	193
4.3.2 Use of the $k-\epsilon$ Boussinesq Viscosity Model with Wall Functions	195
4.3.3 Combination of the Mixing-Length and $k-\epsilon$ Turbulence Models	196
4.3.4 Adaptation of a Simplified ASM in the Core Region of the Tube	199
4.4 Figures	200

## CHAPTER 5 THE TURBULENT FLOW CALCULATIONS

5.1 Validation Tests	210
5.2 Parametric Study of the Result and Comparison with Experimental Data	212
5.2.1 Using the Combination of $k-\epsilon$ and Mixing-Length Turbulence Models	212
• The Velocity Field	212
• Convective Heat Transfer	218
5.2.2 Introduction of the Two Forms of a Simplified ASM into the Core Region of the Solution Domain	224
5.3 Concluding Remarks	226
5.4 Figures	228

		<u>Page</u>
<u>CHAPTER 6</u>	<u>CONCLUSIONS AND RECOMMENDATIONS FOR FURTHER WORK</u>	

6.1	Fulfilment of Objectives	274
	(a) Laminar Regime	274
	(b) Turbulent Regime	276
6.2	Conclusions and Recommendations for Future Work	277
	(a) Laminar Regime	277
	(b) Turbulent Regime	280

APPENDICES

<u>APPENDIX 1</u>	<u>The Computer Code for Generating the Grid Mapping the Solution Domain</u>
-------------------	--

1.1	Introduction	284
1.2	A Brief Description of the Computer Program's Structure	285
1.3	An Important Detail of the Computer Code	286
1.4	The Computer Code	288
1.4a	Glossary of FORTRAN Symbols for the Computer Code	288
1.4b	Listing of the Computer Code	

<u>APPENDIX 2</u>	<u>Derivation of the Equations of Flow in a Straight Spirally Fluted Tube</u>
-------------------	---

2.1	Introduction	291
2.2	Geometry	291
2.2.1	Characterization	291
2.2.2	Co-ordinate System	293
2.2.3	Metric of the Co-ordinate System	293
2.2.4	Normalized Basis	295
2.3	Vector and Tensor Components	299

	<u>Page</u>
2.3.1 Choice of the Components	299
2.3.2 Co-ordinate Transformation	302
2.4 Transport Equations	306
<u>APPENDIX 3</u>	<u>Pressure-Implicit Split Operator (PISO)</u>
3.1 Description of PISO	317
3.2 Derivation of the "Full" Pressure Correction Equation for PISO	319
<u>APPENDIX 4</u>	<u>Derivation of the Equations for <math>c_u</math> and <math>Pr_t</math> for the ASM Turbulence Model including Density Fluctuation Effects</u>
	330
<u>APPENDIX 5</u>	<u>The Computer Program for solving the Dynamic and Temperature Fields in a Spirally Fluted Tube</u>
• Introductory Remarks	336
5.1 User's Guide	336
5.1.1 General Structure	337
5.1.2 Details	340
5.1.2a CALCΦ	341
5.1.2b CALCP	342
5.1.2c LISOLV	344
5.1.2d PROPS	346
• Flow Chart	
5.2.1 Glossary of FORTRAN Symbols	347
5.2.2 Listing of the Computer Code	
References	356

### Acknowledgements

I wish to express my sincere gratitude to my supervisor, Professor B.E. Launder, for his guidance, advice and encouragement throughout this project.

Sincere thanks are offered to Dr. A.D. Gosman of Imperial College for his important contributions and advice in relation to numerical aspects of the research, as well as to Dr. G. Bergeles, Dr. I. Demirdzic and Dr. M.A. Leschziner for their help at various stages of the program .

Thanks must be expressed to Mr. J. Nicholson and the staff of the Computer Section for their eager assistance with the computational work.

I particularly wish to thank Mr. J. Yampolsky for his sympathetic interest and encouragement during critical stages of the work and the U.S. Office of Naval Research for the financial support they provided.

I am also deeply grateful to Mrs. L.J. Ball for her exceptional work in typing the thesis.

I wish to express my gratitude to the Department of Mechanical Engineering for the provision of research facilities.

To my parents and my husband for their encouragement, support and forbearance go my deepest thanks and gratitude.

Abstract

The thesis describes the development and application of a computational procedure (based on the curvilinear-orthogonal TEACH code which incorporates a finite-volume discretization of the describing partial differential equations) for solving both velocity and temperature fields in fully-developed laminar and turbulent flows through spirally fluted tubes.

In the laminar regime, extensive computational results have been obtained for air ( $Pr = 0.708$ ), water ( $Pr = 7.03$ ) and ethylene glycol ( $Pr = 93$ ) at Reynolds numbers ranging up to  $2.5 \times 10^3$ , with flute angles varying from  $0^\circ$  to  $30^\circ$  and with 10, 20 and 30 flutes around the circumference. The results show that both the surface heat transfer coefficients and friction factors increase over the smooth tube values. However, for water and especially for ethylene glycol the increase in skin friction coefficient is substantially lower than that of the heat transfer coefficient. Thus, even in the laminar regime, spirally fluted tubing can be used beneficially for promoting heat transfer in fluids of high Prandtl number.

In the turbulent regime, the study has been based mainly on the  $k-\epsilon$  Boussinesq viscosity model over most of the tube, merged with Van Driest's form of the mixing-length hypothesis in the near-wall region. Three fluids have been tested, air, water and calcium chloride solution 30% ( $Pr = 19.6$ ) in tubes with spiral angles ranging from  $0^\circ$  to  $30^\circ$  for 10, 20 and 30 flutes.

The predicted results show enhancement in both heat transfer and skin friction coefficients over the unfluted tube values. In most of the cases studied, however, the increase in surface heat transfer is considerably higher than that of the pressure drop, a behaviour quite desirable for applications in heat exchangers. The comparison with the available limited experimental data showed a substantial overprediction of the measured friction factors and heat transfer coefficients. However, an important (though brief) enquiry into the nature of the physical processes (viscous behaviour of the flow within the flutes, sensitivity due to swirl) led to a significant improvement of the predicted values in agreement with the experimental data.

Nomenclature

$A$	cross-sectional area
$A_n$	nominal area based on inside diameter
$A_t$	total area
$A_e^\phi, A_w^\phi, A_n^\phi, A_s^\phi$	control volume's east, west, north, south areas
$A_E^\phi, A_W^\phi, A_N^\phi, A_S^\phi$	coefficients for the discretized equations
$A_P^\phi$	$\left( -A_E^\phi + A_W^\phi + A_N^\phi + A_S^\phi - SP^\phi \right)$
$b$	$H/2\pi$
$c_{fin}$	$k_m \delta / (k_f d)$
$c_p$	specific heat at constant pressure
$c_\mu$	turbulence constant
$C_\xi, C_\eta$	convection coefficients
$D_{\xi\phi}, D_{\eta\phi}$	diffusion parameters
$D_h, d_h, d_e$	hydraulic diameter ( $= 4A/P$ )
$\vec{e}_\xi, \vec{e}_\eta, \vec{e}_\zeta$	base vectors in the $\{x^{(\xi)}, x^{(\eta)}, x^{(\zeta)}\}$ co-ordinate system
$\vec{e}_{(\xi)}, \vec{e}_{(\eta)}, \vec{e}_{(\zeta)}$	normalized base vectors in the $\{x^{(\xi)}, x^{(\eta)}, x^{(\zeta)}\}$ co-ordinate system
$f_e, f$	friction factor based on hydraulic diameter $\left( = \left( -\frac{dp}{dz} \right) \frac{4A}{\frac{1}{2}\rho W^2 P} \right)$
$f_p$	friction factor based on mean radius $\left( = \left( -\frac{dp}{dz} \right) \frac{2R_b}{\frac{1}{2}\rho W^2} \right)$
$f_r$	friction factor of a rough surface

$f_s$	friction factor of a smooth surface
$f_{sf}$	friction factor of a spirally fluted tube
$f_{sm}$	friction factor of a smooth tube
$F_{\xi\phi}, F_{\eta\phi}$	convection parameters
$G$	turbulence energy generation rate
$g_r$	body force per unit mass in radial direction
$h$	height of flute
$h_o$	height of a constant- $\eta$ co-ordinate line
$h_\xi, h_\eta, h_\zeta$	magnitudes of base vectors $\vec{e}_\xi, \vec{e}_\eta, \vec{e}_\zeta$
$H$	spiral pitch
$I, J$	indices for dependent variables and co-ordinates
$k$	turbulence energy
$\vec{k}$	vector parallel to the tube-axis
$k_f$	thermal conductivity of the fluid
$k_m$	thermal conductivity of the tape
$k_s^+$	roughness parameter
$l$	fin height
$l_c$	mixing length for a parallel plate channel
$l_p$	pipe mixing length
$l_m$	mixing length
$\dot{m}$	total mass flow rate
$\dot{m}_a$	mass flow rate in the region $R \leq R_a$
$n$	number of flutes
$NI, NJ$	maximum values of indices $I, J$
$Nu$	Nusselt number based on hydraulic diameter including the added surface area due to fluting

$$\left( = \frac{q'' D_p}{\Delta T \cdot k_f} \quad \frac{P}{2\pi R_b} \right)$$



$Nu_p$	pipe Nusselt number including the added surface area due to fluting $\left( = \frac{q'' P}{\pi \cdot \Delta T \cdot k_f} \right)$
$Nu'$	$( = Nu_p \frac{2\pi R_b}{P} )$
$Nu_e = Nu^*$	$( = Nu \frac{2\pi R_b}{P} )$
$Nu_r$	Nusselt number of a rough surface
$Nu_s$	Nusselt number of a smooth surface
$P$	pressure
$P', P'_1, P'_2$	pressure corrections
$P^*$	production of turbulence energy
$P_{ij}^*$	production of Reynolds stresses $\overline{u_i u_j}$
$P_{i\theta}^*$	production of fluxes $\overline{u_i \theta'}$
$P$	perimeter of the fluted tube
$Pe$	Peclet number
$Pr$	Prandtl number
$Pr_t$	turbulent Prandtl number
$P_{ref}$	reference pressure
$P_w$	surface static pressure
$P_{max}, P_{min}$	maximum and minimum static pressures
$\dot{q}''$	heat input to tube per unit surface area
$\dot{q}_e, \dot{q}_w, \dot{q}_n, \dot{q}_s$	total fluxes (convection plus diffusion)
$Q, \dot{Q}'$	heat input to tube per unit length
$R_a$	inner radius of the fluted tube
$R_b$	mean radius of the fluted tube
$Re_e, Re$	Reynolds number based on hydraulic diameter $( = \bar{w} \cdot 4A / (\nu P) )$
$Re_p$	Reynolds number based on mean diameter $( = \bar{w} \cdot 2R_b / \nu )$

$Re_f$	flute Reynolds number
$R_o$	mean radius of a co-ordinate- $\xi$ line
$R_m$	matching radius between the curvilinear and polar parts of grid
$R_w$	radius of the tube wall
$R_\eta$	$(=r/(r^2 + b^2) \partial r/\partial \eta)$
$S_f = S_{flute}$	perimeter of the flute = $\frac{P}{n}$
$S_\phi = \text{source term}$	$(=B_\phi + \Delta_\phi \phi)$
$St$	Stanton number
$SU^\phi, SP^\phi$	source terms
$s$	inter-fin spacing
$T$	mean temperature
$\vec{T}$	stress tensor
$T_b, \bar{T}$	bulk temperature
$T_{ref}$	reference temperature
$T_w$	wall temperature
$T_{w_r}$	temperature on the wall at the trough position
$U_{wall}$	velocity of the wall
$\vec{U}$	velocity vector
$\overline{u_i u_j}$	Reynolds stresses
$\overline{u_i \theta'}$	heat fluxes
$u^{(\xi)}, u^{(\eta)}, u^{(\zeta)}$	velocity components in the $\{x^{(\xi)}, x^{(\eta)}, x^{(\zeta)}\}$ co-ordinate system
$U, u$	mean and fluctuating velocity in direction $\xi$
$URF\phi$	under-relaxation factor for $\phi$
$V, v$	mean and fluctuating velocity in direction $\eta$
$V_\theta, V_r$	circumferential and radial velocity of $(\vec{U} + \vec{V})$

$W, w$	mean and fluctuating velocity in direction $z$
$W_{\max}$	maximum axial velocity
$\bar{W}$	bulk axial velocity
$W_{\xi}$	axial velocity at the pipe axis
$w^{(\xi)}, w^{(\eta)}, w^{(\zeta)}$	velocity components in the $\{z^{(\xi)}, z^{(\eta)}, z^{(\zeta)}\}$ co-ordinate system
$x^{(\xi)}, x^{(\eta)}, x^{(\zeta)}$	co-ordinate system following the spiralling of the flutes
$y$	distance from a node to the nearest node on the wall
$y^+$	$y\sqrt{\rho\tau_w}/\mu$
$z$	axial direction
$z^{(\xi)}, z^{(\eta)}, z^{(\zeta)}$	co-ordinate system following the tube-axis

### Greek Letters

$\alpha$	circumferential angle on the cross-stream plane
$\alpha_{\phi}$	weighting factor accounting for the non-uniformity of the grid
$\beta$	fin angle
$\beta_{\phi}$	weighting factor accounting for the non-uniformity of the grid
$\Gamma_e$	effective diffusivity
$\Gamma_t$	turbulent diffusivity
$\Gamma_T$	thermal diffusion coefficient ( $= \mu/Pr$ )
$\Gamma_{\eta_{\phi}}, \Gamma_{\xi_{\phi}}$	diffusion coefficients

$\delta_{ij}$	Kronecker delta
$\Delta V^\phi$	control volume
$\Delta \eta, \Delta \xi, \Delta z$	distances in $\eta, \xi$ and $z$ directions
$\Delta T$	$(= T_w - \bar{T})$
$\delta, \delta_L$	laminar sublayer thickness
$\delta u, \delta v$	velocity corrections
$\epsilon$	energy dissipation rate
$\vec{e}_\xi, \vec{e}_\eta, \vec{e}_z$	base vectors in the $\{z^{(\xi)}, z^{(\eta)}, z^{(z)}\}$ co-ordinate system
$\vec{e}_{(\xi)}, \vec{e}_{(\eta)}, \vec{e}_{(z)}$	normalized base vectors in the $\{z^{(\xi)}, z^{(\eta)}, z^{(z)}\}$ co-ordinate system
$\zeta$	spiral direction
$\eta, \xi$	curvilinear co-ordinates mapping the cross-section
$\eta_h$	efficiency $\left( = \frac{Nu_r/Nu_s}{f_r/f_s} \right)$
$\theta$	sector angle $\left( = \frac{2\pi}{n} \right)$
$\theta$	normalized temperature $(= T - T_{ref})$
$\theta'$	temperature fluctuation
$\kappa$	Von Karman constant
$\kappa_\xi$	$(= \frac{1}{b} \frac{\partial \xi}{\partial \theta})$
$\kappa_\eta$	$(= \frac{1}{b} \frac{\partial \eta}{\partial \theta})$
$\lambda_\xi$	$(= \frac{1}{h_\xi} \frac{\partial h_\xi}{\partial \eta})$
$\lambda_\eta$	$(= \frac{1}{h_\eta} \frac{\partial h_\eta}{\partial \xi})$
$\mu$	viscosity

x

$\mu_e$	effective viscosity
$\mu_t$	turbulent viscosity
$\mu_w$	viscosity on the wall
$\nu$	kinematic viscosity
$\pi$	3.1468
$\rho$	density
$\rho'$	density fluctuation
$\tau_w$	wall shear stress
$\tau_{\xi\xi}, \tau_{\eta\eta}, \tau_{zz}, \tau_{\xi\eta}$	stresses
$\tau_{\xi z}, \tau_{\eta z}$	
$\phi$	spiral angle $\left( \tan \phi = \frac{2\pi R_p}{H} \right)$
$\Phi$	dependent variable
$\omega$	angular velocity

## CHAPTER 1

### 1. INTRODUCTION AND LITERATURE SURVEY

#### 1.1 Introduction

It has been known for a long time that spiralling indentations on the inside surface of circular tubes enhance considerably surface heat transfer coefficients. However, in most of the cases this improvement is accompanied by substantial increases in friction factor, a feature which deters their application to systems where the pumping power is of primary importance.

However, experiments have shown that the type of spirally fluted tubes evolved by Yampolsky [1], shown in Figure 1.1, possess highly attractive features for use in heat exchanges and condensers for, on the inner surface, the heat transfer coefficient may be more than doubled compared with smooth tube values while the friction factors remain at values associated with unfluted smooth tubes. Moreover, the fabrication technique of rolling flutes on strips and then spiralling and simultaneously welding the strips to form the tubes results in costs not significantly greater than those of commercially welded tubes.

To complement the experimental work currently ongoing by J.C. LaRue and P.A. Libby, the present study has focused attention on the development and application of a numerical solution scheme to laminar and turbulent flows through spirally fluted tubes. The provision of such a procedure would be valuable in optimizing the design of the fluting.

## 1.2 Literature Survey

### Introduction

The thesis describes a numerical study of the velocity field and convective heat transfer characteristics of flow in the spirally fluted tubes evolved by Yampolsky [1], an example of which is shown in Figure 1.1.

The designer of heat transfer equipment has always been attracted to schemes which improve heat transfer coefficients. Considerations of saving energy and materials have led to enormous efforts to produce more efficient heat-exchange equipment. According to Bergles [2] (see Figure 1.2) the number of papers published per year in this area shows a remarkable increase in the last decade, a feature that is unique in the international scientific literature. The main focus of this work is to reduce the size of heat exchanger required for a specified heat duty or to increase the capacity of an existing heat exchanger. In some cases where heat generation rates are fixed, an efficient heat exchanger can prevent excessive temperatures or system destruction.

The various techniques for augmenting heat transfer inside tubes for laminar or turbulent flows may be divided into two categories: passive and active techniques. Passive techniques are those where no external energy is required to augment the heat transfer other than the pump work. Joshi and Bergles [3] in their survey of passive heat transfer augmentation techniques sub-classify these as:

- 1) Surface roughness
  - 2) Internal extended surfaces
  - 3) Displaced promoters
  - 4) Swirl flows
  - 5) Curved or coiled tubes
  - 6) Additives
- and 7) Compound techniques in which more than one of these techniques are employed.

As active techniques, where external energy is required to produce the augmentation, the above reference lists the following:-

- 1) Rotating tubes
- 2) Heated surface vibration
- 3) Fluid pulsation
- 4) Electrostatic fields
- 5) Suction or injection
- 6) Compound techniques

Bergles and different co-workers [ 2 ], [ 3 ], [ 4 ], [ 5 ] have presented an extensive literature survey on heat transfer augmentation techniques. They refer to about 600 publications giving a very short evaluation of the different techniques.

Attempts to increase heat transfer coefficients go back at least to Joule's [ 6 ] work in 1861. Later, similar reports have been published by Whitham in 1896 [ 7 ] and by Royds in 1924 [ 8 ]. Joule reported that significant improvement in the overall heat transfer coefficient for condensation of steam in a tube by single-phase cooling water flowing on



the outside of the tube could be obtained by wending a wire, in spirals, around the tube. Whitham [7] reported an increase in efficiency of a tube boiler by up to 18% when twisted-tape inserts were fixed in the tubes.

In our literature survey we shall restrict attention to passive techniques mainly because the spirally fluted tube belongs to that category. We shall refer to experimental and numerical studies for both turbulent and laminar flows. The augmentation of heat transfer for laminar flows is most important because in that regime the heat transfer coefficients are generally low.

The main problem is that, in the existing literature, for a given augmentation technique, different investigators do not give their results in a common frame of reference. Thus, the evaluation of a technique and, even more so, the comparison of different techniques, becomes very difficult.

Making a brief reference to active techniques we should state that a great amount of work has been published on this topic. For example, the reports of White [9], Harvey et al [10], Murakami et al [11], Nagib et al [12], Canon and Kays [13], McElhiney et al [14], Mori et al [15], Miyazaki [16] and Skiadaressis and Spalding [17] present tubes straight or curved, circular or square, rotating about their own axis or a parallel axis, and give data for both laminar and turbulent flows where generally a moderate increase in heat transfer has been observed mainly for laminar flows.

Bergles [2] reports improvement of heat transfer to both turbulent and laminar flows for liquids with surface vibration. Fluid vibration has

been studied for both air and liquids and reported in reference [2].

The studies of Porter et al [18], Savkar [19] and Newton et al [20] showed an impressive enhancement of heat transfer with electric fields, particularly in the laminar flow region, improvements of at least 100% when voltages in the 10 KV range were applied to oil.

Injection and suction have been demonstrated to improve heat transfer to both laminar and turbulent flows. Relevant reports are those of Kudirka [21], Tauscher et al [22], Kinney [23] and Kinney and Sparrow [24]. It is interesting to note, however, that in all the above references the enhancement of heat transfer is followed by a comparable or even higher increase of the friction factor.

The existing literature on passive techniques can be divided into two categories: experimental studies and numerical studies. In the first category we shall focus attention mainly on results, while in the second we shall discuss as well the numerical procedures used by the authors since our work is a numerical study. (A careful investigation of previous studies, similar to ours, can provide most useful information for comparison as far as the numerical procedure and the results are concerned).

#### 1.2a Experimental Studies

The role of rough surfaces in fluid mechanics and heat transfer has been studied by scientists for a long time. In 1933 Nikuradse [25] reported his experimental work on the effect of roughness on friction and velocity distribution, using pipes roughened by sand grains. In spite of

this complete experimental work, little attention had been focused on the study of the effect of roughness on heat transfer until Cope [26], in 1941, published his studies on heat transfer of rough tubes and Nunner [27], in 1958, reported an extensive work on heat transfer to air using different types of two-dimensional roughness elements.

Schlichting [28], using the experimental results of Nikuradse, showed that friction factor laws for rough tubes can be divided into three different regions depending on the roughness parameter  $k_s^+$  and the laminar sublayer thickness  $\delta_L$ :-

- 1) The hydraulically smooth region, where the roughness elements are within the laminar sublayer and the equation of friction factor is that of a smooth tube

$$\frac{1}{\sqrt{f}} = 2 \log(\text{Re} \sqrt{f}) - 0.8 \quad \left[ 0 < (k_s/\delta_L) < 5 \right]$$

where  $k_s$  = roughness height

$f$  = friction factor

$$k_s^+ = k_s/\delta_L$$

$\text{Re}$  = Reynolds number

- 2) The transition region, where some of the roughness elements are in contact with the turbulent bulk flow increasing the pressure drop and the equation of friction factor is a function not only of  $\text{Re}$  but of  $k_s/d_h$  as well

$$\frac{1}{\sqrt{f}} = 1.74 - 2 \log \left[ 2 \frac{k_s}{d_h} + \frac{18.7}{\text{Re} \sqrt{f}} \right] \quad \left[ 5 < (k_s/\delta_L) < 70 \right]$$

where  $d_h$  = hydraulic diameter

- 3) The fully rough region, where the friction factor depends only on  $k_s/d_h$

$$f = \frac{1}{(2 \log \frac{d_h}{k_s} + 1.74)^2} \quad \left[ (k_s/\delta_L) > 70 \right]$$

However, all the above equations can be used only with close-packed sand roughnesses and cannot be extended to other roughness types.

Similarly, studies of experimental results on heat transfer on rough surfaces led to a number of theoretical correlations conducted by Nunner [27], Dipprey et al [29], Owen et al [30], Martinelli [31] and Galin [32]. Nunner's experimental results were presented in the form

$$\eta_h = \frac{1 + 1.5 \text{Re}^{-1/8} \text{Pr}^{-1/6} (\text{Pr} - 1)}{1 + 1.5 \text{Re}^{-1/8} \text{Pr}^{-1/6} (\text{Pr} (f_r/f_s) - 1)}$$

where  $\text{Pr}$  = Prandtl number

$$\eta_h = \frac{\text{Nu}_r/\text{Nu}_s}{f_r/f_s} \equiv \text{efficiency}$$

(subscripts  $r$  and  $s$  stand for rough and smooth tubes respectively)

$\text{Nu}$  = Nusselt number

The above correlation predicts efficiency always less than unity since  $f_r/f_s$  is equal to or greater than unity. The formula does not fit experimental results for "integral" roughnesses since Nunner's experiments were conducted with "overlapped" roughnesses only. The latter type of roughness can be formed by wires or ribs soldered on the tube surface, inside or outside, being only turbulent promoters. They do not increase the heat transfer surface because of the high thermal resistance between

the smooth surface and the roughness elements. In contrast, integral roughnesses, such as threads, wires, ribs or grooves forming a solid body with the tube, increase the active heat transfer surface. However, the small scattering of data for both integral and overlapped roughnesses indicates that the experimental results for all types of roughnesses can be represented by one equation. In this regard, separate proposals have been made by Dipprey et al [29] and Owen et al [30]. Dipprey used a similarity rule in order to correlate, interpret and extend experimental results for turbulent flow and the equation obtained is:-

$$\eta_h = \frac{1.07 + 12.7 \sqrt{f_s/8} (Pr^{\frac{2}{3}} - 1)}{1 + \sqrt{f_r/8} (5.19(k_s^+)^{0.2} Pr^{0.44} - 8.48)}$$

Owen's equation is:-

$$\eta_h = \frac{1.07 + 12.7 \sqrt{f_s/8} (Pr^{\frac{2}{3}} - 1)}{1 + \sqrt{f_r/8} (0.52(k_s^+)^{0.45} Pr^{0.8}) + 17.8 f_r/8}$$

where  $k_s^+ = k_s/\delta_L$  determines the extent of geometrical influence of a roughness element in turbulent flow. Dipprey's equation is presented on Figures 1.3-1.6, where the efficiency  $\eta_h$  is plotted against the Prandtl number with  $k_s^+ = 30, 60, 100, 250$  as parameters. From these graphs one can see the good agreement between Dipprey's theory and the experimental results for the fully rough region ( $k_s^+ > 70$ ) and for Prandtl numbers from 1 to 7 as well as the level of  $\eta_h$  which becomes greater than 1 for high Pr and  $k_s^+ > 70$ . However, no experimental data exist for high Prandtl numbers for  $k_s^+ > 250$  and  $k_s^+ < 30$ . Figure 1.7 presents the efficiency  $\eta_h$  as a function of  $k_s^+$  for different Prandtl numbers. It is clear that for a given  $k_s^+$   $\eta_h$  increases with Pr, while for a given Prandtl number and

$k_s^+ > 70 \eta_h$  decreases with increasing  $k_s^+$ .

Burck [33] tried to explain the heat transfer mechanism of rough surfaces emphasizing that it cannot be expected that the models proposed by Dipprey or Owen would predict with great accuracy such a complicated behaviour over a large range of Prandtl numbers and roughness parameters. His analysis noted that the heat transported by turbulence in the bulk depends on the amount of heat which can reach that part of the flow transported by conduction through the thermal boundary layer. So, increasing  $k_s$  (namely  $k_s^+$ ), the heat transported to the bulk flow is limited by the thermal resistance of the thermal boundary layer, while the skin friction is increasing, leading to a decrease of efficiency. The heat transfer performance of rough surfaces is not so much influenced by the shape of the roughness elements, but is determined mainly by the type of the roughness elements, namely integral or overlapped.

Smith and Gowen [34] reported heat transfer data for internally threading pipes using UCON with  $Pr = 349$ . They demonstrated an improvement of efficiency (compared with smooth tube's data) for UCON (a polyalkylene glycol) in contrast to the behaviour of water confirming the results from Dipprey's equation.

Gee et al [37] studied another type of roughness, the helical rib-roughness, using air and water with three helix angles ( $30^\circ$ ,  $49^\circ$  and  $70^\circ$ ) all having a rib pitch (H) to height ratio of 15 and covering a Reynolds range from 6000 to 65000. That paper, published in 1980, was the first reporting heat transfer data in circular tubes with helically rib-roughened inner surfaces. Gee et al showed that helical rib-roughness on the inner

surface of a tube gives greater efficiency than transverse rib roughness, as many other investigators before have suggested. The best operating condition, as is shown in Figures 1.8 and 1.9, is  $k_s^+ = 5$  and helix angle of about  $50^\circ$  ( $k_s^+$  is based on the rib height).

Smith et al [38] studied the features of a smooth pipe where a spiral rib was inserted. They found, as in Ref. [37], that for water the smooth tube is always more efficient than the rifled tube but for air, only for Reynolds numbers greater than  $2 \times 10^4$ . Their temperature profiles showed that the rifling has reduced the resistance to heat transfer in the turbulent core, which explains the greater efficiency of rifled tubes at lower Pr since, for a given Reynolds number, the relative resistance to heat transfer in the turbulent core increases with decreasing Prandtl number. In contrast, wall roughness resulted in somewhat steeper dimensionless temperature gradients in the turbulent core since the most important reduction in resistance is at the wall.

White et al [39] reported on helical-rib roughness applied to the outer surface of the inner tube in an annular flow configuration. They transformed their data using an equivalent diameter in order to remove the effect of the smooth outer wall and presented their results as though both walls of the annulus were rough. Their transformed annulus data showed that the highest efficiency was observed at  $33^\circ$  helix angle with rib pitch-to-height ratio of 8.

Considerable progress in the commercial production of tubes with internal roughness has been made in recent years and such tubes are available in the U.S.A. and U.K. as standard catalogue items.

Another method of intensifying heat transfer is the use of internal fins in tubes. Such fins could be either straight or helical in geometry. For most applications this approach can be considered "old technology".

Experimental results for laminar flows have been reported by Marner and Bergles [40] and by Bergles [41]. They reported a 200% increase in Nusselt number for water and 700% for ethylene glycol using longitudinal fins and uniform heat flux, as well as a 230% increase for ethylene glycol using spiral fins and uniform wall temperature. Watkinson et al [42] studied the flow of motor oil ( $Pr = 180 - 450$ ) in tubes with spiral fins and reported an increase of 224% in Nusselt numbers based on constant pumping power comparison.

For turbulent flows, studies have been reported for air by Kubanek et al [43] and for water by Tarassof et al [44] using the same type of tubes for their experiments. They developed correlations using similar parameters; however, those for water do not agree with the correlations for air. The data for friction factor were correlated by an equation of the general form:

$$f_e = c_1 (s/d_e)^a Re_e^b (H/d_e)^d \quad (I)$$

where  $s$  is the inter-fin spacing,  $H$  the pitch of the spiral fins, while the subscript  $e$  stands for 'equivalent'. The different constants are given in the following table:-

		$c_1$	$a$	$b$	$d$
STRAIGHT FINS	WATER	1.624	0.16	-0.39	0
	AIR	0.524	0.17	-0.29	0
SPIRAL FINS	WATER	2.456	0	-0.39	-0.2
	AIR	0.2184	0	-0.15	-0.24



Equation (I) is valid for  $5000 \leq Re_e \leq 75000$ ,  $0.2 \leq s/de \leq 0.5$  and  $9 \leq H/de \leq 80$ . Figures 1.10 and 1.11 show how well the experimental data are correlated by Equation (I), for both straight and spiral fins.

The data for Nusselt number were correlated by an equation of the general form:-

$$Nu_e = c_2 Pr^k Re_e^l (H/de)^m (S/de)^n \left( \frac{\mu}{\mu_w} \right)^p \left( \frac{T_b}{T_w} \right)^q \left( \frac{A_n}{A_t} \right)^r \quad (II)$$

where  $A_n$  is the nominal area based on inside diameter,  $A_t$  the total area,  $T_b$  the bulk temperature,  $T_w$  the wall temperature,  $\mu$  the viscosity and  $\mu_w$  the viscosity on the wall. Again, the different constants are given in the following table:-

		$c_2$	$k$	$l$	$m$	$n$	$p$	$q$	$r$
STRAIGHT FINS	WATER	0.212	0.333	0.60	0	0.34	0.14	0	0
	AIR	4.11	0.4	0.326	0	$\frac{-1.4 \times 10^{-6}}{Re_e^{1.07}}$	0	0.5	1
SPIRAL FINS	WATER	0.369	0.333	0.63	-0.27	0.21	0.14	0	0
	AIR	0.242	0.4	0.645	$\frac{-2.95}{Re_e^{0.23}}$	$0.0045 Re_e^{0.31}$	0	0.5	0

Equation (II) is valid over the same range of  $Re_e$ ,  $H/de$ ,  $s/de$  as Equation (I).

Figures 1.12, 1.13 and 1.14 show the agreement between the experimental data and the values taken from the correlation (II). For both water and air, when the ratio  $(H/de)$  decreases, the Nusselt number increases. For air flow through spirally finned tubes the slope of  $Nu_e$  versus  $(H/de)$  or  $(s/de)$

changes systematically with Reynolds number, in contrast to water where the slope is constant. The same is true as well for straight fin tubes and the slope of  $Nu_e$  versus  $(s/de)$ . We can see this in Figures 1.13 and 1.14 where another interesting feature is that an increase of  $(s/de)$  increases  $Nu_e$  for water in contrast to air.

At constant pumping power the heat transfer performance of smooth and finned tubes can be given by the ratio of the heat transfer coefficients for finned ( $hi,f$ ) and smooth ( $hi,o$ ) surfaces, plotted in Figure 1.15. From that figure it is obvious that for spirally finned tubes the above ratio increases with the inter-fin spacing to pitch ratio for both water and air. It means that the best performance can be obtained using fewer fins and tighter spiralling. For the straight fin tubes, the constant pumping power correlation for water increases with the ratio of inter-fin spacing to diameter, while for air it is almost insensitive to that ratio. In references [43] and [44] the influence of Prandtl number has not been established since the range of  $Pr$  used is very narrow. Kubanek et al [43] pointed out that application of the correlation (II) to liquids of higher Prandtl numbers should give conservative results.

Turbulence promoters such as helically coiled wires or twisted tapes fitted inside tubes are among the techniques used to augment heat transfer. Considerable experimental and theoretical work has been published on twisted tapes but very little on helically coiled wires where the following features are very interesting:-

- a) They produce rotational flow which results in the movement of heavier fluid elements outward and lighter ones inward, improving convection in the case of heating.

- b) They introduce roughness elements which affect the velocity distribution, the turbulence level and the turbulent wall shear.

All these result in increased heat transfer and frictional power loss.

Kumar et al [45] have reported experimental results of forced convection heat transfer and frictional factors for water flowing in a vertical tube with coiled wire turbulence promoters of various diameters and pitch-to-diameter ratios, uniformly heated. Their results show that, at constant Re, a decrease of the pitch-to-diameter ratio increases both the heat transfer and friction factor. The maximum increase in heat transfer is of the order of 280% corresponding to a pitch-to-diameter ratio of one. Their heat transfer data were correlated by the equation:-

$$Nu = 0.175 Re^{0.7} Pr^{\frac{1}{3}} (H/d)^{-0.35}$$

within  $\pm 7.5\%$  irrespective of the wire diameter. Kumar et al [45] concluded that helically coiled wire turbulence promoters increase the heat transfer coefficient compared with that of a smooth tube, but that they increase the friction factor even more. Therefore, they can be used effectively only in cases where the pumping power is not important but reduction in the size and weight is of primary interest.

A twisted tape is sometimes inserted in a circular tube to produce swirl flow, thereby to increase the heat transfer coefficient on the inside tube surface. The tape is a thin metal strip twisted about its longitudinal axis with a width equal to the internal diameter of the tube. When the tape twist ratio  $y$  ( $= H/d$ ,  $H$  being the pitch for  $180^\circ$  of rotation of the twisted tape) becomes infinity, the tube consists of two semi-circular straight

tubes in parallel.

Hong et al [46] experimentally evaluated the heat transfer performance of a laminar twisted-tape flow. The tube was electrically heated but the twisted tape was isolated from the wall, which means  $C_{fin} = 0$  ( $C_{fin} \equiv \frac{k_m \delta}{k_f d}$ ,  $k_m$  is the thermal conductivity of the tape material,  $k_f$  of the fluid). Their friction factor results, shown in Figure 1.16, suggest that the effects due to the tape twist are evident only at large Reynolds numbers, where the data tend to rise above the reference curve. Figure 1.17 shows Hong's results for Nusselt number for  $y = 5.08$  and different Prandtl numbers. It is clear that the swirl motion makes  $Nu$  a function of  $Re$  and  $Pr$ , while for  $y = \infty$  and  $C_{fin} = 0$   $Nu$  is a constant equal to 2.594. Hong's experimental results can be correlated by the equation:-

$$Nu = 5.172 \left\{ 1 + 0.005484 \left[ Pr (Re/y)^{1.78} \right]^{0.7} \right\}^{0.5} \quad (III)$$

which fits a very wide range of Prandtl numbers ( $Pr = 3 - 192$ ). Hong et al concluded that the increase in pressure drop with tape-generated swirl flow in the laminar regime is less than the increase in heat transfer coefficient. The maximum increase in heat transfer coefficient is ten times the empty tube, while the corresponding pressure drop is less than four times the empty tube pressure drop.

Lopina et al [47] reported an experimental study on heat transfer and pressure drop in tape-generated swirl flow of single-phase water for the turbulent region. They developed a method for predicting the heat-transfer coefficient for swirl flow based on the hypothesis that the observed improvement is due to a) the increased flow path created by the tape, b) the increased circulation created with heating due to centrifugal forces

and c) the tape fin effect. Figures 1.18 and 1.19 show the results for friction factor and Nusselt number, while the authors concluded that a comparison of swirl and straight flow at constant pumping power indicated that it should be possible to obtain improvements of at least 20% with swirl flow of water. Their additive correlation shown schematically in Figure 1.20 has been found suitable for a wide range of liquid data. The spiral and centrifugal convection (subscripts sc and cc respectively) can be recognized as modified forms of the conventional relations for turbulent flow in tubes and turbulent free convection. The fin factor  $F$  represents the ratio of total heat transfer to the heat transferred by the walls alone. Other reports and comparison between experimental and numerical data for flows in tubes with twisted tapes will be presented in Part 1.2b of the literature survey.

Marner et al [40] reported an experimental comparison between twisted tape inserts (with twist ratio  $y = 5.4$ ) and spirally finned tubes for laminar flow of water and ethylene glycol. From their results, shown in Figure 1.21, it is obvious that although both configurations show some enhancement, the spirally finned tube (S.F.) is clearly superior to tube with twisted tape (T.T.I.). The subscripts m, a and o stand for mean, augmented and plain tube respectively while  $h$  represents the heat transfer coefficient.

From the discussion so far, it is clear that surface roughness and swirl flow produced by a twisted tape, when applied separately, are among the most effective methods for augmenting heat transfer at low pumping cost. Bergles, Lee and Mimic [48] studied the case where those two techniques were combined since it is reasonable to assume that such a practice would be superior to either technique used separately. Their

findings are shown in Figure 1.22 where the ratio of augmented to non-augmented heat transfer coefficient at constant pumping power is plotted against the Reynolds number. The subscripts o, a and p mean smooth tube without swirl tape, tube modified to augment heat transfer, and constant pumping power comparison respectively. From Figure 1.22 it is clear that at low Reynolds the best choice would be a smooth swirl tube, but at higher Reynolds the rough swirl tube is the top performer. However, the authors emphasize that their comparative data apply to the roughness configuration, tube-tape assembly, fluid and operating conditions used in their experiments. Any change might affect the form or the relative position of the curves in Figure 1.22.

Compound techniques, like the one studied in Ref.[48], are a slowly emerging area of enhancement which promises practical applications since heat transfer coefficients can usually be increased above each of the several techniques acting alone. Some other studies are those of Rooyen et al [49] for internally-finned tubes with twisted-tape inserts, and Kryukov et al [50] for rough cylinders with acoustic vibrations.

Other than twisted-tape inserts, there is a variety of inserts of different types widely used in industry. Marner et al [40] studied two types of static-mixer inserts: the Koch and Kenics static-mixers. Figure 1.23 shows the variation of Nusselt number along the tube apparently for the thermally developing region. Curves I and J are for the Koch mixers, while K is for the Kenics mixers. It is clear that both types of insert give high Nusselt numbers, verifying the manufacturers' reports, such as Koch Engineering Company Inc. Bulletin [51] and Chen, Kenics Corporation Bulletin [52], which report a five-fold increase of Nusselt number for Koch inserts

and a two-fold increase for Kenics inserts, compared with the smooth-tube values. Figure 1.24 shows the variation of friction factor with Reynolds number for both mixers. It is obvious that both types of mixer increase the friction factor, this again being in fair agreement with the manufacturers' recommendations.

The most interesting technique for us, however, is that of spirally corrugated tubes. In the rest of the present section on experimental studies, we shall focus on the existing literature on spirally corrugated tubes and mainly on the results reported by the General Atomic Company who financed our project via a contract from the U.S. Office of Naval Research.

Kidd [53] has reported experimental work on the heat transfer and pressure drop characteristics of gas flow inside spirally corrugated tubes. That type of tube was first studied at the Oak Ridge National Laboratory by Lawson et al [54] whose results showed that spirally corrugated tubes were very effective in enhancing the heat transfer to water. Kidd [53] performed his experiments using tubes with corrugation spacing ( $s$ ) to corrugation depth ( $L$ ) ratios ranging from 16 to 41. His data for Nusselt numbers could be correlated by an expression:-

$$Nu = aRe^m Pr^{0.4}$$

where  $m$  is consistently greater than 0.8 obtained for smooth tubes (Dittus - Boelter correlation), while for other common heat transfer enhancement devices, such as wire coils or twisted tapes, the exponent of  $Re$  is usually near or lower than 0.8. This means that corrugated tubes become better enhancement devices as the flow increases. Kidd's results also suggested that the "rougher" tubes, those with the deepest corrugations and the

smallest  $s/L$  ratios, have the higher value for the exponent  $m$ .

Yorkshire Imperial Alloys published a Technical Memorandum [55] where they report design data for their roped tubes, shown in Figure 1.25, in steam condensers. Figure 1.26 shows the variation of friction factor for  $Re = 10^5$  and for a range of groove depth ( $Li$ ) and pitch ( $H$ ) to diameter ( $Di$ ) ratios. It is clear that the friction factor increases when  $(Li/Di)$  or  $(Di/H)$  increases, the smooth friction factor taken from the equation  $f = 0.067 Re^{-0.235}$ . The variation of Nusselt number can be extracted from the variation of  $C_1$  in Figure 1.27 where  $C_1 = Nu Re^{-0.8} Pr^{-1/4}$ . For given Reynolds and Prandtl numbers the value of  $Nu$  can be calculated from  $Nu = C_1 Re^{0.8} Pr^{1/4}$ . Figure 1.27 shows an increase of  $C_1$  when  $(Li/Di)$  or  $(Di/H)$  increases. Ref.[55] points out that the overall heat transfer coefficient per unit pressure drop can be increased by 30% to 40% using roped tubes and a significant overall cost advantage can be obtained when steam is condensed on the outside of horizontal roped tubes by water in turbulent flow inside the tubes.

Silberman [56] in a recent report presented his experimental results on turbulence in helically corrugated pipe flow. The pipe used in his experiments had a 1 ft. diameter with  $59.5^\circ$  helix angle, while the working fluid was air. Silberman's purpose was to explore experimentally the turbulence mechanism behind the reduction of the friction factor for fully developed flow in helically corrugated pipes as compared with such flow in ordinary corrugated pipes, other factors being the same. Turbulence data have not been reported previously for these configurations.

If  $u$ ,  $v$ ,  $w$  represent the velocities in the axial, radial and tangential



directions of the pipe respectively, Figure 1.28 shows Silberman's experimental turbulence intensities compared with data by Laufer [57] for fully developed rectilinear pipe flow. From Figure 1.28 it is obvious that near the centre of the pipe the axial fluctuations are larger, while the circumferential and radial fluctuations are smaller than Laufer's data. The axial component decreases and the circumferential component increases relative to non-rotating pipe flow further from the axis. Radial fluctuations are remarkably smaller than in Laufer's case. Figure 1.29 shows the distribution of  $\overline{u'w'}$  Reynolds stress with the radius. Silberman concluded that the main differences between non-rotating pipe flow and the flow examined in his report were:-

- 1) The defect in mean axial velocity was increased and the eddy viscosity in the core region of the flow was reduced by nearly one half.
- 2) Turbulence intensities were reduced near the wall.
- 3) The  $\overline{v'w'}$  correlation was reduced near the wall.
- 4) Wall shear stress and friction factor were reduced.  
This is consistent with 1) and 3).
- 5) The  $\overline{u'w'}$  correlation was significant, especially near the wall.

Silberman [58] in a previous study had shown experimentally that for a given pipe diameter the friction factor decreases as the helix angle decreases (helix angle being measured from the tube axis), and that for a given helix angle and depth of roughness, the friction factor decreases as pipe diameter increases.

Spirally fluted tubing has been the object of study from 1979 at the General Atomic Company in U.S.A. by Yampolsky, La Rue and Libby. Ref. [1], [59] and [60] report progress made in the experimental area on single spirally fluted tubes, as well as the latest application to a 7-tube bundle heat exchanger. Their experimental work on single tubes showed that the heat transfer coefficient is increased without an increase in the friction coefficient. Figures 1.30 and 1.31 give the variation of Nusselt number and friction factor with Reynolds number for cooling or heating a single-phase liquid flow, all the variables being calculated on a hydraulic diameter basis.

Yampolsky et al [59] explained the physical process behind the above-mentioned most desirable behaviour of the spirally fluted tubes as follows: The spiral flutes continuously induce rotation of the flow within the flutes and of the bulk flow as a result of the curvature of the flutes. When heat is transferred inwards, the density gradients established close to the wall are de-stabilizing in the presence of rotation, affecting the main source of resistance to the transmission of heat (the laminar sublayer) and therefore increasing the heat diffusivity. Normally, improvement in the rate of radial heat transport in a tube resulting from increase in the turbulence level in the flow results in increase of the momentum loss relative to the increase in heat transfer. However, there are examples of instabilities in the atmospheric boundary layer that result in substantial increase of the thermal diffusivity relative to the momentum diffusivity (see Ref. [61]).

Figure 1.30 indicates that the increase in heat transfer depends on the level of heat flux as well as the direction of heat flow: inwards or outwards. Ref. [1], [59] and [60] also point out that there is uncertainty on

the validity of the experiments plotted in Figure 1.31. Kidd's data are in support of that uncertainty since his results show an increase in the friction factor coefficient, opposite to Figure 1.31. Figure 1.32 shows the variation of the Colburn factor, that is the ratio of the exchange coefficients of heat to momentum with the Reynolds number. There are two interesting features: first, the positive slope of the curves with Reynolds number, and second, the level of the Colburn factor which is always greater than one. In addition to the enhancement of the heat transfer coefficient relative to the friction factor coefficient, the flutes increase the heat exchange area also.

As far as the outside of the tube is concerned, in a vertical configuration an increase in condensation can be achieved. The reason for this is the helpful geometry of the tube since surface tension draws the condensate film from the crests into the troughs, creating a very thin film over the major part of the crests with, of course, reduced resistance to heat flow. The outcome is a substantial improvement in heat transfer over conventional smooth tubes.

Ref. [60] gives an analytical report on the study, design and manufacture of a 7-tube spirally fluted tube bundle for a heat exchanger. Figures 1.33 and 1.34 show the tube bundle being assembled into the shell as well as the tubing as seen through the shell side nozzle. The results on the heat transfer tests for this geometry indicate an enhancement factor relative to a plain tube of 1.59 for the tube side and 2.28 for the shell side. This is in addition to the area extension of 1.6. No variation was found in the level of enhancement with heat flux or heat flux direction, in contrast to what was found from experiments on single spirally fluted tubes,

shown in Figure 1.30. The results for the 7-tube bundle are in agreement with Curve 2 of Figure 1.30, where the enhancement ratio is 1.59 - 1.64. The measurements of the frictional coefficients showed essentially no change from the smooth tube values, which disagrees with the results for single spirally fluted tubes shown in Figure 1.31. This was not surprising since, as we mentioned above, confirming tests were required before the data in Figure 1.31 could be accepted. However, this does not alter the basic fact that enhancement of heat transfer is achieved without a frictional penalty. This unusual feature has provided the stimulus for our numerical study.

#### 1.2b Numerical Studies

Numerical studies of fully developed laminar flow heat transfer in uniformly heated internally finned tubes have been reported by Hu et al [62] and by Masliyah et al [63,64]. Hu et al considered fully developed velocity and temperature profiles together with a uniform heat flux on the walls and uniform heat input per unit tube length in axial direction. Masliyah et al considered axially uniform heat flux with peripherally uniform temperature. The fins were longitudinal of triangular shape (finite thickness) with high thermal conductivity, meaning equal temperature for the wall and fins. A finite element method has been used for the solution of the momentum and temperature equations.

Figure 1.35 shows the variation of friction factor with the number of fins with data taken from Refs.[62] and [63]. The agreement between Hu's and Masliyah's data is very good. For constant Reynolds number, the friction factor increases with the number or the height of the fins, reaching values which are 50 times higher than for the smooth tube value.

Figures 1.36 and 1.37 show the variation of the dimensionless temperature  $\phi \equiv \frac{T-T_w}{Q/k_f}$  ( $Q$  being the heat input per unit tube length (J/ms),  $k_f$  the thermal conductivity of the fluid) with radial position along the middle of the inter-fin spacing, for various numbers of zero thickness fins and two fin heights ( $\ell$ ). These figures show that near the wall ( $r = 1$ )  $\phi$  increases with the number of fins, while at the tube centre (away from the fins) it increases for  $N < 8$  and decreases for  $N > 8$ . For  $\ell = 0.4$  and especially for low values of  $N$ , the shape of  $\phi$  is not very much different from that of a smooth tube, while for  $\ell = 0.8$  and  $N \geq 16$  the fins are so close to each other that they act as an artificial tube where the fluid velocity becomes nearly zero. Two regions are created, the fin region from the tube wall to the fin tips and the core region from the fin tips to the tube centre. In the case where the fins have a finite thickness ( $\beta = 3^\circ$ , half fin angle) the radial distribution of  $\phi$  along the middle of the inter-fin spacing, shown in Figure 1.38, has some interesting features. Curve 4 shows that for  $\ell = 0.6$  there is a region between the fins where  $\phi$  becomes nearly constant, while Curve 5 indicates that for  $\ell = 0.8$ , obvious in Figure 1.37 also, the maximum of  $\phi$  no longer occurs at the tube axis but moves towards the fin region.

The variation of Nusselt number based on the inside diameter is given in Figure 1.39. It is clear that the improvement of  $Nu$ , compared with the smooth tube values, in some cases can be as high as forty-fold. Figures 1.35 and 1.39 indicate that the longitudinal fins are less efficient than the smooth surface for laminar flow in contrast to spiral fins (see Ref.[40]) Figure 1.39 also shows that Nusselt number is a strong function of the fin height, fin thickness and number of fins and for a given fin configuration an optimum fin number exists.

The first numerical study to predict the performance of tubes with straight inner fins for turbulent air flow was conducted by Patankar et al [65]. They have studied the fully developed flow in a finned tube with uniform heat flux and uniform wall temperature at any cross section; they also considered the flow in an annulus with constant heat flux and fins on the inner tube, the outer tube being smooth and adiabatic. The equations were solved in a cylindrical-polar co-ordinate system  $(r, \theta, z)$  with  $(r, \theta)$  mapping the cross-stream section and  $z$  following the axis of the tube.

Various turbulence models were examined while the one finally adopted by the authors was an algebraic model involving the mixing length. Because the tube wall and the fin surface simultaneously affect the mixing length at any point on the cross-stream section, the mixing length was taken from the equation:

$$\frac{1}{l} = \frac{1}{l_p} + \frac{1}{l_c}$$

where  $l_p$  was the mixing length for a pipe without fins and  $l_c$  the mixing length for the inter-fin spacing which was likened to a parallel plate channel.  $l_p$  and  $l_c$  were represented as the product of a Nikuradse-type mixing length  $L$  and the Van Driest damping factor  $DF$ :

$$\begin{aligned} l_p &= (DF)_p L_p \\ l_c &= (DF)_c L_c \end{aligned}$$

The turbulent viscosity was given then by the equation

$$\mu_t = \rho l^2 \left[ \left( \frac{\partial w}{\partial r} \right)^2 + \left( \frac{\partial w}{r \partial \theta} \right)^2 \right]^{\frac{1}{2}}$$

$w$  being the axial velocity.

The solution of the equations (continuity and momentum) was obtained

via finite differences, with the momentum equations being solved first and then used as input to the energy equation.

Figure 1.40 shows the variation of local heat transfer coefficient along the fin height ( $h_f$ ), while Figure 1.41 shows the variation of local heat transfer coefficient along the tube wall ( $h_c$ ) from the fin base ( $\theta/\theta_o = 0$ ) to the middle of the inter-fin spacing ( $\theta/\theta_o = 1$ ). It appears that the assumption of a uniform heat transfer coefficient is a better approximation for the tube wall than for the fin surface. For the case of an annulus, Patankar et al used the same turbulence model as for the finned tube with the replacement of  $\ell_p$  by two mixing lengths, one taking account of the outer tube and one of the inner one. For both pipe and annulus the fins were found to be a more effective transfer surface than the heated wall, on a unit area basis. It would be desirable, of course, to extend the numerical study to higher Prandtl numbers and spiral fins for both laminar and turbulent flows.

Date and Singham [66] reported a numerical study of the laminar flow in tubes containing twisted tapes. They first introduced the ratio  $Re/y$  ( $y$  being the twist ratio) which is similar to Dean number in curved pipe flow and accounts for the centrifugal force effect, in the calculation of friction factor. Their numerical results did not take account of the thickness of the tape which is not negligible if the tube diameter is small. Date and Singham correlated their numerical results by the following equations:

$$(f Re) = \begin{cases} 42.23 & Re/y < 6.7 \\ 38.4 (Re/y)^{0.05} & 6.7 \leq Re/y \leq 100 \\ c (Re/y)^{0.3} & Re/y > 100 \end{cases}$$

where  $c = 8.8201y - 2.1193y^2 + 0.2108y^3 - 0.0069y^4$ .

Date [67] reported a numerical study of a uniform-property flow in a tube containing a twisted tape for both laminar and turbulent regimes. He solved a set of equations by adapting an existing finite difference procedure for two-dimensional elliptic equations to predict friction factor and heat transfer coefficients. He used a co-ordinate system in which the angular co-ordinate was measured always from the surface of the twisted tape, that is a rotating cylindrical polar co-ordinate system  $(r', \theta', z')$  which was related to stationary system  $(r, \theta, z)$  by the equations:

$$r' = r$$

$$z' = z$$

$$\theta' = \theta + \frac{\pi}{H} z$$

The positive sign of  $\frac{\pi}{H} z$  implies anti-clockwise rotation of the tape as  $z$  increases,  $z$  and  $z'$  being in the axial direction and  $\theta$  and  $\theta'$  in the clockwise direction. The equations solved were those for the axial vorticity ( $w$ ), the stream function ( $\psi$ ), the momentum equation for the axial velocity ( $V_z$ ) and the energy equation.

Figure 1.42 shows the friction factor variation with the Reynolds number where the experimental data are from Hong and Bergles [46] and the numerical data are from Date and Singham [66]. Date [67] predicted the same behaviour for the friction factor as Ref.[66]. In Figure 1.43, Date's results for Nusselt number for laminar flow are compared with Hong's [46] experimental data correlated by Equation (III). Date's data, in contrast to Hong's results, show a separate influence of Prandtl on Nusselt number.



The difference is substantial and the strong Prandtl number effect for  $c_{fin} > 0$  predicted by Date needs experimental verification.

Figures 1.44 and 1.45 show the variation of  $Nu$  with  $Re$  for various twist ratios and Prandtl numbers. For a fixed  $Re$ ,  $Nu$  increases as  $y$  decreases or  $Pr$  increases. Both figures indicate that for  $y < \infty$ , when secondary flow exists,  $Nu$  depends on both  $Re$  and  $Pr$ . Another feature of the flow is that the increase in  $Nu$  increases as  $Re$  increases and this can be explained, partly, by the fact that in the energy equation there is an extra convection term due to the axial velocity  $\left( \frac{\pi}{H} V_z \right)$  which is large at high  $Re$ .

Date solved the above-mentioned set of equations with the addition of two more for the turbulent regime. The turbulent transport was represented by the  $k-\epsilon$  model and the additional two equations were for the kinetic energy of turbulence  $k$  and the energy dissipation rate  $\epsilon$ . The turbulent viscosity was calculated by the equation

$$\mu_t = \rho C_\mu \frac{k^2}{\epsilon}$$

where  $C_\mu = 0.09$  was taken from Jones and Launder [68].

The predicted friction factor is plotted in Figure 1.46. It is clear that Date's computations under-predict the experimental data, though the trends are in agreement. Date ascribes the modest agreement to the low value of  $\mu_{eff}$  predicted by the  $(k-\epsilon)$  turbulence model where the constants, taken from Ref.[68], although quite general for flows where the velocity gradients are significant only in one direction, are inadequate for predicting the twisted tape flow characteristics.

Figure 1.47 shows the distribution of  $Nu$  with  $Re$ . Again, the experimental data are under-predicted, although the trends are in agreement. One could suppose that if the friction factor data by some means can be corrected, then so would the  $Nu$  data. Date in his report argues that the disagreements between predictions and experimental data can be cured by using a different turbulence model. A first step in that direction could be the application of a simplified Algebraic Stress Model (ASM) proposed by Gibson and Launder [69].

It has been well established that secondary flow can significantly enhance heat transfer. Secondary flows are also generated by twisted pipes. Masliyah et al [70,71] have reported recently their study on laminar flow through twisted square tubes. They solved numerically in a rotating frame of reference the Navier-Stokes equations in the stream function-vorticity form. The rotating co-ordinate system was preferred, as in Date's [67] report, in order to convert the problem to a 2-D problem. Some validity tests on the numerical procedure were made, such as the case of the straight square tube (by setting  $H = 1000$ ,  $H$  being the dimensionless length of the tube over a rotation of  $\pi$  radians) where the friction factor was found with an error of 0.1%. Further mesh refinement tests indicated that finer grids are needed for low  $H$  ( $H = 2.5$ ) at high  $Re$  ( $Re > 400$ ), where the central-difference scheme fails to give accurate solutions and other schemes should be used, such as those proposed by Spalding [72], Raithby et al [73] and Raithby [74].

It has been found that the swirling motion did not alter the axial velocity profile, in conformity with White's [9] report for a circular tube. Masliyah et al reported that for low  $H$  and high  $Re$  the swirling

motion is not detectable in the core region while it is strong in the annular region; this is contrary to the case of low  $H$  but low  $Re$ . Figure 1.48 shows the variation of friction factor with  $Re$  for different values of  $H$  from which it is clear that the swirling motion affects the friction factor only for  $Re \geq 100$ , while for  $H < 20$  all the curves lie above the reference curve for the straight square tube. Ref.[70] also indicated that as  $H$  decreases, the axial velocity profile changes from that of a straight square tube to that of a straight circular tube.

The heat transfer characteristics arising in the twisted square tube were presented in Ref.[71] where the cases of uniform and non-uniform wall temperature were considered. The situation where opposite walls had the same temperature was found to give the best heat transfer performance where, for  $H = 2.5$ , the overall Nusselt number showed an increase of 122% over a straight square tube. Masliyah et al concluded that a twisted square tube configuration can be useful when several fluids at different temperatures have to be heated or cooled to different extents.

#### Concluding Remarks

In conclusion we may say that the spiral fins and the twisted tape inserts (for the laminar region), the integral roughness, the flutes and some types of static mixers are among the most effective (efficiency  $> 1$ ) enhancement techniques when applied to inner surfaces.

However, many factors enter into the final decision to use a heat transfer augmentation technique: heat duty increase, surface area reduction, pumping power requirements, initial cost, maintenance cost,

safety, reliability, etc. The heat transfer augmentation techniques discussed here should be analysed further, based on various performance evaluation criteria, such as those by Bergles et al [77] and Shah [78].

While most of the above-mentioned publications refer to research studies, the commercial application of this "heat transfer enhancement technology" continuously grows. This is evident from the enormous patent and trade literature. In the U.S.A. alone, nearly 500 patents related to this technology have been issued (Bergles, Nelson and Webb [75]), while hundreds of firms advertise such heat transfer promoters (see Junkan and Webb [76]).

### 1.3 The Problem Considered, Present Contribution and Objectives

The geometry under consideration is that of a spirally fluted tube, shown in Figure 1.1. Tests have shown [1, 59, 60] that for a fixed Reynolds number these tubes give rise to surface heat transfer coefficients in turbulent flow up to three times the smooth tube values without any corresponding increase in friction factors. This discovery naturally raises questions of what flow mechanism produces this highly desirable and unusual behaviour, perhaps unique in the heat transfer literature for it has been consistently found that heat transfer promoters enhance friction factors by at least the same proportion.

La Rue [82] is undertaking a detailed hot-wire study which should provide a good deal of insight into the flow structure, while the aim of the present research was to develop and apply a computational procedure for calculating the flow and temperature fields in fully developed conditions

through this type of tube.

The principal objectives of the research were:

- a) The development and application of a numerical solution scheme for laminar and turbulent flows based on finite-volume discretization of the highly complex partial differential continuity, momentum and energy equations, and an efficient algorithm for the solution of the resulting set of algebraic equations.
- b) The application of advanced turbulence models in the numerical solution scheme to represent the effects of turbulence.

The contribution of a computational study towards the understanding of the flow through spirally fluted tubes is valuable because it can provide a far more detailed mapping of the flow properties than any experimental study. It also permits a parametric study of the flow based on variations of the detailed geometry of the tube, exploration of the connection between changes in the surface performance and changes in the interior flow pattern and thus optimization of the tube design. The experimental work needed for optimization, while notionally possible, would be massive enough to make the task practically impossible.

Some of the results presented below have been published in Barba, Bergeles, Demirdzic, Gosman and Launder [83], in Barba, Bergeles, Gosman and Launder [84] and in Barba, Gosman and Launder [85].

#### 1.4 Organization of Thesis

The thesis is divided into six chapters.

Chapter 1 presents a detailed literature review of the experimental and numerical work in the field of heat transfer enhancement technology. Furthermore, the objectives of the research programme are discussed.

Chapter 2 deals with the computational procedure for the laminar flow calculations focusing attention on the chosen co-ordinate system, the partial differential equations describing the flow through a spirally fluted tube, the boundary conditions and the adoption and solution of the equations by the computer program. Details of the grid generating computer program, the derivation of the equations and the two-stage pressure correction (PISO) used in the computational procedure are presented in Appendices 1, 2 and 3 respectively.

Chapter 3 concerns itself with the presentation of the laminar flow numerical results and the validation tests leading to the acceptance of the correctness of these results. A parametric study of the results is presented for both velocity and temperature fields and conclusions are discussed concerning results and computational procedure.

Chapter 4 presents the turbulent flow computational procedure, with attention directed mainly towards the equations describing the flow and the turbulence modelling. Details of their application into the computer code are given in Appendix 5 where the final version of the computer program is contained, accompanied by a detailed description, while Appendix 4

includes the derivation of the equations for the simplified algebraic stress model applied into the core region of the flow.

Chapter 5 is similar in structure to Chapter 3, dealing with the turbulent flow computational results.

Finally, Chapter 6 summarizes the main conclusions from the present research, and recommendations are given for any further theoretical work considered appropriate.

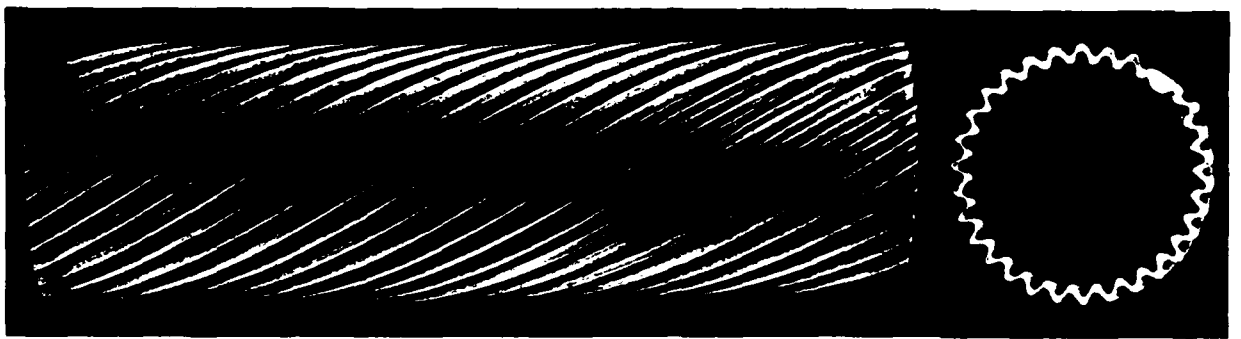


FIG. 1.1 SPIRALLY FLUTED TUBE



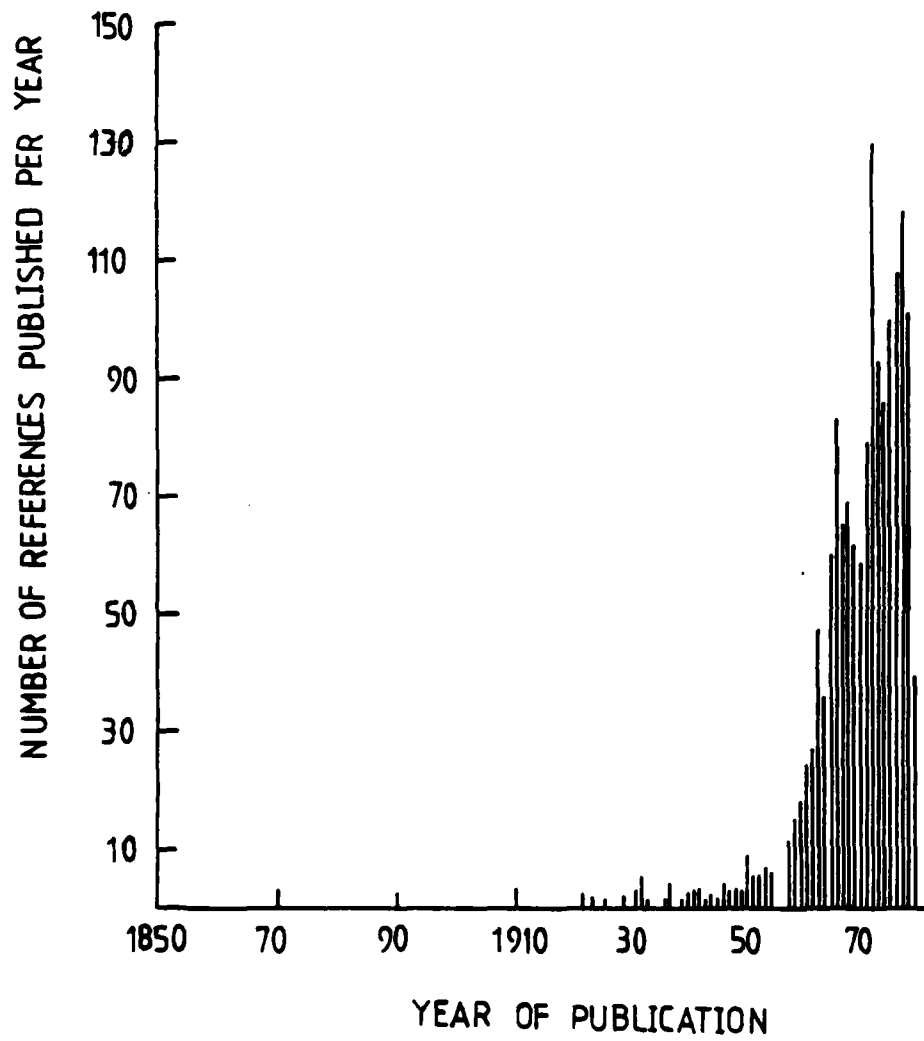


Fig 1-2

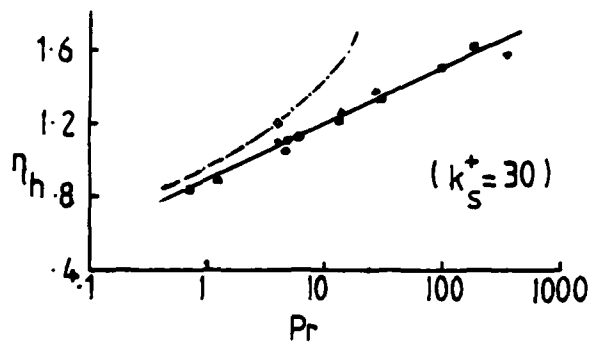


Fig 1-3

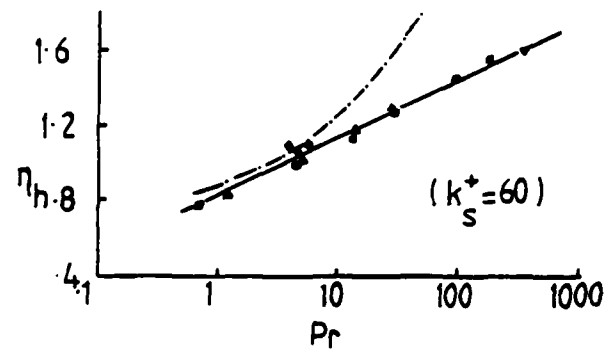


Fig 1-4

- - - Theory D.F.Dipprey  
 Experiments D.F.Dipprey et al  
 V. Kolar [35]  
 J.W. Smith et al [34]  
 E. Skupinski [36]  
 Burck [33]

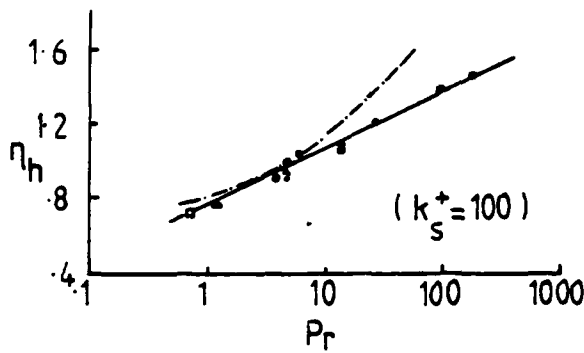


Fig 1-5

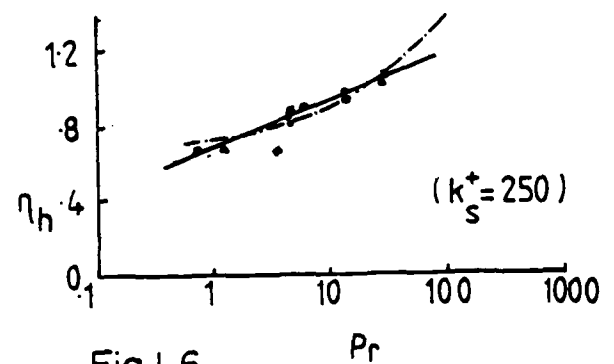


Fig 1-6

Efficiency of integral  
 roughnesses as a function of  $Pr$

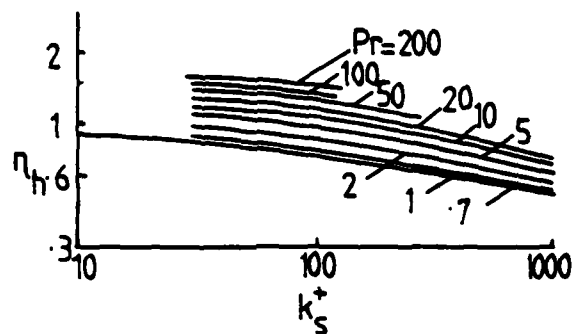


Fig 1.7 Efficiency of integral roughnesses as a function of  $Pr$  &  $k_s^+$

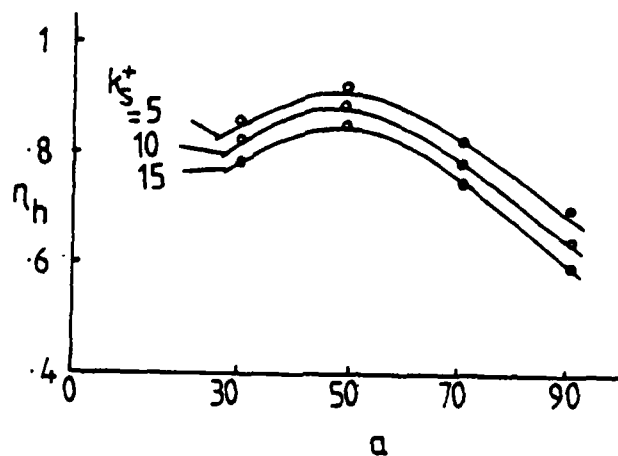


Fig 1.8 Efficiency index  $\eta_h [ = (St_r / St_s) / (f_r / f_s) ]$  vs. helix angle  $\alpha$  ( $Pr = 0.7$ )

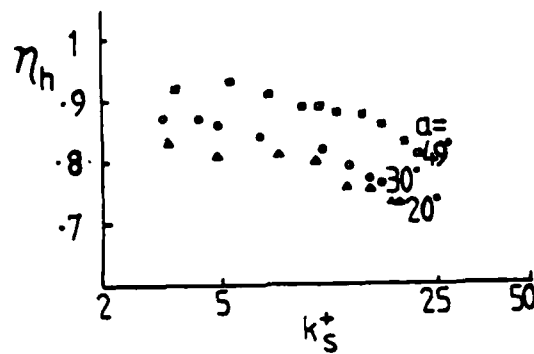
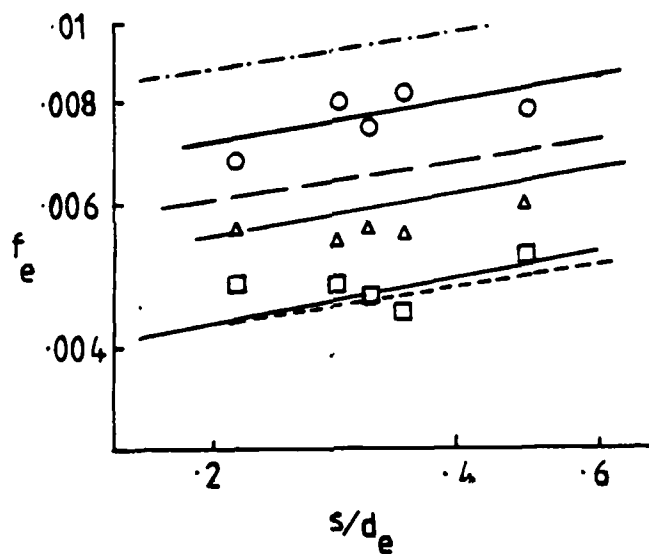
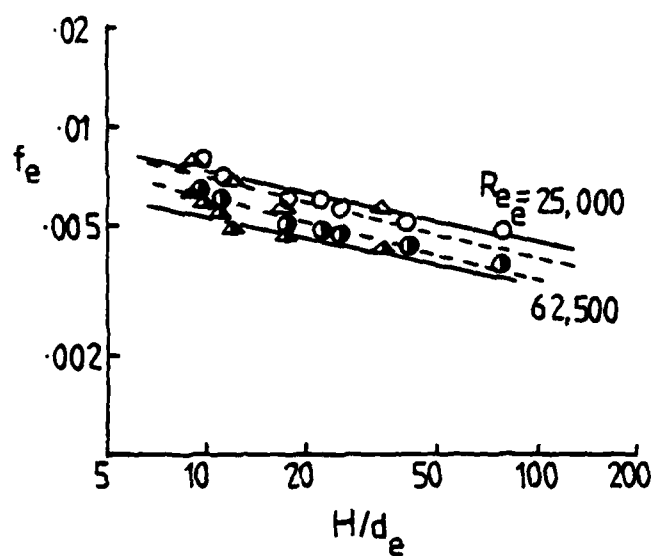


Fig 1-9 Efficiency index  $\eta_h = (St_r/St_s)/(f_r/f_s)$  vs.  $k_s^+$  ( $Pr = 0.7$ )



Experiments (air)	Equation	
$Re_e$	air	water
10,000	—	—
25,000	—	—
62,500	—	—

Fig 1-10 Friction factors for straight fin tubes



### Experiments

$Re_e =$	25,000	62,500	
	○	●	high spiral fins
	△	▲	low spiral fins
			} air
			----- equation - air
			———— equation - water

Fig I-II Friction factors for spiral fin tubes

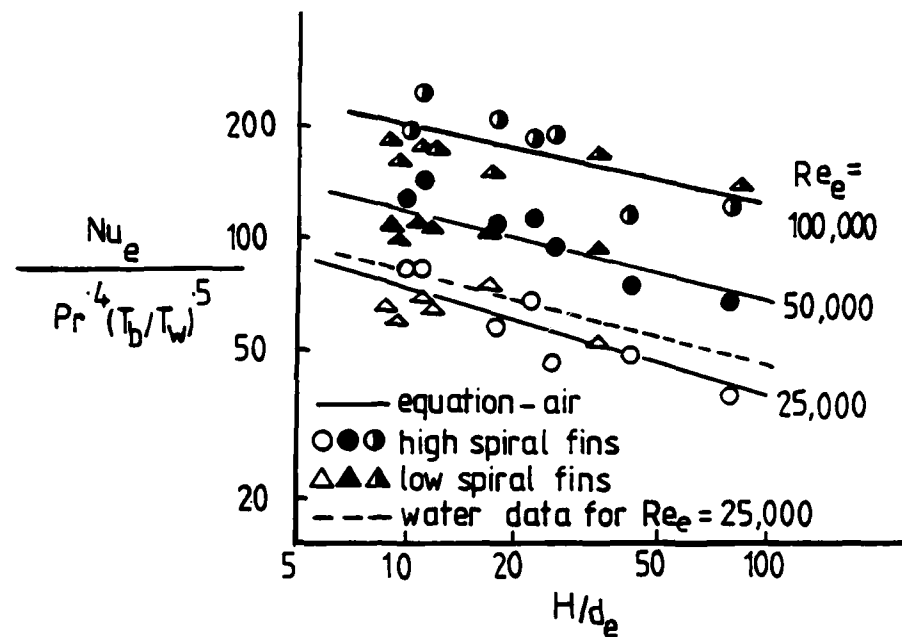


Fig 1-12 Effect of fin spiralling on the Nusselt-Prandtl modulus for spiral fin tubes

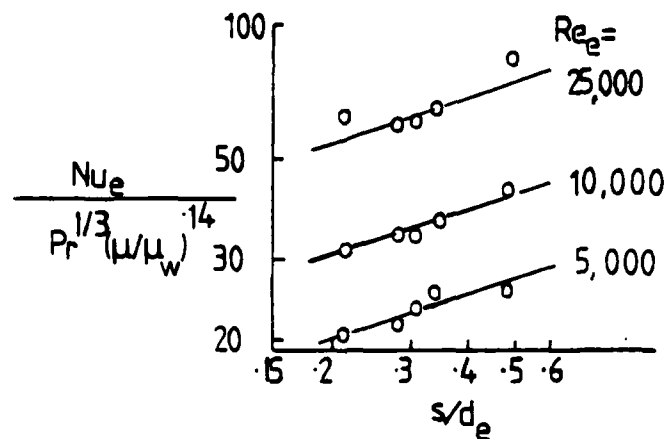


Fig 1-13 Effect of fin spacing to diameter ratio on Nusselt-Prandtl modulus for straight fin tubes (water)

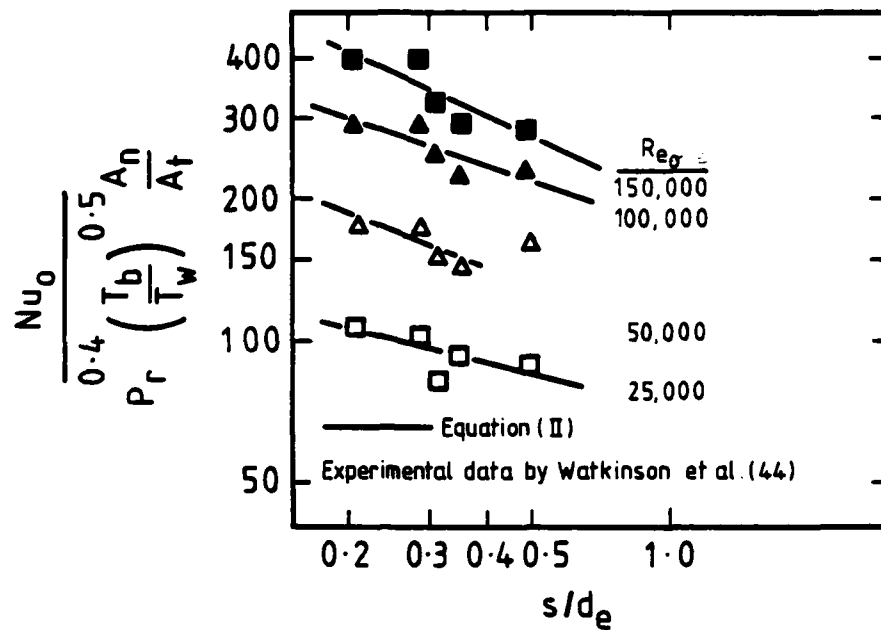


Fig.1.14 Effect of inter - fin spacing on the Nusselt - Prandtl modulus for straight fin tubes (air)

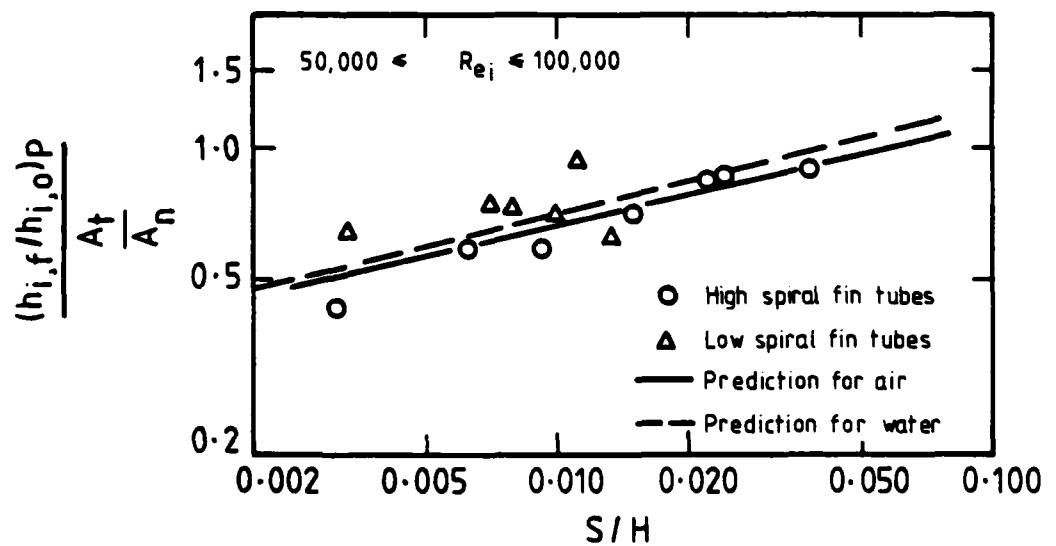


Fig.1.15 Average constant pumping power performance ratio correlation for spiral fin tubes

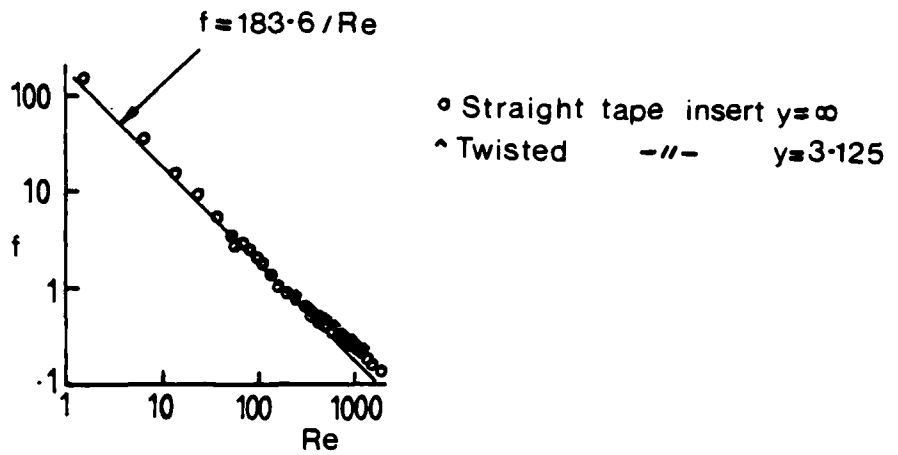


Fig 1-16 Friction factor data for various tape inserts

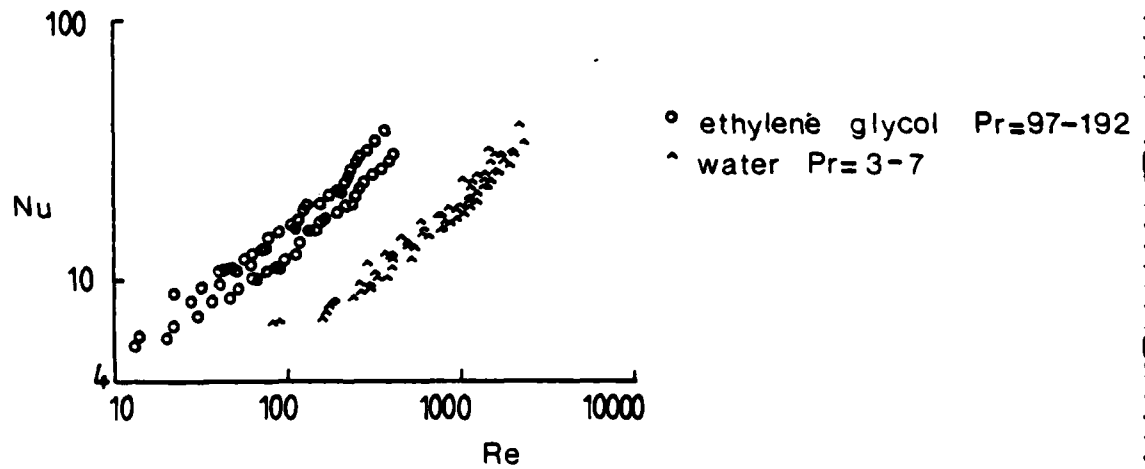


Fig 1-17 Fully developed heat results  $y = 5.08$



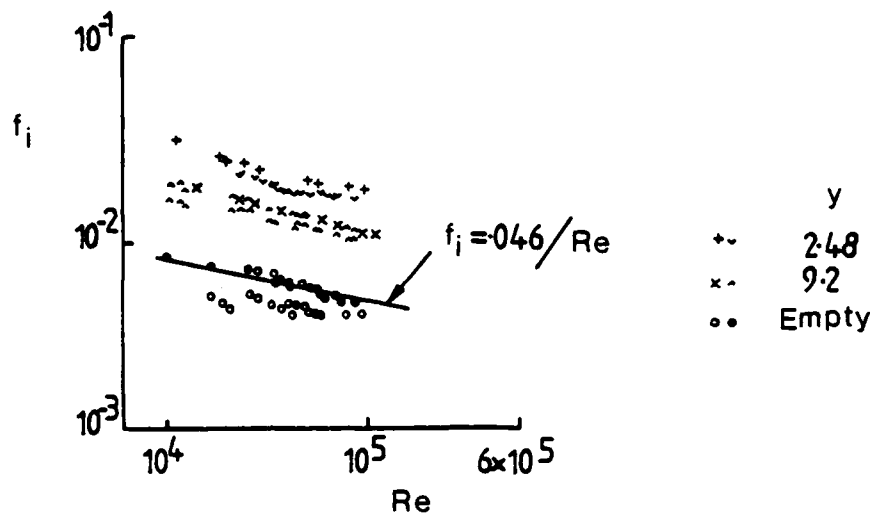


Fig 1.18 Friction factors for isothermal and heated conditions  
( $f = 4f_i$ )

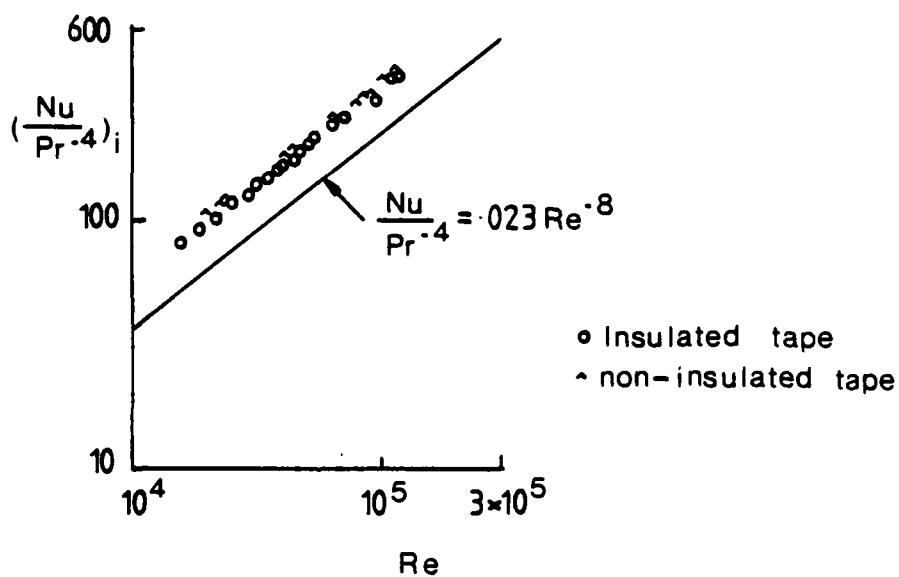


Fig 1.19 Comparison of heat-transfer data for insulated and integral twisted tapes

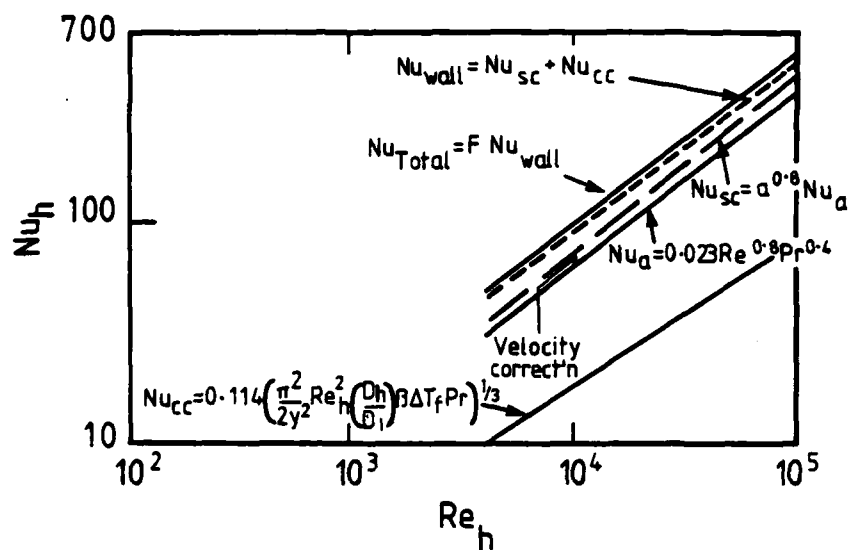


Fig. 1.20 Graphical representation of the swirl flow heat transfer prediction method

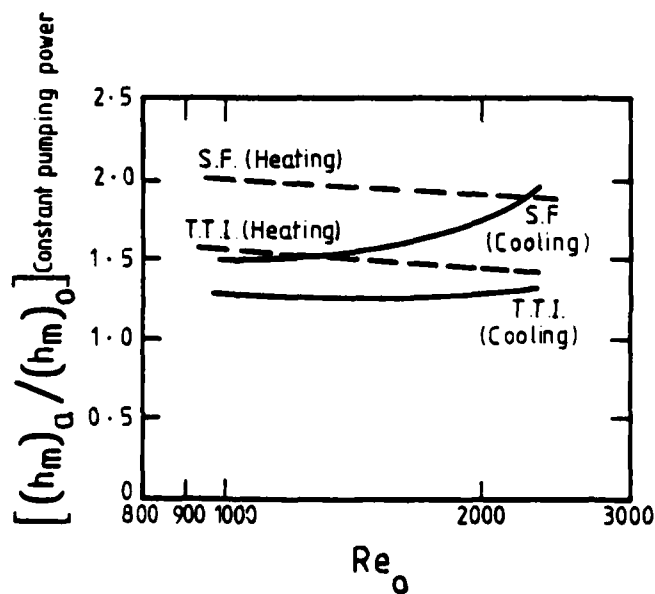


Fig. 1.21 Constant pumping power performance analysis

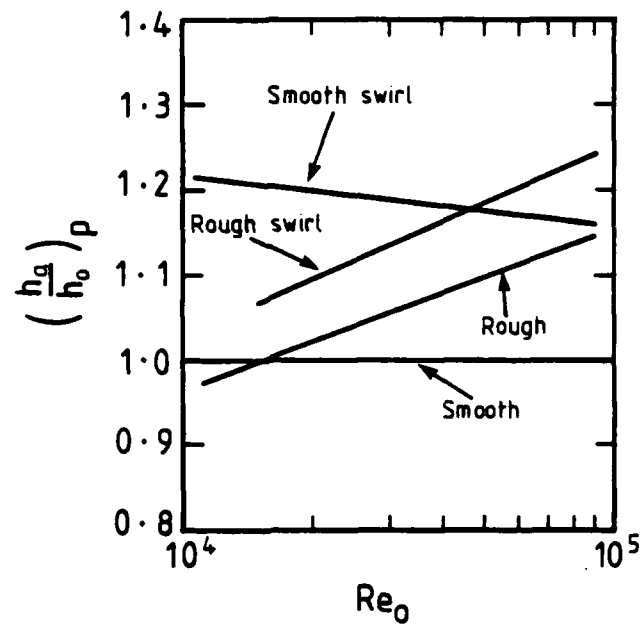


Fig. 1.22 Ratio of augmented and nonaugmented heat transfer coefficients at constant pumping power

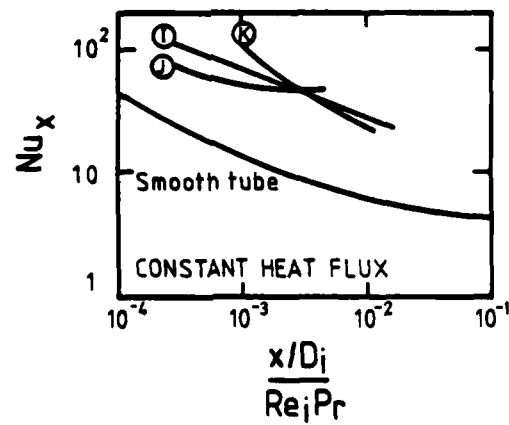


Fig. 1.23 Local Nusselt Numbers for water and ethylene glycol for Koch and Kenics static-mixer inserts

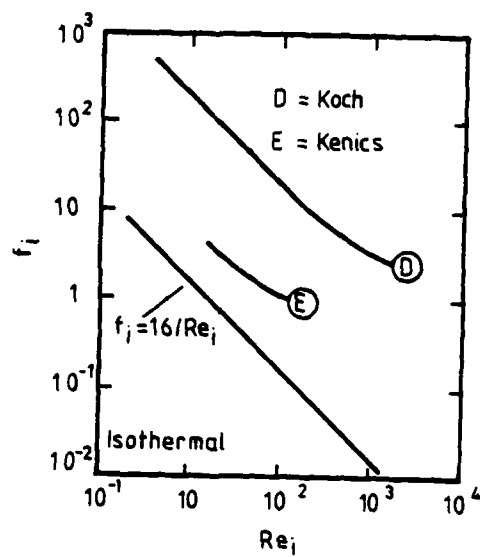


Fig.1.24 Friction factor for Koch and Kenics static-mixer inserts



FIG. 1.25 ROPED TUBES

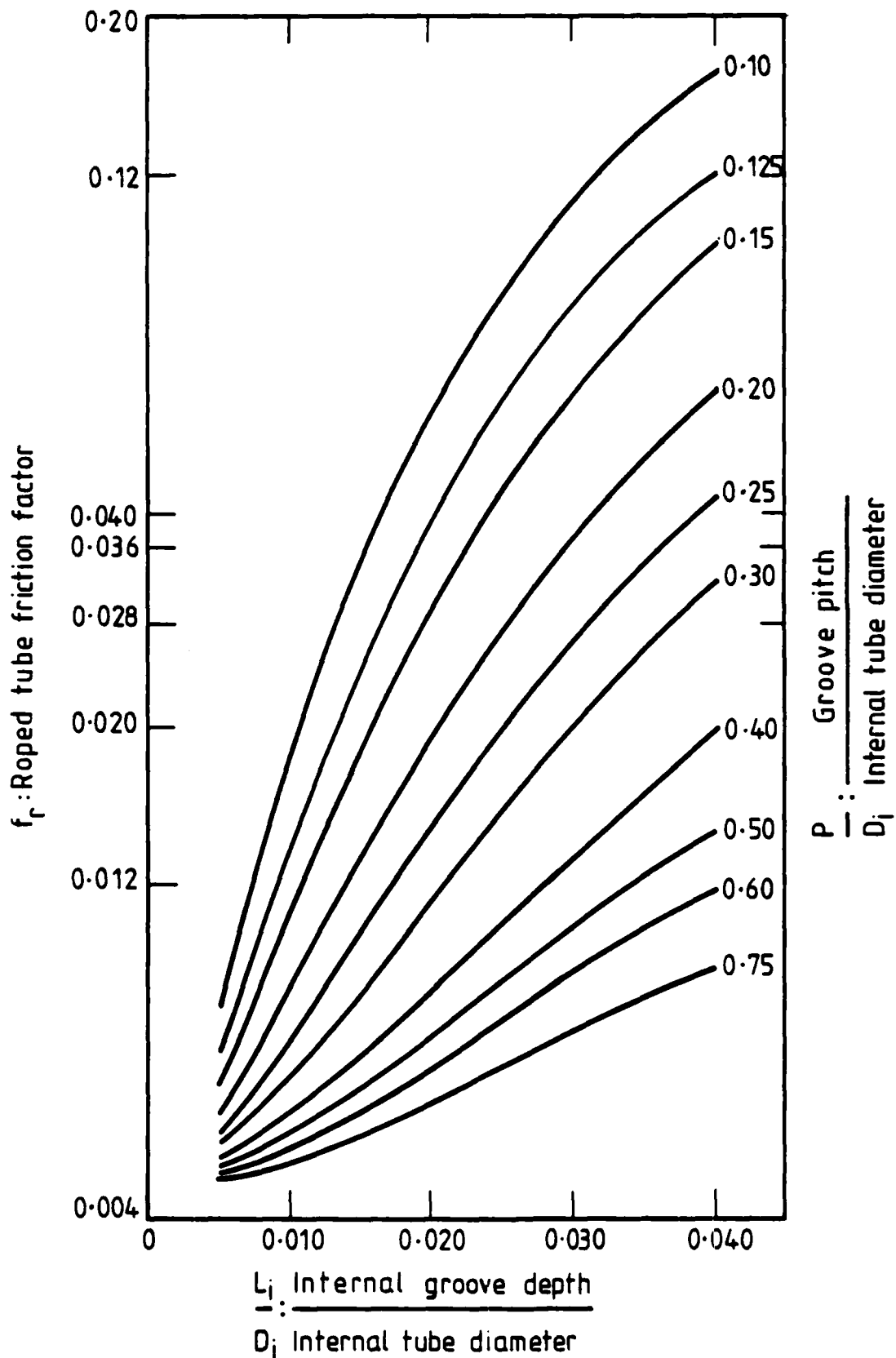


Fig. 1.26 Estimated internal friction factors for a range of tube profiles. (Applicable at Reynolds number = 100000)

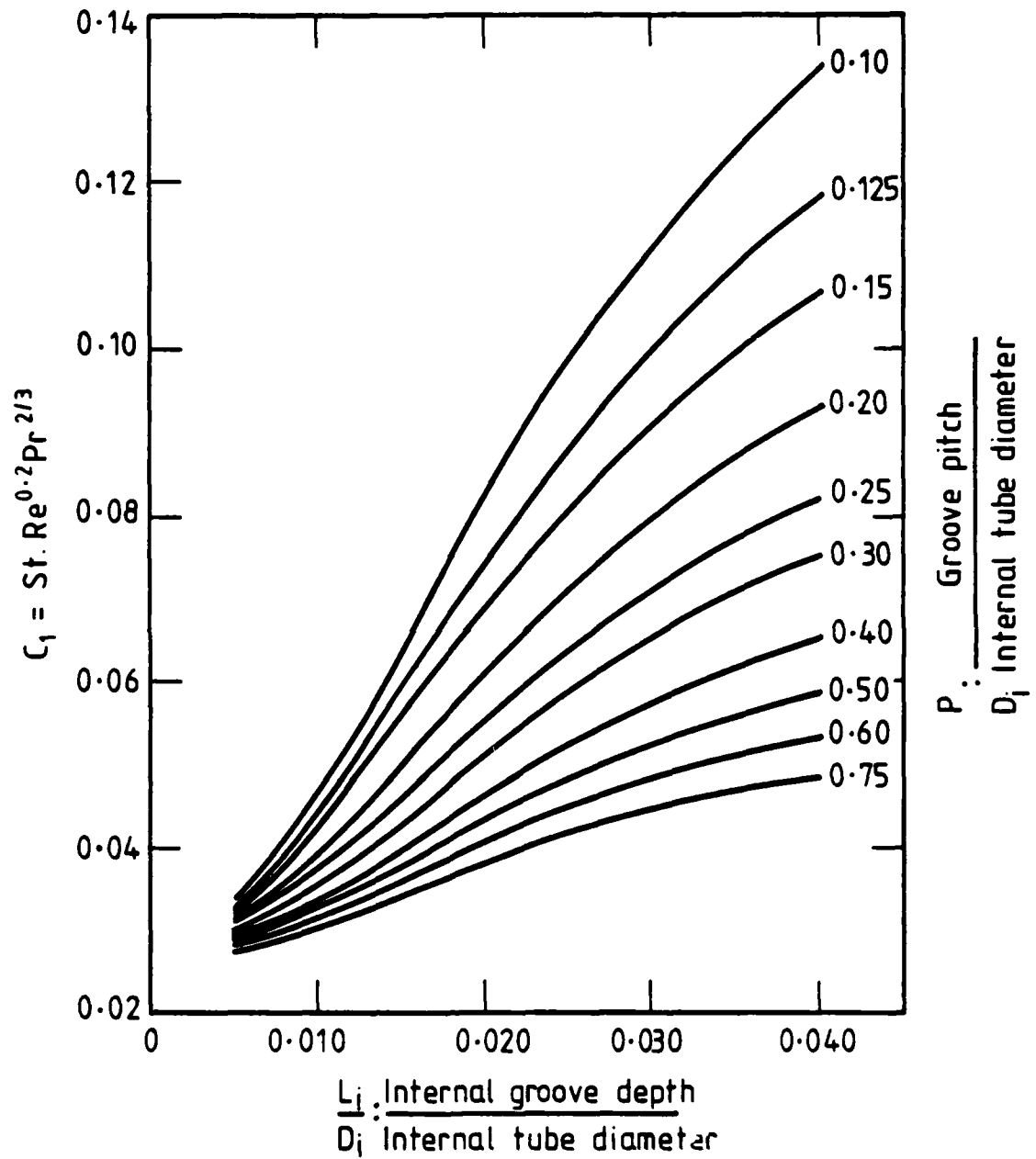


Fig. 1.27 Estimated values of the constant  $C_1$

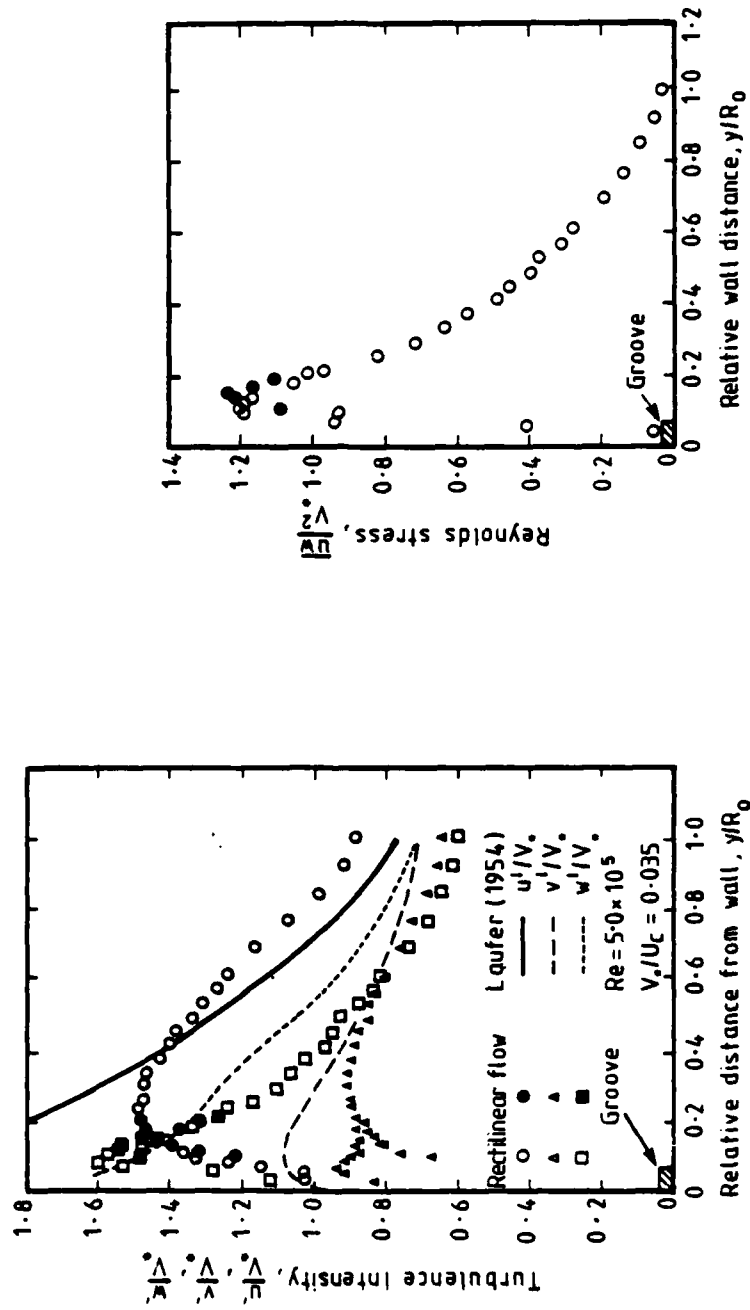


Fig. 1.28 Turbulence in pipe coordinates

Fig. 1.29  $\overline{u'v'}$  Reynolds stress



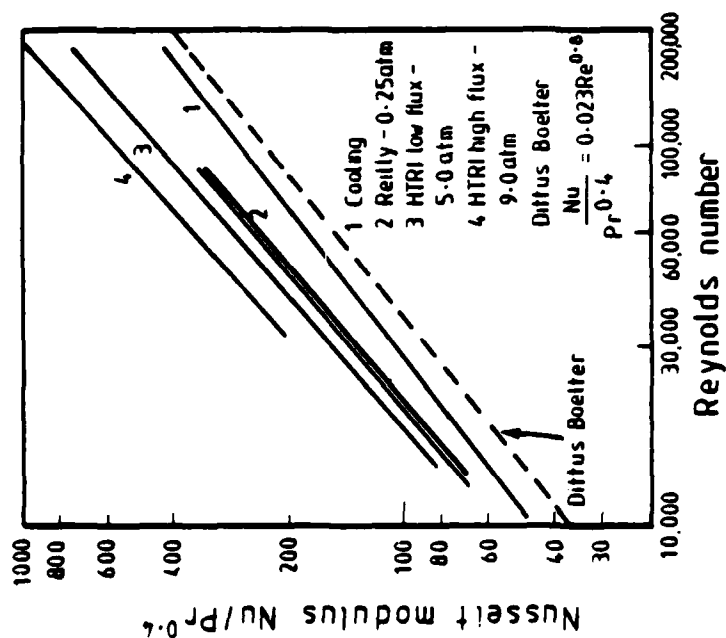


Fig. 1.30 Enhancement of 30° helix for varied heat flux (does not include area extension)

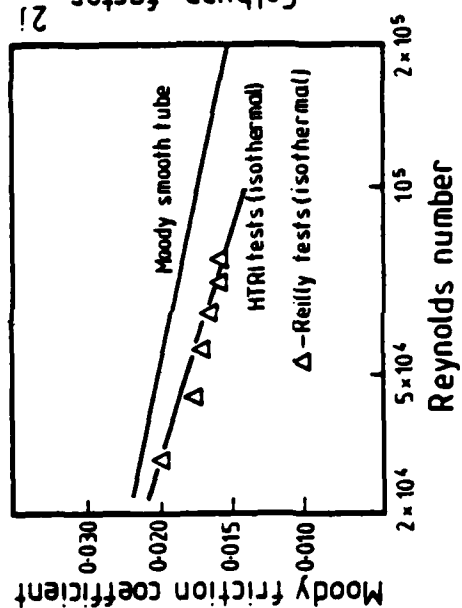


Fig. 1.31 Moody friction coefficient vs Reynolds number for helically fluted tube

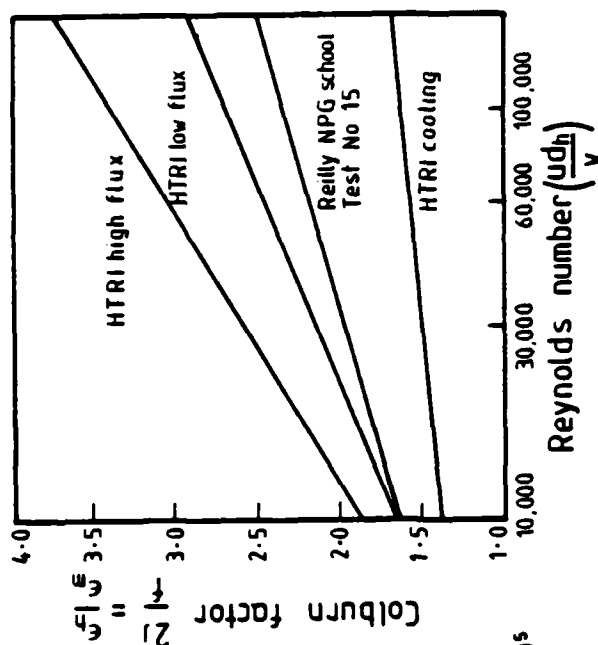


Fig. 1.32 Colburn factor vs. Reynolds number for helically fluted tubes

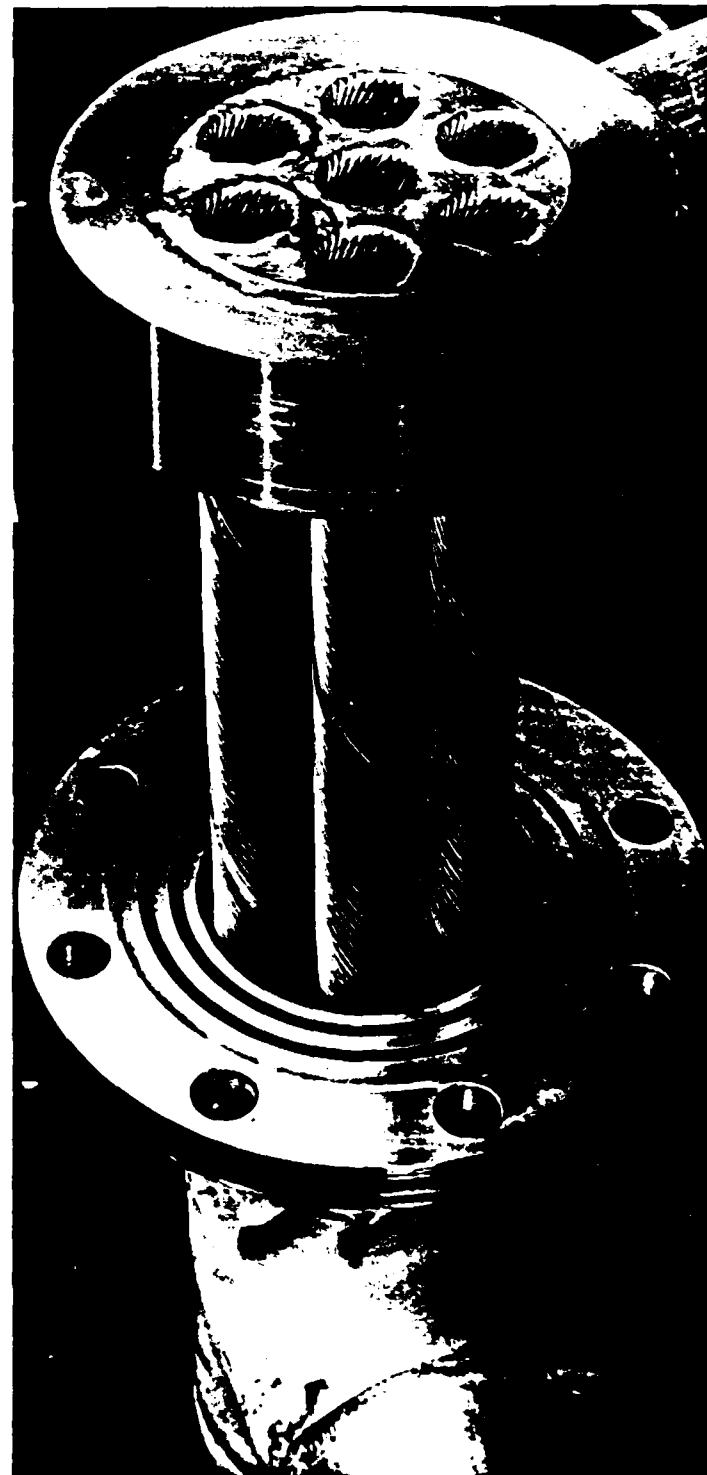


FIG. 1.33 TUBE BUNDLE BEING ASSEMBLED  
INTO THE SHELL

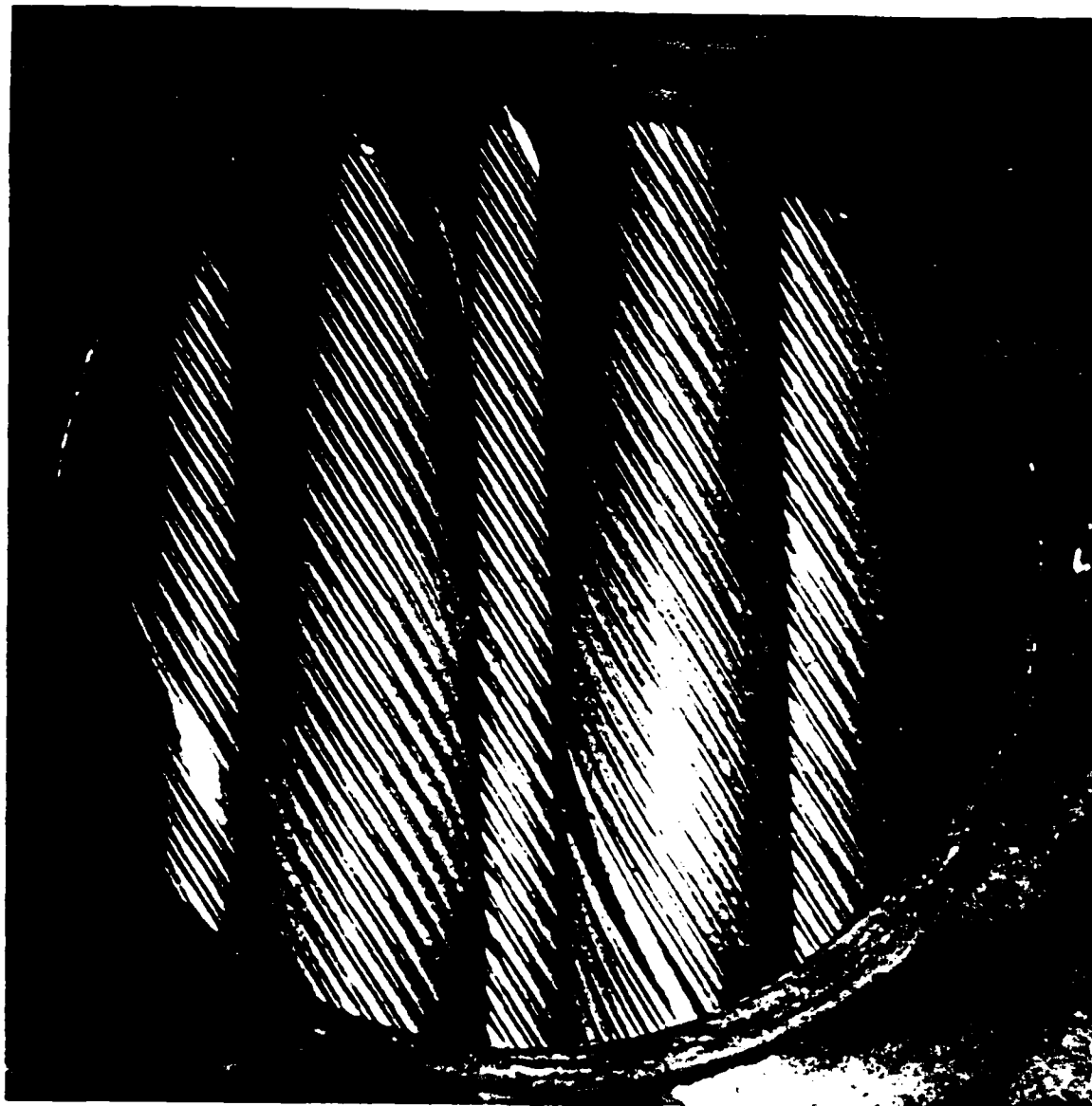


FIG. 1.34 TUBING AS SEEN THROUGH  
THE SHELL SIDE NOZZLE

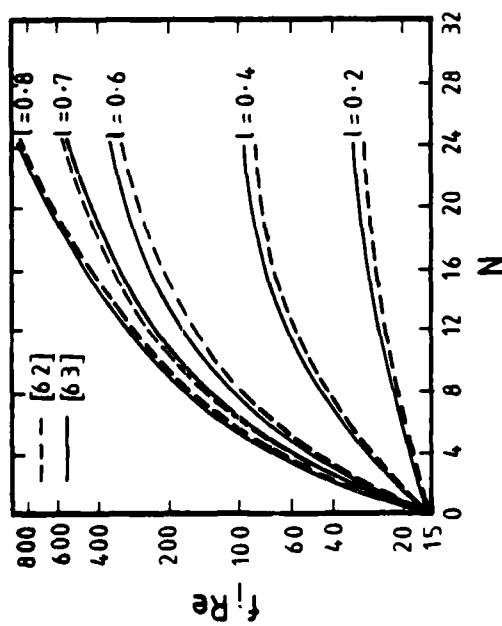


Fig. 1.35 Variation of  $(f_i Re)$  with fin number ( $f=4f_i$ )

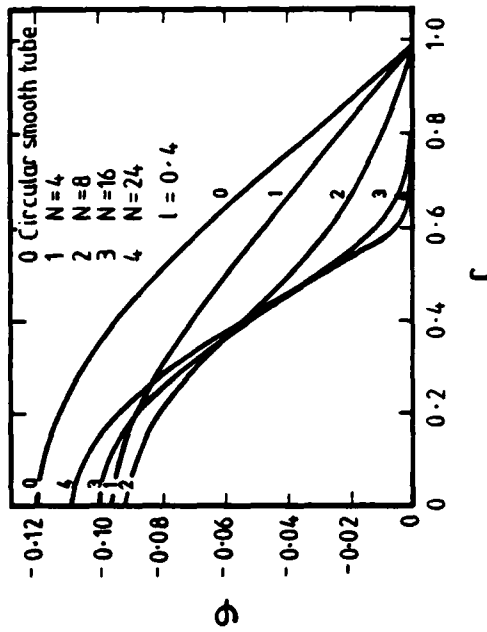


Fig. 1.36 Dimensionless temperature variation in radial direction for  $l=0.4$

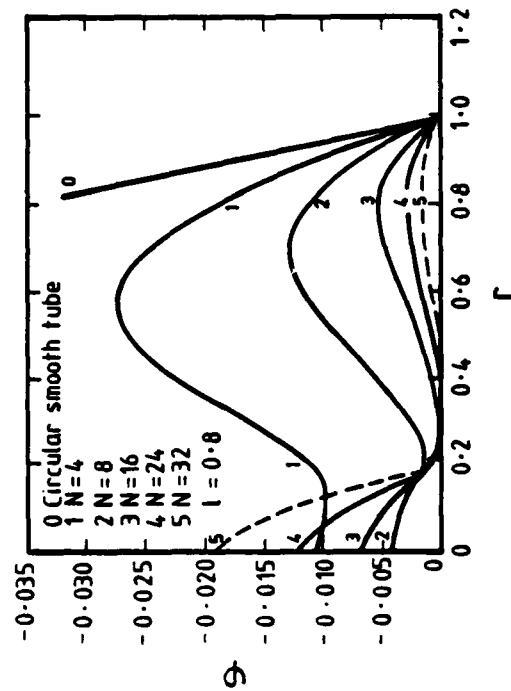


Fig. 1.37 Dimensionless temperature variation in radial direction for  $l=0.8$

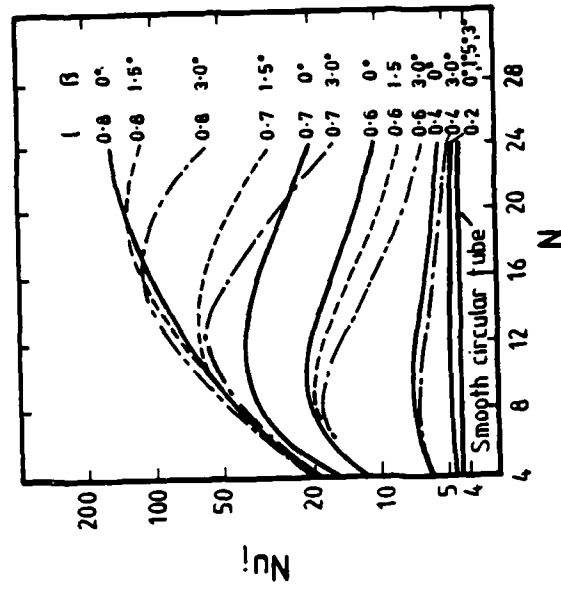


Fig. 1.39 Nusselt number variation with fin number

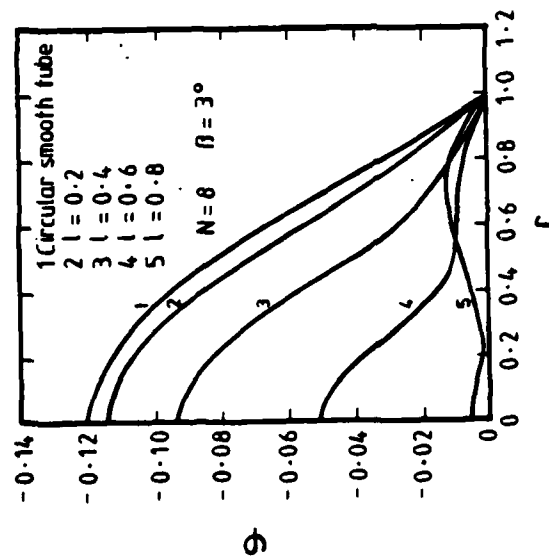


Fig. 1.38 Dimensionless temperature variation in radial direction for  $N=8$  and  $\beta=3^\circ$

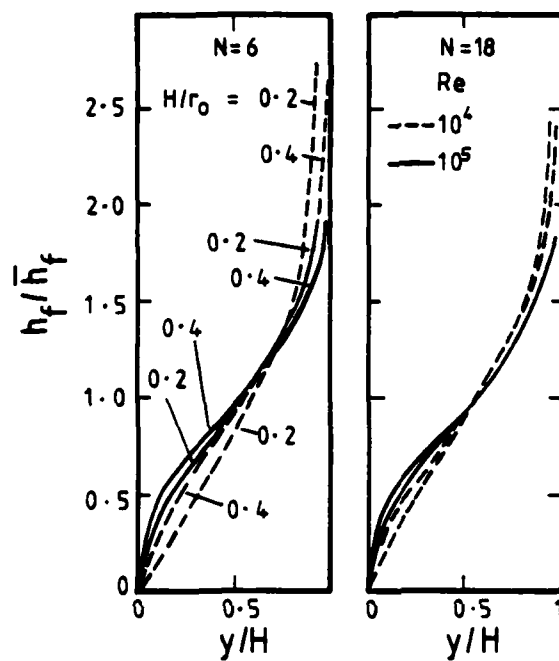


Fig. 1.40 Local heat transfer coefficients along the fin height for internally finned tubes

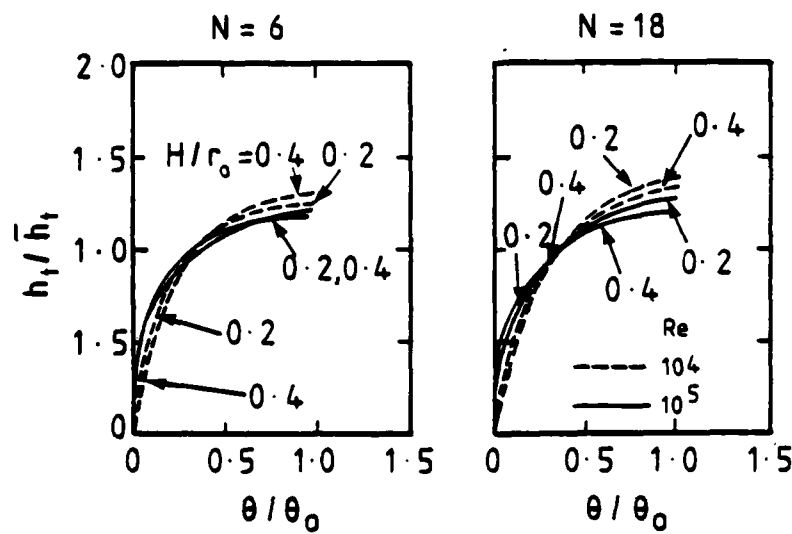


Fig. 1.41 Local heat transfer coefficients along the tube wall for internally finned tubes

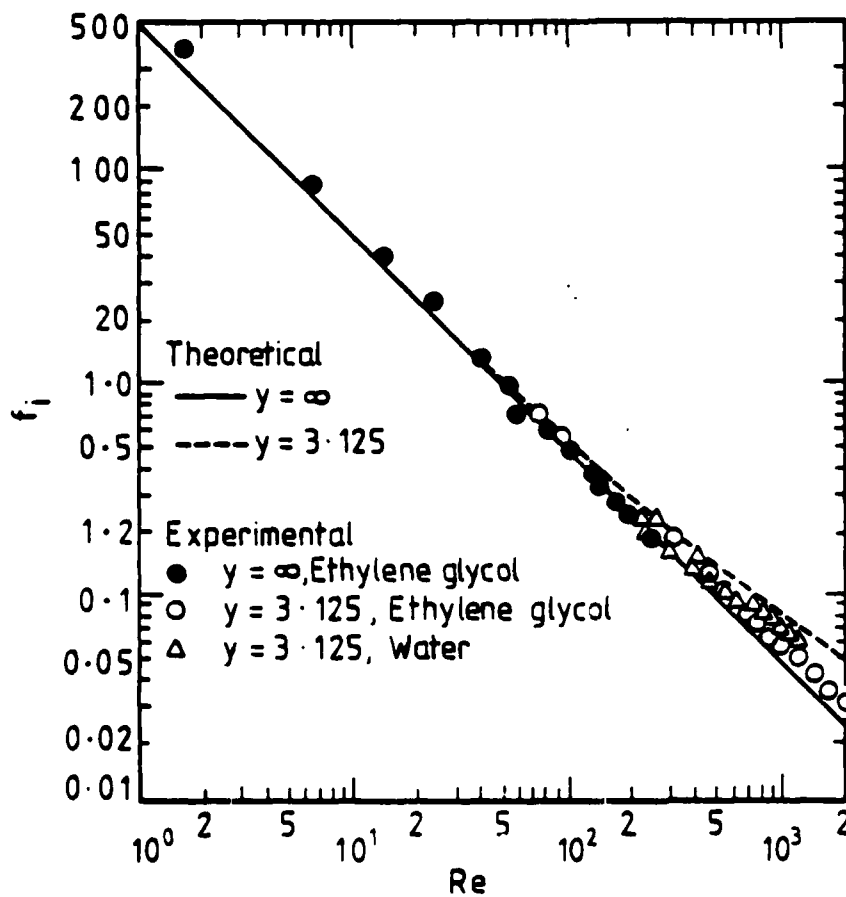


Fig. 1.42 Circular tube with a twisted tape:  $f_i$  as a function of  $Re$  for fully developed laminar flow (from Hong and Bergles [46] ( $f = 4f_i$ ))

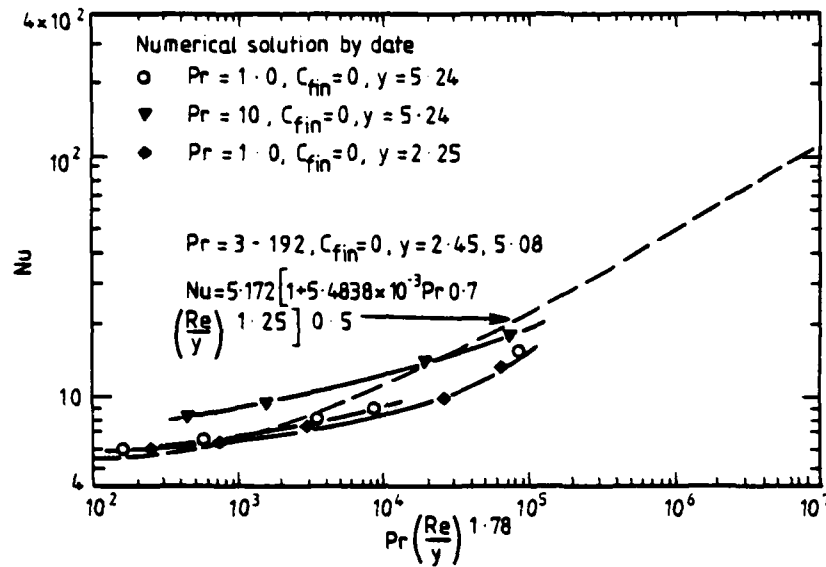
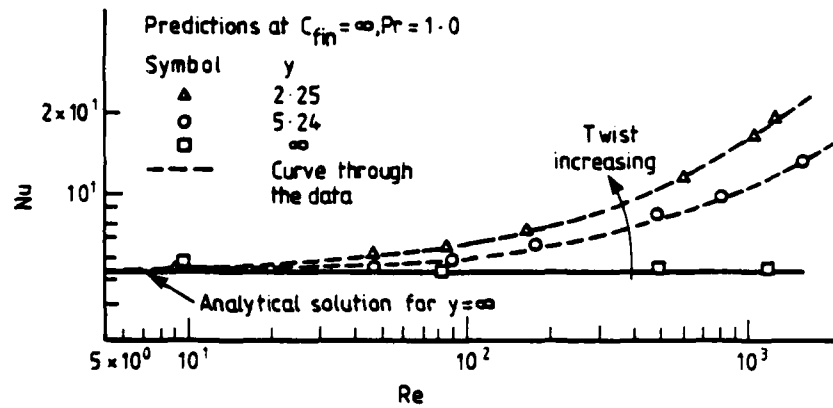
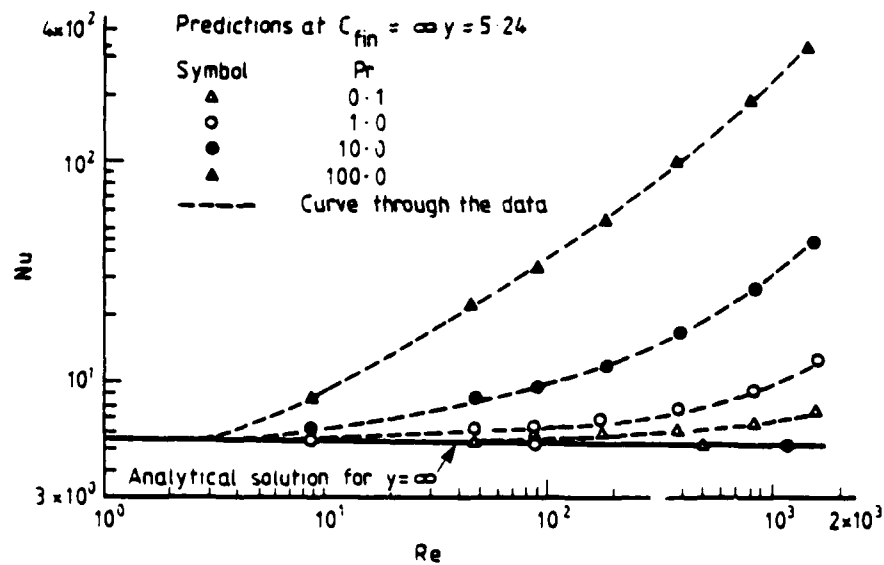


Fig. 1.43 Comparison of present heat transfer correlation with previous analytical predictions

Fig. 1.44 Influence of twist-ratio on Nusselt number at  $C_{fin} = \infty$ Fig. 1.45 Influence of Prandtl number on Nusselt number at  $C_{fin} = \infty$



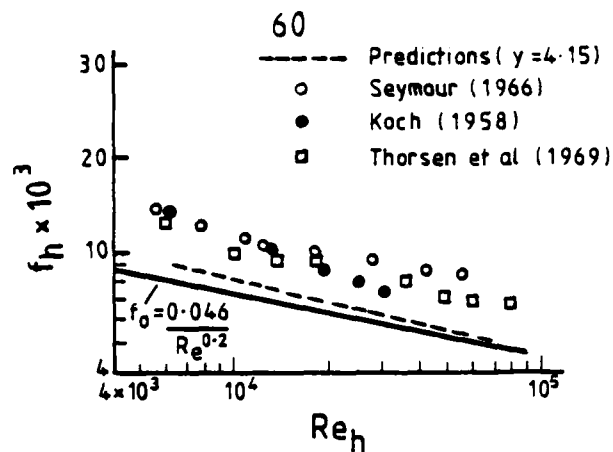


Fig. 1.46 Comparison of predicted and experimental friction factors ( $f_h = 4f$ )

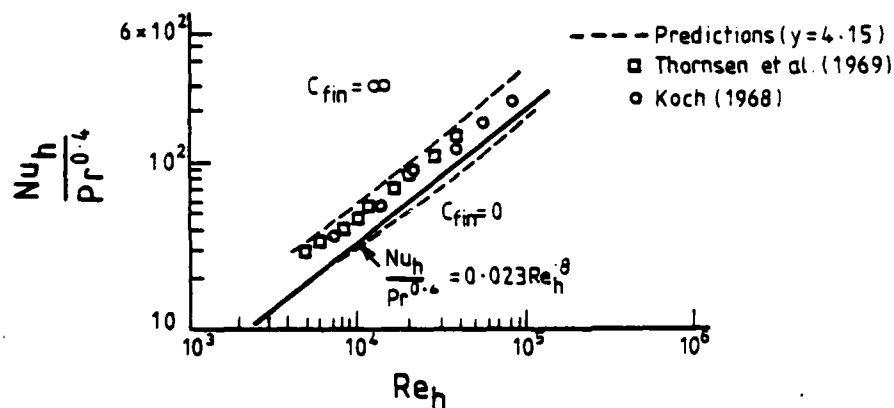


Fig. 1.47 Comparison of predicted and experimental Nusselt numbers

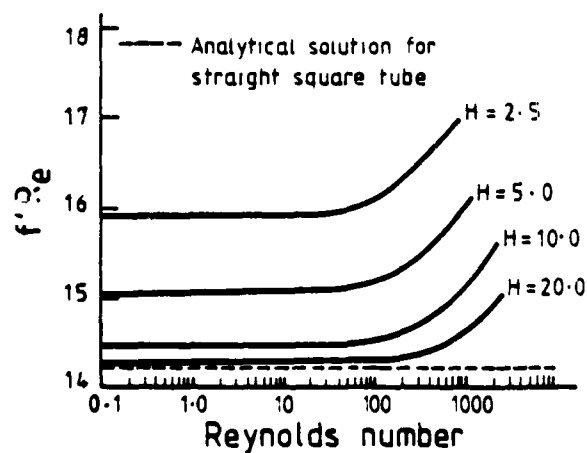


Fig. 1.48 Variation of  $f' Re$  with Reynolds number ( $f' = 4f$ )

## CHAPTER 2

### 2. THE LAMINAR FLOW PROCEDURE

#### 2.1 Introduction

At the beginning of the project available experimental data for the flow through a spirally fluted tube were confined to the turbulent regime. Nothing was known about the tube's behaviour at fairly low Reynolds numbers where laminar flow is expected to be present. There seemed at least the possibility that, in the laminar flow regime, some of the benefits found in turbulent flows could also apply. Thus, the computational procedure developed for the spirally fluted tube has begun by studying the laminar regime.

Nothing was known, too, about the detailed flow pattern in the vicinity of the flutes. However, it was expected that friction and heat transfer should be affected by what is happening in the immediate vicinity of the tube wall (i.e. around the flutes) since the remarkable behaviour of the spirally fluted tubes did not appear to be fully explained by the enhanced turbulent mixing in the core region induced by swirl in the presence of a radial density gradient [1, 59, 60]. So, a numerical procedure could be very useful for it could produce detailed predictions of the highly complex flow structure near the wall which would be very difficult to make experimentally.

The general flow equations for analyzing the flow in a spirally fluted tube with arbitrary shaped flutes have been derived by I. Demirdzic and a detailed description of the procedure followed is presented in Appendix 2. The choice and optimization of the grid, the final form of the equations solved, the boundary conditions applied, the adaptation and solution of the

AD-A150 774

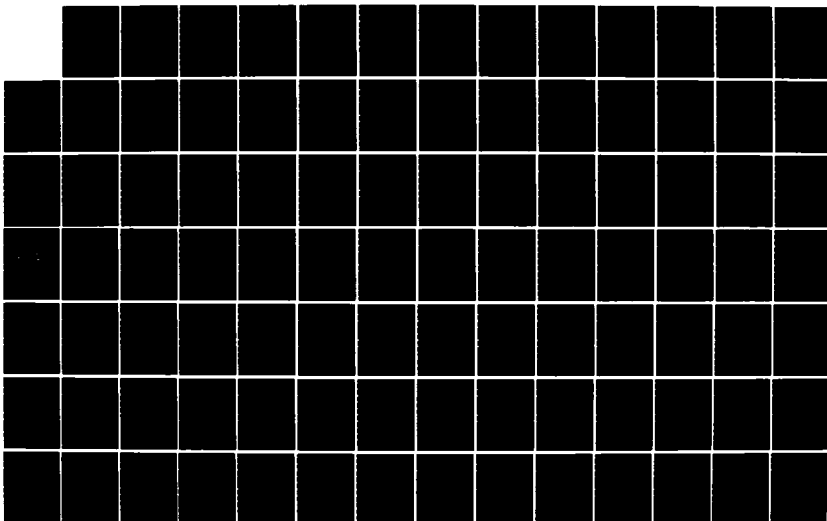
FLUID MECHANICS AND HEAT TRANSFER SPIRALLY FLUTED  
TUBING(U) GA TECHNOLOGIES INC SAN DIEGO CA  
J S YAMPOLSKY ET AL. DEC 84 GA-A17833 N00014-82-C-0721

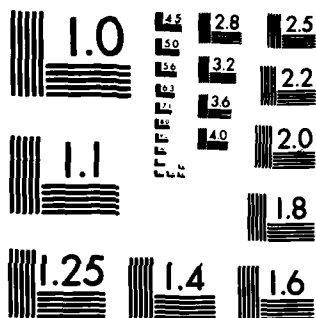
4/8

UNCLASSIFIED

F/G 20/4

NL





MICROCOPY RESOLUTION TEST CHART  
NATIONAL BUREAU OF STANDARDS-1963-A

describing equations by the computer program, the structure of the computer program for solving the laminar flow regime and the computational procedure followed are discussed in the present chapter.

## 2.2 The Co-Ordinate System

The flow field is analyzed over the region shown in Figure 2.1. This represents a part of the tube's cross-section containing one complete rib, being the smallest sector of flow symmetry. The solution domain is bounded on the outer surface by the tube wall and at the inner surface by a circular boundary of radius  $R_a$  whose choice has been decided after tests presented in Chapter 3. The grid-coverage of the complete cross-stream plane of the tube is shown in Figure 2.1a.

The solution domain in the cross-sectional plane is mapped by the orthogonal co-ordinate lines  $\xi$  and  $\eta$  shown in Figure 2.1. Details of the computer program creating the grid as well as the listing of the computer code can be found in Appendix 1. Attention has been focused on the study of tubes with flutes of sinusoidal profile. The radius of the tube wall  $R_w$  as a function of angular position  $\Omega$  is given by the equation:

$$R_w = R_b + h \cos(2\pi\Omega/\theta) \quad (2.1)$$

where  $\theta$  is the sector angle  $\frac{2\pi}{n}$  ( $n$  being the number of flutes around the circumference of the tube) and  $h$  the amplitude of the rib (i.e. the maximum radial departure of the tube radius from the mean radius  $R_b$ ). The tube wall (equation (2.1)) coincides with a line of constant  $\eta$ , while in the vicinity of the wall the other constant- $\eta$  lines imitate with diminishing amplitude the undulation of the wall. The local radius  $r$  of a constant- $\eta$  line is given by:

$$r = R_o + h_o \cos(2\pi\eta/\theta) \quad (2.2)$$

where  $R_o$  is the mean radius of a co-ordinate line of constant  $\eta$  (ranging from  $R_b$  at the wall to  $R_a$  at the inner boundary). The quantity  $h_o/h$  is a prescribed function of  $R_o/R_b$  which initially was chosen to decrease linearly from 1 at the tube wall to zero at radius  $R_a$ . However, the resulting grid, shown in Figure 2.2, gave a quite poor coverage of the solution domain resulting in low numerical accuracy and slow convergence of the computational procedure.

It was found that the best distribution of nodes, for the laminar flow computations, could be achieved by reducing  $h_o$  to zero more rapidly (i.e. by  $R_o/R_b = 0.85 = R_m/R_b$ ) so that over the majority of the solution domain the constant- $\eta$  lines were circular arcs forming a cylindrical-polar mesh. Thus, a composite curvilinear/cylindrical-polar grid (Figure 2.1) is formed and this grid has been adopted for all the results discussed later. The radius  $R_m$  is the matching radius between the two regions of the mesh; its value was taken as  $0.85 R_b$  after tests reported in Chapter 3.

The second family of co-ordinate lines, constant- $\xi$  lines, is constructed numerically orthogonal to the constant- $\eta$  lines. Along the east and west boundaries (trough positions) as well as in the middle of the solution domain (crest position) the constant- $\xi$  lines are radial lines.

The third co-ordinate  $\zeta$  proceeds in the axial direction, shown in Figure 2.3, following the spiralling of the flutes, while the fully developed flow condition is applied with respect to this co-ordinate, i.e.  $\frac{\partial(\dots)}{\partial\zeta} = 0$ . The flow and normalized temperature fields are described in

terms of the independent variables  $\xi$  and  $\eta$ . However, in order to obtain the most suitable form of the momentum equations for numerical solution (see Appendix 2), the latter have been written in terms of the velocity component in the direction  $z$  of the tube-axis rather than in the direction  $\zeta$  of the spiral.

### 2.3 The Describing Equations

The dependent variables chosen for the laminar flow computations of the spirally fluted tube are: the static pressure  $p$ , the velocity components  $U$ ,  $V$  and  $W$  in the  $\xi$ ,  $\eta$ ,  $z$  directions respectively and the normalized temperature  $\theta$ . The equations describing the fully developed laminar flow and giving the distribution of the above variables over the solution domain are presented below:

#### Continuity

$$\frac{\Delta}{\Delta \xi} (\rho U) + \frac{\Delta}{\Delta \eta} (\rho V) = \frac{\Delta}{\Delta \xi} (\kappa_{\xi} \rho W) + \frac{\Delta}{\Delta \eta} (\kappa_{\eta} \rho W) \quad (2.3)$$

#### $\xi$ -Momentum

$$\begin{aligned} \frac{\Delta}{\Delta \xi} (\rho U U) + \frac{\Delta}{\Delta \eta} (\rho U V) = & - \frac{\partial p}{\partial \xi} + \frac{\Delta}{\Delta \xi} (\mu \frac{\partial U}{\partial \xi}) \\ & + \frac{\Delta}{\Delta \eta} (\mu \frac{\partial U}{\partial \eta}) + \frac{\Delta}{\Delta \xi} (\kappa_{\xi} \rho U W) + \frac{\Delta}{\Delta \eta} (\kappa_{\eta} \rho U W) \\ & + \frac{\Delta}{\Delta \xi} (\tau_{\xi \xi} - \mu \frac{\partial U}{\partial \xi} - \kappa_{\xi} \tau_{\xi z}) + \frac{\Delta}{\Delta \eta} (\tau_{\xi \eta} - \mu \frac{\partial U}{\partial \eta} - \kappa_{\eta} \tau_{\xi z}) \\ & + (-\sigma + \kappa_{\xi} \lambda_{\xi} - \kappa_{\eta} \lambda_{\eta}) \times (\rho V W - \tau_{\eta z}) \\ & - \lambda_{\xi} (\rho U V - \tau_{\xi \eta}) + \lambda_{\eta} (\rho V^2 - \tau_{\eta \eta}) \end{aligned} \quad (2.4)$$

$\eta$ -Momentum

$$\begin{aligned}
& \frac{\Delta}{\Delta \xi}(\rho V U) + \frac{\Delta}{\Delta \eta}(\rho V V) = -\frac{\partial p}{\partial \eta} + \frac{\Delta}{\Delta \xi}(\mu \frac{\partial V}{\partial \xi}) \\
& + \frac{\Delta}{\Delta \eta}(\mu \frac{\partial V}{\partial \eta}) + \frac{\Delta}{\Delta \xi}(\kappa_{\xi} \rho V W) + \frac{\Delta}{\Delta \eta}(\kappa_{\eta} \rho V W) \\
& + \frac{\Delta}{\Delta \xi}(\tau_{\eta \xi} - \mu \frac{\partial V}{\partial \xi} - \kappa_{\xi} \tau_{\eta z}) + \frac{\Delta}{\Delta \eta}(\tau_{\eta \eta} - \mu \frac{\partial V}{\partial \eta} - \kappa_{\eta} \tau_{\eta z}) \\
& + (\sigma - \kappa_{\xi} \lambda_{\xi} + \kappa_{\eta} \lambda_{\eta}) \times (\rho U W - \tau_{\xi z}) \\
& + \lambda_{\xi}(\rho U^2 - \tau_{\xi \xi}) - \lambda_{\eta}(\rho U V - \tau_{\xi \eta})
\end{aligned} \tag{2.5}$$

 $z$ -Momentum

$$\begin{aligned}
& \frac{\Delta}{\Delta \xi}(\rho U W) + \frac{\Delta}{\Delta \eta}(\rho V W) = -\frac{\partial p}{\partial z} + \frac{\Delta}{\Delta \xi}(\mu \frac{\partial W}{\partial \xi}) \\
& + \frac{\Delta}{\Delta \eta}(\mu \frac{\partial W}{\partial \eta}) + \frac{\Delta}{\Delta \xi}(\kappa_{\xi} \rho W W) + \frac{\Delta}{\Delta \eta}(\kappa_{\eta} \rho W W) \\
& + \frac{\Delta}{\Delta \xi}(\tau_{\xi z} - \mu \frac{\partial W}{\partial \xi} - \kappa_{\xi} \tau_{zz}) + \frac{\Delta}{\Delta \eta}(\tau_{z \eta} - \mu \frac{\partial W}{\partial \eta} - \kappa_{\eta} \tau_{zz})
\end{aligned} \tag{2.6}$$

Energy Equation

$$\begin{aligned}
& \frac{\Delta}{\Delta \xi} \left[ \rho U \Theta \right] + \frac{\Delta}{\Delta \eta} \left[ \rho V \Theta \right] + \frac{\Delta}{\Delta \zeta} \left[ \frac{h_{\zeta}}{b} \rho W T_{\text{ref}} \right] = \\
& \frac{\Delta}{\Delta \xi} \left[ \Gamma_T \frac{\partial \Theta}{\partial \xi} \right] + \frac{\Delta}{\Delta \eta} \left[ \Gamma_T \frac{\partial \Theta}{\partial \eta} \right] \\
& + \frac{\Delta}{\Delta \xi} \left[ \kappa_{\xi} \rho W \Theta \right] + \frac{\Delta}{\Delta \eta} \left[ \kappa_{\eta} \rho W \Theta \right] \\
& - \frac{\Delta}{\Delta \xi} \left[ \kappa_{\xi} \Gamma_T \left( -\kappa_{\xi} \frac{\partial \Theta}{\partial \xi} - \kappa_{\eta} \frac{\partial \Theta}{\partial \eta} + \frac{h_{\zeta}}{b} \frac{dT_{\text{ref}}}{d\zeta} \right) \right] \\
& - \frac{\Delta}{\Delta \eta} \left[ \kappa_{\eta} \Gamma_T \left( -\kappa_{\xi} \frac{\partial \Theta}{\partial \xi} - \kappa_{\eta} \frac{\partial \Theta}{\partial \eta} + \frac{h_{\zeta}}{b} \frac{dT_{\text{ref}}}{d\zeta} \right) \right]
\end{aligned} \tag{2.7}$$



The undefined symbols appearing in the above equations have the following meaning:

$$\begin{aligned}
 \tau_{\xi\xi} &= 2\mu\left(\frac{\partial U}{\partial \xi} + \lambda_{\xi} V\right) & \tau_{\eta\eta} &= 2\mu\left(\frac{\partial V}{\partial \eta} + \lambda_{\eta} U\right) \\
 \tau_{zz} &= 2\mu\left(-\kappa_{\xi} \frac{\partial W}{\partial \xi} - \kappa_{\eta} \frac{\partial W}{\partial \eta}\right) \\
 \tau_{\xi\eta} &= \mu\left(\frac{\partial U}{\partial \eta} + \frac{\partial V}{\partial \xi} - \lambda_{\xi} U - \lambda_{\eta} V\right) \\
 \tau_{\xi z} &= \mu\left(\frac{\partial W}{\partial \xi} - \kappa_{\xi} \frac{\partial U}{\partial \xi} - \kappa_{\eta} \frac{\partial U}{\partial \eta} + (\sigma - \kappa_{\xi} \lambda_{\xi} + \kappa_{\eta} \lambda_{\eta}) V\right) \\
 \tau_{\eta z} &= \mu\left(\frac{\partial W}{\partial \eta} - \kappa_{\xi} \frac{\partial V}{\partial \xi} - \kappa_{\eta} \frac{\partial V}{\partial \eta} + (-\sigma + \kappa_{\xi} \lambda_{\xi} - \kappa_{\eta} \lambda_{\eta}) U\right)
 \end{aligned}$$

(2.8)

while  $\sigma = (\kappa_{\xi} \kappa_{\xi} + \kappa_{\eta} \kappa_{\eta} + 1) R_{\eta} / \kappa_{\xi}$

$$\begin{aligned}
 \kappa_{\xi} &= \frac{1}{b} \frac{\partial \xi}{\partial \theta} & \kappa_{\eta} &= \frac{1}{b} \frac{\partial \eta}{\partial \theta} \\
 \lambda_{\xi} &= \frac{1}{h_{\xi}} \frac{\partial h_{\xi}}{\partial \eta} & \lambda_{\eta} &= \frac{1}{h_{\eta}} \frac{\partial h_{\eta}}{\partial \xi} \\
 h_{\xi} &= |\vec{e}_{\xi}| & h_{\eta} &= |\vec{e}_{\eta}| \\
 R_{\eta} &= \frac{r}{(r^2 + b^2)} \frac{\partial r}{\partial \eta} & b &= \frac{H}{2\pi} \\
 \sqrt{r^2 + b^2} &= |\vec{e}_{\zeta}| & \frac{h_{\zeta}}{b} &= \sqrt{\kappa_{\xi} \kappa_{\xi} + \kappa_{\eta} \kappa_{\eta} + 1}
 \end{aligned}$$

$$\frac{\Delta(\dots)}{\Delta \xi} = \frac{1}{h_{\eta}} \frac{\partial}{\partial \xi} (h_{\eta}(\dots))$$

$$\frac{\Delta(\dots)}{\Delta \eta} = \frac{1}{h_{\xi}} \frac{\partial}{\partial \eta} (h_{\xi}(\dots))$$

$$\Theta = T - T_{\text{ref}}$$

$$\Gamma_T = \frac{\mu}{Pr}$$

(2.9)

where  $\vec{e}_\xi$ ,  $\vec{e}_\eta$ ,  $\vec{e}_\zeta$  are the base vectors,  $h_\xi$ ,  $h_\eta$ ,  $h_\zeta$  their magnitudes,  $H$  is the spiral pitch,  $Pr$  the Prandtl number of the fluid and  $T_{ref}$  a reference temperature at some interior node whose choice does not affect the normalized temperatures, heat fluxes or in any way the results from the energy equation.

The term  $\frac{h_\zeta}{b} \frac{\partial T_{ref}}{\partial \zeta}$  of the energy equation, using equation (A2.46) of Appendix 2 and applying the conservation of energy principle, takes the form:

$$\frac{h_\zeta}{b} \frac{\partial T_{ref}}{\partial \zeta} = \frac{\partial T_{ref}}{\partial z} = \frac{\dot{q}'' P \cdot dz}{\dot{m} c_p}$$

where  $\dot{q}''$  is the heat input to the tube per unit surface area,  $P$  the perimeter of the fluted tube,  $\dot{m}$  the total mass flow rate, and  $C_p$  the fluid specific heat at constant pressure. Details of the derivation of the above set of equations can be found in Appendix 2.

#### 2.4 The Boundary Conditions

The boundary conditions are shown in Figure 2.4. At the north boundary of the solution domain which coincides with the tube wall, all the velocity components are set to zero and a uniform heat flux is applied, i.e:

$$U = 0, V = 0, W = 0, \frac{d\theta}{d\eta} = \frac{\dot{q}''}{k_f}$$

where  $k_f$  is the thermal conductivity of the fluid. Although the computations could have been extended to the tube axis, this was not done for it was felt that the effect of the flutes would not carry to the centre. Computing times and storage could be saved by imposing at some radius  $R_a$  the require-

ment of solid-body rotation for the circumferential velocity, zero value for the radial velocity, the parabolic profile appropriate to fully-developed pipe flow under a prescribed pressure gradient for the axial velocity and a fixed heat output for the energy equation, i.e:

$$\frac{dU}{dr} = \frac{U}{r}, \quad v = 0, \quad \frac{dW}{dr} = \frac{Ra}{2\mu} \frac{dp}{dz}, \quad \frac{d\theta}{dr} = \frac{\dot{m}_a}{\dot{m}} \frac{\dot{Q}'}{2\pi Ra \cdot k_f}$$

where  $\dot{Q}'$  is the heat input per unit length of the tube and  $\dot{m}_a$  is the mass flow rate in the region  $r \leq R_a$  (calculated from the analytical solution of the axial velocity). The results confirmed the appropriateness of this treatment.

The cyclic character of the flow from one flute to the next is imposed by applying the values of the dependent variables at the east boundary equal to those at the west boundary and vice versa. In addition, in the computer program, namely in sub-routine LISOLV whose function is simply to solve a set of linear algebraic equations (whose coefficients form a tri-diagonal matrix) produced by the finite-volume discretization of the partial differential equations (2.3) - (2.7), a special section has been added to take care of the cyclic nature of the flow. Details of this treatment can be found in Section 2.5 c.

## 2.5 Discretization and Solution of the Equations by the Computer Program

### Introductory Remarks

The computer program used has been developed from the curvilinear orthogonal TEACH code of Antonopoulos et al [86] developed originally for the study of flow over tube banks. This procedure incorporates a finite-volume discretization of the equations presented in Section 2.3 in the  $\xi$ - $\eta$

plane and in which the velocity components and scalar quantities  $p$  and  $\theta$  (for the turbulent flow computations, the turbulent energy  $k$  and its rate of dissipation  $\epsilon$  as well) are evaluated on a staggered mesh. The  $\xi$ - $\eta$  plane is sub-divided by the constant- $\eta$  and constant- $\xi$  lines into many curvilinear cells forming the control volumes on which the pressure, temperature and axial momentum equations (as well as the equations for the turbulent energy  $k$  and its dissipation rate  $\epsilon$  for the turbulent flow calculations) are solved, see Figure 2.5. The  $U$  and  $V$  velocity nodes are located in the middle of the scalar control volume faces while their control volumes are formed by passing constant- $\eta$  or constant- $\xi$  lines through the scalar nodes surrounding the velocity in question. This formation of a 'staggered grid' has the benefit that the variables  $U$ ,  $V$  and  $p$  are located in such a way that the pressure differences which drive the velocities  $u$  and  $v$  are obtained without interpolation. Moreover, the velocities are stored in positions where convective fluxes of scalar quantities have to be computed.

In the following paragraphs attention is focused on the finite-volume discretization of the partial differential equations and the solution of the resultant algebraic equations by the computer code.

### 2.5 a Formulation and Organization of the Finite-Difference Equations

The partial differential equations (2.4) to (2.6) are in a quite compact form. Substituting the expressions (2.8) for the stresses into (2.4), (2.5) and (2.6), the following equations are formed:

$\xi$ -Momentum

$$\begin{aligned}
\frac{\Delta}{\Delta \xi} (\rho u u) + \frac{\Delta}{\Delta \eta} (\rho u v) = & - \frac{\partial p}{\partial \xi} + \frac{\Delta}{\Delta \xi} \left( \mu \frac{\partial u}{\partial \xi} \right) + \frac{\Delta}{\Delta \eta} \left( \mu \frac{\partial u}{\partial \eta} \right) \\
& + \frac{\Delta}{\Delta \xi} (\kappa_{\xi} \rho u w) + \frac{\Delta}{\Delta \eta} (\kappa_{\eta} \rho u w) \\
& + \frac{\Delta}{\Delta \xi} \left[ \mu \frac{\partial u}{\partial \xi} + 2\mu \lambda_{\xi} v - \kappa_{\xi} \mu \left\{ \frac{\partial w}{\partial \xi} - \kappa_{\xi} \frac{\partial u}{\partial \xi} - \kappa_{\eta} \frac{\partial u}{\partial \eta} \right. \right. \\
& \left. \left. + (\sigma - \kappa_{\xi} \lambda_{\xi} + \kappa_{\eta} \lambda_{\eta}) v \right\} \right] \\
& + \frac{\Delta}{\Delta \eta} \left[ \mu \frac{\partial v}{\partial \xi} - \mu \lambda_{\xi} u - \mu \lambda_{\eta} v - \kappa_{\eta} \mu \left\{ \frac{\partial w}{\partial \xi} - \kappa_{\xi} \frac{\partial u}{\partial \xi} - \kappa_{\eta} \frac{\partial u}{\partial \eta} \right. \right. \\
& \left. \left. + (\sigma - \kappa_{\xi} \lambda_{\xi} + \kappa_{\eta} \lambda_{\eta}) v \right\} \right] \\
& + (-\sigma + \kappa_{\xi} \lambda_{\xi} - \kappa_{\eta} \lambda_{\eta}) \times \left( \rho v w - \mu \left\{ \frac{\partial w}{\partial \eta} - \kappa_{\xi} \frac{\partial v}{\partial \xi} - \kappa_{\eta} \frac{\partial v}{\partial \eta} \right. \right. \\
& \left. \left. + (-\sigma + \kappa_{\xi} \lambda_{\xi} - \kappa_{\eta} \lambda_{\eta}) u \right\} \right) \\
& - \lambda_{\xi} \left( \rho u v - \mu \left\{ \frac{\partial u}{\partial \eta} + \frac{\partial v}{\partial \xi} - \lambda_{\xi} u - \lambda_{\eta} v \right\} \right) \\
& + \lambda_{\eta} \left( \rho v^2 - 2\mu \left\{ \frac{\partial v}{\partial \eta} + \lambda_{\eta} u \right\} \right)
\end{aligned} \tag{2.10}$$

 $\eta$ -Momentum

$$\begin{aligned}
\frac{\Delta}{\Delta \xi} (\rho v u) + \frac{\Delta}{\Delta \eta} (\rho v v) = & - \frac{\partial p}{\partial \eta} + \frac{\Delta}{\Delta \xi} \left( \mu \frac{\partial v}{\partial \xi} \right) + \frac{\Delta}{\Delta \eta} \left( \mu \frac{\partial v}{\partial \eta} \right) \\
& + \frac{\Delta}{\Delta \xi} (\kappa_{\xi} \rho v w) + \frac{\Delta}{\Delta \eta} (\kappa_{\eta} \rho v w) \\
& + \frac{\Delta}{\Delta \xi} \left[ \mu \frac{\partial v}{\partial \eta} - \mu \lambda_{\xi} u - \mu \lambda_{\eta} v - \kappa_{\xi} \mu \left\{ \frac{\partial w}{\partial \eta} - \kappa_{\xi} \frac{\partial v}{\partial \xi} - \kappa_{\eta} \frac{\partial v}{\partial \eta} \right. \right. \\
& \left. \left. + (-\sigma + \kappa_{\xi} \lambda_{\xi} - \kappa_{\eta} \lambda_{\eta}) u \right\} \right] \\
& + \frac{\Delta}{\Delta \eta} \left[ \mu \frac{\partial v}{\partial \eta} + 2\mu \lambda_{\eta} u - \kappa_{\eta} \mu \left\{ \frac{\partial w}{\partial \eta} - \kappa_{\xi} \frac{\partial v}{\partial \xi} - \kappa_{\eta} \frac{\partial v}{\partial \eta} \right. \right.
\end{aligned}$$

$$\begin{aligned}
& + (-\sigma + \kappa_\xi \lambda_\xi - \kappa_\eta \lambda_\eta) u \} ] \\
& + (\sigma - \kappa_\xi \lambda_\xi + \kappa_\eta \lambda_\eta) \times \left[ \rho u w - \mu \left\{ \frac{\partial w}{\partial \xi} - \kappa_\xi \frac{\partial u}{\partial \xi} - \kappa_\eta \frac{\partial u}{\partial \eta} \right. \right. \\
& \left. \left. + (\sigma - \kappa_\xi \lambda_\xi + \kappa_\eta \lambda_\eta) v \right\} \right] \\
& + \lambda_\xi \left[ \rho u^2 - 2\mu \left\{ \frac{\partial u}{\partial \xi} + \lambda_\xi v \right\} \right] \\
& - \lambda_\eta \left[ \rho u v - \mu \left\{ \frac{\partial u}{\partial \eta} + \frac{\partial v}{\partial \xi} - \lambda_\xi u - \lambda_\eta v \right\} \right]
\end{aligned}
\tag{2.11}$$

#### z-Momentum

$$\begin{aligned}
\frac{\Delta}{\Delta \xi} (\rho u w) + \frac{\Delta}{\Delta \eta} (\rho v w) = & - \frac{\partial p}{\partial z} + \frac{\Delta}{\Delta \xi} \left[ \mu \frac{\partial w}{\partial \xi} \right] + \frac{\Delta}{\Delta \eta} \left[ \mu \frac{\partial w}{\partial \eta} \right] \\
& + \frac{\Delta}{\Delta \xi} (\kappa_\xi \rho w w) + \frac{\Delta}{\Delta \eta} (\kappa_\eta \rho w w) \\
& + \frac{\Delta}{\Delta \xi} \left\{ \mu \left\{ -\kappa_\xi \frac{\partial u}{\partial \xi} - \kappa_\eta \frac{\partial u}{\partial \eta} + (\sigma - \kappa_\xi \lambda_\xi + \kappa_\eta \lambda_\eta) v \right\} \right. \\
& \left. - \kappa_\xi 2\mu \left\{ -\kappa_\xi \frac{\partial w}{\partial \xi} - \kappa_\eta \frac{\partial w}{\partial \eta} \right\} \right] \\
& + \frac{\Delta}{\Delta \eta} \left\{ \mu \left\{ -\kappa_\xi \frac{\partial v}{\partial \xi} - \kappa_\eta \frac{\partial v}{\partial \eta} + (-\sigma + \kappa_\xi \lambda_\xi + \kappa_\eta \lambda_\eta) u \right\} \right. \\
& \left. - \kappa_\eta 2\mu \left\{ -\kappa_\xi \frac{\partial w}{\partial \xi} - \kappa_\eta \frac{\partial w}{\partial \eta} \right\} \right]
\end{aligned}
\tag{2.12}$$

From equations (2.7), (2.10), (2.11) and (2.12) it is clear that a general equation could be formed:

<p>CONVECTION TERMS</p> <p><u>                    </u></p>	<p>DIFFUSION TERMS</p> <p><u>                    </u></p>
$\frac{\Delta}{\Delta \xi} (\rho c_\xi \phi) + \frac{\Delta}{\Delta \eta} (\rho c_\eta \phi)$	$= \frac{\Delta}{\Delta \xi} \left[ \Gamma_{\xi_\phi} \frac{\partial \phi}{\partial \xi} \right] + \frac{\Delta}{\Delta \eta} \left[ \Gamma_{\eta_\phi} \frac{\partial \phi}{\partial \eta} \right] + s_\phi$

(2.13)

where  $C_\xi, C_\eta$  are the convection coefficients,  $\Gamma_{\xi_\phi}, \Gamma_{\eta_\phi}$  the diffusion coefficients and  $S_\phi$  the source term taking the form  $S_\phi = B_\phi + \Delta_\phi \cdot \phi$ . The quantities  $\Gamma_{\xi_\phi}, \Gamma_{\eta_\phi}$  and  $S_\phi$  ( $B_\phi, \Delta_\phi$ ) are specific to a particular meaning of  $\phi$  which stands for  $U, V, W, \Theta$  (as well as turbulent kinetic energy  $k$  and energy dissipation  $\epsilon$  for the turbulent flow computations). The expressions of all those coefficients and source terms are given below:

$$C_\xi = U - \kappa_\xi W, \quad C_\eta = V - \kappa_\eta W \quad (2.14)$$

if  $\phi \equiv U$ , from equations (2.10), (2.13)

$$\Gamma_{\xi_U} = \mu(1 + \kappa_\xi^2) \quad (2.15)$$

$$\Gamma_{\eta_U} = \mu(1 + \kappa_\eta^2) \quad (2.16)$$

$$\begin{aligned} B_U = \frac{\Delta}{\Delta\xi} & \left[ \mu \frac{\partial U}{\partial \xi} + 2\mu\lambda_\xi V - \kappa_\xi \mu \left\{ \frac{\partial W}{\partial \xi} - \kappa_\eta \frac{\partial U}{\partial \eta} \right. \right. \\ & \left. \left. + (\sigma - \kappa_\xi \lambda_\xi + \kappa_\eta \lambda_\eta) \nabla \right\} \right] \\ & + \frac{\Delta}{\Delta\eta} \left[ \mu \frac{\partial V}{\partial \xi} - \mu\lambda_\xi U - \mu\lambda_\eta V - \kappa_\eta \mu \left\{ \frac{\partial W}{\partial \xi} - \kappa_\xi \frac{\partial U}{\partial \xi} \right. \right. \\ & \left. \left. + (\sigma - \kappa_\xi \lambda_\xi + \kappa_\eta \lambda_\eta) \nabla \right\} \right] \\ & + (-\sigma + \kappa_\xi \lambda_\xi - \kappa_\eta \lambda_\eta) \times \left\{ \rho VW - \mu \left\{ \frac{\partial W}{\partial \eta} - \kappa_\xi \frac{\partial V}{\partial \xi} - \kappa_\eta \frac{\partial V}{\partial \eta} \right\} \right\} \\ & + \lambda_\xi \mu \left( \frac{\partial U}{\partial \eta} + \frac{\partial V}{\partial \xi} - \lambda_\eta V \right) + \lambda_\eta \left( \rho V^2 - 2\mu \frac{\partial V}{\partial \eta} \right) \\ & - \lambda_\xi \rho VU - \frac{\partial p}{\partial \xi} \end{aligned} \quad (2.17)$$

and

$$\Delta_U = \mu(\sigma - \kappa_\xi \lambda_\xi + \kappa_\eta \lambda_\eta)^2 - \mu\lambda_\xi^2 - 2\mu\lambda_\eta^2 \quad (2.18)$$

if  $\Phi \equiv V$ , equations (2.11), (2.13) give:

$$\Gamma_{\xi_V} = \mu(1 + \kappa_\xi^2) \quad (2.19)$$

$$\Gamma_{\eta_V} = \mu(1 + \kappa_\eta^2) \quad (2.20)$$

$$\begin{aligned} B_V = & \frac{\Delta}{\Delta\xi} \left[ \mu \frac{\partial U}{\partial \eta} - \mu \lambda_\xi U - \mu \lambda_\eta V - \kappa_\xi \mu \left\{ \frac{\partial W}{\partial \eta} - \kappa_\eta \frac{\partial V}{\partial \eta} \right. \right. \\ & \left. \left. + (-\sigma + \kappa_\xi \lambda_\xi - \kappa_\eta \lambda_\eta) U \right\} \right] \\ & + \frac{\Delta}{\Delta\eta} \left[ \mu \frac{\partial V}{\partial \eta} + 2\mu \lambda_\eta U - \kappa_\eta \mu \left\{ \frac{\partial W}{\partial \eta} - \kappa_\xi \frac{\partial V}{\partial \xi} \right. \right. \\ & \left. \left. + (-\sigma + \kappa_\xi \lambda_\xi - \kappa_\eta \lambda_\eta) U \right\} \right] \\ & + (\sigma - \kappa_\xi \lambda_\xi + \kappa_\eta \lambda_\eta) \times \left( \rho U W - \mu \left\{ \frac{\partial W}{\partial \xi} - \kappa_\xi \frac{\partial U}{\partial \xi} - \kappa_\eta \frac{\partial U}{\partial \eta} \right\} \right) \\ & + \lambda_\xi \left( \rho U^2 - 2\mu \frac{\partial U}{\partial \xi} \right) + \lambda_\eta \mu \left( \frac{\partial U}{\partial \eta} + \frac{\partial V}{\partial \xi} - \lambda_\xi U \right) \\ & - \lambda_\eta \rho U V - \frac{\partial p}{\partial \eta} \end{aligned} \quad (2.21)$$

$$\text{and } \Delta_V = -\mu(\sigma - \kappa_\xi \lambda_\xi + \kappa_\eta \lambda_\eta)^2 - 2\mu \lambda_\xi^2 - \mu \lambda_\eta^2 \quad (2.22)$$

if  $\Phi \equiv W$ , equations (2.12), (2.13) yield:

$$\Gamma_{\xi_W} = \mu(1 + 2\kappa_\xi^2) \quad (2.23)$$

$$\Gamma_{\eta_W} = \mu(1 + 2\kappa_\eta^2) \quad (2.24)$$

$$\begin{aligned} B_W = & \frac{\Delta}{\Delta\xi} \left[ \mu \left\{ -\kappa_\xi \frac{\partial U}{\partial \xi} - \kappa_\eta \frac{\partial U}{\partial \eta} + (\sigma - \kappa_\xi \lambda_\xi + \kappa_\eta \lambda_\eta) V \right\} \right. \\ & \left. + \kappa_\xi 2\mu \kappa_\eta \frac{\partial W}{\partial \eta} \right] \\ & + \frac{\Delta}{\Delta\eta} \left[ \mu \left\{ -\kappa_\xi \frac{\partial V}{\partial \xi} - \kappa_\eta \frac{\partial V}{\partial \eta} + (-\sigma + \kappa_\xi \lambda_\xi + \kappa_\eta \lambda_\eta) U \right\} \right. \\ & \left. + \kappa_\eta 2\mu \kappa_\xi \frac{\partial W}{\partial \xi} \right] - \frac{\partial p}{\partial \xi} \end{aligned} \quad (2.25)$$



$$\text{and } \Delta_w = 0 \quad (2.26)$$

while if  $\Phi \equiv \theta$ , equations (2.7), (2.13) give:

$$\Gamma_{\xi\theta} = \Gamma_T(1 + \kappa_\xi^2) = \frac{\mu}{Pr}(1 + \kappa_\xi^2) \quad (2.27)$$

$$\Gamma_{\eta\theta} = \Gamma_T(1 + \kappa_\eta^2) = \frac{\mu}{Pr}(1 + \kappa_\eta^2) \quad (2.28)$$

where  $Pr$  is the molecular Prandtl number

$$\begin{aligned} B_\theta = & -\frac{\Delta}{\Delta\xi} \left[ \kappa_\xi \Gamma_T \left( -\kappa_\eta \frac{\partial \theta}{\partial \eta} + \frac{h_\xi}{b} \frac{dT_{ref}}{d\xi} \right) \right] \\ & -\frac{\Delta}{\Delta\eta} \left[ \kappa_\eta \Gamma_T \left( -\kappa_\xi \frac{\partial \theta}{\partial \xi} + \frac{h_\eta}{b} \frac{dT_{ref}}{d\eta} \right) \right] \\ & -\frac{\Delta}{\Delta\xi} \left( \frac{h_\xi}{b} \rho w T_{ref} \right) \end{aligned} \quad (2.29)$$

$$\text{and } \Delta_\theta = 0. \quad (2.30)$$

Having formed the differential equations (2.13) to (2.30) and the proper grid for storage of the variables, the finite-difference equations can be produced following the steps described below:

Integration of the equation (2.13) over the  $\Phi$  control volumes, shown in Figure 2.5, gives:

$$\begin{aligned} & \iiint_V \left\{ \frac{\Delta}{\Delta\xi} (\rho C_\xi \Phi) \right\} dV + \iiint_V \left\{ \frac{\Delta}{\Delta\eta} (\rho G_\eta \Phi) \right\} dV = \\ & \iiint_V \left\{ \frac{\Delta}{\Delta\xi} \left( \Gamma_{\xi\Phi} \frac{\partial \Phi}{\partial \xi} \right) \right\} dV + \iiint_V \left\{ \frac{\Delta}{\Delta\eta} \left( \Gamma_{\eta\Phi} \frac{\partial \Phi}{\partial \eta} \right) \right\} dV + \\ & \iiint_V S_{\Phi P} dV \end{aligned} \quad (2.31)$$

where  $dV$  is given in equation (A2.11) of Appendix 2 and is shown in Figure 3

of the same appendix.

So, the equation (2.31) becomes:

$$\begin{aligned}
 & \left\{ (\rho C_{\xi}^{\bar{\Phi}})_{e_{\bar{\Phi}}} A_{e_{\bar{\Phi}}}^{\bar{\Phi}} - (\rho C_{\xi}^{\bar{\Phi}})_{w_{\bar{\Phi}}} A_{w_{\bar{\Phi}}}^{\bar{\Phi}} \right\} + \left\{ (\rho C_{\eta}^{\bar{\Phi}})_{n_{\bar{\Phi}}} A_{n_{\bar{\Phi}}}^{\bar{\Phi}} \right. \\
 & \left. - (\rho C_{\eta}^{\bar{\Phi}})_{s_{\bar{\Phi}}} A_{s_{\bar{\Phi}}}^{\bar{\Phi}} \right\} = \left\{ \left[ \Gamma_{\xi}^{\bar{\Phi}} \frac{\partial \bar{\Phi}}{\partial \xi} \right]_{e_{\bar{\Phi}}} A_{e_{\bar{\Phi}}}^{\bar{\Phi}} - \left[ \Gamma_{\xi}^{\bar{\Phi}} \frac{\partial \bar{\Phi}}{\partial \xi} \right]_{w_{\bar{\Phi}}} A_{w_{\bar{\Phi}}}^{\bar{\Phi}} \right\} \\
 & + \left\{ \left[ \Gamma_{\eta}^{\bar{\Phi}} \frac{\partial \bar{\Phi}}{\partial \eta} \right]_{n_{\bar{\Phi}}} A_{n_{\bar{\Phi}}}^{\bar{\Phi}} - \left[ \Gamma_{\eta}^{\bar{\Phi}} \frac{\partial \bar{\Phi}}{\partial \eta} \right]_{s_{\bar{\Phi}}} A_{s_{\bar{\Phi}}}^{\bar{\Phi}} \right\} + S_{\bar{\Phi}P} \Delta V^{\bar{\Phi}}
 \end{aligned} \tag{2.32}$$

where  $e_{\bar{\Phi}}$ ,  $w_{\bar{\Phi}}$ ,  $n_{\bar{\Phi}}$ ,  $s_{\bar{\Phi}}$  stand for east, west, north and south positions of the control volume surrounding  $\bar{\Phi}$  (see Figure 2.5).  $A_{e_{\bar{\Phi}}}^{\bar{\Phi}}$ ,  $A_{w_{\bar{\Phi}}}^{\bar{\Phi}}$ ,  $A_{n_{\bar{\Phi}}}^{\bar{\Phi}}$ ,  $A_{s_{\bar{\Phi}}}^{\bar{\Phi}}$  denote the control volume's east, west, north and south areas respectively, while  $\Delta V^{\bar{\Phi}}$  is its volume. The value of  $S_{\bar{\Phi}P}$  is calculated at the P position which is located in the centre of the control volume for  $\bar{\Phi}$ . If  $\bar{\Phi} \equiv U$ , then:

$$\begin{aligned}
 A_{e_{\bar{\Phi}}}^U &= 0.5 \left[ \Delta \eta_{(I,J)} + \Delta \eta_{(I+1,J)} \right] \times \Delta z \\
 A_{w_{\bar{\Phi}}}^U &= 0.5 \left[ \Delta \eta_{(I,J)} + \Delta \eta_{(I-1,J)} \right] \times \Delta z \\
 A_{n_{\bar{\Phi}}}^U &= 0.5 \left[ \Delta \xi_{(I,J+1)} + \Delta \xi_{(I-1,J+1)} \right] \times \Delta z \\
 A_{s_{\bar{\Phi}}}^U &= 0.5 \left[ \Delta \xi_{(I,J)} + \Delta \xi_{(I-1,J)} \right] \times \Delta z \\
 \Delta V^U &= 0.25 \left[ \Delta \xi_{(I,J)} + \Delta \xi_{(I-1,J)} \right] \times \left[ \Delta \eta_{(I,J)} + \Delta \eta_{(I+1,J)} \right] \times \Delta z
 \end{aligned} \tag{2.33}$$

where  $\Delta z \equiv 1$  and the distance  $\Delta \eta$  and  $\Delta \xi$  are shown in Figure 2.5.

If  $\bar{\Phi} \equiv V$  then:

$$\begin{aligned}
A_e^V &= 0.5 \left[ \Delta\eta_{(I+1,J-1)} + \Delta\eta_{(I+1,J)} \right] \times \Delta z \\
A_w^V &= 0.5 \left[ \Delta\eta_{(I,J-1)} + \Delta\eta_{(I,J)} \right] \times \Delta z \\
A_n^V &= 0.5 \left[ \Delta\xi_{(I,J)} + \Delta\xi_{(I,J+1)} \right] \times \Delta z \\
A_s^V &= 0.5 \left[ \Delta\xi_{(I,J)} + \Delta\xi_{(I,J-1)} \right] \times \Delta z \\
\Delta V^V &= 0.25 \left[ \Delta\xi_{(I,J)} + \Delta\xi_{(I,J-1)} \right] \times \left[ \Delta\eta_{(I+1,J-1)} + \Delta\eta_{(I+1,J)} \right] \times \Delta z
\end{aligned}
\tag{2.34}$$

If  $\Phi \equiv W, \theta, p'$  (or  $k, \epsilon$  for the turbulent flow computations) then:

$$\begin{aligned}
A_e^{\Phi} &= \Delta\eta_{(I+1,J)} \times \Delta z \\
A_w^{\Phi} &= \Delta\eta_{(I,J)} \times \Delta z \\
A_n^{\Phi} &= \Delta\xi_{(I,J+1)} \times \Delta z \\
A_s^{\Phi} &= \Delta\xi_{(I,J)} \times \Delta z \\
\Delta V^{\Phi} &= \Delta\eta_{(I+1,J)} \times \Delta\xi_{(I,J)} \times \Delta z
\end{aligned}
\tag{2.35}$$

In evaluating the values of the variables  $\Phi$  at their cell boundaries central differencing has been used throughout. Patankar [87], Leonard [88], [89] and Han et al [90] report that central differencing may lead to unphysical oscillatory behaviour in an implicit scheme or to non-convergence in an explicit scheme in a flow where convection dominates diffusion (i.e. the Peclet number  $Pe = \frac{\rho U \cdot \Delta x}{\Gamma} > 2$ ). However, in the present computations no such problems have been encountered since the cell Peclet numbers (based on the velocity components in the  $\xi$ - $\eta$  plane) were always less than 2. A typical value for the results discussed in the next chapter was  $10^{-1}$ . In such cases

the exclusive use of central differencing undoubtedly offers a satisfactory compromise between the requirements for accuracy and computational economy.

Equation (2.32) can be written in the form:

$$\dot{q}_e - \dot{q}_w + \dot{q}_n - \dot{q}_s - S_{\phi_P} \Delta V^{\phi} = 0 \quad (2.36)$$

$$\begin{aligned} \text{where } \dot{q}_e &= \left[ (\rho C_{\xi}^{\phi})_{e_{\phi}} - \left( \Gamma_{\xi_{\phi}} \frac{\partial \phi}{\partial \xi} \right)_{e_{\phi}} \right] \times A_e^{\phi} \\ \dot{q}_w &= \left[ (\rho C_{\xi}^{\phi})_{w_{\phi}} - \left( \Gamma_{\xi_{\phi}} \frac{\partial \phi}{\partial \xi} \right)_{w_{\phi}} \right] \times A_w^{\phi} \\ \dot{q}_n &= \left[ (\rho C_{\eta}^{\phi})_{n_{\phi}} - \left( \Gamma_{\eta_{\phi}} \frac{\partial \phi}{\partial \eta} \right)_{n_{\phi}} \right] \times A_n^{\phi} \\ \dot{q}_s &= \left[ (\rho C_{\eta}^{\phi})_{s_{\phi}} - \left( \Gamma_{\eta_{\phi}} \frac{\partial \phi}{\partial \eta} \right)_{s_{\phi}} \right] \times A_s^{\phi} \end{aligned} \quad (2.37)$$

the total fluxes (convection plus diffusion). Equation (2.36) shows that the above discretization is conservative since continuity of the fluxes  $\dot{q}$  is satisfied around the cell boundaries. However, the presence of the curvature terms in the diffusion and convection coefficients makes it difficult to judge if overall momentum conservation is explicitly satisfied. If all the values of  $\phi$ , appearing in equations (2.37), are calculated using central differencing, equation (2.36) takes the form:

$$A_P^{\phi} \phi_P = A_E^{\phi} \phi_E + A_W^{\phi} \phi_W + A_N^{\phi} \phi_N + A_S^{\phi} \phi_S + S U^{\phi} \quad (2.38)$$

where for central differencing ( $Pe < 2$ )

$$A_E^{\phi} = \left[ D_{\xi_{\phi}} - \alpha_{\phi} F_{\xi_{\phi}} \right]_{e_{\phi}}$$

$$A_W^\phi = \left[ D_{\xi_\phi} + (1 - \alpha_\phi) F_{\xi_\phi} \right]_{w_\phi}$$

$$A_N^\phi = \left[ D_{\eta_\phi} - \beta_\phi F_{\eta_\phi} \right]_{n_\phi}$$

$$A_S^\phi = \left[ D_{\eta_\phi} + (1 - \beta_\phi) F_{\eta_\phi} \right]_{s_\phi}$$

$$A_P^\phi = A_E^\phi + A_W^\phi + A_N^\phi + A_S^\phi - SP^\phi$$

(2.39)

where  $SP^\phi = \Delta_{\phi_P} \cdot \Delta v^\phi$

$$SU^\phi = B_{\phi_P} \cdot \Delta v^\phi$$

$\Delta_\phi, \beta_\phi$  are given by the equations (2.17), (2.18), (2.21), (2.22), (2.25), (2.26), (2.29) and (2.30)

and  $\left[ D_{\xi_\phi} \right]_{e_\phi} = \left[ \Gamma_{\xi_\phi} \right]_{e_\phi} \cdot A_e^\phi \cdot \Delta \xi_{e_\phi}$

$$\left[ D_{\xi_\phi} \right]_{w_\phi} = \left[ \Gamma_{\xi_\phi} \right]_{w_\phi} \cdot A_w^\phi \cdot \Delta \xi_{w_\phi}$$

$$\left[ D_{\eta_\phi} \right]_{n_\phi} = \left[ \Gamma_{\eta_\phi} \right]_{n_\phi} \cdot A_n^\phi \cdot \Delta \eta_{n_\phi}$$

$$\left[ D_{\eta_\phi} \right]_{s_\phi} = \left[ \Gamma_{\eta_\phi} \right]_{s_\phi} \cdot A_s^\phi \cdot \Delta \eta_{s_\phi}$$

$$\left[ F_{\xi_\phi} \right]_{e_\phi} = \rho \left[ C_{\xi} \right]_{e_\phi} \cdot A_e^\phi$$

$$\left[ F_{\xi\phi} \right]_{w\phi} = \rho \left[ C_{\xi} \right]_{w\phi} \cdot A_w^{\phi}$$

$$\left[ F_{\eta\phi} \right]_{n\phi} = \rho \left[ C_{\eta} \right]_{n\phi} \cdot A_n^{\phi}$$

$$\left[ F_{\eta\phi} \right]_{s\phi} = \rho \left[ C_{\eta} \right]_{s\phi} \cdot A_s^{\phi}$$

(2.40)

The equations for  $\Gamma_{\xi\phi}$ ,  $\Gamma_{\eta\phi}$ ,  $C_{\xi}$ ,  $C_{\eta}$  have been given above ((2.14), (2.15), (2.16), (2.19), (2.20), (2.23), (2.24), (2.27), (2.28)), as well as the equations for  $A_e^{\phi}$ ,  $A_w^{\phi}$ ,  $A_n^{\phi}$ ,  $A_s^{\phi}$  ((2.33), (2.34), (2.35)), while:

$$\text{if } \phi \equiv U: \Delta \xi_{e_U} = 0.5 \left( \Delta \xi_{(I,J)} + \Delta \xi_{(I,J+1)} \right)$$

$$\Delta \xi_{w_U} = 0.5 \left( \Delta \xi_{(I-1,J)} + \Delta \xi_{(I-1,J+1)} \right)$$

$$\Delta \eta_{n_U} = 0.5 \left( \Delta \eta_{(I,J)} + \Delta \eta_{(I,J+1)} \right)$$

$$\Delta \eta_{s_U} = 0.5 \left( \Delta \eta_{(I,J)} + \Delta \eta_{(I,J-1)} \right)$$

(2.41)

$$\text{if } \phi \equiv V: \Delta \xi_{e_V} = 0.5 \left( \Delta \xi_{(I,J)} + \Delta \xi_{(I+1,J)} \right)$$

$$\Delta \xi_{w_V} = 0.5 \left( \Delta \xi_{(I,J)} + \Delta \xi_{(I-1,J)} \right)$$

$$\Delta \eta_{n_V} = 0.5 \left( \Delta \eta_{(I,J)} + \Delta \eta_{(I+1,J)} \right)$$

$$\Delta \eta_{s_V} = 0.5 \left( \Delta \eta_{(I,J-1)} + \Delta \eta_{(I+1,J-1)} \right)$$

(2.42)

and if  $\phi \equiv W, \Theta(k, \epsilon)$ :

$$\begin{aligned}
\Delta \xi_{e_\phi} &= 0.25 \left[ \Delta \xi_{(I,J)} + \Delta \xi_{(I,J+1)} + \Delta \xi_{(I+1,J)} + \Delta \xi_{(I+1,J+1)} \right] \\
\Delta \xi_{w_\phi} &= 0.25 \left[ \Delta \xi_{(I,J)} + \Delta \xi_{(I,J+1)} + \Delta \xi_{(I-1,J)} + \Delta \xi_{(I-1,J+1)} \right] \\
\Delta \eta_{n_\phi} &= 0.25 \left[ \Delta \eta_{(I,J)} + \Delta \eta_{(I+1,J)} + \Delta \eta_{(I,J+1)} + \Delta \eta_{(I+1,J+1)} \right] \\
\Delta \eta_{s_\phi} &= 0.25 \left[ \Delta \eta_{(I,J)} + \Delta \eta_{(I+1,J)} + \Delta \eta_{(I,J-1)} + \Delta \eta_{(I+1,J-1)} \right]
\end{aligned}
\tag{2.43}$$

$\alpha_\phi$  and  $\beta_\phi$  in equations (2.39) are weighting factors accounting for the non-uniformity of the grid. Their values are given below:

$$\begin{aligned}
\text{if } \phi \equiv U \quad & \alpha_U = 0.5 \\
& \beta_U = \Delta \eta_{(I,J)} / \left[ \Delta \eta_{(I,J)} + \Delta \eta_{(I,J+1)} \right] \\
\text{if } \phi \equiv V \quad & \alpha_V = \Delta \xi_{(I,J)} / \left[ \Delta \xi_{(I,J)} + \Delta \xi_{(I+1,J)} \right] \\
& \beta_V = 0.5 \\
\text{if } \phi \equiv W, \theta(k, \epsilon) \quad & \alpha_\phi = \left[ \Delta \xi_{(I,J)} + \Delta \xi_{(I,J+1)} / \left[ \Delta \xi_{(I,J)} + \Delta \xi_{(I+1,J)} \right. \right. \\
& \quad \left. \left. + \Delta \xi_{(I,J+1)} + \Delta \xi_{(I+1,J+1)} \right] \right] \\
& \beta_\phi = \left[ \Delta \eta_{(I,J)} + \Delta \eta_{(I+1,J)} / \left[ \Delta \eta_{(I,J)} + \Delta \eta_{(I+1,J)} \right. \right. \\
& \quad \left. \left. + \Delta \eta_{(I,J+1)} + \Delta \eta_{(I+1,J+1)} \right] \right]
\end{aligned}
\tag{2.44}$$

For grid cells adjacent to the boundaries of the solution domain the coefficients  $A_E^\phi$ ,  $A_W^\phi$ ,  $A_N^\phi$ ,  $A_S^\phi$  and the source term of (2.38) have been modified to include the various boundary conditions. The iterative procedure followed by the computer code and described in a following section of the present chapter has to be stable and, hopefully, rapidly convergent. Certain modifications in equation (2.38) have been proved to secure these requirements:

- a) During an iteration the net mass flux from a control volume is generally non-zero. If SMP is this non-zero mass flux in a cell, stability can be improved by adding the term  $SMP \cdot \phi_P$  in the SU term and subtracting it from SP.
- b) Instability can also be eliminated by using under-relaxation factors (URF $\phi$ ). Their application in equation (2.38) yields:

$$\begin{aligned} \phi_P' &= \phi_P + URF\phi \frac{1}{A_P^\phi} \left[ -A_P^\phi \phi_P + A_E^\phi \phi_E + A_W^\phi \phi_W \right. \\ &\quad \left. + A_N^\phi \phi_N + A_S^\phi \phi_S + SU^\phi \right] \\ \Rightarrow A_P^\phi \phi_P' &= A_P^\phi \phi_P - URF\phi A_P^\phi \phi_P + URF\phi \left[ A_E^\phi \phi_E + A_W^\phi \phi_W \right. \\ &\quad \left. + A_N^\phi \phi_N + A_S^\phi \phi_S \right] + URF\phi \cdot SU^\phi \\ \Rightarrow \frac{A_P^\phi}{URF\phi} \phi_P' &= A_E^\phi \phi_E + A_W^\phi \phi_W + A_N^\phi \phi_N + A_S^\phi \phi_S \end{aligned}$$



$$+ \left[ \frac{A_P^\phi}{URF\phi} (1 - URF\phi) \phi_P + SU^\phi \right]$$

$$\text{So, } \frac{A_P^\phi}{URF\phi} = (A_P^\phi)'$$

$$\text{and } SU^\phi + (1 - URF\phi) \frac{A_P^\phi}{URF\phi} \phi_P = (SU^\phi)'$$

The use of improper under-relaxation factors may also cause instability. In such cases, adjustment of the under-relaxation factors is needed. The variables  $(A_P^\phi)'$  and  $(SU^\phi)'$  give the expressions for  $A_P^\phi$  and  $SU^\phi$  formed after the application of the under-relaxation factors.

## 2.5b The Special Treatment of Pressure

The TEACH program in its original form incorporates the SIMPLE algorithm (Semi-Implicit Method for Pressured Linked Equations) (see Patankar and Spalding [81], Patankar [87]) in order to adjust successively the pressure field and satisfy eventually the continuity equation throughout the solution domain. Initial runs using SIMPLE indicated extremely slow rates of convergence although simple test cases were computed. At the same time, similar difficulties had been experienced by a research group at Imperial College working on a different project using also cyclic boundary conditions. In their case, the problem had been overcome by devising a new algorithm for the solution of pressure-correction equation (see Issa [79] and Gosman, Issa, Watkins [80]).

This new algorithm, PISO (Pressure Implicit Split Operator) is based

on the recognition that the assumption of a linear relation between velocity and pressure perturbations, used in SIMPLE, has to be improved. So, it relates the velocity perturbations at some point not only with the pressure perturbations but also with velocity fluctuations at adjacent nodes. A full description of the new algorithm is given in Appendix 3. The equation (A3.18) describing the "full" exact pressure correction equation has the same form with the discretized momentum and energy equations given by (2.38) where  $\Phi \equiv p'$  and  $SU \equiv I + II$  given below. In order to apply equation (A3.18) into the computer code, modified to solve the flow through the spirally fluted tube, the source term of the continuity equation (2.3):

$$\frac{\Delta}{\Delta \xi} (\kappa_{\xi} \rho W) + \frac{\Delta}{\Delta \eta} (\kappa_{\eta} \rho W)$$

has to be included. Thus, equation (A3.18) becomes:

$$\begin{aligned} A_p^p p_p' = & A_E^p p_E' + A_W^p p_W' + A_N^p p_N' + A_N^p p_N' + A_S^p p_S' \\ & - \left\{ \left( \rho A_e^p U_e^* \right) - \left( \rho A_w^p U_w^* \right) \right. \\ & + \left. \left( \rho A_n^p V_n^* \right) - \left( \rho A_s^p V_s^* \right) \right\} \\ & - \left\{ \left( \rho A_e^p W_e^* \kappa_{\xi_e} \right) - \left( \rho A_w^p W_w^* \kappa_{\xi_w} \right) \right. \\ & + \left. \left( \rho A_n^p W_n^* \kappa_{\eta_n} \right) - \left( \rho A_s^p W_s^* \kappa_{\eta_s} \right) \right\} \end{aligned} \quad \left. \vphantom{\begin{aligned} A_p^p p_p' = & A_E^p p_E' + A_W^p p_W' + A_N^p p_N' + A_N^p p_N' + A_S^p p_S' \\ & - \left\{ \left( \rho A_e^p U_e^* \right) - \left( \rho A_w^p U_w^* \right) \right. \\ & + \left. \left( \rho A_n^p V_n^* \right) - \left( \rho A_s^p V_s^* \right) \right\} \\ & - \left\{ \left( \rho A_e^p W_e^* \kappa_{\xi_e} \right) - \left( \rho A_w^p W_w^* \kappa_{\xi_w} \right) \right. \\ & + \left. \left( \rho A_n^p W_n^* \kappa_{\eta_n} \right) - \left( \rho A_s^p W_s^* \kappa_{\eta_s} \right) \right\} } \right\} I$$

$$\begin{aligned}
& - \left\{ \left( \rho A_e^p \right) \cdot \left[ \frac{A_{Ee}^U}{A_{Pe}^U} \delta u_{Ee} + \frac{A_{We}^U}{A_{Pe}^U} \delta u_{We} \right. \right. \\
& \quad \left. \left. + \frac{A_{Ne}^U}{A_{Pe}^U} \delta u_{Ne} + \frac{A_{Se}^U}{A_{Pe}^U} \delta u_{Se} \right] \right. \\
& - \left( \rho A_w^p \right) \cdot \left[ \frac{A_{Ew}^U}{A_{Pw}^U} \delta u_{Ew} + \frac{A_{Ww}^U}{A_{Pw}^U} \delta u_{Ww} \right. \\
& \quad \left. + \frac{A_{Nw}^U}{A_{Pw}^U} \delta u_{Nw} + \frac{A_{Sw}^U}{A_{Pw}^U} \delta u_{Sw} \right] \\
& + \left( \rho A_n^p \right) \cdot \left[ \frac{A_{En}^V}{A_{Pn}^V} \delta v_{En} + \frac{A_{Wn}^V}{A_{Pn}^V} \delta v_{Wn} \right. \\
& \quad \left. + \frac{A_{Nn}^V}{A_{Pn}^V} \delta v_{Nn} + \frac{A_{Sn}^V}{A_{Pn}^V} \delta v_{Sn} \right] \\
& - \left( \rho A_s^p \right) \cdot \left[ \frac{A_{Es}^V}{A_{Ps}^V} \delta v_{Es} + \frac{A_{Ws}^V}{A_{Ps}^V} \delta v_{Ws} \right. \\
& \quad \left. + \frac{A_{Ns}^V}{A_{Ps}^V} \delta v_{Ns} + \frac{A_{Ss}^V}{A_{Ps}^V} \delta v_{Ss} \right] \left. \right\} \quad \text{II} \\
\end{aligned} \tag{2.45}$$

where  $p' = p_1' + p_2'$ ,  $A_e^p$ ,  $A_w^p$ ,  $A_n^p$ ,  $A_s^p$  are areas given by equations (2.35),  $A_E^\phi$ ,  $A_W^\phi$ ,  $A_N^\phi$ ,  $A_S^\phi$  the coefficients for velocity  $\phi$  ( $\phi \equiv U$  or  $V$ ) given by

equations (2.39) calculated at positions e or w for U and n or s for V (see Figures 1a and 1b of Appendix 3), while

$$\begin{aligned}
 A_E^P &= \rho \cdot A_e^P \cdot A_e^P \\
 A_W^P &= \rho \cdot A_w^P \cdot A_w^P \\
 A_N^P &= \rho \cdot A_n^P \cdot A_n^P \\
 A_S^P &= \rho \cdot A_s^P \cdot A_s^P \\
 A_P^P &= A_E^P + A_W^P + A_N^P + A_S^P
 \end{aligned}
 \tag{2.46}$$

It is difficult to give a physical meaning to these finite-difference coefficients. However, they can be looked on as proportionality factors which, if multiplied by pressure gradient perturbations, give velocity fluctuations:

$$\delta u_{W_e} = A_W^P \cdot (p_{I-1} - p_I) \quad \text{etc.}$$

$$\delta v_{S_n} = A_S^P \cdot (p_{J-1} - p_J) \quad \text{etc.}$$

where  $p_{I-1}$ ,  $p_I$ ,  $p_{J-1}$ ,  $p_J$  are the pressures located at positions shown in Figures 1a and 1b of Appendix 3.

Equation (2.45) can be decomposed into two pressure correction equations (for  $p'_1$  and  $p'_2$ , say) which differ only in their source terms (source term I for the first equation and II for the second). The velocity components  $u^*$ ,  $v^*$  are calculated at the previous iteration while  $\delta u$  and  $\delta v$  are calculated after the first pressure correction equation has been applied.

### 2.5c Solution of the Difference Equations

The finite-difference equations have been solved using a line-by-line iteration procedure. Thus, for solution along N-S lines with W-E sweeps equation (2.38) can be written as:

$$-A_N^{\phi} \phi_N + A_P^{\phi} \phi_P - A_S^{\phi} \phi_S = SU^{\phi} + A_E^{\phi} \phi_E + A_W^{\phi} \phi_W \quad (2.48)$$

If 1, 2, ...,  $\kappa$ , ...,  $n$  are the nodes shown in Figure 2.6, the equation (2.48) can take the form:

$$-A_{\kappa}^{\phi} \phi_{\kappa+1} + D_{\kappa}^{\phi} \phi_{\kappa} - B_{\kappa}^{\phi} \phi_{\kappa-1} = C_{\kappa} \quad (2.49)$$

where

$$\begin{aligned} D_{\kappa}^{\phi} &= A_P^{\phi} \\ B_{\kappa}^{\phi} &= A_S^{\phi} \\ A_{\kappa}^{\phi} &= A_N^{\phi} \\ C_{\kappa} &= SU^{\phi} + A_E^{\phi} \phi_E + A_W^{\phi} \phi_W \\ \phi_{\kappa} &= \phi_P \\ \phi_{\kappa-1} &= \phi_S \\ \phi_{\kappa+1} &= \phi_N \end{aligned}$$

Applying equation (2.49) to nodes  $\kappa = 2, 3, \dots, n-1$

$$\begin{aligned} -A_2^{\phi} \phi_3 + D_2^{\phi} \phi_2 &= B_2^{\phi} \phi_1 + C_2 \\ -A_3^{\phi} \phi_4 + D_3^{\phi} \phi_3 &= B_3^{\phi} \phi_2 + C_3 \\ &\vdots \\ -A_{n-1}^{\phi} \phi_n + D_{n-1}^{\phi} \phi_{n-1} &= B_{n-1}^{\phi} \phi_{n-2} + C_{n-1} \end{aligned} \quad (2.50)$$

where  $\phi_1, \phi_n$  are known boundary values.

Dividing the first member of equations (2.50) by  $D_2$ :

$$-\frac{A_2}{D_2} \phi_3 + \phi_2 = \frac{B_2}{D_2} \phi_1 + \frac{C_2}{D_2} = \frac{C_2^*}{D_2} \quad (2.51)$$

or 
$$\phi_2 = A_2' \phi_3 + C_2' \quad (2.52)$$

where 
$$A_2' = A_2 / D_2$$

$$C_2' = C_2^* / D_2 = (B_2 \phi_1 + C_2) / D_2$$

Multiplying equation (2.52) with  $B_3$ :

$$-B_3 A_2' \phi_3 + B_3 \phi_2 = C_2' B_3 \quad (2.53)$$

Adding equation (2.53) to the second one of equations (2.50) one can get:

$$-B_3 A_2' \phi_3 - A_3 \phi_4 + D_3 \phi_3 = C_3 + C_2' B_3 \quad \rightarrow$$

$$(D_3 - B_3 A_2') \phi_3 - A_3 \phi_4 = C_3 + C_2' B_3 \quad \rightarrow$$

$$\phi_3 - \frac{A_3}{(D_3 - B_3 A_2')} \phi_4 = \frac{C_3 + C_2' B_3}{(D_3 - B_3 A_2')} \quad \rightarrow$$

$$\phi_3 = A_3' \phi_4 + C_3' \quad (2.54)$$

$$\text{where } A_3' = \frac{A_3}{(D_3 - B_3 A_2')} , \quad C_3' = \frac{C_3 + C_2' B_3}{(D_3 - B_3 A_2')}$$

Similarly, from the rest of equations (2.50) the following relations can be derived:

$$\begin{aligned} \phi_4 &= A_4' \phi_5 + C_4' \\ \phi_5 &= A_5' \phi_6 + C_5' \\ &\vdots \\ \phi_{n-1} &= A_{n-1}' \phi_n + C_{n-1}' \end{aligned} \tag{2.55}$$

$$\begin{aligned} \text{where } A_4' &= \frac{A_4}{(D_4 - B_4 A_3')} , \quad C_4' = \frac{C_4 + C_3' B_4}{(D_4 - B_4 A_3')} \\ &\vdots \\ A_{n-1}' &= \frac{A_{n-1}}{(D_{n-1} - B_{n-1} A_{n-2}')} , \quad C_{n-1}' = \frac{C_{n-1} + C_{n-2}' B_{n-1}}{(D_{n-1} - B_{n-1} A_{n-2}')} \end{aligned}$$

In equations (2.55)  $\phi_n$  is a known boundary value. Using equations (2.55), in reverse order, the values of  $\phi_{n-1}, \phi_{n-2} \dots \phi_4$  can be calculated, while equations (2.54) and (2.53) give  $\phi_3$  and  $\phi_2$ .

The above sequence of forming the new coefficients and extracting the  $\phi$ 's is followed by a similar one applied along W-E lines with N-S sweeps. However, a special treatment has been introduced here in order to take account of the cyclic nature of the boundary conditions along the east and west boundaries. Again, the line-by-line iteration procedure has been used to solve the finite-difference equations along these lines

with N-S sweeps. Equation (2.38) can now be written as:

$$-A_E^\phi \phi_E + A_P^\phi \phi_P - A_W^\phi \phi_W = SU^\phi + A_N^\phi \phi_N + A_S^\phi \phi_S \quad (2.56)$$

If  $1, 2, \dots, \kappa, \dots, n$  are the nodes shown in Figure 2.7 the above equation can take the form:

$$-A_\kappa \phi_{\kappa+1} + D_\kappa \phi_\kappa - B_\kappa \phi_{\kappa-1} = C_\kappa$$

or  $D_\kappa \phi_\kappa = A_\kappa \phi_{\kappa+1} + B_\kappa \phi_{\kappa-1} + C_\kappa \quad (2.57)$

where  $D_\kappa = A_P^\phi$

$$A_\kappa = A_E^\phi$$

$$B_\kappa = A_W^\phi$$

$$C_\kappa = SU^\phi + A_N^\phi \phi_N + A_S^\phi \phi_S$$

$$\phi_\kappa = \phi_P$$

$$\phi_{\kappa-1} = \phi_W$$

$$\phi_{\kappa+1} = \phi_E$$

Applying equation (2.57) to nodes  $1, 2, \dots, n$  one obtains:

$$D_1 \phi_1 = A_1 \phi_2 + B_1 \phi_n + C_1$$

$$D_2 \phi_2 = A_2 \phi_3 + B_2 \phi_1 + C_2$$

$$\vdots$$

$$D_n \phi_n = A_n \phi_1 + B_n \phi_{n-1} + C_n \quad (2.58)$$



As before, we re-organize the equations to relate  $\phi_\kappa$  to  $\phi_{\kappa+1}$  starting from  $\kappa=2$  to  $\kappa=n-1$ . Equations (2.58) then become:

$$\begin{aligned}
 \phi_1 &= A'_1 \phi_2 + B'_1 \phi_n + C'_1 \\
 \phi_2 &= A'_2 \phi_3 + B'_2 \phi_n + C'_2 \\
 &\vdots \\
 \phi_{n-1} &= A'_{n-1} \phi_n + B'_{n-1} \phi_n + C'_{n-1} \\
 \phi_n &= A'_n \phi_1 + B'_n \phi_n + C'_n
 \end{aligned}
 \tag{2.59}$$

where 
$$A'_\kappa = \frac{A_\kappa}{(D_\kappa - A'_{\kappa-1} B_\kappa)}$$

$$B'_\kappa = \frac{B_\kappa B'_{\kappa-1}}{(D_\kappa - A'_{\kappa-1} B_\kappa)}$$

$$C'_\kappa = \frac{C_\kappa + C'_{\kappa-1} B_\kappa}{(D_\kappa - A'_{\kappa-1} B_\kappa)}$$

for  $\kappa = 2, \dots, n$

and 
$$A'_\kappa = A_1/D_1$$

$$B'_\kappa = B_1/D_1$$

$$C'_\kappa = C_1/D_1$$

for  $\kappa = 1$

Substituting  $\phi_{\kappa+1}$  to  $\phi_\kappa$  starting from  $\kappa = n-2$  to  $\kappa=1$  equations (2.59) yield:

$$\begin{aligned}
 \phi_1 &= B_1'' \phi_n + C_1'' \\
 \phi_2 &= B_2'' \phi_n + C_2'' \\
 &\vdots \\
 \phi_{n-1} &= B_{n-1}'' \phi_n + C_{n-1}''
 \end{aligned}
 \tag{2.60}$$

where  $B_{\kappa}'' = A_{\kappa}' B_{\kappa+1}'' + B_{\kappa}'$

$$C_{\kappa}'' = A_{\kappa}' C_{\kappa+1}'' + C_{\kappa}'$$

for  $\kappa = 1, \dots, n-2$

and  $B_{n-1}'' = B_{n-1}' + A_{n-1}'$

$$C_{n-1}'' = C_{n-1}'$$

The first equation of set (2.60) can be combined with the last equation of set (2.59) to give:

$$\phi_n = \frac{C_n' + A_n' C_1''}{1 - B_n' - A_n' B_1''}
 \tag{2.61}$$

which defines the value of  $\phi_n$ . This value can then be substituted into each of the equations (2.60) to yield values of  $\phi_{\kappa}$  for  $\kappa = 1, \dots, n-1$ .

The application of the above treatments for line-by-line solution of the finite-difference equations along W-E and N-S lines can be found in Appendix 5 (sub-routine LISOLV).

## 2.6 Outline of the Computer Program - General Structure

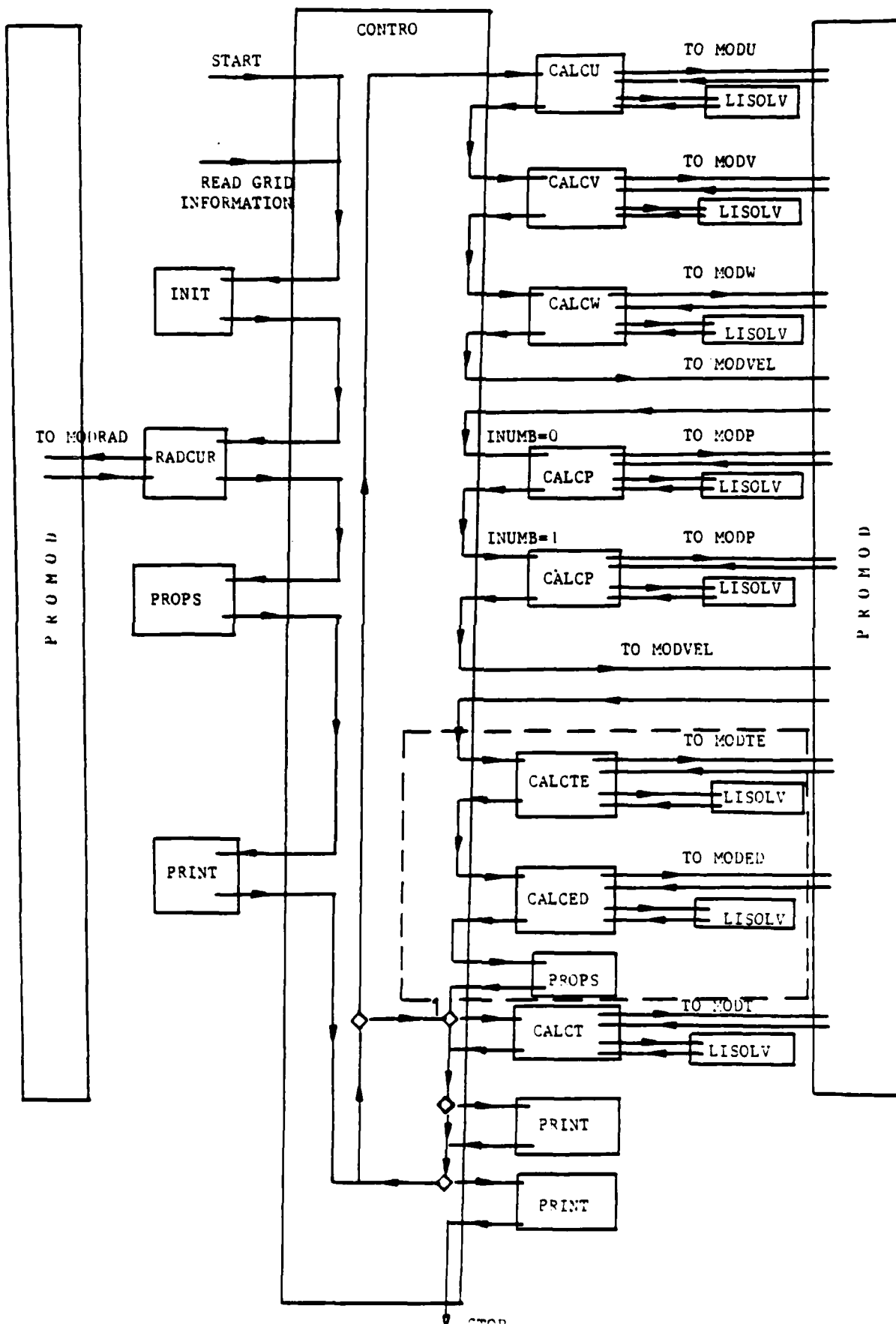
The original computer code (TEACH), written by Antonopoulos, Gosman and Issa [86], has been devised for the solution of steady, two-dimensional, turbulent (or laminar) recirculating flows and can be modified to cover three-dimensional flows as well as parabolic ones.

The computer program consists of 14 sub-routines. Each sub-routine is divided into chapters to facilitate understanding. The structure of the computer program is given in the following flow chart while a broad description of the program and the main functions of each sub-routine are outlined in a subsequent section.

CONTRO is the main sub-routine responsible for the overall control of the operations by calling in a fixed order the rest of the sub-routine. First, in CONTRO, the various parameters, fluid properties, turbulence constants (for the turbulent flow computations) are initiated. Next, geometric quantities, such as control volume dimensions, solution domain features (i.e.  $R_g$ ,  $h$ ,  $n$ ) are read in as data.

INIT is the first sub-routine called by CONTRO. This calculates the geometric interpolation coefficients and sets most of the working arrays to zero.

CONTRO then calls sub-routine RADCUR where quantities related to the curvature of the co-ordinates are calculated, while a special treatment of the boundary surfaces is introduced by section MODRAD of sub-routine PROMOD. PROMOD, as its name implies, is responsible for the introduction of the



boundary conditions (PROblem MODifications). This sub-routine is divided into sections with individual entry points defined as MOD followed by some characteristic symbol (for example, MODRAD). So, every section plays the role of an independent sub-routine.

The next sub-routine to be called by CONTRO is PROPS. This sets the fluid properties over the whole solution domain. Since only incompressible flows are considered, the density is set to a constant value, while viscosity is calculated from the proper equations depending on the turbulence model, if turbulent flow computations are performed, or set to a constant value if the laminar regime is examined. A more detailed description of CONTRO can be found in Appendix 5.

Called next is sub-routine PRINT which prints the initial values of the variables while at that point both the iteration and marching loops begin.

During the marching procedure, CONTRO calls CALCU, CALCV, CALCW, CALCP (and CALCTE, CALCED for the turbulent flow computations) in that order for the solution of the finite-difference equations described in Sections 2.5a, 2.5b and 2.5c. Depending on whether the fluid viscosity ( $\mu$ ) is variable, PROPS is called at the end of the above sequence. CALCU, CALCV, CALCW, (CALCTE and CALCED) are described in Appendix 5, as well as CALCP with its special features for the solution of the pressure correction equation. Just after CALCW, when the velocity field has been calculated from the momentum equations, CONTRO calls MODVEL which, as its name implies, is a section of PROMOD updating the boundary velocities. MODVEL is called twice, the second call being made after the velocity field is adjusted by the correction process in CALCP. Once the marching loop has been completed, CONTRO calls

again the above-mentioned sequence of sub-routines and so on. At the end of every marching loop an intermediate printout is used. This gives the summed residuals, the computed variables at some reference point in the solution domain, as well as the velocity, pressure (and  $k$ ,  $\epsilon$ ,  $\mu$ ) fields if the number of iterations is an exact multiple of a value (INDPRI) fixed at the beginning of CONTRO. At point 1 in the flow chart, a termination test for the iteration procedure is performed. All the residual sums calculated in CALC $\phi$ s and RESORM (calculated in CALCP) are checked against a value introduced at the beginning of CONTRO (SORMAX). If all these residuals are smaller than this control value ( $10^{-3}$ ), the dynamic field is considered to have converged and the iteration sequence is terminated. Then, a small iteration loop is initiated where only the temperature equation is solved, controlled by a similar termination test. Once the temperature equation has converged, a printout for all the computed variables is issued covering the whole solution domain.

In the last chapter of CONTRO, final operations, such as the calculation of friction factors and Nusselt numbers, normalization of profiles as well as the final output, are performed.

Gosman and Ideriah [9], in their TEACH manual, point out that, since computer resources in time and storage are limited, measures must be taken to ensure minimization of these demands. Such measures are:

- Good specification of initial field; for example, starting from a previous calculation can improve the computing times considerably.
- Optimization of grid; that implies the use of a

fine grid in regions of steep gradients (for example, near a wall) and a coarse grid in the rest of the solution domain.

- Minimization of the extent of the calculation domain.
- Optimization of the under-relaxation factors.
- Specification of a realistic convergence criterion.

All the above measures have been followed in the present computations and specific reference to them is made in the appropriate chapters.

The additional modifications introduced into the computer program for the solution of turbulent flows are described in Chapter 4 and Appendix 5.

## 2.7 Experiences in Applying the Computer Program

The initial programming effort has been concerned with introducing the very large number of "source terms" arising from the expression of the describing equations in the co-ordinate system  $(\xi, \eta, \zeta)$ . An impression of the difficulty of the task can be gained by referring to equations (2.17), (2.18), (2.21), (2.22), (2.25), (2.29) which express the source terms for the momentum and energy equations. Moreover, the form of the diffusion coefficients given by equations (2.15), (2.16), (2.19), (2.20), (2.23), (2.24), (2.27), (2.28) and convection coefficients given by equation (2.14) raised questions as far as the extra terms added to the conventional ones are concerned. However, the inclusion of these extra terms in the source

terms proved to be unsuccessful since it produced instability of the computational procedure. Equations (2.39) and (2.40) give the final forms of the diffusion coefficients, convection coefficients and source terms introduced into the computer code, being compatible with the already existing program.

Another major task has been the incorporation of the PISO algorithm into the computer code for solving the pressure-correction equation, presented in Section 2.5b. After introducing this new scheme, the convergence rates of the solution procedure were improved by more than an order of magnitude.

Despite this improvement, the problem of slow convergence for some cases remained. Indeed, the convergence of the solution has been a very difficult task throughout the project, for both laminar and turbulent regimes. Computing times on a CDC7600 for solving both the velocity and temperature fields starting from a uniform initial distribution, for laminar flow computations, ranged from 50 cps to 800 cps using an  $(18 \times 20)$  grid which has been found to give acceptably grid-independent solutions. However, the practice of using a uniform initial field was not normally followed. Actually, once a solution has been obtained for a fixed number of flutes, it was used as the initial distribution for the further computations (at a different Reynolds number or with minor variations in tube geometry). By this means, the computing times were reduced to just 10-20% of those reported above.

As has been shown in the flow chart of the computer program, the temperature equation was solved only when the momentum equations were fully



converged and the velocities were stored. Thus, the study of different fluids could be obtained by using, for a given flute geometry and Reynolds number, the same dynamic field with a dummy thermal conductivity  $k_f$  ( $k_f = \frac{\mu \cdot C_p}{Pr}$  where  $C_p$  and  $Pr$  are the specific heat at constant pressure and the Prandtl number of the used fluid) for the temperature equation. Again, this practice reduced the computing times to 10-20% of the times reported initially.

Following the suggestions of Gosman et al [9] for obtaining fast convergence of the computational procedure, many sets of under-relaxation factors have been applied to the discretized form of the describing equations. For low Reynolds number, the under-relaxation factors giving the fastest convergence rates are: 0.5 for the pressure ( $p$ ), 1.0 for the axial velocity ( $W$ ), 1.0 for the  $\xi$ -velocity component ( $U$ ) and 0.9 for the  $\eta$ -velocity component ( $V$ ), while for high Reynolds numbers, 0.9 for  $W$  and 0.8 for both  $U$  and  $V$ . The integer values of  $NSWP\phi$ , which determine how many times sub-routine LISOLV will be called from  $CALC\phi$  to solve the discretized form of the describing equations, were 4 for  $CALCP$  and  $CALCU$  and 2 for  $CALCV$  and  $CALCW$ . Any increase in these values did not make any substantial difference in the total number of iterations needed.

Figures 2.8 to 2.11 show the convergence of the largest residuals with the number of iterations for different Reynolds numbers and flute configurations. Figure 2.8 shows, at a Reynolds number of 330 and for three pipe geometries (i.e. 10, 20 and 30 flutes), the convergence of  $\xi$ -momentum equation. It is clear that for the higher flute density ( $n=30$ ) although the convergence rate is fast for the first 70 iterations, it slows down and only reaches a satisfactorily converged level after 1650 iterations.

Analogous behaviour is shown in Figure 2.9 where a high Reynolds number flow is examined and the largest residual is that for the axial velocity  $W$ . Figures 2.10 and 2.11 present the influence of the spiral angle  $\phi$  on the convergence rates in two different situations: first, for high Reynolds number and low flute density, and, second, for low Reynolds number and high number of flutes. For both cases, the higher the spiral angle  $\phi$  the slower the convergence rate of the corresponding largest residual.

Many tests have been performed in order to identify the reasons behind the slow convergence rates of the computational procedure. In this direction, the effectiveness of the TDMA (Tri-Diagonal Matrix Algorithm) used in LISOLV for solving the discretized form of the describing equations (described in a previous section) has been questioned. However, when the residuals were checked after every call of LISOLV, TDMA proved to perform quite satisfactorily since the residual of  $U$  decreased by a factor of 3.4, the residual of  $V$  by 3.2 and the residual of  $W$  by 1.04. (This small value of  $W$  was not felt to be significant as the axial momentum equation had already converged at the time the test was introduced).

It is obvious from Figures 2.8 to 2.11 that the higher computing times were obtained with flute configurations which gave rise to grid cells of high aspect ratio, i.e. for large number of flutes of high amplitude  $h$  (see Figure 2.12). Moreover, in the early stages of the research when grid networks like the one shown in Figure 2.2 were used, the convergence rates were even slower. It is believed that this deterioration in convergence rates could be cured if the high aspect ratio grid cells could be avoided. One way of achieving this would have been to adopt a non-orthogonal grid in

which the  $\eta$  lines were all radial lines. This interesting possibility was recognized only when research with the orthogonal system had proceeded so far that a changeover was not practicable.

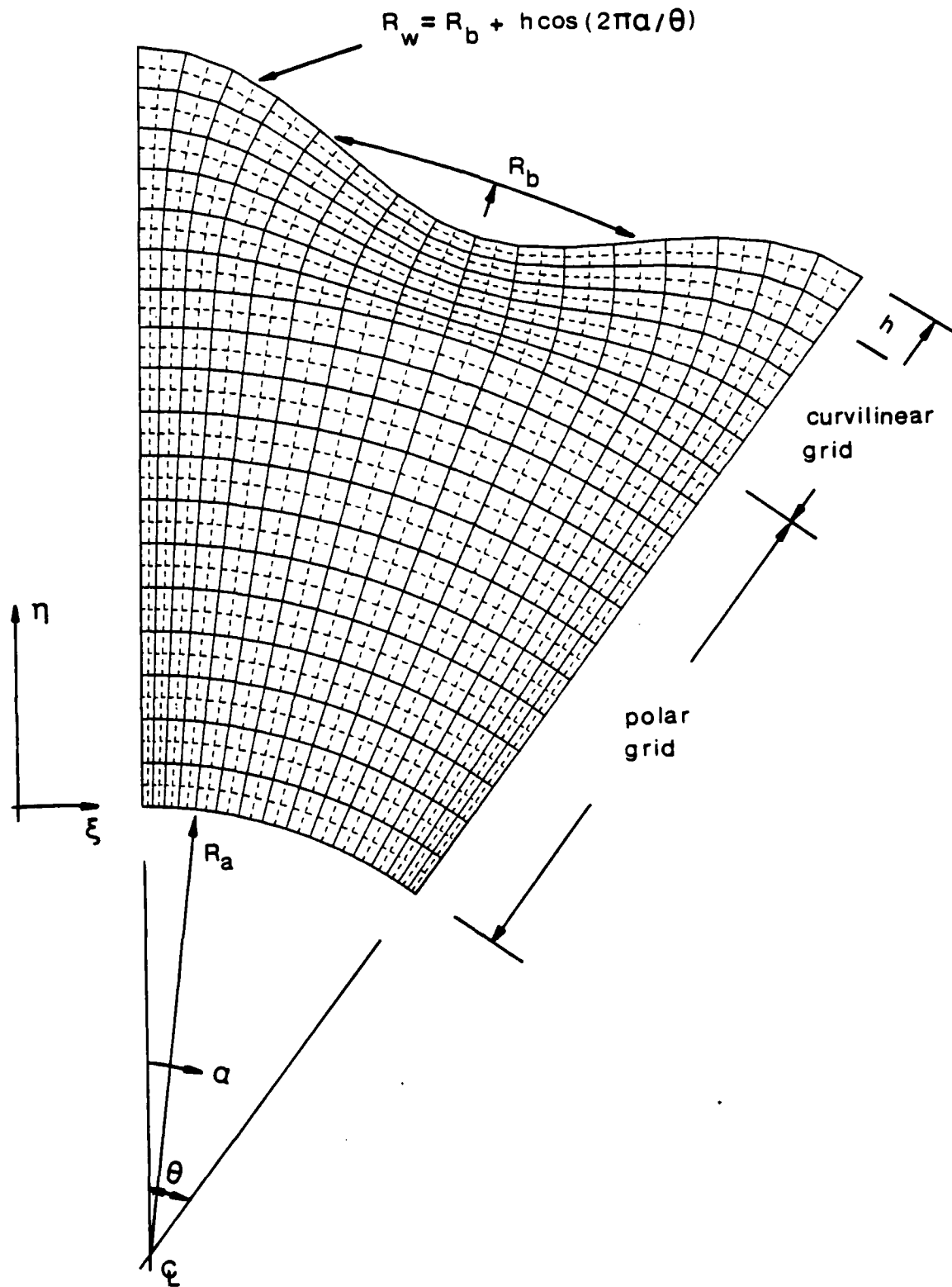


Fig 2-1 Curvilinear/polar grid

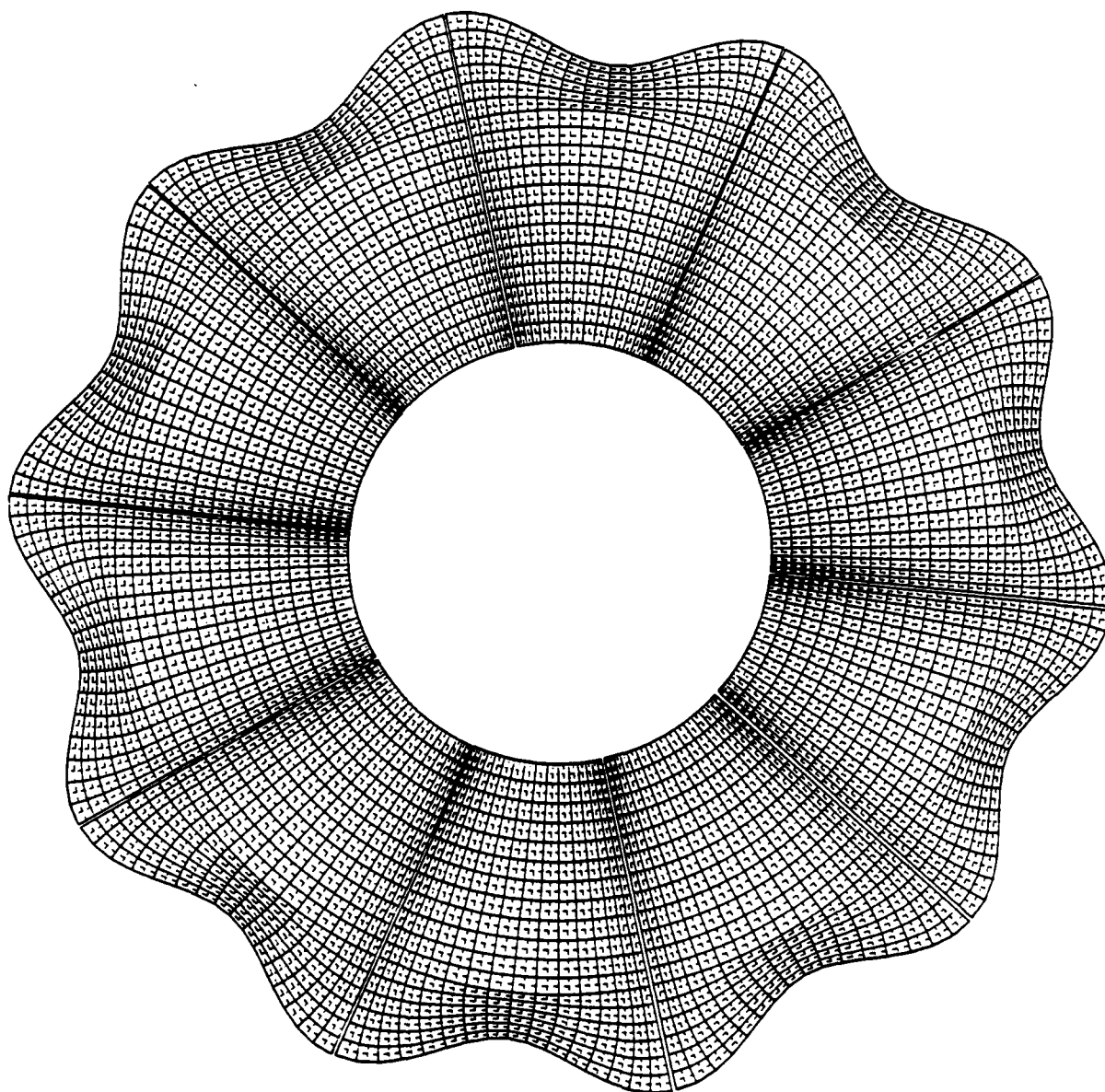


FIG 2-1a GRID COVERAGE OF THE CROSS  
STREAM PLANE

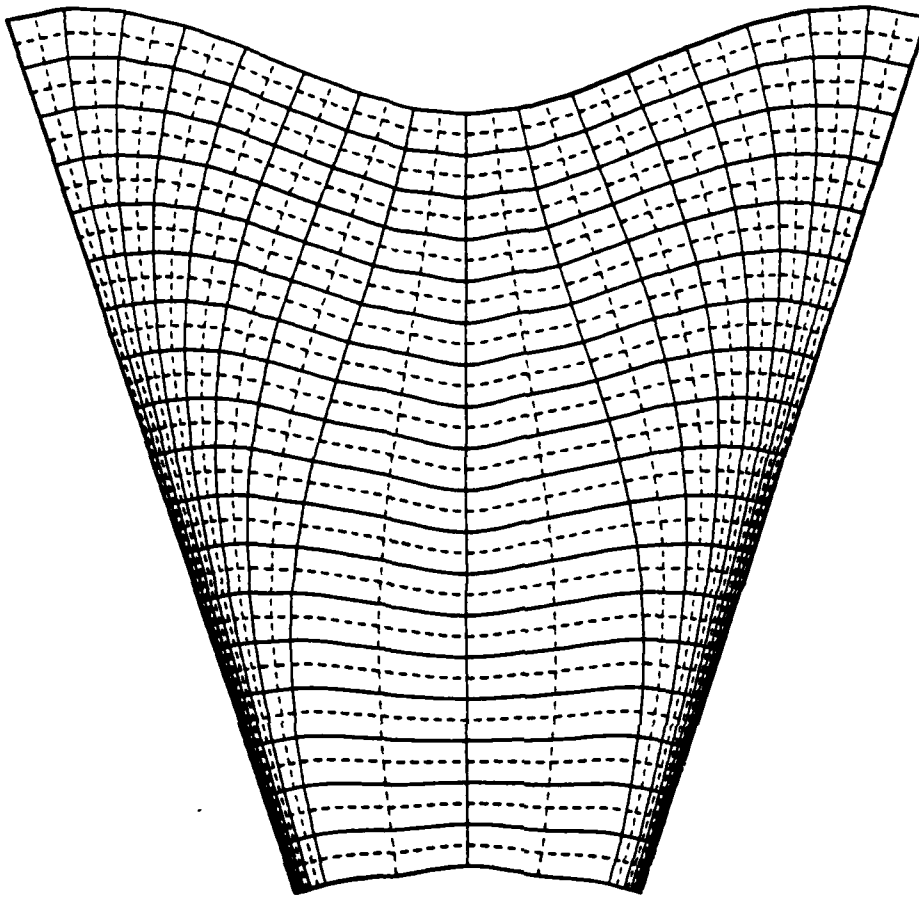


Fig 2-2 Fully curvilinear grid

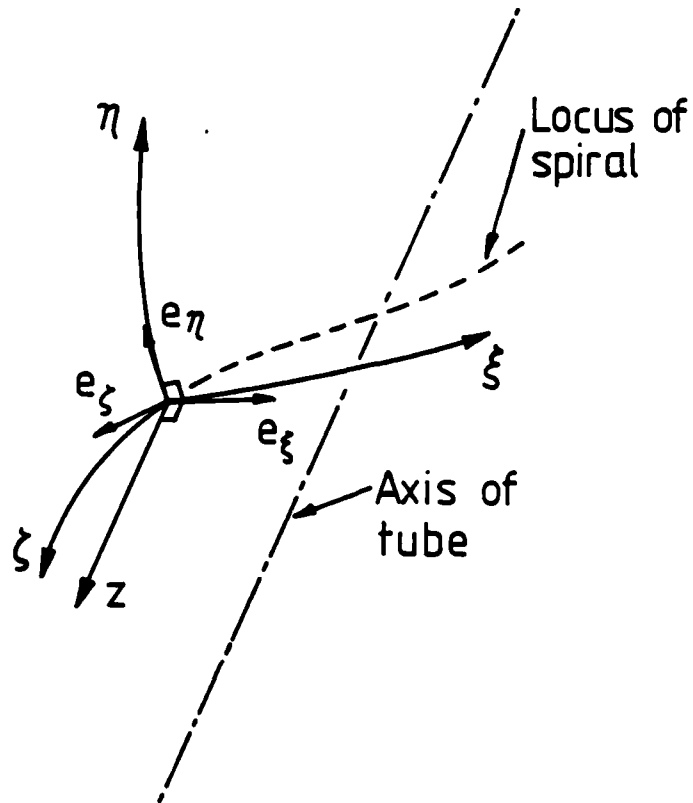


Fig 2-3 The coordinate system

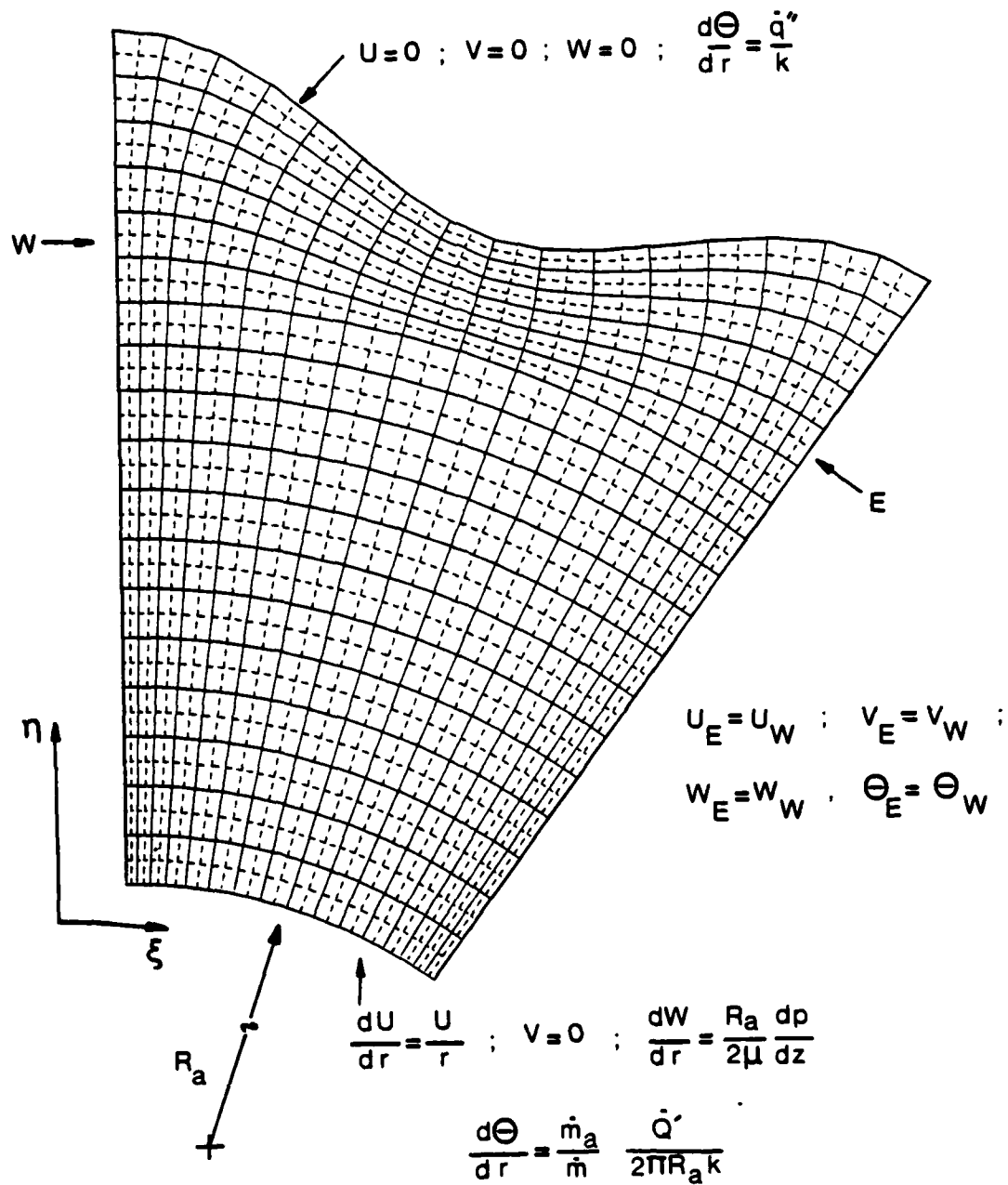
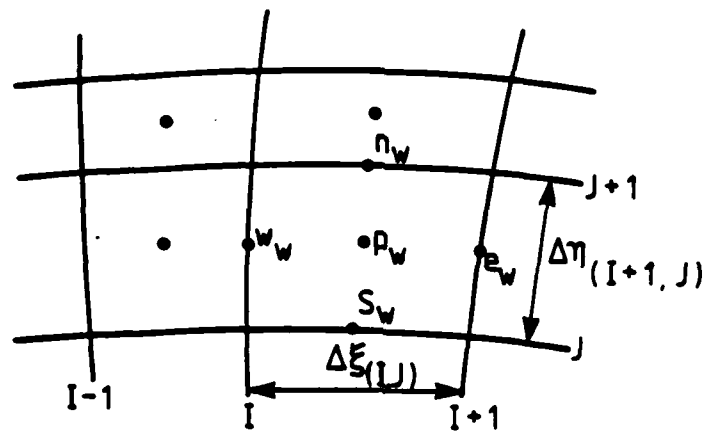


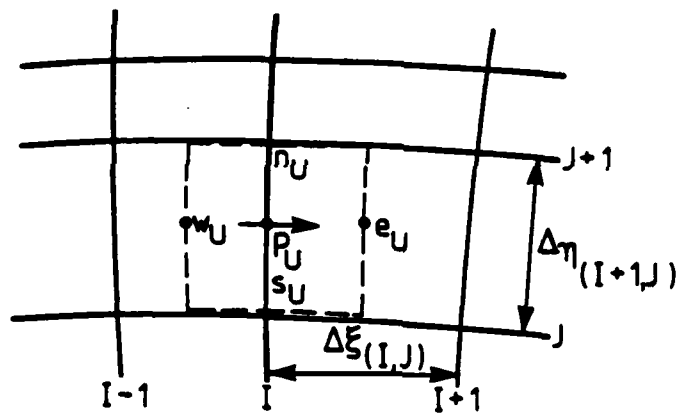
Fig 2-4 Boundary conditions



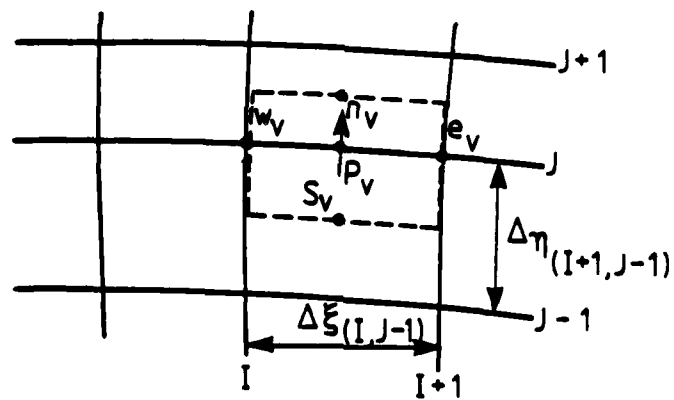


(a)

Scalar control volume



(b)

 $\xi$  Momentum control volume

(c)

 $\eta$  Momentum control volume

Fig. 2.5.

The control volume

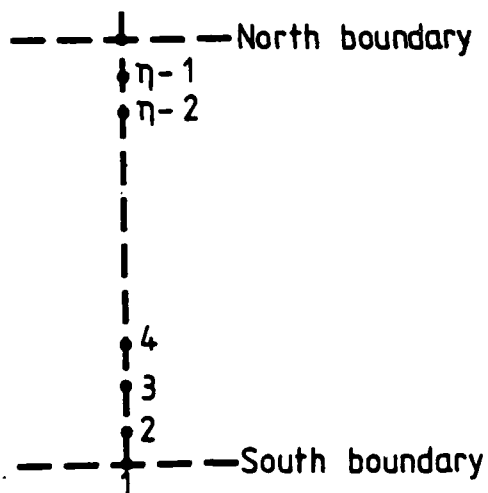


Fig. 2.6 W-E sweeps in LISOLV

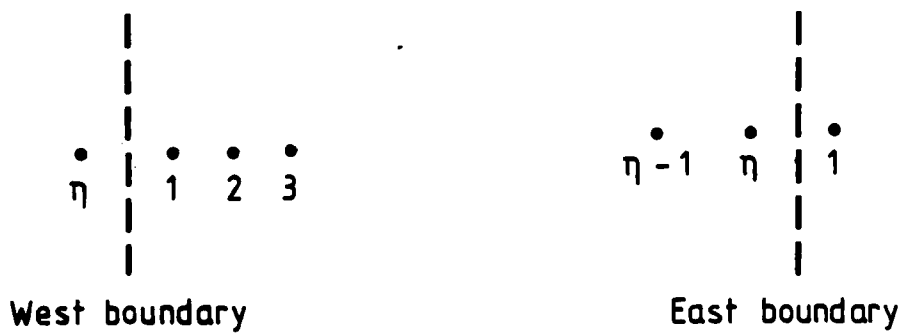


Fig. 2.7 N-S sweeps in LISOLV (cyclic treatment)

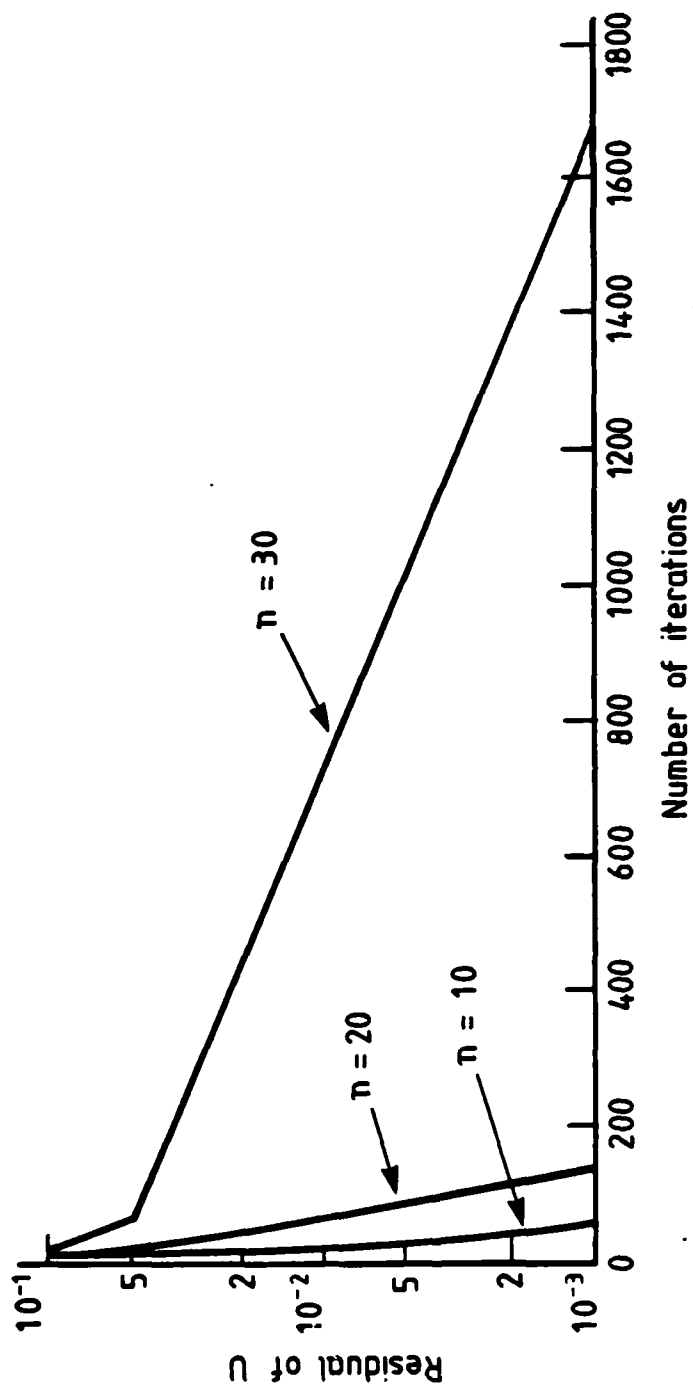


Fig. 2.8 Convergence rates of the numerical solution for different flute densities for

$$\varphi = 15^\circ, \text{Re} \approx 330$$

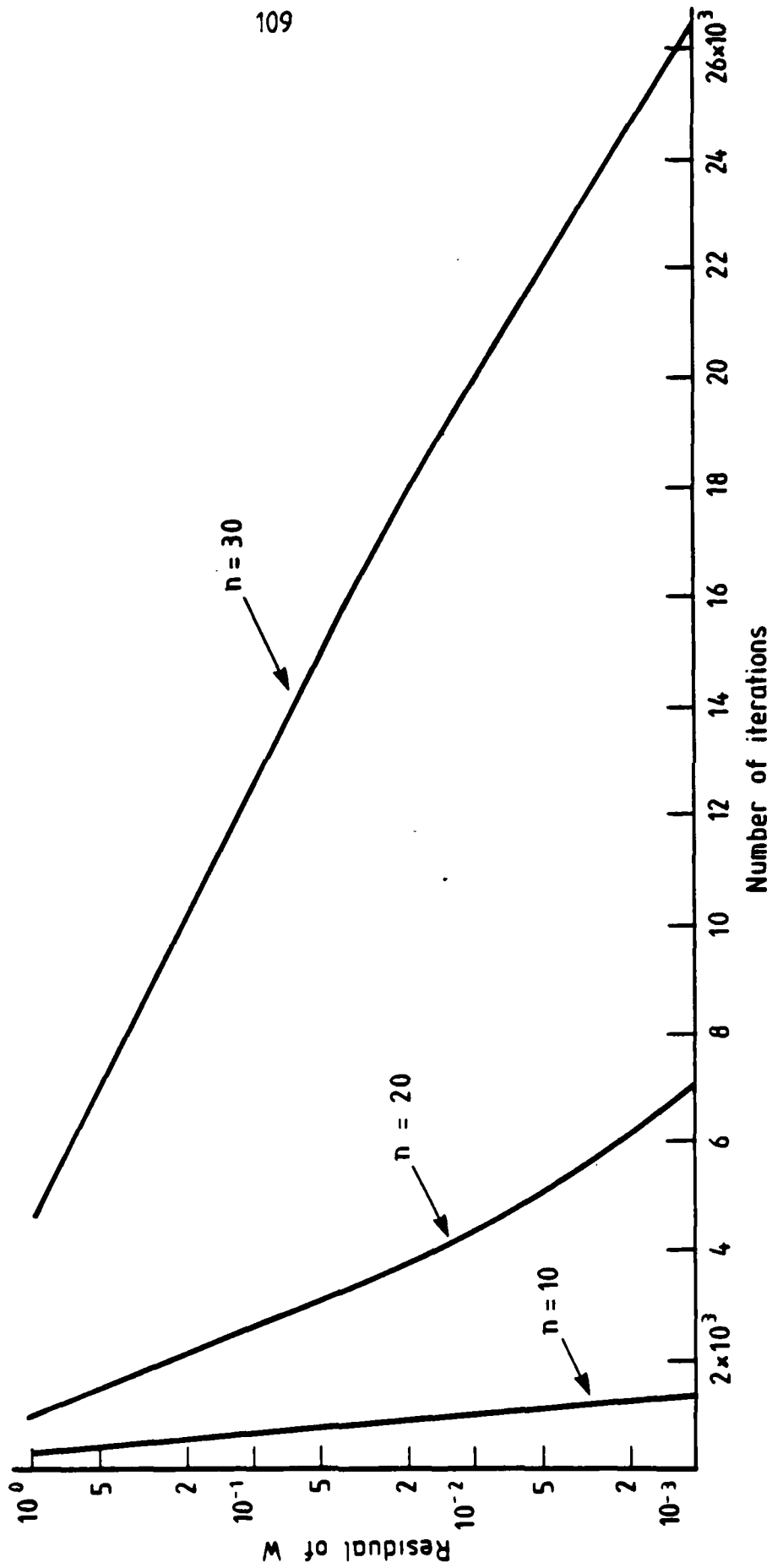


Fig. 2.9 Convergence rates of the numerical solution for different flute densities for  $\varphi = 15^\circ$ ,  $Re \approx 2700$

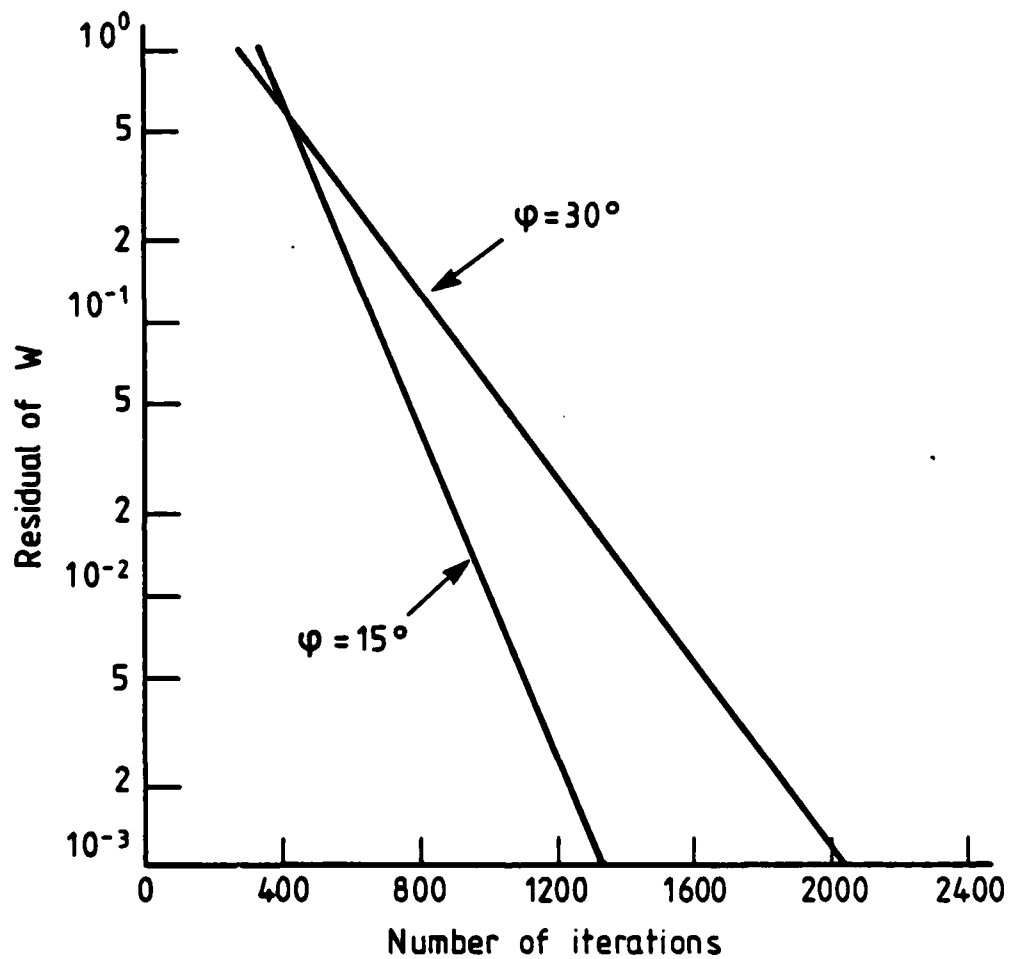


Fig. 2.10 Dependence of convergence rates of the numerical solution on number of iterations and spiral angles for  $n=10$ ,  $Re \simeq 2700$

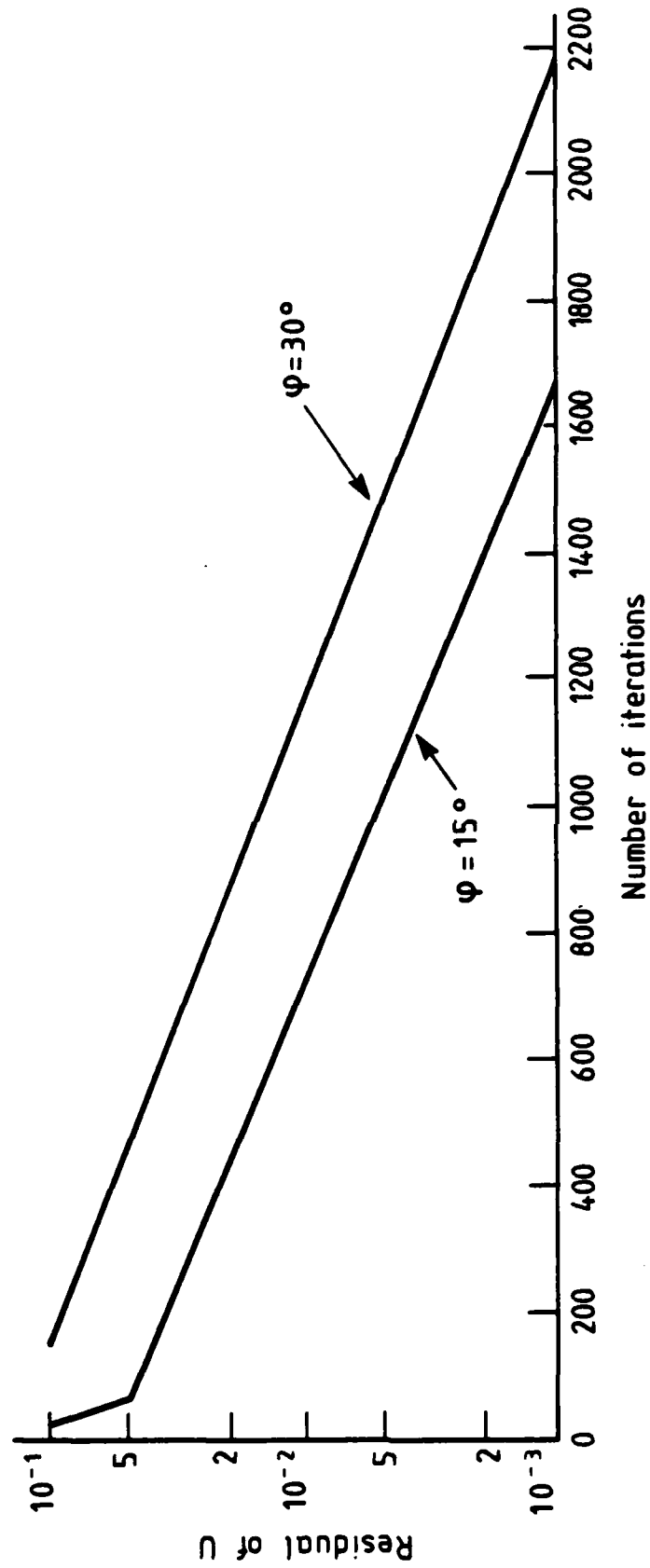


Fig. 2.11 Dependence of convergence rates of the numerical solution on number of iterations and spiral angles for  $n = 30$ ,  $Re \simeq 330$

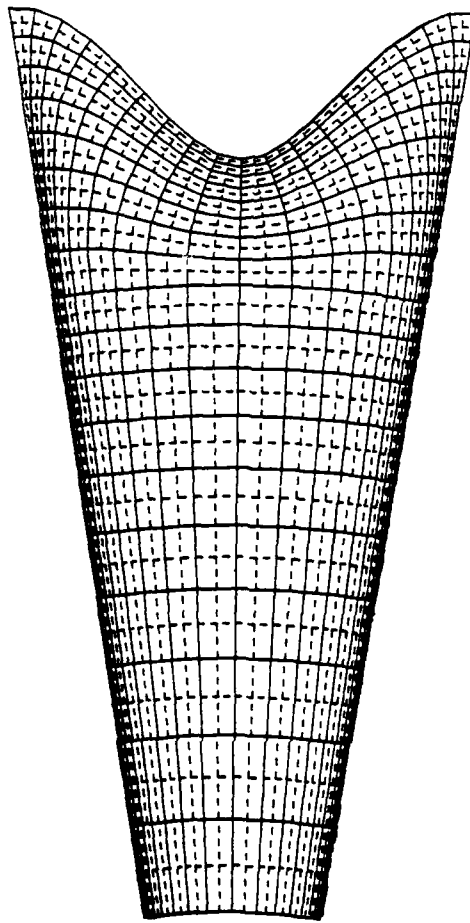


Fig 2-12 Grid ;  $n=20$   $h=-.06 R_b$

### CHAPTER 3

## 3. THE LAMINAR FLOW CALCULATIONS

### 3.1 Introduction

The complex form of the transport equations, presented in Section 2.5 of Chapter 2, has provided many opportunities for errors to appear in the derivation of the differential equations or later in their finite volume discretization and finally incorporation into the computer code. Since no experimental data were available, the calculation of simple flows with known analytical solutions using the computational procedure discussed in Chapter 2 was therefore believed to be a highly important aspect of the work. In fact, several levels of error did come to light in the initial rounds of testing against the exact solutions. The final validation tests performed as well as the parametric explorations (including changes in the number of flutes, spiral angle, height of ribs, Reynolds and Prandtl numbers) are reported in the present chapter.

#### 3.1.1 Validation Tests

##### 3.1.1 a. Velocity Field

The validation test cases considered were the fully-developed flow in a straight circular-sectioned tube and the flow in a concentric annulus in which the core tube is stationary and the outer cylinder rotates at prescribed speed. These geometries could have been easily examined by setting the helix angle and flute height to zero. If that had been done, the goal of these validation tests would have been lost since it is the presence of the spiral fluting that makes the equations so complex. Instead, a 10-flute grid with a  $15^\circ$  spiral angle was adopted. Of course, because of



the 'fluting' of the grid, the outer boundary of the solution domain did not coincide with the purely circular boundary surfaces of the test flows. The exact analytical values were therefore applied to the finite volume code for the outer row of cells. The values calculated for the interior nodes were then compared with those of the analytical solution. These tests proved valuable in helping differential and coding errors to be detected.

The flow in the circular tube was computed with 20 nodes in the  $\eta$ -direction and a flute amplitude of  $0.03 R_b$ . The maximum departure of the computed axial velocity from the parabolic analytical profile was 0.8%. Figure 3.1 shows the comparison between computations and analytical solution of the axial velocity ratio  $W/\bar{W}$  at the trough position of the 'fluted' grid. Although the exact solution requires zero motion in the cross stream plane, the momentum equations for velocity components  $U$  and  $V$  in the plane  $\xi - \eta$  were also solved. The largest velocity computed was  $10^{-6}$  times the axial velocity; value which has been accepted to be almost zero. It may be mentioned here, however, that first attempts at computing this flow produced a swirl velocity of order  $10^{-2}$  times the axial velocity, a discovery that helped an error in the differential equations to be detected.

The annular flow computations were performed for a radius ratio of 0.4 with the outer cylinder rotating at a velocity as large as the mean axial velocity using a grid with a flute amplitude of  $0.06 R_b$  (while a 3% flute amplitude has been used for the smooth pipe flow discussed above) decreasing linearly to zero from the outer boundary to inner radius  $R_a$ . Despite the unsuitable nature of the grid, shown in Figure 2.2 of Chapter 2, the maximum error in axial velocity was 1.5% and in circumferential velocity 3%. Figure 3.2 shows a comparison of the circumferential velocity ratio

$U/U_{\text{wall}}$  and axial velocity ratio  $W/W_{\text{max}}$  at the trough position of the 'fluted' grid between computations and analytical solution.

At the beginning of computations on spirally fluted tubes, the question of positioning the inner boundary arose. The condition of solid body rotation was applied at three different values of the inner boundary  $R_a$  : 0.62, 0.42 and 0.3 times the mean radius,  $R_b$ . The enlargement of the calculation domain was obtained by adding extra nodes, leaving the grid in the area common to three solutions unchanged. Figure 3.3 shows the three nodal distributions. The flow in a tube with ten flutes and 6% flute height at a Reynolds number of 300 has been used as the basis for comparisons. No differences between the solutions with  $R_a = 0.42 R_b$  and  $R_a = 0.03 R_b$  have been detected over the common region. For  $R_a = 0.62 R_b$ , however, although the flow pattern in the vicinity of the flutes was identical to those obtained with  $R_a = 0.3 R_b$  and  $R_a = 0.42 R_b$ , the tangential velocity displayed a 15% variation around the inner boundary indicating a violation of the solid body rotation condition imposed there. Figure 3.4, which presents the distribution of  $U/\bar{W}$  with the radius at the trough and crest radii, clearly shows all the characteristics mentioned above. Figure 3.5 gives an impression of the velocity direction lines for the three solution domains used. The pattern seems identical in all three plottings for the near-wall region, while for  $R_a = 0.62 R_b$  near the inner boundary, some divergence from solid body rotation can be seen from the difference in the lengths of the arrows at a given radius. On the basis of these tests, the inner boundary conditions in all the computations for laminar flows were applied at  $0.4 R_b$ , although for 30 flutes this choice was not the best one since the solid body rotation region extended up to  $0.73 R_b$  and matching at  $R_a = 0.7 R_b$  would not have altered the results.

Another question, which arose when the mixed curvilinear/cylindrical grid had been found to give the best mapping of the solution domain, was the influence of the abrupt change in grid spacing, due to the switch from one grid type to the other, on the flow pattern. Runs were made with the changeover radius ranged from  $0.6 R_b$  to  $0.85 R_b$ . No differences in results have been found if the change occurred for  $R \geq 0.7 R_b$ . For smaller radii and 30 flutes, unjustified circumferential non-uniformities appeared because of the poor mesh coverage. For all the subsequent computations of laminar flows the value of  $0.85 R_b$  was applied to changeover radius.

### 3.1.1 b. Convective Heat Transfer

The computation of convective heat transfer in a smooth tube with a uniform surface heat flux has been used as a further test of the solving scheme's numerical accuracy. Again, a (20 x 18) 'fluted' grid has been used with 6% rib height and  $15^\circ$  spiral angle. The exact analytical values of temperature were supplied at the nodes of the outermost row of cells. This test case proved valuable in detecting coding errors in the energy equation. When these had been corrected, the calculated Nusselt number for a grid with  $45^\circ$  spiral angle and zero flute amplitude agreed within 0.1% with the value of 4.364.

### 3.1.2 Parametric Study of the Results

#### 3.1.2 a. Velocity Field

In the parametric study of the laminar flow through a spirally fluted tube, reported below, the tube with 10 flutes, 6% flute height,  $15^\circ$  spiral

angle has been chosen as the basis for parametric variations.

The pattern of the flow created in the spirally fluted tube is broadly the same for all the variations considered (number, height or angle of flutes). However, some significant detailed differences can be detected and are reported below. This general flow pattern is clearly shown by the velocity-direction lines mapping the  $\xi$ - $\eta$  plane of the tube. Figure 3.6 presents the flow pattern for 10, 20 and 30 flutes at a Reynolds number of 300, while Figure 3.7 shows the velocity-direction lines covering the whole cross-stream plane of the tube. It is clear from these two figures that the flow encountering a flute (spiralling around the circumference in a clockwise direction) creates a region of high pressure on the leading face of the flute which forces adjacent fluid clockwise and to smaller radius. In contrast, on the trailing face of the flute a low pressure region is created and, because of the pressure difference between the two flute faces, some fluid spills anti-clockwise over the flute crest despite the overall clockwise flow-direction. The difference in length and direction of the arrows in the near-flutes region indicates that the circumferential variations are quite strong, in contrast to the core region where no changes can be detected from the purely circumferential direction of the velocity-direction lines. It is obvious from Figure 3.6 that as the number of flutes increases, the flute-affected region moves closer to the tube wall while the solid body rotation region (no circumferential variations) covers a larger part of the flow. The same behaviour is encountered when the Reynolds number increases, as shown in Figure 3.8 where the flow patterns for two Reynolds numbers are presented.

Figures 3.8a and 3.8b show two alternative presentations of vector lines on the cross-stream plane of a 10-flute tube at  $\phi = 30^\circ$ . The first one

illustrates the distribution of velocity vectors given by:

$$(\vec{U} + \vec{V}) - \omega \vec{R}$$

where  $\vec{U}$ ,  $\vec{V}$  are velocity vectors in  $\xi$  and  $\eta$  directions respectively, while  $\omega$  is the angular velocity of the core region for the particular case. Thus, Figure 3.8a shows how the secondary flow "vectors" appear to an observer rotating with the core of the fluid and consequently the velocity over the core region of the solution domain where the solid-body rotation takes place appears as zero. It is clear from the figure that near the flutes some fluid is rotating clockwise faster than the "solid-body" rotation rate while nearby fluid is proceeding much more slowly.

Figure 3.8b shows the distribution of velocity vectors given by the correlation:

$$\left[ \vec{V}_{n\theta} + \vec{V}_r \right]$$

where

$$V_{n\theta} = (V_\theta \cos \phi - W \sin \phi) \cos \phi$$

$$\phi = \text{spiral angle} \quad W = \text{axial velocity}$$

$V_\theta$  and  $V_r$  are the circumferential and radial velocity components of the resultant velocity vector  $(\vec{U} + \vec{V})$ . Velocity  $V_{n\theta}$  is the circumferential velocity on the "cross-stream" plane formed by slicing the tube normal to the flutes. It is clear from the anticlockwise direction of the arrows that over most of the tube the fluid is not spinning clockwise as fast as the flutes, i.e. it is gliding backwards relative to the flutes. Deep within the flutes, however, the shrinkage of the velocity "vectors" to a mere dot indicates that here the fluid is very nearly following the grooves of the fluting. We shall see later in Chapter 5 that this pattern is in marked contrast with that found in turbulent flow. The corresponding velocity vector presentations for a 20-flute tube at  $30^\circ$  spiral angle are presented in Figures 3.8c and 3.8d where no distinctive differences can be detected from those for 10 flutes.

Figure 3.9 also shows the influence of the Reynolds number on the cross-stream flow pattern discussed above. This figure displays the distribution of the velocity ratio  $U/U_{\max}$  as a function of Reynolds number at two radial lines passing through the trough and the crest of the flute, since it is believed that these two positions illustrate as clearly as possible the effects which different modifications in the flow parameters or flute geometry have on the cross-stream flow. Three different Reynolds numbers are considered showing that the higher the Reynolds number the smaller the distance from the tube wall to which the flutes affect the flow. This trend is entirely plausible since an increase in Reynolds number entails a decrease in the diffusion velocity relative to the convection velocity especially when the convection coefficients have the form of equation (2.14) where extra terms, including the axial velocity, are present. Figure 3.10 shows the same behaviour as Figure 3.9 but for the effect of spiral angle. It is clear that the spiral angle also displays a trend to confine the flute-affected region near the wall. Figure 3.11 shows that, for spiral angles ranging from  $15^\circ$  to  $45^\circ$ , the circumferential velocity increases in roughly the same ratio as the tangents of the spiral angles.

In spite of the above-mentioned effects of Reynolds number and flute angle, their effects on the shape of the circumferential velocity profile is very small. In contrast, changes in the number of flutes display a much more profound effect on the velocity profile. This can be seen in Figure 3.12 where two different flute densities are plotted and where, for 30 flutes, the fluid is in solid body rotation for radii less than about  $0.75 R_p$  while more swirling flow is transferred to the core region of the tube. This is best shown in Figure 3.13 where the ratio  $U/\bar{W}$  is plotted against the number of flutes at radius  $0.5 R_p$ . For 30 flutes, although the "back flow"

over the crest is stronger, it is confined to a thinner region, while a very weak and limited reverse flow also appears in the trough. Since the flow pattern for 20 flutes is intermediate between that for 10 and 30 flutes, it has been omitted for clarity.

The rib amplitude has a considerable effect on the amount of swirl generated, as shown in Figure 3.14 where the 6% flute height produces circumferential velocities almost three times as large as for flutes of 3% amplitude for a tube with 10 flutes, 15° spiral angle at a Reynolds number of approximately 300.

Figures 3.15 and 3.16 show the effects that the flute density and spiral angle have on the axial velocity profiles. The main feature to note is that for 30 flutes (Figure 3.15) the velocity level within the trough is very much lower than for 10 flutes due to the proximity of the flute surfaces and the enhanced viscous retardation that results. The influence of spiral angle, however, over the range 0° - 45° is not significant, as can be seen from Figure 3.16.

The distribution of surface pressure  $((p - p_{ref})/\rho \bar{W}^2)$  can be seen in Figures 3.17 and 3.18. As has been pointed out above, at the leading face of the flute a high pressure region is created, in contrast to the trailing face which is characterized by low pressures. Figures 3.17 and 3.18 show exactly that. From Figure 3.17 one can see that the maxima and minima occur near the crest at positions located one quarter of the distance between trough and crest on each face of the flute. This distribution, however, depends highly on the number of flutes; the higher the flute density the more abrupt the change from maximum to minimum surface pressure moving

towards the crest. Analogous behaviour is shown in Figure 3.18 where the effect of flute angle on static pressure around the flute is presented. The only difference here is that the position of the maxima and minima seems to be almost independent of the spiral angle, over the range considered.

Figure 3.19 displays the distribution of the pressure coefficient  $(p_{\max} - p_{\min})/\rho W^2$  with Reynolds number. It is clear that at low Reynolds numbers this coefficient shows a  $Re^{-1}$  dependence while at high Reynolds numbers ( $10^3 < Re < 2.5 \times 10^3$ ) the dependence on  $Re$  can be approximated by an exponent of  $-\frac{1}{2}$ . This distribution can be explained by the fact that if changes in surface pressure around the flute were only due to dynamic effects, the pressure coefficient would be independent of  $Re$ , while if the dynamic effects were negligible it would vary as  $Re^{-1}$ . Two different numbers of flutes are plotted in Figure 3.19; the 20-flute tube displays a stronger dependence on  $Re^{-1}$  which becomes, at high Reynolds numbers,  $Re^{-\frac{1}{2}}$ . This behaviour can be explained by the higher flute Reynolds numbers

$$Re_f = \frac{(W \sin \phi - V_\theta \cos \phi) \cos \phi (2h)}{v}$$

(based on velocity  $(W \sin \phi - V_\theta \cos \phi) \cos \phi$ , which is the projection on the cross-stream plane of the velocity normal to flutes direction and rib height) observed for the lower flute density tubes at Reynolds numbers ( $Re$ ) between 400 and 1500; for example, for a Reynolds number of 1300, the ratio of flute Reynolds numbers for 10 and 20 flutes is 2.3  $\left[ \frac{Re_{f(n=10)}}{Re_{f(n=20)}} = 2.3 \right]$ .

The variation of friction factor with Reynolds number is shown in Figures 3.20 and 3.21 for two different definitions of friction factor.



Figure 3.20 illustrates the variation of friction factor defined as:

$$f = \left( -\frac{dp}{dz} \right) 4A / (\frac{1}{2}\rho \bar{W}^2) / P \quad (3.1)$$

where A is the tube's cross-sectional area and P its perimeter, while

$$Re = \bar{W} \cdot 4A / \nu / P \quad (3.2)$$

The term  $4A / P$  gives the conventional equivalent diameter ( $D_h$ ). It is clear that while all the friction factors lie below the smooth tube line ( $f = 64 / Re$ ) they also display a -1 dependence on Reynolds number over the range studied. This behaviour indicates that, for 10 flutes, form drag (which is roughly proportional to the pressure coefficient shown in Figure 3.19) has a small effect on the total pressure drop. The fact that all the friction factor lines lie below the smooth tube line can be explained by the behaviour shown in Figures 3.15 and 3.16. As has been pointed out earlier, in the troughs the axial velocity and consequently the wall shear stress are clearly much lower than in a smooth tube. Thus, the mean wall shear stress is lower and eventually the friction factor.

Figure 3.21 shows the variation of "pipe" friction factor, defined as:

$$f_p = \left( -\frac{dp}{dz} \right) 2R_b / (\frac{1}{2}\rho \bar{W}^2) \quad (3.3)$$

with Reynolds number:

$$Re_p = 2\bar{W} R_b / \nu \quad (3.4)$$

Using these definitions a comparison can be made between the pressure drop through the spirally fluted tube and that through a smooth tube of the same mean radius under the same mass flow rate. It is clear that the increase

is almost insignificant. Although only the line for 10 flutes has been drawn, all the other lines ( $n = 20$ ,  $n = 30$  and even  $\phi = 30^\circ$ ,  $\phi = 45^\circ$ ) are not discernibly different from this line, so they have been omitted for clarity. Now, the fluted tube's friction factors lie above the smooth tube's line but the increase, even for  $n = 30$ ,  $\phi = 30^\circ$ , is less than 10%.

### 3.1.2 b. Convective Heat Transfer

The heat transfer enhancement of the spirally fluted tube can be ascribed to two different factors: the increase, due to fluting, of heat transfer surface area per unit length of the tube and the convective transport, due to the secondary flow produced by the spiral flutes. It is well known that the Nusselt number of fully-developed laminar flow in smooth tubes is constant ( $Nu = 4.364$ ) while generally in fully-developed flows with no net circumferential convection the Nusselt numbers are independent of Reynolds and Prandtl numbers. As has been reported in the literature survey in Chapter 1, a sensitivity of Nusselt number to  $Re$  or  $Pr$  can be found when a secondary flow is present. This is what Figure 3.22 indicates, illustrating the dependence of mean Nusselt number of the spirally fluted tube on Reynolds and Prandtl numbers. The Nusselt number plotted in this figure and used in all the results reported below has been defined as:

$$Nu_P = \frac{\dot{q}'' 2R_b}{\Delta T \cdot k_f} \cdot \frac{P}{2\pi R_b} \quad (3.5)$$

where  $\dot{q}''$  is the heat input to the tube per unit surface area,  $P$  is the perimeter of the fluted tube,  $k_f$  is the thermal conductivity and

$$\Delta T = T_w - \bar{T}$$

$T_w$  being the wall temperature and  $\bar{T}$  the bulk mean temperature of the fluid. The definition (3.5) shows what, for a given total heat input, would be the reduction in pipe wall temperature from the presence of fluting for the same mean radius and flow conditions. If the added surface area, due to fluting, had not been taken into account, equation (3.5) would have the form:

$$Nu' = Nu_p \cdot \frac{2\pi R_b}{P} = \frac{\dot{q}'' 2R_b}{\Delta T \cdot k_f} \quad (3.6)$$

Another definition of Nusselt number based on the hydraulic diameter ( $D_h$ ) could be:

$$Nu = Nu_p \frac{D_h}{2R_b} = \frac{\dot{q}'' D_h}{\Delta T \cdot k_f} \cdot \frac{P}{2\pi R_b} \quad (3.7)$$

or the one corresponding to (3.6):

$$Nu^* = Nu \frac{2\pi R_b}{P} = \frac{\dot{q}'' D_h}{\Delta T \cdot k_f} \quad (3.8)$$

All the above definitions of Nusselt number stand for the local values around the flute. The mean value of  $Nu_p$ , plotted in Figure 3.22, has been calculated from the local ones (equation (3.5)) using the correlation:

$$A_{\text{mean}} = \frac{1}{(P/n)} \sum_{i=2}^{I-1} A_{\text{local}} \cdot \Delta \xi_i \quad (3.9)$$

where A stands for the Nusselt number or any other variable calculated around the flute, P the perimeter of the fluted tube, n the number of flutes around the circumference,  $\Delta \xi$  the control volume face coinciding with the

wall and I the number of constant- $\xi$  lines mapping the solution domain.

Three different fluids have been considered in all the convective heat transfer studies: air ( $Pr = 0.708$ ), water (7.03) and ethylene glycol ( $Pr = 93$ ) at  $20^\circ\text{C}$ . Figure 3.22 shows the distribution of mean  $Nu_p$  with Reynolds number  $Re_p$  (equation (3.4)) for those three Prandtl numbers for tubes of 10, 20 and 30 flutes. It is clear that for air there is no considerable increase of Nusselt number with Reynolds number, while for water there is an increase depending on the number of flutes. The greater the number of flutes the less sensitive the Nusselt number of water to Reynolds number. So, for 10 flutes, the Nusselt number at  $Re_p = 2500$  is about 5% above that at  $Re_p = 300$ , while for 30 flutes the Nusselt number is almost insensitive to Reynolds number. However, the effect of Reynolds number on Nusselt number is much stronger for ethylene glycol ( $Pr = 93$ ) showing a two-fold increase when the Reynolds number increases from 40 to 2500 for the tube with 10 flutes. This augmentation becomes important even at  $Re_p = 100$  while for 20 flutes there is also an enhancement of Nusselt number, though it is less than that for 10 flutes and becomes significant only at Reynolds numbers above 500. The same characteristics can be seen for the tube with 30 flutes; however, the augmentation of Nusselt number in this case is even smaller, becoming noticeable only for  $Re_p > 800$ .

The explanation of the contrasting behaviour between the different fluids used can be found in the way that heat is transmitted through them: at a Reynolds number of 2500 and  $n = 10$ , the flute Peclet number for air, based on peak circumferential velocity and flute height  $\left[Pe = \frac{\rho \cdot U \cdot 2h}{\mu / Pr}\right]$ , is only 0.2. This means that convective transport has a minor effect, compared

with diffusive transport, on the heat transmission across the near-wall zone. However, for ethylene glycol ( $Pr = 93$ ) the flute Peclet number is more than a hundred times larger ( $93/0.708$ ) so convection is the principal mechanism in transferring heat from the fluted wall into the fluid.

Another feature of Figure 3.22 is that for a fixed Prandtl number the increase of Nusselt number increases with Reynolds number. This can be explained partly by referring to equation (2.14) of Chapter 2 where an extra convection term due to the axial velocity ( $\kappa_{\xi}W$  or  $\kappa_{\eta}W$ ) appears in the energy equation which obviously increases with Reynolds number. The same type of behaviour has been found in Date's [67] study of twisted tape inserts reported in the literature survey.

Figure 3.22 also shows that for ethylene glycol and high Reynolds numbers the level of Nusselt number for the 10-flute tube is higher than that for 20 or 30 flutes. A similar behaviour is also evident for 20 flutes when it is compared with the 30-flute tube. The superiority of the low flute-density tubes is primarily due to the fact that, in these geometries, fluid from the vicinity of the flutes is carried further into the core fluid (this behaviour has been discussed in the previous section and is shown in Figure 3.12). So, the fact that the enhancement of Nusselt number for 30 flutes is lower than for 20 or 10 flutes can be ascribed to two factors: first, the confinement of the fluid circulating in the flutes closer to the wall (Figure 3.12), and second, the low values of flute Peclet numbers, even for ethylene glycol; at  $Re_p = 300$  and  $n = 30$  for  $Pr = 93$ , the flute Peclet number is only 2. The increase in the level of Nusselt number with the number of flutes, shown in Figure 3.22, arises from the definition of Nusselt number itself. If, instead of equation (3.5), the definition given

by equation (3.6) has been used, the levels of Nusselt number would have fallen below the smooth tube value as the number of flutes was increased; that is, for 30 flutes and  $Re_p \leq 300$ , to 3.6. A similar distribution is produced if the definition (3.7) is used.

Figure 3.23 shows for 10 flutes at  $Re_p \approx 300$  that the mean Nusselt number ( $Nu_p$ ) increases with the helix angle, that increase being quite steady for  $Pr = 93$ . As pointed out above in Section 3.12 a. (Figure 3.11), for spiral angles ranging from  $15^\circ$  to  $45^\circ$  the maximum circumferential velocity increases in roughly the same ratio as the tangent of the helix angles. So, for the same Reynolds number and number of flutes, the flute Peclet number of a fluid (water or ethylene glycol) will increase in the same ratio as the maximum circumferential velocity when the spiral angle of the flutes increases, explaining the behaviour shown in Figure 3.23. An analogous behaviour would have been shown if the height of flutes rather than the spiral angle had been increased. A significant enhancement of  $Nu_p$  with  $\phi$  is also found with water but only if 20 or 30 flutes are employed (Figure 3.24). For 10 flutes there is very little augmentation.

Figure 3.25 gives, for ethylene glycol and a 10-flute tube, the  $Nu_p - Re_p$  distribution for two spiral angles:  $\phi = 15^\circ$  and  $30^\circ$ . For  $\phi = 30^\circ$  the enhancement of mean Nusselt number at  $Re_p > 2000$  becomes more than 100%.

Perhaps the most useful dimensionless quantity to consider is a measure of the relative increase of heat transfer and frictional losses. This can be given by the normalized ratio of Stanton number to friction factor expressed in the form:

$$\frac{\text{Pr.St.}}{f_p} = \frac{\text{Nu}_p / \text{Re}_p}{f_p} = \frac{\text{Nu}_p / \text{Re}_p}{\tau_w / (\frac{1}{8} \rho \bar{w}^2)} \quad (3.10)$$

For a smooth tube, equation (3.10) takes the value 0.068. Again, while the above equation expresses local values around the flute, the mean value can be calculated using equation (3.9). Figure 3.26 presents the distribution of the mean value of  $\frac{\text{Pr.St.}}{f_p}$  with the spiral angle for both water and ethylene glycol, while Figure 3.27 gives its distribution with the helix angle for water for three different numbers of flutes ( $n = 10, 20, 30$ ). These two figures, being analogous to Figures 3.23 and 3.24 discussed above, show a significant increase of  $\frac{\text{Pr.St.}}{f_p}$  over the smooth tube value indicating that the spirally fluted tubes, even for moderate Prandtl numbers ( $\text{Pr} = 7.03$ ) in laminar flow situations, can raise the heat transfer coefficients substantially more than the frictional losses.

The dimensionless temperature ratio

$$\frac{T - T_{w_r}}{\bar{T} - T_{w_r}}$$

( $T_{w_r}$ , the temperature on the wall at the trough position) distribution along two radii passing through the trough and crest of the flute is given in Figures 3.28, 3.29 and 3.30. Figure 3.28 displays this distribution for both water and ethylene glycol in a tube with 10 flutes and  $15^\circ$  spiral angle. Differences in the temperature ratio distribution between trough and crest, for all the fluids and Reynolds numbers shown in Figure 3.28, are discernible only for  $\frac{R_b - R}{R_b} < 0.2$ . Since the distribution of

$\frac{T - T_{wr}}{\bar{T} - T_{wr}}$  shows no distinctive features for  $Pr = 7.03$ , its distribution at  $Re_p = 700$  has been omitted in Figure 3.28 for clarity. However, at  $Re_p = 2345$ , a quite interesting difference in shapes between water and ethylene glycol can be detected. It is clear that for ethylene glycol the temperature profile is divided into two distinct regions: the core region, where the radial heat transport is by conduction, and the region near the flutes where, due to the fluid mixing (fluid spills over the crest), the temperature becomes uniform. These two regions become less noticeable for lower Reynolds numbers (see Figures 3.28 and 3.29). Masliyah et al [63, 64] (see literature survey in Chapter 1) have encountered the same shape in the distribution of the temperature ratio (see Figure 1.38) when they studied the heat transfer performance of fully-developed laminar flows through uniformly heated internally-finned tubes. The two distinct regions are clearly shown on curve 4 of Figure 1.38. Figure 3.30 displays the distribution of the dimensionless temperature ratio at the trough and crest radii for ethylene glycol at  $Re_p$  of 2345 for both 10 and 30 flutes. It is obvious from this figure that for  $n = 10$  the region of uniform temperature is more extensive than for  $n = 30$ . This is due to the fact that a reduction in the number of flutes increases the distance from the tube wall over which the fluid is mixed.

Figure 3.31 shows the variation of local Nusselt number ( $Nu_p$ ) around the flute at two different Reynolds numbers for both water and ethylene glycol. For the low Prandtl number the distribution of  $Nu_p$  is symmetric with the maximum value near the crest and the minimum in the trough of the flute. For an increase of Reynolds number from 300 to 1700 the local  $Nu_p$  increases in the trough but decreases at the crest, the result being to increase the level of the mean  $Nu_p$  (calculated by (3.9)) by about 3%.



However, for the high Prandtl fluid ( $Pr = 93$ ) for the same increase of Reynolds number, the level of the mean Nusselt number rises by about 25%, the distribution of the local  $Nu_p$  at both Reynolds numbers (300 and 1700) being considerably asymmetric. This distribution strengthens the suggestion that, for ethylene glycol, convective transport is the dominant mechanism in transferring heat across the near-wall zone, while for water it makes a minor addition to diffusive transport.

The variation of local  $\frac{St.Pr}{f_p}$  around the flute for water and ethylene glycol for the same tube geometry and Reynolds numbers as the distributions shown in Figure 3.31, is shown in Figure 3.32. For both water and ethylene glycol the distribution of local  $\frac{St.Pr}{f_p}$  is quite symmetric with the minimum value near the flute crest and the maximum value occurring in the trough. It is obvious that there is a large difference in the levels of the minimum and maximum values for all the cases plotted in Figure 3.32. For water, the two curves ( $Re_p = 300$  and 1700) are almost indistinguishable while for ethylene glycol a 23% rise in the mean value of  $\frac{St.Pr}{f_p}$  for the same increase in Reynolds number can be easily identified.

### 3.2 Concluding Remarks

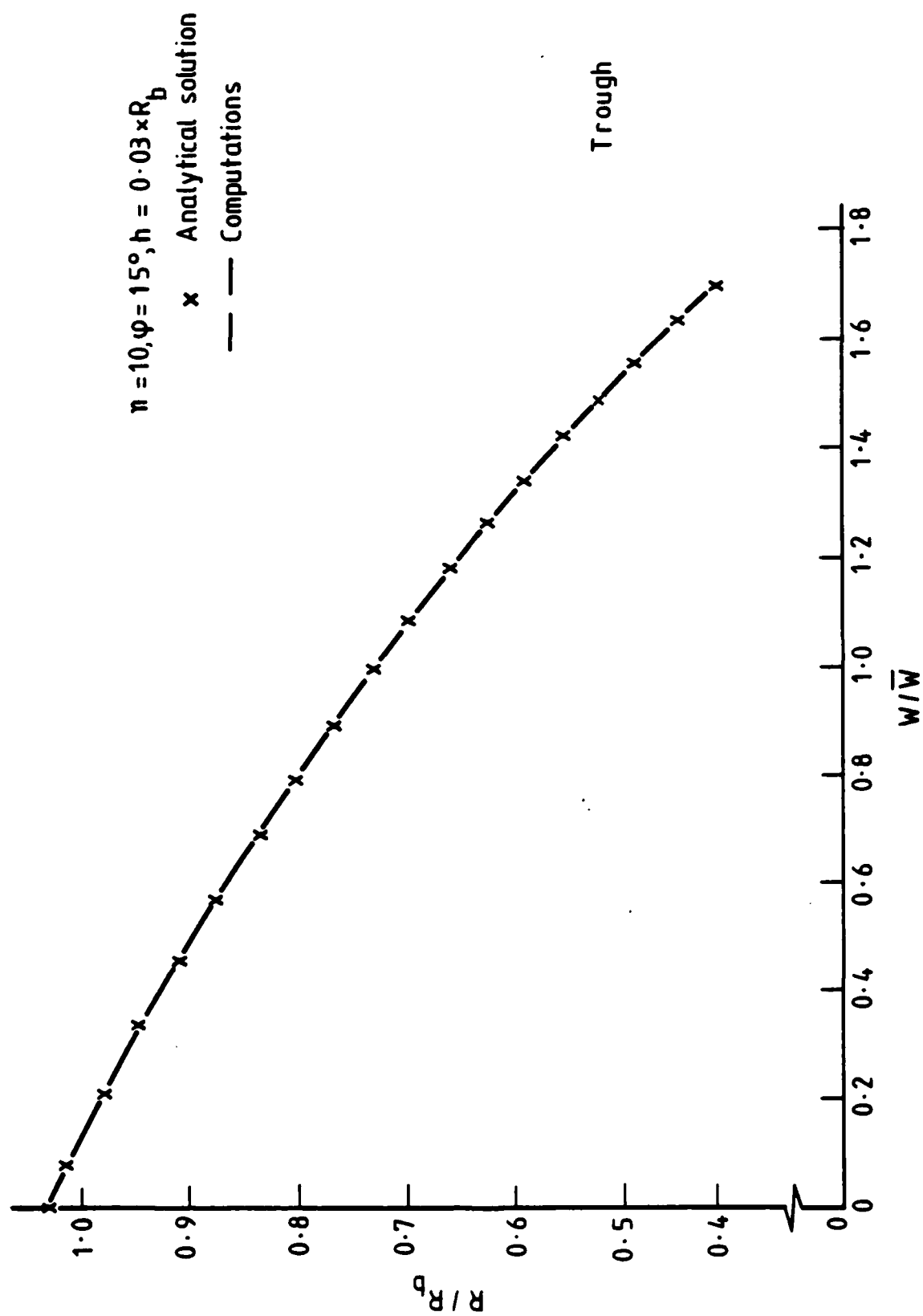
Chapters 2 and 3 have presented the successful adaptation of the general orthogonal TEACH code for solving the laminar velocity and temperature fields in a spirally fluted tube. The principal steps which improved the convergence of the solution were the inclusion of the two-stage pressure-correction procedure, the so-called PISO scheme, and the use of a mixed curvilinear/cylindrical-polar grid instead of the original curvilinear one. However, in cases of high flute density where high aspect

ratio cells are still present, the convergence is not entirely satisfactory. The adoption of a non-orthogonal grid should solve this problem and lead to a more rapid convergence of the iterative solution.

The effects of different parameter variations and, generally, the flow pattern produced by the computations now seem entirely plausible. However, at the beginning of the project, since no experimental data for laminar flows were available, it was very difficult to imagine what flow pattern would actually be produced in such a tube. There has, to the author's knowledge, been nothing reported on computational studies of flows in pipes with such a combination of complexities encountered during the study of the spirally fluted tubes. In view of the experimental difficulties referred to, it is believed that the computational procedure here developed can be usefully applied to the optimization of the design of spirally fluted tubes.

The numerical results show clearly the mechanism behind the heat transfer augmentation and explain why there is no marked effect on the level of friction factor due to the fluting. These results also verify the suggestion that friction and heat transfer must be considerably affected by what is happening in the immediate vicinity of the tube wall. It is very interesting that even for water the increase in heat transfer is several times greater than the increase in friction factor. Considering that all other enhancement techniques for internal flows raise the friction factors substantially more than the heat transfer coefficients, the fact that the spirally fluted tube produces a contrary behaviour, even for moderate Prandtl numbers, indicates that this type of tube could be used, quite beneficially, in heat exchangers. A far better improvement is found

for ethylene glycol, meaning that spiral fluting could be adopted in oil coolers since the circulation of oils often takes place in the laminar regime. In this case, low flute density and tight spiralling gives the best performance, while for low Prandtl numbers (i.e. water), high flute density and tight spiralling tubes should be adopted. Of course, beyond a certain helix angle, the improvement will be reversed, though the identification of this limit has not been possible in the present research programme.



Fin 3 1 Laminar flow in a smooth pipe

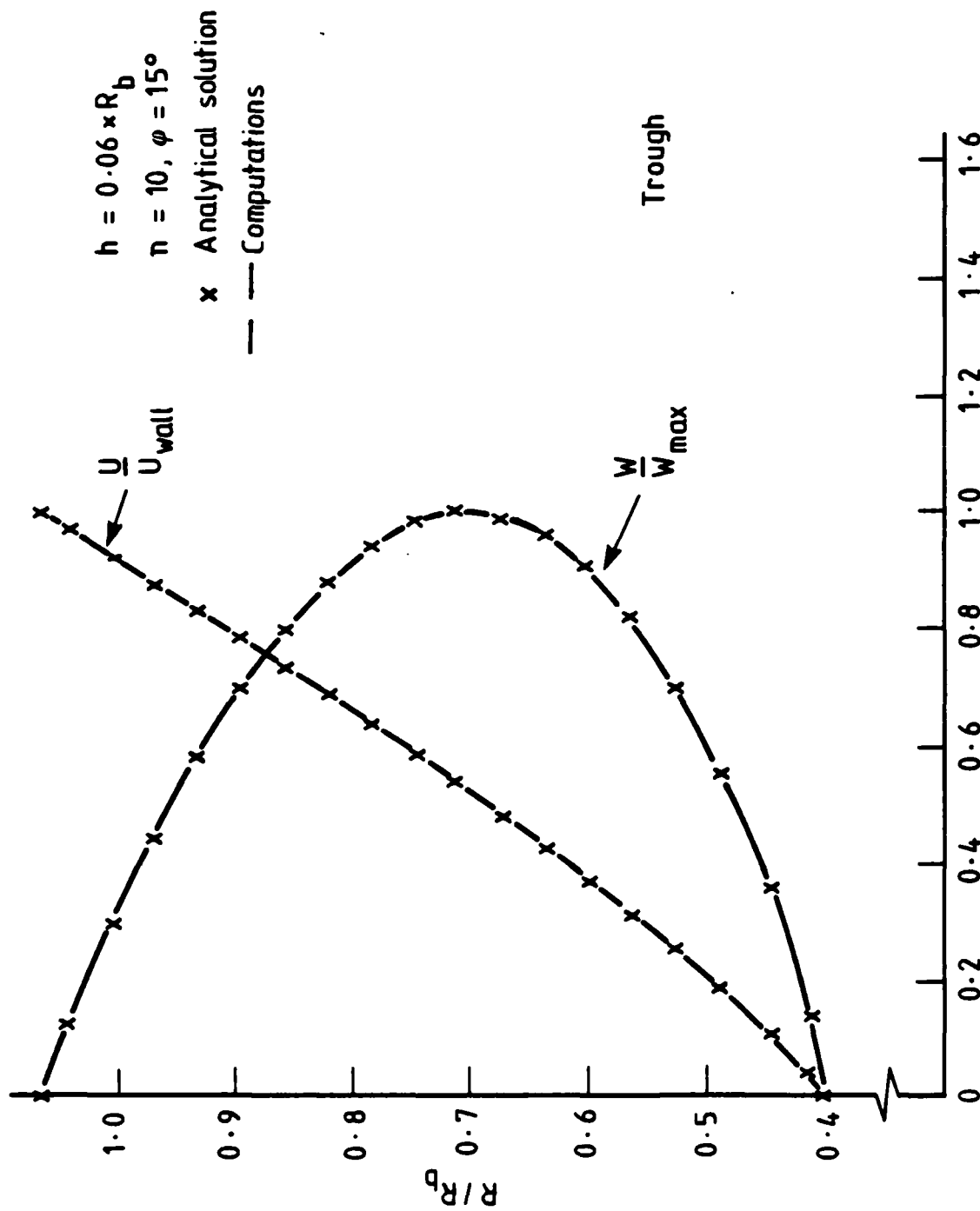


Fig. 3.2 Laminar flow in annulus with rotation on the outer wall

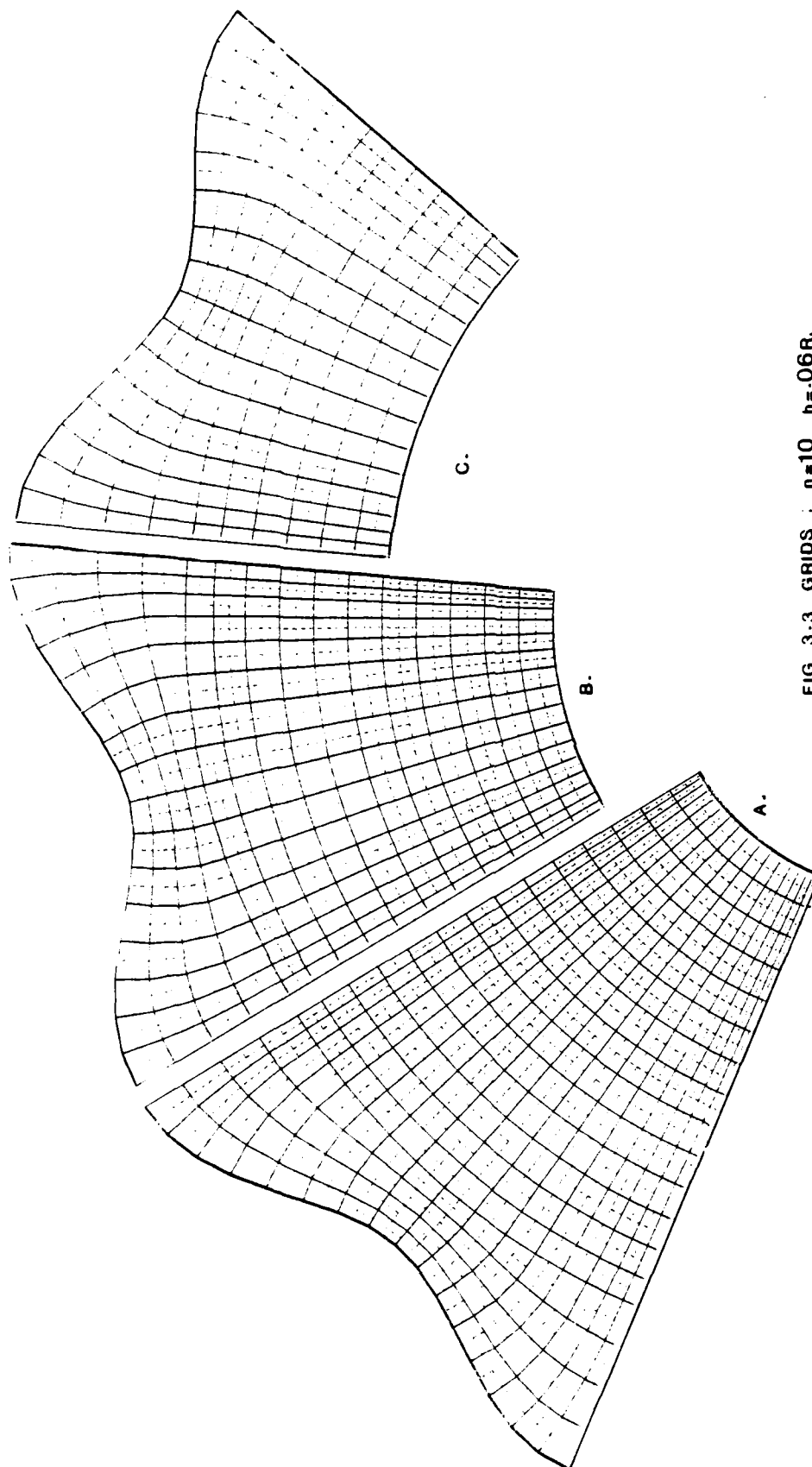


FIG 3-3 GRIDS :  $n=10$   $h=.06R_b$

A.  $R_a = .3R_b$

B.  $R_a = .42R_b$

C.  $R_a = .62R_b$

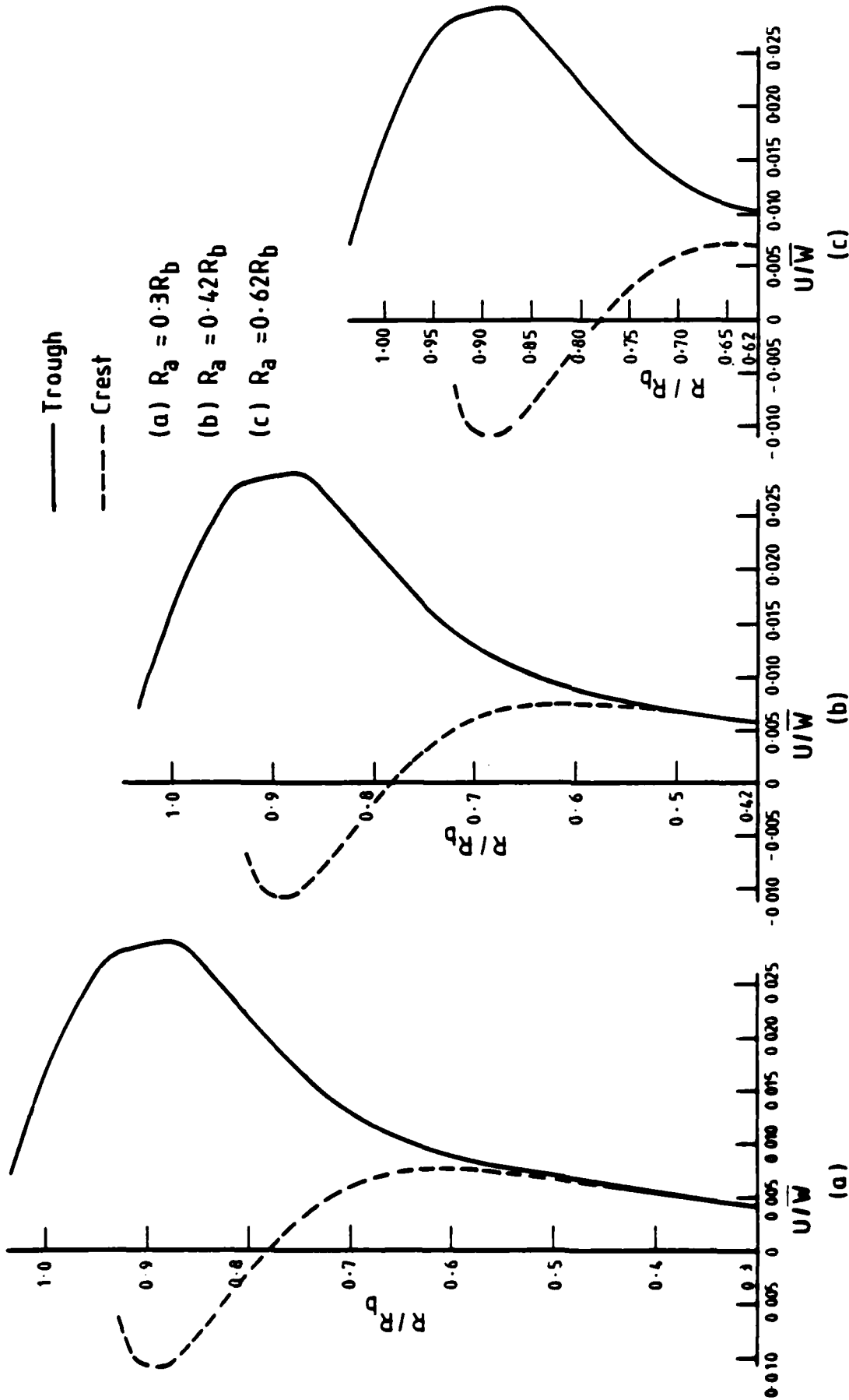


Fig. 3.6 Distribution of  $U/\bar{W}$  with  $R/R_b$ ,  $\eta = 10$ ,  $h = 0.06R_b$

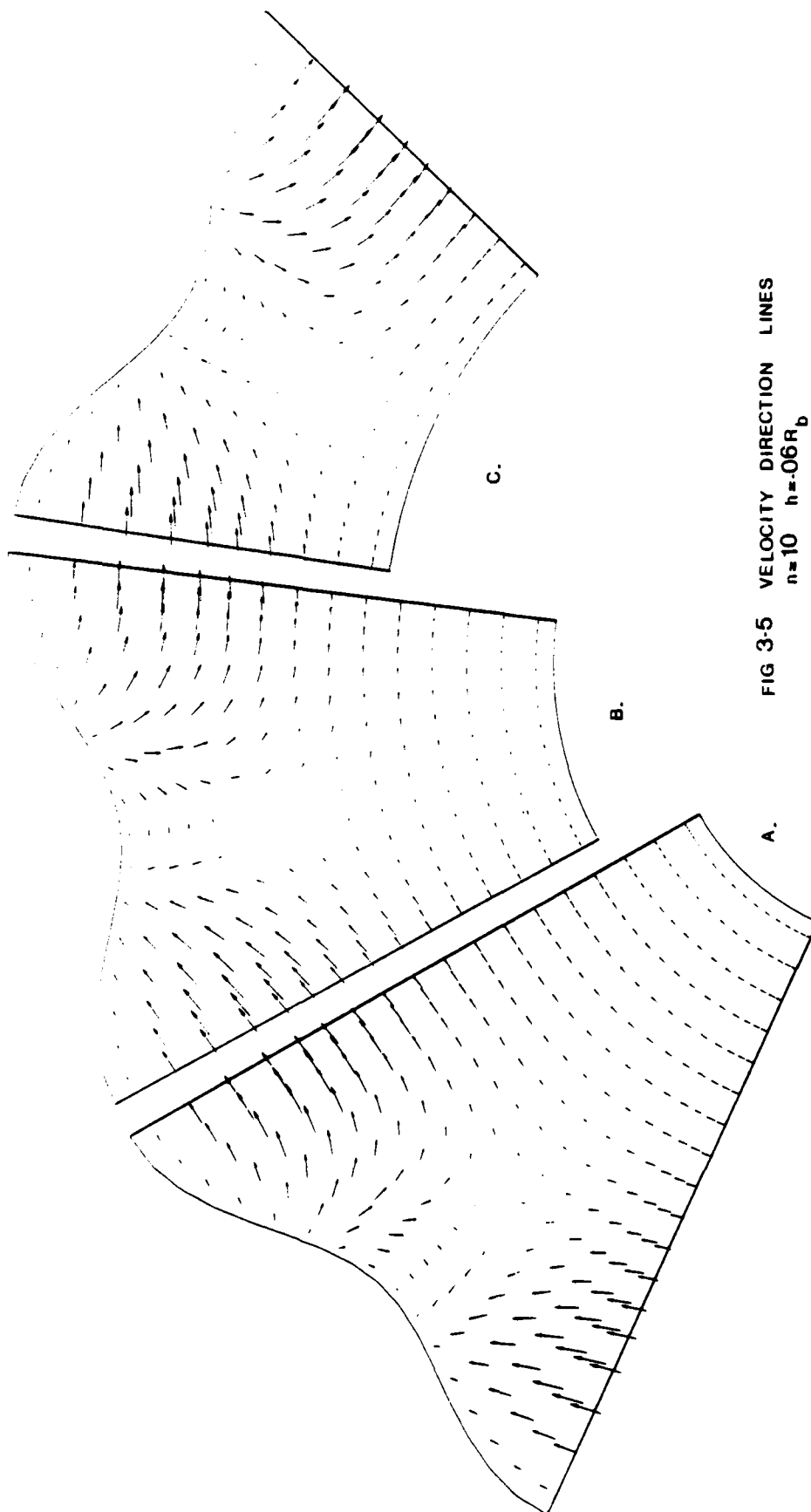


FIG 3-5 VELOCITY DIRECTION LINES  
 $n=10$   $h=0.6R_b$

A.  $R_a = 3R_b$

B.  $R_a = 4.2R_b$

C.  $R_a = 6.2R_b$



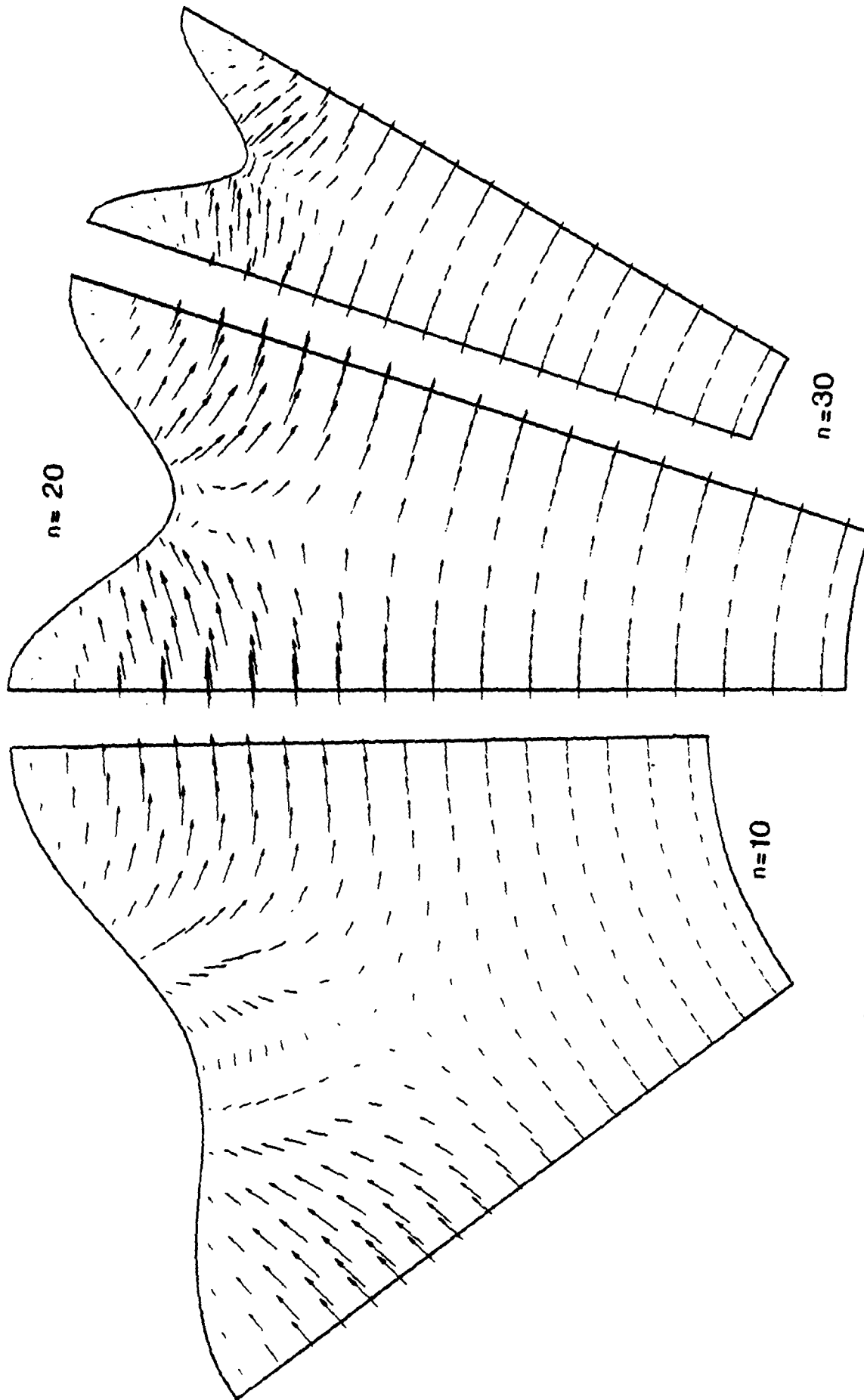


Fig 3-6 Velocity direction lines in  $\xi$ - $\eta$  plane  $h=0.6R_b$   $Re=300$

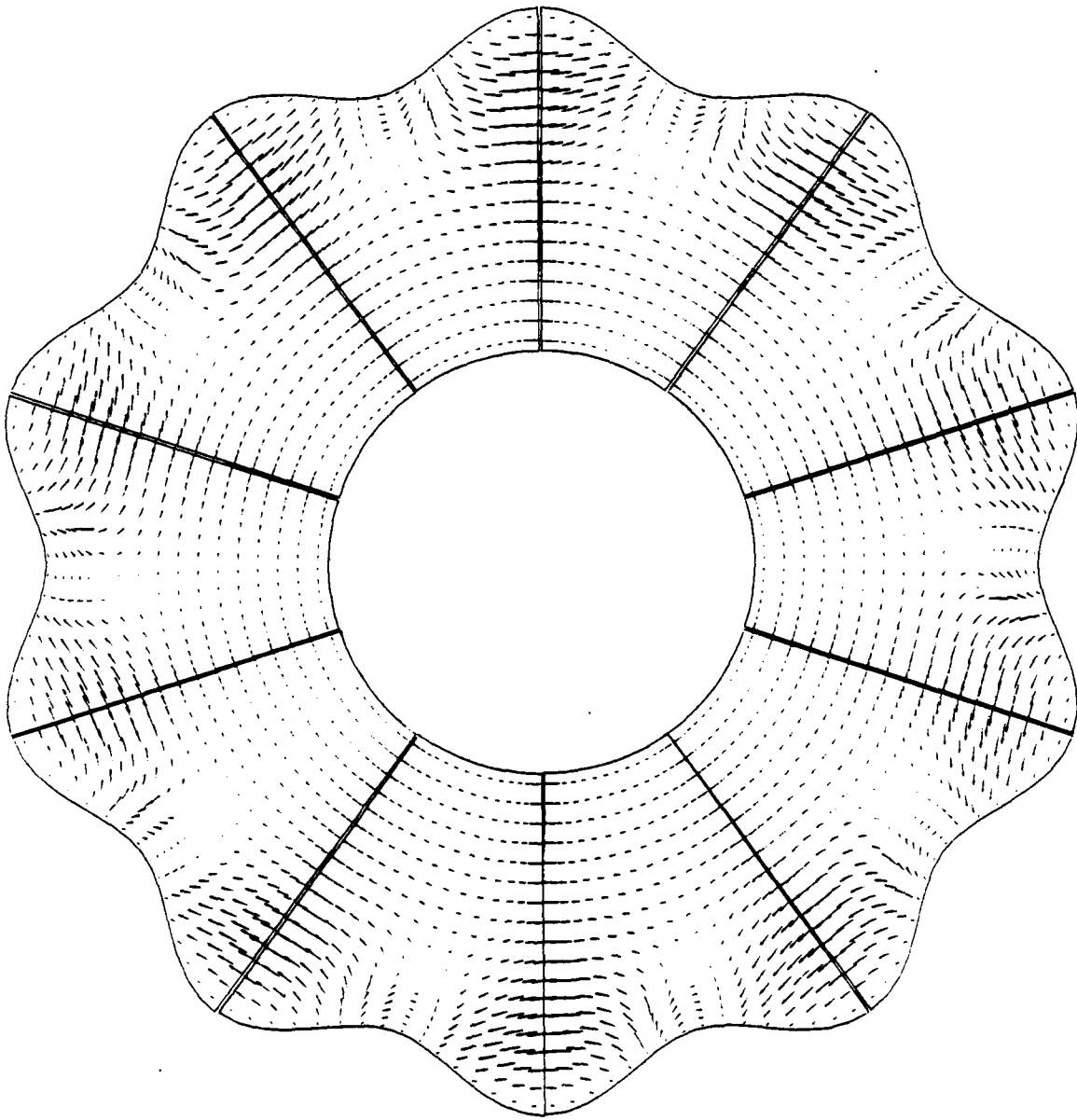


FIG 3-7 VELOCITY DIRECTION LINES

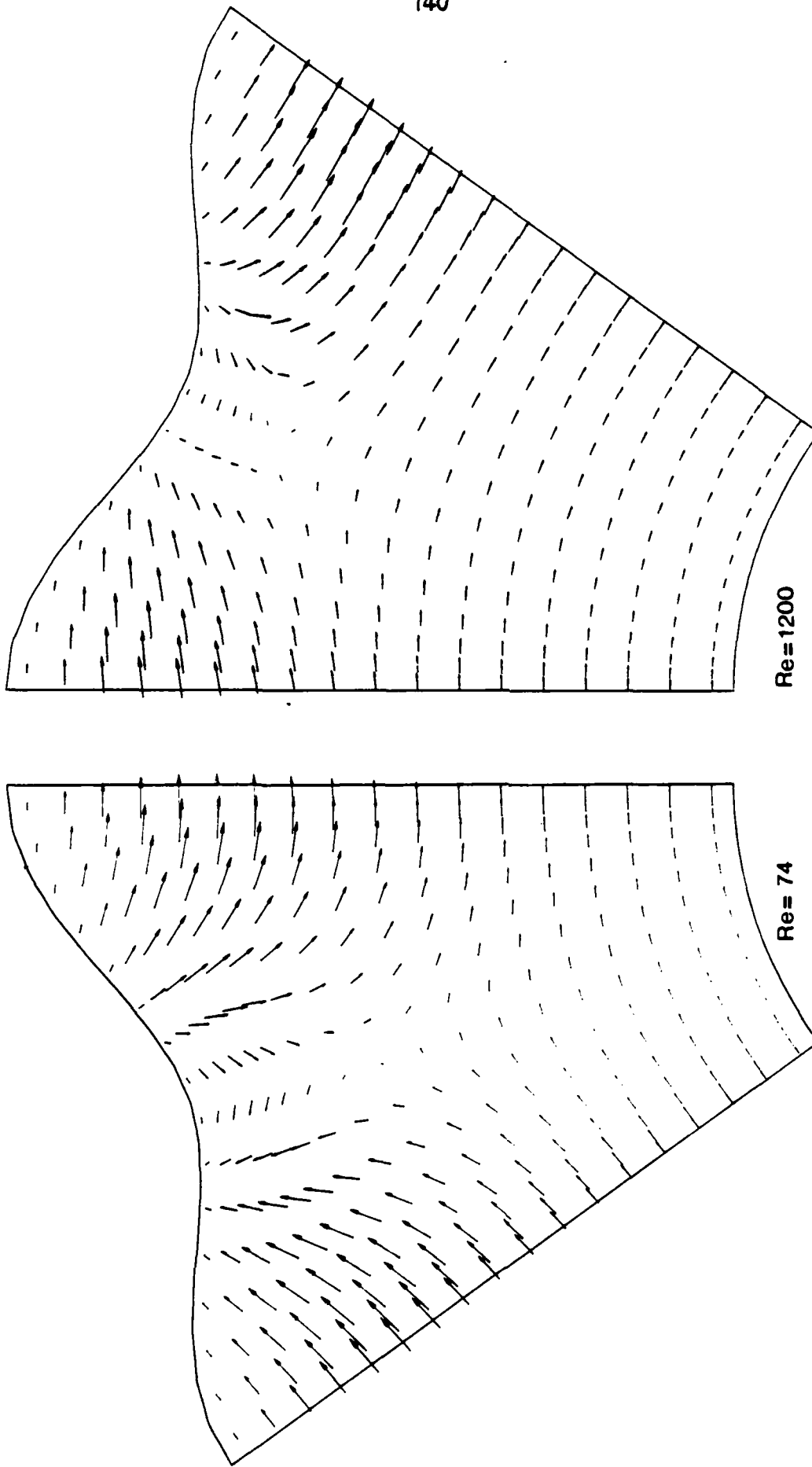


Fig 3-8 Velocity-direction lines in  $\xi$ - $\eta$  plane ;  $n=10$   $h=-0.6R_b$

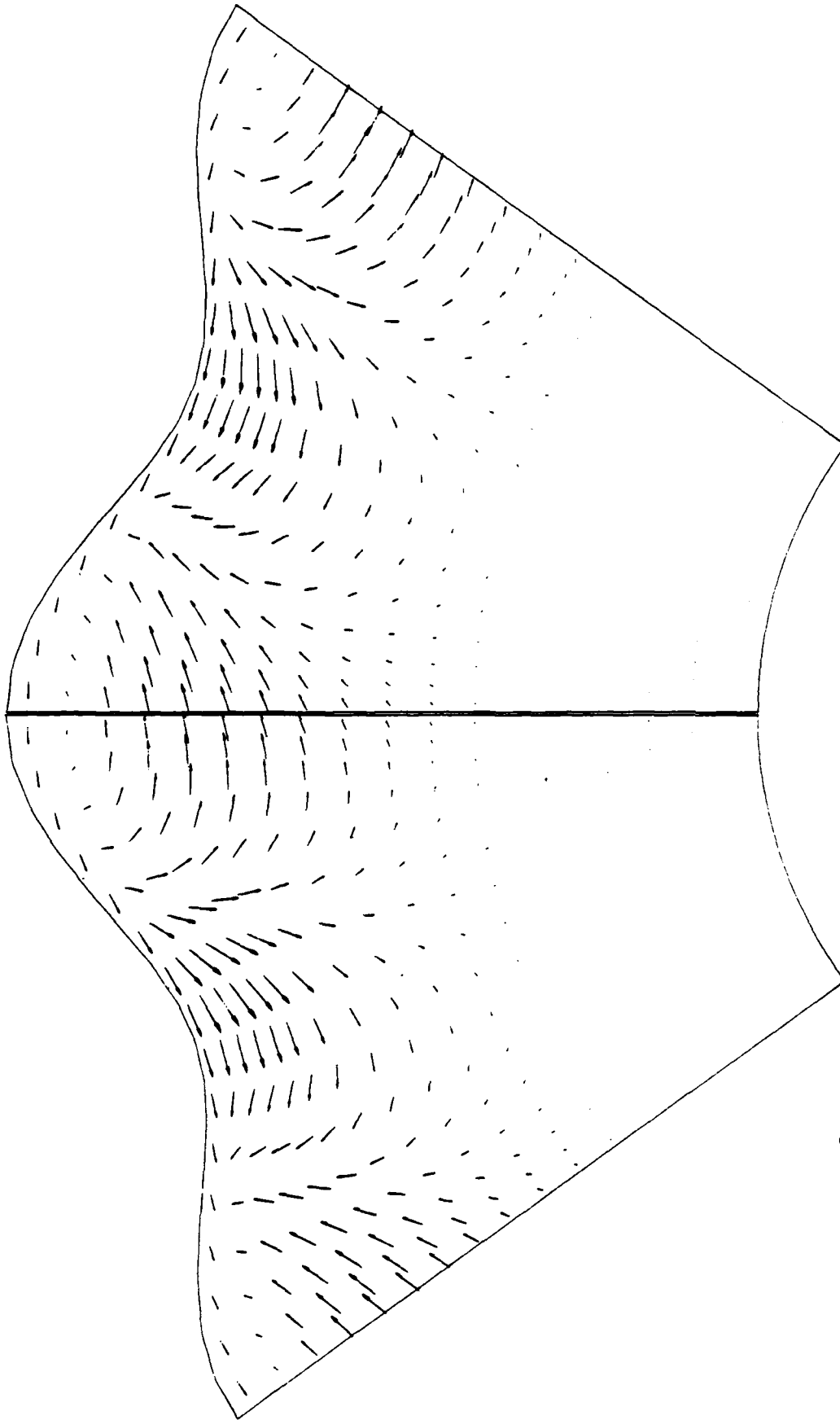
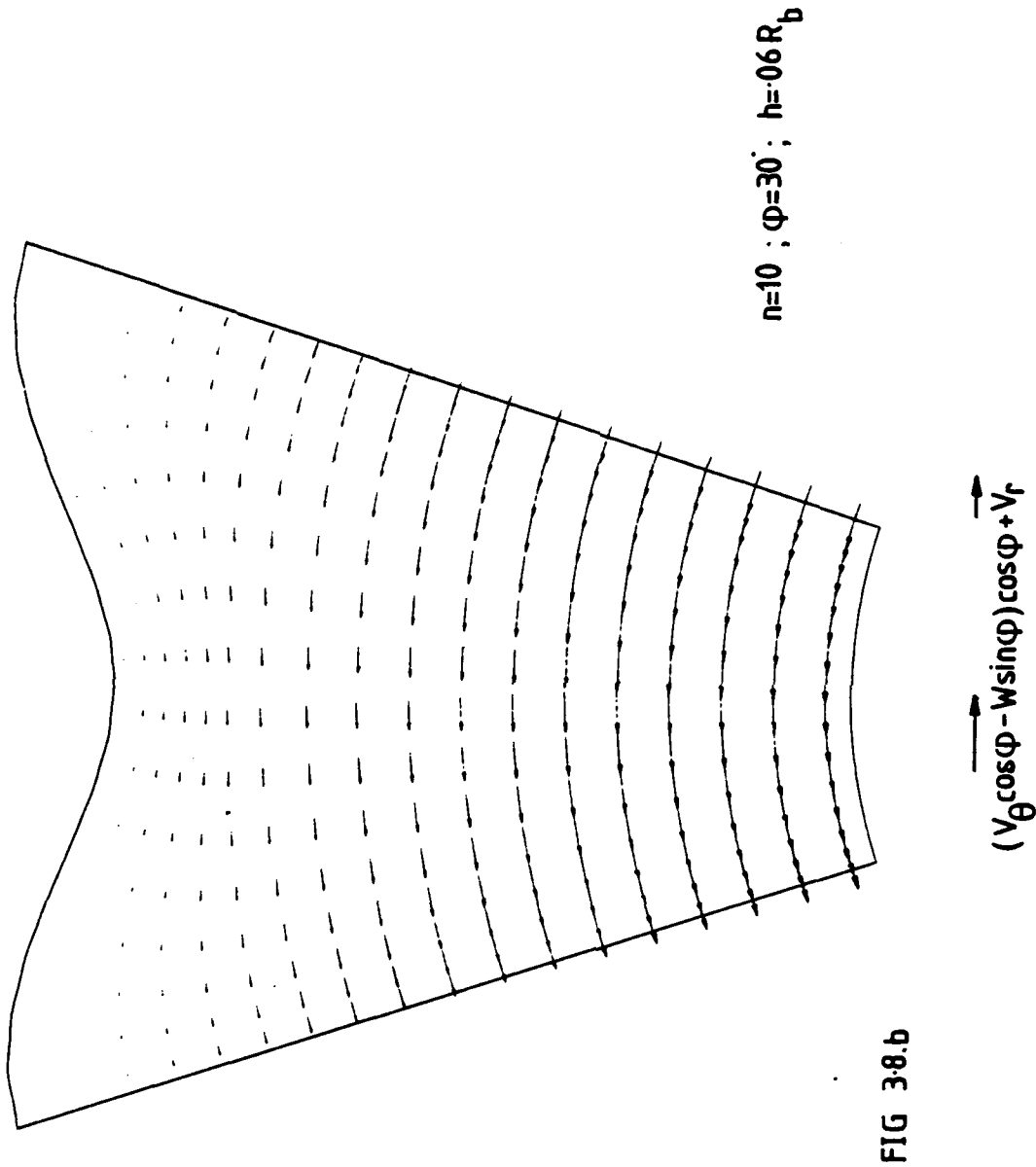
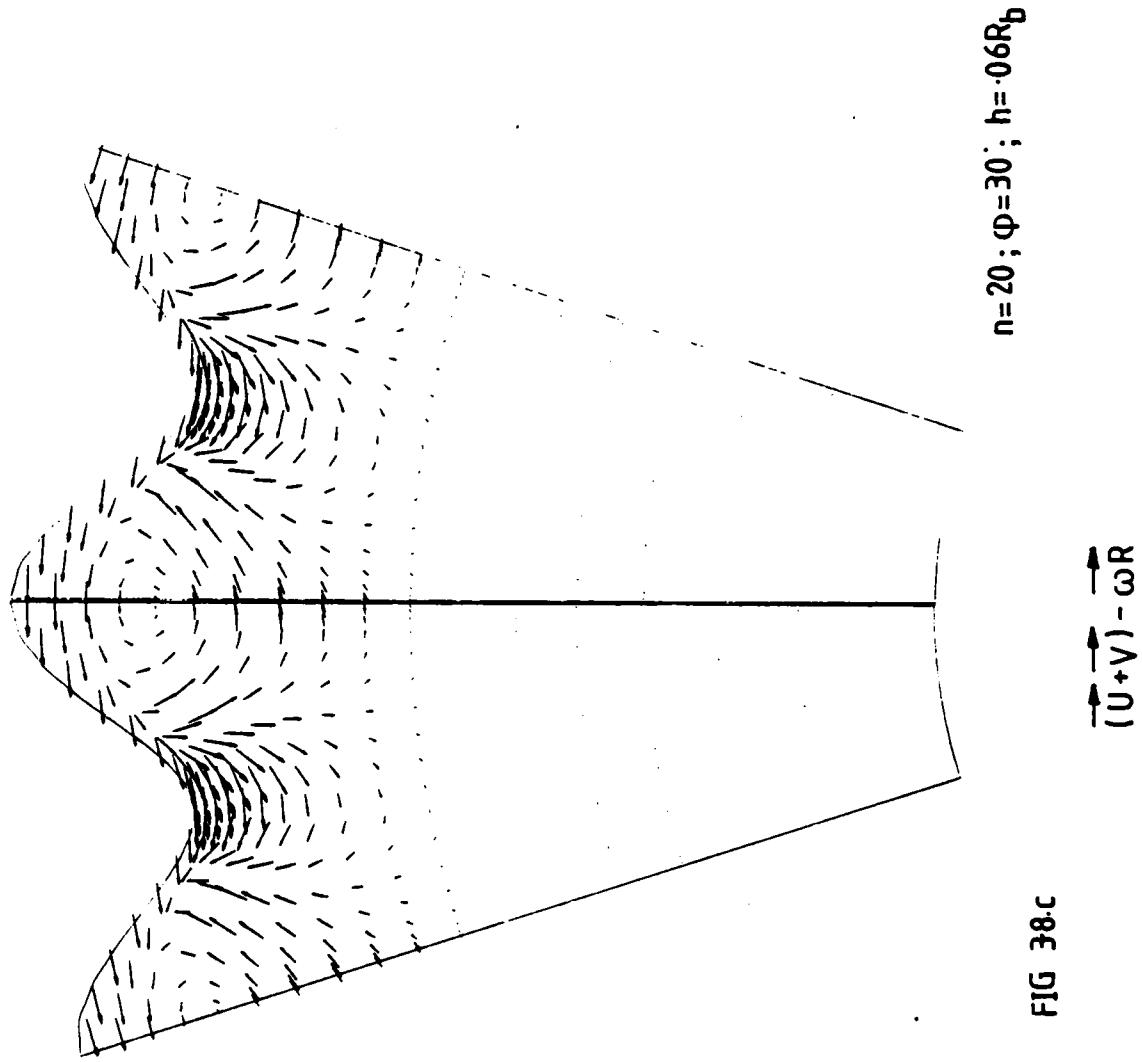


FIG 3.8.a

$n=10$  ;  $\varphi=30^\circ$  ;  $h=0.6 R_b$

$$(\vec{U} + \vec{V}) - \omega \vec{R}$$





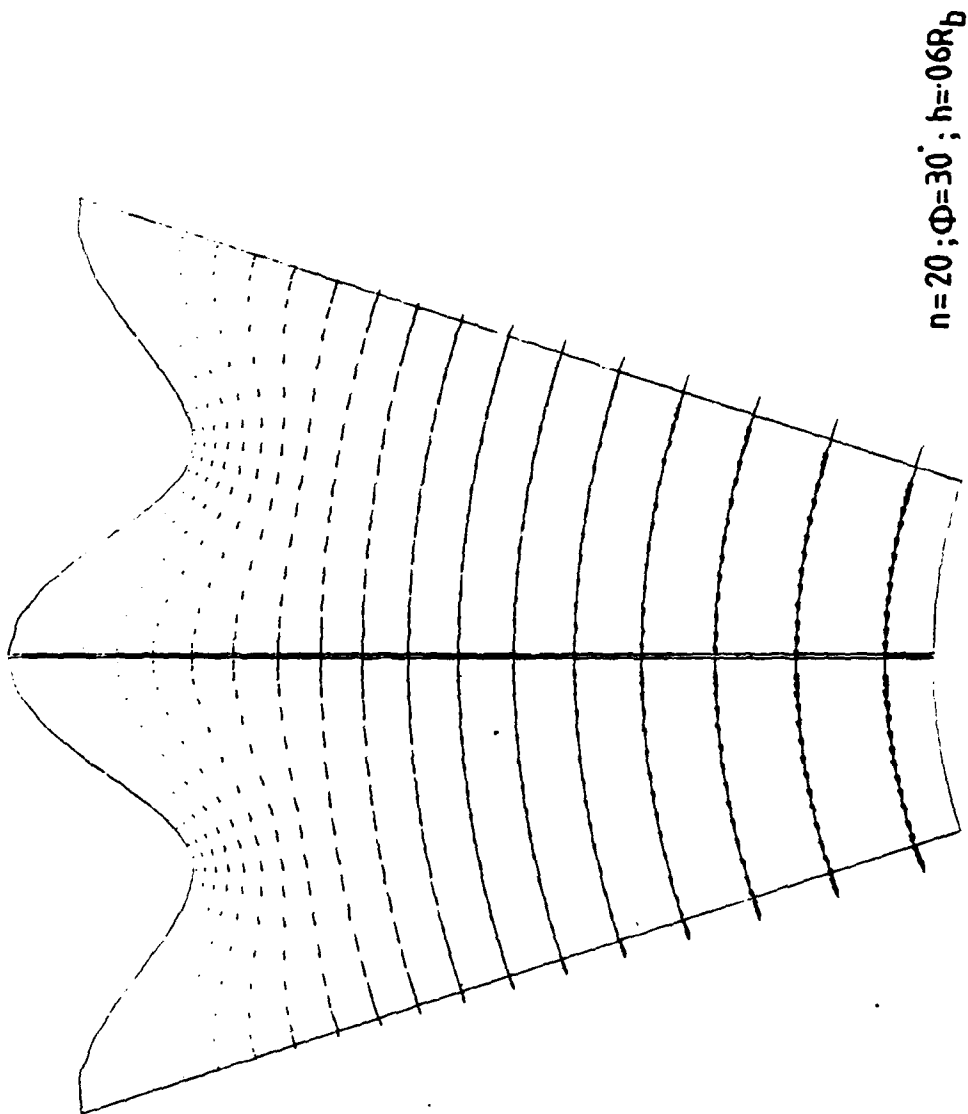


FIG 38d

$$(V_{\theta} \cos \Phi - W \sin \Phi) \cos \Phi + V_r$$

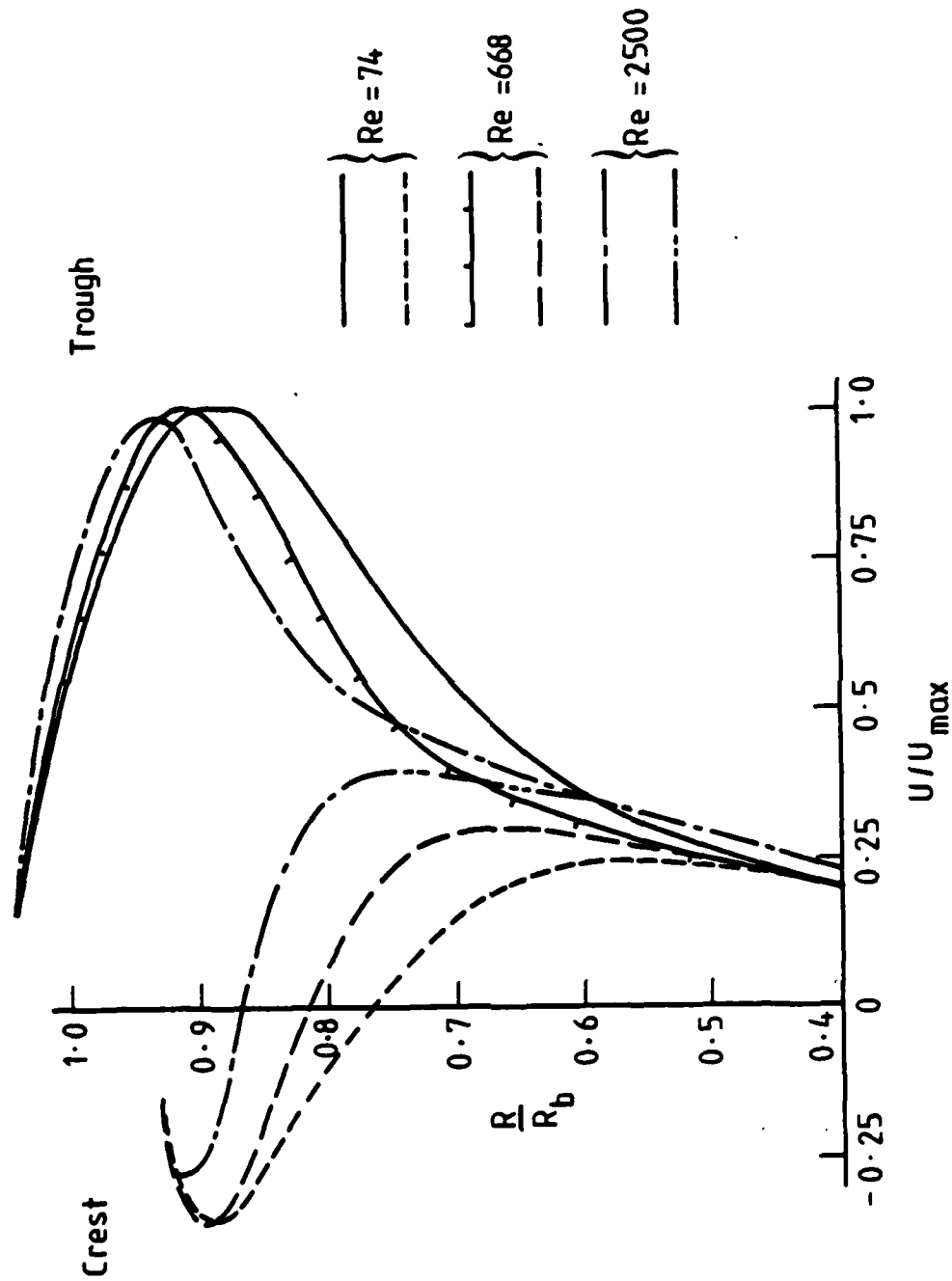


Fig. 3.9. Effect of Reynolds number on circumferential velocity profile along radii passing through crest and trough.  $h = 0.06 R_b$ ,  $n = 10$ ,  $\phi = 15^\circ$



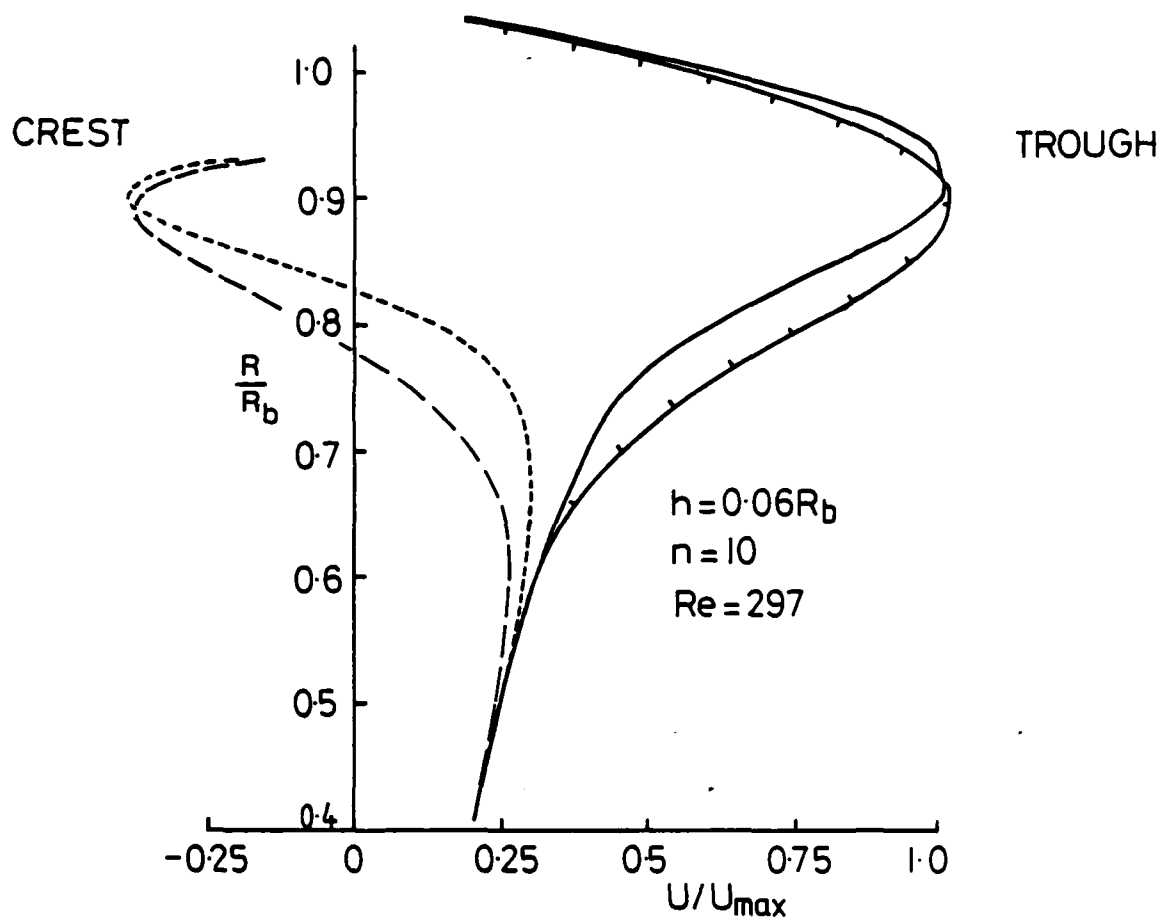


Fig 3-10 Effect of flute angle on  
 circumferential velocity  
 $h = 0.06R_b$   $n = 10$   $Re = 297$

——  $\phi = 15^\circ$       ——  $\phi = 30^\circ$   
 - - - - -

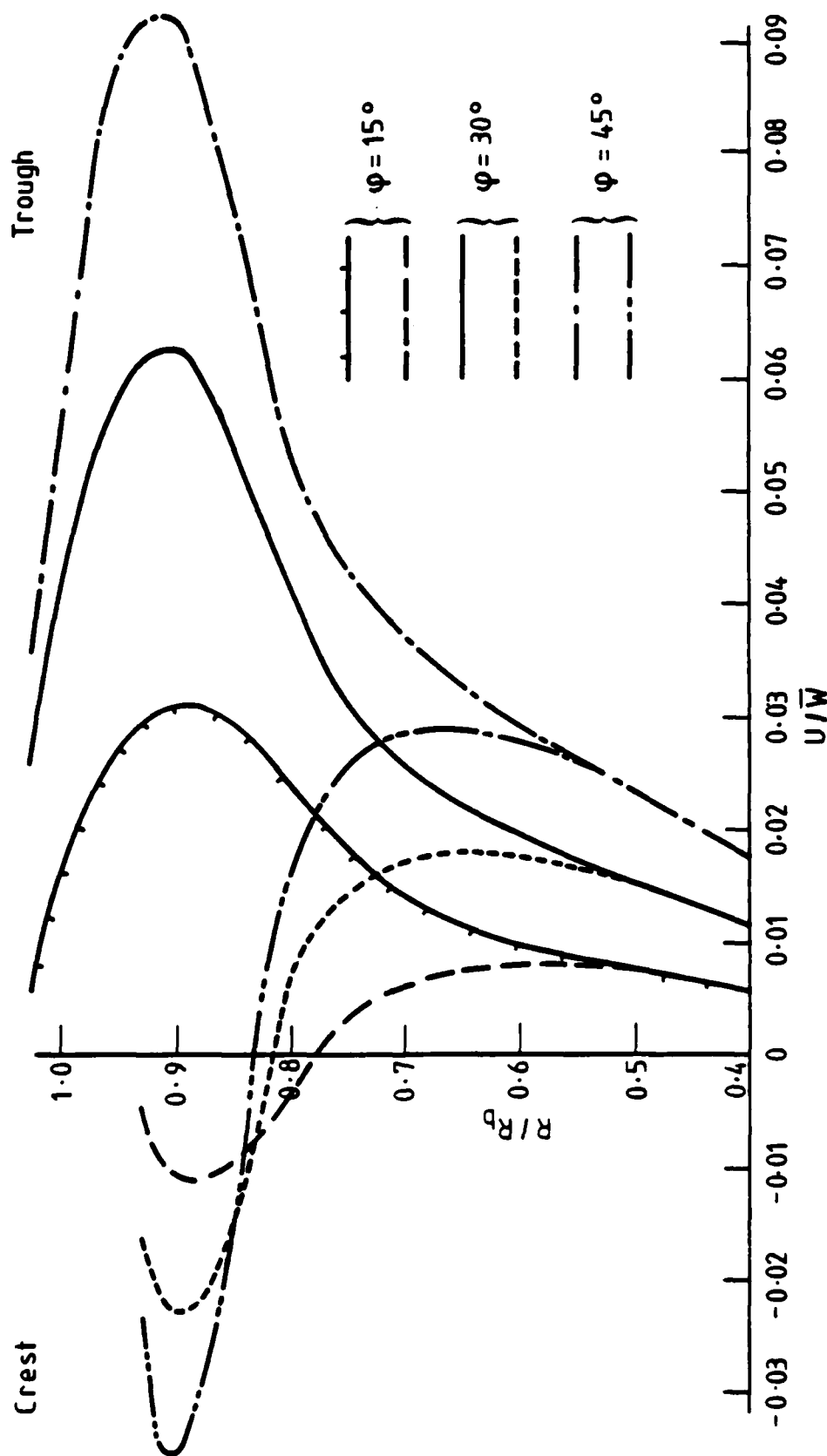


Fig 3.11 Effect of flute angle on circumferential velocity profile along crest and trough radii,  $h = 0.06 R_b$ ,  $n = 10$ ,  $Re = 297$

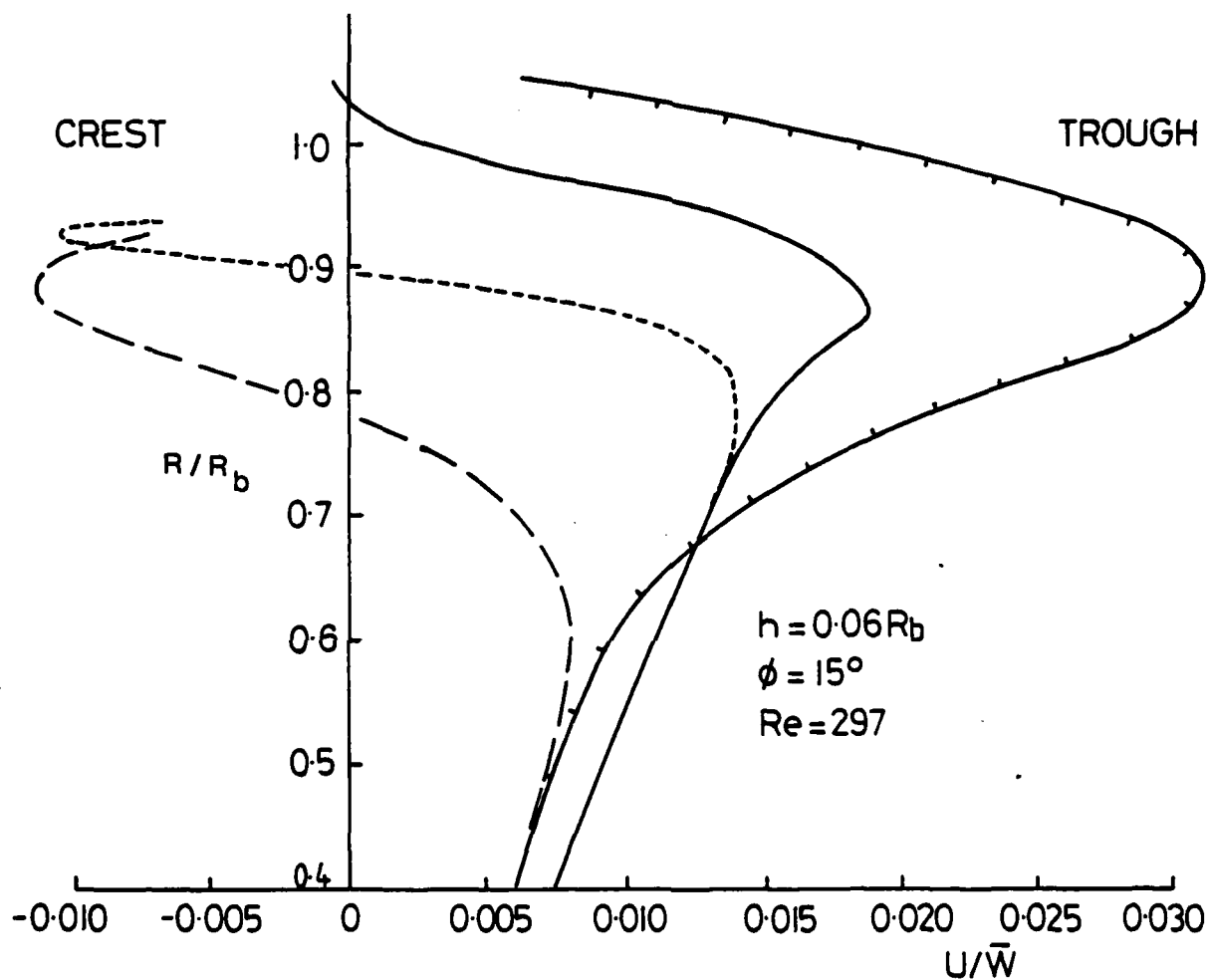


Fig 3-12 Effect of number of flutes on circumferential velocity profile along crest and trough radii

$\text{---} \quad n=10$ 
 $\text{---} \quad n=30$

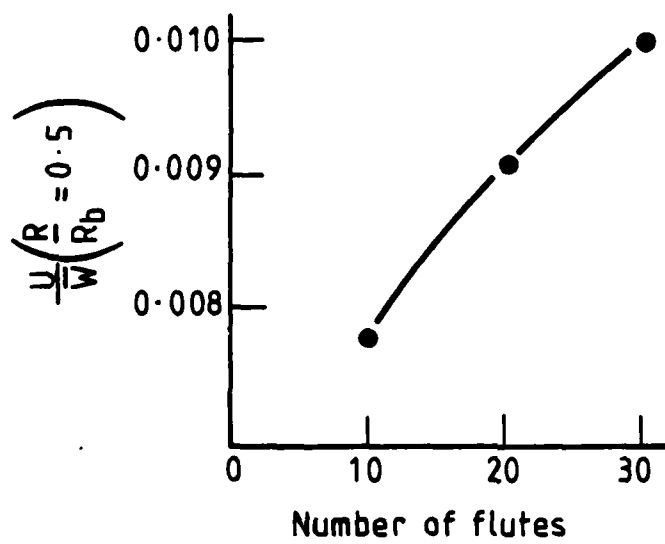


Fig. 3.13 Swirl imparted at  $R/R_b = 0.5$  for different number of flutes ( $Re \approx 300$ )

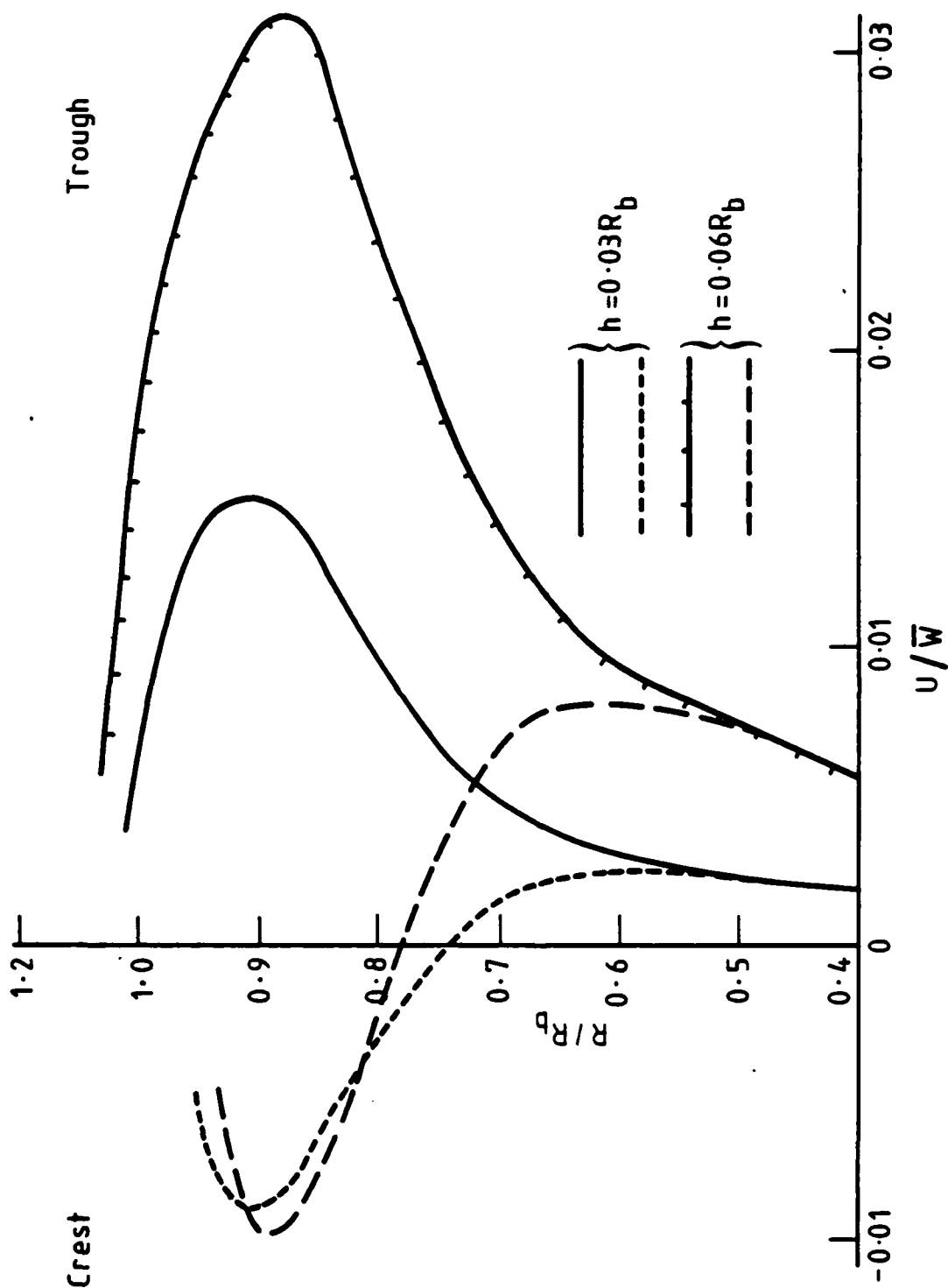


Fig. 3.14 Effect of flute height on circumferential velocity profile along crest and trough radii  $n = 10$ ,  $\omega = 15^\circ$ ,  $Re = 297$

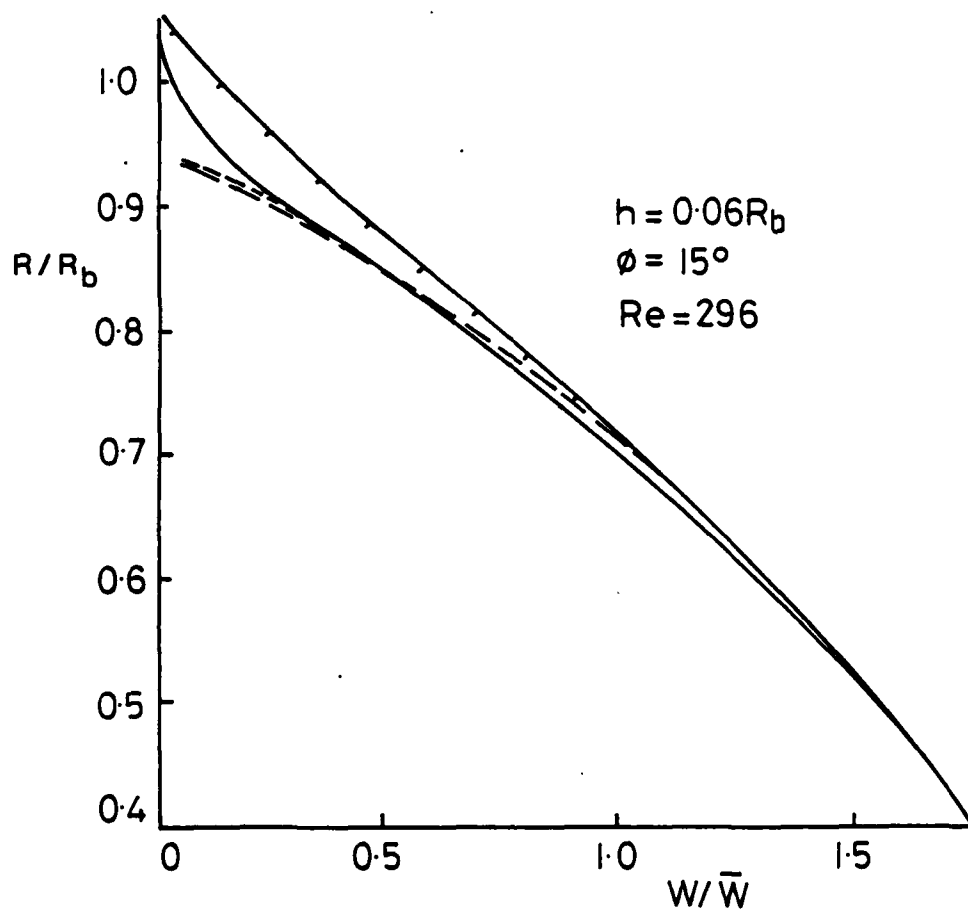


Fig 3-15 Effect of number of flutes on axial velocity profile along crest and trough radii

—•—•—•— n = 10      ——— n = 30  
- - - - -

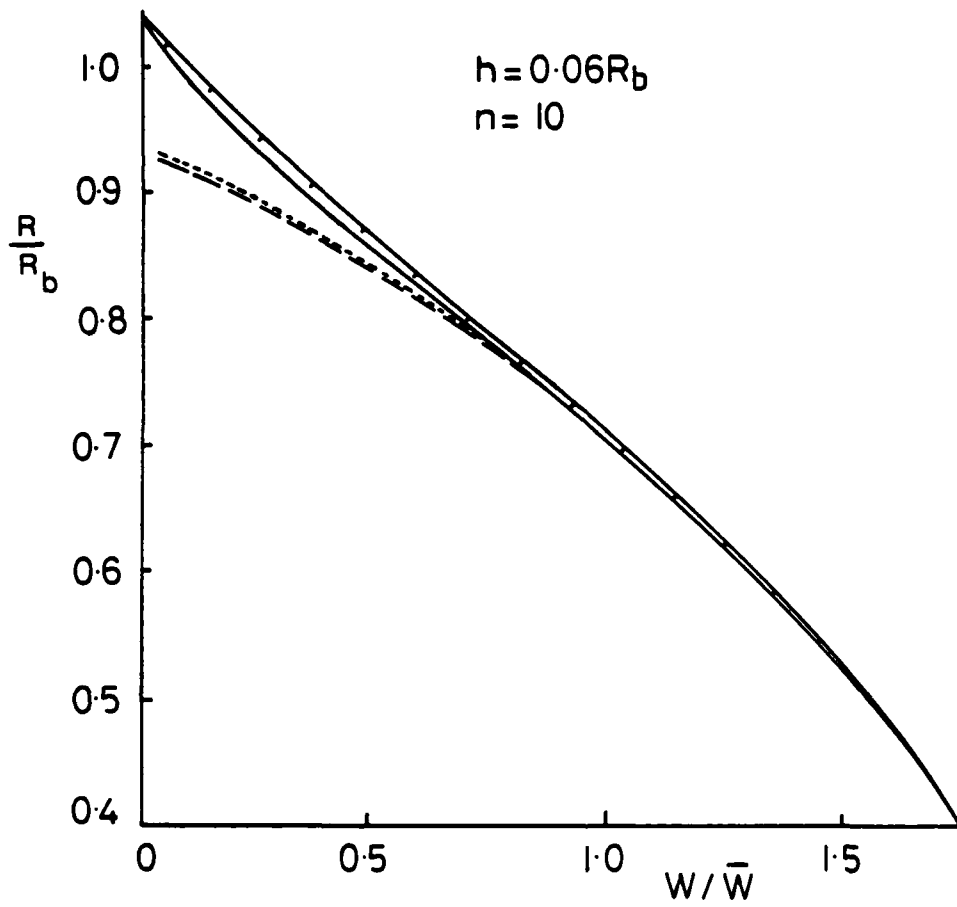


Fig 3-16 Effect of flute angle on axial velocity profile along trough and crest radii

$\text{---} \quad \phi = 0^\circ$        $\text{---} \quad \phi = 45^\circ$   
 $\text{---} \quad \text{---}$        $\text{---} \quad \text{---}$

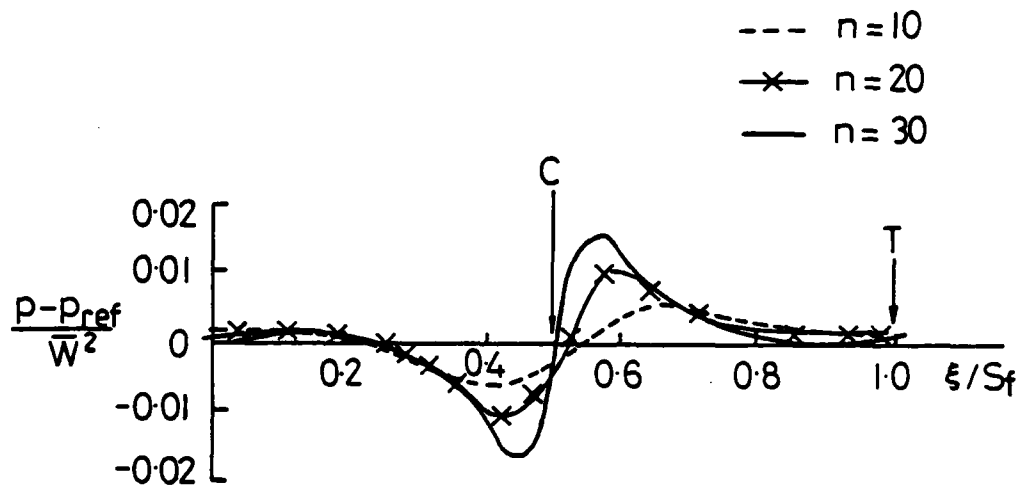


Fig 3-17 Distribution of static pressure  
around flute: Effect of number  
of flutes  $h = 0.06R_b$   $\Phi = 15^\circ$   
 $Re = 297$



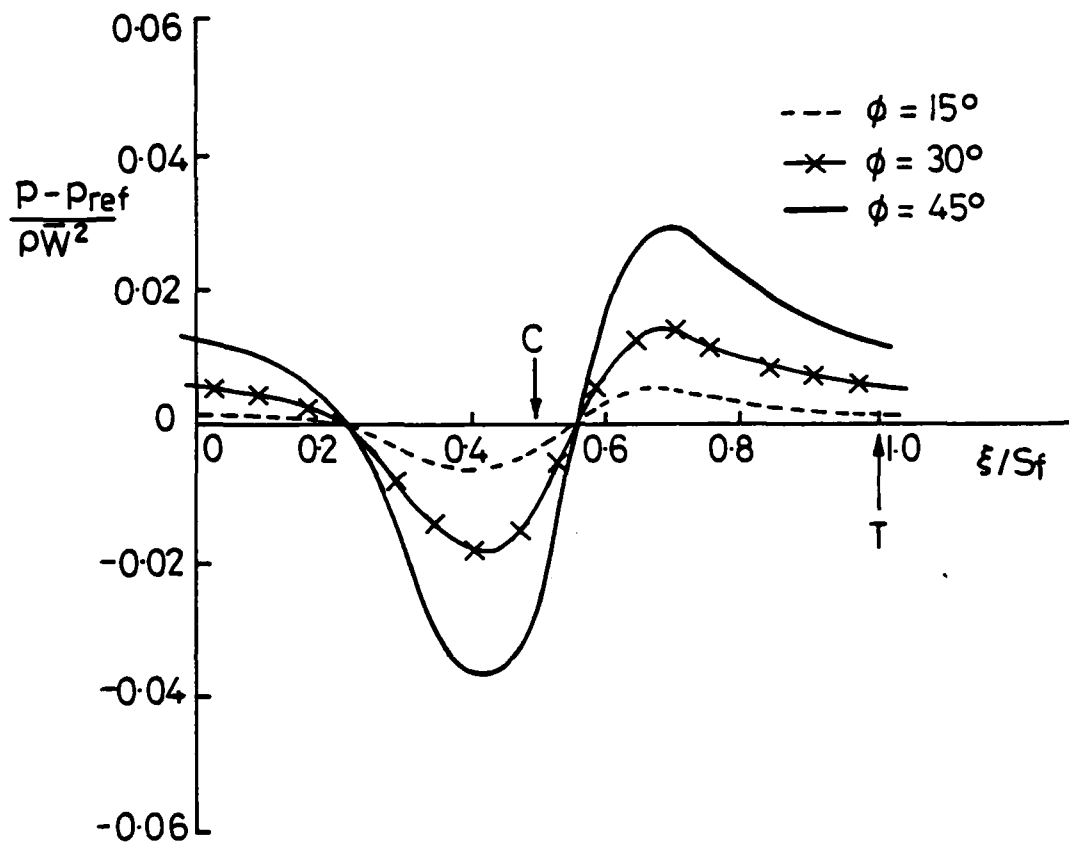


Fig 3-18 Distribution of static pressure around flute: effect of flute angle  $h = 0.06R_b$   $n = 10$   $Re = 297$

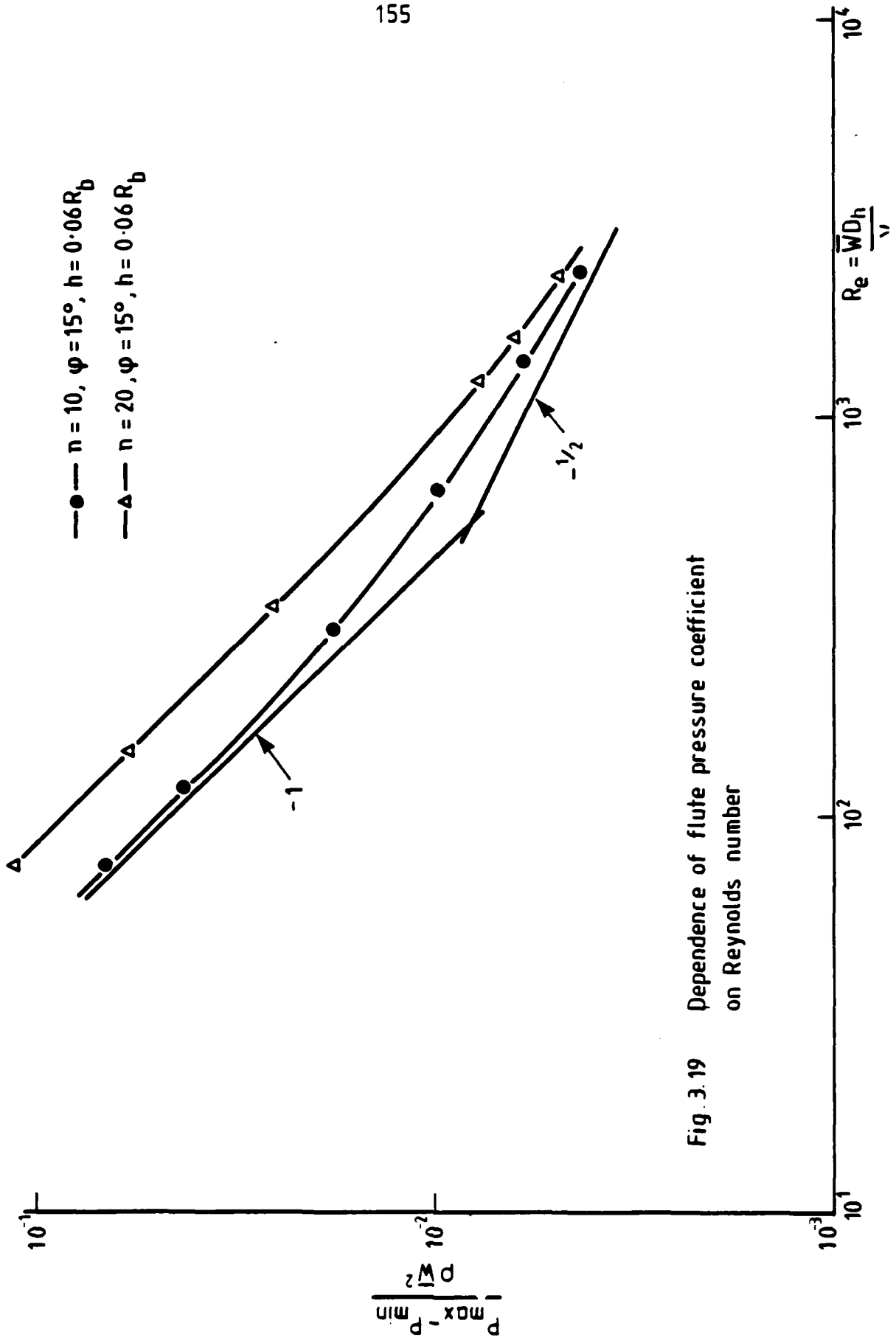
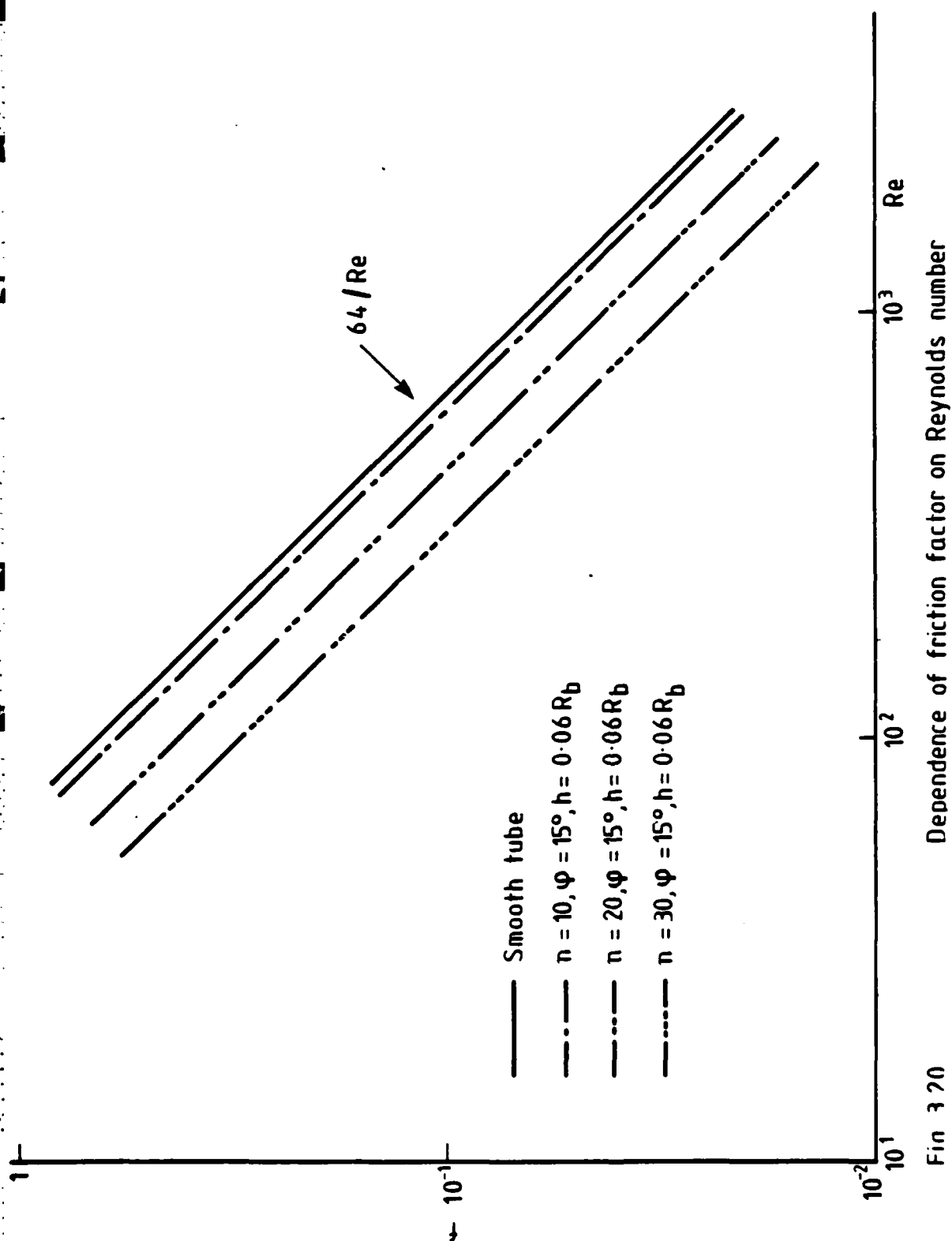


Fig. 3.19 Dependence of flute pressure coefficient on Reynolds number



Fin 3 20  
Dependence of friction factor on Reynolds number

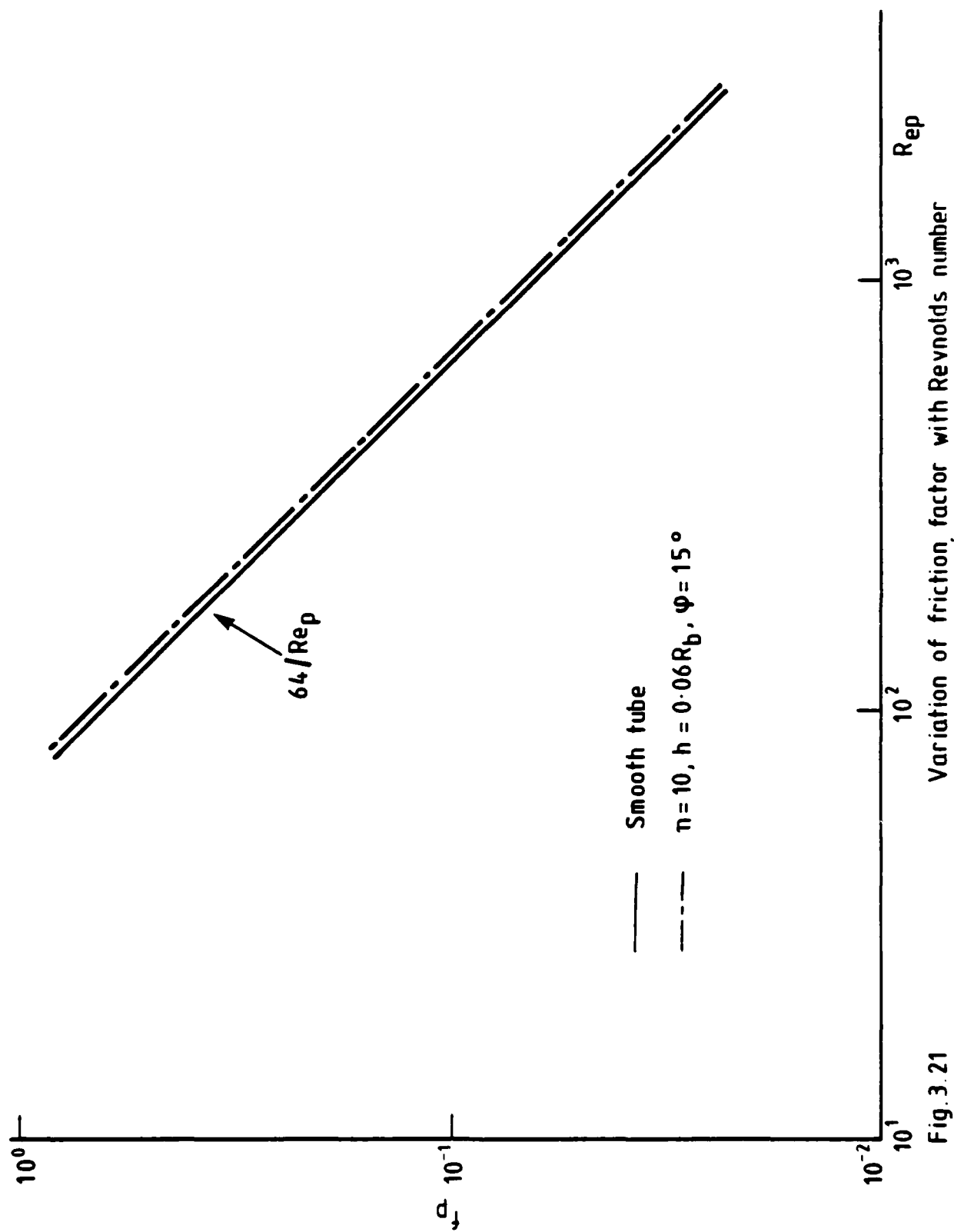


Fig. 3.21

AD-A150 774

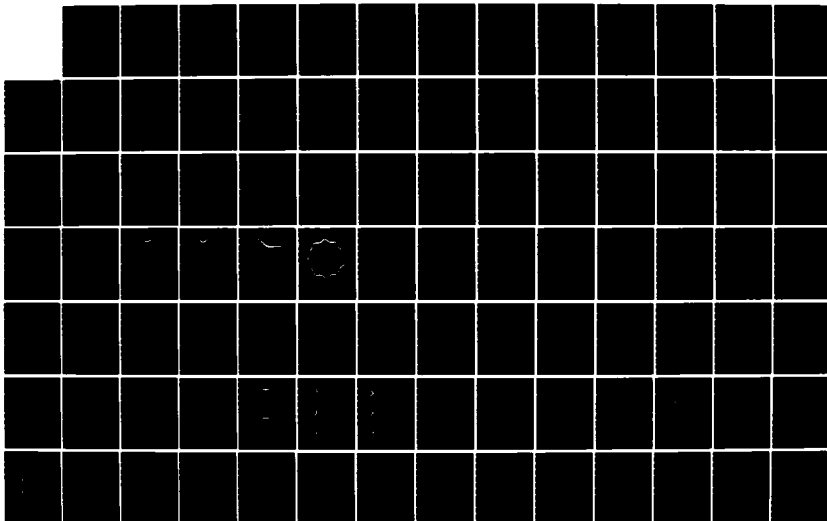
FLUID MECHANICS AND HEAT TRANSFER SPIRALLY FLUTED  
TUBING(U) GA TECHNOLOGIES INC SAN DIEGO CA  
J S YAMPOLSKY ET AL. DEC 84 GA-A17833 N00014-82-C-0721

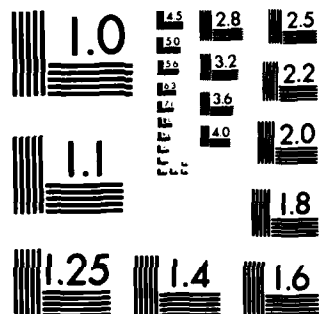
518

UNCLASSIFIED

F/G 28/4

NL





MICROCOPY RESOLUTION TEST CHART  
NATIONAL BUREAU OF STANDARDS-1963-A

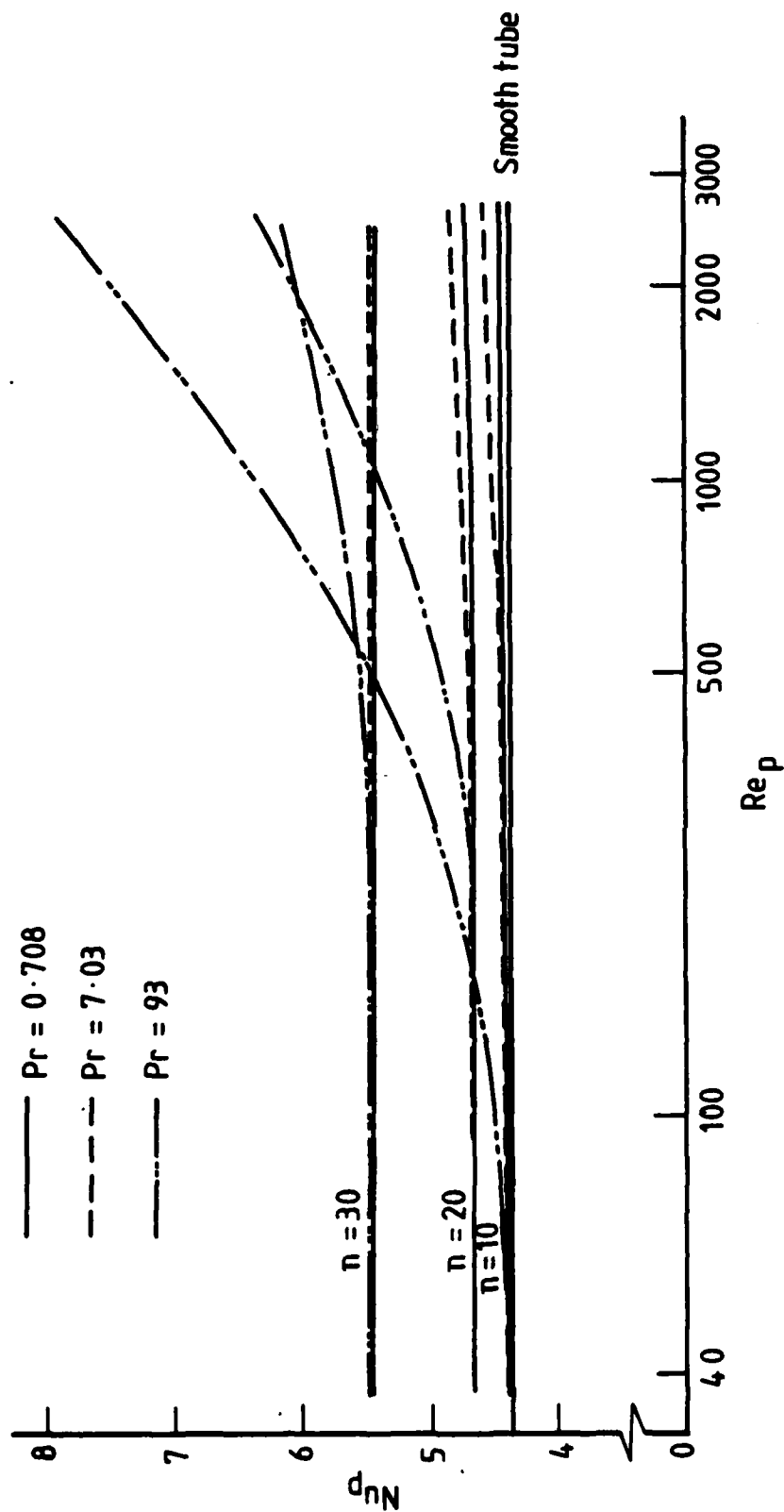


Fig. 3.22. Dependence of Nusselt number on Reynolds and Prandtl number for

$$\varphi = 15^\circ, \quad n = 10, 20, 30, \quad h = 0.06 R_b$$

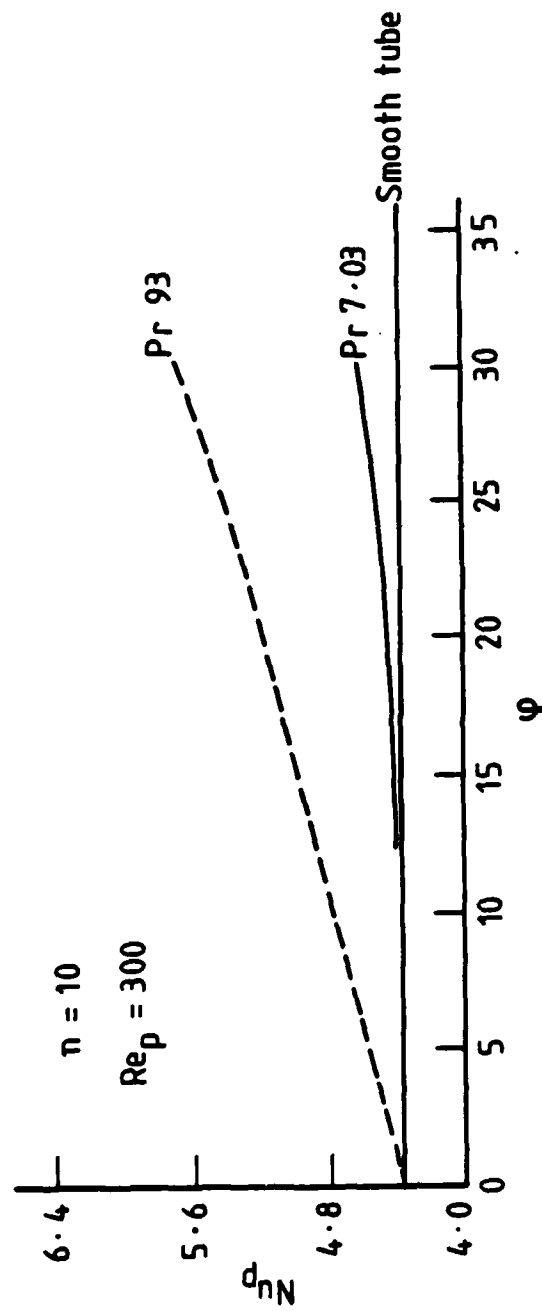


Fig. 3.23 Dependence of Nusselt number on spiral angle :  $h = 0.06 R_b$ ,  $n = 10$ ,  $Re_p = 300$



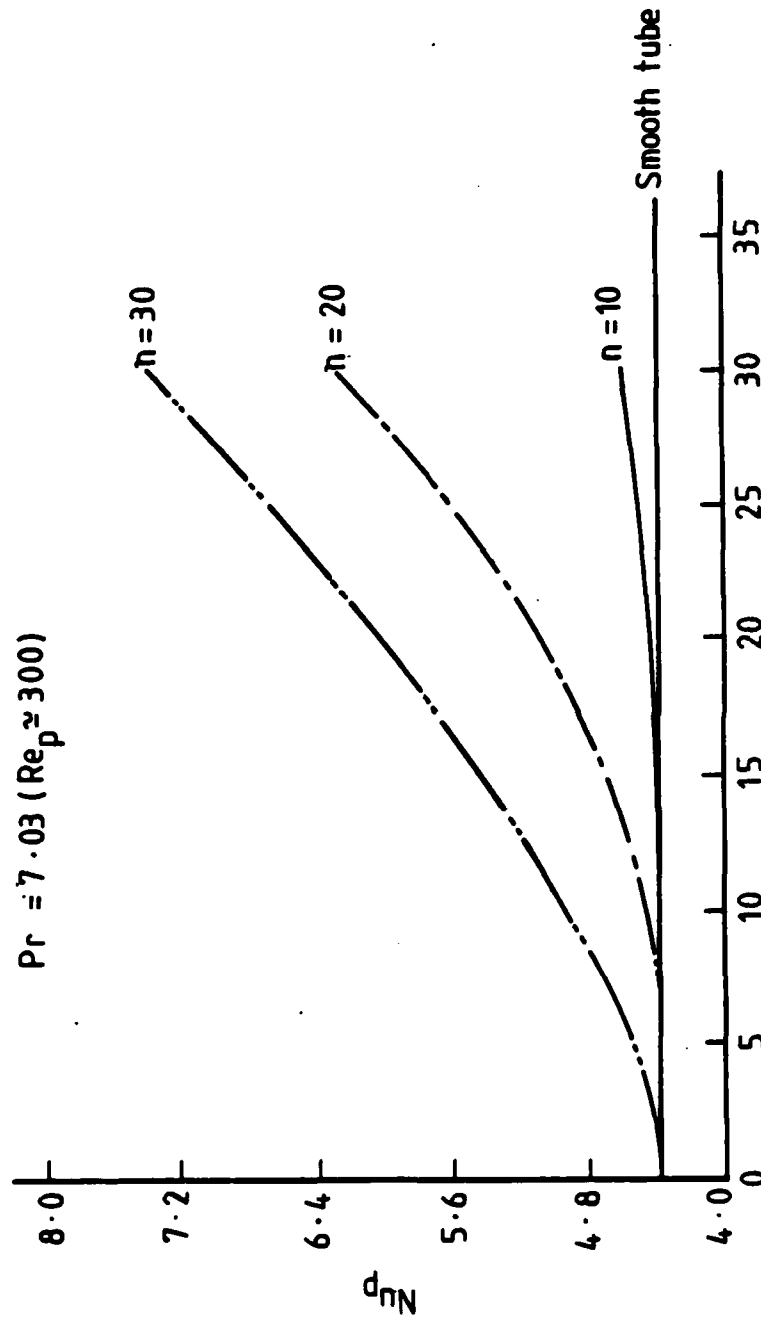


Fig. 3.24 Dependence of Nusselt number on spiral angle :  $h = 0.06 R_b, Re_p \approx 300$ ,

$Pr = 7.03$

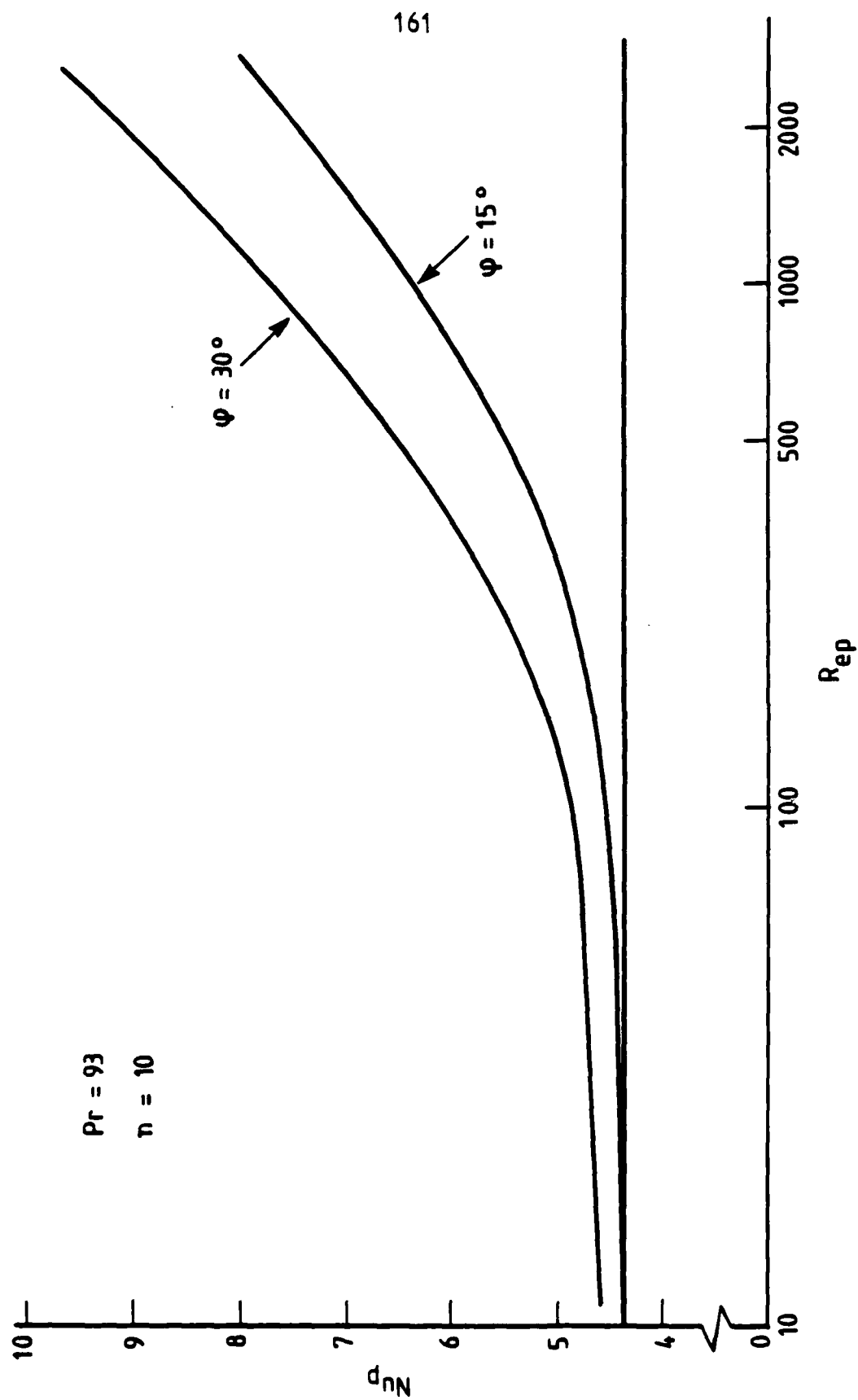


Fig. 3.25 Dependence of Nusselt number on Reynolds number and spiral angle :  $n = 10$ ,  $h = 0.06R_b$ ,  
Pr = 93

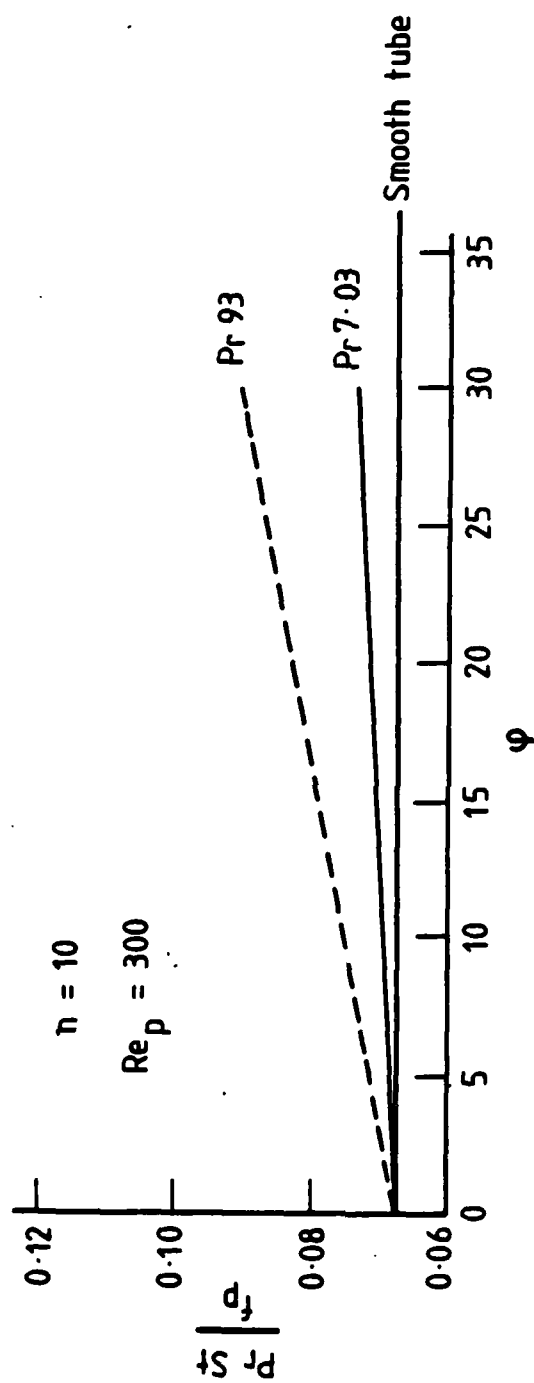


Fig. 3.26 Relative augmentation of heat transfer and friction factor

$h = 0.06 R_b$ ,  $n = 10$ ,  $Re_p \approx 300$

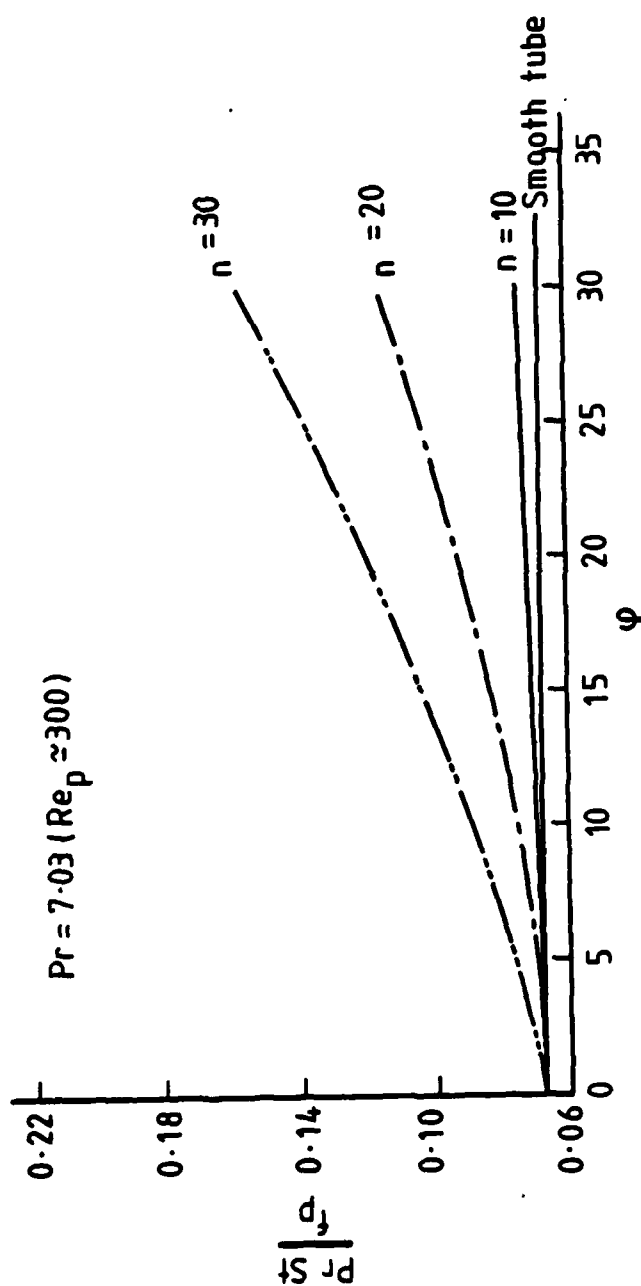


Fig. 3.27 Relative augmentation of heat transfer and friction factor:  $h = 0.06 R_b$ ,  $Re_p \approx 300$

$Pr = 7.03$

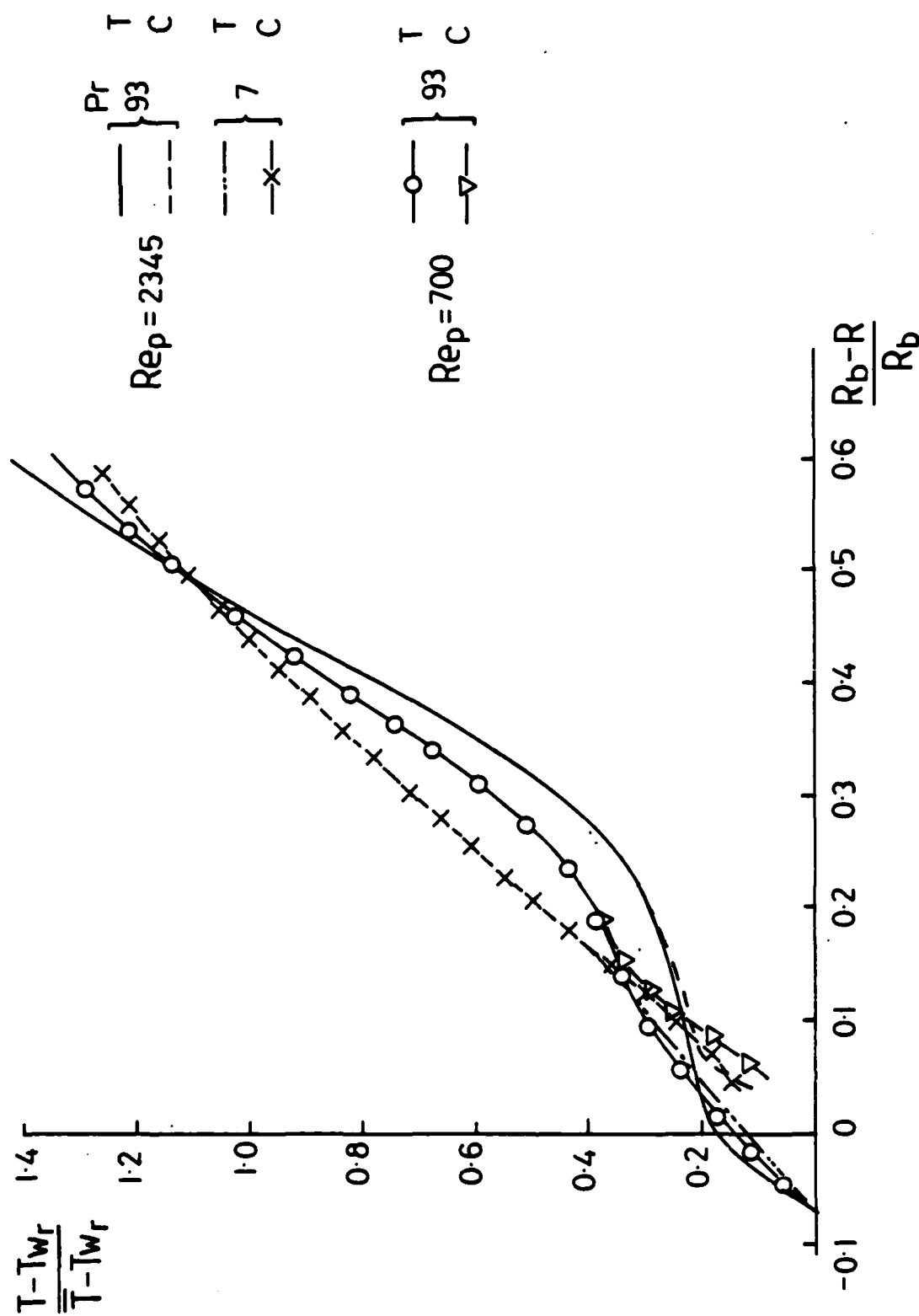


Fig 3-28 Dimensionless temperature profile  
 $n = 10$   $h = 0.06 R_b$   $\Phi = 15^\circ$

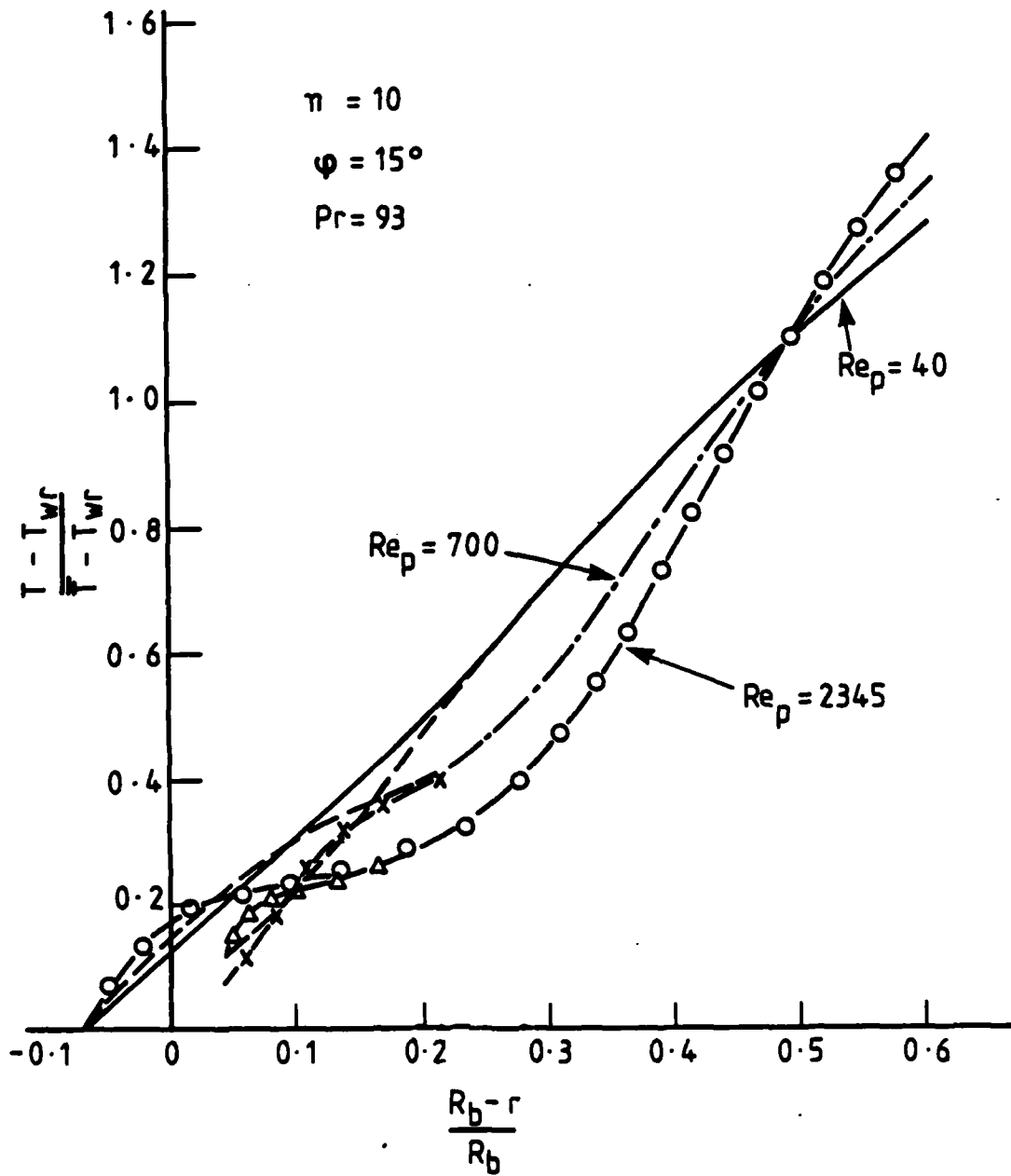


Fig. 3.29 Dimensionless temperature :  $n = 10$ ,  $\varphi = 15^\circ$ ,  $h = 0.06 R_b$   
 profiles  $Pr = 93$

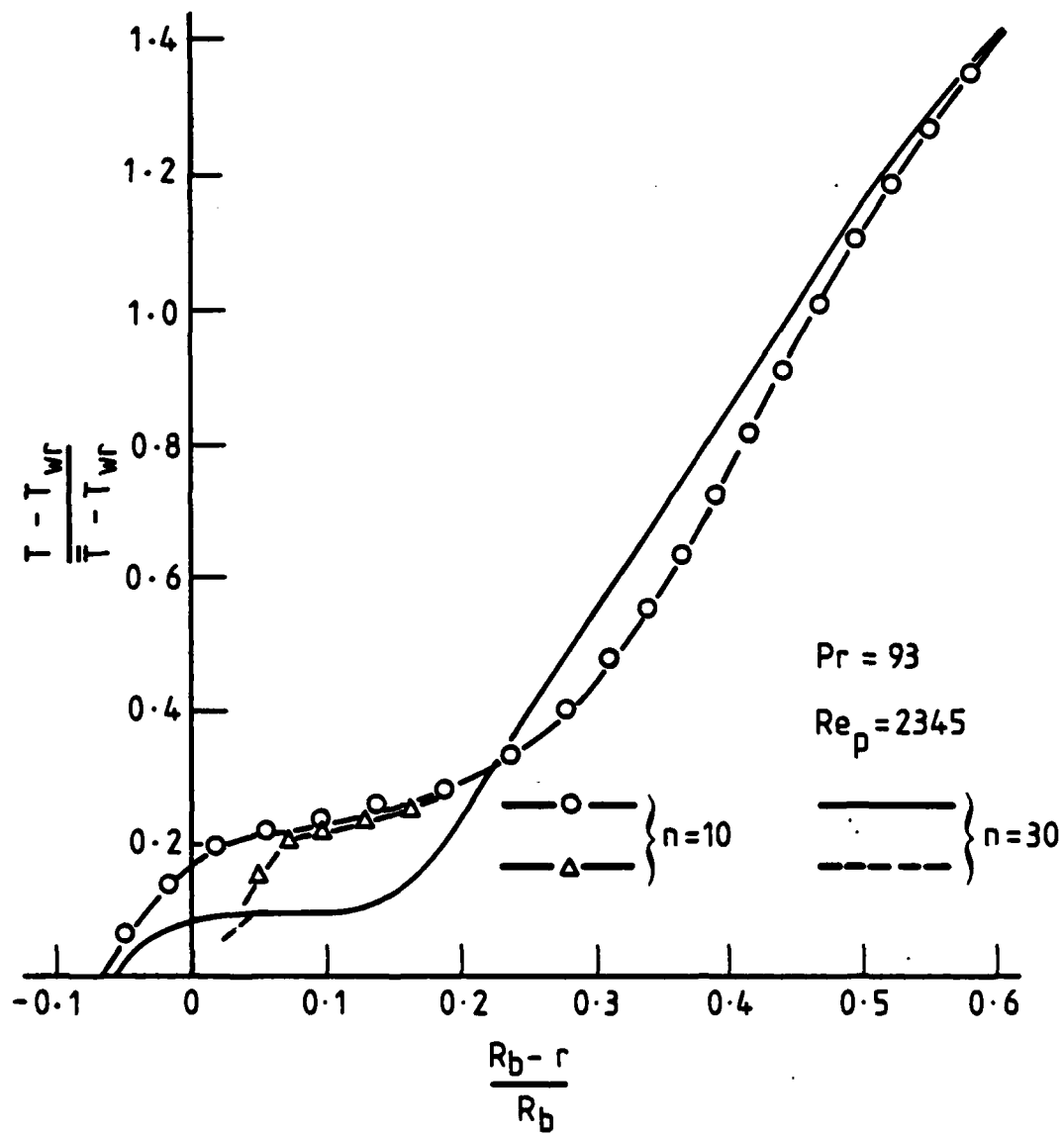


Fig. 3.30 Dimensionless temperature profile:  $\varphi = 15^\circ$ ,  $h = 0.06R_b$ ,  
 $Pr = 93$ ,  $Re_p = 2345$

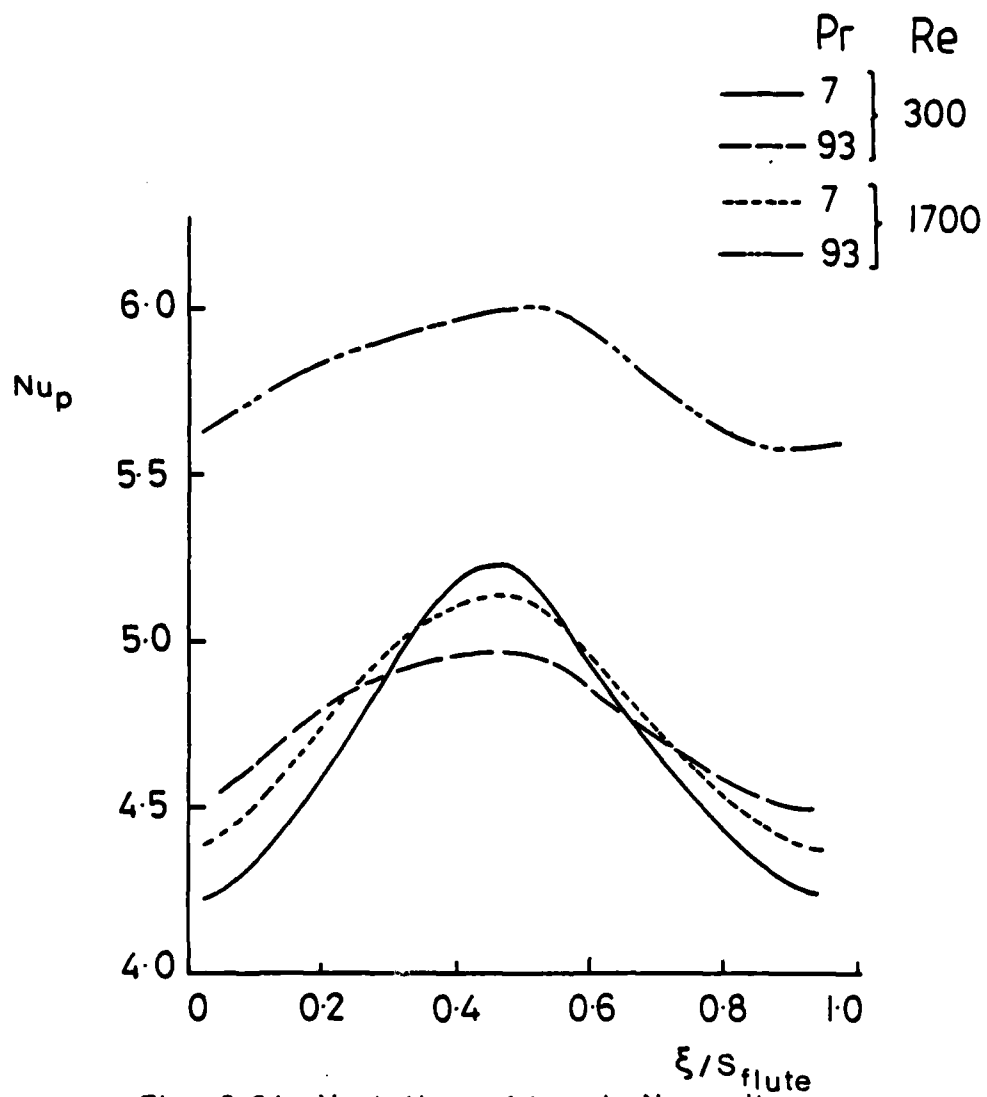


Fig 3-31 Variation of local Nusselt number around the flute  
 $h = .06R_b$   $n = 20$   $\Phi = 15^\circ$



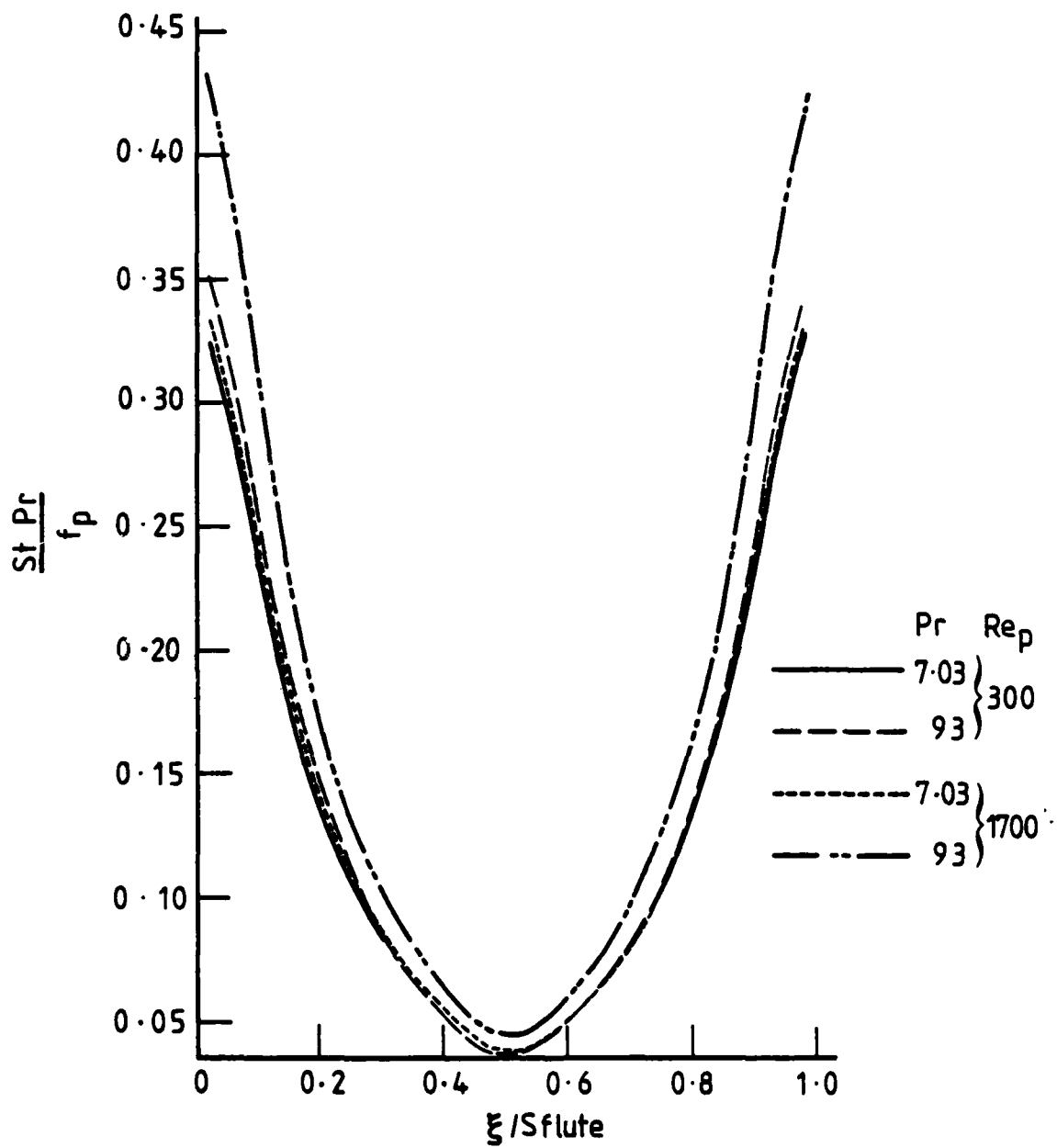


Fig. 3.32. Variation of local  $\frac{St \, Pr}{f_p}$  around the flute  
 $h = 0.06 R_b, n = 20, \varphi = 15^\circ$

CHAPTER 44. THE TURBULENT FLOW PROCEDUREIntroduction

The next step in the development of the procedure reported in Chapters 2 and 3 has been the calculation of turbulent flow since in this regime lie most of the industrial applications of spirally fluted tubes.

The present chapter reports all the modifications and additions made in the computational procedure (reported in Chapter 2) in order to handle turbulent flows. The following sections describe the grid adopted, the equations solved, the boundary conditions applied, the turbulence models used and the computational solution procedure followed in order to overcome the problems arising in the prediction of such a complex flow.

4.1 The Turbulence Models Adopted4.1.1 General Considerations

Although the usual practice in the solution of turbulent elliptic flows is to adopt wall functions for the near-wall region, apart from preliminary calculations, that practice has not been followed in the present work. It was felt that strong skewing of the velocity profile that occurs very near the flute surface could only be correctly predicted by adopting a fine grid and a low-Reynolds-number model of turbulence. So far as the choice of such a model was concerned, it was thought desirable, at least for this initial study, to adopt a simple turbulence model like the mixing

length hypothesis including already established viscous-damping effects for it was clear that the most important physical features to express were the suppression of turbulence by the flutes and the associated viscous flow behaviour.

For the rest of the solution domain, it was believed that a purely Boussinesq stress-strain law would not be sufficient to express the complex strain field of the flow. It seemed that the most appropriate model of turbulence to adopt was an algebraic stress closure (see Launder [92]). However, because of the complexity of the equations solved, instead of a full algebraic stress model, a  $k-\epsilon$  Boussinesq turbulence model has been used, followed by a simplified algebraic stress model to allow some of the conjectures on the physical mechanisms at work to be tested. The more complex turbulence models have been adopted in the region where a cylindrical-polar grid was applied (the grid description can be found in Section 4.2.1). The fact that the use of a cylindrical-polar grid for most of the solution domain had been found numerically beneficial for laminar flow computations was very fortunate since it was much easier to adopt an algebraically complex turbulence model in this region than in the region of the flutes where the curvilinear grid was applied.

A short description follows on the different turbulence models which have been adopted in different regions of the solution domain.

#### 4.1.2 Mixing Length Hypothesis

Within the immediate vicinity of the flutes, where molecular transport becomes significant, a fine mesh has been adopted (shown in Figure 4.1 for

three different geometries:  $n = 10, 20$  and  $30$ ). The turbulent viscosity  $\mu_t$  is prescribed by way of Prandtl's mixing length hypothesis with Van Driest's damping function. With this formulation

$$\mu_t = \rho l_m^2 \left| \frac{\partial w}{\partial \eta} \right| \quad (4.1)$$

where

$$l_m = \kappa y \left[ 1 - e^{-y^+/26} \right]$$

$$y^+ \equiv \frac{y \sqrt{\rho \tau_w}}{\mu}$$

$\kappa$  is the Von Karman constant here given the value  $0.4187$  (Patel and Head [108]),  $\rho$  is the density,  $\mu$  the laminar viscosity,  $\tau_w$  the local wall shear stress and  $y$  the distance from the node in question to the nearest node on the wall.

The choice of the equation for the turbulent thermal diffusivity  $\Gamma_t$  has been a difficult task since more than thirty analytical models of turbulent thermal transport processes have been reported in the last twenty-five years. An impression of the variety of the proposed models can be gained by studying the report of Reynolds [99]. Launder [98], reviewing Reynolds' [99] comprehensive survey of models for turbulent Prandtl numbers, classifies these in three groups depending on the idea behind their derivation:

- i) Mixing-Length models: where lumps of fluid are displaced from one region to another and in movement lose heat by conduction to the surrounding fluid;

- ii) Surface-Renewal models: similar to the previous group except that attention is focused on the "residence time" of an eddy;
- and iii) Lagrangian Diffusivity models: where the effective diffusivity is expressed in terms of Lagrangian length scales.

Although Patankar [96] uses a constant turbulent Prandtl number of 0.9 for his study of turbulent boundary layers with pressure gradients, our computations of smooth tubes have shown that Cebeci's model [94] gives better agreement with the experimental data reported by Kays [97]. In this case the maximum error in Nusselt numbers was 2.5% for a calcium chloride solution ( $Pr = 19.6$ ) and high Reynolds numbers.

Cebeci [95] gives an expression for the turbulent Prandtl number as a function of molecular Prandtl number for the near-wall region and a constant, 0.9, for the rest of the solution domain. Cebeci reports that his model gives results in good agreement with the experimental data for low, medium and high molecular Prandtl numbers. He also reports that several incompressible turbulent flows have shown that with variable turbulent Prandtl numbers the temperature profiles are in better agreement with experiments than those obtained by using a constant turbulent Prandtl number. His equation for the turbulent thermal diffusivity has the form:

$$\tau = \rho l_h l_m \left| \frac{\partial W}{\partial \eta} \right| \quad (4.2)$$

where

$$l_h = \kappa' y \left[ 1 - e^{-y^+/B^+} \right]$$

$$\kappa' = 0.44$$

$$B^+ = B^{++}/\sqrt{Pr}$$

$B^{++}$  is given in reference [95] in graphical form and to which the following expressions have been fitted in the present study:

$$B^{++} = 476.2 Pr^2 - 188.1 Pr + 38.57, \quad 0.02 \leq Pr \leq 0.3$$

$$B^{++} = 0.102 Pr^2 + 9.08 Pr + 22.4, \quad 0.3 < Pr < 7$$

$$B^{++} = 5.16 Pr + 58.9, \quad 7 \leq Pr$$

#### 4.1.3 The k-ε Boussinesq Viscosity Model

Except for the thin region around the flutes, the k-ε Boussinesq viscosity model, described in Jones and Launder [68] and Launder and Spalding [100], has been used in its high Reynolds number form to determine the turbulent viscosity  $\mu_t$ :

$$\mu_t = c_\mu \rho k^2 / \epsilon \quad (4.3)$$

where the turbulent kinetic energy  $k$  and its rate of viscous dissipation  $\epsilon$  were obtained from the following approximate transport equations:

#### k equation

$$\begin{aligned} \frac{\Delta}{\Delta \xi} (\rho U k) + \frac{\Delta}{\Delta \eta} (\rho V k) &= \frac{\Delta}{\Delta \xi} \left[ \Gamma_k \frac{\partial k}{\partial \xi} \right] + \frac{\Delta}{\Delta \eta} \left[ \Gamma_k \frac{\partial k}{\partial \eta} \right] \\ &+ \frac{\Delta}{\Delta \xi} (\kappa_\xi \rho W k) + \frac{\Delta}{\Delta \eta} (\kappa_\eta \rho W k) \\ &- \frac{\Delta}{\Delta \xi} \left[ \kappa_\xi \Gamma_k \left( -\kappa_\xi \frac{\partial k}{\partial \xi} - \kappa_\eta \frac{\partial k}{\partial \eta} \right) \right] \end{aligned}$$

$$\begin{aligned}
& - \frac{\Delta}{\Delta \eta} \left[ \kappa_{\eta} \Gamma_k \left( - \kappa_{\xi} \frac{\partial k}{\partial \xi} - \kappa_{\eta} \frac{\partial k}{\partial \eta} \right) \right] \\
& + G - \rho \cdot \epsilon
\end{aligned} \tag{4.4}$$

$\epsilon$  equation

$$\begin{aligned}
& \frac{\Delta}{\Delta \xi} (\rho U \epsilon) + \frac{\Delta}{\Delta \eta} (\rho V \epsilon) = \frac{\Delta}{\Delta \xi} \left[ \Gamma_{\epsilon} \frac{\partial \epsilon}{\partial \xi} \right] + \frac{\Delta}{\Delta \eta} \left[ \Gamma_{\epsilon} \frac{\partial \epsilon}{\partial \eta} \right] \\
& + \frac{\Delta}{\Delta \xi} (\kappa_{\xi} \rho W \epsilon) + \frac{\Delta}{\Delta \eta} (\kappa_{\eta} \rho W \epsilon) \\
& - \frac{\Delta}{\Delta \xi} \left[ \kappa_{\xi} \Gamma_{\epsilon} \left( - \kappa_{\xi} \frac{\partial \epsilon}{\partial \xi} - \kappa_{\eta} \frac{\partial \epsilon}{\partial \eta} \right) \right] \\
& - \frac{\Delta}{\Delta \eta} \left[ \kappa_{\eta} \Gamma_{\epsilon} \left( - \kappa_{\xi} \frac{\partial \epsilon}{\partial \xi} - \kappa_{\eta} \frac{\partial \epsilon}{\partial \eta} \right) \right] \\
& + c_1 \frac{\epsilon}{k} G - c_2 \rho \frac{\epsilon^2}{k}
\end{aligned} \tag{4.5}$$

At the pipe axis the boundary conditions

$$\frac{dk}{dr} = 0 \quad , \quad \frac{d\epsilon}{dr} = 0 \tag{4.6}$$

were applied.

In the above equations:  $\Gamma_k \equiv \mu + \frac{\mu_t}{\sigma_k}$  ;  $\Gamma_{\epsilon} \equiv \mu + \frac{\mu_t}{\sigma_{\epsilon}}$  , while the turbulence model coefficients were assigned the following standard values:

$$\sigma_k = 1.0$$

$$\sigma_{\epsilon} = c_{\mu}^{\frac{1}{2}} k^2 / (c_2 - c_1) = 1.21$$

$$c_1 = 1.44$$

$$c^2 = 1.92$$

$$K = 0.4187$$

$$c_\mu = 0.09$$

The turbulence energy generation rate  $G$  is given by

$$G = \frac{1}{2\mu_t} \left[ \left( \tau_{\xi\xi}^t \right)^2 + \left( \tau_{\eta\eta}^t \right)^2 + \left( \tau_{zz}^t \right)^2 + 2 \left[ \left( \tau_{\xi\eta}^t \right)^2 + \left( \tau_{\xi z}^t \right)^2 + \left( \tau_{\eta z}^t \right)^2 \right] \right] \quad (4.7)$$

where  $\tau_{\xi\xi}^t$  is the stress  $\tau_{\xi\xi}$ , given in Section 2.3, with  $\mu_t$  replacing  $\mu$  etc.

The turbulent thermal conductivity in the region where the  $k-\epsilon$  turbulence model has been used was obtained by assuming a constant turbulent Prandtl number of 0.9, so:

$$\Gamma_t = \mu_t / 0.9 \quad (4.8)$$

Launder and Spalding [100] in their study of numerical computation of turbulent flows conclude that, after application in a wide range of flows, the  $k-\epsilon$  model has been proved to be "the simplest kind of model that permits prediction of both near-wall and free-shear-flow phenomena without adjustments to constants or functions". They also point out the need for replacement of the isotropic viscosity formula by more general expressions connecting the stress and strain fields in turbulent flows. In this direction, the Algebraic-Stress-Model has been derived, a simplified form of which has been used in the present research and is described below.



#### 4.1.4 Simplified Algebraic-Stress-Model

The exact equation expressing the transport of Reynolds stresses for an incompressible buoyancy-affected fluid has the form:

$$\begin{aligned}
 \frac{D \overline{u_i u_j}}{Dt} = & - \underbrace{\left\{ \overline{u_i u_k} \frac{\partial U_j}{\partial x_k} + \overline{u_j u_k} \frac{\partial U_i}{\partial x_k} \right\}}_{P_{ij}} - \underbrace{\frac{\alpha}{T} \left\{ g_j \overline{u_i T'} + g_i \overline{u_j T'} \right\}}_{G_{ij}} \\
 & - \underbrace{2\nu \frac{\partial \overline{u_i}}{\partial x_k} \frac{\partial \overline{u_j}}{\partial x_k}}_{\epsilon_{ij}} - \underbrace{\frac{\overline{p'}}{\rho} \left( \frac{\partial \overline{u_i}}{\partial x_j} + \frac{\partial \overline{u_j}}{\partial x_i} \right)}_{\phi_{ij}} \\
 & - \underbrace{\frac{\partial}{\partial x_k} \left( \overline{u_i u_j u_k} + \delta_{jk} \frac{\overline{u_i p'}}{\rho} + \delta_{ik} \frac{\overline{u_j p'}}{\rho} - \nu \frac{\partial \overline{u_i u_j}}{\partial x_k} \right)}_{D_{ij}} \quad (4.9)
 \end{aligned}$$

where  $U$  and  $T$  stand for mean velocity and temperature respectively,  $u$  and  $T'$  for velocity and temperature fluctuations,  $p'$  for pressure fluctuation,  $\nu$  for kinematic viscosity and  $\delta_{ij}$  for the kronecker delta. Also,  $g_i$  is the body force per unit mass in direction  $x_i$  and  $\alpha$  the dimensionless volumetric coefficient of expansion given by the equation:

$$\alpha = - \frac{T}{\rho} \left( \frac{\partial \rho}{\partial T} \right)_p$$

In the above equation, terms  $P_{ij}$  and  $G_{ij}$  represent the production of the stresses  $\overline{u_i u_j}$ , term  $\epsilon_{ij}$  the dissipation, term  $\phi_{ij}$  the non-diffusive pressure interaction and term  $D_{ij}$  the diffusion. So, the above equation

can take the form:

$$\frac{D \overline{u_i u_j}}{Dt} = P_{ij} + G_{ij} - \epsilon_{ij} + \phi_{ij} + D_{ij} \quad (4.9a)$$

In this equation the stress generation terms  $P_{ij}$  and  $G_{ij}$  may be considered as exactly representable. However, in order to solve (4.9a), all the other terms must be modelled using correlations consisting of the mean velocities, Reynolds stresses and one or more parameters characterizing a length scale of turbulence or some parameter such as the turbulence energy dissipation rate (see Launder [107]). In local equilibrium approximation, the contribution of  $\frac{D \overline{u_i u_j}}{Dt}$  and  $D_{ij}$  is neglected. This leaves only the terms  $\epsilon_{ij}$  and  $\phi_{ij}$  to be modelled. The most widely recommended forms for high Re free flows (Launder [103]) are:

$$\epsilon_{ij} = \frac{2}{3} \delta_{ij} \epsilon \quad (4.10a)$$

$$\phi_{ij} = -c_1 \frac{\epsilon}{k} (\overline{u_i u_j} - \frac{2}{3} \delta_{ij} k) - c_2 (P_{ij} + G_{ij} - \frac{2}{3} \delta_{ij} (P + G)) \quad (4.10b)$$

where  $P = - \overline{u_i u_j} \frac{\partial u_i}{\partial x_j}$

and  $G = \frac{\alpha g_i}{T} \overline{u_i T'}$

Thus, the equation (4.9a) can be organized into the form:

$$\frac{(\overline{u_i u_j} - \frac{2}{3} \delta_{ij} k)}{k} = \left[ \frac{1 - c_2}{c_1} \right] \frac{(P_{ij} + G_{ij} - \frac{2}{3} \delta_{ij} (P + G))}{\epsilon} \quad (4.11)$$

which is known as the Algebraic Stress Model (ASM). The corresponding

exact form of the energy flux equation is:

$$\begin{aligned}
 \frac{D \overline{u_i T'}}{Dt} = & - \underbrace{\left( \overline{u_i u_k} \frac{\partial T}{\partial x_k} + \overline{T' u_k} \frac{\partial u_i}{\partial x_k} \right)}_{\text{I}} - \underbrace{\frac{\alpha \overline{T'^2} g_i}{T}}_{\text{II}} \\
 & - \underbrace{\left( \frac{\Gamma_T}{\rho} + \nu \right) \frac{\partial T'}{\partial x_k} \frac{\partial u_i}{\partial x_k}}_{\text{III}} + \underbrace{\frac{p}{\rho} \frac{\partial T'}{\partial x_i}}_{\text{IV}} \\
 & - \underbrace{\frac{\partial}{\partial x_k} \left( \overline{u_k u_i T'} + \frac{\overline{p t'}}{\rho} \delta_{ik} \right)}_{\text{V}}
 \end{aligned} \tag{4.12}$$

By ignoring terms III and V and modelling term IV (Launder [103]), the following equation is formed:

$$-\overline{u_i T'} = \phi_T \frac{k}{\epsilon} \overline{u_i u_k} \frac{\partial T}{\partial x_k} - \phi_T' \frac{k}{\epsilon} (P_{iT} + G_{iT}) \tag{4.13}$$

where  $\phi_T = 1/C_{1T}$  ;  $C_{1T} = 3.2$

$\phi_T' = \phi_T (1 - C_{2T})$  ;  $C_{2T} = 0.5$

$$P_{iT} = - \overline{u_k T'} \frac{\partial u_i}{\partial x_k}$$

$$G_{iT} = - \frac{\alpha g_i}{T} \overline{T'^2}$$

The original plan had been to explore fully the above equations. However, the extreme time for convergence of the solution procedure even with the k-ε model meant that this was not feasible. Therefore, it has been necessary to limit attention to two very much simplified forms of the above

equations, each of which reduces to the same form as the  $k-\epsilon$  Boussinesq viscosity model but with variable  $C_\mu$  and  $Pr_t$ .

Two distinct physical effects of swirl are considered which, in the case of the flow through a spirally fluted tube, are simultaneously present: (a) the effect of swirl associated with the additional strain it introduces, and (b) the effect of "buoyancy" in which, due to the swirl, heavy fluid packages are centrifuged preferentially outwards. Effect (a) arises through the term  $P_{ij}$ , while (b) is due to  $G_{ij}$ . Here, these two effects are considered separately so that the importance of each can be readily assessed. The limited aim of the study has been to ascertain whether the remarkable behaviour of spirally fluted tubes, which is not adequately predicted with purely isotropic models, can plausibly be attributed to either of the effects which, in other flows, these models have been found to mimic satisfactorily.

The forms of the equations adopted are strictly applicable only in flows remote from the influence of the wall. In the vicinity of the wall, pressure reflections from the surface modify the relative distribution of turbulence energy among the components. In the present work no additional terms have been introduced to simulate wall reflections. There were three reasons for this:

- 1) Corrections are only well established for a flat surface (Launder [10]) which, of course, is very different from a spirally fluted surface.
- 2) Even to use the plane flow corrections would greatly complicate the application of the model.

- 3) In the cylindrical polar region (which includes only the region up to  $0.8 R_0$ ) the effects of the wall pressure reflections are relatively minor.

(a) Swirl Flow Treatment

Younnis [102] has recently shown that for axisymmetric swirling flows equation (4.11) leads to broadly the correct development of free swirling jets if  $c_2 = 0.3$  and  $c_1 = 3.0$ . In cylindrical polar co-ordinates, if only radial gradients are retained, the following expressions are obtained for the Reynolds stress components (see Launder, Reece, Rodi [93]):

$$-\overline{wv} = \frac{(1-c_2)}{c_1} \frac{k}{\epsilon} \overline{v}^2 \frac{\partial w}{\partial r} \left( 1 - \frac{(2-c_2)}{(1-c_2)} \frac{\overline{uw}}{\overline{v}^2} \frac{U/r}{\partial W/\partial r} \right) \quad (4.14a)$$

$$-\overline{vu} = \frac{(1-c_2)}{c_1} \frac{k}{\epsilon} \overline{v}^2 \left( \frac{\partial U}{\partial r} - \frac{U}{r} \right) \left( 1 + \frac{(2-c_2)}{(1-c_2)} \frac{(\overline{v}^2 - \overline{u}^2)}{\overline{v}^2} \frac{U/r}{\left( \frac{\partial U}{\partial r} - \frac{U}{r} \right)} \right) \quad (4.14b)$$

$$-\overline{uw} = \overline{wv} \frac{k}{\epsilon} \frac{1}{c_1} \left( \frac{U}{r} + (1-c_2) \frac{\partial U}{\partial r} \right) + \overline{vu} (1-c_2) \frac{k}{\epsilon} \frac{1}{c_1} \frac{\partial W}{\partial r} \quad (4.14c)$$

and 
$$\overline{v}^2 = \frac{2}{3} k \left[ 1 + \frac{(c_2-1)}{c_1} + \frac{3(2-c_2)}{c_1} \frac{\overline{vu}}{\epsilon} \frac{W}{r} \right] \quad (4.14d)$$

From the equations (4.14a) to (4.14d), the following equation can be formed:

$$-\overline{wv} = \frac{\partial W}{\partial r} \frac{k^2}{\epsilon} \frac{\overline{v}^2}{k} \frac{(1-c_2)}{c_1} \frac{1}{\left[ 1 + \frac{(2-c_2)}{c_1^2} \frac{U}{r} \frac{k^2}{\epsilon^2} \left( \frac{U}{r} + (1-c_2) \frac{\partial U}{\partial r} \right) \right]} \quad (4.15a)$$

which can also be presented as:

$$-\bar{w}v = \frac{\partial W}{\partial r} \frac{k^2}{\epsilon} c_\mu \quad (4.15b)$$

where

$$c_\mu = \frac{\bar{v}^2}{k} \frac{(1-c_2)}{c_1} \frac{1}{\left[ 1 + \frac{(2-c_2)}{c_1^2} \frac{U}{r} \frac{k^2}{\epsilon^2} \left( \frac{U}{r} + (1-c_2) \frac{\partial U}{\partial r} \right) \right]} \quad (4.15c)$$

(b) Buoyancy Effects due to Swirl

From equations (4.11) and (4.13) (based on recommendations by Gibson and Launder[69] and Launder [104] and applied in the cylindrical-polar region of the solution domain where only the radial gradients are important) the following equations can be derived (see Appendix 4):

$$-\bar{w}v = \frac{\partial W}{\partial r} \frac{k^2}{\epsilon} \frac{\bar{v}^2}{k} B = \frac{\partial W}{\partial r} \frac{k^2}{\epsilon} c_\mu \quad (4.16)$$

and

$$-\bar{v}\theta' = \frac{\partial \Theta}{\partial r} \frac{k^2}{\epsilon} \frac{\Gamma 2/3 (1 - \Phi P^*/\epsilon)}{(1 - 2A\Gamma)} = \frac{\partial \Theta}{\partial r} \frac{k^2}{\epsilon} \frac{c_\mu}{Pr_t} \quad (4.17)$$

where

$$c_\mu = \left[ \frac{2}{3} (1 - \Phi P^*/\epsilon) - \frac{\Phi}{\epsilon} \frac{2\alpha g_r}{T} \bar{v}\theta' \right] \cdot B \quad (4.18)$$

$$B = \frac{\Phi}{(1 - \Phi\phi_{TA})} + \frac{\Phi\phi_{TA}'A}{\left[ (1 - \Phi\phi_{TA}) (1 - \phi_{TA}'c_{TA}'A) + \phi_{TA}'^2 \left( \frac{k}{\epsilon} \right)^2 \frac{U}{r} \frac{\partial U}{\partial r} \right]}$$

$$\Phi = \left( \frac{1 - c_2}{c_1} \right) = 0.204$$

$$A = \frac{\alpha g_r}{T} \left( \frac{k}{\epsilon} \right)^2 \frac{\partial \theta}{\partial r}$$

$$g_r = \frac{1}{r} \left( U^2 + \frac{2}{3} k \right)$$

$$Pr_t = c_\mu \frac{(1-2A\Gamma)}{r^{2/3} (1-\phi P^*/\epsilon)} \quad (4.20)$$

$$\text{and } \Gamma = \frac{\phi_T (1 - \phi_T \phi A)}{\left[ (1 - \phi \phi_T A) (1 - \phi_T' c_T' A) + \phi_T' \left( \frac{k}{\epsilon} \right)^2 \frac{U}{r} \frac{\partial U}{\partial r} \right]} \quad (4.21)$$

$\theta$  being the temperature difference ( $T - T_{ref}$ ),  $\theta'$  its fluctuation and  $P^* = P + G$ .

Gibson and Launder [69] have applied a slightly more elaborate form of equations (4.18) and (4.20) to the calculation of horizontal shear flows. The physics of gravitational modification to turbulent mixing of such flows is analogous to that of the radial centrifuging of heavy eddies in a spirally fluted tube, due to the swirling motion induced. In the latter case, the effective "gravitational acceleration" is  $U^2/r$  and, unlike  $g$ , varies from point to point in the flow.

#### 4.1.5 Matching the Near-Wall and Fully Turbulent Regions

For most of the results, discussed in the next chapter, two turbulence models have been used at the same time in different regions of the solution domain: the mixing-length hypothesis with the Van Driest damping function (see Section 4.1.2) for the low-Reynolds-number region near the tube wall,

and the  $k$ - $\epsilon$  Boussinesq viscosity model (see Section 4.1.3) in the region where molecular effects were negligible. The junction of the two turbulence models has been achieved by applying, at the first  $\xi$ -direction row of cells just outside the  $k$ - $\epsilon$  region and inside the mixing-length hypothesis region, the following boundary conditions for turbulent energy  $k$  and its dissipation  $\epsilon$ :

$$k = \left( \frac{\epsilon \mu_t}{\rho \cdot c_\mu} \right)^{1/2} \quad (4.22)$$

where  $\epsilon = \frac{G}{\rho} \quad (4.23)$

$G$  is the generation term given by equation (4.7) and calculated using the values from the mixing-length region, including  $\mu_t$ . The same applies for equation (4.22) where, again,  $\mu_t$  is calculated from equation (4.1):

$$\mu_t = \rho l m^2 \left| \frac{\partial W}{\partial \eta} \right|$$

For some of the results, discussed in Chapter 5, a third turbulence model has been added to the previous two. Two forms of the simplified algebraic-stress model (see Section 4.1.4) have been applied separately to the core region of the tube. Figure 4.2 shows the regions of application of the various turbulence models.

## 4.2 Numerical Aspects of Treatment for Turbulent Flows

### 4.2.1 The Describing Equations and Boundary Conditions

As in the laminar flow calculations, attention was limited to turbulent flows which were fully developed in the direction following the



spiralling of the flutes ( $\zeta$ ). The flow field was analysed over the region shown in Figure 4.3 created by the grid-program reported in Appendix 1 and Section 2.2 of Chapter 2. However, the numerical computations of turbulent flows were not confined to the region bounded by radius  $R_a$  but extended to the pipe axis. Since it had been proved experimentally that, over a substantial proportion of the core, circumferential variations were entirely negligible, for radii less than  $R_a$ , the describing equations have been solved along just one radial string of nodes with circumferential variations set to zero in order to save core memory and computing time. The above practice has been adopted for, unlike laminar flow, there is no analytical solution to which the flow could be matched at some radius  $R_a$ . Figure 4.4 shows the grid coverage of the complete cross-stream plane of the tube. The co-ordinate system used has been described in Section 2.2. The main differences are the values of the boundary radius  $R_a$  and the matching radius  $R_m$  as well as the way  $h_o/h$  decreases from one at the tube wall to zero at  $R_m$ . For the turbulent flow computations,  $R_a$  has been chosen  $0.54 R_b$  (or  $0.65 R_b$  for 20 and 30 flutes) because it was expected that solid body rotation would affect a larger part of the flow than for the laminar regime, while  $R_m$  took the value  $0.88 R_b$  since a better distribution of nodes was produced. Because (as explained later) a very fine grid was required near the tube wall, a linear decrease of  $h_o/h$  was no longer suitable. Figure 4.5 shows the new distribution of  $h_o/h$  given by the equation

$$\frac{h_o}{h} = \left[ \frac{2}{\pi} \left( \tan^{-1} \left( \frac{\beta}{\left( 1 - R_o/R_b \right) - \beta} \right) - \frac{\pi}{4} \right) \right]^Y \quad (4.24)$$

where  $\beta = \frac{1 - R_m/R_b}{2}$

and  $\gamma$  takes constant values depending on the number of flutes.

The continuity, momentum and energy equations solved have the form:

#### Continuity

$$\frac{\Delta}{\Delta \xi} (\rho U) + \frac{\Delta}{\Delta \eta} (\rho V) = \frac{\Delta}{\Delta \xi} (\kappa_{\xi} \rho W) + \frac{\Delta}{\Delta \eta} (\kappa_{\eta} \rho W) \quad (4.25)$$

#### $\xi$ -Momentum

$$\begin{aligned} \frac{\Delta}{\Delta \xi} (\rho U U) + \frac{\Delta}{\Delta \eta} (\rho U V) = & - \frac{\partial p}{\partial \xi} + \frac{\Delta}{\Delta \xi} (\mu_e \frac{\partial U}{\partial \xi}) \\ & + \frac{\Delta}{\Delta \eta} (\mu_e \frac{\partial U}{\partial \eta}) + \frac{\Delta}{\Delta \xi} (\kappa_{\xi} \rho U W) + \frac{\Delta}{\Delta \eta} (\kappa_{\eta} \rho U W) \\ & + \frac{\Delta}{\Delta \xi} (\tau_{\xi \xi} - \mu_e \frac{\partial U}{\partial \xi} - \kappa_{\xi} \tau_{\xi z}) + \frac{\Delta}{\Delta \eta} (\tau_{\xi \eta} - \mu_e \frac{\partial U}{\partial \eta} - \kappa_{\eta} \tau_{\xi z}) \\ & + (-\sigma + \kappa_{\xi} \lambda_{\xi} - \kappa_{\eta} \lambda_{\eta}) \times (\rho V W - \tau_{\eta z}) \\ & - \lambda_{\xi} (\rho U V - \tau_{\xi \eta}) + \lambda_{\eta} (\rho V^2 - \tau_{\eta \eta}) \end{aligned} \quad (4.26)$$

#### $\eta$ -Momentum

$$\begin{aligned} \frac{\Delta}{\Delta \xi} (\rho V U) + \frac{\Delta}{\Delta \eta} (\rho V V) = & - \frac{\partial p}{\partial \eta} + \frac{\Delta}{\Delta \xi} (\mu_e \frac{\partial V}{\partial \xi}) \\ & + \frac{\Delta}{\Delta \eta} (\mu_e \frac{\partial V}{\partial \eta}) + \frac{\Delta}{\Delta \xi} (\kappa_{\xi} \rho V W) + \frac{\Delta}{\Delta \eta} (\kappa_{\eta} \rho V W) \\ & + \frac{\Delta}{\Delta \xi} (\tau_{\eta \xi} - \mu_e \frac{\partial V}{\partial \xi} - \kappa_{\xi} \tau_{\eta z}) + \frac{\Delta}{\Delta \eta} (\tau_{\eta \eta} - \mu_e \frac{\partial V}{\partial \eta} - \kappa_{\eta} \tau_{\eta z}) \\ & + (\sigma - \kappa_{\xi} \lambda_{\xi} + \kappa_{\eta} \lambda_{\eta}) \times (\rho U W - \tau_{\xi z}) \\ & + \lambda_{\xi} (\rho U^2 - \tau_{\xi \xi}) - \lambda_{\eta} (\rho U V - \tau_{\xi \eta}) \end{aligned} \quad (4.27)$$

z-Momentum

$$\begin{aligned}
\frac{\Delta}{\Delta \xi}(\rho UW) + \frac{\Delta}{\Delta \eta}(\rho VW) = & -\frac{\partial p}{\partial z} + \frac{\Delta}{\Delta \xi}(\mu_e \frac{\partial W}{\partial \xi}) \\
+ \frac{\Delta}{\Delta \eta}(\mu_e \frac{\partial W}{\partial \eta}) + \frac{\Delta}{\Delta \xi}(\kappa_\xi \rho WW) + \frac{\Delta}{\Delta \eta}(\kappa_\eta \rho WW) \\
+ \frac{\Delta}{\Delta \xi}(\tau_{\xi z} - \mu_e \frac{\partial W}{\partial \xi} - \kappa_\xi \tau_{zz}) + \frac{\Delta}{\Delta \eta}(\tau_{z\eta} - \mu_e \frac{\partial W}{\partial \eta} - \kappa_\eta \tau_{zz}) \quad (4.28)
\end{aligned}$$

Energy Equation

$$\begin{aligned}
\frac{\Delta}{\Delta \xi}(\rho U \Theta) + \frac{\Delta}{\Delta \eta}(\rho V \Theta) + \frac{\Delta}{\Delta \zeta} \left( \frac{h_\zeta}{b} \rho W T_{\text{ref}} \right) \\
= \frac{\Delta}{\Delta \xi} \left( \Gamma_e \frac{\partial \Theta}{\partial \xi} \right) + \frac{\Delta}{\Delta \eta} \left( \Gamma_e \frac{\partial \Theta}{\partial \eta} \right) + \frac{\Delta}{\Delta \xi}(\kappa_\xi \rho W \Theta) + \frac{\Delta}{\Delta \eta}(\kappa_\eta \rho W \Theta) \\
- \frac{\Delta}{\Delta \xi} \left[ \kappa_\xi \Gamma_e \left( -\kappa_\xi \frac{\partial \Theta}{\partial \xi} - \kappa_\eta \frac{\partial \Theta}{\partial \eta} + \frac{h_\zeta}{b} \frac{dT_{\text{ref}}}{d\zeta} \right) \right] \\
- \frac{\Delta}{\Delta \eta} \left[ \kappa_\eta \Gamma_e \left( -\kappa_\xi \frac{\partial \Theta}{\partial \xi} - \kappa_\eta \frac{\partial \Theta}{\partial \eta} + \frac{h_\zeta}{b} \frac{dT_{\text{ref}}}{d\zeta} \right) \right] \quad (4.29)
\end{aligned}$$

The undefined symbols appearing in the above equations have the following significance:

$$\begin{aligned}
\tau_{\xi\xi} &= 2\mu_e \left( \frac{\partial U}{\partial \xi} + \lambda_\xi V \right) & \tau_{\eta\eta} &= 2\mu_e \left( \frac{\partial V}{\partial \eta} + \lambda_\eta U \right) \\
\tau_{zz} &= 2\mu_e \left( -\kappa_\xi \frac{\partial W}{\partial \xi} - \kappa_\eta \frac{\partial W}{\partial \eta} \right) \\
\tau_{\xi\eta} &= \mu_e \left( \frac{\partial U}{\partial \eta} + \frac{\partial V}{\partial \xi} - \lambda_\xi U - \lambda_\eta V \right) \\
\tau_{\xi z} &= \mu_e \left( \frac{\partial W}{\partial \xi} - \kappa_\xi \frac{\partial U}{\partial \eta} - \kappa_\eta \frac{\partial U}{\partial \xi} + (\sigma - \kappa_\xi \lambda_\xi + \kappa_\eta \lambda_\eta) V \right) \\
\tau_{\eta z} &= \mu_e \left( \frac{\partial W}{\partial \eta} - \kappa_\xi \frac{\partial V}{\partial \xi} - \kappa_\eta \frac{\partial V}{\partial \eta} + (-\sigma + \kappa_\xi \lambda_\xi - \kappa_\eta \lambda_\eta) U \right)
\end{aligned}$$

The rest of the symbols are given in Section 2.3 of Chapter 2 (equation (2.9)).

For the core region (from the tube axis to radius  $R_a$ ) where no changes in the circumferential direction exist, the equations describing the flow (solved along one radial string of nodes) may be written:

$\xi$ -Momentum

$$\frac{d^2 U}{dr^2} = 0 \quad \text{or} \quad \frac{1}{r} \frac{d}{dr} \left[ r \mu_e \frac{dU}{dr} \right] = \mu_e \frac{U}{r^2} + \frac{dU}{dr} \frac{d\mu_e}{dr} \quad (4.31)$$

$\eta$ -Momentum

$$\frac{dp}{dr} = \rho \frac{U^2}{r} \quad (4.32)$$

$z$ -Momentum

$$\frac{1}{r} \frac{d}{dr} \left[ \mu_e r \frac{dW}{dr} \right] = \frac{dp}{dz} \quad (4.33)$$

Continuity Equation

$$v = 0 \quad (4.34)$$

Energy Equation

$$\frac{1}{r} \frac{d}{dr} \left[ r \Gamma_e \frac{d\theta}{dr} \right] = \rho W \frac{dT_{ref}}{dz} \quad (4.35)$$

Equations (4.31) - (4.35) can be easily derived from (4.25) - (4.29) after applying the simplifications associated with the core region.

The equations for turbulent kinetic energy  $k$  and its rate of dissipation  $\epsilon$  (4.4) and (4.5) for the one-dimensional region take the forms:

$k$ -Equation

$$\frac{1}{r} \frac{d}{dr} \left[ r \Gamma_k \frac{dk}{dr} \right] = -\mu_t \left( \frac{dW}{dr} \right)^2 + \rho \epsilon \quad (4.36)$$

$\epsilon$ -Equation

$$\frac{1}{r} \frac{d}{dr} \left[ r \epsilon \frac{d\epsilon}{dr} \right] = - \frac{\epsilon}{k} \left[ c_1 \mu_t \left( \frac{dW}{dr} \right)^2 - c_2 \rho \epsilon \right] \quad (4.37)$$

The finite volume discretization of the above equations and their successful incorporation into the computer code are presented in Section 4.2.2.

The boundary conditions are the same as those described in Section 2.4 for laminar flows except for the south boundary. At the tube surface the velocity components are all set to zero and a uniform heat flux is applied. The cyclic character of the flow from one flute to the next is achieved by setting the dependent variables at the left-hand boundary equal to those on the right and vice versa, in addition to the special treatment introduced in the sub-routine which solves the discretized form of the partial differential equations. At the tube axis the radial and circumferential velocity components are set to zero, as is the radial gradient of the streamwise component and the temperature. So, on the tube axis the conditions

$$U = 0, \quad V = 0, \quad \frac{dW}{dr} = 0, \quad \frac{d\theta}{dr} = 0 \quad (4.38)$$

have been applied.

#### 4.2.2 Discretization of the Partial Differential Equations

##### 4.2.2a Two-Dimensional Region

Equations (4.25) to (4.29) are identical to those presented in

Section 2.3 for the laminar regime except that the effective value of viscosity is used instead of the molecular one. Thus, all the equations derived in 2.5a may be taken over for the turbulent case, provided that  $\mu$  is replaced by  $\mu_e$ . Equations (4.4) and (4.5) for the turbulent kinetic energy  $k$  and its rate of viscous dissipation  $\epsilon$  can be converted to the general form of equation (2.13) (Section 2.5a) if we take

$$C_{\xi} = U - \kappa_{\xi} W, \quad C_{\eta} = V - \kappa_{\eta} W \quad (4.39)$$

while if  $\phi \equiv k$ :  $\Gamma_{\xi k} = \Gamma_k (1 + \kappa_{\xi}^2)$

$$\Gamma_{\eta k} = \Gamma_k (1 + \kappa_{\eta}^2)$$

$$B_k = \frac{\Delta}{\Delta \xi} \left[ \kappa_{\xi} \Gamma_k \left( \kappa_{\eta} \frac{\partial k}{\partial \eta} \right) \right] + \frac{\Delta}{\Delta \eta} \left[ \kappa_{\eta} \Gamma_k \left( \kappa_{\xi} \frac{\partial k}{\partial \xi} \right) \right] + G$$

$$\Delta_k = -\rho^2 c_{\mu} \frac{k}{\mu_t} \quad (4.40)$$

and if  $\phi \equiv \epsilon$ :  $\Gamma_{\xi \epsilon} = \Gamma_{\epsilon} (1 + \kappa_{\xi}^2)$

$$\Gamma_{\eta \epsilon} = \Gamma_{\epsilon} (1 + \kappa_{\eta}^2)$$

$$B_{\epsilon} = \frac{\Delta}{\Delta \xi} \left[ \kappa_{\xi} \Gamma_{\epsilon} \left( \kappa_{\eta} \frac{\partial \epsilon}{\partial \eta} \right) \right] + \frac{\Delta}{\Delta \eta} \left[ \kappa_{\eta} \Gamma_{\epsilon} \left( \kappa_{\xi} \frac{\partial \epsilon}{\partial \xi} \right) \right]$$

$$+ c_1 G \rho c_{\mu} \frac{k}{\mu_t}$$

$$\Delta_{\epsilon} = -c_2 \rho \frac{\epsilon}{k} \quad (4.41)$$

The extra feature which must be introduced here is the treatment of the core region, namely the derivation of the finite-difference equations for

the one-dimensional region and their inclusion in the computer code.

#### 4.2.2b One-Dimensional Region

Since no circumferential variations are present in the core region (the radial velocity is zero (solid body rotation) and  $\kappa_\eta = 0$  (radial string of nodes) ) equation (2.13) takes the form:

$$\frac{\Delta}{\Delta\eta} \left( r_{\eta_\phi} \frac{\partial \phi}{\partial \eta} \right) + S_\phi = 0 \quad (4.42)$$

$$\text{or} \quad \frac{1}{r} \frac{d}{dr} \left( r \Gamma_\phi \frac{d\phi}{dr} \right) + S_\phi = 0 \quad (4.43)$$

where  $\phi$  may stand for  $U$ ,  $W$  or  $\theta$  (and  $k, \epsilon$  if the  $(k-\epsilon)$  turbulence model is used. Equations (4.43) and (4.31) - (4.37) yield:

$$\begin{aligned} \text{if } \phi \equiv U \quad \Gamma_U &= \mu_e \\ S_U &= -\mu_e \frac{U}{r^2} - \frac{dU}{dr} \frac{d\mu_e}{dr} \end{aligned} \quad (4.44)$$

$$\begin{aligned} \text{if } \phi \equiv W \quad \Gamma_W &= \mu_e \\ S_W &= -\frac{dp}{dz} \end{aligned} \quad (4.45)$$

$$\begin{aligned} \text{if } \phi \equiv \theta \quad \Gamma_\theta &= \Gamma_e \\ S_\theta &= -\rho W \frac{dT_{ref}}{dz} \end{aligned} \quad (4.46)$$

$$\begin{aligned} \text{if } \phi \equiv k \quad \Gamma_k &= \mu + \frac{\mu_t}{\sigma_k} \\ S_k &= \mu_t \left( \frac{dW}{dr} \right)^2 - \rho^2 c_\mu \frac{k^2}{\mu_t} \end{aligned} \quad (4.47)$$

and if  $\phi \equiv \epsilon$   $\Gamma_{\epsilon} = \mu + \frac{\mu_t}{\sigma_{\epsilon}}$

$$S_{\epsilon} = c_1 \mu_t \left( \frac{dW}{dr} \right)^2 - c_2 \rho \frac{\epsilon^2}{k} \quad (4.48)$$

Integrating equation (4.43) over the distance  $\Delta r$  shown in Figure 4.6, the following equation is formed:

$$r_n \Gamma_{\phi_n} \left( \frac{d\phi}{dr} \right)_n - r_s \Gamma_{\phi_s} \left( \frac{d\phi}{dr} \right)_s + S_{\phi_P} \Delta r = 0 \quad (4.49)$$

where n, s, P are north, south and middle positions respectively of the distance  $\Delta r$ , indicated in Figure 4.6. Analysing further the derivatives  $\frac{d\phi}{dr}$  equation (4.49) becomes:

$$r_n \Gamma_{\phi_n} \frac{\phi_N - \phi_P}{\Delta r} - r_s \Gamma_{\phi_s} \frac{\phi_P - \phi_S}{\Delta r} + S_{\phi_P} \Delta r = 0$$

or  $\left( r_n \Gamma_{\phi_n} + r_s \Gamma_{\phi_s} \right) \phi_P = r_n \Gamma_{\phi_n} \phi_N + r_s \Gamma_{\phi_s} \phi_S + S_{\phi_P} \Delta r^2 \quad (4.50)$

Equation (4.50) is similar to (2.38) since it can be written as:

$$A_P^{\phi} \phi_P = A_N^{\phi} \phi_N + A_S^{\phi} \phi_S + S U^{\phi} \quad (4.51)$$

where  $A_N^{\phi} = r_n \Gamma_{\phi_n}$

$$A_S^{\phi} = r_s \Gamma_{\phi_s}$$

$$A_P^{\phi} = r_n \Gamma_{\phi_n} + r_s \Gamma_{\phi_s} - S P^{\phi} = A_N^{\phi} + A_S^{\phi} - S P^{\phi}$$

$$S_{\phi_P} = S U^{\phi} + S P^{\phi} \phi \quad (4.52)$$



$$\begin{aligned}
 \text{while for } \phi \equiv U \quad SU^U &= - \left( \frac{dU}{dr} \frac{du_e}{dr} \right)_p \\
 SP^U &= - \left( \frac{\mu_e}{r^2} \right)_p
 \end{aligned} \tag{4.53}$$

$$\begin{aligned}
 \text{for } \phi \equiv W \quad SU^W &= - \frac{dp}{dz} \\
 SP^W &= 0
 \end{aligned} \tag{4.54}$$

$$\begin{aligned}
 \text{for } \phi \equiv \Theta \quad SU^\Theta &= - \rho W \frac{dT_{ref}}{dz} \\
 SP^\Theta &= 0
 \end{aligned} \tag{4.55}$$

$$\begin{aligned}
 \text{for } \phi \equiv k \quad SU^k &= \mu_t \left( \frac{dW}{dr} \right)^2 \\
 SP^k &= - \rho^2 c_\mu \frac{k}{\mu_t}
 \end{aligned} \tag{4.56}$$

$$\begin{aligned}
 \text{for } \phi \equiv \epsilon \quad SU^\epsilon &= c_1 \mu_t \left( \frac{dW}{dr} \right)^2 \\
 SP^\epsilon &= -c_2 \rho \frac{\epsilon^2}{k}
 \end{aligned} \tag{4.57}$$

The radial momentum equation is not solved in the core region since  $V = 0$  (equation (4.34)).

A detailed description of the computer code used for the solution of the above equations can be found in Appendix 5.

### 4.3 Experiences in Applying the Computer Program

#### 4.3.1 Use of the Mixing-Length Hypothesis for the Whole Solution Domain

The initial computations adopted the mixing-length hypothesis throughout the solution domain for the calculation of turbulent flows in a smooth pipe. The cross-stream section was covered by a polar grid with 44 radial nodes where, for the 20 nodes closest to the pipe axis, the dependent variables were held in a one-dimensional string. The matching radius  $R_a$  between the two-dimensional and the one-dimensional regions was  $0.9 R_b$  (although for a smooth tube a distinction between one-dimensional and two-dimensional regions in the solution domain is not necessary, this arrangement was maintained for uniformity) and the error found for the friction factor, compared with the values given from equation  $f = 0.3164 Re^{-0.25}$ , was about 0.4%. Although this accuracy in the calculation of friction factor was satisfactory, the fine grid used near the wall was very difficult to be achieved for the real geometry of the fluted wall. The problem was overcome by applying a cubic spline to represent the highly non-linear variations in turbulent transport coefficients at the surfaces of the scalar cells near the wall. This allowed acceptable accuracy with a relatively coarse grid. For example, the number of radial nodes needed for 0.4% accuracy in friction factor in the two-dimensional region could be decreased from 24 to 18, while an acceptable error of 0.8% was produced when the radial nodes were decreased further to 14. The above-mentioned cubic-spline treatment of the near-wall region has been maintained throughout the turbulent flow computations as long as the mixing-length hypothesis was applied.

The next step in the procedure was to switch to the real geometry

using the mixing-length hypothesis for the whole solution domain.

Computations have been made using 18 nodes to span the circumferential arc covering one flute and 40 radial nodes. Of the latter, 20 nodes mapped the one-dimensional region, while of the remaining 20 nodes, 12 were in the cylindrical-polar part and 8 in the curvilinear near the wall.

Figure 4.7 shows this grid where  $R_a = 0.4 R_b$ ,  $R_m = 0.88 R_b$ ,  $h = 0.06 R_b$ ,  $n = 10$  and  $\phi = 15^\circ$ .

Convergence of the solution proved to be difficult to secure. After many tests (for the grid used and the effect of each one of the equations on the solution convergence), the following combination of under-relaxation factors was found to give the best convergence behaviour (lowering the residuals to an acceptable level of  $1 \times 10^{-2}$  after 2000 iterations for a Reynolds number of  $3 \times 10^4$ ): for the  $\xi$ -direction velocity 0.6 increased to 0.7 after 500 iterations, for the  $\eta$ -direction velocity 0.6, for the axial velocity 0.8 decreased to 0.7 at about the same time the under-relaxation factor for  $U$  changes, for the pressure 1.0, and for viscosity 0.8. It should be pointed out that, as in the laminar flow computations (see Section 2.5b), the equations were solved by the recently developed PISO algorithm described in Issa [79], Gosman et al [80] and Appendix 3. This new algorithm allowed the use of high under-relaxation factors for pressure (1.0), thus improving the convergence rate of the solution procedure and reducing computing times.

For all the turbulent flow computations, the under-relaxation factors used for the one-dimensional region were the same with those applied in the rest of the solution domain.

#### 4.3.2 Use of the $k$ - $\epsilon$ Boussinesq Viscosity Model with Wall Functions

As an initial test, a coarse-grid wall-function approach has also been adopted in the numerical solution scheme. As in the case of the mixing-length hypothesis, the new model has been tested against the flow through a straight unfluted tube. Using a polar grid with 42 radial nodes from which 20 were covering the one-dimensional region from  $R_a = 0.3 R_b$  to the pipe axis, an agreement of 1% has been found for the friction factor compared with the value given by the analytical Blasius equation  $f = 0.3164 Re^{-0.25}$ .

The real geometry of the spirally fluted tube has been solved by using the grid shown in Figure 4.8 where  $R_a = 0.3 R_b$ ,  $R_m = 0.85 R_b$ ,  $h = 0.06 R_b$ ,  $n = 10$  and  $\phi = 15^\circ$ . Again, 18 nodes span the circumferential arc, while from the 42 radial nodes, 20 are in the one-dimensional region, 16 in the cylindrical-polar part of the grid and 6 in the curvilinear part near the wall. The solution converged easily after 1000 iterations to a level of  $1 \times 10^{-3}$  using the following under-relaxation factors: for the  $\xi$ -direction velocity 0.9, for the  $\eta$ -direction velocity 0.8, for the axial velocity 0.95, for the pressure 1.0, for viscosity 0.8 and for kinetic energy  $k$  and its dissipation  $\epsilon$  0.8. Figure 4.9 shows the induced swirl velocity on two radial lines passing through the trough and the crest of the flute for both the turbulence models used separately, mixing-length hypothesis and  $k$ - $\epsilon$  Boussinesq viscosity model. It is clear that the latter gives its maximum value at the near-wall node, so no certainty could be placed on this value.

#### 4.3.3 Combination of the Mixing-Length and k- $\epsilon$ Turbulence Models

A fine-grid analysis was introduced in the near-wall region where the mixing-length hypothesis with Van Driest's damping function was used to predict the low-Reynolds-number area, while in the rest of the solution domain the k- $\epsilon$  Boussinesq viscosity model was adopted, the changeover taking place as soon as all the nodes on a  $\xi$ -direction row of cells were located in fully turbulent flow. The grid used is shown in Figure 4.1. The solution for 10 flutes,  $15^\circ$  spiral angle and Reynolds number of  $3 \times 10^4$  converged to a level of  $5 \times 10^{-2}$  after 1700 iterations using the same under-relaxation factors as in the case mentioned in Section 4.3.1. However, bearing in mind that this geometry was the easiest one as far as the convergence of the solution procedure was concerned and the Reynolds number low, it was felt to be essential to explore ways of accelerating convergence rates and reducing computing times.

Arising from this exploration, the parabolic-sublayer treatment (PSL), described in Iacovides and Launder [105], has been adopted which has improved the rates of convergence for tubes with 10 flutes by a factor of 3, while giving final results that were negligibly different from those obtained by applying the elliptic solver throughout. For a turbulent elliptic flow, three alternative near-wall treatments can be applied, shown in Figure 4.10 (taken from Launder [106]), where since the computer code is based on a finite-volume discretization, a column of scalar cells normal to the wall has been drawn for each of the three methods. Column (a) presents the wall-function approach where the near-wall node is placed in fully turbulent fluid, while column (b) illustrates, the usual alternative to the use of wall functions, an elliptic fine grid over which some low-Reynolds-

number turbulence models are used (in our case, the mixing-length hypothesis). Column (c) shows the parabolic sublayer approach where, for a thin band in the immediate vicinity of the tube wall (covering 2 or 3 rows of control volumes next to the surface), the pressure is taken equal to that at the node just outside this band. So, no extra work has to be done for any pressure-correction procedure while the  $\eta$ -momentum equation is not solved, the values of  $V$  within this band being calculated by application of the continuity equation to each pressure control volume. For most of the runs, the PSL treatment has replaced the conventional elliptic treatment while its adaptation into the computer code is presented in Appendix 5.

As in the laminar flow computations for a given number of flutes, once a solution has been obtained, the effects of Reynolds number or variations in the tube geometry were examined using this existing solution as the initial field for the further studies. The velocity field was solved first and stored prior to solving the energy equation. For the latter, although the grids, shown in Figure 4.5, were quite fine near the wall, two extra grid points were placed in the row of cells attached to the wall in order to solve the high Reynolds numbers or high Prandtl numbers cases (see Appendix 5).

The rates of convergence depended greatly on the number of flutes and the Reynolds number. For 10 flutes the number of iterations required, starting from a uniform initial field, increased from about 500 at a Reynolds number of  $3 \times 10^4$  to approximately 850 for  $Re = 8 \times 10^4$ . The under-relaxation factors used were: 0.8 for the  $\xi$ -direction velocity and  $\eta$ -direction velocity, 0.9 for the axial velocity, 0.8 for the turbulence energy  $k$  and its dissipation  $\epsilon$ , 0.7 for the viscosity and 0.5 for pressure.

In the case of 30 flutes, complete convergence for  $Re = 3 \times 10^4$  has only been achieved after 7000 iterations, while for higher Reynolds numbers or higher spiral angles (i.e.  $\phi = 30^\circ$ ), no exact figure can be reported since the initial field used was the converged solution of a simpler case (lower  $Re$  or  $\phi = 15^\circ$ ). The under-relaxation factors used were: 0.7 for the  $\xi$ -direction velocity, 0.6 for the  $\eta$ -direction velocity, 0.9 for the axial velocity, 1.0 for pressure, 0.7 for viscosity, 0.7 for turbulence energy  $k$  and its dissipation  $\epsilon$ . In addition, the indices which set the number of times sub-routine LISOLV will be called to solve the discretized form of the equations were changed as follows from those used for 10 flutes: for the  $\xi$ -direction velocity  $U$  from 4 to 8, for pressure  $p$  from 4 to 2, while for axial velocity  $W$ ,  $\eta$ -direction velocity  $V$ , turbulence energy  $k$  and energy dissipation  $\epsilon$  were unchanged (10, 2, 2, 2 respectively). Computing times on a CDC 7600 for a (18, 40) grid were about 0.55 cps/iteration.

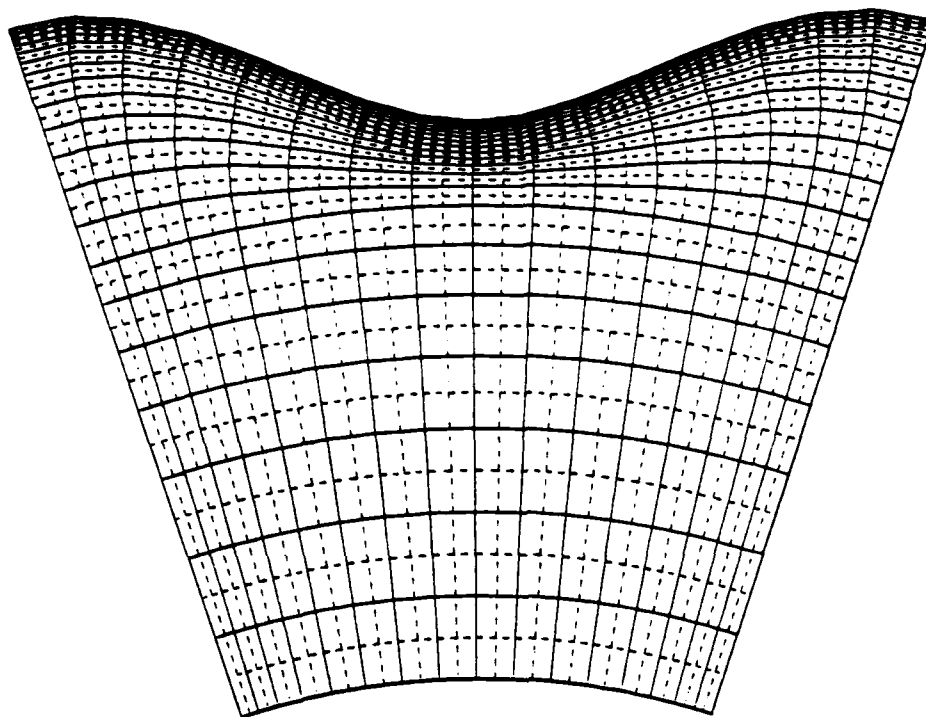
Figure 4.11 shows the distribution of the swirl velocity across trough and crest radii for the cases where the mixing-length model is matched with the  $k$ - $\epsilon$  scheme and where the  $k$ - $\epsilon$  model is matched to wall functions. It is obvious that the low-Reynolds-number mixing-length treatment gives levels of secondary flow some 25% higher than those predicted by wall functions. In view of the fact that with the latter treatment the maximum swirl velocity always occurred at the near-wall node, it was felt that little reliance could be placed on its value. Turning to heat transfer for 10 flutes,  $15^\circ$  spiral angle, the low-Reynolds-number treatment led to predicted Nusselt numbers for water ( $Pr = 7.03$ ) 20% higher than for a smooth tube, while the wall functions predicted only a 5% rise. In view of these indications, the low-Reynolds-number treatment was used for the

main programme of explorations.

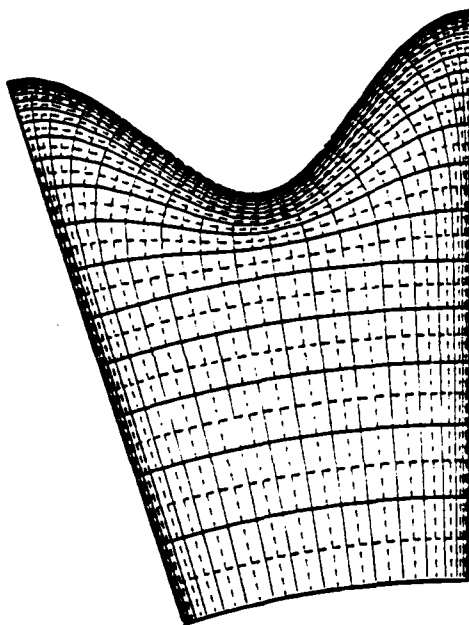
#### 4.3.4 Adaptation of a Simplified ASM in the Core Region of the Tube

In the final stages of the present project, a third type of turbulence model has been added in the core region of the flow; a simplified algebraic stress model. This scheme has been applied in the cylindrical-polar part of the grid as well as in the one-dimensional solution area where the fluid is in solid-body rotation (see Figure 4.2). The only change that the new turbulence model introduced into the standard  $k-\epsilon$  model was the evaluation, as functions, of the quantities  $c_\mu$  and  $Pr_\epsilon$  which take constant values with the usual  $k-\epsilon$  model.

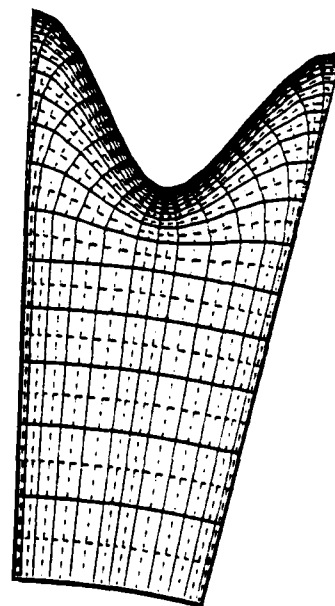




a.  $n=10$  ;  $R_a = -54R_b$  ;  $NI=18$  ;  $NJ=22$



b.  $n=20$  ;  $R_a = -65R_b$   
 $NI=20$  ;  $NJ=20$



c.  $n=30$  ;  $R_a = -65R_b$   
 $NI=18$  ;  $NJ=20$

Fig 4.1

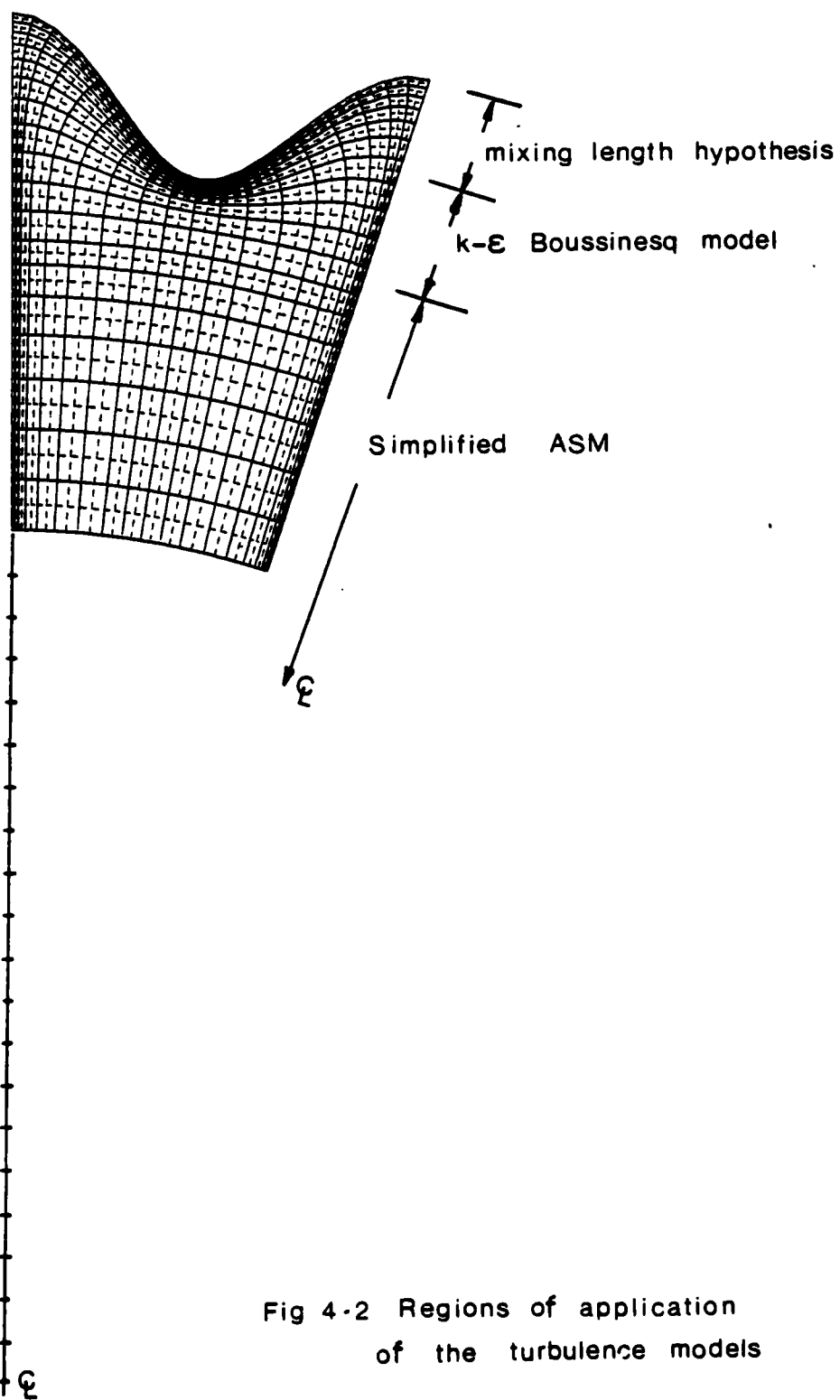


Fig 4-2 Regions of application  
of the turbulence models

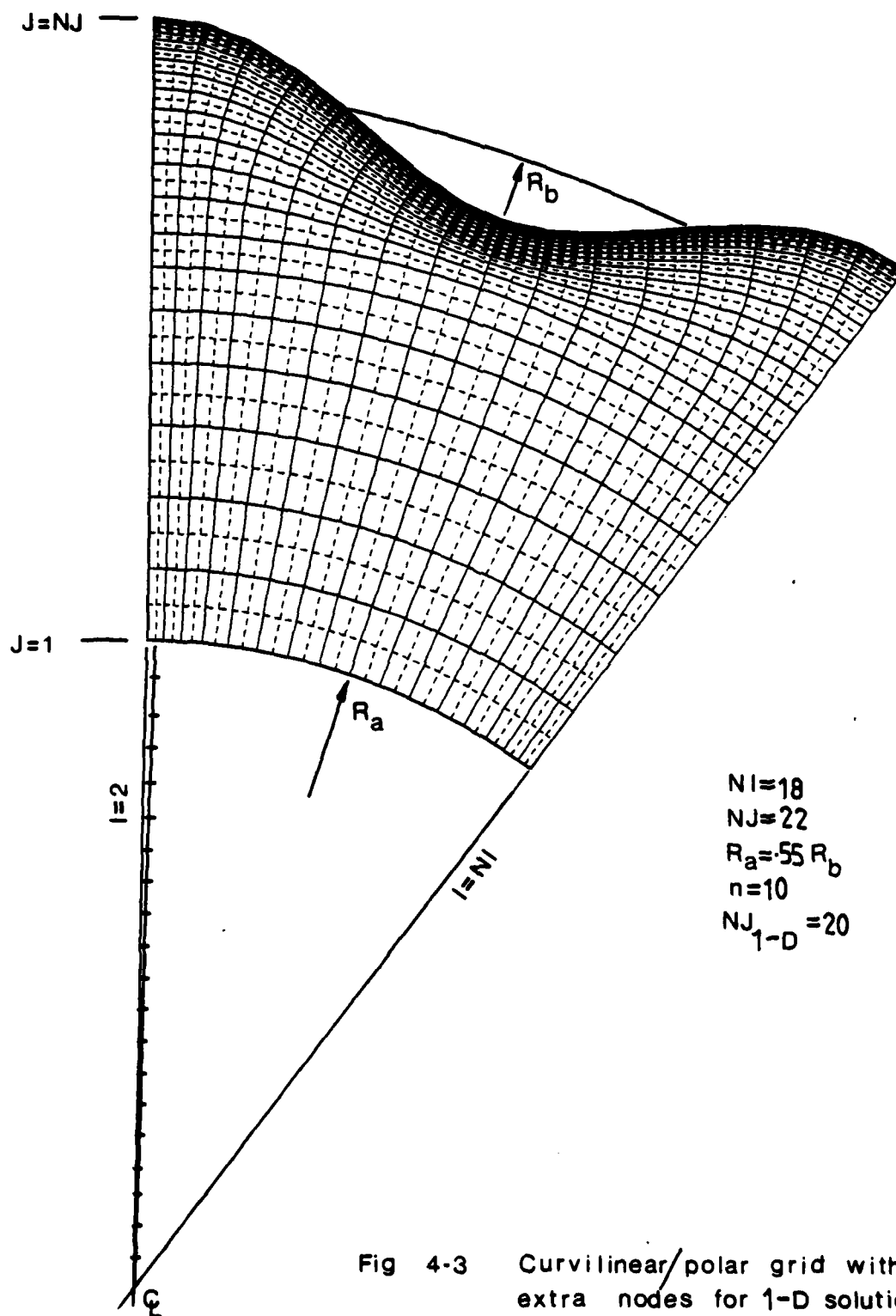


Fig 4-3 Curvilinear/polar grid with extra nodes for 1-D solution up to pipe axis

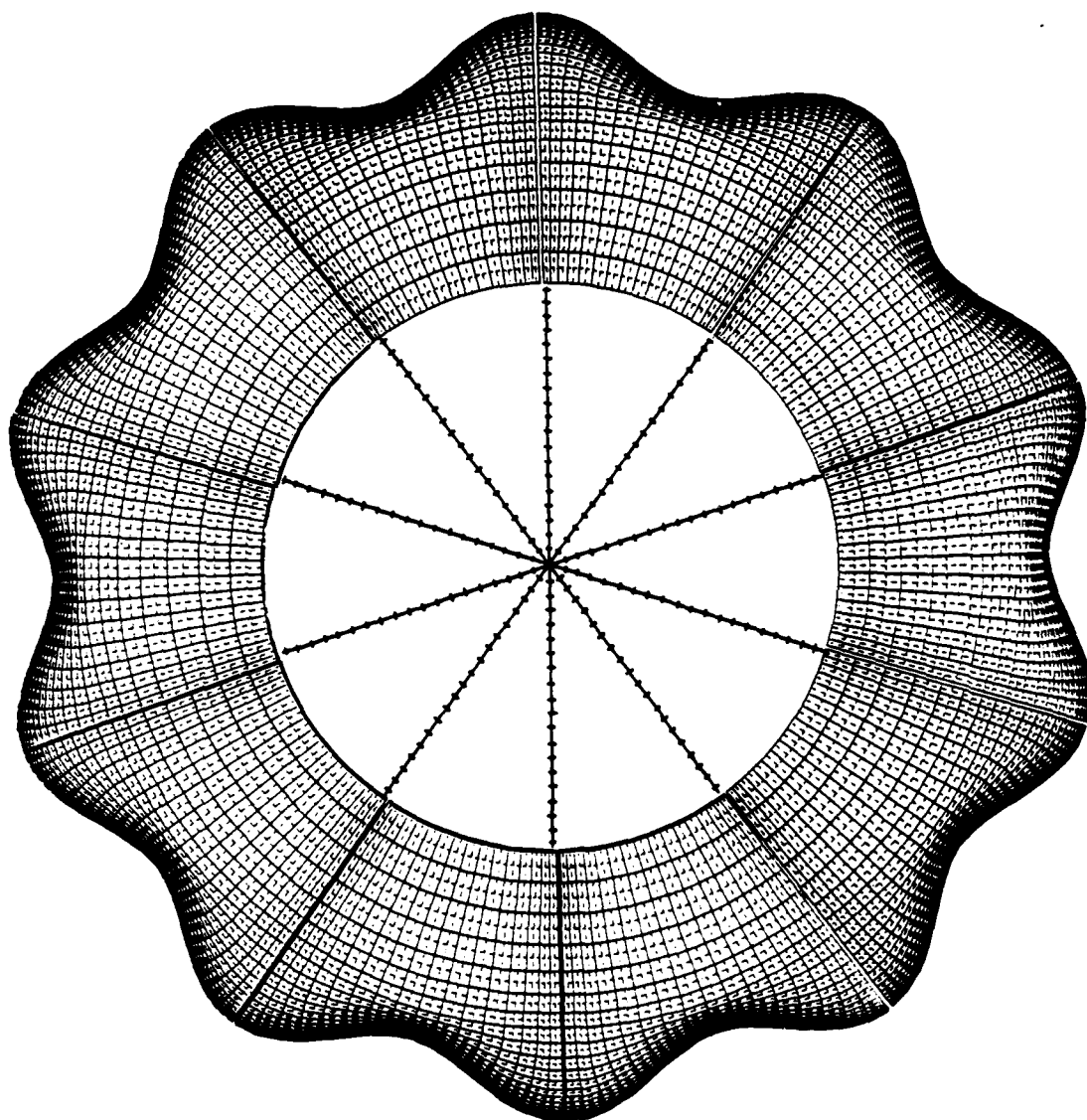
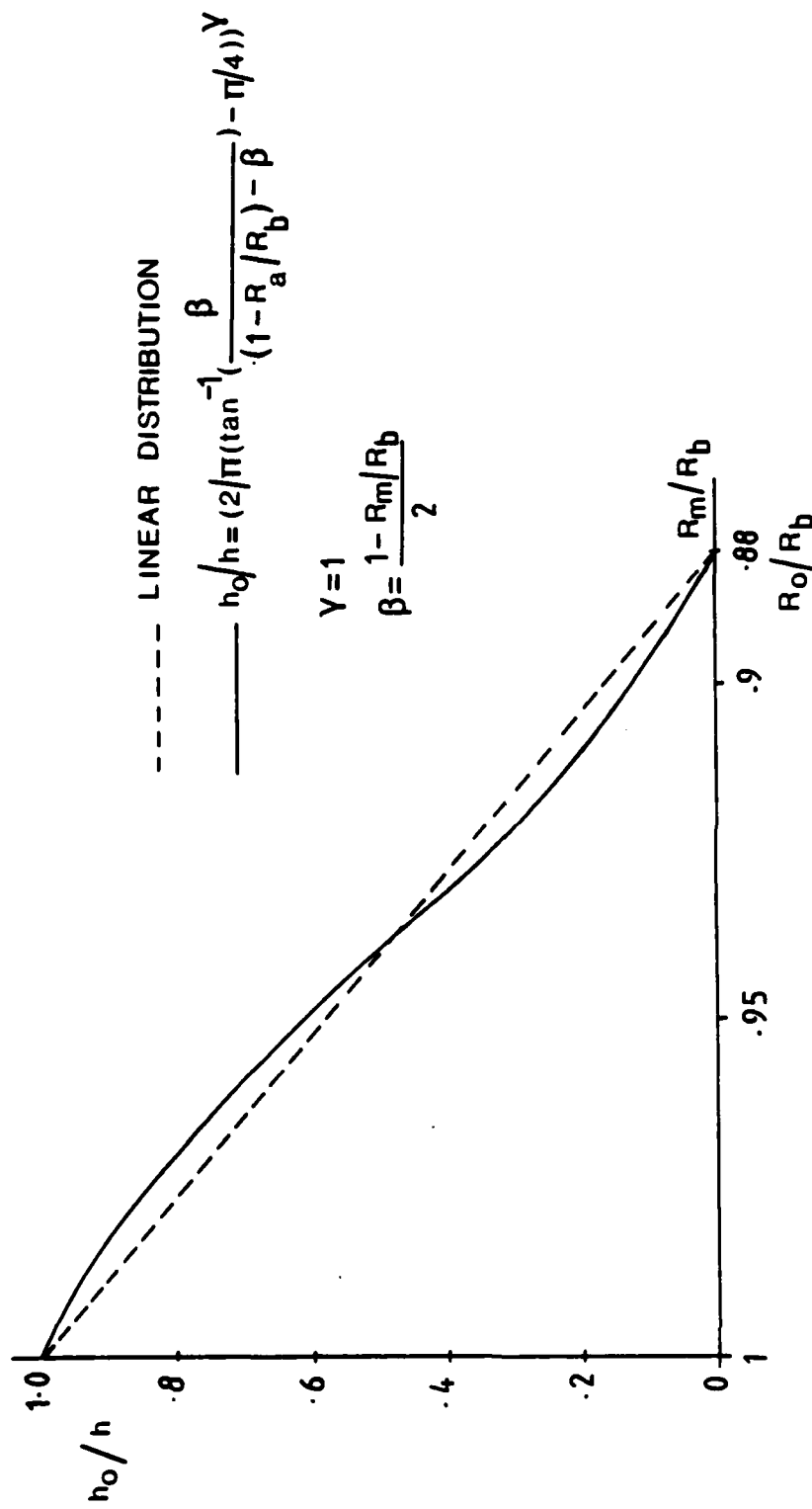


FIG 4-4 GRID COVERAGE OF THE COMPLETE  
CROSS-STREAM SECTION

Fig 45 DISTRIBUTION OF  $h_o/h$  VERSUS  $R_o/R_b$

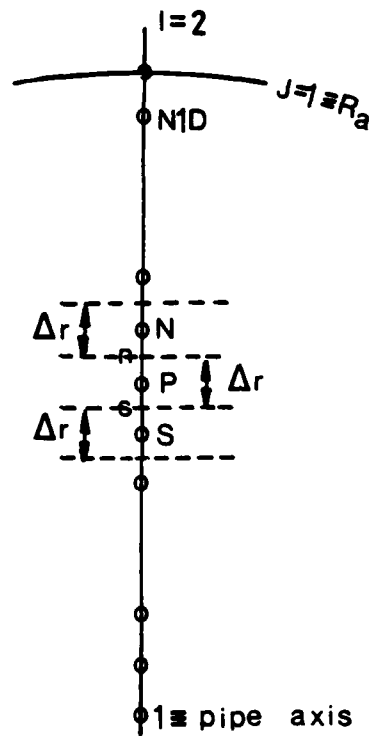


Fig 4-6 Radial node-distribution  
for the 1-D region

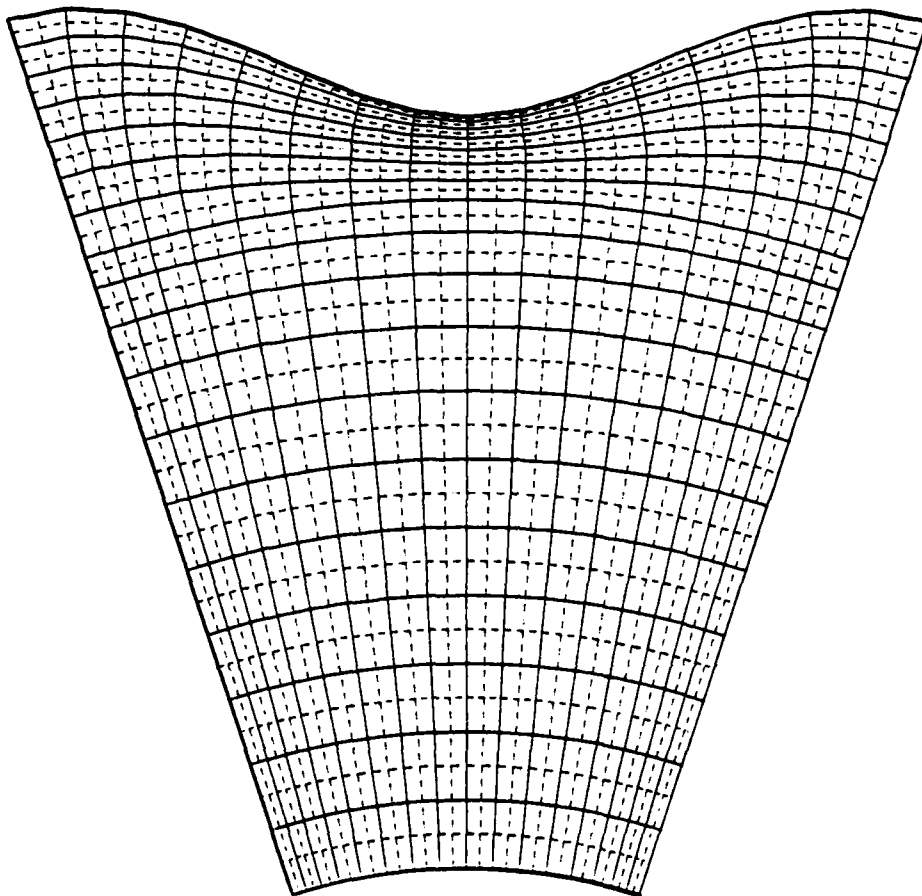


Fig 4-7 Grid  $n=10$   $h=-0.6R_b$   $R_a=-4R_b$

MIXING LENGTH HYPOTHESIS

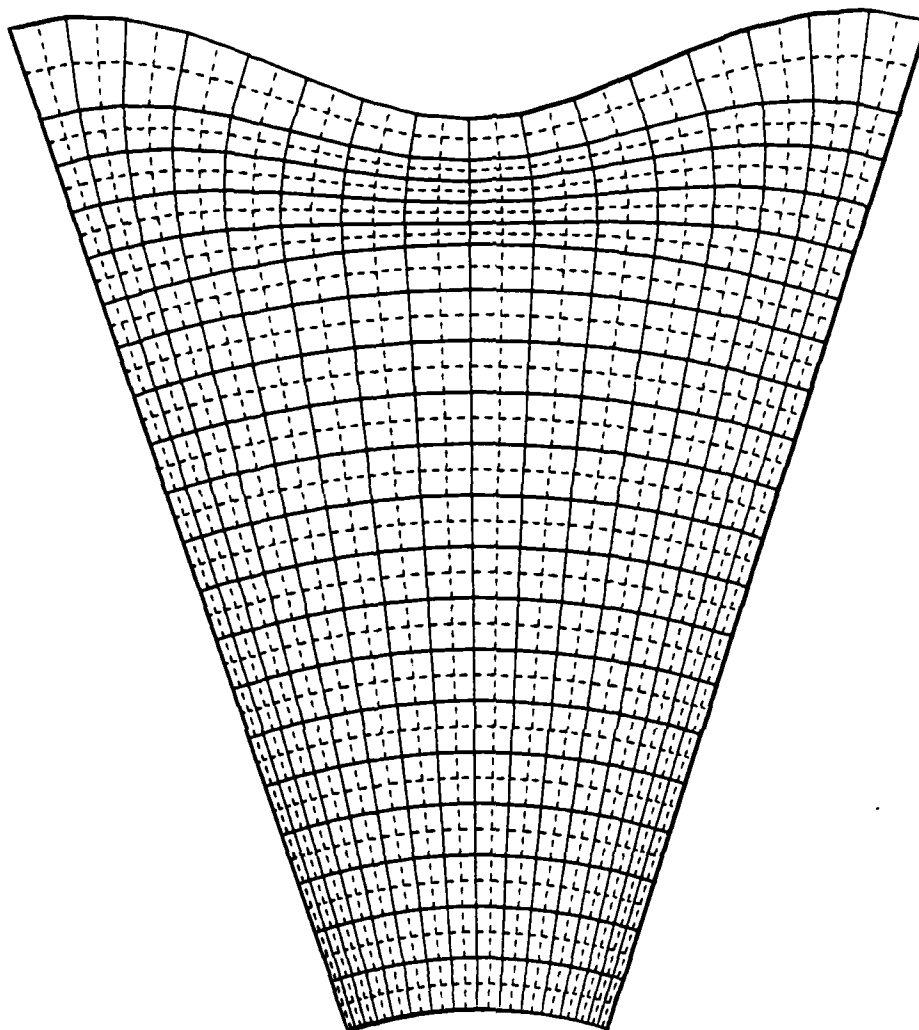


Fig 4-8 Grid  $n=10$   $h=0.6R_b$   $R_a=3R_b$

k- $\epsilon$  BOUSSINESQ VISCOSITY  
MODEL



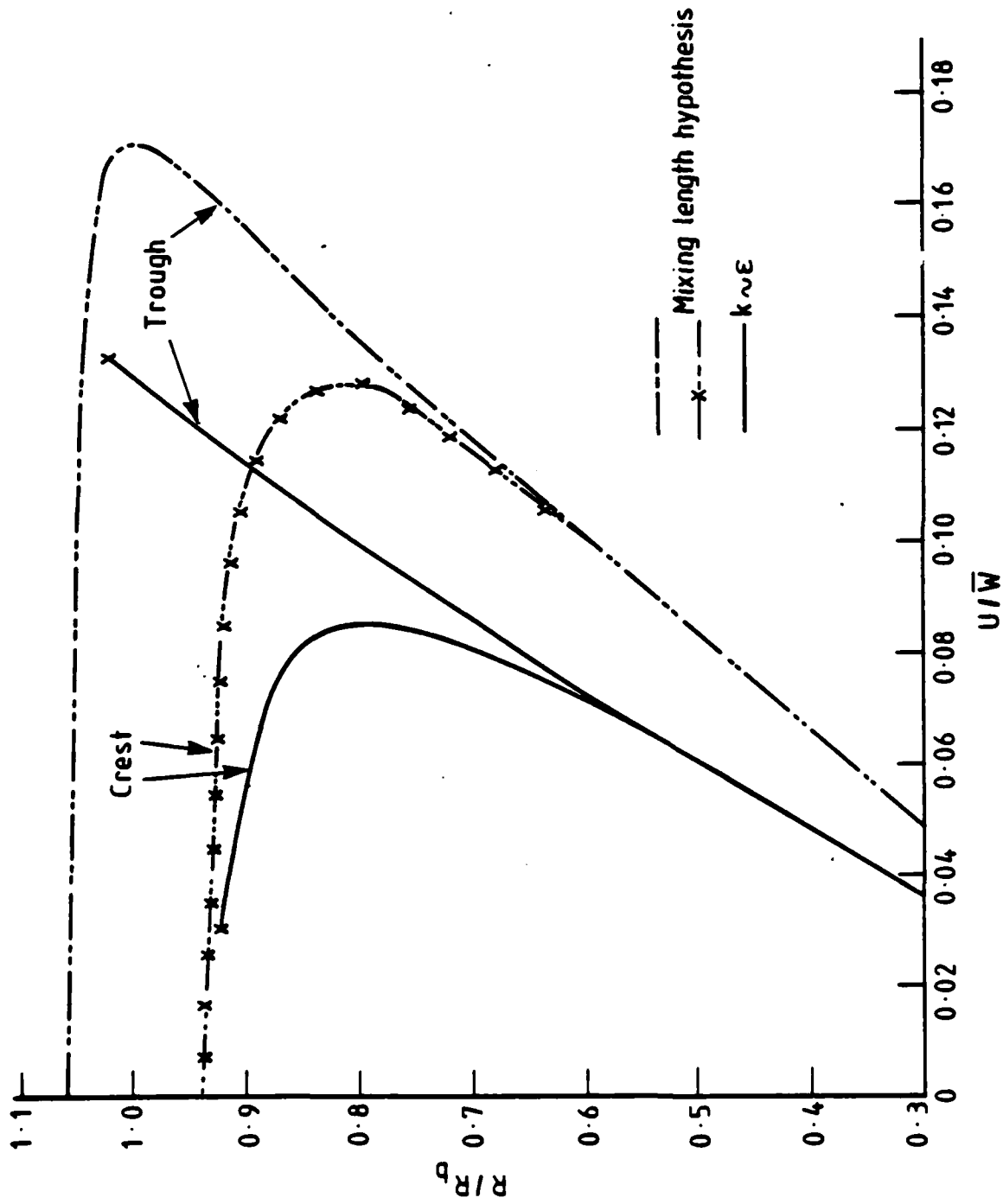


Fig. 4.9 Induced swirl velocities in flow through a spirally fluted tube  $h = 0.06R_b$ ,  $\eta = 10$ ,  $\varphi = 15^\circ$ ,  $Re = 3 \times 10^4$

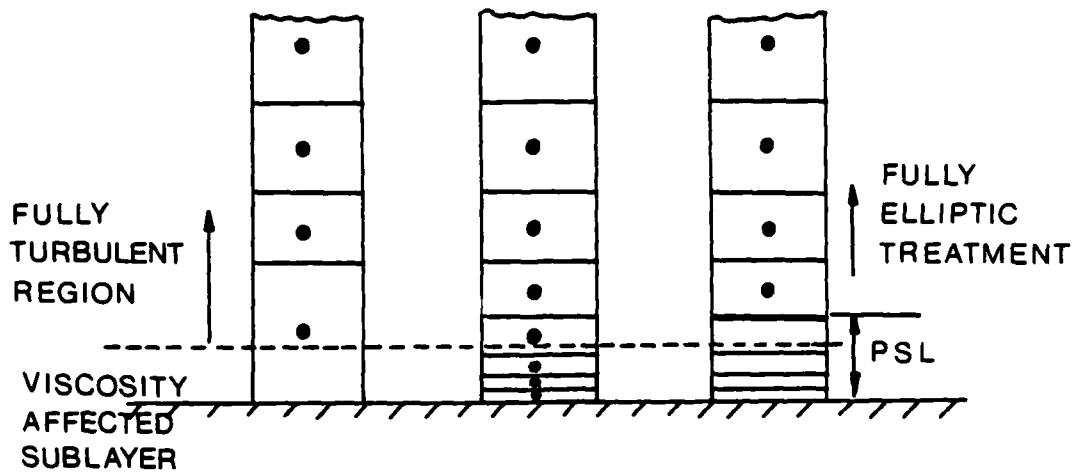


FIG 4.10 ALTERNATIVE NEAR-WALL  
APPROACHES FOR TURBULENT  
ELLIPTIC FLOWS

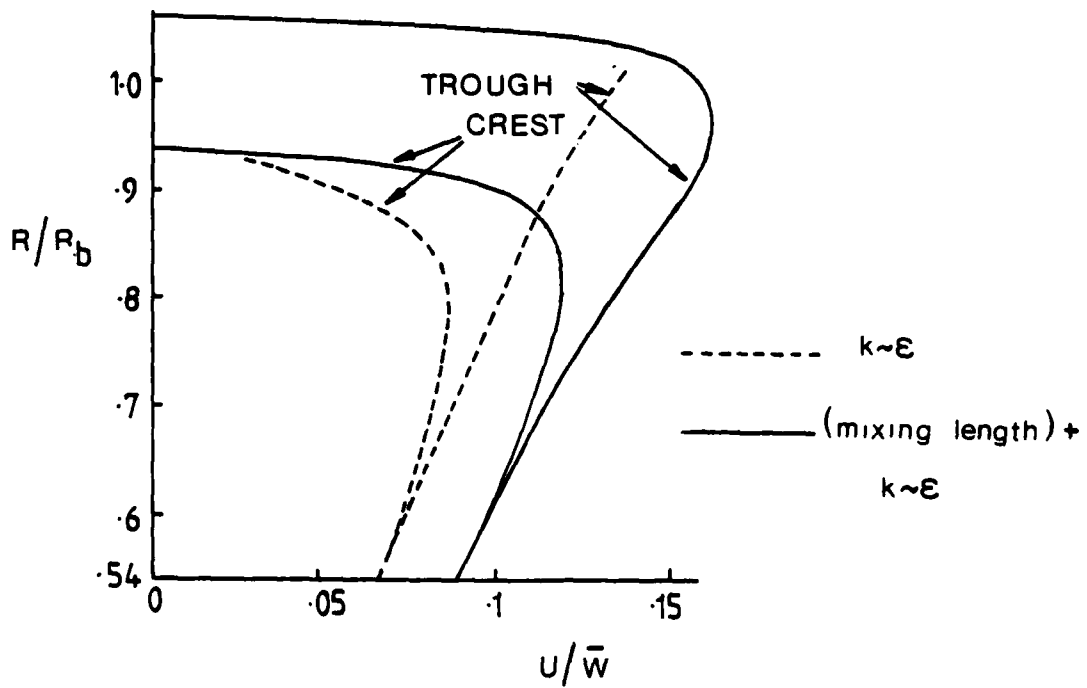


FIG 4.11 SWIRL VELOCITY  
 $h = -0.06 R_b$  ;  $n = 10$  ;  $\phi = 15^\circ$  ;  $Re = 30000$

## CHAPTER 5

### 5. THE TURBULENT FLOW CALCULATIONS

The present chapter reports the validation tests performed and the computational results obtained from a parametric exploration of the turbulent flow through spirally fluted tubes. This exploration includes changes in the number of flutes, spiral angles, Reynolds and Prandtl numbers. Finally, a comparison between the computational results and experimental data reported by LaRue [82] is presented from which useful conclusions may be drawn on directions for achieving better predictions of this highly complex flow.

#### 5.1 Validation Tests

In Chapter 3, several validation tests of the computational procedure have been reported, such as the computation of laminar flow through a straight circular-sectioned tube or through a concentric annulus with a rotating outer cylinder at a prescribed speed. In Chapter 4, the computation of friction factors for turbulent flows through smooth pipes, applying different near-wall treatments, has been reported as a further test of the correctness of the complex equations given by (4.25) - (4.29) for the two-dimensional part of the solution domain and by (4.31) - (4.37) for the core region. As a test of the energy equation, the prediction of heat transfer coefficients for fully-developed turbulent flows in straight unfluted tubes has been considered by setting the flute height to zero while the spiral angle was kept at  $15^\circ$ . The mixing-length hypothesis with Van Driest's damping function has been adopted in the near-wall region merged with the  $k-\epsilon$  Boussinesq viscosity model over the rest of the solution domain. Three different fluids have been tested: air ( $Pr = 0.708$ ), water

(Pr = 7.03) and eutectic calcium chloride solution 30% (Pr = 19.6). For all these fluids the computed Nusselt numbers agreed within 2.5% with the following analytic correlations given by Kays [97]:

$$\text{for } Pr < 1 \quad Nu = 0.022 Re^{0.8} Pr^{0.6} \quad (5.1)$$

$$\text{for } 1 \leq Pr < 19 \quad Nu = 0.0155 Re^{0.83} Pr^{0.5} \quad (5.2)$$

$$\text{for } 19 \leq Pr \quad Nu = 0.0118 Re^{0.9} Pr^{0.3} \quad (5.3)$$

Figure 5.1 shows the comparison between the computations and the above correlations (5.1), (5.2), (5.3).

An additional test has been carried out by setting the spiral angle of a fluted tube ( $n = 20$ ,  $h = 0.06 R_b$ ) to zero. The computation of turbulent flow through this tube showed (see Figure 5.2) that lower Nusselt numbers than the smooth tube values are obtained. However, the two Nusselt number lines of Figure 5.2 would appear to coincide if they were extended to  $Re > 8 \times 10^5$ . The definition of Nusselt number is based on the equivalent diameter  $D_h$  ( $= 4A/P$ ) given by the equation:

$$Nu^* = \frac{\dot{q}'' D_h}{\Delta \bar{T} k} \quad (5.4)$$

while water has been used as the working fluid. The above definition (equation (5.4)) does not take account of the added surface area by the flutes expressed by the ratio  $\frac{P}{2\pi R_b}$ . If this term had been included into equation (5.4) the Nusselt numbers predicted for  $n = 20$ ,  $\phi = 0^\circ$ ,  $h = 0.06 R_b$  would have increased to slightly higher values than those computed for smooth tubes (presented in Figure 5.2 by the solid line).

## 5.2 Parametric Study of the Results and Comparison with Experimental Data

### 5.2.1 Using the Combination of $k-\epsilon$ and Mixing-Length Turbulence Models

#### The Velocity Field

For the parametric study of turbulent flow through spirally fluted tubes reported below, the case of 10 flutes,  $15^\circ$  spiral angle and 6% flute height has been considered as the "base case". For the results reported here, in the low-Reynolds-near-wall region, the mixing-length hypothesis with Van Driest's damping function has been applied, being matched to the  $k-\epsilon$  Boussinesq viscosity model as soon as all the nodes belonging to a constant- $\eta$  row of cells were located in fully turbulent region. The grids used to calculate the turbulent flow through tubes with 10, 20 or 30 flutes are given in Figures 5.3, 5.4 and 5.5 respectively. For each case, more than one grid pattern is presented displaying the writer's attempts at near-wall grid-refinement in order to achieve grid-independent solutions. Figure 5.6 shows the distribution of local Nusselt number around a flute for the three types of grid presented in Figure 5.4 ( $n = 20$ ). It is clear that for air ( $Pr = 0.708$ ) no changes can be detected in the distribution of local Nusselt number using the three grids. However, for water ( $Pr = 7.03$ ) and calcium chloride solution ( $Pr = 19.6$ ) grid 1 gives a substantially different Nusselt distribution from grids 2 and 3. Moreover, one could say, considering the distributions predicted using grids 2 and 3, that a virtually grid-independent solution has been achieved, at least for water. For calcium chloride solution, however, further refinement is needed for obtaining a grid-independent solution. The same type of behaviour has also been found for 10 and 30 flutes, while for a constant Prandtl number, it has, not unexpectedly, been found that the higher the flute density the more

near-wall grid-refinement is needed in order to achieve a grid-independent solution. An extensive discussion on the local Nusselt number distribution around the flutes can be found in the following section where the convective heat transfer results are reported.

The velocity direction lines for a 10-flute tube at a Reynolds number of  $1.66 \times 10^4$  are shown in Figure 5.7. From this figure, it is clear that as the fluid encounters the flute spiralling clockwise, a high pressure region is created on the leading face of the flute pushing the fluid clockwise and away from the wall. Comparing this flow pattern with Figure 3.6, which shows the corresponding one for laminar flow in a 10-flute pipe at a Reynolds number of 300, one can note the following: firstly, the confinement of the flute-affected region closer to the wall; secondly, the complete absence of "back-flow" over the crest of the flute. Figure 3.10 shows that, for  $Re = 300$ , significant circumferential variations occur over a large proportion of the cross-section ( $R/R_b > 0.45$ ), while from Figure 5.10, where the distribution of the  $\xi$ -velocity component along the trough and crest radii for tubes with 10, 20 and 30 flutes at  $15^\circ$  is presented, it is clear that for the lower flute density the fluid is in solid-body rotation for radii less than about  $0.6 R_b$ . For higher flute densities, however, this value becomes  $0.7 R_b - 0.75 R_b$ . The higher the flute density the lower the distance from the tube wall to which the flute effects penetrate. The velocity direction lines for 20 and 30 flutes are illustrated in Figure 5.8. An interesting feature shown in both figures (5.8 and 5.10) is the existence of "back-flow" at the crest position of the flute.

Figures 5.9a, 5.9b and 5.9c show three alternative presentations of vector lines on the cross-stream plane of a 20-flute tube at  $15^\circ$  spiral

angle. Figure 5.9a gives the usual presentation, while 5.9b shows the distribution of velocity vectors given by the correlation:

$$\left( \vec{U} + \vec{V} \right) = \overline{\omega} \cdot \vec{R} \quad (5.5)$$

where  $\vec{U}$  and  $\vec{V}$  are the vectors for the  $\xi$  and  $\eta$  velocity components respectively, while  $\left( \vec{U} + \vec{V} \right)$  is the resultant vector plotted in 5.9a.  $\overline{\omega}$  is the angular velocity of the central core for the test in question. This figure thus shows how the secondary flow "vectors" appear to an observer rotating with the core of the fluid. So, over the part of the pipe in solid-body rotation, the velocity appears as zero.

Figure 5.9c presents the distribution of velocity vectors given by:

$$\left( \vec{V}_{n\theta} + \vec{V}_r \right) \quad (5.6)$$

The meaning of the vectors appearing in (5.6) can be found in Chapter 3. Figure 5.9c actually shows the velocity direction lines seen by an observer placed on the flute spiralling clockwise around the tube. Over most of the domain the arrows are signifying an anti-clockwise flow, i.e. that fluid in the tube is not spinning clockwise as fast as the flutes (so, relative to the flutes fluid is gliding backwards). This particular presentation conveys a striking impression of how the flutes promote mixing of the near-wall fluid. The corresponding alternative presentations of vector lines for  $n = 30$ ,  $\phi = 30^\circ$  are presented in Figures 5.9d, 5.9e and 5.9f. The patterns show no distinctive differences from those for 20 flutes.

The circumferential velocity along trough and crest radial lines for various flute densities has been shown in Figure 5.10, while the effect of

Reynolds number on this distribution for a 20-flute tube with a  $15^\circ$  spiral angle is shown in Figure 5.11. This figure shows an increase in the extent of the region of solid-body rotation with Reynolds although this change is small since, even for  $Re = 16500$ , the solid-body rotation region covers most of the solution domain. Moreover, in Figure 5.10, for the higher flute density a very weak and limited reverse flow in the trough can be detected. One can note the marked increase of the secondary flow as the number of flutes is raised from 10 to 20. However, for a further increase from 20 to 30, the increase in circumferential velocity is only slight. Figure 5.10 also shows that the additional flutes produce a higher level of swirl, not only in the core region but also in the near-wall region in contrast to the laminar flow computations (see Figure 3.12) where a lower maximum level of secondary flow is produced with the high flute density tube.

Figure 5.12 shows the effect of flute angle on the circumferential velocity profile for  $n = 30$  and  $Re = 18000$ . From this figure it is clear that the circumferential velocity increases in roughly the same ratio as the tangents of the spiral angle (the same has been shown in Figure 3.11 for the laminar flow computations), while the higher the flute angle the stronger the "back-flow" over the crest and trough although very limited and, in the trough, still very weak.

A similar behaviour is also shown in Figure 5.13 where the effect of spiral angle on circumferential velocity profile is given for a tube with 20 flutes at a Reynolds number around  $5.1 \times 10^4$ . This figure shows that although for  $\phi = 15^\circ$  no "back-flow" exists over the crest, for  $\phi = 30^\circ$  a weak one is present even at this high Reynolds number.



The effects that the flutes exert on the axial velocity profiles are presented in Figure 5.14. It is obvious that the velocity distribution for 10 flutes is similar to that for a fully-developed flow through a smooth tube with a known pressure gradient, while the higher the flute density the more curved the distribution of the axial velocity due to the proximity of the flute surfaces and the greater velocity retardation that they cause.

The only velocity-field experimental data available are for 30-flute tubes at  $30^\circ$  spiral angle; the data plotted below have been measured by J.C. LaRue [82] at the University of California, Irvine. Although the computational results for this geometry ( $n = 30$ ,  $\phi = 30^\circ$ ) do not exceed a Reynolds number of 26300 (due to the increasing difficulty in converging the solution procedure), comparisons have been drawn between the predictions and the experimental data for higher Reynolds numbers. This comparison seems reasonable to make (though, of course, one needs to be slightly wary of Re influences in such complex geometry). The distribution of axial velocity ratio  $W/W_c$  ( $W_c$  = axial velocity at the tube axis) along the trough and crest radii is shown in Figures 5.15 and 5.16 respectively. Despite the difference in Reynolds numbers between LaRue's and the predicted data, the profiles are almost identical.

Figure 5.17 presents the variation of predicted friction factor  $f$  with Reynolds number based on the conventional hydraulic diameter of the tube (see equation (3.1)) for three flute densities ( $n = 10, 20, 30$ ) and a  $15^\circ$  spiral angle. One may note that for  $n = 10$  the spirally fluted tube friction factor is almost identical to that for a smooth tube. Its increase over the smooth tube values ranges from -2.1% to +2.6% for Reynolds numbers

varying from  $10^4$  to  $8 \times 10^4$ . For 20 flutes, the spirally fluted tube friction factor at  $Re = 10^4$  is again 2.1% lower than the circular tube value but 11% higher at  $Re = 8 \times 10^4$ , while for 30 flutes at  $Re = 2 \times 10^4$  it is already 18% higher and displays an increase as the Reynolds number is raised. Thus, at  $Re = 4 \times 10^4$  it is almost 50% higher than for a smooth tube at the same Reynolds number.

The variation of friction factor with Reynolds number for the different flute densities with a  $30^\circ$  spiral angle is shown in Figure 5.18. The notable feature of Figure 5.18 is that all the friction factors lie above the smooth tube line with increases ranging from 10% for  $n = 10$  at  $Re = 8 \times 10^4$  to 118% for  $n = 30$  at  $Re = 3 \times 10^4$ . Again, the values for the higher flute density show an increase with Reynolds number.

This behaviour of the friction factor with the number of flutes can be partly explained by the increasingly asymmetric distribution of the surface static pressure around the flute. Figure 5.19 presents the distribution of the surface static pressure around the flute at a Reynolds number of  $6 \times 10^4$  for two different flute densities and a  $15^\circ$  spiral angle. Clearly, for 20 flutes the profile is more asymmetric about the crest than for 10 showing a marked double maxima. The effect of the spiral angle on the pressure distribution for a tube with 20 flutes at the same Reynolds number ( $6 \times 10^4$ ) is illustrated in Figure 5.20. From both Figures 5.19 and 5.20 it is clear that the effect of the static pressure on the leading face of the flute ( $0.5 < \xi < 1.0$ ) opposing the downstream motion of the flow is more than on the trailing surface pushing the fluid downstream. However, the higher the flute density or spiral angle or Reynolds number, the stronger this difference and the higher the friction factor compared with

the circular tube values. In Figure 5.21 the case of 30 flutes,  $30^\circ$  spiral angle is presented for two Reynolds numbers, while Figure 5.22 illustrates the surface static pressure distribution for a tube with 30 flutes but  $15^\circ$  flute angle. All the above-mentioned characteristics are noticeable in these two figures also.

A comparison of predicted and measured friction factors is given in Figure 5.23. This figure presents the friction factor-Reynolds number distribution revealing a serious disagreement with the experimental data. At a Reynolds number of  $2 \times 10^4$  the computed friction factor is 47% above the experimental level (by LaRue) displaying a steady increase as the Reynolds number is raised, in contrast to the measurements (where the level of friction factor drops even below the smooth tube line at Reynolds numbers above  $6 \times 10^4$ ). Consequently, at a Reynolds number of  $3 \times 10^4$  the difference becomes almost 80%. The causes of this disagreement and possible cures are considered later. First, however, we examine the convective heat transfer results associated with the above hydrodynamic predictions.

#### Convective Heat Transfer

The factors which may tend to enhance the heat transfer performance of the spirally fluted tubes are: the increase of heat transfer surface area per unit length of tube due to the fluting, the convective transport due to the swirl flow generated by the spiralling of the flutes and the augmentation of turbulent transport coefficients. Taking into account the added surface area for the definition of Nusselt number (see equation (3.7) based on the conventional hydraulic diameter) a comparison is presented in Figure 5.24 between smooth-tube Nusselt number values and those for tubes

of 10, 20 and 30 flutes at  $15^\circ$  spiral angle for air ( $Pr = 0.708$ ), water ( $Pr = 7.03$ ) and calcium chloride solution ( $Pr = 19.6$ ). The smooth pipe results shown in Figure 5.24 are those recommended by Kays [96]. One may note the substantial increase of mean Nusselt number for every fluid and geometry studied. These increases range from 12% for 10 flutes and 39% for 20 flutes to up to 120% for 30 flutes, the enhancement for the last two geometries depending on Prandtl number. (Thus, for a 30-flute tube, while the increase for air is around 55%, for water it is 93% and for calcium chloride solution 120%).

The mean Nusselt number distribution with Reynolds number for the same fluids and flute densities at a higher spiral angle ( $\phi = 30^\circ$ ) is presented in Figure 5.25. Again, the enhancement of heat transfer performance is remarkable especially for the higher Prandtl numbers. From both figures (5.24, 5.25) one notes that the higher the number of flutes the stronger the augmentation of Nusselt number over the smooth tube values. For  $n = 10$  the increases range from 10% for air and 16% for water up to 20% for calcium chloride solution, while for  $n = 30$  from 130% for air and 240% for water up to 315% for calcium chloride solution! Moreover, the augmentations for 20 flutes are intermediate between those for 10 and 30 flutes. Thus, the increase of friction factor mentioned in the previous section, even for  $n = 30$  at  $30^\circ$  spiral angle for  $Re = 3 \times 10^4$  (118%), can be considered modest compared with the three-fold increase of the Nusselt number.

It is interesting to note how the number of flutes, the level of Reynolds and Prandtl numbers and the spiral angle affect the distribution of the local Nusselt number around the flutes. Figures 5.26 to 5.30 display all these effects. The behaviour for 10 flutes is shown in Figure 5.26 for two Reynolds numbers and three different fluids. For the lowest

Prandtl number (air) at both Reynolds numbers there is only a 15% variation in the distribution of Nusselt number about its mean value with a maximum at the crest position ( $\xi/S_{\text{flute}} = 0.5$ ). The same behaviour has also been found in the laminar flow computations shown in Figure 3.31. For water, the distribution of Nusselt number is different since its maximum value has shifted halfway down the leading face of the flute ( $0.5 < \xi/S_{\text{flute}} < 1$ ) while at a higher Reynolds number ( $\approx 6.5 \times 10^4$ ) a further modification in the shape of the distribution can be detected mainly on the trailing side of the flute. For the highest Prandtl number the behaviour of the local Nusselt number is similar to that for water but with the maximum shifted still further away from the crest on the pressure side.

The corresponding variation of local Nusselt number for 20 flutes is given in Figure 5.27. At a low Reynolds number the distribution for air is similar to that for 10 flutes; however, at  $Re \approx 6 \times 10^4$  it develops a double maximum one at each face of the flute (pressure and suction); this feature is also present at higher Prandtl numbers. The maximum appearing at the suction face of the flute may be understood by reference to the behaviour of the velocity direction lines shown in Figure 5.9c. This figure shows at the trailing side of the flute an impinging flow which leads to the peak on the local Nusselt distribution. (Similar remarks could be made about the distribution of surface static pressure presented above which also shows a maximum on the suction face of the flute). Figure 5.28 shows the variation of local Nusselt number for a 30-flute tube.

Figure 5.29 shows the effect of higher spiral angles on the local

Nusselt number distribution for 20 flutes. It is interesting to note the substantial difference, for the higher Prandtl numbers, in the level of the two maxima occurring on the two flute faces. Again, the highest levels are those of the suction face. A similar behaviour is shown in Figure 5.30 for  $n = 30$  and  $\phi = 30^\circ$ .

Figure 5.31 draws comparisons between experimental and predicted data for the convective heat transfer behaviour. The computed Nusselt numbers for air show a 120% increase over the smooth tube values while the experiments indicate only a small augmentation. Moreover, the computed Nusselt numbers for water flow and uniform fluid properties (low heat flux) display a 200% increase over the unfluted tube values while the experimental data suggest an increase only about half that found numerically. This can be seen in Figure 5.31 where the Nusselt modulus  $Nu/Pr^{0.4}$  for water is plotted against the Reynolds numbers for different heat fluxes and heat flux directions.(inward or outward). The predicted values should be compared with Reilly's data [94] (line 2) since a low heat-flux situation has been considered. The Nusselt number is based on the conventional hydraulic diameter not including the area extension due to the fluting (see equation (5.4)).

It is also interesting to include here the comparison of predicted and experimental data for the turbulent kinetic energy distribution along the crest and trough radii. It is clear from Figures 5.32 and 5.33 that the computations overpredict the experimental level giving values which are almost three times larger than the measured ones along the crest radius and over four times larger along the trough radius. The predictions of a 10-flute tube at  $30^\circ$  spiral angle are also presented in Figures 5.32 and 5.33

and in contrast with the foregoing these results show an almost identical distribution to LaRue's data. The higher values predicted for 30 flutes compared with the predictions for 10 flutes may be explained by referring to Figure 5.14. From this figure it is clear that at a radius of  $0.88 R_b$ , where the matching of the mixing-length hypothesis and the  $k-\epsilon$  Boussinesq viscosity model takes place, the gradient of the axial velocity is steeper for the 30-flute geometry than for the 10. Thus, for the higher flute density a larger production of turbulence is created giving values of  $k$  at that radius which, as mentioned above, are several times larger than those for 10 flutes.

Our computations so far have succeeded in showing the favourable heat transfer performance of spirally fluted tubes; however, for both momentum and heat transfer the enhancement is too strong. This should clearly suggest that the turbulent transport coefficients are too high in some respect .

One possibility we felt worth considering was that within the flute itself turbulent mixing might be suppressed, the flow here being essentially viscous. Up to now the computational solution gives substantial turbulent transport in the flutes except within the viscous sublayer whose thickness depends on the value assigned to the Van Driest damping "constant"  $A^+$  which in the present computations has taken the standard value of 26. (The viscous sublayer thickness of course becomes thinner as the Reynolds number is raised). To mimic approximately the conjectured suppression of turbulent transport in the region within the flutes, the turbulent term in the effective viscosity has been dropped in this part of the solution domain. The resultant predictions of friction factor and heat transfer coefficients

show some improvement in agreement with the experimental data. Figure 5.34 shows that the computed skin friction has been decreased by 20% at  $Re = 2 \times 10^4$  and by 26% at  $Re = 3 \times 10^4$  compared with the values computed initially; for the same two Reynolds numbers the excess of the predicted values over the experimental data (by LaRue) is only 18% and 32% respectively (instead of 47% and 80% mentioned above). What is particularly encouraging is that the suppression of turbulence in the flute gives a friction factor distribution that decreases as the Reynolds number is raised. Figure 5.35 illustrates the corresponding effects on the heat transfer coefficients for air and water flow. For both fluids the suppression of turbulent transport within the flutes has brought about a decrease in the computed Nusselt numbers. However, while for air flow the decrease is almost comparable with that of friction factor (13%), for water the decrease is only 7%. This behaviour comes about because of the way that heat is transmitted in the region within the flutes. For water, convection by the secondary flow is more important than diffusion in the flute region. For air flow, however, diffusion is also important, so the damping of turbulent diffusion has produced a larger decrease in heat transfer coefficients. Figure 5.36 shows the effect on the secondary flow due to the change in effective viscosity within the flutes. One can see an increase in the level of the circumferential velocity and a decrease in the "back-flow" over the crest. No substantial change has been found in the distribution of the ratio  $W/W_Q$  shown in Figures 5.15 and 5.16. Figures 5.37 and 5.38 show the corresponding effect on the turbulent kinetic energy distribution where one can see an improvement of the predicted values by 28% at the tube axis and by 45% at the outer boundary of the trough position.

The results shown in Figures 5.34 to 5.38 suggest that the replace-



ment of the mixing-length hypothesis by the  $k-\epsilon$  Boussinesq viscosity model in its low-Reynolds-number form could give a better agreement with experiments by predicting the suppression of turbulence in the region within the flutes since this model has been successful in predicting "laminarizing" phenomena in several other situations (Jones and Launder [110], [111], Durst and Rastogi [112]).

### 5.2.2 Introduction of the Two Forms of a Simplified ASM into the Core Region of the Solution Domain

In the foregoing calculations the level of predicted Nusselt number is independent of the heat flux magnitude since the (thermal) energy equation is uncoupled from the momentum equations and linear in  $\theta$  ( $\theta = T - T_{ref}$ ). However, Yampolsky [1] (Figure 1.30) showed an enhancement of water Nusselt numbers as heat flux increases, suggesting that the buoyancy effect associated with the swirl was the physical source of the enhancement. Thus, limited calculations have been made with the simplified buoyancy ASM of Gibson and Launder [109] (see Section 4.1.4b of Chapter 4) applied in the core region of the solution domain. Only the case of 20 flutes at  $15^\circ$  spiral angle for a Reynolds number of 17000 has been examined. For these runs the dynamic and temperature fields were solved at the same time, resulting to an increase of the computing times from 0.55 cp sec/iteration (see Section 4.3.3) to 0.63 cp sec/iteration. However, no significant enhancement in Nusselt number has been found, suggesting that buoyant centrifuging in the main part of the tube is not significant. Possibly, the effect could be important in the region immediately adjacent to ribs where very rapid gradients in velocity and density are present. (However, turbulence generation by shear is also large and this will tend to obscure

the buoyant contribution). The above possibility could not be explored because to incorporate the ASM model into the curvilinear region would introduce too great a complexity. Perhaps a more likely reason for "heat flux ratio" having such a marked effect is the strong dependence of viscosity on temperature. A high "heat flux" implies a large decrease in viscosity in the flute region compared with the core flow, thus facilitating larger secondary and primary flow deep in the flutes (a scenario that seems certain to lead to higher heat transfer rates). Unfortunately, the assumption of fully-developed flow to which the present study is confined does not allow for an exploration of the effect of fluid property variations.

The conclusions so far are that it seems quite probable that the flow in the flute region is laminarized but this mechanism alone is unable to account for the differences between computations and measurements. The other mechanism considered is the sensitivity due to swirl. In a swirling jet, where predominantly angular momentum decreases with radius, the effect is to augment turbulent mixing but in the spirally flute tube, where the angular momentum increases from the axis to the crest of the ribs, the tendency will be to inhibit turbulent transport. Thus, the incorporation into the core region of the solution domain of a simplified ASM including the effect of swirl associated with the additional strains it introduces into the flow (see Section 4.1.4a of Chapter 4) led to a 4.5% decrease in friction factor for a tube of 20 flutes at  $15^\circ$  spiral angle. No corresponding changes have been introduced into the heat flux equations. Figure 5.39 shows the variation of ratio  $f_{sf}/f_{sm}$  (where  $f_{sf}$  is the friction factor for spirally fluted tube, while  $f_{sm}$  is the friction factor for smooth tube) with the Reynolds number for the 20-flute,  $15^\circ$  tube, while Figure 5.40 illustrates a similar distribution for a 30-flute,  $30^\circ$  tube. In the

latter geometry the decrease of friction factor is about 7% while the corresponding decrease of Nusselt number for water is almost 5%.

Finally, some calculations have been made applying both the treatments that have been found to improve the comparison between predictions and measurements when they have been used separately. Thus, suppressing the turbulent transport in the near-wall region and applying the simplified ASM including the swirl effects at the core region of the solution domain for a 30-flute,  $30^\circ$  tube, the friction factors have been decreased by 28% at  $Re = 2 \times 10^4$  and by 33% at  $Re = 3 \times 10^4$ , compared with the values computed initially, while for the same two Reynolds numbers the increase over the experimental data (by LaRue) is only 7% and 20% respectively (instead of 47% and 80% found initially). These results are shown in Figure 5.41. The predicted Nusselt numbers for water are 4.5% lower than those shown in Figure 5.35 for the suppression of turbulent diffusion within the flutes.

### 5.3 Concluding Remarks

Chapters 4 and 5 have reported the adaptation and application of the TEACH computer code for solving turbulent flow through spirally fluted tubes. Although several tests have been made adopting different near-wall approaches, the final results reported above have been based mainly on the  $k-\epsilon$  Boussinesq viscosity model over most of the solution domain merged with Van Driest's form of the mixing-length hypothesis in the near-wall region. The problem of converging the solution procedure (also serious in the laminar flow computations) has been alleviated by applying the parabolic sublayer treatment in the immediate vicinity of the flutes. The use of a

mixed curvilinear/cylindrical-polar grid and the inclusion of the two-stage pressure correction procedure must have contributed to the improvement of convergence although no turbulent runs have been made using either the original SIMPLE procedure or the fully curvilinear grid. However, for a 30-flute tube at  $30^\circ$  spiral angle, the convergence rate of the solution procedure is still intolerably slow. This is why the results reported above for this tube geometry do not exceed a Reynolds number of 26300.

Despite the remaining disagreements between predicted and experimental data reported above, the predicted data cover an extensive parametric study showing how valuable a numerical solution can be in developing insight into a complex flow. Moreover, the interfacing of two or three turbulence models in different parts of the solution domain shows the flexibility of a computational solution for predicting a difficult turbulent flow.

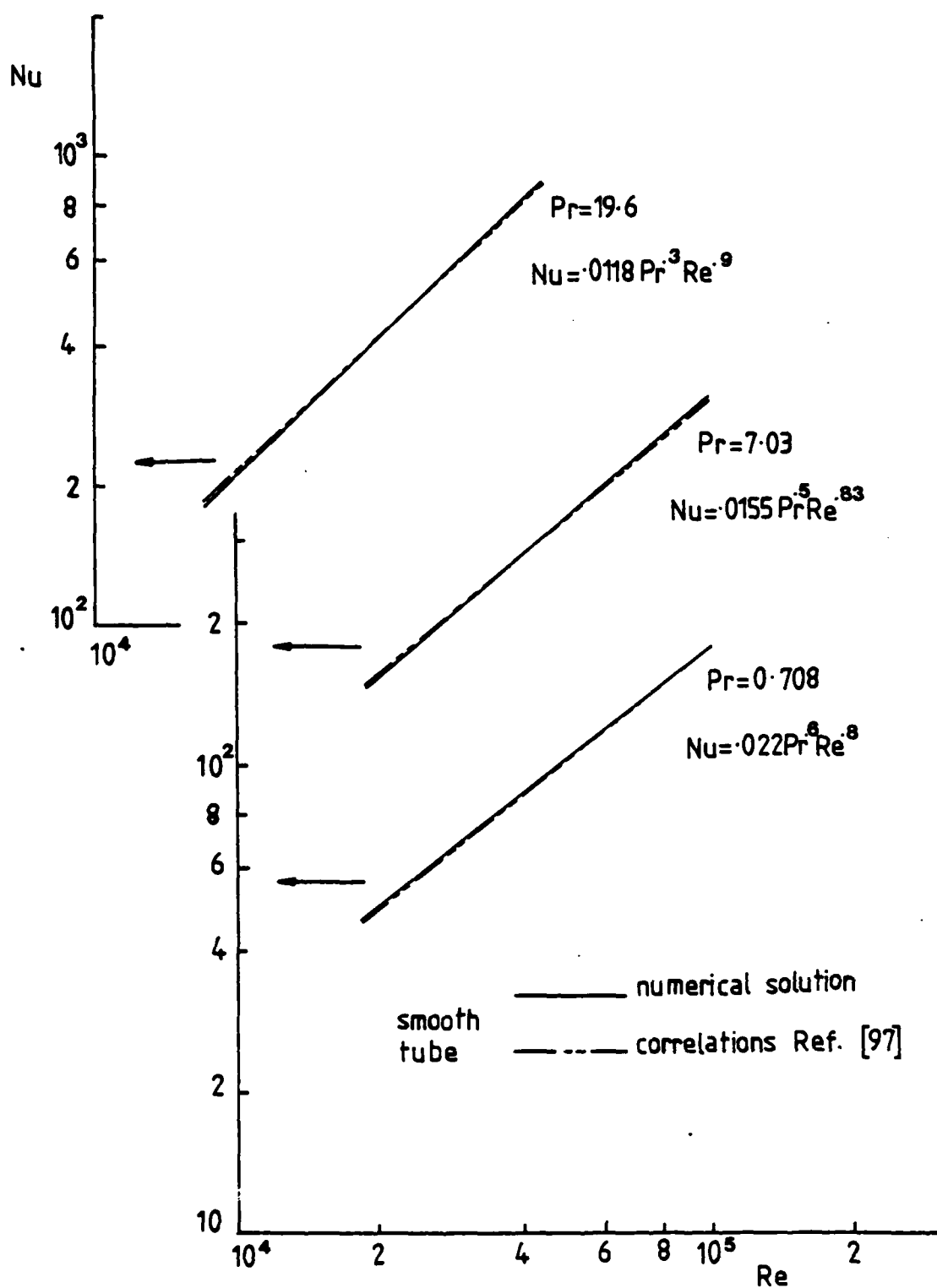


FIG 5-1 Comparison between numerical results and correlations (Ref. [97] ) for a smooth tube

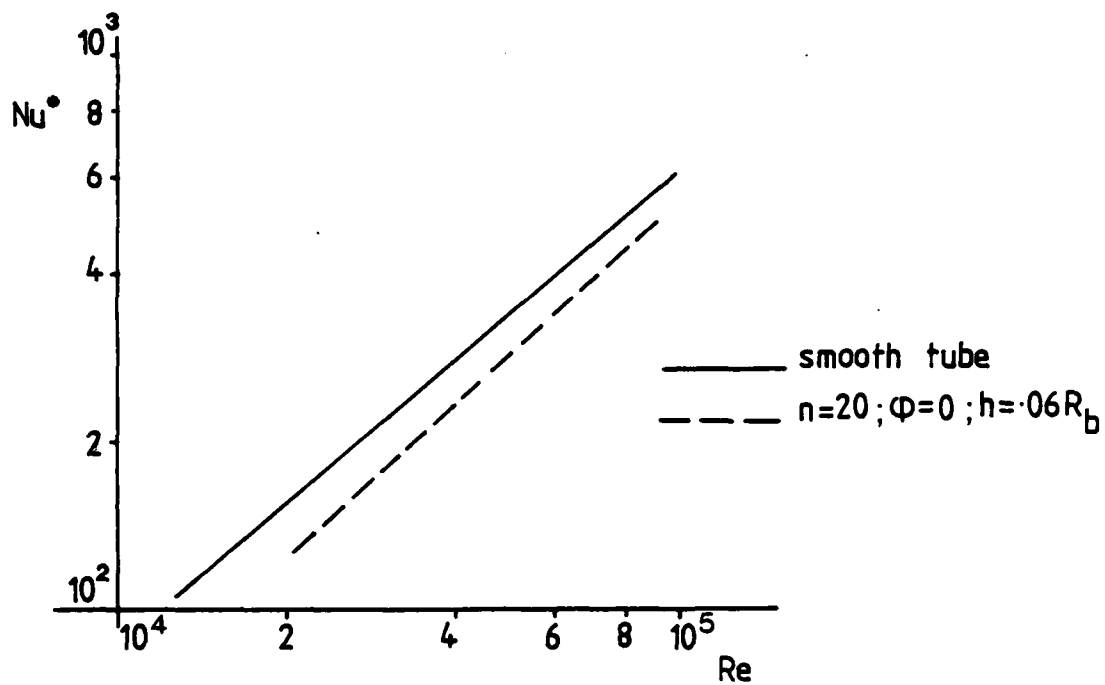
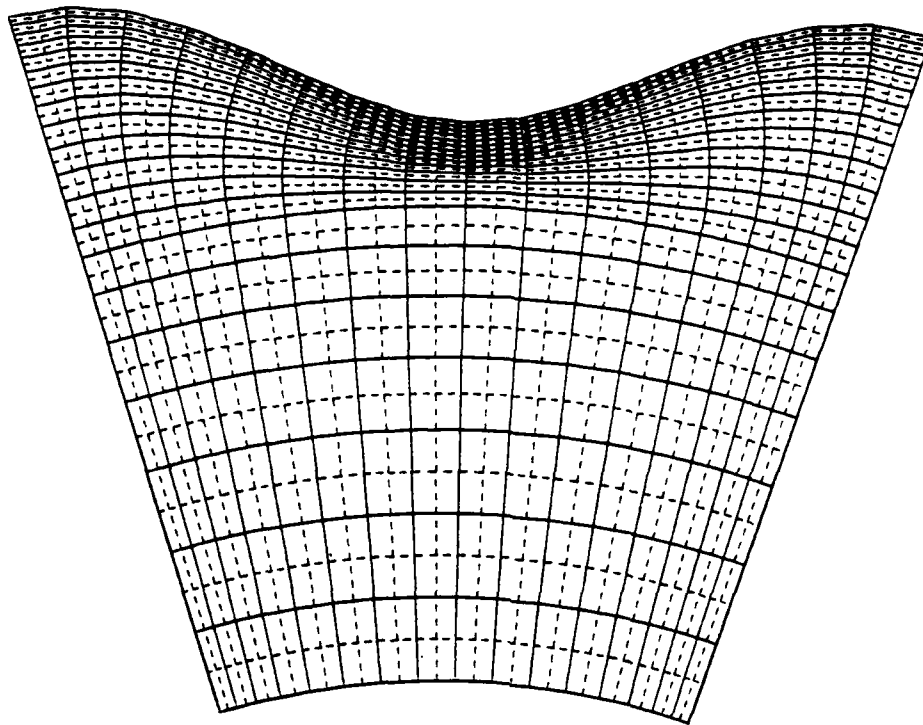
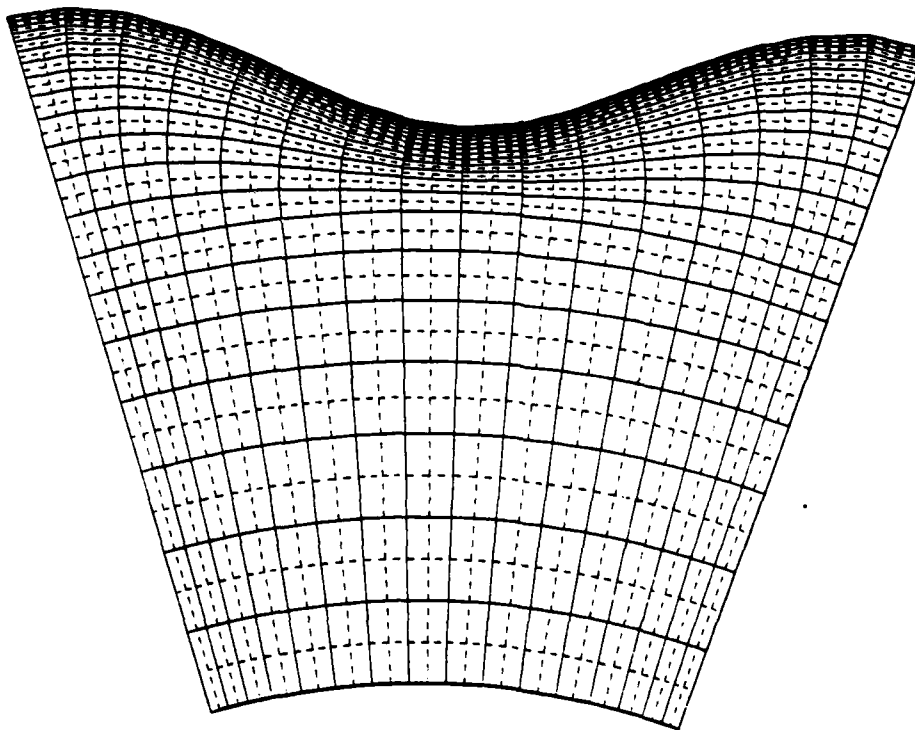


FIG 5-2  $Nu-Re$  distribution ( $Pr=7.03$ )

$$Nu = \frac{\bar{q}'' D_h}{\Delta T k}$$

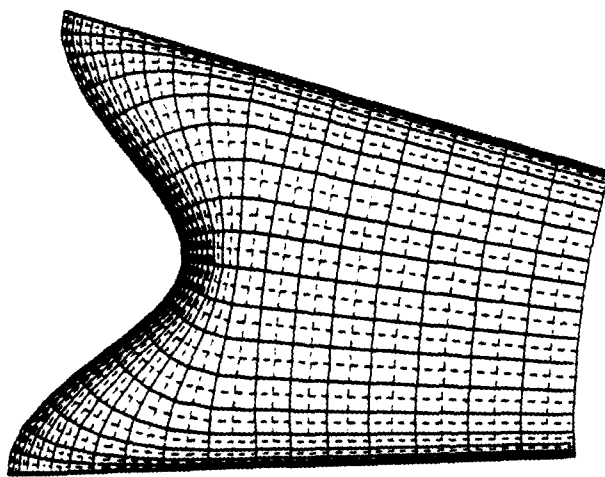


a. Grid 1

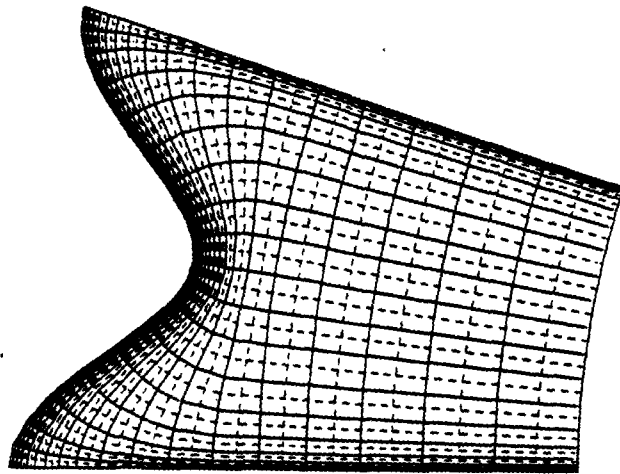


b. Grid 2

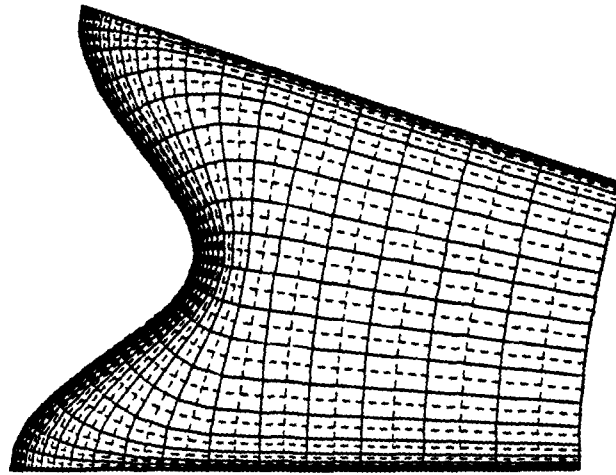
FIG 5-3  $n=10$  ;  $h=.06R_b$  ;  $R_a=.55R_b$



a. Grid 1



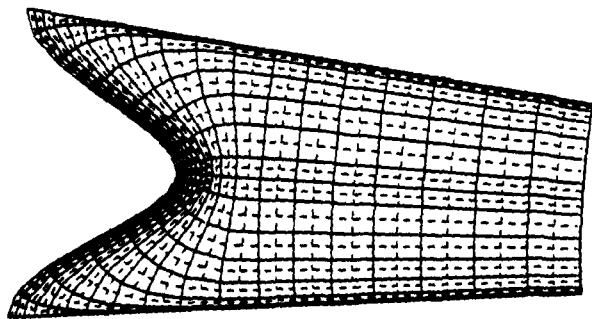
b. Grid 2



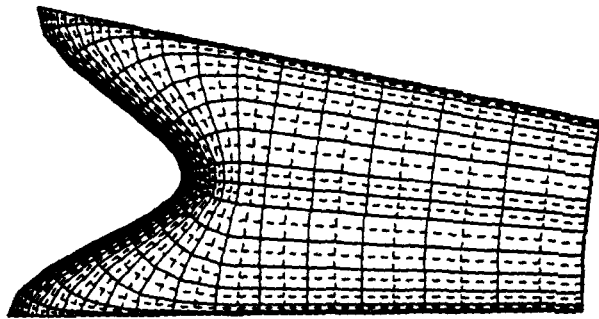
c. Grid 3

Fig 5.4  $n=20$ ;  $h=0.6R_b$ ;  $R_a=65R_b$

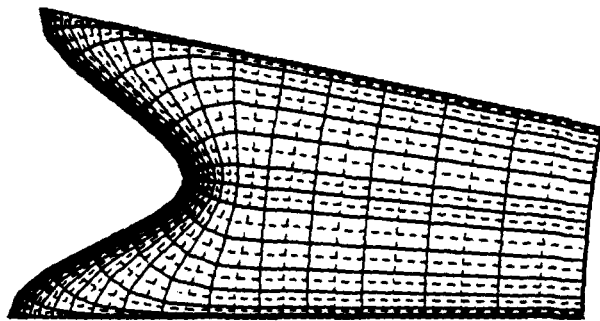




a. Grid 1



b. Grid 2



c. Grid 3

FIG 5-5  $n=30$  ;  $h=.06R_b$  ;  $R_a=.65R_b$

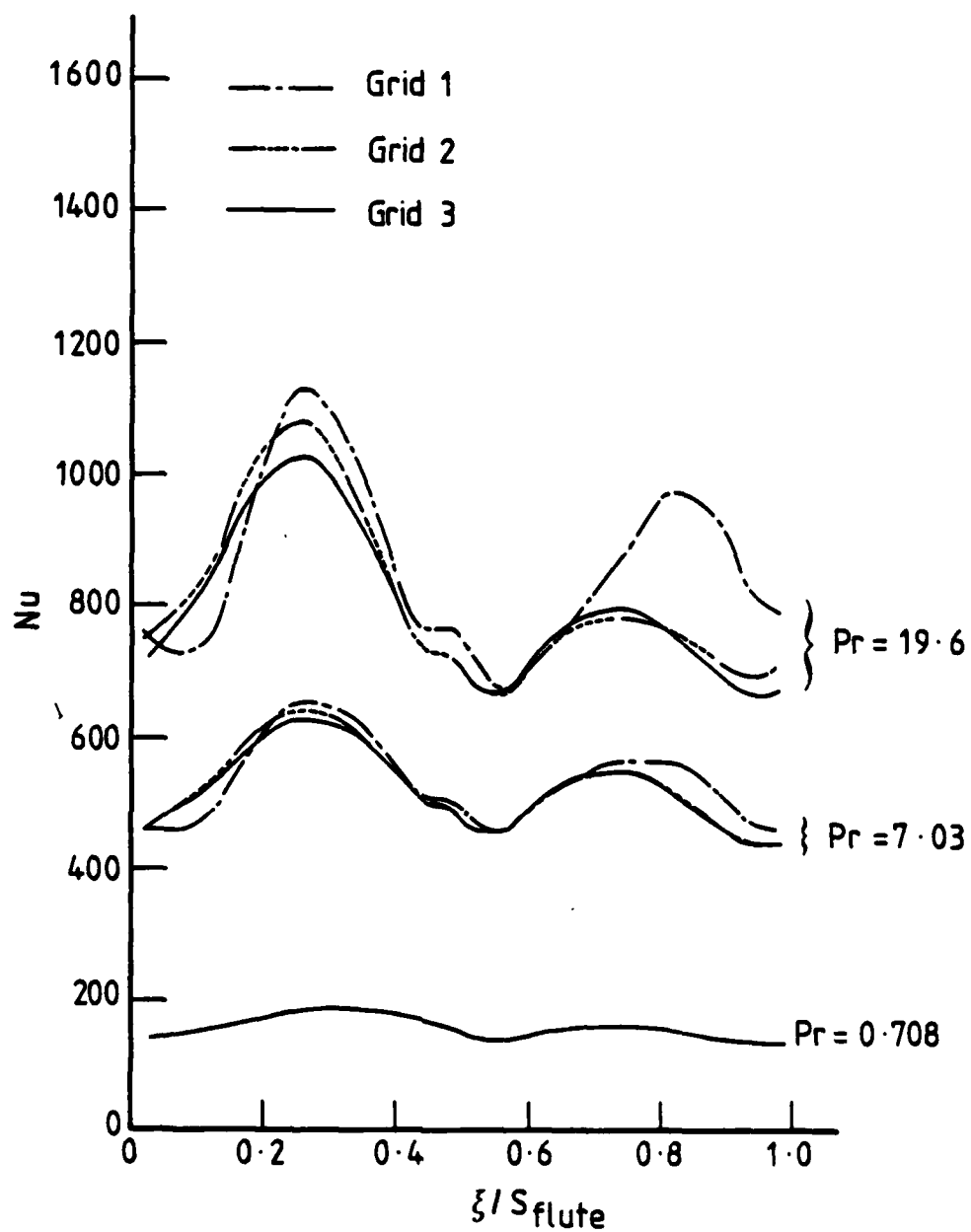


Fig. 5.6 Comparison of the results taken with the grids shown in Fig. 5.4,  $n = 20$ ,  $\varphi = 15^\circ$ ,  $Re \approx 60000$

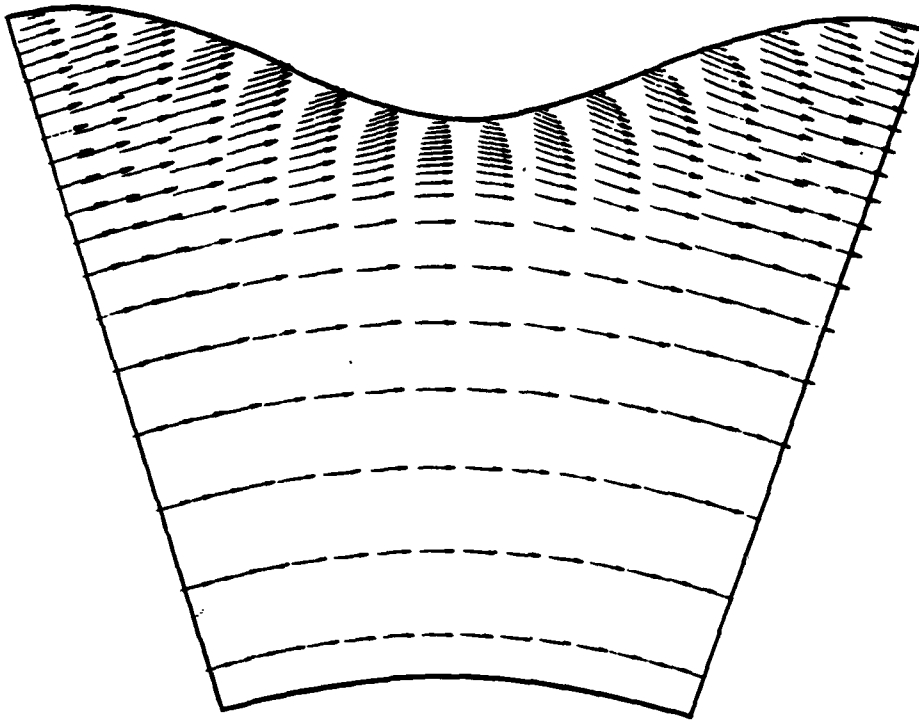
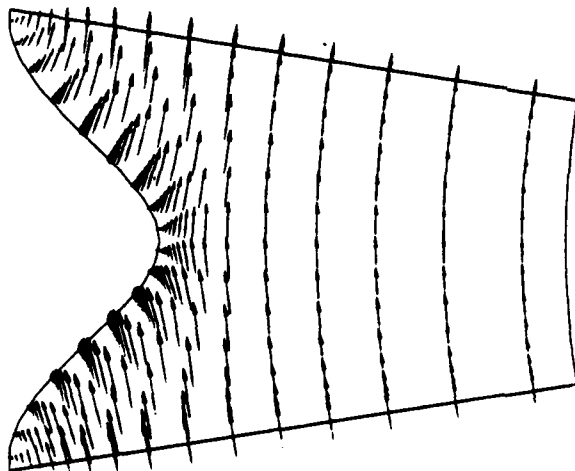
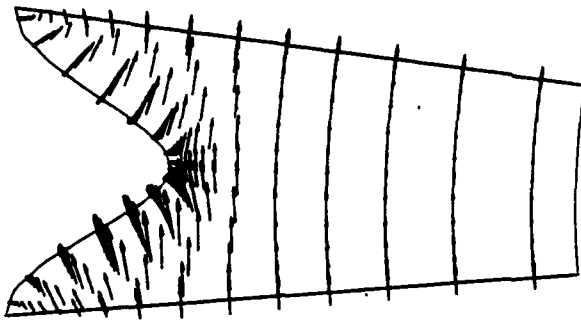


FIG 5-7  $(\vec{U} + \vec{V})$  for  $n=10$ ;  $\varphi=15^\circ$ ;  $Re=18000$

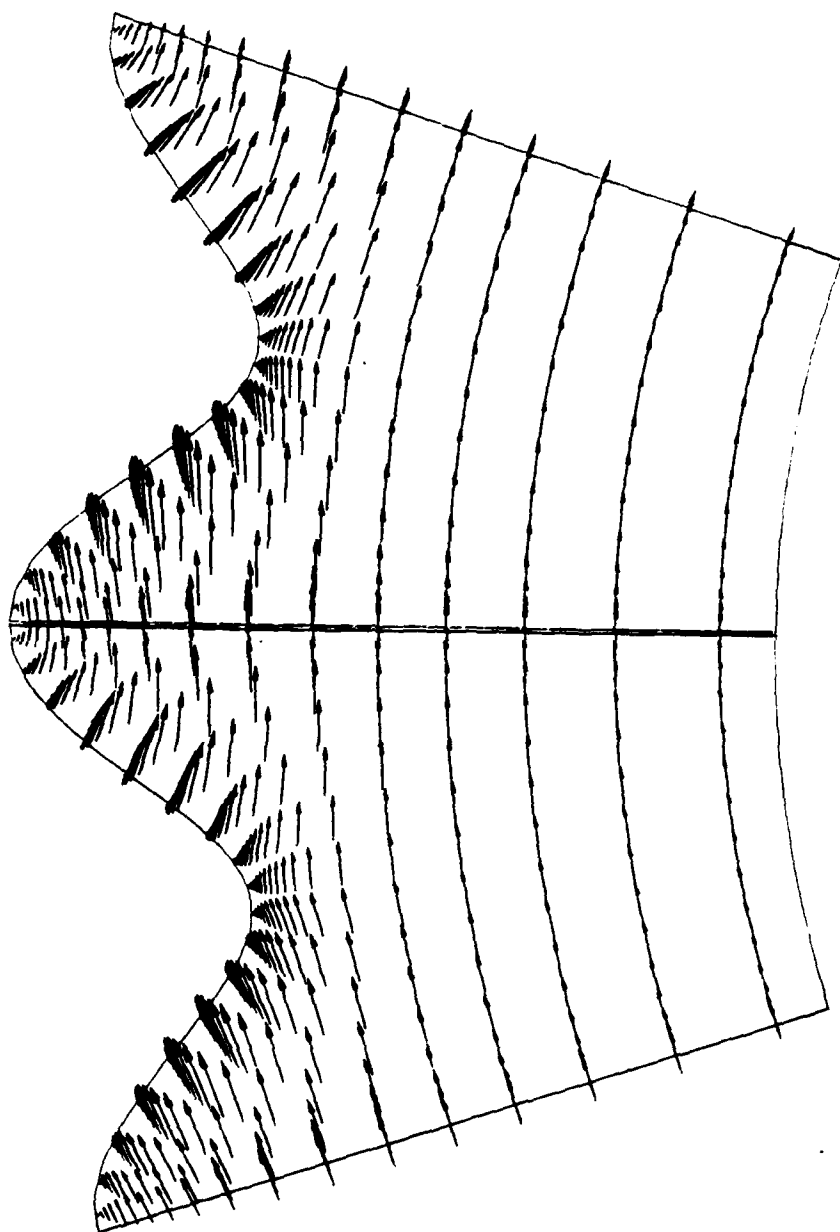


a. 20 flutes



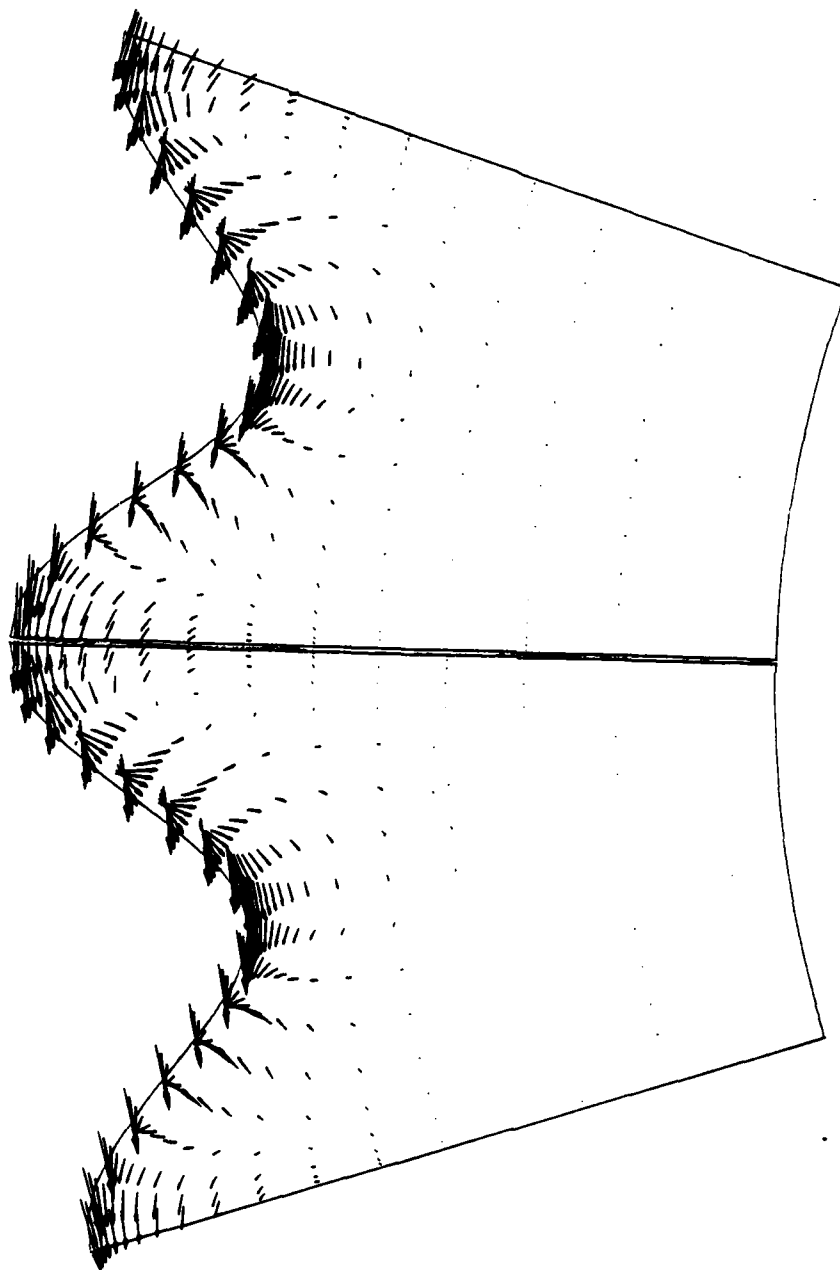
b. 30 flutes

FIG 5-8  $\vec{U} + \vec{V}$  ;  $\phi = 15^\circ$  ;  $h = 0.6 R_D$  ;  $Re = 18000$



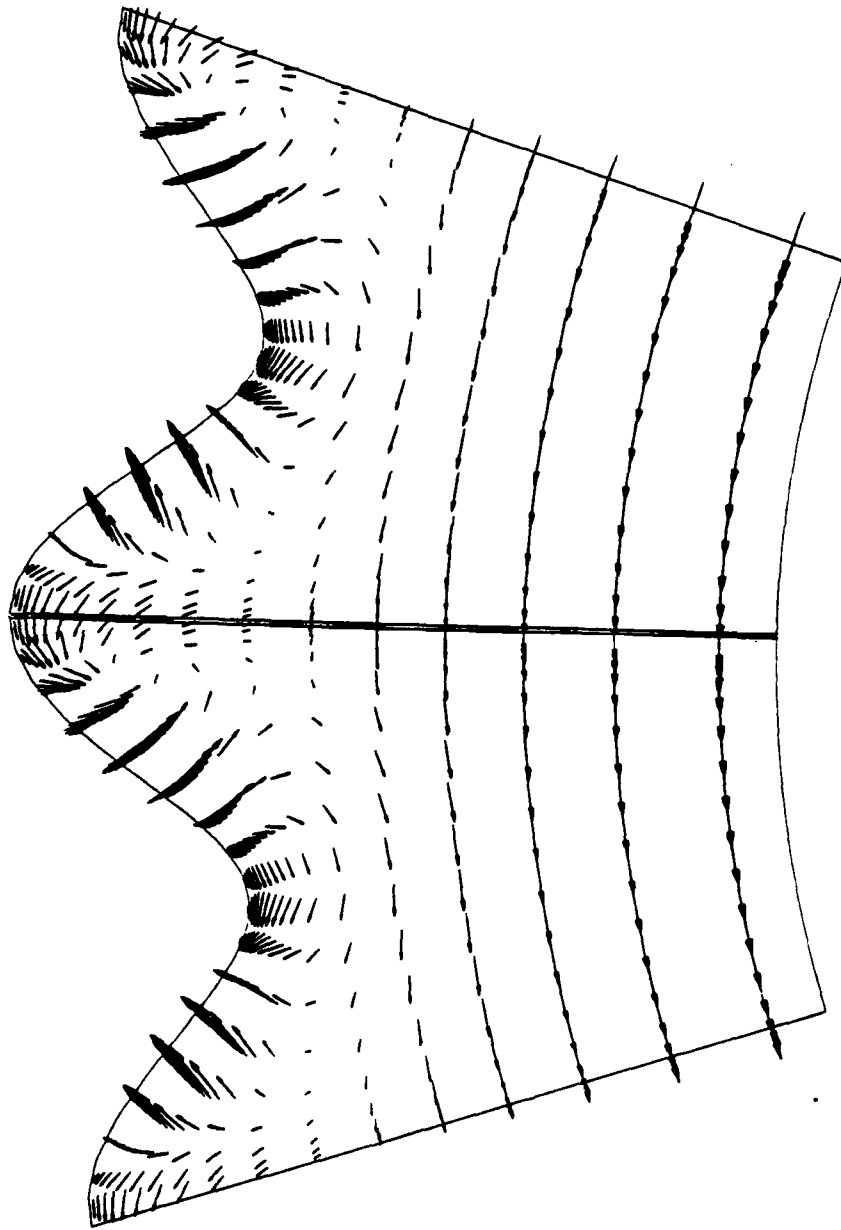
$n=20$ ;  $\varphi=15$ ;  $h=.06R_b$

FIG 5.9.a  $\vec{(U+V)}$



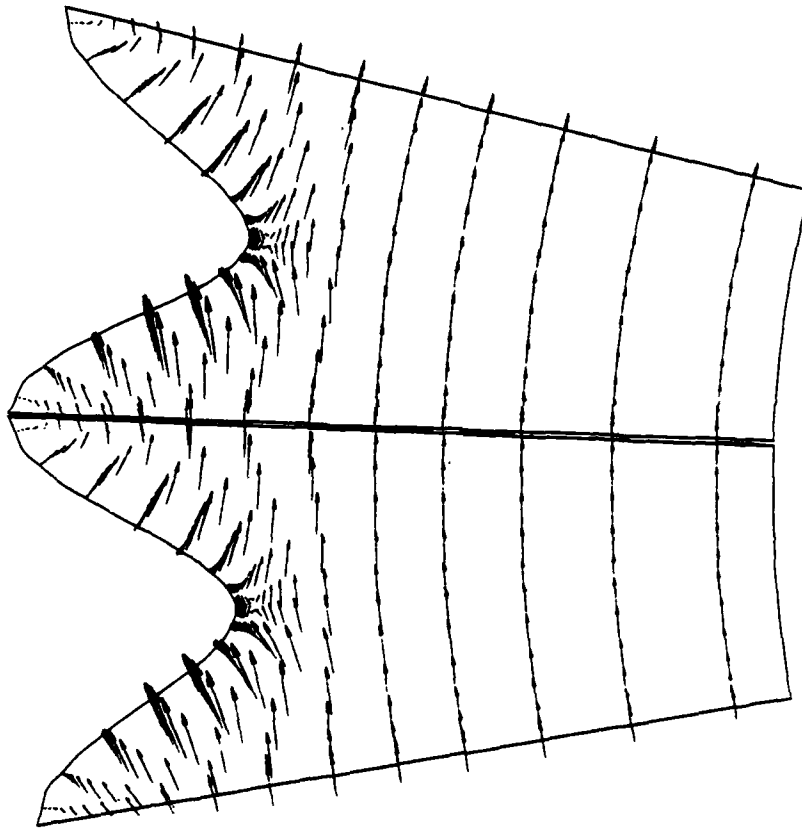
$n=20 ; \varphi=15 ; h=0.6R_b$

FIG 5.9.b  $(\vec{U} + \vec{V}) - \vec{\omega R}$



$n=20; \varphi=15; h=0.6R_D$

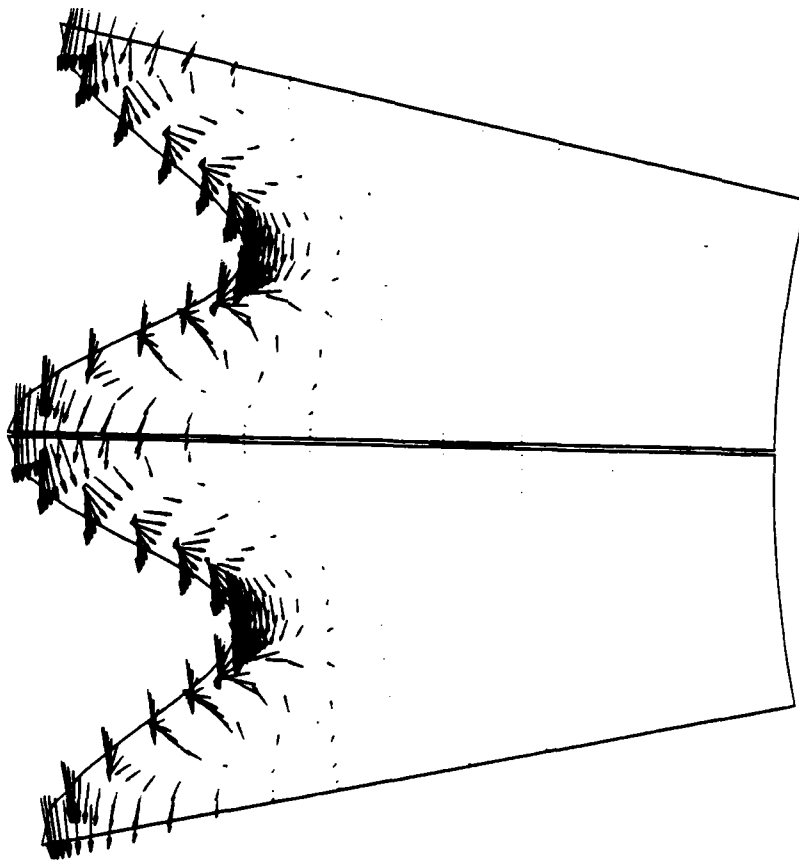
FIG 5-9.c  $(V_{\theta} \cos \varphi - W \sin \varphi) \cos \varphi + V_r$



$n=30 ; \phi=30 ; h=.06R_b$

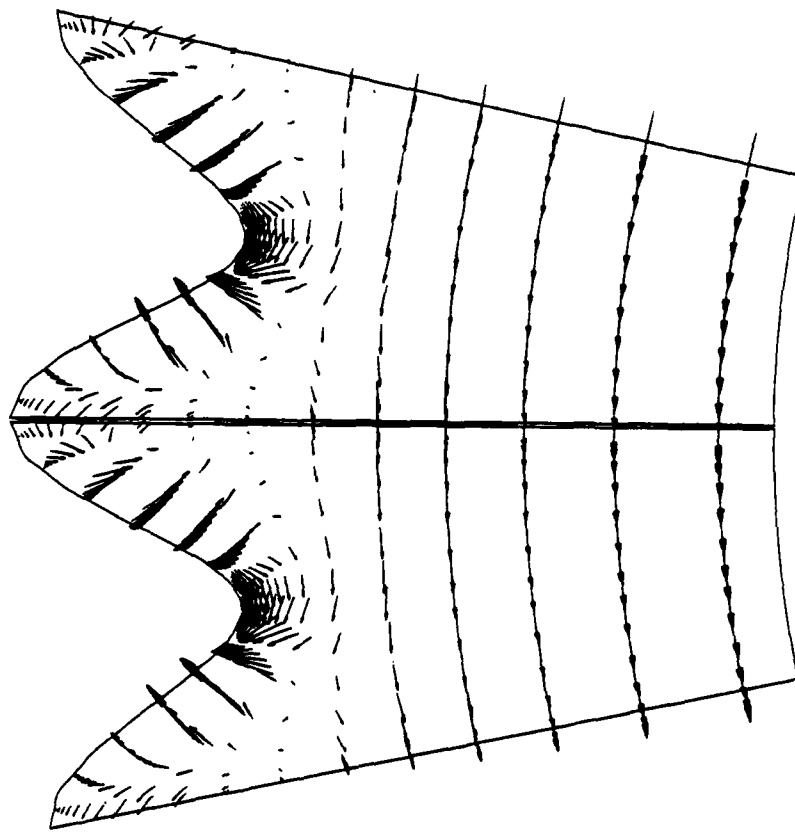
FIG 5.9d  $(\vec{U}+\vec{V})$





$$n=30; \varphi=30; h=0.6R_b$$

FIG 5.9.e  $(\vec{U} + \vec{V}) - \vec{\omega R}$



$n=30 ; \varphi=30 ; h=.06 R_D$

FIG 5-9f  $\overrightarrow{V_\theta \cos \varphi - W \sin \varphi} \cos \varphi + \overrightarrow{V_r}$

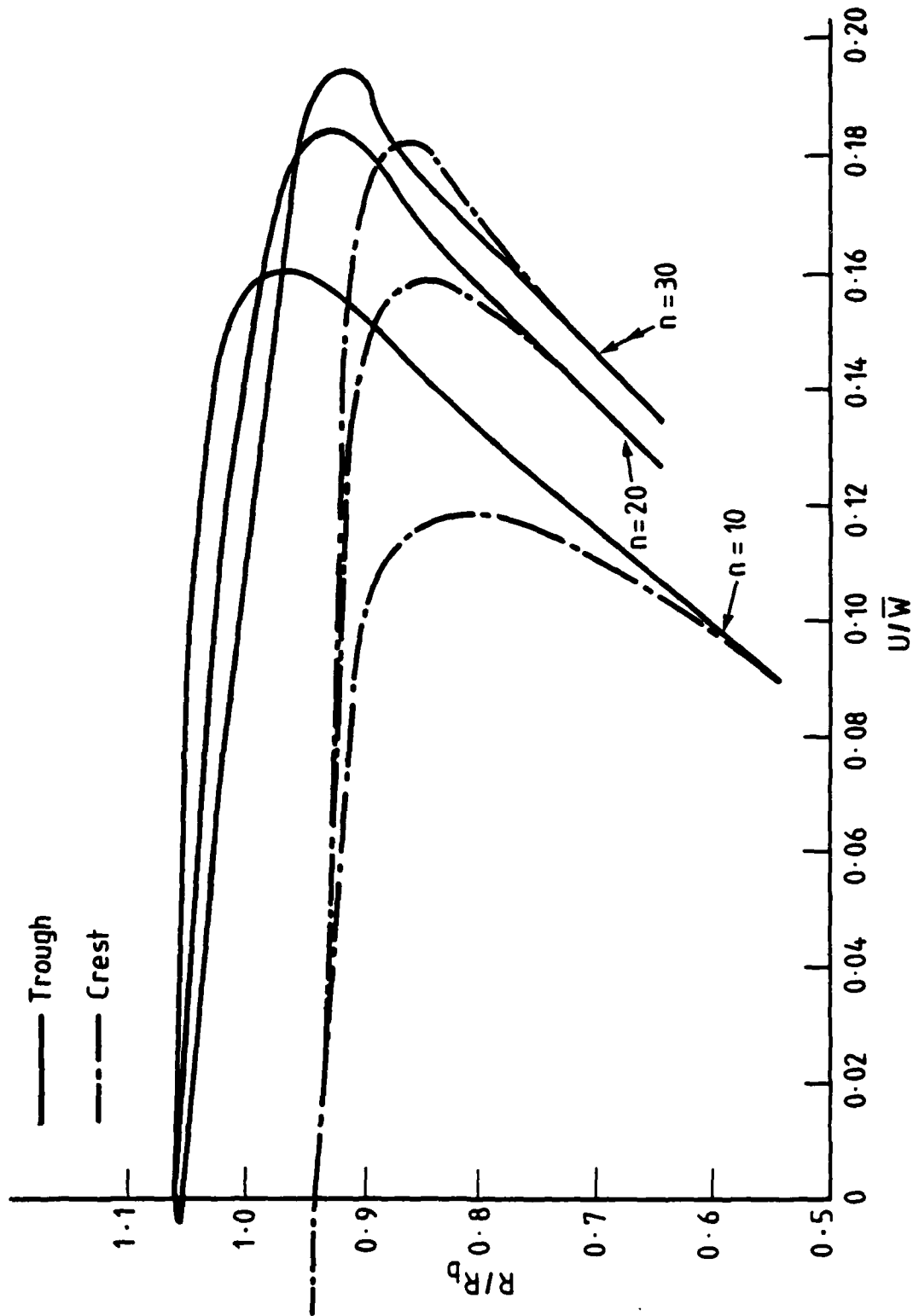


Fig. 5.10 Distribution of circumferential velocity along trough and crest radii  $\phi = 15^\circ$ ,  $Re = 18,000$

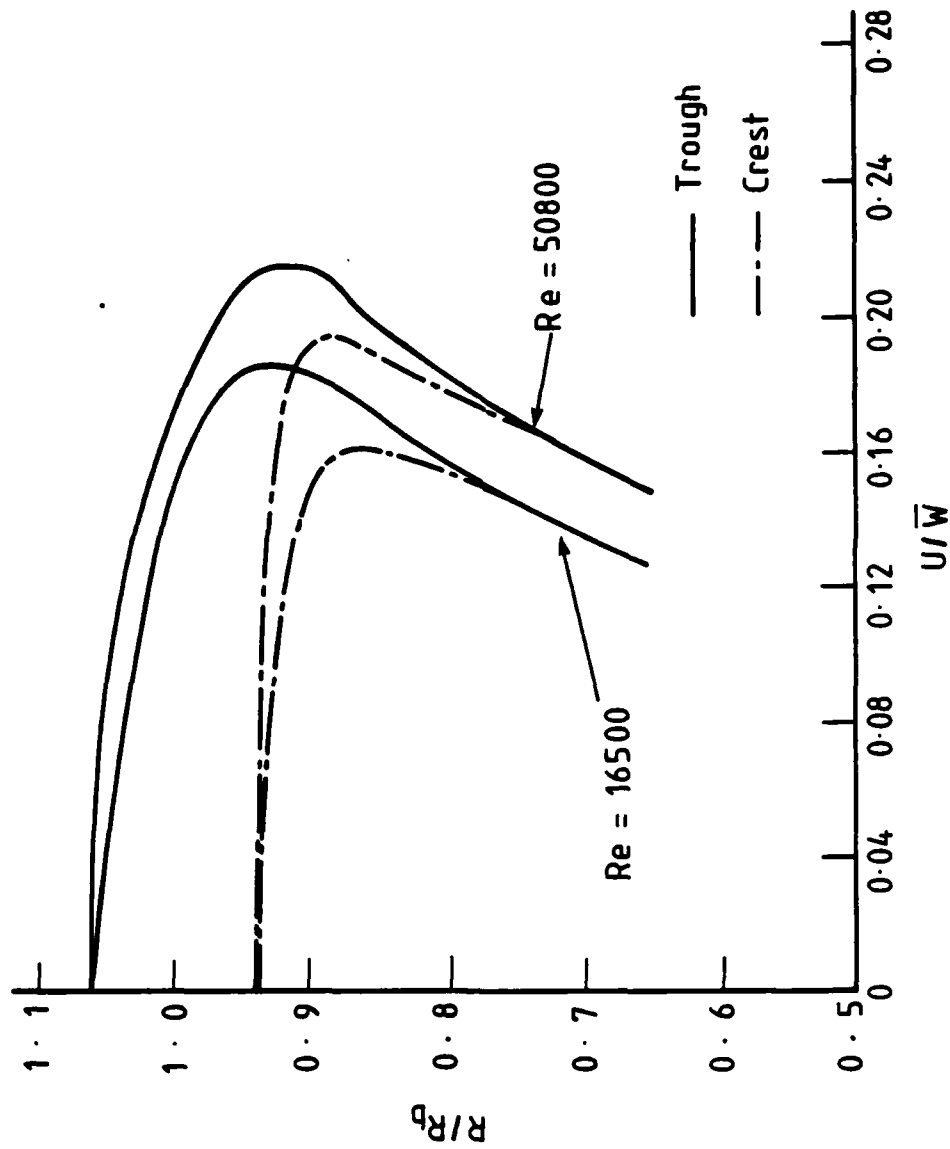


Fig. 5.11 Effect of the Reynolds number on the distribution of circumferential velocity along trough and crest radii,  $n = 20$ ,  $\phi = 15^\circ$

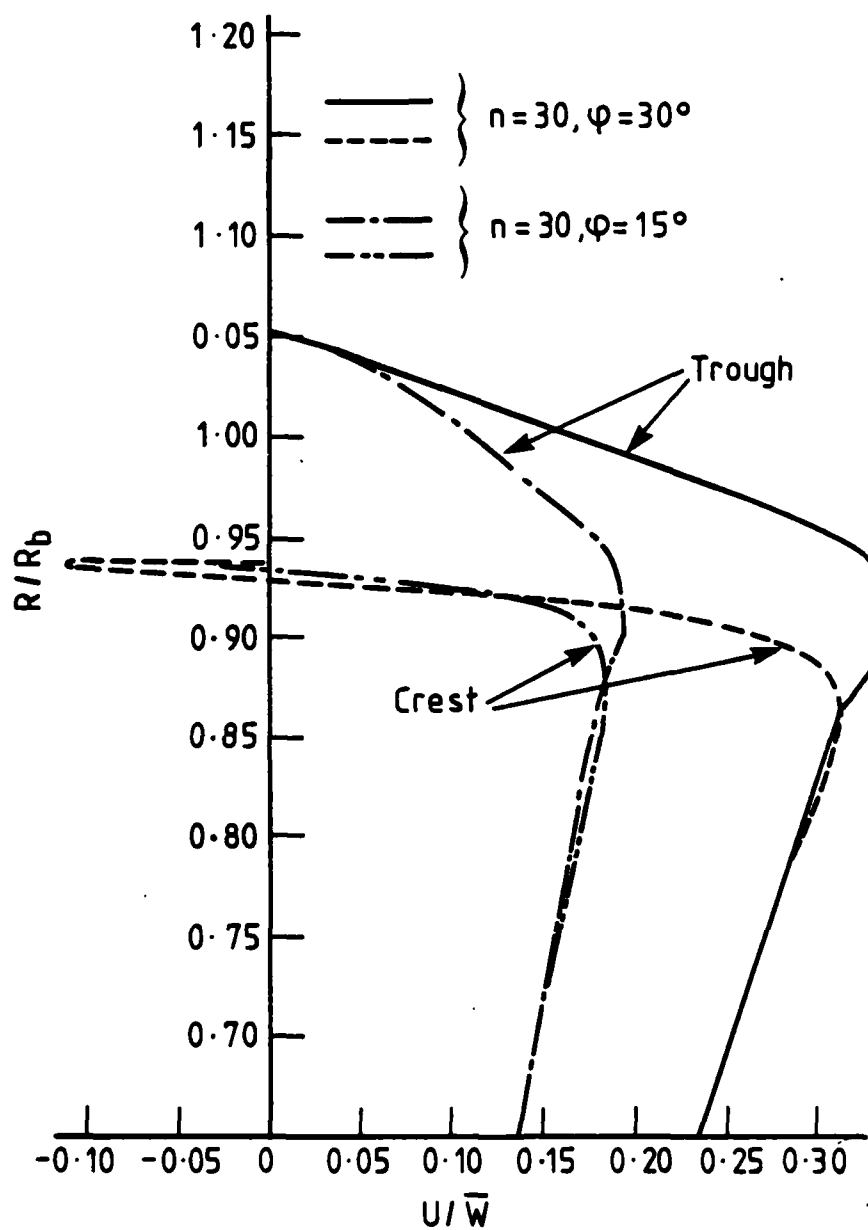


Fig. 5.12 Effect of the spiral angle  $\varphi$  on the distribution of circumferential velocity along trough and crest radii for  $n = 30$ ,  $Re \approx 18000$

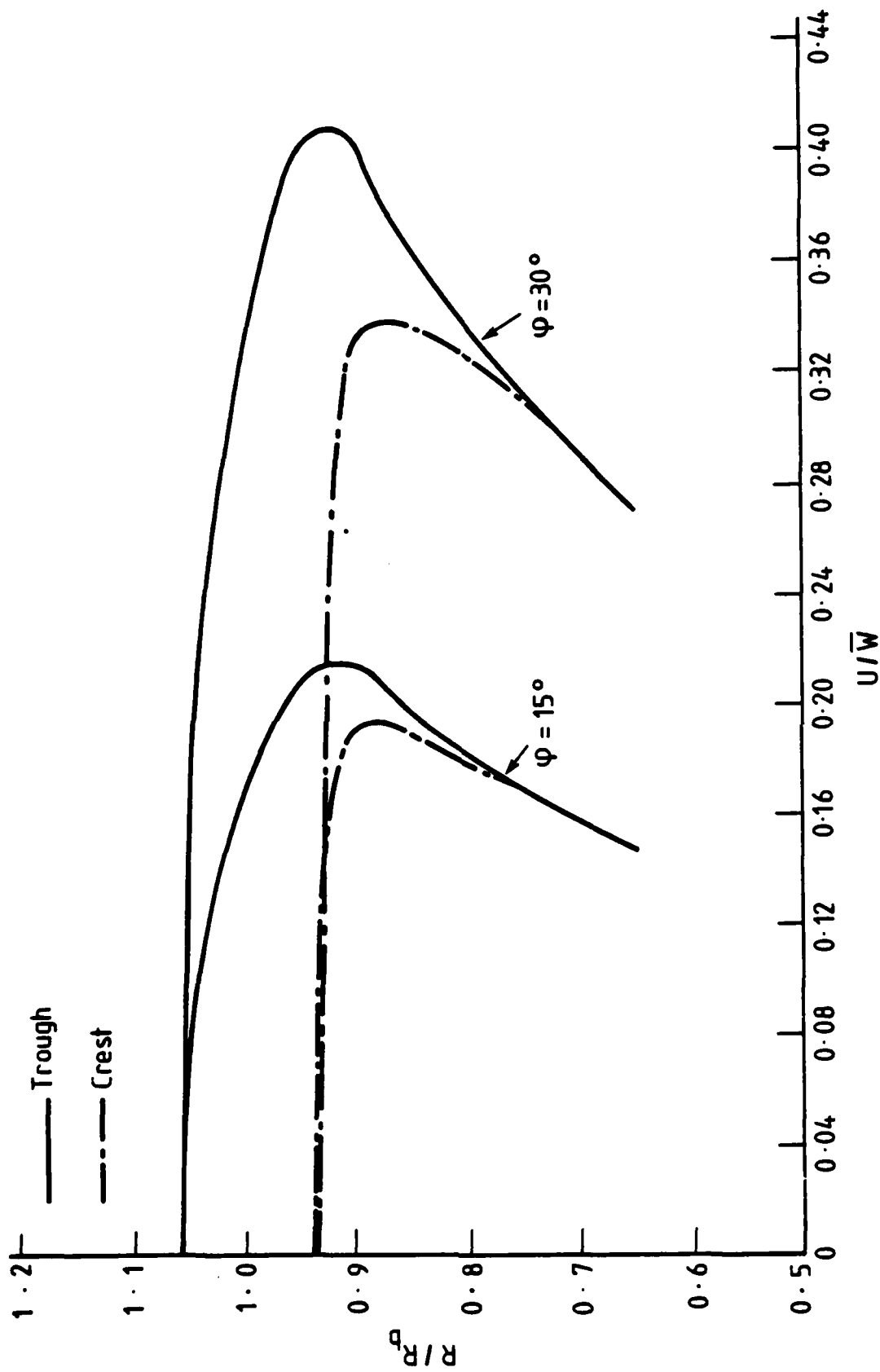


Fig. 5.13 Effect of the spiral angle on the circumferential velocity profiles  $n = 20$ ,  $Re = 5.1 \times 10^4$

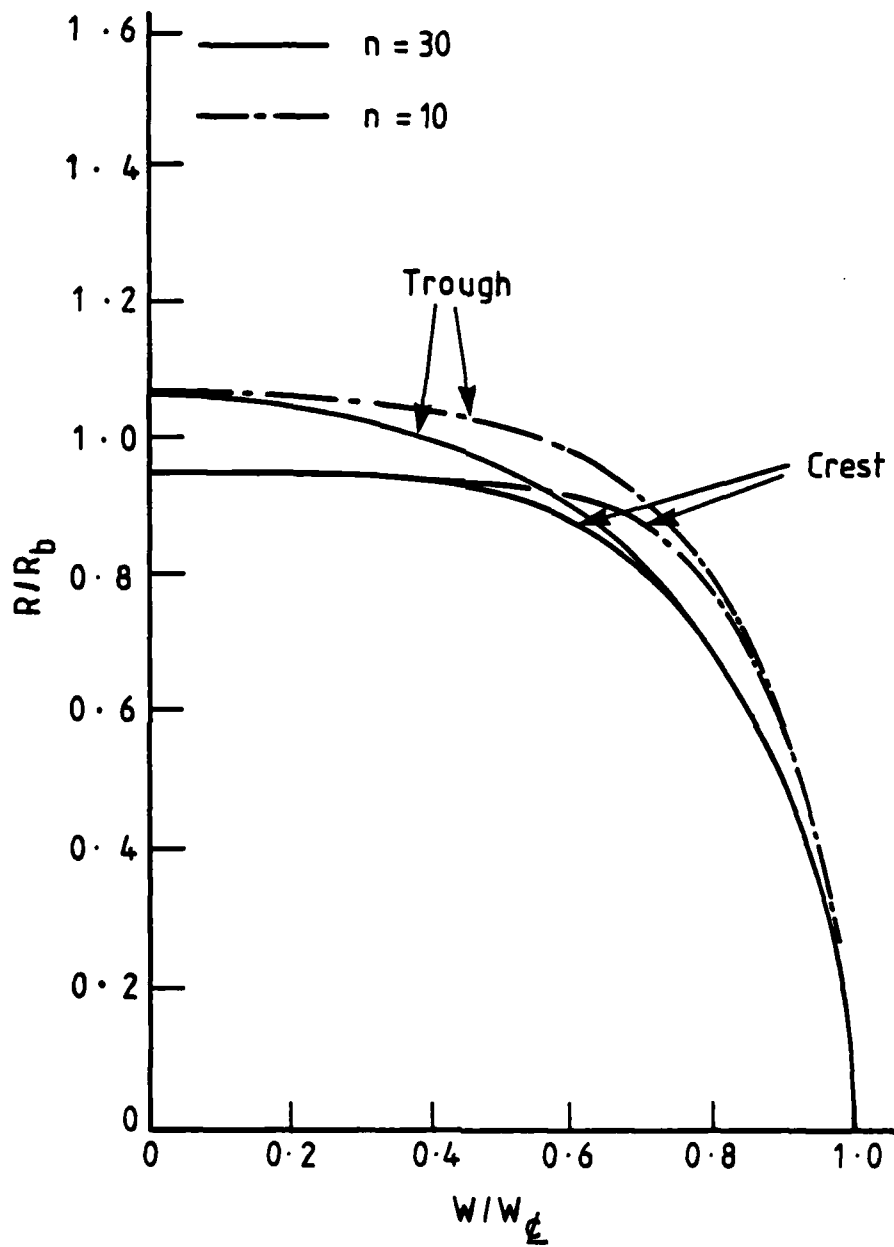


Fig. 5.14 Effect of flute density on the distribution of the axial velocity  $\varphi = 30^\circ$ ,  $Re \approx 26300$

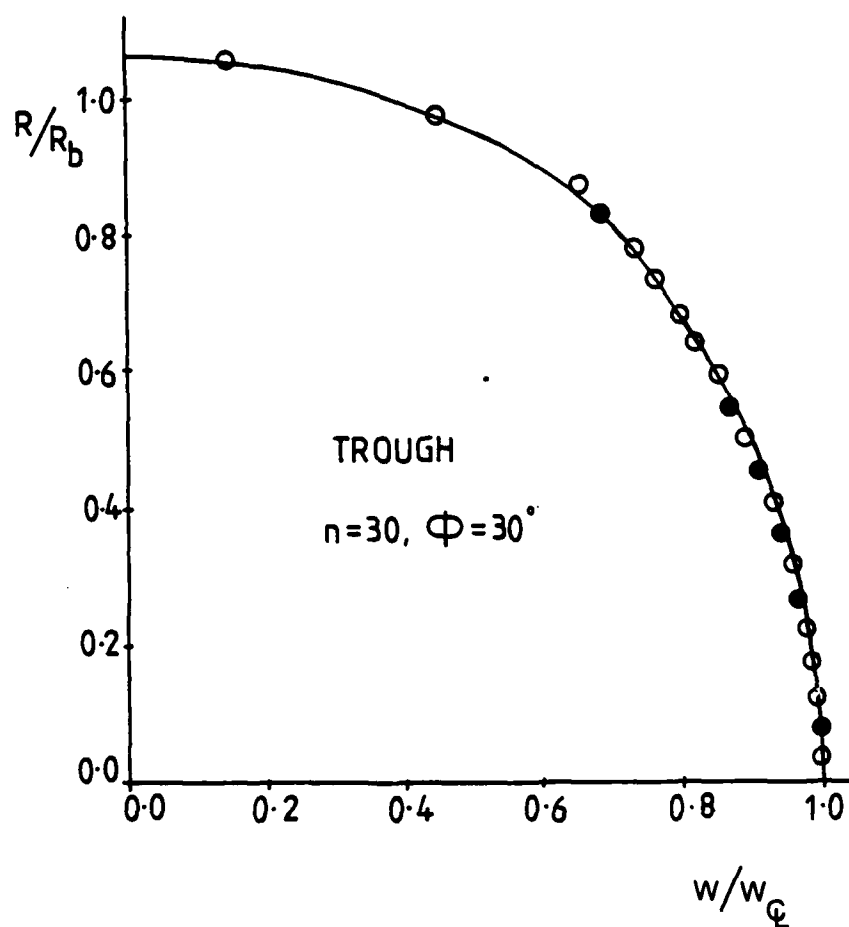


FIG 5-15 Comparison of predicted and experimental data for the axial velocity distribution

○ ● Experiments (LaRue)  $Re=47847$

— Computations  $Re=26300$



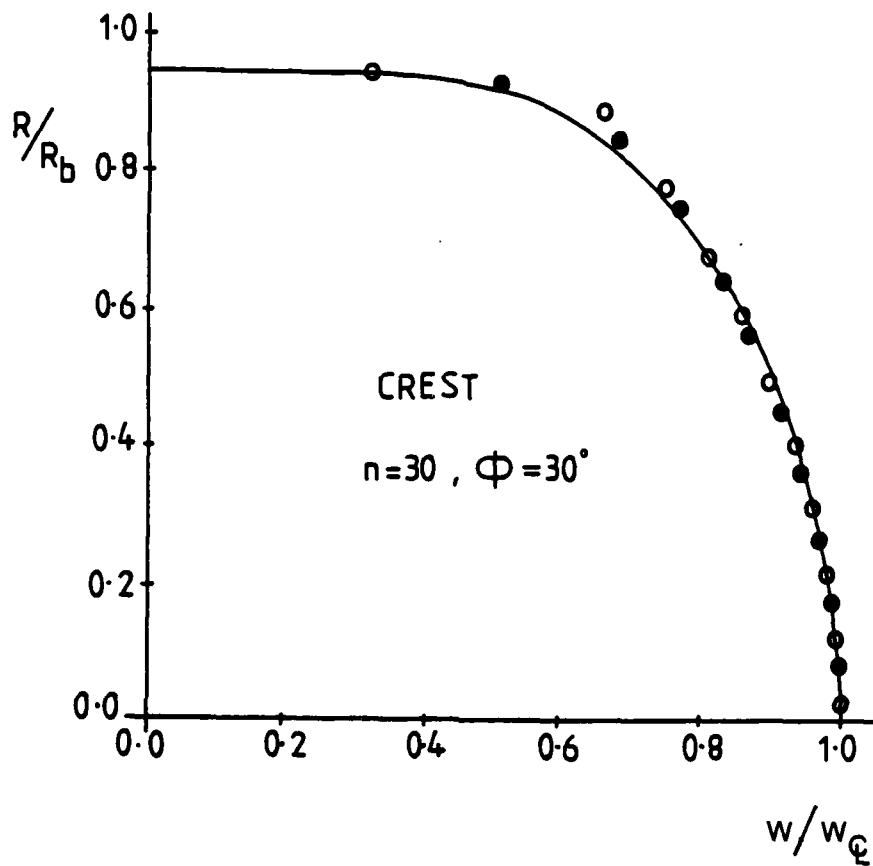


FIG 5-16 Comparison of predicted and experimental data for the axial velocity distribution

o • Experiments (LaRue)  $Re=47287$

— Computations  $Re=26300$

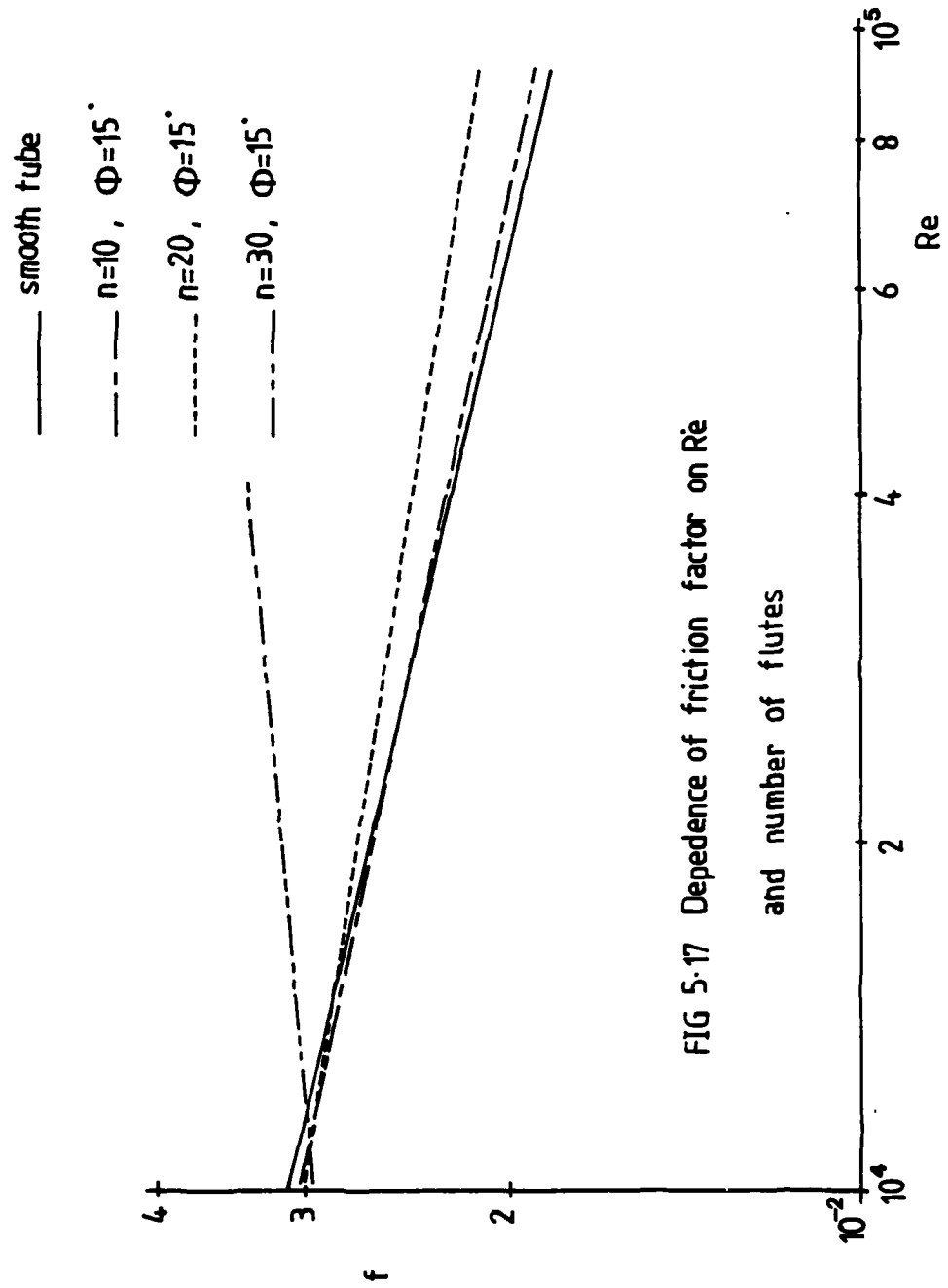


FIG 5-17 Dependence of friction factor on  $Re$   
and number of flutes

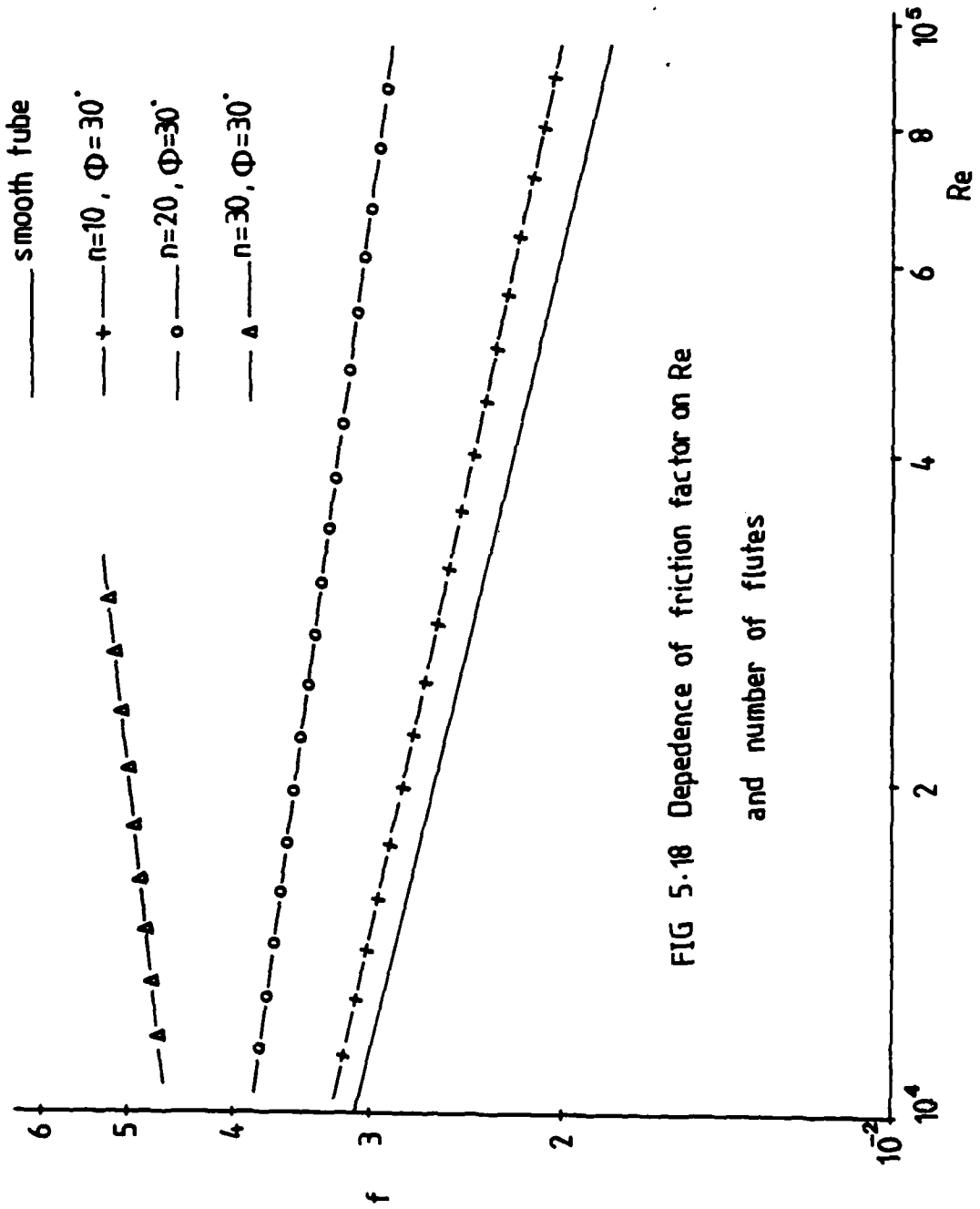


FIG 5.18 Dependence of friction factor on Re  
and number of flutes

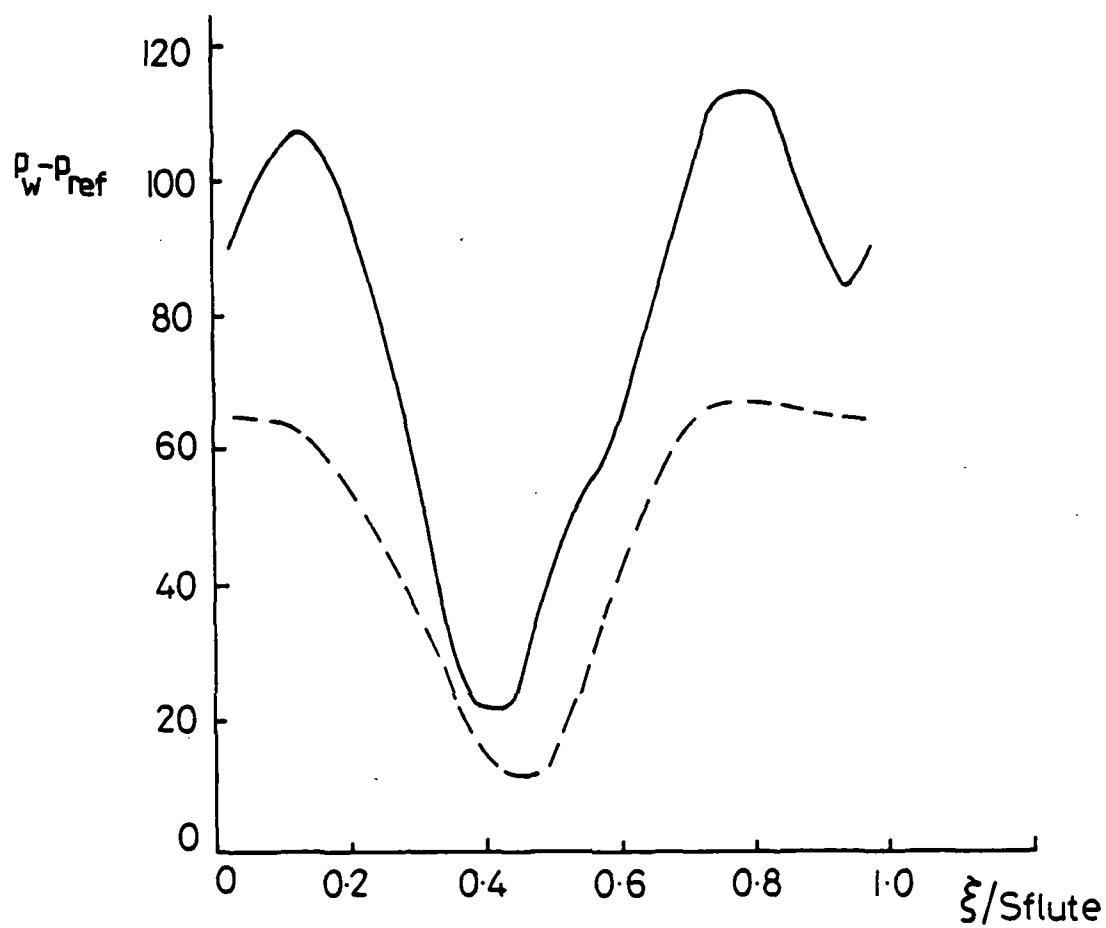


FIG 5-19 Effect of flute density on the distribution of surface pressure  
 $Re=6 \times 10^4$

— —  $n=10$   $\varphi=15^\circ$

—  $n=20$   $\varphi=15^\circ$

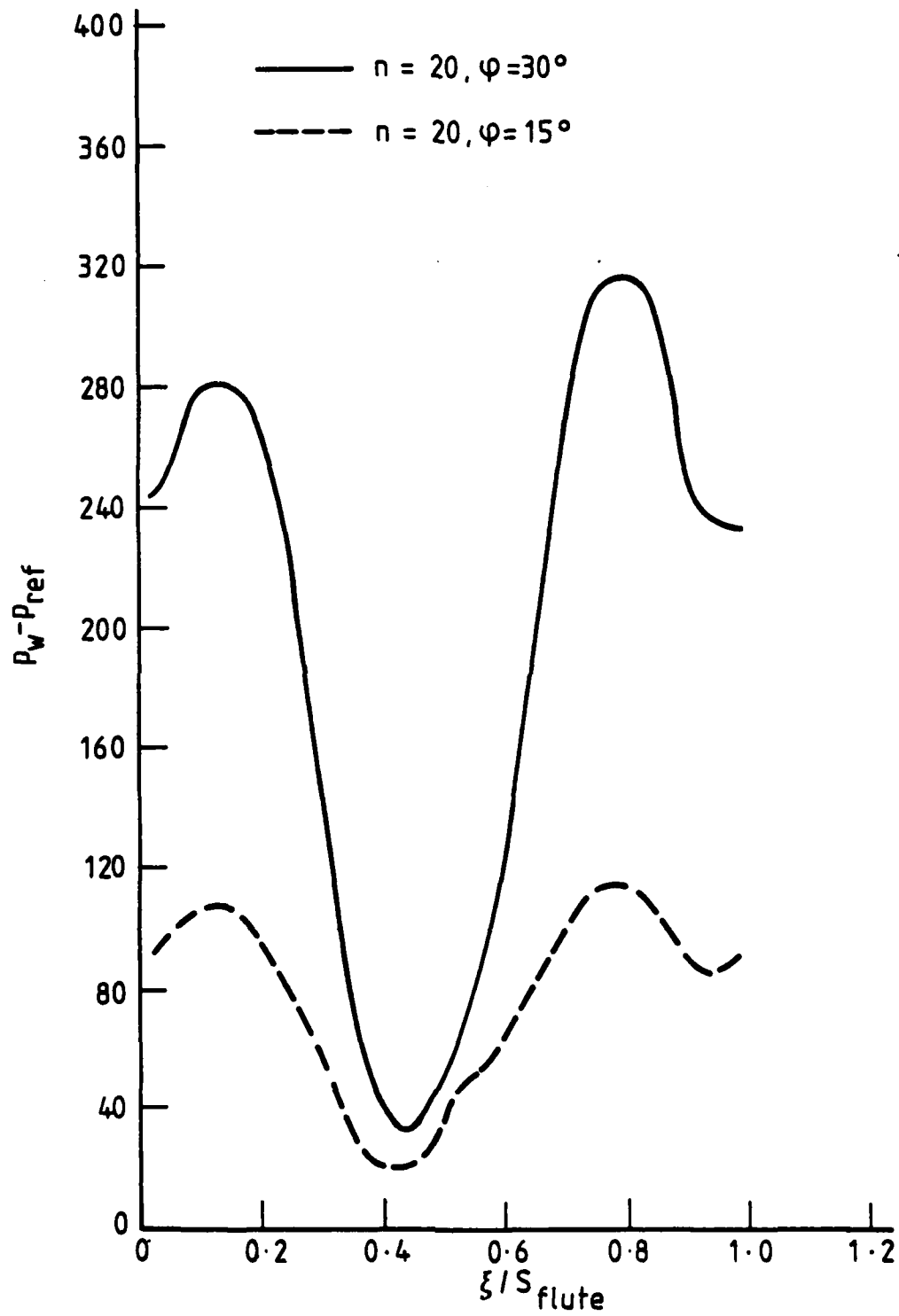


Fig. 5.20 Effect of spiral angle on the distribution of surface pressure for  $Re = 6 \times 10^4$

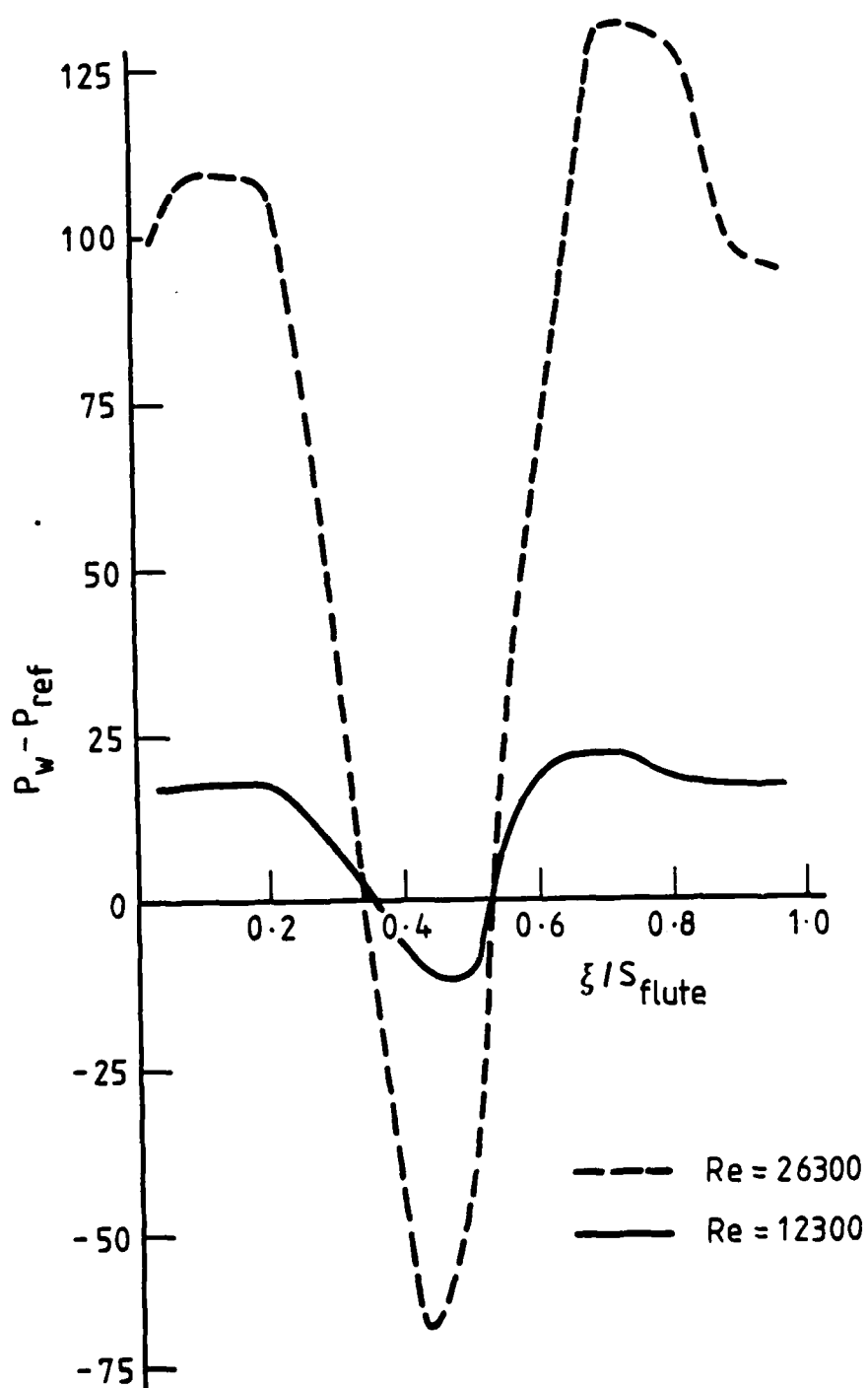


Fig. 5.21 Effect of Reynolds number on surface pressure distribution for  $n = 30$ ,  $\varphi = 30^\circ$

AD-A150 774

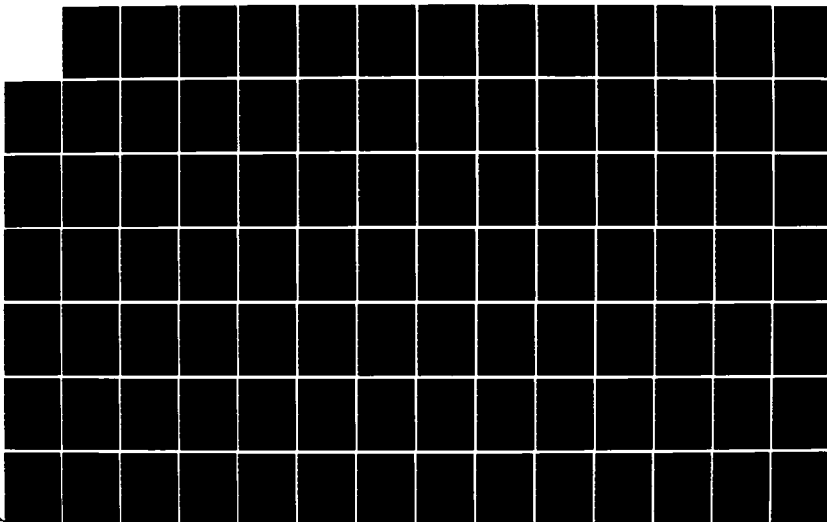
FLUID MECHANICS AND HEAT TRANSFER SPIRALLY FLUTED  
TUBING(U) GA TECHNOLOGIES INC SAN DIEGO CA  
J S YAMPOLSKY ET AL. DEC 84 GA-A17833 N00014-82-C-0721

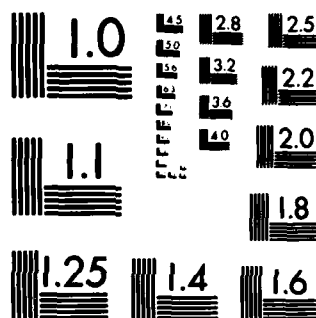
6/8

UNCLASSIFIED

F/G 20/4

NL





MICROCOPY RESOLUTION TEST CHART  
NATIONAL BUREAU OF STANDARDS-1963-A



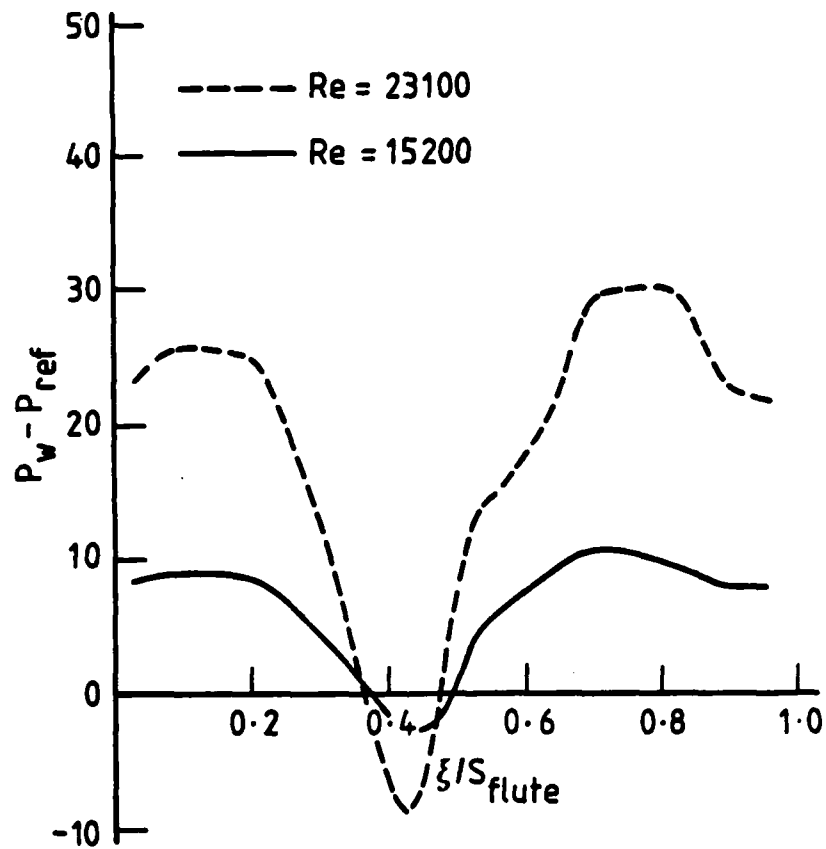


Fig. 5.22 Effect of Reynolds number on surface pressure distribution for  $n=30, \varphi=15$

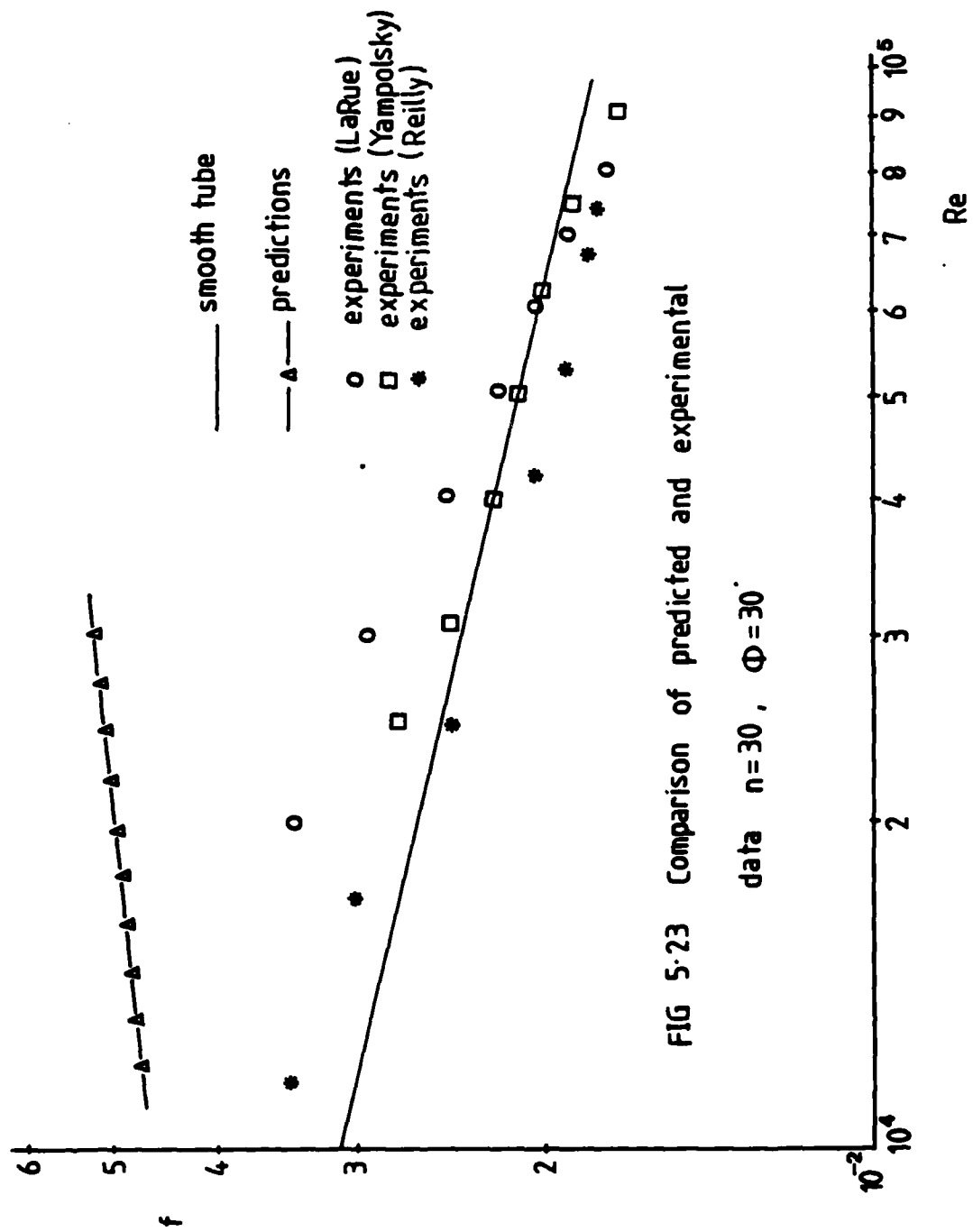


FIG 5-23 Comparison of predicted and experimental

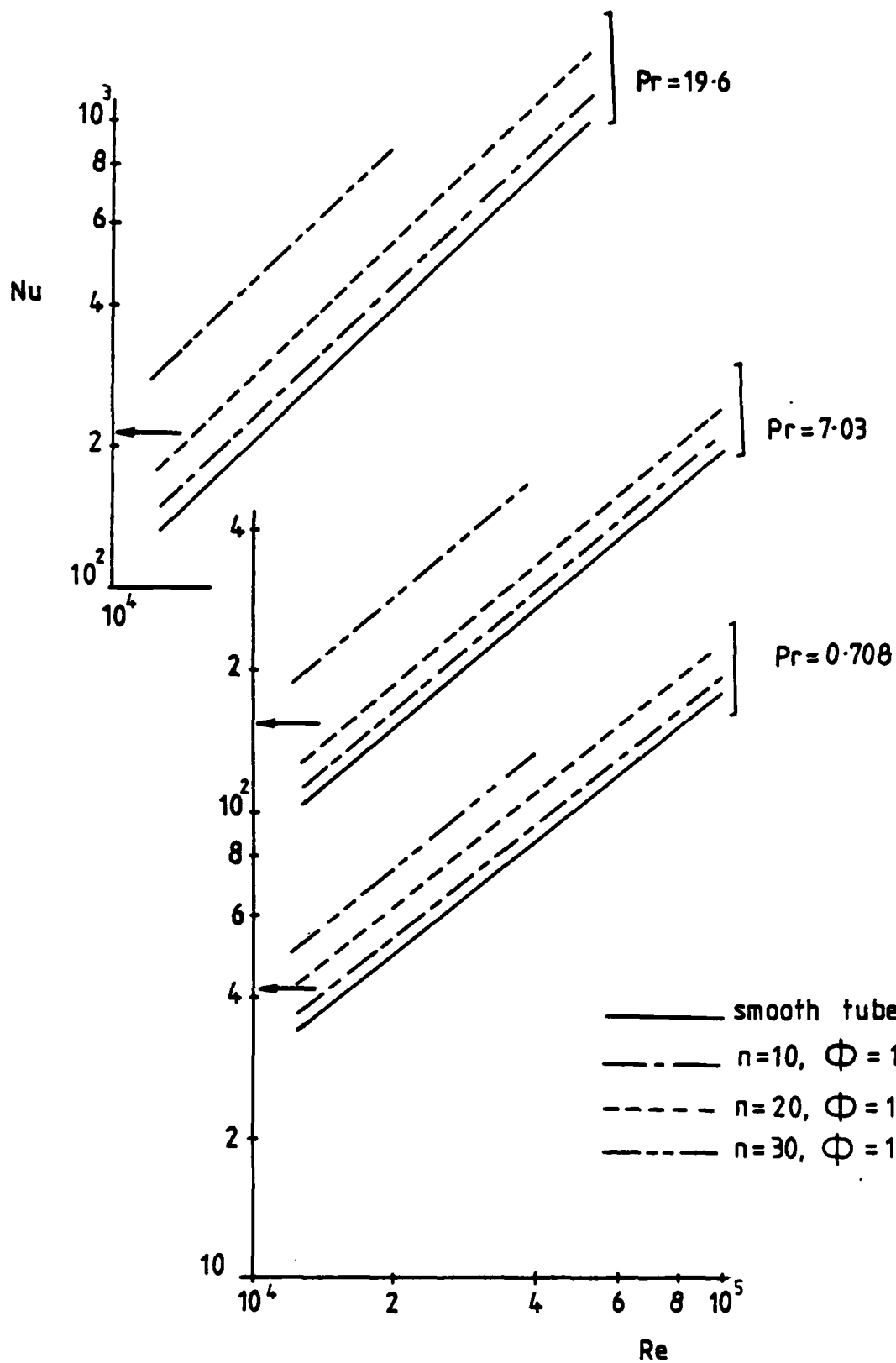


FIG 5-24 Dependence of  $Nu$  on  $Re$   
and number of flutes

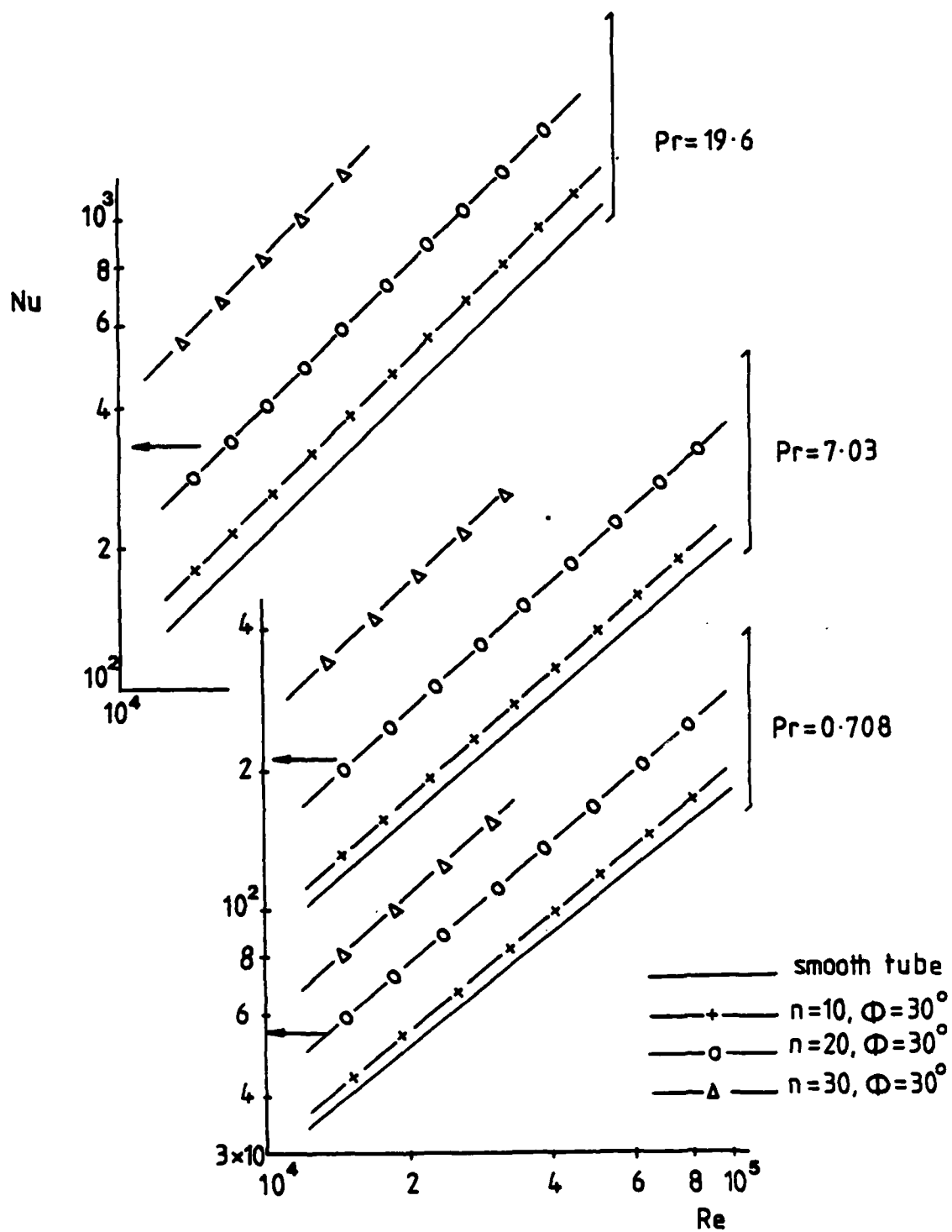


FIG 5-25 Dependence of  $Nu$  on  $Re$  and number of flutes

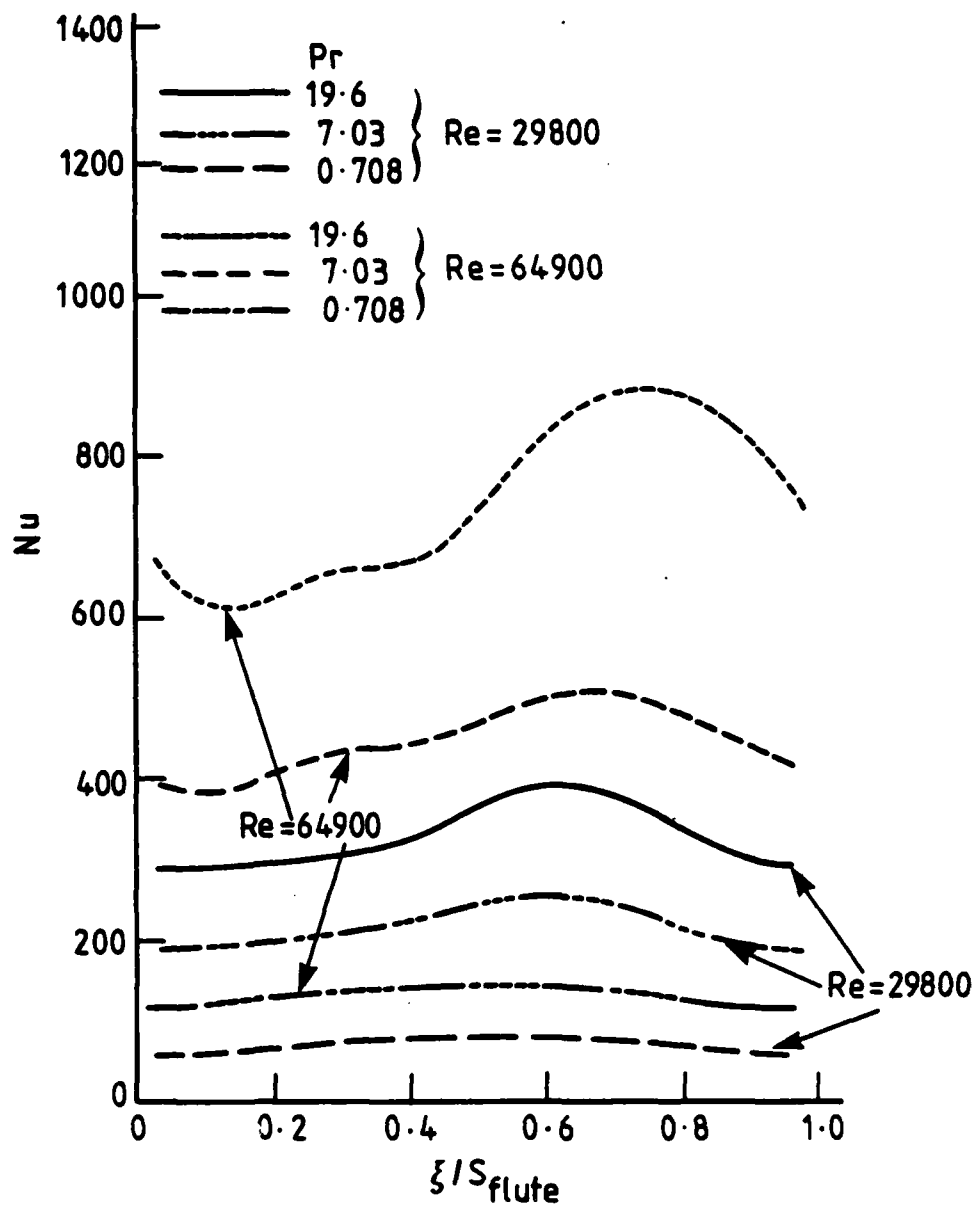


Fig. 5.26 Variation of local Nusselt number around flute  
 $n = 10, \varphi = 15^\circ$

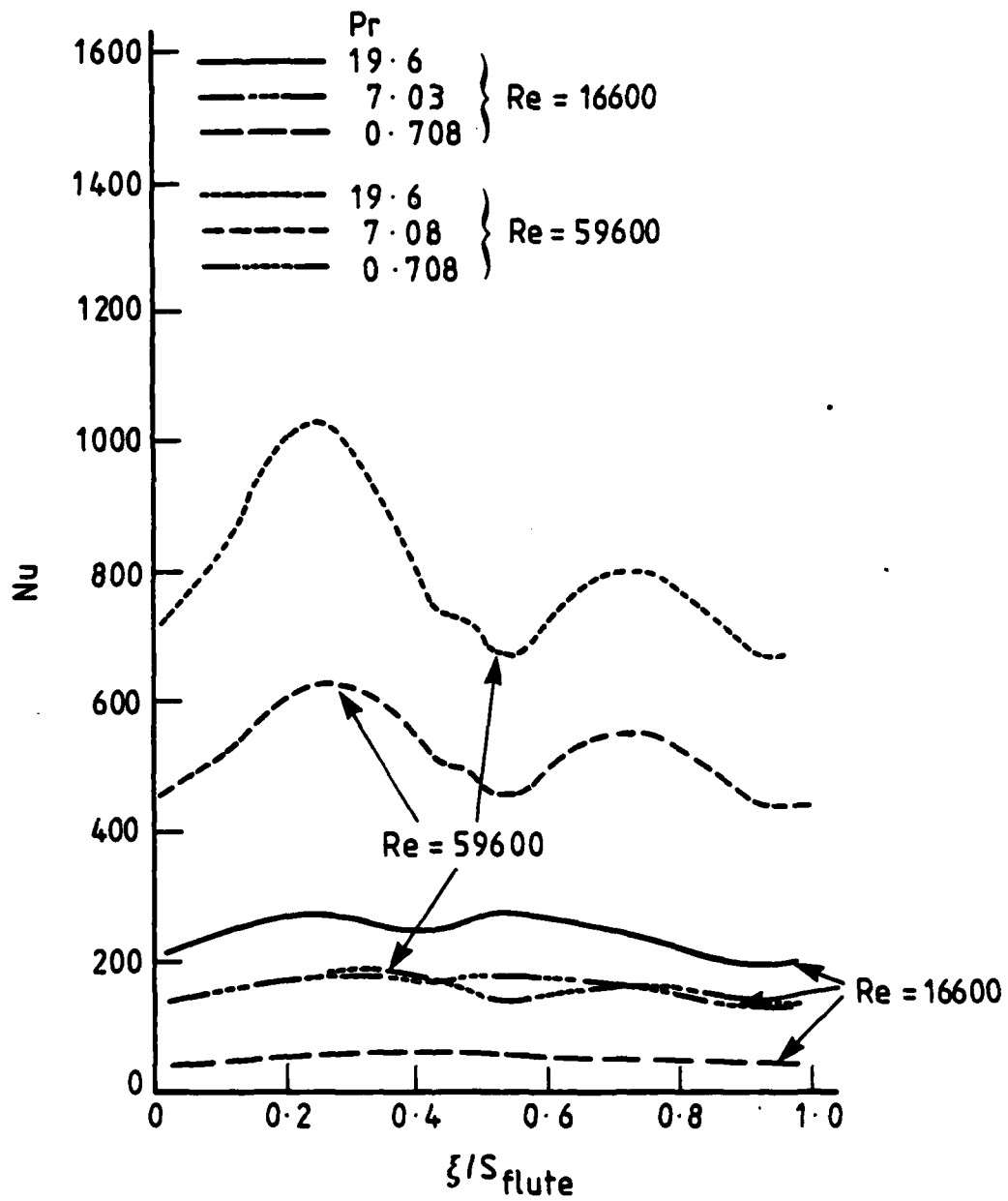


Fig. 5.27 Variation of local Nusselt number around flute  
 $n = 20$ ,  $\varphi = 15^\circ$

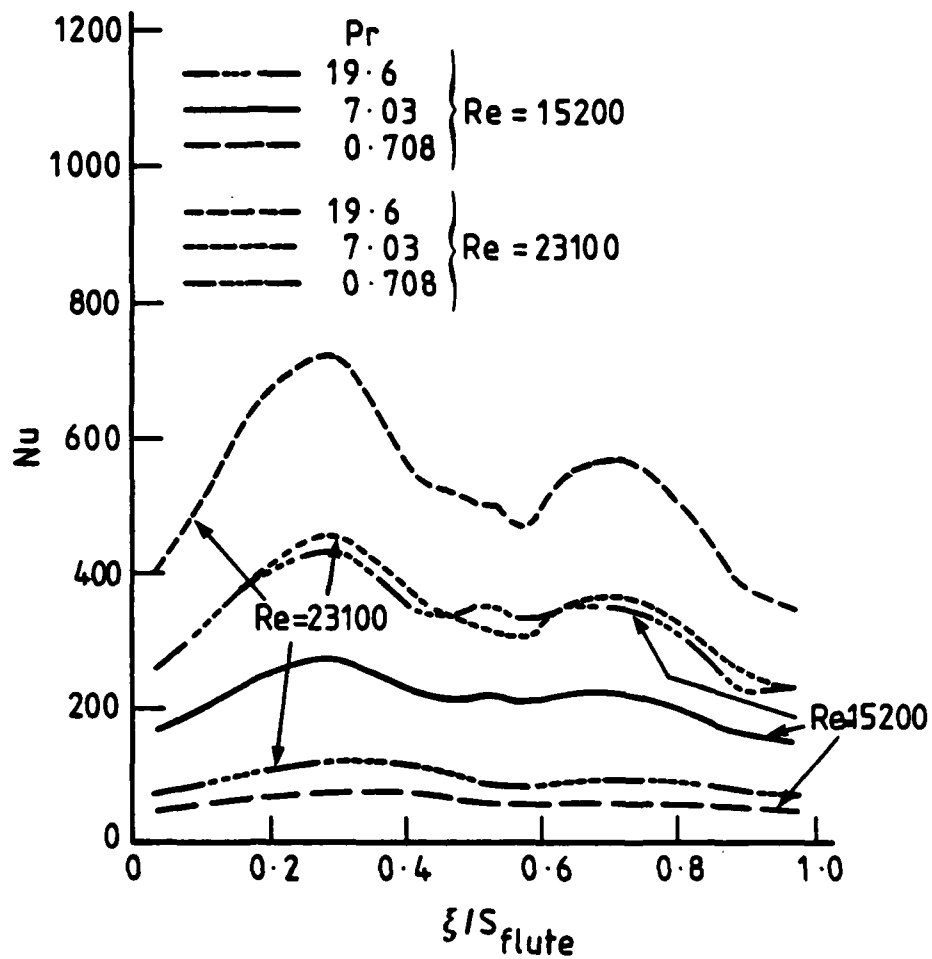


Fig. 5.28 Variation of local Nusselt number around flute  
 $n = 30, \varphi = 15^\circ$

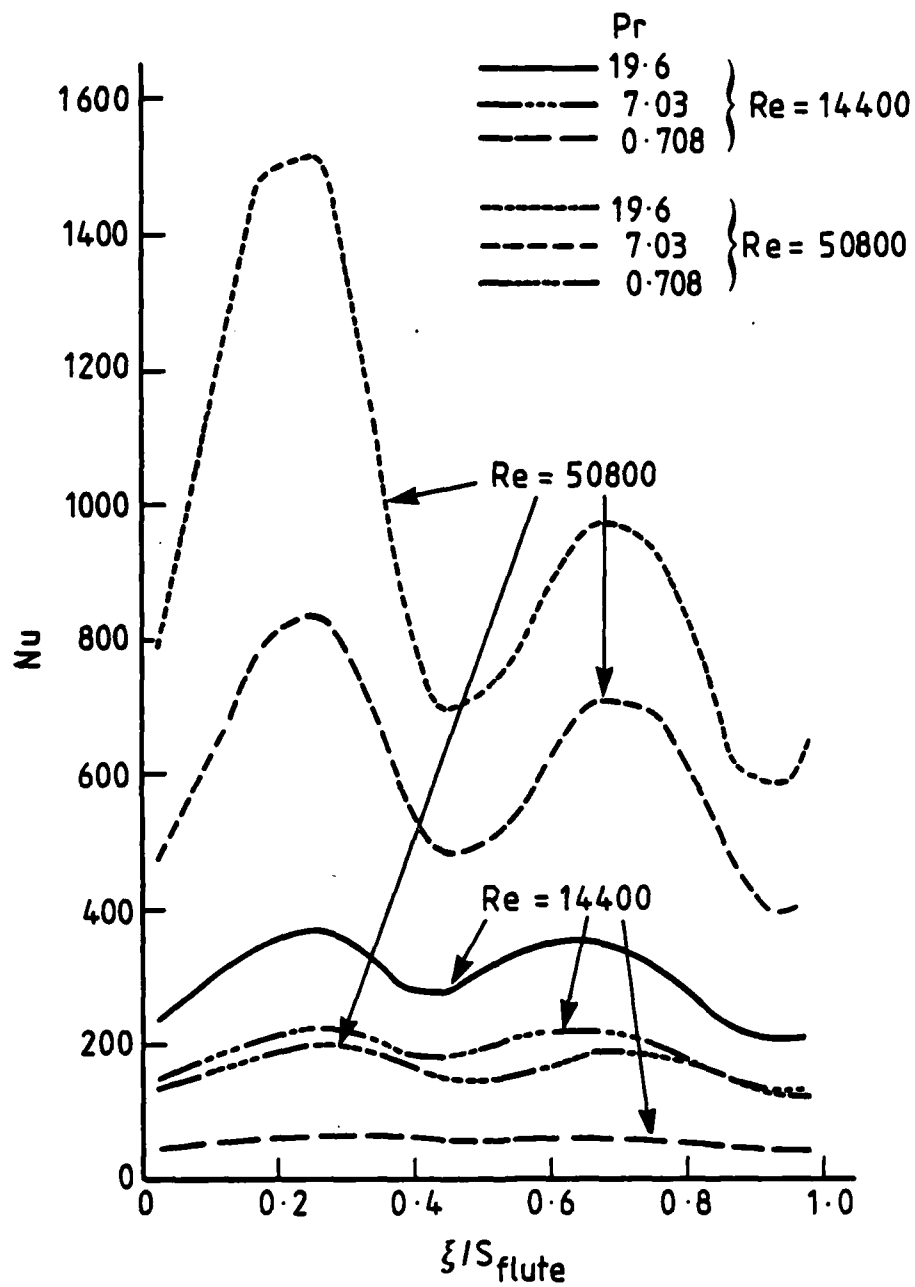


Fig. 5.29 Variation of local Nusselt number around flute  
 $n = 20, \varphi = 30^\circ$



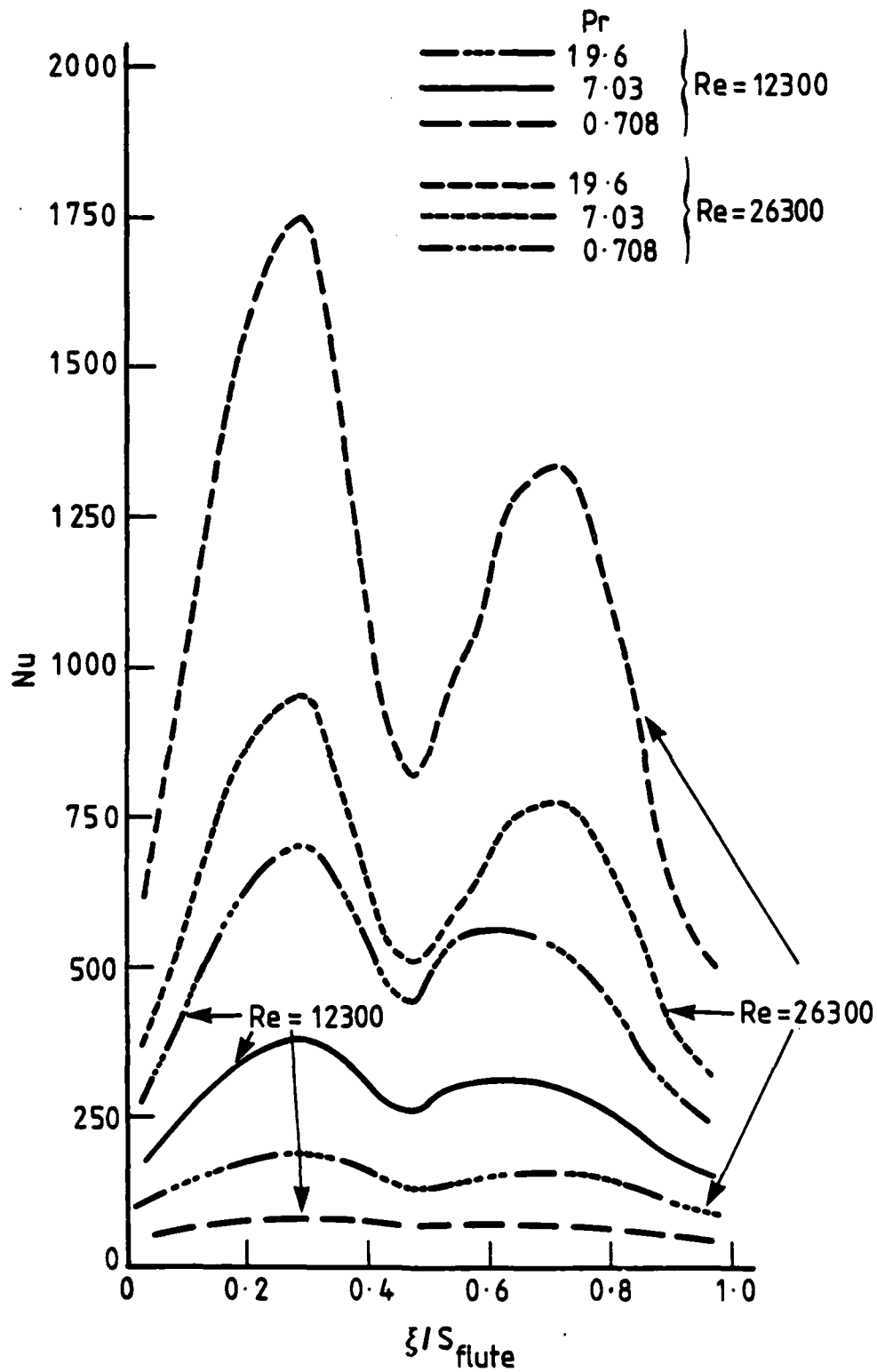


Fig. 5.30 Variation of local Nusselt number around flute  
 $n = 30$ ,  $\varphi = 30^\circ$

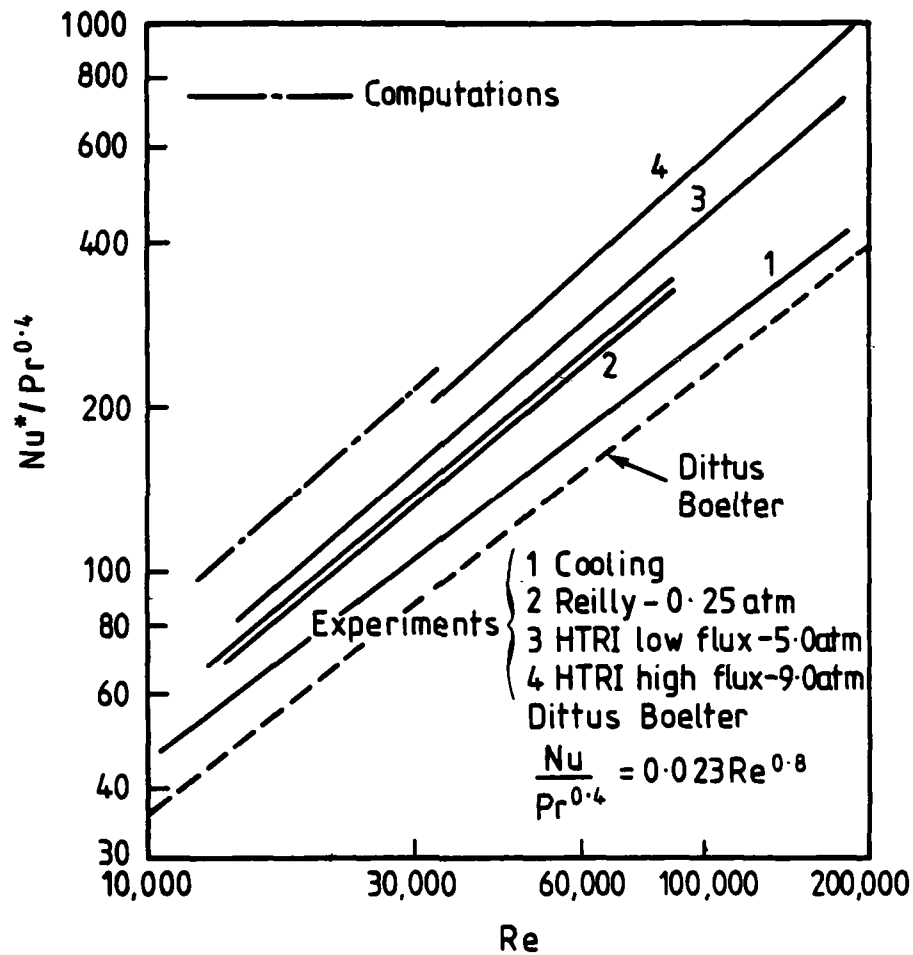


Fig. 5.31 Comparison of predicted and experimental data  
for Nusselt modulus  $n = 30, \phi = 30^\circ$

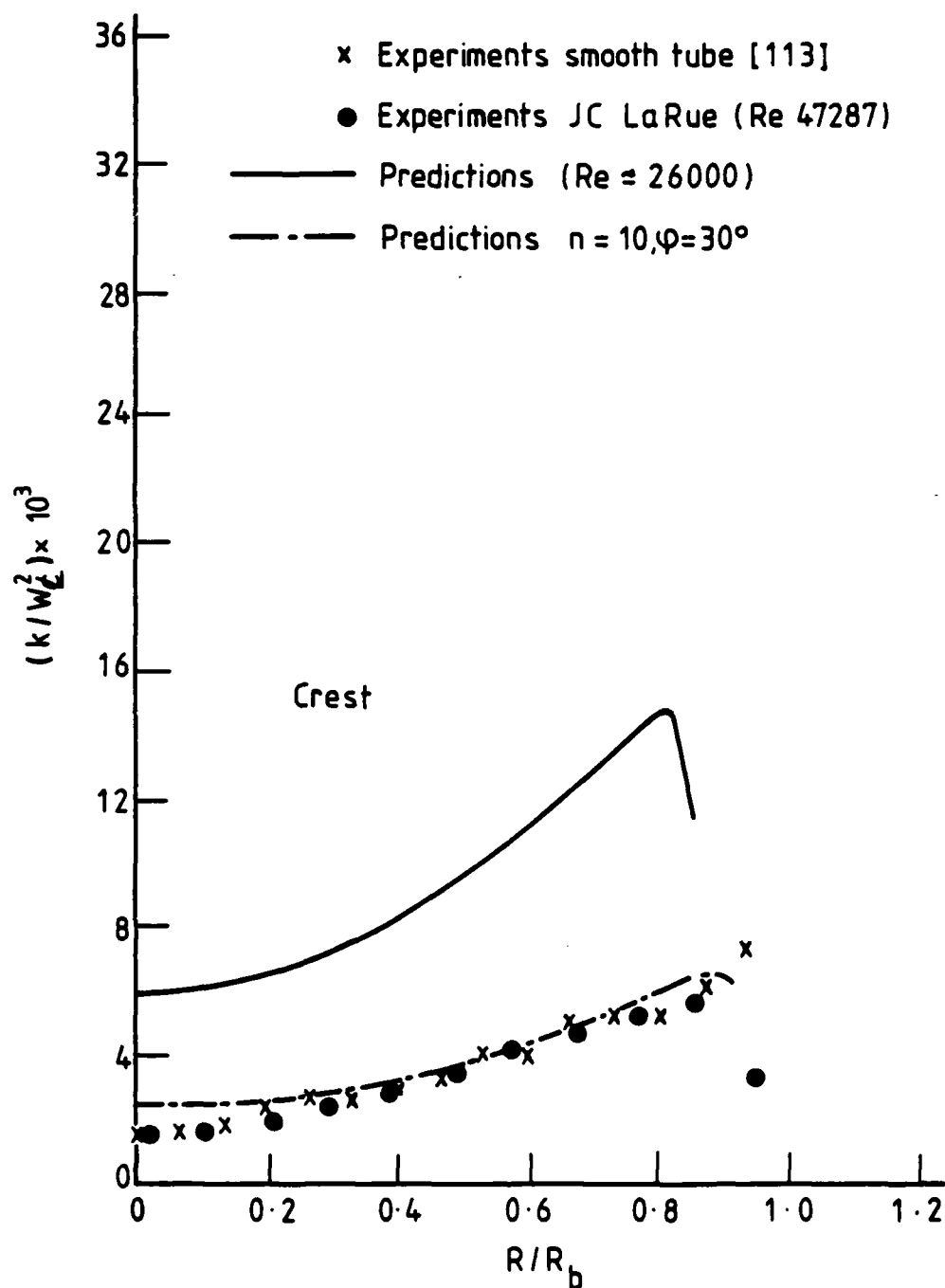


Fig. 5.32 Comparison of predicted and experimental data for the  $k$  distribution along the crest  $n = 30, \varphi = 30^\circ$

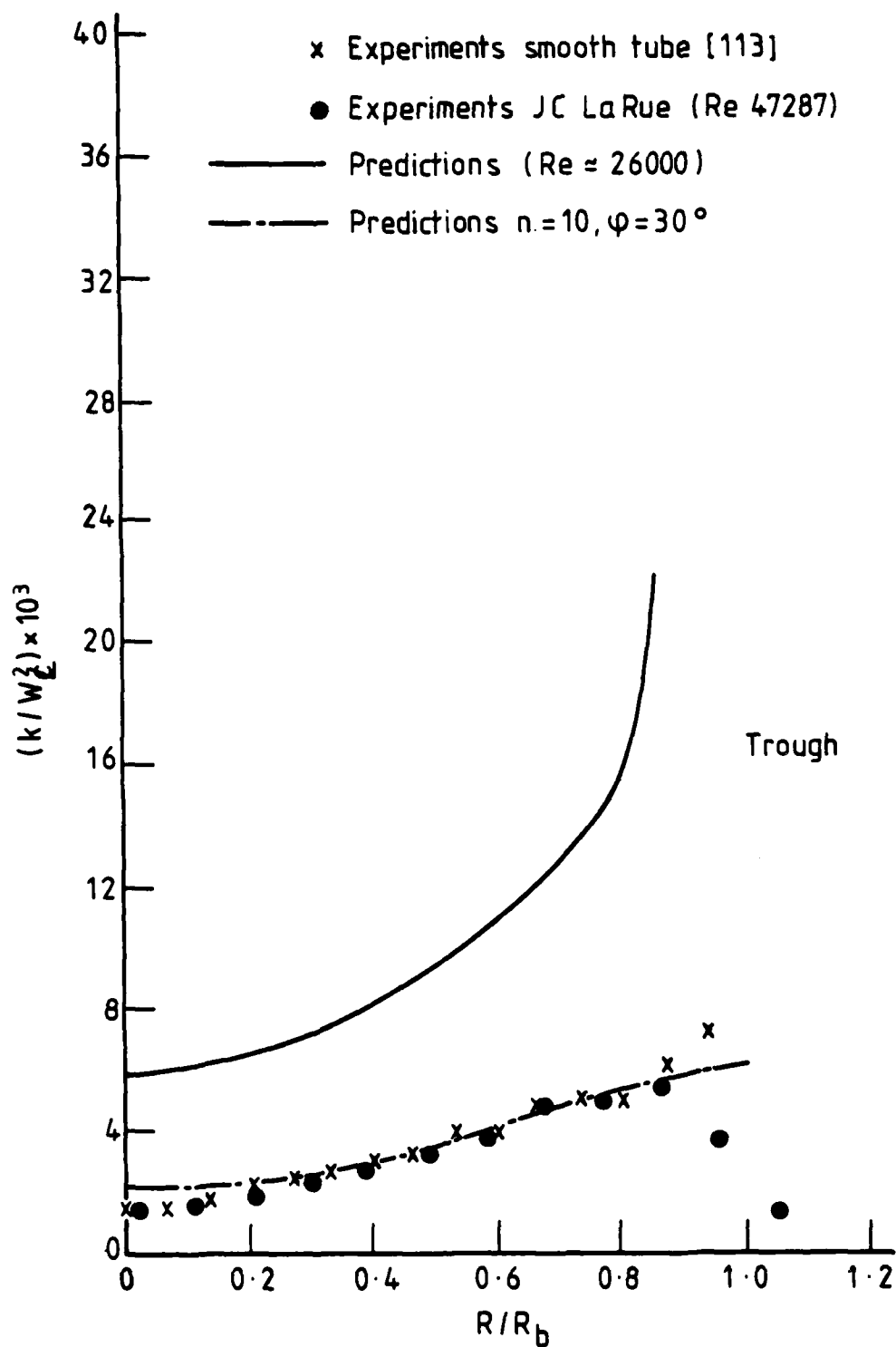


Fig. 5.33 Comparison of predicted and experimental data for the  $k$  distribution along the trough  $n=30, \phi=30^\circ$

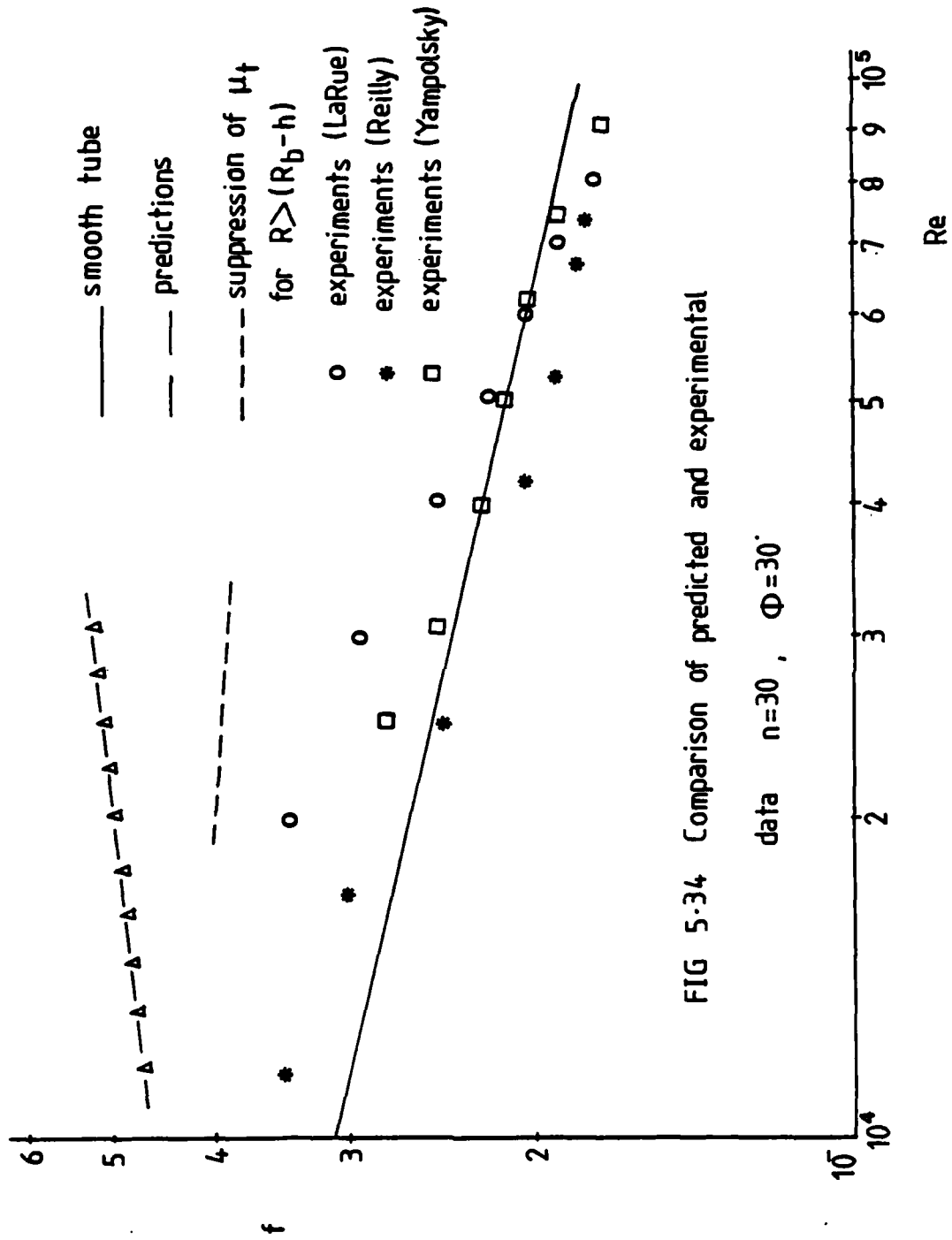


FIG 5-34 Comparison of predicted and experimental

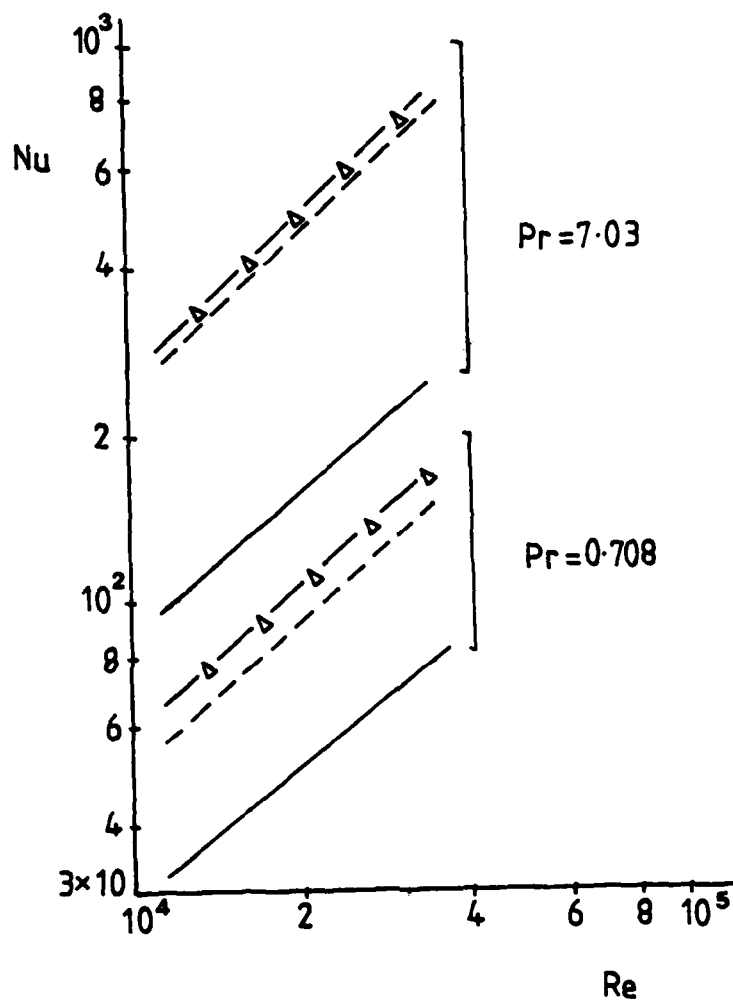


FIG 5-35 Dependence of predicted  $Nu$  on  $Re$ ;  $n=30$ ,  $\Phi=30^\circ$

— smooth tube  
 —  $\Delta$  — predictions  
 - - - suppression of  $\mu_+$   
 for  $R > (R_0 - h)$

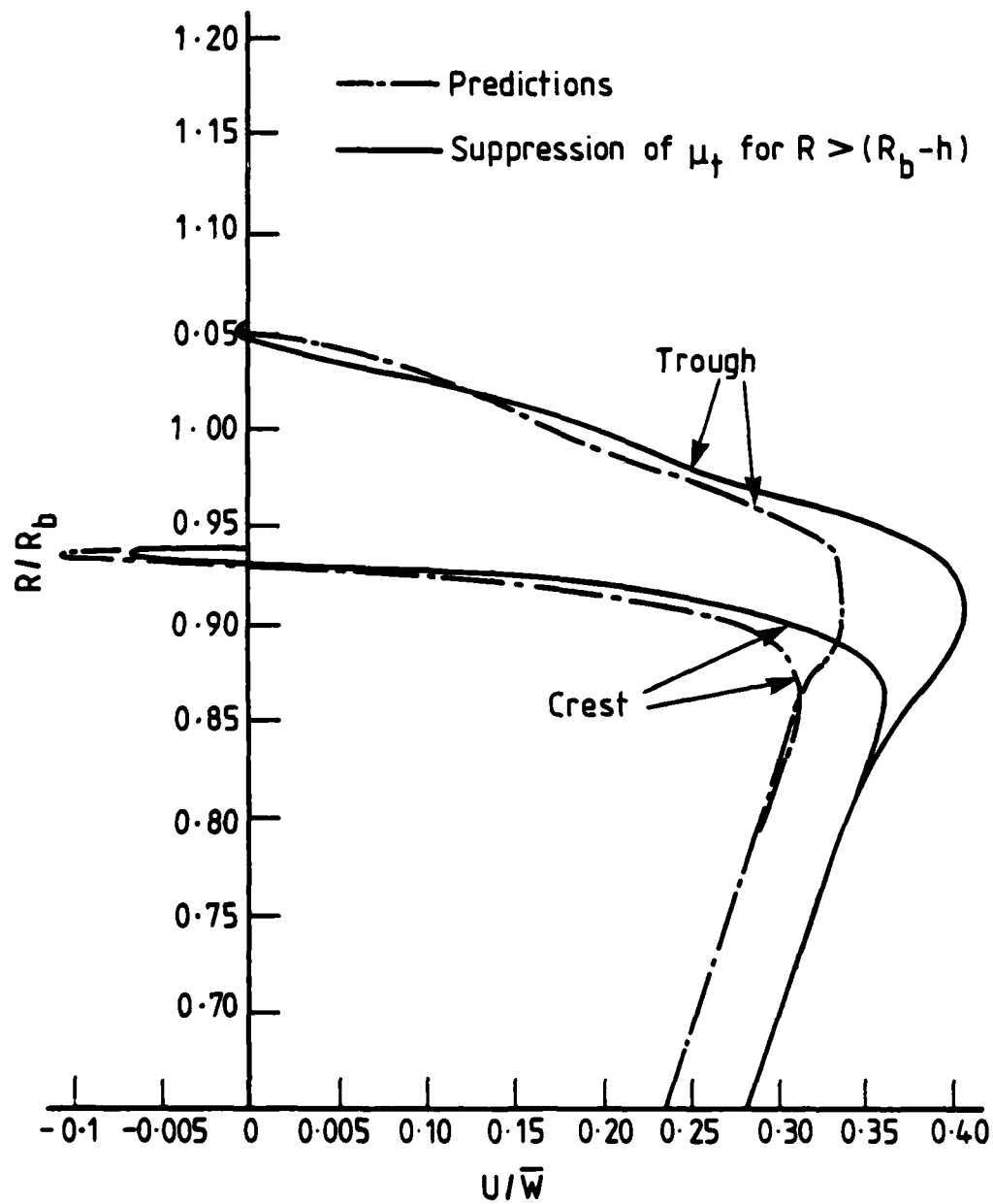


Fig. 5.36 Variation of circumferential velocity for  $n=30, \varphi=30^\circ$

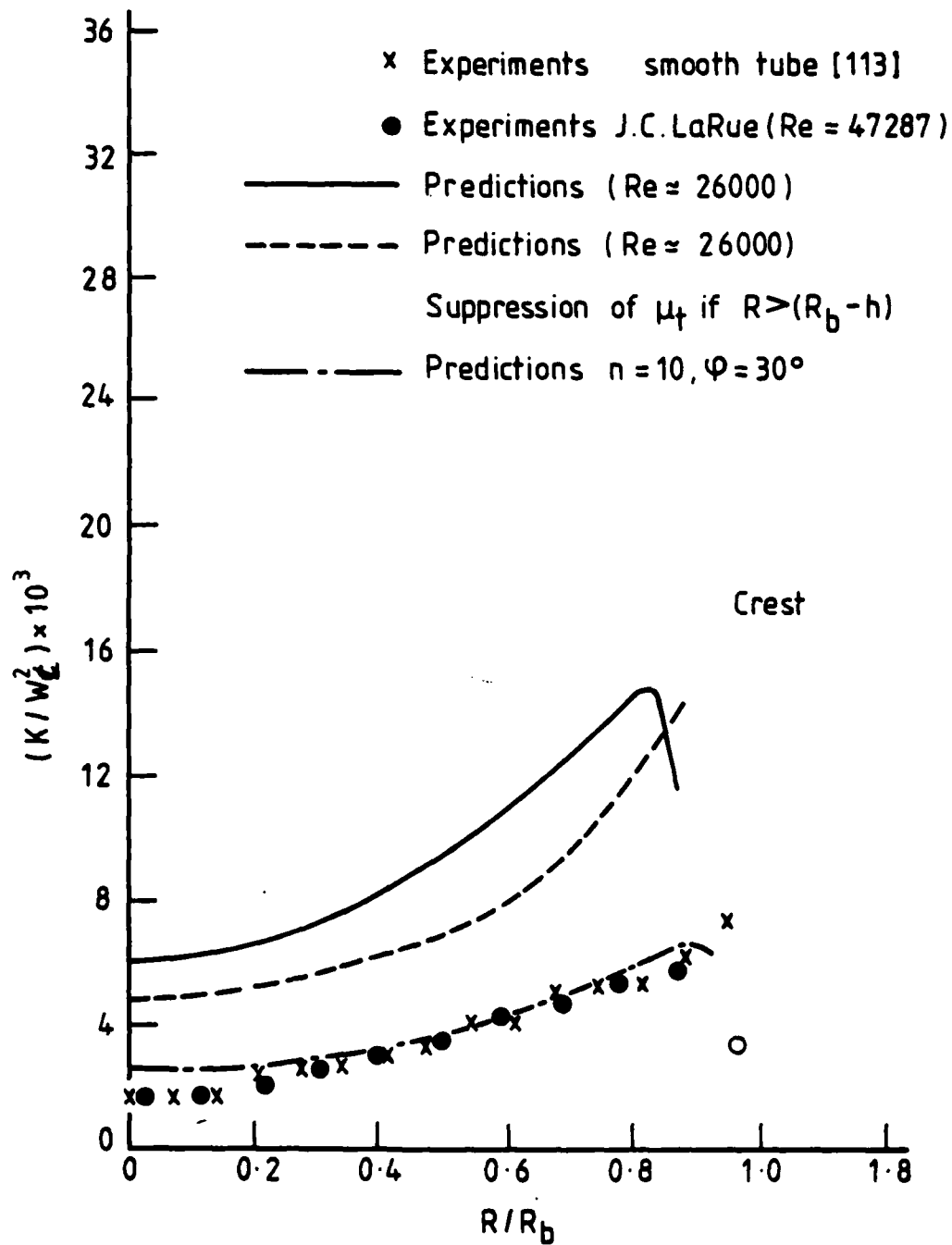


Fig.5.37 Comparison of predicted and experimental data for the  $k$  distribution along the crest,  $n = 30, \varphi = 30^\circ$



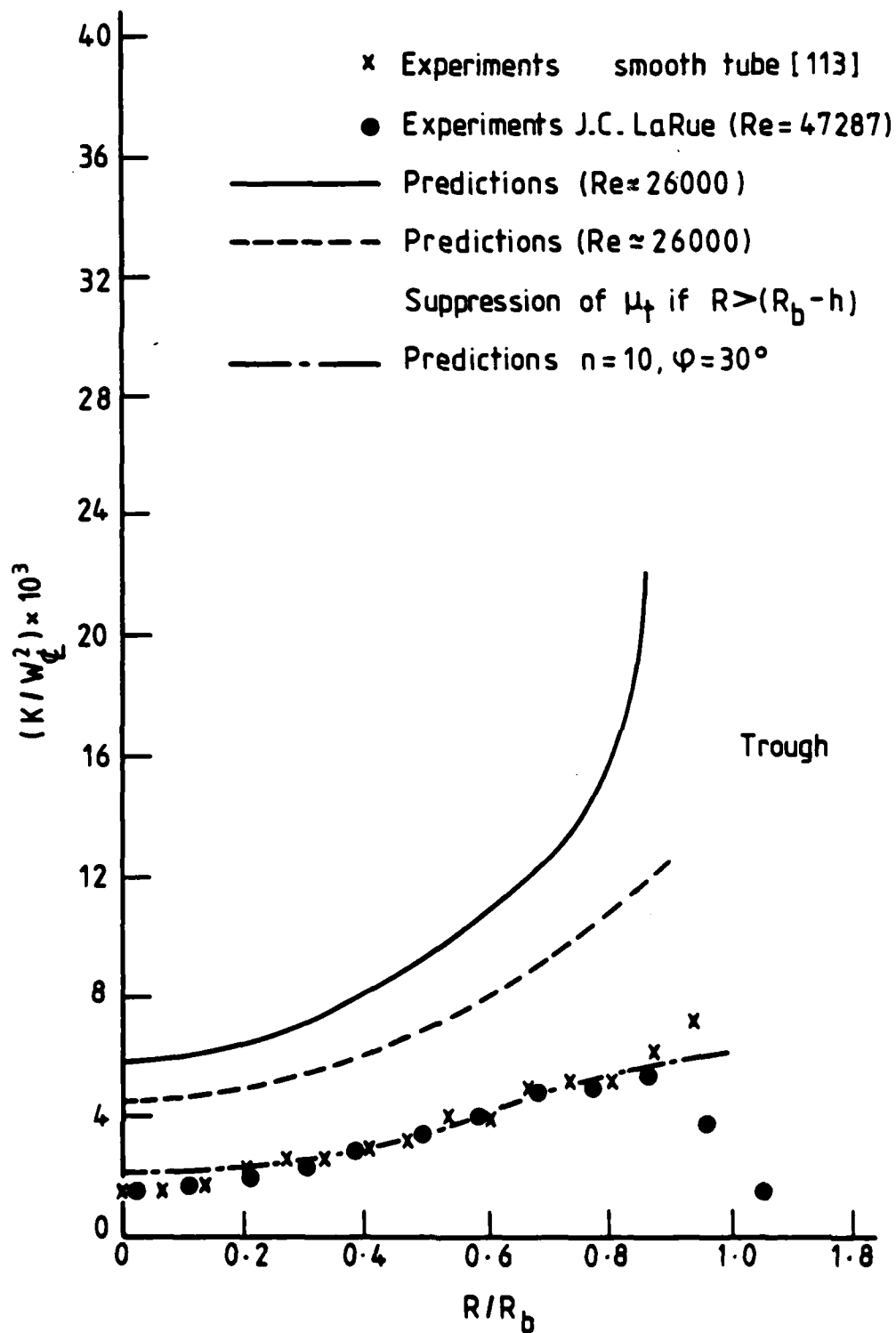


Fig. 5.38 Comparison of predicted and experimental data for the  $k$  distribution along the trough,  $n=30, \varphi=30^\circ$

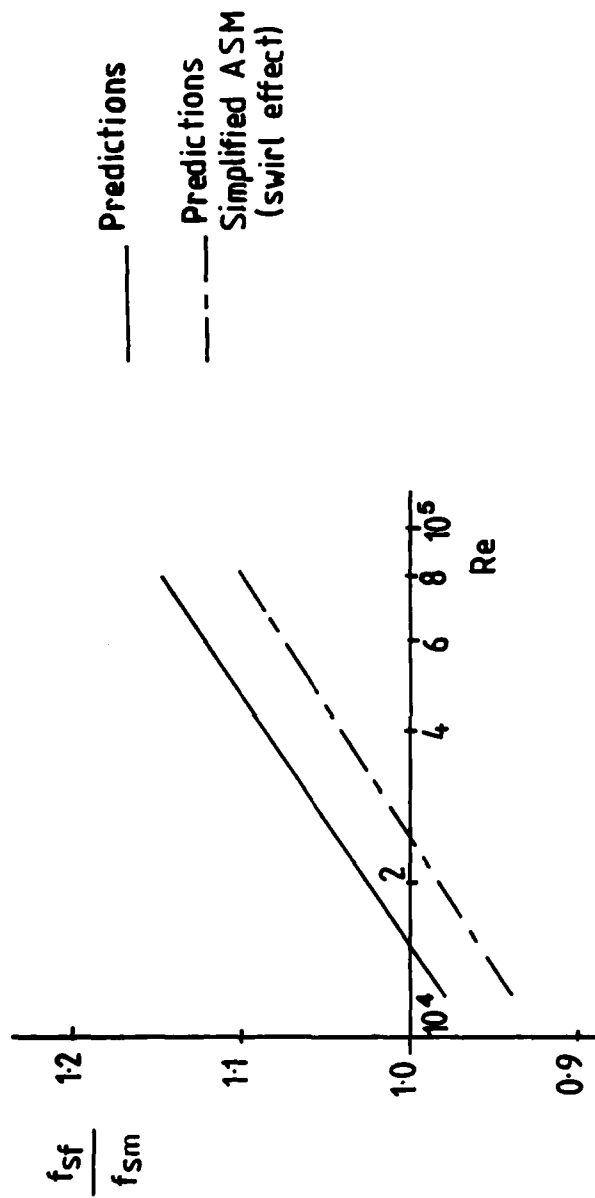


FIG 5-39 Variation of  $\frac{f_{sf}}{f_{sm}}$  with  $Re$ ,  $n=20$ ,  $\Phi=15^\circ$

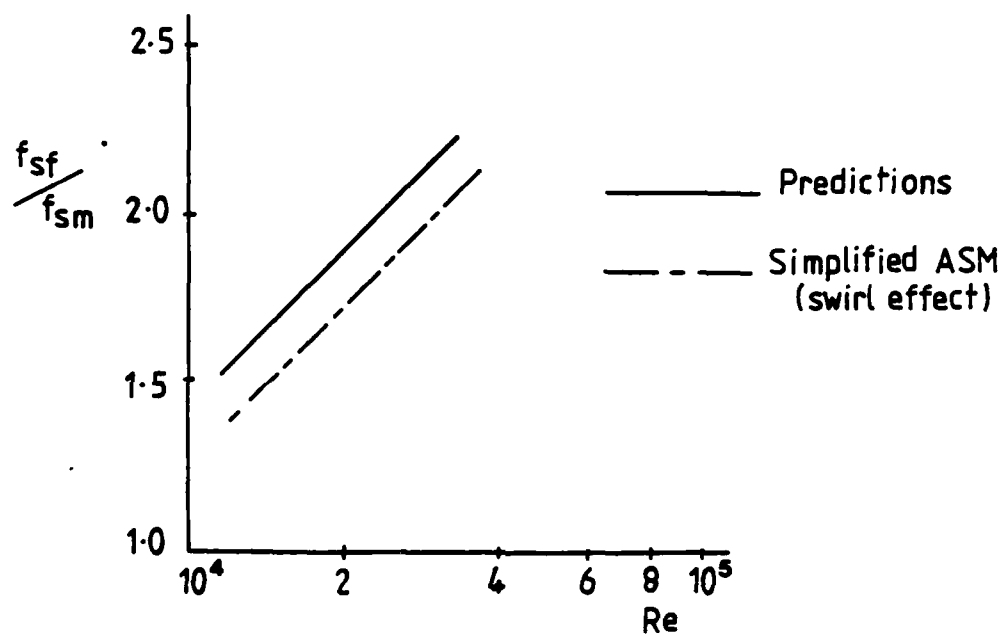


FIG 5.40 Variation of  $f_{sf}/f_{sm}$  with  $Re$   
 $n=30$ ,  $\Phi=30^\circ$

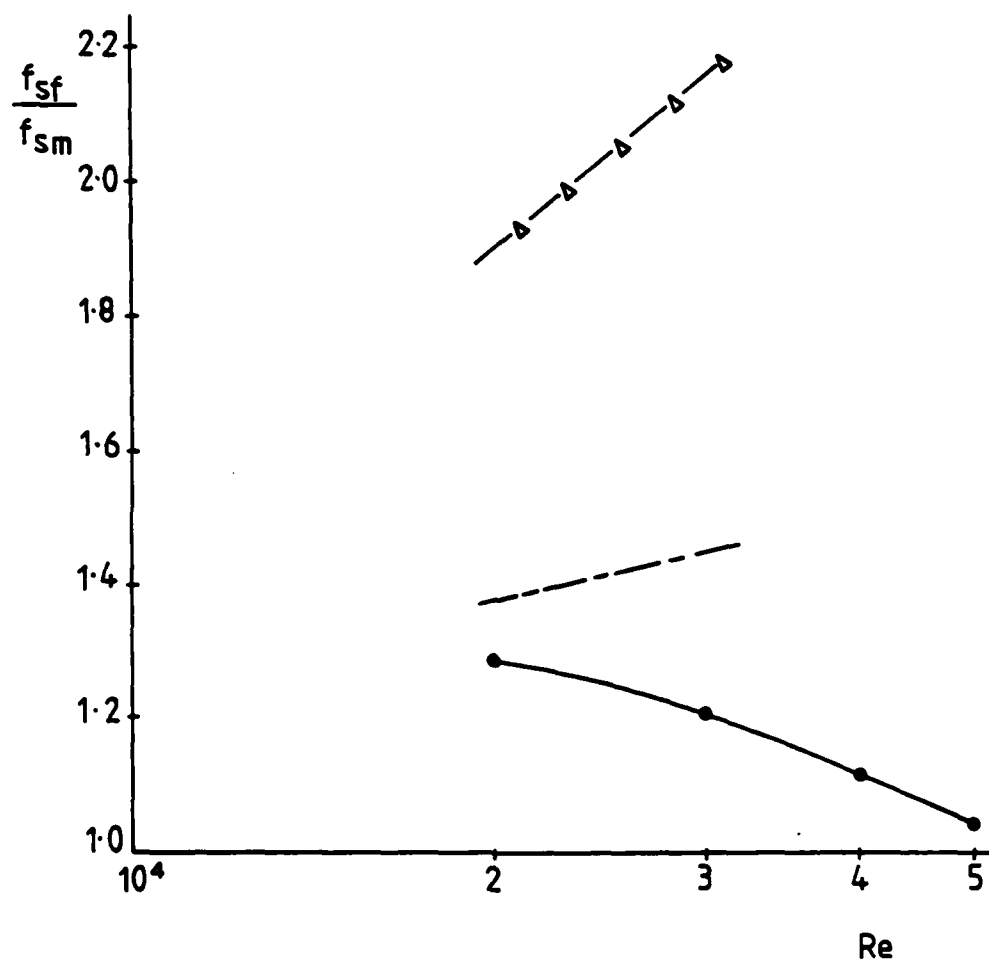


FIG 5-41 Variation of  $f_{sf}/f_{sm}$  with  $Re$

$n=30$ ,  $\Phi=30^\circ$

—●— experiments (LaRue)

—△— predictions

--- suppression of  $\mu_t$  for  $R > (R_b - h)$

+ Simplified ASM (swirl effect)

## CHAPTER 6

### 6. CONCLUSIONS AND RECOMMENDATIONS FOR FURTHER WORK

#### 6.1 Fulfilment of Objectives

The main objectives of the present work (stated in Section 1.3 of Chapter 1) were:

- a) The development and application of an efficient computer code for solving the flow through the spirally fluted tube in both laminar and turbulent regimes.
- b) The introduction of advanced turbulence models in the numerical solution scheme in order to represent the complex turbulence behaviour for the prediction of turbulent flows since in this regime lie most of the industrial applications of spirally fluted tubes.

Thus, the present work may be briefly summarized by noting the main steps towards the accomplishment of the above objectives.

#### (a) Laminar Regime

- 1) The derivation of the differential equations describing the flow through the spirally fluted tube. The discretization of these equations using a finite volume approach and adaptation of the computer code originally written by Antonopoulos, Gosman and Issa [86] to reflect these discretized equations.

- 2) The development and application of a computer code for generating a curvilinear/cylindrical-polar grid covering the part of a flute bounded on the outer surface by the tube wall and at the inner surface by an arc of radius  $R_a$ .
- 3) The introduction into the computer code of a special treatment for handling the cyclic boundary conditions applied at the east and west boundaries of the solution domain.
- 4) The solution of the discretized equations by the recently developed PISO algorithm (see Issa [79] and Gosman et al [80]) based on the idea that the velocity perturbations at some point of the solution domain depend not only on pressure perturbations but also on velocity perturbations at adjacent nodes.
- 5) The test of the resultant solving scheme's numerical accuracy by applying it to the computation of simple flows with known analytical solutions since the complex form of the describing equations makes it easy for errors to appear in their derivation, discretization or incorporation into the computer code.
- 6) The application of the computer code to the computation of the dynamic and temperature fields of the flow through the spirally fluted tube. The parametric study of the flow including changes in the number, height or angle of the flutes

and in Reynolds and Prandtl numbers.

(b) Turbulent Regime

- 7) The extension of the solution domain to the tube axis by means of a radial string of nodes along which the describing equations were solved with circumferential variations set to zero. The discretization of the describing equations in the one-dimensional (core region) and incorporation into the computer code. The introduction into the numerical procedure of a special treatment for the simultaneous solution of both regions (two-dimensional and one-dimensional).
- 8) The application of the Parabolic Sublayer treatment (PSL) within a thin band in the immediate vicinity of the tube wall (covering the two or three rows of cells next to the surface).
- 9) The application of various turbulence models and near-wall approaches to the computation of the turbulent flow through the spirally fluted tube. The incorporation of special treatments for viscosity and temperature in the fine grid approach finally adopted for the solution of the near-wall region.
- 10) The application of the resultant computer code (incorporating the  $k-\epsilon$  Boussinesq viscosity model over most of the pipe

merged with Van Driest's form of the mixing-length hypothesis in the immediate vicinity of the flutes) for solving the flow through the spirally fluted tube. The parametric study of the flow including changes in the number or angle of flutes, in Reynolds and Prandtl numbers.

- 11) The comparison with the experimental data available for the turbulent regime, for a tube with 30 flutes at  $30^\circ$  spiral angle.
- 12) The exploration of different physical models in the light of the comparison with experiments.

## 6.2 Conclusions and Recommendations for Future Work

### (a) Laminar Regime

- 1) The convergence of the solution procedure, while being a serious problem throughout the present work, has been considerably improved for most of the geometries studied. The steps mostly contributing to it were the introduction of PISO algorithm into the computer code and the adoption of the mixed curvilinear/cylindrical-polar grid.
- 2) In geometries of high flute density where high aspect ratio cells appear near the east and west boundaries the convergence of the solution procedure is still not satisfactory. The use of a non-orthogonal grid could avoid the large variation



in cell size and thus probably lead to more rapid convergence of the solution. Alternatively, if the orthogonal grid is retained, some improvement may be achieved by ignoring the high aspect ratio cells and solving the describing equations in a domain where the east and west boundaries are appropriately modified.

- 3) Since no experimental data for laminar flows are available, no comparison can be given with the values predicted. The numerical results show that even in the laminar regime this type of tubing can be beneficial since it enhances heat transfer coefficients while keeping the friction factors to levels almost equal with those of smooth tubes. Moreover, bearing in mind that all other enhancement techniques for internal flows increase the friction factors substantially more than the heat transfer coefficients, the behaviour of spirally fluted tubes is quite special.
- 4) The flow pattern produced by the computations provides an insight into the thermal characteristics predicted. Viewing the flow from upstream, the spiralling follows a clockwise direction which is also the general direction of the flow given by the velocity direction lines. At the leading face of the flute a high pressure region pushes the fluid away from the wall and to lower radii, while over the trailing face a low pressure region is created. Thus, because of the difference in pressure some fluid spills over the crest. The fact that the friction factors (based on hydraulic diameter) of the spirally fluted

tubes are lower than the unfluted tube values can be explained by the distribution of the axial velocity near the wall. As has been shown in Figures 3.15 and 3.16, due to the proximity of the flute surfaces and the resultant viscous retardation, the axial velocity and consequently the mean wall shear stress are lower than in a smooth tube. Moreover, the heat transfer enhancement of the fluted tube can be ascribed to two different factors: the increase, due to the flutes, of the surface area per unit length of tube, and the convective transport, due to the secondary flow produced by the spiralling. The importance of the second factor, for a constant Reynolds number and flute geometry, depends on the fluid used. Thus, for a high Prandtl number fluid, convective transport becomes much more important than diffusive transport in conveying heat across the near-wall zone.

- 5) Even for water ( $Pr = 7.03$ ) the enhancement of heat transfer coefficients is several times greater than the increase in friction factors. In this case, high flute density and tight spiralling should be adopted. A far better improvement has been found for high Prandtl number fluids (ethylene glycol). This means that spirally fluted tubes could be used beneficially in oil coolers since the circulation of oils often takes place in the laminar regime. For these fluids, tubes of low flute density and tight spiralling give the best performance.
- 6) The beneficial effect of spiral angle on the thermal behaviour is going to be reversed beyond a certain angle. Although this

limit has not been reached in the present computations, its identification would be something one would need to explore in order to optimize the flute design.

(b) Turbulent Regime

The computation of turbulent flows through the spirally fluted tubes using the standard  $(k-\epsilon)/(mlh)$  treatment revealed the following behaviour:

- 7) The flow pattern in the cross-stream plane indicates significant differences from that for laminar regime. Firstly, the radial motion produced by the flutes is less pronounced, and secondly, the "back-flow" over the crest is either absent or, in tubes of high flute density, very close to the wall. The flow pattern seen by an observer placed on the flute spiralling clockwise gives a clear picture of how the flutes enhance mixing of the near-wall fluid.
- 8) The computed friction factors of the spirally fluted tube are higher than the smooth tube values. Moreover, for tubes of 30 flutes at  $30^\circ$  spiral angle the computed friction factors display an increase in  $f$  as  $Re$  is raised. In this case, at  $Re = 3 \times 10^4$  the friction factor is almost 118% above the unfluted tube value.
- 9) The predicted Nusselt numbers are also higher than the ones for influted tubes. For air, for a tube of 30 flutes at  $30^\circ$  spiral angle and a Reynolds number of  $3 \times 10^4$  the increase is 130%

while for ethylene glycol solution it is almost 315%. Thus, the predicted behaviour indicates, at least for the high Prandtl number fluid ( $Pr = 19.6$ ), a two-fold increase of the heat transfer coefficient compared with the increase of the skin friction. This, of course, is very desirable since, from the literature survey reported in Chapter 1, it is clear that not many other "enhancement techniques" exhibit such a behaviour.

However, the comparison of the predicted values with the experimental data (available only for tubes with  $n = 30$ ,  $\phi = 30^\circ$ ) showed serious disagreements.

- 10) The experimental friction factors are sensibly the same as for a smooth tube displaying a decrease as  $Re$  increases. Thus, the predicted  $f$  values for the spirally fluted tube are not only higher than the experimental ones but also show the opposite trend as  $Re$  is raised.
- 11) The experimental Nusselt numbers for air show only a small increase over the smooth tube values, while the computations give an almost 130% increase. For water, at low heat flux (uniform property flow) the predicted Nusselt numbers are two times the measured ones.
- 12) No significant enhancement in Nusselt, due to the variation on heat flux levels, has been computed with uniform fluid properties (but with density fluctuation effects on Reynolds stresses

included in the core region of the solution domain), though the experimental data show a substantial effect.

It was felt that a major contributor to the disagreements mentioned in paragraphs 10) and 11) may arise from the actual flow exhibiting a viscous behaviour in the region within the flutes, while the computations give a turbulent behaviour (except from the viscous sublayer). Thus, in order to reproduce the conjectured viscous fluid behaviour the turbulent transport within this region was suppressed, a modification that resulted in a far better agreement with the experiments since:

- 13) It reduced the friction factors by almost 20% from the originally predicted values while reversing the trend of the skin friction-Reynolds number behaviour for the case of 30 flutes,  $30^\circ$  spiral angle.
- 14) It reduced the Nusselt numbers for air by an amount comparable with that found in skin friction (13%).
- 15) It reduced the Nusselt numbers for water by only 7% since in this case the suppression of turbulent diffusion does not reduce (indeed leads to an increase in) convection which is the main mechanism in conveying heat.

The above test suggests that the mixing-length hypothesis adopted in the near-wall region should be replaced by a turbulence model capable of predicting laminarization of the flow within the flutes, for example the low-Reynolds-number  $k-\epsilon$  model (see Jones and Launder [110], [111], Durst

and Rastogi [112]).

The disagreement reported in paragraph 12) suggests that the buoyancy effect associated with the swirl is not important in the core region of the solution domain. This effect could be important in the near-wall region, though the introduction of the simplified buoyancy ASM of Gibson and Launder [69] into the curvilinear grid has not been attempted here, due to the complexity involved. However, this possibility could be explored in the future. As an alternative physical source of the enhanced heat transfer under high heating we note that the temperature dependence of viscosity is rather substantial for water flow. The present computations, however, do not include property variations because strictly the assumption of fully-developed flow is not compatible with these.

Finally, the introduction of the simplified ASM (including swirl effects) into the core region of the solution domain and at the same time the suppression of turbulent diffusion within the flutes produced a substantial improvement of the predicted skin friction bringing results much closer to the experimental data (see Figure 5.41). Thus, in the Reynolds number range considered, the predicted friction factors are only 7% - 20% higher than the measured values by LaRue.

In view of the satisfactory agreement reported above and the experimental difficulties stated in [1], [59], [60], it is believed that the ultimate objective of developing a computer code useful for the optimization of the tube design has been substantially achieved.

APPENDIX 1The Computer Code for Generating the GridMapping the Solution Domain1.1 Introduction

A short program has been written for generating the grid used in the main program (described in Appendix 5). The original program has been written at Imperial College; however, many changes and additions have been introduced by the author of the present thesis. All the geometrical parameters are set in the grid-generation code and they are written to a file that the main code can call.

The program creates a grid which covers a flute bounded on the outer surface by the tube wall itself and at the inner surface by a circular boundary of radius  $R_a$  on the cross-stream plane of the spirally fluted tube (an example is shown in Figure 2.1).

The grid produced is divided into two regions: an orthogonal curvilinear part in the vicinity of the wall and a polar part over the rest of the solution domain. This mixed grid has been found to be very effective for producing a far more uniform coverage of the solution domain when compared with a fully curvilinear grid, shown in Figure 2.2. An orthogonal curvilinear grid has been used near the wall because it is only by using "body fitted" co-ordinates that one can refine the grid satisfactorily to resolve the regions of steep gradients. The grid has been created by defining one family of lines (constant  $\eta$  lines) and calculating the second family (constant  $\xi$  lines) normal to the first.

## 1.2 A Brief Description of the Computer Program's Structure

The computer program comprises only one routine. Initially, parameters, constants, indices and geometrical characteristics of the fluted duct are defined. Then, a distribution of points is fixed on the constant  $\eta$  line representing the wall and defined by the sinusoidal equation

$$R_w = R_b + h \cos(2\pi\Omega/\theta)$$

where  $R_b$  is the mean radius,  $h$  the rib height,  $\Omega$  the angular position and  $\theta$  the sector's angle given by the equation

$$\theta = 2\pi/n$$

$n$  being the number of flutes around the circumference of the tube. The local radius of all members of this family of lines is given by

$$R = R_o + h_o \cos(2\pi\Omega/\theta)$$

where  $R_o$  is the mean radius and  $h_o/h$  a prescribed function of  $R_o/R_b$  whose variation has been described in Sections 2.2 and 4.2.1.

The second family of co-ordinate lines is drawn orthogonal to the first using an iterative procedure described in the following section.

Next, the polar part of the grid is calculated and for the whole solution domain a number of geometrical variables, such as control volume lengths, boundary radii, rib heights, spiral angles, etc., are defined, which are stored on a tape called at the beginning of the main computer program (described in Appendix 5).



At the end, the orthogonality of  $\eta$  and  $\xi$  co-ordinate lines is tested and several variables are calculated and stored for subsequent use by the plotting-program.

### 1.3 An Important Detail of the Computer Code

The idea used for generating the second family of co-ordinate lines (constant  $\xi$  lines) orthogonal to the first (constant  $\eta$  lines) is given below:

Suppose that  $f(x, y)$  and  $g(x, y)$  are functions representing two lines in a  $(x, y)$  Cartesian co-ordinate system and  $(x_1, y_1)$  is a known point on  $f(x, y)$ . The problem arising is "how a line can be drawn orthogonal to both  $f(x, y)$  and  $g(x, y)$  passing from  $(x_1, y_1)$ ". The equations which can be written are:

$$y_1 = Qx_1^2 + \beta x_1 + \gamma \quad (A1.1)$$

which represents the unknown line at  $(x_1, y_1)$

$$2Qx_1 + \beta = -1/\lambda_1 \quad (A1.2)$$

representing the orthogonality of the unknown line and  $f(x, y)$ ,  $\lambda_1$  being the the tangent to  $f(x, y)$  at  $(x_1, y_1)$

$$2Qx_2 + \beta = -1/\lambda_2 \quad (A1.3)$$

representing the orthogonality of the unknown line and  $g(x, y)$ ,  $\lambda_2$  being the tangent to  $g(x, y)$  at  $(x_2, y_2)$

$$g(x_2, y_2) = 0 \quad (A1.4)$$

and 
$$y_2 = \alpha x_2^2 + \beta x_2 + \gamma \quad (A1.5)$$

confirming that  $(x_2, y_2)$  is a common point to both  $g(x, y)$  and the unknown line. Subtracting (A1.1) from (A1.5) and (A1.2) from (A1.3) we get:

$$y_2 - y_1 = \alpha [x_2^2 - x_1^2] + \beta [x_2 - x_1] \quad (A1.6)$$

$$\alpha = \frac{1}{2(x_2 - x_1)} \left[ \frac{1}{\lambda_1} - \frac{1}{\lambda_2} \right] \quad (A1.7)$$

while substituting (A1.7) into (A1.2) we find:

$$\beta = -\frac{1}{\lambda_1} - \frac{x_1}{x_2 - x_1} \left[ \frac{1}{\lambda_1} - \frac{1}{\lambda_2} \right] \quad (A1.8)$$

Substituting (A1.7) and (A1.8) into (A1.6) we get:

$$y_2 - y_1 = -\frac{x_2}{2} \left[ \frac{1}{\lambda_2} + \frac{1}{\lambda_1} \right] + \frac{x_1}{2} \left[ \frac{1}{\lambda_2} + \frac{1}{\lambda_1} \right]$$

$$\Rightarrow x_2 = x_1 + \frac{2(y_1 - y_2)}{1/\lambda_1 + 1/\lambda_2} \quad (A1.9)$$

Equations (A1.4) and (A1.9) can be solved iteratively and so the unknowns  $x_2, y_2$  can be calculated. Thus, from equations (A1.5), (A1.7), (A1.8) the values of  $\alpha, \beta, \gamma$  of the unknown line  $y = \alpha x^2 + \beta x + \gamma$  can be found.

The above procedure has been applied for just half of the solution

domain (the sector between trough and crest radii) since the other half can be calculated as symmetric to the first.

#### 1.4 The Computer Code

##### 1.4 a. Glossary of Fortran Symbols for the Computer Code

$$\text{COST}(I,J) = \cos(\star \eta, y)$$

$$\text{COSAPT}(I,J) = \cos(\star \xi, y)$$

$$\text{COSR}(I,J) = \cos F$$

$$\text{DYDX}(I,J) = \tan(\star \eta, y)$$

$$\text{DXC}(I,J) = \text{length of the control volume surface in } \xi\text{-direction}$$

$$\text{DYC}(I,J) = \text{length of the control volume surface in } \eta\text{-direction}$$

$$\text{DKIDF}(I,J) = \frac{\partial \xi}{\partial F} \text{ at } (I,J)$$

$$\text{DETADF}(I,J) = \frac{\partial \eta}{\partial F} \text{ at } (I,J)$$

$$\text{DRDXI}(I,J) = \frac{r}{r^2 + b^2} \frac{\partial r}{\partial \xi} \text{ at } (I,J)$$

$$\text{DRDETA}(I,J) = \frac{r}{r^2 + b^2} \frac{\partial r}{\partial \eta} \text{ at } (I,J)$$

$$F = \tan^{-1}(Y/X) = \Omega$$

$$\text{FIAXIS} = \text{spiral angle} = \phi$$

$$\text{HTHR}(I,J) = \frac{\sqrt{r^2 + b^2}}{b} = \frac{h}{b}$$

$$H = h$$

$$I = \text{index for dependent variables in } \xi\text{-direction}$$

$$J = \text{index for dependent variables in } \eta\text{-direction}$$

$$\text{NI} = \text{number of } \eta \text{ lines}$$

$$\text{NJ} = \text{number of } \xi \text{ lines}$$

NFLUT = n

NIH =  $\eta$  line representing the crest position

NPOLAR = number of polar  $\xi$  lines

PIH =  $\tan \phi = 1/b$

RAD(I,J) = radius of (I,J)

RR(I,J) = RAD(I,J)

RB =  $R_b$

RA =  $R_a$

RM = matching radius between curvilinear and polar parts of grid

R = radius of (I,J) =  $R_b + h \cos(2\pi F/THETA)$

SINT(I,J) =  $\sin(\eta, Y)$

SINAPT(I,J) =  $\sin(\xi, Y)$

SINR(I,J) = SINF

THETA =  $2\pi/n = \theta$

X(I,J) = Cartesian co-ordinate of (I,J)  
 Y(I,J) =                      - // -                      }  $Q \equiv (x,y) = (0,0)$

XX(I,J) = X(I,J)  $R_b$  (in cm)

YY(I,J) = Y(I,J)  $R_b$  (in cm)

XN(I,J) = 0.5 (XX(I-1,J) + XX(I,J))

YN(I,J) = 0.5 (YY(I-1,J) + YY(I,J))

XE(I,J) = 0.5 (XX(I,J) + XX(I,J-1))

YE(I,J) = 0.5 (YY(I,J) + YY(I,J-1))

XC(I,J) = 0.5 (XN(I,J) + XN(I,J-1))

YC(I,J) = 0.5 (YN(I,J) + YN(I,J-1))

X1(I,J) = X(I,J)  $R_b$  (in m)

Y1(I,J) = Y(I,J)  $R_b$  (in m)

X2(I,J) = X(I,NJ)  $R_b$  (in m)

$$Y2(I,J) = Y(I,NJ) R_b \quad (\text{in m})$$

XML(I) = distance from (I,J) to node I on the wall

XMLL(I,J) = distance from (I,J) to the nearest node on the wall

$$YL(I,J) = R(I,J)/R_b$$

## 1-4-b Listing of the computer code

```

C*****
C   PROGRAM FOR GENERATING ORTHOGONAL GRID COVERING A PART OF A   *
C   FLUTE ( FROM THE WALL UP TO A RADIUS RA ) ON THE CROSS-STREAM *
C   PLANE OF A SPIRALLY FLUTED TUBE.
C*****
PROGRAM GRID(INPUT,OUTPUT,TAPE5=INPUT,TAPE6=OUTPUT,TAPE11,TAPE8R,
1   TAPE22)
  DIMENSION X(25,25),Y(25,25),DYDY(25,25),RAD(25,25)
  DIMENSION SX(25,25),SY(25,25),DYC(25,25),DYC(25,25)
  DIMENSION DXIDF(25,25),DETADF(25,25)
  DIMENSION DZDX(25,25)
  DIMENSION DRDXI(25,25),DRDETA(25,25)
  DIMENSION HTHR(25,25),RR(25,25),ANGL(25,25),FF(25,25)
  DIMENSION XX(25,25),YY(25,25),XN(25,25),YN(25,25),XF(25,25)
  DIMENSION YE(25,25),XC(25,25),YC(25,25),COST(25,25),SINT(25,25)
  DIMENSION COSAPT(25,25),SINAPT(25,25)
  DIMENSION COSR(25,25),SINR(25,25)
  DIMENSION X1(25,25),Y1(25,25),X2(25,25),Y2(25,25),XML(25,25)
  DIMENSION XMLL(25,25),YL(25,25)
C*****
C   PARAMETERS AND CONSTANTS   *
C*****
  E=1.E-2
  MAXIT=120
  SMALL=1.E-30
  PI=3.14159
  IIPFX=.4
  IIPFY=.4
C*****
C   GEOMETRY OF FLUTED DUCT   *
C*****
C   INITIAL VALUE FOR RB
C   -----
  RB=1.
  RRI=RB
  RM=.88*RB
C   INITIAL VALUE FOR RA
C   -----
  RA=RM
  H=.06*RB
  AH=H
  NFLUIT=30
  THETA=2.*PI/FLOAT(NFLUIT)
C*****
C   INDICES   *
C*****
  NI=17
C   NUMBER OF XI LINES FOR THE CURVILINEAR PART OF GRID
C   -----
  NJ=14
  IPOLAR=1
  NPOLAR=5
  JG=NPOLAR+2
  NJM1=NI-1
  NJM1=NJ-1
  NTP1=NI+1
  NJP1=NJ+1

```

```

      NJM3=NJ-3
      NIH=(NI+1)/2
      NIHP1=NIH+1
      NIHM3=NI-3
      NIHM1=NIH-1
      NIHM2=NIH-2
      NIHM3=NIH-3
      NIHS=NI-5
C*****
C      RADIUS DECREMENTS      *
C*****
      DP=(RP-RA)*(1.-1.25)/(1.-1.25*(NJ-1))
      DJ=DP
C*****
C      INITIALISATION OF VARIABLES *
C*****
      DO 501 I=1,25
      DO 501 J=1,25
      DXC(I,J)=1.
      DYC(I,J)=1.
      DXIDF(I,J)=1.
      DFTADF(I,J)=1.
      DRDXI(I,J)=1.
      DRDFTA(I,J)=1.
      ANGL(I,J)=1.0
      FF(I,J)=1.0
      RP(I,J)=1.0
      XX(I,J)=1.
      YY(I,J)=1.
      XN(I,J)=1.
      YN(I,J)=1.
      XF(I,J)=1.
      YF(I,J)=1.
      XC(I,J)=1.
      YC(I,J)=1.
      COST(I,J)=1.
      SINT(I,J)=1.
      COSAPT(I,J)=1.
      SINAPT(I,J)=1.
      COSP(I,J)=1.0
      SINR(I,J)=1.0
501 CONTINUE
C*****
C      XT LINES ARE DEFINED AND FTA LINES ARE CALCULATED *
C      INITIAL DISTRIBUTION OF X AND Y ON THE SPECIFIED XI LINE *
C      FOR J=1 REPRESENTING THE WALL , J=NJ REPRESENTS RADIUS PM *
C*****
      J=1
      DO 101 I=1,NIH
      IF(I.EQ.1) F=0.0
      IF(I.EQ.2) F=THETA*0.08
      IF(I.EQ.3) F=0.16*THETA
      IF(I.EQ.4) F=THETA*0.24
      IF(I.EQ.5) F=THETA*0.31
      IF(I.EQ.6) F=THETA*0.37
      IF(I.EQ.7) F=THETA*0.43
      IF(I.EQ.8) F=THETA*.48

```

```

      IF(I.EQ.9) F=THETA*.5
1931 CONTINUE
      R=RR+H*COS(2.*PI*F/THETA)
      X(I,J)=R*SIN(F)
      Y(I,J)=R*COS(F)
      DYDX(I,J)=(-R*SIN(F)-COS(F)*H*2.*PI/THETA*SIN(2.*PI*F/THETA))/
1(SMALL+R*COS(F)-SIN(F)*H*2.*PI/THETA*SIN(2.*PI*F/THETA))
101 CONTINUE
      DO 102 J=2,NJ
C*****
C SPECIFY GENERAL SHAPE OF XI LINES FOR J GREATER OR EQUAL TO 2 *
C*****
      IF(J.NE.2) DR=DR*1.25
      RR=RH-DR
C CALCULATION OF H FOR J GREATER OR EQUAL TO 2
C -----
      AA=ATAN((RBI-RA)/2./RPI/((RPI-RR)/RPI-
1(PRI-RA)/2./RBI))
      IF(AA.LT.0.) AA=AA+PI
      IF(AA.GT.PI) AA=AA-PI
      H=(AA-PI/4.)*1.25*AH*(2./PI)*1.25
      WRITE(6,1734) RR,H
1734 FORMAT(1H,1E10.4,5X,1E10.4)
C*****
C ITERATIVE PROCEDURE FOR CALCULATING X,Y ON THE SPECIFIED *
C XT LINES AND ETA LINES FOR HALF THE SOLUTION DOMAIN *
C*****
      DO 103 I=1,NIH
      NITER=0
104 NITER=NITER+1
      IF(NITER.EQ.1) X(I,J)=X(I,J-1)
      IF(NITER.EQ.1) Y(I,J)=Y(I,J-1)
      F=ATAN(X(I,J)/(SMALL+Y(I,J)))
      R=RR+H*COS(2.*PI*F/THETA)
      DYDX(I,J)=(-R*SIN(F)-COS(F)*H*2.*PI/THETA*SIN(2.*PI*F/THETA))/
1(SMALL+R*COS(F)-SIN(F)*H*2.*PI/THETA*SIN(2.*PI*F/THETA))
      AX=X(I,J)
      X(I,J)=X(I,J-1)+2.*(Y(I,J-1)-Y(I,J))/(1./(SMALL+DYDX(I,J-1))
1+1./(DYDX(I,J)+SMALL))
      X(I,J)=HURFX*X(I,J)+(1.-HURFX)*AX
      AY=Y(I,J)
      Y(I,J)=HURFY*Y(I,J)+(1.-HURFY)*AY
      IF(J.EQ.NJ) Y(I,J)=SQRT(R**2-X(I,J)**2)
      IF(I.EQ.NIH) X(I,J)=R*SIN(THETA/2.)
      IF(I.EQ.NIH) Y(I,J)=R*COS(THETA/2.)
301 CONTINUE
      XP=X(I,J)
      YP=Y(I,J)
      IF(NITER.GT.MAXIT) GO TO 105
      GO TO 104
105 CONTINUE
103 CONTINUE
102 CONTINUE
C*****

```



```

C      CALCULATION OF THE SECOND HALF OF THE GRID USING THE VALUES      *
C      JUST FOUND FOR ITS SYMMETRIC HALF                                  *
C*****
      H=AH
      DO 131 J=1,NJ
      IF(J.EQ.1) RB=RRI
      IF(J.GT.2) DRI=DRI*1.25
      IF(J.GT.1) RB=RR-DHI
      AA=ATAN((RBI-RA)/7./RRI/((RBI-RR)/RRI-
1(RBI-RA)/2./RBI))
      IF(AA.LT.0.0) AA=AA+PI
      IF(AA.GT.PI) AA=AA-PI
      IF(J.GT.1) H=(AA-PI/4.)*1.25*AH*(2./PI)*1.25
      WRITE(6,2345) RR,H
2345  FORMAT(1H,1E10.4,5X,1E10.4)
      DO 131 I=NI+1,NI
      F=ATAN(X(NI-I+1,J)/(SMALL+Y(NI-I+1,J)))
      F=THETA-F
      R=SQRT(X(NI-I+1,J)**2+Y(NI-I+1,J)**2)
      DYDX(I,J)=(-R*SIN(F)-COS(F)*H*2.*PI/THETA*SIN(2.*PI*F/THETA))/
1(SMALL+R*COS(F)-SIN(F)*H*2.*PI/THETA*SIN(2.*PI*F/THETA))
      X(I,J)=R*SIN(F)
      Y(I,J)=R*COS(F)
131  CONTINUE
C*****
C      CALCULATION OF THE POLAR PART OF THE GRID                        *
C*****
      IF(IPOLAR.EQ.0) GO TO 1731
      NJPOL=NJ+NPOLAR
      NJ1=NJ+1
      D1=0.034
      DO 7856 J=NJ1,NJPOL
      IF(J.EQ.(NJ1+1)) D1=0.039
      IF(J.EQ.(NJ1+2)) D1=0.045
      IF(J.EQ.(NJ1+3)) D1=0.052
      IF(J.GT.(NJ1+3)) D1=0.06
      DO 7856 I=1,NI
      F=ATAN(X(I,NJ)/Y(I,NJ))
      Y(I,J)=Y(I,J-1)-D1*COS(F)
      X(I,J)=X(I,J-1)-D1*SIN(F)
      DYDX(I,J)=DYDX(I,NJ)
7856  CONTINUE
C      NUMBER OF XI LINES FOR BOTH CURVILINEAR AND POLAR PARTS OF GRID
C      -----
      NJ=NJPOL
      NJP1=NJ+1
      NJM1=NJ-1
1731  CONTINUE
C*****
C      INTERCHANGE LINES J=1 AND NJ FOR THIS PROBLEM                  *
C*****
      DO 106 I=1,NI
      DO 106 J=1,NJ
      DZDX(I,J)=X(I,J)
106  CONTINUE
      DO 107 I=1,NI
      DO 107 JJ=1,NJ

```

```

      J=NJ-JJ+1
      X(I,J)=DZDX(I,JJ)
107 CONTINUE
      DO 154 I=1,NI
      DO 154 J=1,NJ
      DZDX(I,J)=Y(I,J)
154 CONTINUE
      DO 164 I=1,NI
      DO 164 JJ=1,NJ
      J=NJ-JJ+1
      Y(I,J)=DZDX(I,JJ)
164 CONTINUE
      DO 706 I=1,NI
      DO 706 J=1,NJ
706 DZDX(I,J)=DYDX(I,J)
      DO 707 I=1,NI
      DO 707 JJ=1,NJ
      J=NJ-JJ+1
707 DYDX(I,J)=DZDX(I,JJ)
C*****
C      CALCULATE LENGTHS OF CONTROL VOLUMES *
C*****
      DO 108 J=1,NJ
      SX(1,J)=0.
      DO 108 I=2,NI
      DX=X(I,J)-X(I-1,J)
      DY=Y(I,J)-Y(I-1,J)
      SY(I,J)=SX(I-1,J)+SQRT(DX*DX+DY*DY)
108 CONTINUE
      DO 110 I=1,NI
      SY(I,1)=0.
      DO 110 J=2,NJ
      DX=X(I,J)-X(I,J-1)
      DY=Y(I,J)-Y(I,J-1)
      SY(I,J)=SY(I,J-1)+SQRT(DX*DX+DY*DY)
110 CONTINUE
      DO 111 J=2,NJP1
      DO 111 I=2,NI
      DX=X(I,J)-X(I-1,J-1)
      DYC(I,J)=SX(I,J-1)-SX(I-1,J-1)
111 CONTINUE
      DO 112 J=2,NJ
      DO 112 I=2,NIP1
      DYC(I,J)=SY(I-1,J)-SY(I-1,J-1)
112 CONTINUE
C*****
C      CALCULATION OF GEOMETRICAL VARIABLES USEFUL FOR THE SOLUTION *
C      OF VELOCITY AND TEMPERATURE FIELDS IN A SPIRALLY FLUTED TUBE *
C*****
      DO 1321 I=1,NI
      DO 1321 J=1,NJ
      IF(J.LT.NJ) X1(I,J+1)=X(I,J)
      IF(J.LT.NJ) Y1(I,J+1)=Y(I,J)
      IF(J.EQ.NJ) X2(I)=X(I,NJ)
      IF(J.EQ.NJ) Y2(I)=Y(I,NJ)
1321 CONTINUE
      DO 1322 I=1,NI
      X1(I,1)=X1(I,2)

```

```

      Y1(I,1)=Y1(I,2)
1322 CONTINUE
      DO 1323 I=1,NI
      DO 1323 J=1,NJ
      DO 1324 II=1,NI
      XML(IT)=SQRT((X2(IT)-Y1(I,J))**2+(Y2(IT)-Y1(I,J))**2)
      IF(II.EQ.1) XMLL(I+1,J)=XML(IT)
      XMLL(I+1,J)=AMIN1(XMLL(I+1,J),XML(IT))
1324 CONTINUE
1323 CONTINUE
      DO 1325 J=1,NJ
1325 XMLL(1,J)=XMLL(NI,J)
      NTP1=NI+1
      NJP1=NJ+1
      DO 1326 I=1,NJP1
1326 XMLI(I,NJP1)=0.0
      DO 113 I=1,NI
      DO 113 J=1,NJ
      RAD(I,J)=SQRT(X(I,J)*Y(I,J)+Y(I,J)*Y(I,J))
      RP(I+1,J+1)=RAD(I,J)
113 CONTINUE
      DO 707 I=1,NI
      DO 707 J=1,NJ
      DO 708 RP(1,J+1)=RP(NI,J+1)
      DO 708 RP(1,1)=RP(NI,1)
      FIAXIS=4.*ATAN(1.)/12.
      PIH=TAN(FIAXIS)
      DO 135 I=1,NI
      DO 135 J=1,NJ
      IF(PIH.EQ.0.0) GO TO 3569.
      RFACT=RAD(I,J)/(RAD(I,J)**2+(1./PIH)**2)
      HTHR(I+1,J+1)=SQRT(RAD(I,J)**2+(1./PIH)**2)
      1/(1./PIH)
      IF(I.EQ.1) DWDXT(I+1,J+1)=(RAD(I+1,J)-RAD(I,J))
      1/DXC(I+1,J+1)+RFACT
      IF(I.GT.1.AND.I.LT.NI) DRDXT(I+1,J+1)=(RAD(I+1,J)-
      1-RAD(I-1,J))/(DXC(I+1,J+1)+DXC(I,J+1))*RFACT
      IF(I.EQ.NI) DRDXT(I+1,J+1)=(RAD(I,J)-RAD(I-1,J))
      1/DXC(I,J+1)+RFACT
      IF(J.EQ.1) DRDETA(I+1,J+1)=(RAD(I,J+1)-RAD(I,J))
      1/DYC(I+1,J+1)+RFACT
      IF(J.GT.1.AND.J.LT.NJ) DRDETA(I+1,J+1)=(RAD(I,J+1)-
      1-RAD(I,J-1))/(DYC(I+1,J+1)+DYC(I,J+1))*RFACT
      IF(J.EQ.NJ) DRDETA(I+1,J+1)=(RAD(I,J)-RAD(I,J-1))
      1/DYC(I+1,J+1)+RFACT
      GO TO 3579
3569 HTHR(I+1,J+1)=1.0
      DRDXT(I+1,J+1)=0.0
      DRDETA(I+1,J+1)=0.0
3579 CONTINUE
135 CONTINUE
      DO 319 I=1,NIH
      DO 319 J=1,NJ
      ANGET=ATAN(DYDX(I,J))
      ANGET=ARS(ANGET)
      ANGR=PI/2.-ATAN(Y(I,J)/(X(I,J)+SMALL))

```

```

      ANGP=ARS(ANGR)
      ANGL(I+1,J+1)=ANGET-ANGR
319 CONTINUE
      DO 142 I=NIHP1,NI
      DO 142 J=1,NJ
142 ANGL(I+1,J+1)=ANGL(NI-I+2,J+1)
      DO 3842 I=1,NI
      DO 3842 J=1,NJ
      DXIDF(I+1,J+1)=RAD(I,J)/COS(ANGL(I+1,J+1))
      DETADF(I+1,J+1)=DXIDF(I+1,J+1)*TAN(ANGL(I+1,J+1))*(-1.)
3842 CONTINUE
C*****
C      STORE RESULTS ON TAPE WHICH IS CALLED BY THE MAIN PROGRAM *
C      FOR THE SOLUTION OF VELOCITY AND TEMPERATURE FIELDS IN A *
C      SPIRALLY FINITED TUBE *
C*****
      WRITE(11) DXC,DYC,DXIDF,DETADF,DRDXT,DRDETA,HTRP,PP,ANGL,
      1,RR,RA,AM,NFLUT,FIAXIS,JG,XMLI
      NJP1=NJ+1
      NIP1=NI+1
      DO 3996 JJ=1,NJP1
      J=NJ+1
      WRITE(6,115) (J,(XMLI(I,J),I=1,NIP1))
3996 CONTINUE
      DO 4124 I=2,NIP1
      DO 4124 J=2,NJ
4124 YL(I,J)=-5*(RR(I,J+1)+RR(I,J))
      DO 4125 I=2,NIP1
      YL(I,1)=RR(I,1)
4125 YL(I,NJP1)=RR(I,NJP1)
      DO 4126 J=1,NJP1
4126 YL(1,J)=YL(NI,J)
      WRITE(22) YL
      REWIND 22
C*****
C      PRINT OUT *
C*****
      WRITE(6,201)
      DO 114 JJ=1,NJ
      J=NJ-JJ+1
      WRITE(6,115) (J,(X(I,J),I=1,NI))
114 CONTINUE
      WRITE(6,202)
      DO 116 JJ=1,NJ
      J=NJ-JJ+1
      WRITE(6,115) (J,(Y(I,J),I=1,NI))
116 CONTINUE
      WRITE(6,203)
      DO 117 JJ=1,NJ
      J=NJ-JJ+2
117 WRITE(6,118) (DXC(I,J),I=2,NI)
      WRITE(6,204)
      DO 119 JJ=2,NJ
      J=NJ-JJ+2
119 WRITE(6,118) (DYC(I,J),I=2,NIP1)
      WRITE(6,205)
      DO 121 JJ=1,NJ

```

```

      J=NI-JJ+1
121 WRITE(6,118) (RAD(I,J),I=1,NI)
      WRITE(6,206)
      DO 123 JJ=1,NJ
      J=NI-JJ+1
123 WRITE(6,207) (J,(DXIDF(I,J),I=1,NI))
      WRITE(6,208)
      DO 124 JJ=1,NJ
      J=NI-JJ+1
124 WRITE(6,207) (J,(DETADE(I,J),I=1,NI))
      DO 377 JJ=1,NJ
      J=NI-JJ+1
      WRITE(6,207) (J,(DRDXI(I,J),I=1,NI))
377 CONTINUE
      DO 388 JJ=1,NJ
      J=NI-JJ+1
388 WRITE(6,207) (J,(DRDETA(I,J),I=1,NI))
      DO 445 JJ=1,NJ
      J=NI-JJ+1
445 WRITE(6,207) (J,(HTHR(I,J),I=1,NI))
      WRITE(6,118) (RP(I),I=1,NJP1)
C*****
C      TEST FOR ORTHOGONALITY OF ETA AND XI LINES *
C*****
      DO 901 I=1,NI
      DO 901 JJ=2,NJ
      J=NI-JJ+1
      D1=-1./(SMALL+DYDX(I,J+1))+1./(SMALL+DYDX(I,J))
      ALFA=-5/(X(I,J+1)-X(I,J))*D1
      BETA=-ALFA*X(I,J+1)*2.-1./(SMALL+DYDX(I,J+1))
      IF(JJ.EQ.2) D7DX(I,J+1)=2.*ALFA*X(I,J+1)+BETA
      D7DY(I,J)=2.*ALFA*X(I,J)+BETA
      IF(JJ.EQ.2) D7DX(I,J+1)=ATAN(DZDX(I,J+1))
      D7DX(I,J)=ATAN(DZDX(I,J))
901 CONTINUE
      WRITE(6,904)
904 FORMAT(24H INCLINATION OF XI LINES)
      DO 902 JJ=1,NJ
      J=NI-JJ+1
902 WRITE(6,903) (J,(D7DX(I,J),I=1,NI))
903 FORMAT(5X,I5,(10E10.4))
      DO 354 I=1,NI
      DO 354 J=1,NJ
      DYDX(I,J)=ATAN(DYDX(I,J))
354 CONTINUE
      WRITE(6,401)
401 FORMAT(25H INCLINATION OF ETA LINES)
      DO 302 JJ=1,NJ
      J=NI-JJ+1
302 WRITE(6,402) (DYDX(I,J),I=1,NI)
C*****
C      WRITE RESULTS ON TAPE AND REWIND *
C*****
      DO 477 I=1,NI
      DO 477 J=1,NJ
      XX(I+1,J+1)=X(I,J)
      YY(I+1,J+1)=Y(I,J)

```

```

      COST(I+1,J+1)=COS(DYDV(I,J))
      SYNT(I+1,J+1)=SIN(DYDV(I,J))
      COSAPT(I+1,J+1)=COS(D7DX(I,J))
      SYNAPT(I+1,J+1)=SIN(D7DX(I,J))
477 CONTINUE
      DO 471 I=2,NIP1
      XX(I,1)=XX(I,2)
      YY(I,1)=YY(I,2)
      COST(I,1)=COST(I,2)
      SYNT(I,1)=SYNT(I,2)
      COSAPT(I,1)=COSAPT(I,2)
471 SINAPT(I,1)=SINAPT(I,2)
      DO 488 I=1,NI
      DO 488 J=1,NJ
      DYDX(I,J)=ATAN(Y(I,J)/(X(I,J)+SMALL))
      COSP(I+1,J+1)=COS(DYDX(I,J))
      RRH SINR(I+1,J+1)=SIN(DYDX(I,J))
      DO 489 I=2,NIP1
      COSP(I,1)=COSP(I,2)
      RR9 SINR(I,1)=SINR(I,2)
      DO 499 J=2,NJP1
      COSP(1,J)=COSP(NI,J)
      RR9 SINR(1,J)=SINR(NI,J)
      COSP(1,1)=COSP(NJ,1)
      SINR(1,1)=SINR(NI,1)
      NI=NI+1
      NJ=NJ+1
      NIM=NJ-1
      NJM=NJ-1
      NIHM1=NI-2
      NJHM1=NJ-2
      DO 478 I=2,NI
      DO 478 J=1,NJ
      XN(I,J)=.5*(XX(I,J)+XY(I-1,J))
478 YN(I,J)=.5*(YY(I,J)+YV(I-1,J))
      DO 480 I=1,NI
      DO 480 J=2,NJ
      XF(I,J)=.5*(XX(I,J)+XY(I,J-1))
480 YF(I,J)=.5*(YY(I,J)+YV(I,J-1))
      DO 481 I=1,NI
      XF(I,1)=XX(I,1)
      YF(I,1)=YY(I,1)
481 CONTINUE
      DO 482 I=1,NI
      DO 482 J=2,NJ
      XC(I,J)=.5*(XN(I,J)+XN(I,J-1))
      YC(I,J)=.5*(YN(I,J)+YN(I,J-1))
482 CONTINUE
      DO 483 I=1,NI
      XC(I,1)=XN(I,1)
483 YC(I,1)=YN(I,1)
      WRITE(RR) NI,NJ,NIM,NIP,NJHM1,NJHM1,
1      ((XX(I,J),J=1,NJ),I=1,NI),((YY(I,J),J=1,NJ),I=1,NI),
2      ((XC(I,J),J=1,NJ),I=1,NI),((YC(I,J),J=1,NJ),I=1,NI),
3      ((XF(I,J),J=1,NJ),I=1,NI),((YF(I,J),J=1,NJ),I=1,NI),
4      ((XN(I,J),J=1,NJ),I=1,NI),((YN(I,J),J=1,NJ),I=1,NI),
5      ((COST(I,J),J=1,NJ),I=1,NI),((SYNT(I,J),J=1,NJ),I=1,NI),

```

```

6 ((COSAPT(I,J),J=1,NJ),I=1,NI),((SINAPT(I,J),J=1,NJ),I=1,NI)
7,((RR(I,J),J=1,NJ),I=1,NI),((COSR(I,J),J=1,NJ),I=1,NI),
8 ((SINR(I,J),J=1,NJ),I=1,NI)
      REWIND 88
      NI=NI-1
      NJ=NJ-1
      DO 303 I=1,NI
      DO 303 J=1,NJ
      DYDX(I,J)=ATAN(Y(I,J)/(X(I,J)+SMALL))
303 CONTINUE
      WRITE(6,403)
403 FORMAT(27H INCLINATION OF RADIUS)
      DO 304 JJ=1,NJ
      J=NJ-JJ+1
304 WRITE(6,402) (DYDX(I,J),I=1,NI)
      DO 532 JJ=1,NJP1
      J=NJP1-JJ+1
532 WRITE(6,402) (ANGL(I,J),I=1,NJP1)
      WRITE(6,205)
      DO 731 JJ=1,NJP1
      J=NJP1-JJ+1
731 WRITE(6,402) (RR(I,J),I=1,NJP1)
402 FORMAT(/,(10E10.4))
C*****
C      FORMATS *
C*****
201 FORMAT(/,14H X COORDINATES,/)
202 FORMAT(/,14H Y COORDINATES,/)
203 FORMAT(/,17H DXC LENGTHS,/)
204 FORMAT(/,12H DYC LENGTHS,/)
205 FORMAT(/,13H LOCAL RADIUS,/)
115 FORMAT(I5.5X,(10E10.4))
118 FORMAT(5X,(10E10.4))
206 FORMAT(/,6H DXIDF)
208 FORMAT(/,7H DETADF)
207 FORMAT(/,15,(10E10.4))
      STOP
      END

```

APPENDIX 2

Derivation of the equations of flow  
in a straight spirally fluted tube

2.1 Introduction

The present appendix is largely drawn from the report of I. Demirdzic [109] on the derivation of equations for flow through the spirally fluted tube. This had been prepared at the start of the project. Changes, however, have been introduced in the nomenclature used, for maintaining uniformity with the remainder of the thesis.

The objective was to derive the equations of motion in a form which includes a co-ordinate system suitable for describing the complex shape of the tube cross section and which allows the condition of fully-developed flow to be expressed in a computationally convenient way.

2.2 Geometry2.2.1 Characterization

A circular helix (spiral) is described by the following equation in a Cartesian co-ordinate system:

$$\vec{r} = r \cos \theta \vec{i} + r \sin \theta \vec{j} + b \theta \vec{k} \quad (\text{A2.1})$$

or in cylindrical co-ordinates:

$$\vec{r} = r \vec{e}_r + b \theta \vec{k} \quad (\text{A2.2})$$



(see Figure 1), where the following relationships hold between Cartesian  $(\vec{i}, \vec{j}, \vec{k})$  and cylindrical  $(\vec{e}_r, \vec{e}_\theta, \vec{k})$  base vectors:

$$\begin{aligned}\vec{e}_r &= \cos \theta \vec{i} + \sin \theta \vec{j}, \\ \vec{e}_\theta &= -r \sin \theta \vec{i} + r \cos \theta \vec{j} = r \frac{\partial \vec{e}_r}{\partial \theta}\end{aligned}\quad (\text{A2.3})$$

From (A2.1) and (A2.2) follows

$$\frac{d\vec{r}}{d\theta} = -r \sin \theta \vec{i} + r \cos \theta \vec{j} + b\vec{k} = \vec{e}_\theta + b\vec{k}, \quad (\text{A2.4})$$

$$\frac{d^2\vec{r}}{d\theta^2} = -r \cos \theta \vec{i} - r \sin \theta \vec{j} = -r\vec{e}_r \quad (\text{A2.5})$$

The differential arc length of the spiral is

$$ds = \sqrt{dx^2 + dy^2 + dz^2} = \sqrt{r^2 + b^2} d\theta. \quad (\text{A2.6})$$

It follows that the unit tangent and normal vectors to the spiral are

$$\begin{aligned}\vec{m} &= \frac{d\vec{r}}{ds} = \frac{d\vec{r}}{d\theta} \frac{d\theta}{ds} = \frac{1}{\sqrt{r^2 + b^2}} (\vec{e}_\theta + b\vec{k}), \\ \vec{n} &= \frac{1}{\kappa} \frac{d\vec{m}}{ds} = \frac{1}{\kappa} \frac{d\vec{m}}{d\theta} \frac{d\theta}{ds} = -\vec{e}_r,\end{aligned}\quad (\text{A2.7})$$

where

$$\kappa = \frac{1}{R} = \frac{r}{r^2 + b^2} \quad (\text{A2.8})$$

is the curvature of the spiral.

### 2.2.2 Co-ordinate System

A suitable co-ordinate system for the complex duct configuration illustrated in Figure 1 is defined as follows. A general orthogonal curvilinear system  $x^\xi - x^\eta$  is defined in the cross-sectional plane  $xOy$ , with the third co-ordinate  $x^\zeta$  aligned (naturally) with the tangent to the spiral, as illustrated in Figure 2. The vectors

$$\vec{e}_t = \frac{\partial \mathbf{x}}{\partial x^t} \vec{i} + \frac{\partial \mathbf{y}}{\partial x^t} \vec{j} + \frac{\partial \mathbf{z}}{\partial x^t} \vec{k} \quad (t = \xi, \eta, \zeta) \quad (\text{A2.9})$$

are tangent to the co-ordinate lines  $x^t$  and form the natural bases of the co-ordinate system employed.

The vectors

$$\vec{e}^t = \frac{\partial \mathbf{x}}{\partial x^t} \vec{i} + \frac{\partial \mathbf{y}}{\partial x^t} \vec{j} + \frac{\partial \mathbf{z}}{\partial x^t} \vec{k} \quad (t = \xi, \eta, \zeta) \quad (\text{A2.10})$$

are orthogonal to the co-ordinate surfaces  $x^t = \text{const}$  and reciprocal  $(\vec{e}_i \cdot \vec{e}^j = \delta_i^j)$  to the vectors  $\vec{e}_t$ .

The elementary control volume defined by this co-ordinate system is presented in Figure 3. Its elemental volume is given by

$$dV = d\xi d\eta d\zeta \sin\Phi = d\xi d\eta dz. \quad (\text{A2.11})$$

### 2.2.3 Metric of the Co-ordinate System

The metric of the co-ordinate system is defined by the covariant and contravariant metric tensor component

$$g_{ts} = \vec{e}_t \cdot \vec{e}_s ; \quad g^{ts} = \vec{e}^t \cdot \vec{e}^s, \quad (\text{A2.12})$$

where

$$g_{\xi\xi} = h_{\xi}^2 = \left( \frac{\partial \mathbf{x}}{\partial x^{\xi}} \right)^2 + \left( \frac{\partial y}{\partial x^{\xi}} \right)^2 + \left( \frac{\partial z}{\partial x^{\xi}} \right)^2,$$

$$g_{\xi\eta} = g_{\eta\xi} = 0,$$

$$g_{\eta\eta} = h_{\eta}^2 = \left( \frac{\partial \mathbf{x}}{\partial x^{\eta}} \right)^2 + \left( \frac{\partial y}{\partial x^{\eta}} \right)^2 + \left( \frac{\partial z}{\partial x^{\eta}} \right)^2,$$

$$g_{\zeta\zeta} = h_{\zeta}^2 = r^2 + b^2,$$

$$g_{\zeta\xi} = g_{\xi\zeta} = h_{\xi}^2 \frac{\partial x^{\xi}}{\partial \theta}, \quad g_{\zeta\eta} = g_{\eta\zeta} = h_{\eta}^2 \frac{\partial x^{\eta}}{\partial \theta},$$

$$g^{\xi\xi} = \frac{1}{h_{\xi}^2} + \frac{1}{b^2} \left( \frac{\partial x^{\xi}}{\partial \theta} \right)^2, \quad g^{\eta\eta} = \frac{1}{h_{\eta}^2} + \frac{1}{b^2} \left( \frac{\partial x^{\eta}}{\partial \theta} \right)^2,$$

$$g^{\xi\eta} = g^{\eta\xi} = \frac{1}{b^2} \left( \frac{\partial x^{\xi}}{\partial \theta} \right) \left( \frac{\partial x^{\eta}}{\partial \theta} \right), \quad g^{\zeta\zeta} = \frac{1}{b^2}$$

$$g^{\zeta\xi} = g^{\xi\zeta} = -\frac{1}{b^2} \left( \frac{\partial x^{\xi}}{\partial \theta} \right), \quad g^{\zeta\eta} = g^{\eta\zeta} = -\frac{1}{b^2} \left( \frac{\partial x^{\eta}}{\partial \theta} \right) \quad (\text{A2.13})$$

Since the base vectors  $\vec{e}_t$  are not in general constant vectors, their derivatives

$$\frac{\partial \vec{e}_t}{\partial x^s} = \left\{ \begin{matrix} m \\ t \ s \end{matrix} \right\} \vec{e}_m$$

(A2.14)

are expressed in terms of Christoffel symbols defined as follows:

$$\left\{ \begin{matrix} t \\ s \ k \end{matrix} \right\} = \frac{1}{2} g^{tm} \left( \frac{\partial g_{sm}}{\partial x^k} + \frac{\partial g_{km}}{\partial x^s} - \frac{\partial g_{sk}}{\partial x^m} \right) \quad (\text{A2.15})$$

that characterize certain geometrical properties of the curvilinear co-ordinate system. (Note that the Einstein summation convention is used henceforth. That is matching upper and lower indices are to be summed).

#### 2.2.4 Normalized Basis

If physical vector and tensor components are to be employed, the normalized base vectors and their reciprocal vectors should be introduced:

$$\vec{e}_{(t)} = \frac{\vec{e}_t}{h_t} \quad ; \quad \vec{e}^{(t)} = h_t \vec{e}^t \quad (\text{no summation}) \quad (\text{A2.16})$$

One can see that  $\vec{e}_{(t)}$  are non-dimensional unit vectors tangent to the co-ordinate lines  $t$ , while  $\vec{e}^{(t)}$  are also non-dimensional, but are not unit vectors. The two sets are related to each other by

$$\begin{aligned} \vec{e}^{(\xi)} &= \vec{e}_{(\xi)} - \kappa_{\xi} \vec{k} , \\ \vec{e}^{(\eta)} &= \vec{e}_{(\eta)} - \kappa_{\eta} \vec{k} , \\ \vec{e}^{(\zeta)} &= \frac{h_{\zeta}}{b} \left[ \frac{h_{\zeta}}{b} \vec{e}_{(\zeta)} - \kappa_{\xi} \vec{e}_{(\xi)} - \kappa_{\eta} \vec{e}_{(\eta)} \right] = \frac{h_{\zeta}}{b} \vec{k} , \end{aligned} \quad (\text{A2.17})$$

where

$$\begin{aligned} \kappa_{\xi} &= \frac{h_{\xi}}{b} \frac{\partial x^{\xi}}{\partial \theta} = \frac{\partial \xi}{b \partial \theta} , \\ \kappa_{\eta} &= \frac{h_{\eta}}{b} \frac{\partial x^{\eta}}{\partial \theta} = \frac{\partial \eta}{b \partial \theta} , \\ \kappa_{\zeta} &= 0 \quad (\text{included for generality, see Section 4}) \end{aligned} \quad (\text{A2.18})$$

Vectors and tensors in the curvilinear frame can now be expressed in terms of their components relative to the base vectors  $\vec{e}_{(t)}$ . For example:

$$\begin{aligned}\vec{a} &= a^{(t)} \vec{e}_{(t)}, \\ A &= A^{(ts)} \vec{e}_{(t)} \otimes \vec{e}_{(s)},\end{aligned}\tag{A2.19}$$

where  $a^{(t)}$  and  $A^{(ts)}$  are physical vector and tensor components respectively. The operator  $\otimes$  stands for the tensor product.

The metric can also be defined in terms of the physical metric tensor components

$$g_{(ts)} = \vec{e}_{(t)} \cdot \vec{e}_{(s)}\tag{A2.20}$$

and

$$g^{(ts)} = \vec{e}^{(t)} \cdot \vec{e}^{(s)}$$

where  $g_{(ts)}$  represent the cosines of the angles between vectors  $\vec{e}_{(t)}$  and  $\vec{e}_{(s)}$ , i.e.

$$g_{(ts)} = \cos \angle (\vec{e}_{(t)}, \vec{e}_{(s)})\tag{A2.21}$$

and

$$\begin{aligned}g^{(\xi\xi)} &= 1 + \kappa_{\xi}^2, \\ g^{(\xi\eta)} &= g^{(\eta\xi)} = \kappa_{\xi} \kappa_{\eta}, \\ g^{(\eta\eta)} &= 1 + \kappa_{\eta}^2, \\ g^{(\xi\zeta)} &= g^{(\zeta\xi)} = -\frac{h_{\xi}}{b} \kappa_{\xi}, \\ g^{(\eta\zeta)} &= g^{(\zeta\eta)} = -\frac{h_{\eta}}{b} \kappa_{\eta}, \\ g^{(\zeta\zeta)} &= \frac{h_{\zeta}^2}{b^2}.\end{aligned}\tag{A2.22}$$

Relationships equivalent to the Christoffel symbols can now be defined from the physical components thus:

$$\frac{\partial \vec{e}_{(t)}}{\partial x^{(s)}} = \frac{\partial \vec{e}_{(t)}}{h_s \partial x^s} = \begin{Bmatrix} m \\ t \ s \end{Bmatrix} \vec{e}_{(m)}, \quad (\text{A2.23})$$

where

$$\begin{Bmatrix} m \\ t \ s \end{Bmatrix} = \frac{h_m}{h_t h_s} \left( \begin{Bmatrix} m \\ t \ s \end{Bmatrix} - \delta_t^m \frac{g_{tn}}{g_{tt}} \begin{Bmatrix} n \\ t \ s \end{Bmatrix} \right) \quad (\text{summation on } n \text{ only}) \quad (\text{A2.24})$$

are the physical Christoffel symbols. Note that (generally)

$$\begin{Bmatrix} m \\ t \ s \end{Bmatrix} \neq \begin{Bmatrix} m \\ s \ t \end{Bmatrix}. \quad (\text{A2.25})$$

Since the  $x^\xi - x^\eta$  co-ordinate surface is planar, and bearing in mind that the derivative of the unit vector  $\vec{e}_{(\zeta)} = \vec{m}$  is parallel to this plane (see equation (A2.7)), the following physical Christoffel symbols turn out to be equal to zero:

$$\begin{aligned} \begin{Bmatrix} \xi \\ \zeta \ \xi \end{Bmatrix} &= \begin{Bmatrix} \xi \\ \xi \ \zeta \end{Bmatrix} = \begin{Bmatrix} \xi \\ \xi \ \xi \end{Bmatrix} = \begin{Bmatrix} \xi \\ \xi \ \eta \end{Bmatrix} = \begin{Bmatrix} \eta \\ \eta \ \xi \end{Bmatrix} = \begin{Bmatrix} \eta \\ \eta \ \eta \end{Bmatrix} = \begin{Bmatrix} \zeta \\ \xi \ \xi \end{Bmatrix} = \\ \begin{Bmatrix} \zeta \\ \xi \ \eta \end{Bmatrix} &= \begin{Bmatrix} \eta \\ \eta \ \zeta \end{Bmatrix} = \begin{Bmatrix} \zeta \\ \eta \ \zeta \end{Bmatrix} = \begin{Bmatrix} \zeta \\ \eta \ \xi \end{Bmatrix} = \begin{Bmatrix} \zeta \\ \eta \ \eta \end{Bmatrix} = \begin{Bmatrix} \zeta \\ \xi \ \zeta \end{Bmatrix} = \begin{Bmatrix} \eta \\ \zeta \ \eta \end{Bmatrix} = \\ \begin{Bmatrix} \zeta \\ \zeta \ \zeta \end{Bmatrix} &= 0 \end{aligned} \quad (\text{A2.26})$$

The values of non-zero physical Christoffel symbols are:

$$\begin{aligned}
 \begin{pmatrix} \xi \\ \eta \xi \end{pmatrix} &= \lambda_{\xi}, & \begin{pmatrix} \xi \\ \eta \eta \end{pmatrix} &= -\lambda_{\eta}, \\
 \begin{pmatrix} \eta \\ \xi \eta \end{pmatrix} &= \lambda_{\eta}, & \begin{pmatrix} \eta \\ \xi \xi \end{pmatrix} &= -\lambda_{\xi}, \\
 \begin{pmatrix} \xi \\ \zeta \zeta \end{pmatrix} &= -R_{\xi}, & \begin{pmatrix} \eta \\ \zeta \zeta \end{pmatrix} &= -R_{\eta}, \\
 \begin{pmatrix} \zeta \\ \zeta \xi \end{pmatrix} &= -R_{\xi}, & \begin{pmatrix} \zeta \\ \zeta \eta \end{pmatrix} &= -R_{\eta},
 \end{aligned}
 \tag{A2.27'}$$

$$\begin{pmatrix} \xi \\ \eta \zeta \end{pmatrix} = \begin{pmatrix} \xi \\ \zeta \eta \end{pmatrix} = \frac{h_{\zeta}}{b} \frac{R_{\eta}}{\kappa_{\xi}} = -\frac{h_{\zeta}}{b} \frac{R_{\xi}}{\kappa_{\eta}} = -\begin{pmatrix} \eta \\ \xi \zeta \end{pmatrix}$$

$$\begin{pmatrix} \eta \\ \xi \zeta \end{pmatrix} = \begin{pmatrix} \eta \\ \zeta \xi \end{pmatrix} = \frac{h_{\zeta}}{b} \frac{R_{\xi}}{\kappa_{\eta}} = -\frac{h_{\zeta}}{b} \frac{R_{\eta}}{\kappa_{\xi}} = -\begin{pmatrix} \xi \\ \eta \zeta \end{pmatrix}
 \tag{A2.27''}$$

where

$$\lambda_{\xi} = \frac{1}{h_{\xi}} \frac{\partial h_{\xi}}{\partial \eta},$$

$$\lambda_{\eta} = \frac{1}{h_{\eta}} \frac{\partial h_{\eta}}{\partial \xi},$$

$$R_{\xi} = \frac{r}{r^2 + b^2} \frac{\partial r}{\partial \xi},$$

$$R_{\eta} = \frac{r}{r^2 + b^2} \frac{\partial r}{\partial \eta},$$

$$\kappa_{\xi} = \frac{\partial \xi}{b \partial \theta},$$

$$\kappa_{\eta} = \frac{\partial \eta}{b \partial \theta}.$$

(A2.28)

## 2.3 Vector and Tensor Components

### 2.3.1 Choice of the Components

Perhaps the most obvious practice would be to use physical vector and tensor components defined with respect to the  $x^t$  co-ordinate system, i.e. in terms of the normalized base vectors  $\vec{e}_{(t)}$ .

In this case the velocity vector would have the components

$$\vec{v} = u^{(t)} \vec{e}_{(t)} = u^{(\xi)} \vec{e}_{(\xi)} + u^{(\eta)} \vec{e}_{(\eta)} + u^{(\zeta)} \vec{e}_{(\zeta)} \quad (\text{A2.29})$$

and stress tensor would be

$$\vec{T} = T^{(ts)} \vec{e}_{(t)} \otimes \vec{e}_{(s)}, \quad (\text{A2.30})$$

where

$$T^{(ts)} = -pg^{(ts)} + \tau^{(ts)}, \quad (\text{A2.31})$$

where  $p$  is the pressure and

$$\tau^{(ts)} = \mu \left[ g^{(sm)} \nabla_{(m)} u^{(t)} + g^{(tm)} \nabla_{(m)} u^{(s)} \right] \quad (\text{A2.32})$$

Here  $\nabla_{(s)} u^{(t)}$  is the covariant derivative of the physical vector components, defined by

$$\nabla_{(s)} u^{(t)} = \frac{\partial u^{(t)}}{\partial x^{(s)}} + u^{(m)} \begin{bmatrix} t \\ m \ s \end{bmatrix}. \quad (\text{A2.33})$$

It has been found, however, that the resulting expressions for the stress tensor components are very complicated and time-consuming to evaluate.



Therefore an alternative practice is recommended whereby the base vector  $\vec{e}_{(\zeta)}$  is replaced by the constant vector  $\vec{k}$ , parallel to the tube axis. This leads to the  $z^t$  co-ordinate system with the following orthonormal basis (see Figure 4):

$$\begin{aligned}\vec{e}_{(\xi)} &= \vec{e}^{(\xi)} = \vec{e}_{(\xi)} , \\ \vec{e}_{(\eta)} &= \vec{e}^{(\eta)} = \vec{e}_{(\eta)} , \\ \vec{e}_{(z)} &= \vec{e}^{(z)} = \frac{h_z}{b} \vec{e}_{(\zeta)} - \kappa_\xi \vec{e}_{(\xi)} - \kappa_\eta \vec{e}_{(\eta)} = \vec{k} \quad (\text{A2.34})\end{aligned}$$

The corresponding metric tensor components are

$$\gamma_{(ts)} = \gamma^{(ts)} = \begin{pmatrix} 1 & 0 & 0 \\ 0 & 1 & 0 \\ 0 & 0 & 1 \end{pmatrix} \quad (\text{A2.35})$$

It is obvious that the only non-zero Christoffel symbols in the  $z^t$  co-ordinate system are  $\begin{pmatrix} \xi \\ \eta \xi \end{pmatrix}$ ,  $\begin{pmatrix} \xi \\ \eta \eta \end{pmatrix}$ ,  $\begin{pmatrix} \eta \\ \xi \xi \end{pmatrix}$ ,  $\begin{pmatrix} \eta \\ \xi \eta \end{pmatrix}$  given by equations (A2.27). The velocity vector is now:

$$\begin{aligned}\vec{U} &= w^{(t)} \vec{e}_{(t)} = w^{(\xi)} \vec{e}_{(\xi)} + w^{(\eta)} \vec{e}_{(\eta)} + w^{(z)} \vec{e}_{(z)} , \\ &= U \vec{e}_{(\xi)} + V \vec{e}_{(\eta)} + W \vec{k} \quad (\text{A2.36})\end{aligned}$$

where components  $w^{(t)}$  can be related to the components  $u^{(t)}$  as follows:

$$\begin{aligned}u^{(\xi)} &= U - \kappa_\xi W = w^{(\xi)} - \kappa_\xi w^{(z)} \\ u^{(\eta)} &= V - \kappa_\eta W = w^{(\eta)} - \kappa_\eta w^{(z)} \\ u^{(\zeta)} &= \frac{h_z}{b} W = \frac{h_z}{b} w^{(z)} \quad (\text{A2.37})\end{aligned}$$

The stress tensor now has the components

$$\vec{T} = T^{(ts)} \vec{e}_{(t)} \otimes \vec{e}_{(s)} \quad (\text{A2.38})$$

where

$$T^{(ts)} = -p\gamma^{(ts)} + \tau^{(ts)} \quad (\text{A2.39})$$

and

$$\tau^{(ts)} = \mu \left[ \gamma^{(sm)} \nabla_{(m)} w^{(t)} + \gamma^{(tm)} \nabla_{(m)} w^{(s)} \right] \quad (\text{A2.40})$$

where

$$\nabla_{(s)} w^{(t)} = \frac{\partial w^{(t)}}{\partial z^{(s)}} + w^{(m)} \left[ \begin{matrix} t \\ m \end{matrix} \right]_{s} . \quad (\text{A2.41})$$

Consequently the stress tensor components in the  $z^t$  co-ordinate system are:

$$\begin{aligned} T^{(\xi\xi)} &= -p + 2\mu \left[ \frac{\partial U}{\partial \xi} + \left[ \begin{matrix} \xi \\ \eta \end{matrix} \right]_{\xi} V \right] , \\ T^{(\xi\eta)} &= T^{(\eta\xi)} = \mu \left[ \frac{\partial U}{\partial \eta} + \left[ \begin{matrix} \xi \\ \eta \end{matrix} \right]_{\eta} V + \frac{\partial V}{\partial \xi} + \left[ \begin{matrix} \eta \\ \xi \end{matrix} \right]_{\xi} U \right] , \\ T^{(\eta\eta)} &= -p + 2\mu \left[ \frac{\partial V}{\partial \eta} + \left[ \begin{matrix} \eta \\ \xi \end{matrix} \right]_{\eta} U \right] , \\ T^{(\xi z)} &= T^{(z\xi)} = \mu \left[ \frac{\partial U}{\partial z} + \frac{\partial W}{\partial \xi} \right] , \\ T^{(\eta z)} &= T^{(z\eta)} = \mu \left[ \frac{\partial V}{\partial z} + \frac{\partial W}{\partial \eta} \right] , \\ T^{(zz)} &= -p + 2\mu \frac{\partial W}{\partial z} . \end{aligned} \quad (\text{A2.42})$$

Since the control volume continues to be defined in terms of the original  $x^t$  co-ordinate system (see Figure 3), in the new frame the convection terms in the fluid transport equations become more complicated (due to the fluxes of  $\rho w$  through the  $x^\xi$ - $x^\zeta$  and  $x^\eta$ - $x^\zeta$  co-ordinate surfaces), but this is more than compensated by the appearance of much simpler diffusion terms in the momentum equations and a simple expression for the generation of turbulent kinetic energy. However, there is a further stage of manipulation required which is connected with the present choice of control volume. All derivations have to be expressed in terms of  $x^t$  and this requires that relations be derived between derivations in the  $z^t$  and  $x^t$  co-ordinate systems. These relations can be obtained by a co-ordinate transformation as outlined below.

### 2.3.2 Co-ordinate Transformation

The orthogonal curvilinear co-ordinates  $z^\xi$  and  $z^\eta$  can be expressed as functions of  $r$  and  $\theta$  thus:

$$\begin{aligned} z^\xi &= f_1(r, \theta) \\ z^\eta &= f_2(r, \theta) \\ z^z &= z \end{aligned} \quad (A2.43)$$

If one introduces the transformation

$$\begin{aligned} r' &= r \\ \theta' &= \theta - \frac{z}{b} \\ z' &= z \end{aligned} \quad (A2.44)$$

this has the effect of rotating the shaded area in the position vertically above the same area in the  $z = 0$  plane (Figure 5) and one gets:

$$\begin{aligned} x^\xi &= f_1(r', \theta') \\ x^\eta &= f_2(r', \theta') \\ x^\zeta &= \frac{1}{b} z' \quad (\text{Equ. (A2.1)} \Rightarrow z^z = z = b\Delta\theta \Rightarrow \Delta\theta = \frac{z}{b}) \\ &\quad (\text{Equ. (A2.6)} \Rightarrow h_\zeta x^\zeta = h_\zeta \Delta\theta = h_\zeta \frac{z}{b} \Rightarrow x^\zeta = \frac{z}{b} = \frac{z'}{b}) \end{aligned} \quad (\text{A2.45})$$

Therefore it follows that:

$$\begin{aligned} \frac{\partial}{\partial z^{(\xi)}} (\dots) &= \frac{\partial}{\partial x^{(\xi)}} (\dots) = \frac{\partial}{\partial \xi} (\dots) \\ \frac{\partial}{\partial z^{(\eta)}} (\dots) &= \frac{\partial}{\partial x^{(\eta)}} (\dots) = \frac{\partial}{\partial \eta} (\dots) \\ \frac{\partial}{\partial z} (\dots) &= \frac{h_\zeta}{b} \frac{\partial}{\partial x^{(\zeta)}} (\dots) - \kappa_\xi \frac{\partial}{\partial \xi} (\dots) - \kappa_\eta \frac{\partial}{\partial \eta} (\dots) \end{aligned} \quad (\text{A2.46})$$

The first two of these relations are obvious since the rotation does not change derivatives. The third relation follows from:

$$\begin{aligned} \frac{\partial}{\partial z} (\dots) &= \frac{\partial}{\partial x^{(\xi)}} (\dots) \frac{\partial x^{(\xi)}}{\partial z} + \frac{\partial}{\partial x^{(\eta)}} (\dots) \frac{\partial x^{(\eta)}}{\partial z} + \frac{\partial (\dots)}{\partial x^{(\zeta)}} \frac{\partial x^{(\zeta)}}{\partial z} \\ &= \frac{\partial x^{(\xi)}}{\partial z} \frac{\partial}{\partial x^{(\xi)}} (\dots) + \left[ \frac{\partial x^{(\eta)}}{\partial r'} \frac{\partial r'}{\partial z} + \frac{\partial x^{(\eta)}}{\partial \theta'} \frac{\partial \theta'}{\partial z} \right] \frac{\partial}{\partial x^{(\eta)}} (\dots) \\ &\quad + \left[ \frac{\partial x^{(\xi)}}{\partial r'} \frac{\partial r'}{\partial z} + \frac{\partial x^{(\xi)}}{\partial \theta'} \frac{\partial \theta'}{\partial z} \right] \frac{\partial}{\partial x^{(\xi)}} (\dots), \end{aligned}$$

$$\text{or} \quad \frac{\partial}{\partial z} (\dots) = \frac{1}{b} \frac{\partial (\dots)}{\partial x^{(\xi)}} - \frac{1}{b} \frac{\partial x^{(\eta)}}{\partial \theta'} \frac{\partial (\dots)}{\partial x^{(\eta)}} - \frac{1}{b} \frac{\partial x^{(\xi)}}{\partial \theta'} \frac{\partial (\dots)}{\partial x^{(\xi)}} ,$$

$$\text{i.e.} \quad \frac{\partial}{\partial z} (\dots) = \frac{h_{\xi}}{b} \frac{\partial}{\partial \xi} (\dots) - \kappa_{\xi} \frac{\partial (\dots)}{\partial \xi} - \kappa_{\eta} \frac{\partial (\dots)}{\partial \eta} , \quad (\text{A2.47})$$

which is identical to the last relation (A2.46).

In order to obtain  $\partial U/\partial z$ ,  $\partial V/\partial z$ ,  $\partial W/\partial z$ , one should apply (A2.47) to the vector  $\vec{U}$  (not to its components):

$$\begin{aligned} \frac{\partial \vec{U}}{\partial z} &= \frac{h_{\xi}}{b} \frac{\partial \vec{U}}{\partial \xi} - \kappa_{\xi} \frac{\partial \vec{U}}{\partial \xi} - \kappa_{\eta} \frac{\partial \vec{U}}{\partial \eta} = \\ &= \frac{h_{\xi}}{b} \left[ \frac{\partial U}{\partial \xi} \vec{e}_{(\xi)} + U \frac{\partial \vec{e}_{(\xi)}}{\partial \xi} + \frac{\partial V}{\partial \xi} \vec{e}_{(\eta)} + V \frac{\partial \vec{e}_{(\eta)}}{\partial \xi} \right. \\ &\quad \left. + \frac{\partial W}{\partial \xi} \vec{e}_{(z)} + W \frac{\partial \vec{e}_{(z)}}{\partial \xi} \right] \\ &- \kappa_{\xi} \left[ \frac{\partial U}{\partial \xi} \vec{e}_{(\xi)} + U \frac{\partial \vec{e}_{(\xi)}}{\partial \xi} + \frac{\partial V}{\partial \xi} \vec{e}_{(\eta)} + V \frac{\partial \vec{e}_{(\eta)}}{\partial \xi} \right. \\ &\quad \left. + \frac{\partial W}{\partial \xi} \vec{e}_{(z)} + W \frac{\partial \vec{e}_{(z)}}{\partial \xi} \right] \\ &- \kappa_{\eta} \left[ \frac{\partial U}{\partial \eta} \vec{e}_{(\xi)} + U \frac{\partial \vec{e}_{(\xi)}}{\partial \eta} + \frac{\partial V}{\partial \eta} \vec{e}_{(\eta)} + V \frac{\partial \vec{e}_{(\eta)}}{\partial \eta} \right. \\ &\quad \left. + \frac{\partial W}{\partial \eta} \vec{e}_{(z)} + W \frac{\partial \vec{e}_{(z)}}{\partial \eta} \right] \\ &= \nabla_{(z)} W^{(\tau)} \vec{e}_{(\tau)} . \end{aligned} \quad (\text{A2.48})$$

Using (A2.34) and (A2.29) one gets:

$$\begin{aligned}
 \frac{\partial \vec{U}}{\partial z} &= \frac{h_z}{b} \left\{ \frac{\partial U}{\partial \zeta} \vec{e}_{(\xi)} + U \left[ \begin{pmatrix} \xi \\ \xi \ \zeta \end{pmatrix} \vec{e}_{(\xi)} + \begin{pmatrix} \eta \\ \xi \ \zeta \end{pmatrix} \vec{e}_{(\eta)} + \cancel{\begin{pmatrix} \xi \\ \xi \ \zeta \end{pmatrix}} \right] \right. \\
 &\quad \left. + \frac{b}{h_z} \left( \kappa_\xi \vec{e}_{(\xi)} + \kappa_\eta \vec{e}_{(\eta)} + \vec{e}_{(z)} \right) \right] + \frac{\partial V}{\partial \zeta} \vec{e}_{(\eta)} + \frac{\partial W}{\partial \zeta} \vec{e}_{(z)} \\
 &\quad + V \left[ \begin{pmatrix} \xi \\ \eta \ \zeta \end{pmatrix} \vec{e}_{(\xi)} + \begin{pmatrix} \eta \\ \eta \ \zeta \end{pmatrix} \vec{e}_{(\eta)} + \cancel{\begin{pmatrix} \zeta \\ \eta \ \zeta \end{pmatrix}} \frac{b}{h_z} \left( \kappa_\xi \vec{e}_{(\xi)} + \kappa_\eta \vec{e}_{(\eta)} + \vec{e}_{(z)} \right) \right] \Bigg\} \\
 &\quad - \kappa_\xi \left[ \frac{\partial U}{\partial \xi} \vec{e}_{(\xi)} + U \begin{pmatrix} \eta \\ \xi \ \xi \end{pmatrix} \vec{e}_{(\eta)} + \frac{\partial V}{\partial \xi} \vec{e}_{(\eta)} + V \begin{pmatrix} \xi \\ \eta \ \xi \end{pmatrix} \vec{e}_{(\xi)} + \frac{\partial W}{\partial \xi} \vec{e}_{(z)} \right] \\
 &\quad - \kappa_\eta \left[ \frac{\partial U}{\partial \eta} \vec{e}_{(\xi)} + U \begin{pmatrix} \eta \\ \xi \ \eta \end{pmatrix} \vec{e}_{(\eta)} + \frac{\partial V}{\partial \eta} \vec{e}_{(\eta)} + V \begin{pmatrix} \xi \\ \eta \ \eta \end{pmatrix} \vec{e}_{(\xi)} + \frac{\partial W}{\partial \eta} \vec{e}_{(z)} \right] \\
 &= \nabla_{(z)} W(z) \vec{e}_{(z)} \tag{A2.49}
 \end{aligned}$$

$$\begin{aligned}
 \Rightarrow \quad \frac{\partial U}{\partial z} &= \nabla_{(z)} U = \frac{h_z}{b} \left[ \frac{\partial U}{\partial \zeta} + U \cancel{\begin{pmatrix} \xi \\ \xi \ \zeta \end{pmatrix}} + V \begin{pmatrix} \xi \\ \eta \ \zeta \end{pmatrix} \right] \\
 &\quad - \kappa_\xi \left[ \frac{\partial U}{\partial \xi} + V \begin{pmatrix} \xi \\ \eta \ \xi \end{pmatrix} - U \cancel{\begin{pmatrix} \zeta \\ \xi \ \zeta \end{pmatrix}} - V \begin{pmatrix} \zeta \\ \eta \ \zeta \end{pmatrix} \right] \\
 &\quad - \kappa_\eta \left[ \frac{\partial U}{\partial \eta} + V \begin{pmatrix} \xi \\ \eta \ \eta \end{pmatrix} \right] \\
 \frac{\partial V}{\partial z} &= \nabla_{(z)} V = \frac{h_z}{b} \left[ \frac{\partial V}{\partial \zeta} + U \begin{pmatrix} \eta \\ \xi \ \zeta \end{pmatrix} + V \cancel{\begin{pmatrix} \eta \\ \eta \ \zeta \end{pmatrix}} \right] \\
 &\quad - \kappa_\xi \left[ \frac{\partial V}{\partial \xi} + U \begin{pmatrix} \eta \\ \xi \ \xi \end{pmatrix} \right]
 \end{aligned}$$

$$\begin{aligned}
& - \kappa_{\eta} \left[ \frac{\partial V}{\partial \eta} + U \begin{pmatrix} \eta \\ \xi \eta \end{pmatrix} - U \begin{pmatrix} \zeta \\ \xi \zeta \end{pmatrix} - V \begin{pmatrix} \zeta \\ \eta \zeta \end{pmatrix} \right] \\
\frac{\partial W}{\partial z} &= \nabla_{(z)} W = \frac{h_{\zeta}}{b} \frac{\partial W}{\partial \zeta} + U \begin{pmatrix} \zeta \\ \xi \zeta \end{pmatrix} + V \begin{pmatrix} \zeta \\ \eta \zeta \end{pmatrix} \\
& - \kappa_{\xi} \frac{\partial W}{\partial \xi} - \kappa_{\eta} \frac{\partial W}{\partial \eta}
\end{aligned} \tag{A2.50}$$

#### 2.4 Transport Equations

The transport equations for mass, scalar and momentum can now be written in the form:

$$\begin{aligned}
\frac{\partial \rho}{\partial t} + \frac{\Delta}{\Delta x(s)} \left[ \rho \vec{U} \cdot \vec{e}(s) \right] &= S_m, \\
\frac{\partial}{\partial t} (\rho \vec{\Phi}) + \frac{\Delta}{\Delta x(s)} \left[ (\rho \vec{U} \vec{\Phi} - \vec{q}) \cdot \vec{e}(s) \right] &= S_{\vec{\Phi}}, \\
\frac{\partial}{\partial t} (\rho \vec{U}) + \frac{\Delta}{\Delta x(s)} \left[ (\rho \vec{U} \otimes \vec{U} - \vec{T}) \cdot \vec{e}(s) \right] &= \vec{S}_U,
\end{aligned} \tag{A2.51}$$

where the following differential operator is introduced ( $g = \det(g_{ts})$ )

$$\frac{\Delta}{\Delta x(s)} [\dots] = \sqrt{\frac{g_{ss}}{g}} \frac{\partial}{\partial x(s)} \left[ \sqrt{\frac{g}{g_{ss}}} (\dots) \right] \tag{A2.52}$$

If, as proposed, the vector and tensor components are defined with

respect to the  $z^t$  co-ordinate system, then the velocity  $\vec{U}$ , flux vector  $\vec{q}$  and stress tensor  $\vec{T}$  have the following forms:

$$\begin{aligned}\vec{U} &= w^{(t)} \vec{e}_{(t)} , \\ \vec{q} &= \Gamma_\phi \frac{\partial \Phi}{\partial z^{(t)}} \vec{e}_{(t)} , \\ \vec{T} &= T^{(ts)} \vec{e}_{(t)} \otimes \vec{e}_{(s)}\end{aligned}\tag{A2.53}$$

and therefore

$$\begin{aligned}\vec{U} \cdot \vec{e}^{(s)} &= c^{(s)} w^{(s)} - \kappa_s W , \\ \vec{q} \cdot \vec{e}^{(s)} &= \Gamma_\phi \left[ c^{(s)} \frac{\partial \Phi}{\partial z^{(s)}} - \kappa_s \frac{\partial \Phi}{\partial z} \right] , \\ &= \Gamma_\phi \left[ c^{(s)} \frac{\partial \Phi}{\partial z^{(s)}} - \kappa_s \left( \frac{h_\zeta}{b} \frac{\partial \Phi}{\partial \zeta} - \kappa_\xi \frac{\partial \Phi}{\partial \xi} - \kappa_\eta \frac{\partial \Phi}{\partial \eta} \right) \right] , \\ (\vec{U} \otimes \vec{U}) \cdot \vec{e}^{(s)} &= w^{(t)} \left[ c^{(s)} w^{(s)} - \kappa_s W \right] \vec{e}_{(t)} , \\ \vec{T} \cdot \vec{e}^{(s)} &= \left[ c^{(s)} T^{(ts)} - \kappa_s T^{(tz)} \right] \vec{e}_{(t)} ,\end{aligned}\tag{A2.54}$$

where the vector

$$c^{(s)} = \left( 1, 1, \frac{h_\zeta}{b} \right)\tag{A2.55}$$

has been introduced for generality.

The transport equations can now be written in terms of the quantities just defined as:



$$\frac{\partial \rho}{\partial t} + \frac{\Delta}{\Delta x(s)} \left[ \rho (c(s) w(s) - k_s w) \right] = S_m, \quad (A2.56)$$

$$\frac{\partial}{\partial t} (\rho \Phi) + \frac{\Delta}{\Delta x(s)} \left[ c(s) \left( \rho w(s) \Phi - \Gamma_\Phi \frac{\partial \Phi}{\partial z(s)} \right) - k_s \left( \rho w \Phi - \frac{\partial \Phi}{\partial z} \Gamma_\Phi \right) \right] = S_\Phi, \quad (A2.57)$$

$$\begin{aligned} \frac{\partial}{\partial t} \left[ \rho w(t) \vec{e}_{\epsilon(t)} \right] + \frac{\Delta}{\Delta x(s)} \left\{ \left[ c(s) \left( \rho w(t) w(s) - T(tz) \right) \right. \right. \\ \left. \left. - k_s \left( \rho w(t) w - T(tz) \right) \right] \vec{e}_{\epsilon(t)} \right\} = S_w^{(t)} \vec{e}_{\epsilon(t)} \end{aligned} \quad (A2.58)$$

The expanded form of the equation (A2.56) is

$$\begin{aligned} \frac{\partial \rho}{\partial t} + \frac{\Delta}{\Delta \xi} (\rho U) + \frac{\Delta}{\Delta \eta} (\rho V) + \frac{\Delta}{\Delta \zeta} \left( \frac{h_\zeta}{b} \rho W \right) \\ = \frac{\Delta}{\Delta \xi} (\kappa_\xi \rho W) + \frac{\Delta}{\Delta \eta} (\kappa_\eta \rho W) + S_m \end{aligned} \quad (A2.59)$$

The expanded form of the equation (A2.57) is

$$\begin{aligned} \frac{\partial}{\partial t} (\rho \Phi) + \frac{\Delta}{\Delta \xi} (\rho U \Phi) + \frac{\Delta}{\Delta \eta} (\rho V \Phi) + \frac{\Delta}{\Delta \zeta} \left( \frac{h_\zeta}{b} \rho W \Phi \right) = \\ = \frac{\Delta}{\Delta \xi} \left[ \Gamma_\Phi \frac{\partial \Phi}{\partial \xi} \right] + \frac{\Delta}{\Delta \eta} \left[ \Gamma_\Phi \frac{\partial \Phi}{\partial \eta} \right] + \frac{\Delta}{\Delta \zeta} \left[ \frac{h_\zeta^2}{b^2} \Gamma_\Phi \frac{\partial \Phi}{\partial \zeta} \right] + S_\Phi \\ + \frac{\Delta}{\Delta \xi} (\kappa_\xi \rho W \Phi) + \frac{\Delta}{\Delta \eta} (\kappa_\eta W \Phi) \\ - \frac{\Delta}{\Delta \xi} \left[ \kappa_\xi \Gamma_\Phi \left( \frac{h_\zeta}{b} \frac{\partial \Phi}{\partial \zeta} - \kappa_\xi \frac{\partial \Phi}{\partial \xi} - \kappa_\eta \frac{\partial \Phi}{\partial \eta} \right) \right] \end{aligned}$$

$$\begin{aligned}
& - \frac{\Delta}{\Delta \eta} \left[ k_{\eta} \Gamma_{\phi} \left( \frac{h_{\zeta}}{b} \frac{\partial \phi}{\partial \zeta} - \kappa_{\xi} \frac{\partial \phi}{\partial \xi} - \kappa_{\eta} \frac{\partial \phi}{\partial \eta} \right) \right] \\
& - \frac{\Delta}{\Delta \zeta} \left[ \frac{h_{\zeta}}{b} \Gamma_{\phi} \left( \kappa_{\xi} \frac{\partial \phi}{\partial \xi} + \kappa_{\eta} \frac{\partial \phi}{\partial \eta} \right) \right]
\end{aligned}
\tag{A2.60}$$

If one introduces the following notation:

$$\begin{aligned}
\rho_w(t) w(s) - T(ts) &= \rho_w(t) w(s) - \tau(ts) + p_Y(ts) = \\
&= \sigma(ts) + p_Y(ts)
\end{aligned}
\tag{A2.61}$$

the momentum equation (A2.58) takes the form:

$$\begin{aligned}
& \frac{\partial}{\partial t} \left[ \rho_w(t) \vec{e}(t) \right] + \frac{\Delta}{\Delta x(s)} \left[ c(s) \sigma(ts) - \kappa_s \sigma(tz) \right] \vec{e}(t) + \\
& + \left[ c(s) \sigma(ts) - \kappa_s \sigma(tz) \right] \frac{\partial \vec{e}(t)}{\partial x(s)} = \left[ -\gamma(ts) \frac{\partial p}{\partial z}(t) + S_w(t) \right] \vec{e}(t)
\end{aligned}
\tag{A2.62}$$

If the expression (A2.23) is used, the above equation can also be written in the form:

$$\begin{aligned}
& \left\{ \frac{\partial}{\partial t} \rho_w(t) + \frac{\Delta}{\Delta x(s)} \left[ c(s) \sigma(ts) - \kappa_s \sigma(tz) \right] + \right. \\
& \left. \left\langle \left[ c(s) \sigma(ms) - \kappa_s \sigma(mz) \right] \left[ \frac{1}{c(t)} \begin{pmatrix} t \\ m \end{pmatrix} + \kappa_s \frac{b}{h_{\zeta}} \begin{pmatrix} \zeta \\ m \end{pmatrix} \right] \right\rangle \right\} \\
& \cdot \vec{e}(t) = \left[ -\gamma(ts) \frac{\partial p}{\partial z}(t) + S_w(t) \right] \vec{e}(t)
\end{aligned}
\tag{A6.23}$$

where the term in  $\langle \rangle$  brackets is equal to zero for  $m = z$ , since

$\partial \vec{\epsilon}_{(z)} / \partial x^{(t)} = 0$  and  $\vec{\epsilon}_{(z)} = \vec{k} = \text{const.}$  where, from (A2.61),

$$\sigma^{(ts)} = \rho_w^{(t)} w^{(s)} - \tau^{(ts)} \quad (\text{A2.64})$$

and, from (A2.42), (A2.50), (A2.27)  $\Rightarrow$

$$\tau^{(\xi\xi)} = \tau_{\xi\xi} = 2\mu \left[ \frac{\partial U}{\partial \xi} + \lambda_{\xi} V \right],$$

$$\tau^{(\xi\eta)} = \tau_{\xi\eta} = \tau^{(\eta\xi)} = \tau_{\eta\xi} = \mu \left[ \frac{\partial U}{\partial \eta} + \frac{\partial V}{\partial \xi} - \lambda_{\xi} U - \lambda_{\eta} V \right],$$

$$\tau^{(\eta\eta)} = \tau_{\eta\eta} = 2\mu \left[ \frac{\partial V}{\partial \eta} + \lambda_{\eta} U \right],$$

$$\begin{aligned} \tau^{(\xi z)} = \tau_{\xi z} = \tau^{(z\xi)} = \tau_{z\xi} = & \mu \left[ \frac{\partial W}{\partial \xi} + \frac{h_{\xi}}{b} \frac{\partial U}{\partial \zeta} - \kappa_{\xi} \frac{\partial U}{\partial \xi} - \kappa_{\eta} \frac{\partial U}{\partial \eta} \right. \\ & \left. + \left( \kappa_{\eta} \lambda_{\eta} - \kappa_{\xi} \lambda_{\xi} + \frac{h_{\xi}}{b} \begin{pmatrix} \xi & \eta \\ \eta & \zeta \end{pmatrix} \right) V \right], \end{aligned}$$

$$\begin{aligned} \tau^{(\eta z)} = \tau_{\eta z} = \tau^{(z\eta)} = \tau_{z\eta} = & \mu \left[ \frac{\partial W}{\partial \eta} + \frac{h_{\eta}}{b} \frac{\partial V}{\partial \zeta} - \kappa_{\xi} \frac{\partial V}{\partial \xi} - \right. \\ & \left. \kappa_{\eta} \frac{\partial V}{\partial \eta} + \left( \kappa_{\xi} \lambda_{\xi} - \kappa_{\eta} \lambda_{\eta} + \frac{h_{\eta}}{b} \begin{pmatrix} \eta & \xi \\ \xi & \zeta \end{pmatrix} \right) U \right], \end{aligned}$$

$$\tau^{(zz)} = 2\mu \left[ \frac{h_{\zeta}}{b} \frac{\partial W}{\partial \zeta} - \kappa_{\xi} \frac{\partial W}{\partial \xi} - \kappa_{\eta} \frac{\partial W}{\partial \eta} \right]$$

Using (A2.27'') and the equation  $\frac{h_{\zeta}^2}{b^2} = (\kappa_{\xi} \kappa_{\xi} + \kappa_{\eta} \kappa_{\eta} + 1)$ , one gets:

$$\tau_{\eta z} = \tau_{z\eta} = \mu \left[ \frac{\partial W}{\partial \eta} + \frac{h_{\eta}}{b} \frac{\partial V}{\partial \zeta} - \kappa_{\xi} \frac{\partial V}{\partial \xi} - \kappa_{\eta} \frac{\partial V}{\partial \eta} \right]$$

$$\begin{aligned}
& + \left( \kappa_{\xi} \lambda_{\xi} - \kappa_{\eta} \lambda_{\eta} - \sigma \right) U \Big] \\
\tau_{\xi z} = \tau_{z\xi} = & \mu \left[ \frac{\partial W}{\partial \xi} + \frac{h_{\xi}}{b} \frac{\partial U}{\partial z} - \kappa_{\xi} \frac{\partial U}{\partial \xi} - \kappa_{\eta} \frac{\partial U}{\partial \eta} \right. \\
& \left. + \left( \kappa_{\eta} \lambda_{\eta} - \kappa_{\xi} \lambda_{\xi} + \sigma \right) V \right] \quad (A2.65)
\end{aligned}$$

where  $\sigma = (\kappa_{\xi} \kappa_{\xi} + \kappa_{\eta} \kappa_{\eta} + 1) R_{\eta} / \kappa_{\xi}$ .

Finally, one can extract the equations for the individual momentum components as follows:

#### $\xi$ Momentum

$$\begin{aligned}
\frac{\partial}{\partial t}(\rho U) + \frac{\Delta}{\Delta \xi}(\rho U U) + \frac{\Delta}{\Delta \eta}(\rho U V) + \frac{\Delta}{\Delta z} \left( \frac{h_{\xi}}{b} \rho U W \right) = & - \frac{\partial p}{\partial \xi} + \frac{\Delta}{\Delta \xi} \left( \mu \frac{\partial U}{\partial \xi} \right) \\
& + \frac{\Delta}{\Delta \eta} \left( \mu \frac{\partial U}{\partial \eta} \right) + \frac{\Delta}{\Delta z} \left( \frac{h_{\xi}}{b} \mu \frac{\partial U}{\partial z} \right) + \frac{\Delta}{\Delta \xi}(\kappa_{\xi} \rho U W) + \frac{\Delta}{\Delta \eta}(\kappa_{\eta} \rho U W) \\
& + \frac{\Delta}{\Delta \xi} \left( \tau_{\xi \xi} - \mu \frac{\partial U}{\partial \xi} - \kappa_{\xi} \tau_{\xi z} \right) + \frac{\Delta}{\Delta \eta} \left( \tau_{\xi \eta} - \mu \frac{\partial U}{\partial \eta} - \kappa_{\eta} \tau_{\xi z} \right) \\
& + \frac{\Delta}{\Delta z} \left[ \frac{h_{\xi}}{b} \left( \tau_{\xi z} - \mu \frac{\partial U}{\partial z} \right) \right] \\
& + \left( -\sigma + \kappa_{\xi} \lambda_{\xi} - \kappa_{\eta} \lambda_{\eta} \right) \times (\rho V W - \tau_{\eta z}) \\
& - \lambda_{\xi}(\rho U V - \tau_{\xi \eta}) + \lambda_{\eta}(\rho V^2 - \tau_{\eta \eta}) \quad (A2.66)
\end{aligned}$$

#### $\eta$ Momentum

$$\begin{aligned}
\frac{\partial}{\partial t}(\rho V) + \frac{\Delta}{\Delta \xi}(\rho V U) + \frac{\Delta}{\Delta \eta}(\rho V V) + \frac{\Delta}{\Delta z} \left( \frac{h_{\eta}}{b} \rho V W \right) = & - \frac{\partial p}{\partial \eta} + \frac{\Delta}{\Delta \xi} \left( \mu \frac{\partial V}{\partial \xi} \right) \\
& + \frac{\Delta}{\Delta \eta} \left( \mu \frac{\partial V}{\partial \eta} \right) + \frac{\Delta}{\Delta z} \left( \frac{h_{\eta}}{b} \mu \frac{\partial V}{\partial z} \right) + \frac{\Delta}{\Delta \xi}(\kappa_{\xi} \rho V W) + \frac{\Delta}{\Delta \eta}(\kappa_{\eta} \rho V W)
\end{aligned}$$

$\eta$  Momentum (cont.)

$$\begin{aligned}
& + \frac{\Delta}{\Delta \xi} (\tau_{\eta \xi} - \mu \frac{\partial V}{\partial \xi} - \kappa_{\xi} \tau_{\eta z}) + \frac{\Delta}{\Delta \eta} (\tau_{\eta \eta} - \mu \frac{\partial V}{\partial \eta} - \kappa_{\eta} \tau_{\eta z}) \\
& + \frac{\Delta}{\Delta \zeta} \left[ \frac{h_{\zeta}}{b} \left( \tau_{\eta z} - \mu \frac{\partial V}{\partial \zeta} \right) \right] \\
& + (\sigma - \kappa_{\xi} \lambda_{\xi} + \kappa_{\eta} \lambda_{\eta}) \times (\rho U W - \tau_{\xi z}) \\
& + \lambda_{\xi} (\rho U^2 - \tau_{\xi \xi}) - \lambda_{\eta} (\rho U V - \tau_{\xi \eta})
\end{aligned}
\tag{A2.67}$$

 $z$  Momentum

$$\begin{aligned}
\frac{\partial}{\partial t} (\rho W) + \frac{\Delta}{\Delta \xi} (\rho U W) + \frac{\Delta}{\Delta \eta} (\rho V W) + \frac{\Delta}{\Delta \zeta} \left[ \frac{h_{\zeta}}{b} \rho W W \right] &= - \frac{\partial p}{\partial z} + \frac{\Delta}{\Delta \xi} (\mu \frac{\partial W}{\partial \xi}) \\
& + \frac{\Delta}{\Delta \eta} (\mu \frac{\partial W}{\partial \eta}) + \frac{\Delta}{\Delta \zeta} \left[ \frac{h_{\zeta}}{b} \mu \frac{\partial W}{\partial \zeta} \right] + \frac{\Delta}{\Delta \xi} (\kappa_{\xi} \rho W W) + \frac{\Delta}{\Delta \eta} (\kappa_{\eta} \rho W W) \\
& + \frac{\Delta}{\Delta \xi} (\tau_{\xi z} - \mu \frac{\partial W}{\partial \xi} - \kappa_{\xi} \tau_{zz}) + \frac{\Delta}{\Delta \eta} (\tau_{z \eta} - \mu \frac{\partial W}{\partial \eta} - \kappa_{\eta} \tau_{zz}) \\
& + \frac{\Delta}{\Delta \zeta} \left[ \frac{h_{\zeta}}{b} \left( \tau_{zz} - \mu \frac{\partial W}{\partial \zeta} \right) \right]
\end{aligned}
\tag{A2.68}$$

Generation of Turbulent Kinetic Energy

If (k- $\epsilon$ ) turbulence model is used the generation of turbulent kinetic energy should be calculated. It is defined (in terms of  $w^{(t)}$ ) as

$$G = \gamma_{(tm)} \tau_t^{(sm)} \nabla_{(s)} w^{(t)} \tag{A2.69}$$

Since in  $z^t$  co-ordinate system (orthogonal one)

$$\tau_t^{(ts)} = \mu_t \left[ \nabla_{(t)} w^{(s)} + \nabla_{(s)} w^{(t)} \right] = \tau_{ts}^t \tag{A2.70}$$

it follows that

$$G = \frac{1}{2} \mu_t \left\{ \left( \tau_{\xi\xi}^t \right)^2 + \left( \tau_{\eta\eta}^t \right)^2 + \left( \tau_{zz}^t \right)^2 + \right. \\ \left. + 2 \left[ \left( \tau_{\xi\eta}^t \right)^2 + \left( \tau_{\xi z}^t \right)^2 + \left( \tau_{\eta z}^t \right)^2 \right] \right\} \quad (\text{A2.71})$$

where  $\tau_{ts}^t$  are given by relations (A2.65) for  $\mu = \mu_t$ .

#### Steady and Fully Developed Flow

In the case of the steady flow

$$\frac{\partial}{\partial t}(\dots) = 0 \quad (\text{A2.72})$$

and in the case of the fully developed flow in the  $x^{(\zeta)}$  direction

$$\frac{\partial}{\partial \zeta}(\dots) = 0$$

and (see (A2.52)).

$$\frac{\Delta}{\Delta \zeta}(\dots) = 0 . \quad (\text{A2.73})$$

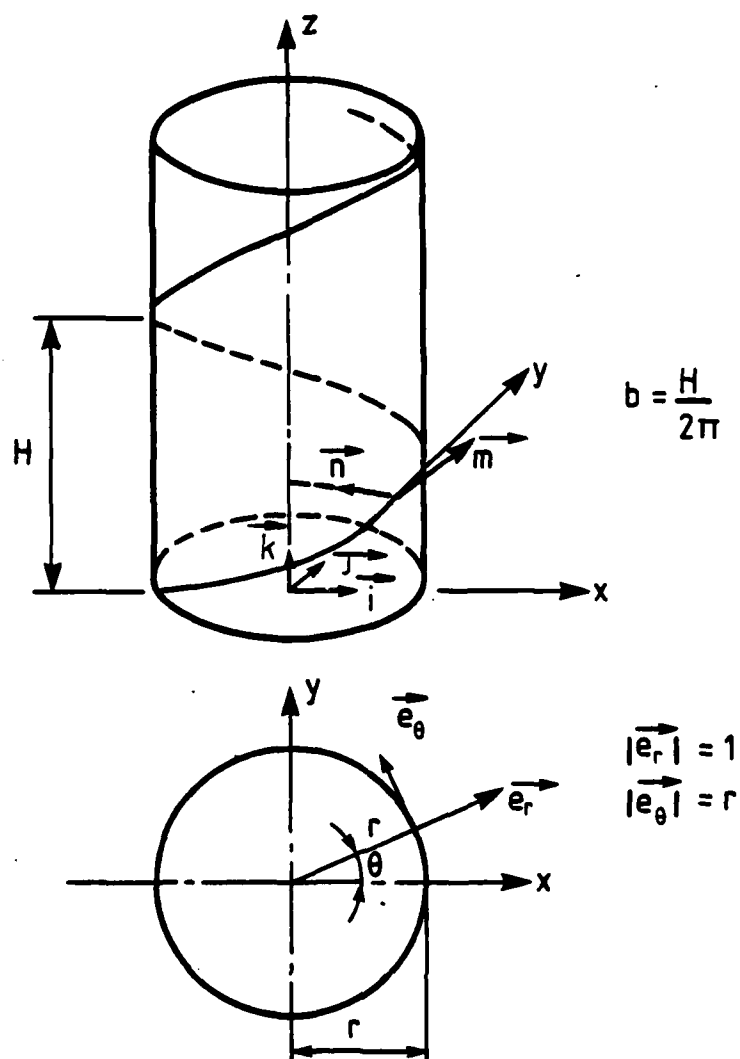


Fig. 1 Mathematical description of a circular helix

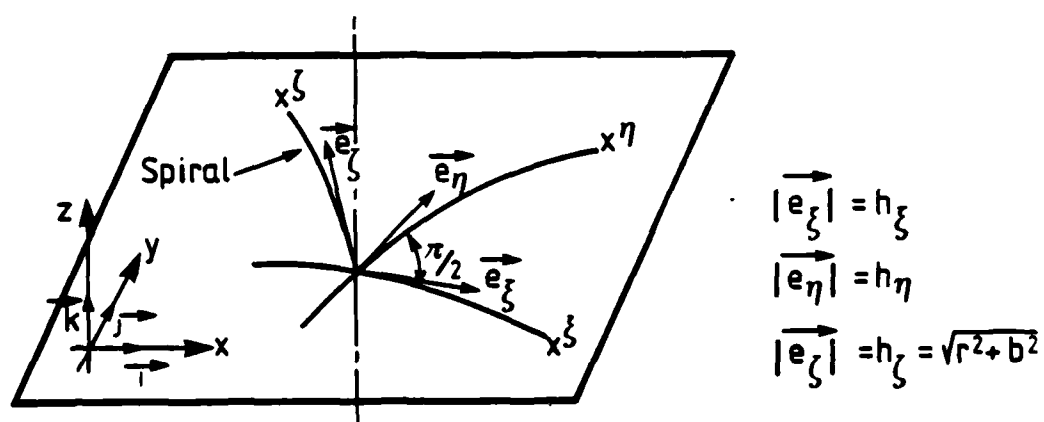


Fig. 2 Illustration of base vectors of curvilinear coordinate frame

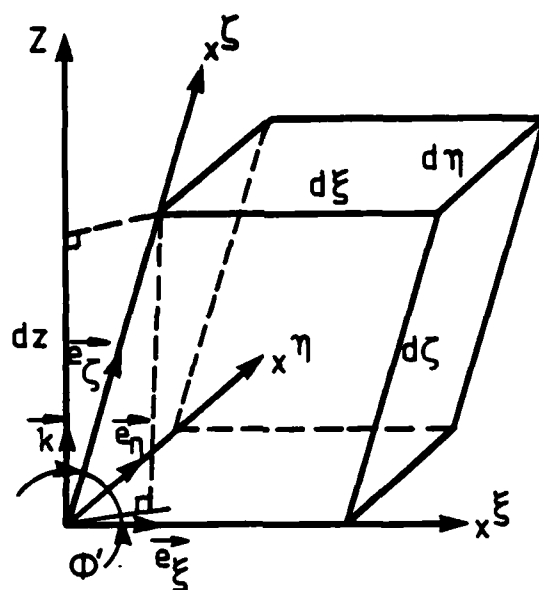


Fig. 3 Elementary control volume in curvilinear coordinate frame

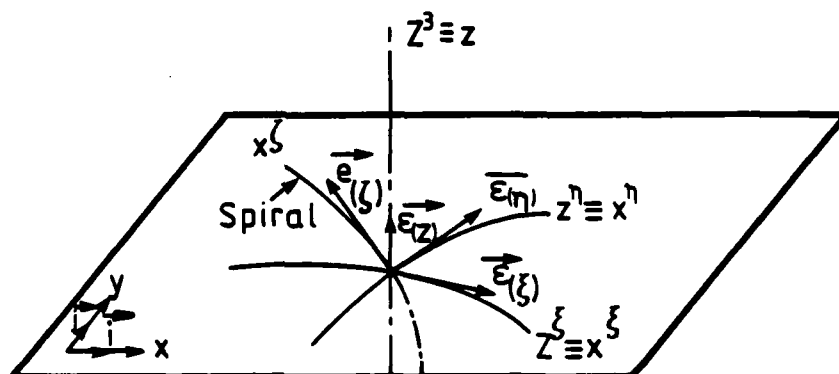


Fig. 4 The new basis



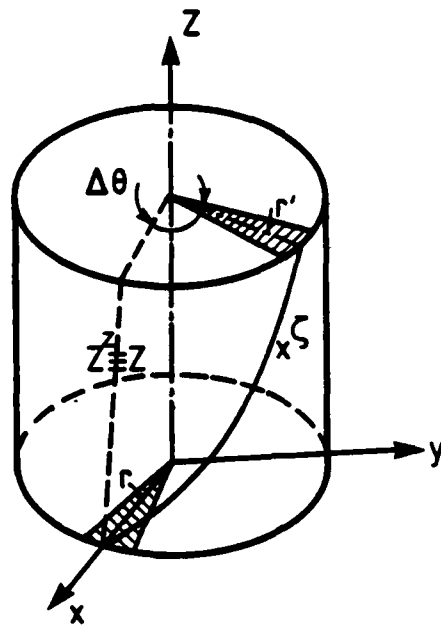


Fig. 5 Illustration of effect of the coordinate transformation

APPENDIX 3Pressure-Implicit Split Operator (PISO)3.1 Description of PISO

The so-called PISO algorithm (described by Issa [79] and Gosman, Issa and Watkins [80]) is a scheme which applies repetitively a predictor-corrector procedure to the discretized momentum and continuity equations in order to calculate the pressure correction by assuming that the velocity corrections depend not only on the pressure corrections but also on the velocity corrections at neighbouring nodes.

The predictor-corrector procedure can be described by using a general representation of the discretized momentum equations

$$\underline{U}_p = H\{\underline{U}_d\} + G.p \quad (A3.1)$$

where:  $\underline{U}$  denotes the velocity vector at a node P or its neighbours,  $H\{\}$  is a linear operator applied to velocity-dependent terms, and G a linear operator giving the pressure gradient. Using the pressure field  $p^*$  calculated at the previous iteration of the computational procedure one can solve equation (A3.1) in order to find the velocity field  $\underline{U}^*$

$$\underline{U}_p^* = H\{\underline{U}_d^*\} + G.p^* \quad (A3.2)$$

Then, corrections  $\underline{U}'$  and  $p'_1$  are applied to the velocity and pressure fields such that

$$\underline{U}^{**} = \underline{U}^* + \underline{U}'$$

and 
$$p^{**} = p^* + p'_1 \quad (A3.3)$$

satisfy the momentum and continuity equations given by:

$$\underline{U}_p^{**} \approx H\{\underline{U}_n^*\} + G p^{**} \quad (A3.4)$$

and 
$$\text{div}(\rho \underline{U}^{**}) = \text{div}(\rho \underline{U}^*) + \text{div}(\rho \underline{U}') = 0 \quad (A3.5)$$

This can be achieved by solving a Poisson equation for  $p'_1$ :

$$\text{div}(\rho G p'_1) = -\text{div}(\rho \underline{U}^*) \quad (A3.6)$$

which can be found by subtracting (A3.2) from (A3.4) and using the result in (A3.5).

Further corrections  $\underline{U}''$  and  $p'_2$  are applied, in a similar procedure, to velocity and pressure fields such that:

$$\underline{U} = \underline{U}^{**} + \underline{U}''$$

and 
$$p = p^{**} + p'_2 \quad (A3.7)$$

satisfy again the momentum and continuity equations expressed by:

$$\underline{U}_p \approx H\{\underline{U}_n^{**}\} + G p \quad (A3.8)$$

and 
$$\text{div}(\rho \underline{U}) = \text{div}(\rho \underline{U}^{**}) + \text{div}(\rho \underline{U}'') = 0 \quad (A3.9)$$

which can be achieved by solving a Poisson equation for  $p'_2$  deduced in a similar way as (A3.6)

$$\text{div}(\rho G p'_2) = -\text{div}(\rho H\{\underline{U}_n'\}) \quad (A3.10)$$

The above procedure up to equation (A3.6) is similar to the Patankar-

Spalding SIMPLE algorithm [81]. Although it is possible to continue the corrections of velocity and pressure fields further, the analysis of Issa [79] showed that no additional improvement would be gained. One can notice that equations (A3.6) and (A3.10) differ only in their right-hand sides which can be translated to a minimization of the additional work needed for calculating the second stage of the above procedure.

The application of the above procedure in the equations describing the flow through the spirally fluted tube is given in the following section.

### 3.2 Derivation of the 'Full' Pressure Correction Equation for PISO

#### Continuity Equation

$$(\rho U \Delta \eta \Delta z)_w^e + (\rho V \Delta \xi \Delta z)_s^n + (\rho W \Delta \eta \Delta \xi)_u^d = 0 \quad (\text{A3.11})$$

$$\text{where} \quad \left( \begin{array}{c} \\ \end{array} \right)_w^e = \left( \begin{array}{c} \\ \end{array} \right)_e - \left( \begin{array}{c} \\ \end{array} \right)_w$$

$$\left( \begin{array}{c} \\ \end{array} \right)_s^n = \left( \begin{array}{c} \\ \end{array} \right)_n - \left( \begin{array}{c} \\ \end{array} \right)_s$$

$$\left( \begin{array}{c} \\ \end{array} \right)_u^d = \left( \begin{array}{c} \\ \end{array} \right)_d - \left( \begin{array}{c} \\ \end{array} \right)_u$$

#### Momentum Equations

$$U_e = \sum_{i_e} \frac{A_{i_e}^U}{A_P^U} U_{i_e} + \frac{D_e^U}{A_P^U} (p_P - p_E) + S_P^U$$

$$U_w = \sum_{i_w} \frac{A_{i_w}^U}{A_P^U} U_{i_w} + \frac{D_w^U}{A_P^U} (p_w - p_p) + S_p^U$$

$$V_n = \sum_{i_n} \frac{A_{i_n}^V}{A_P^V} V_{i_n} + \frac{D_n^V}{A_P^V} (p_p - p_n) + S_p^V$$

$$V_s = \sum_{i_s} \frac{A_{i_s}^V}{A_P^V} V_{i_s} + \frac{D_s^V}{A_P^V} (p_s - p_p) + S_p^V$$

$$W_d = \sum_{i_s} \frac{A_{i_s}^W}{A_P^W} W_{i_d} + \frac{D_d^W}{A_P^W} (p_p - p_D) + S_p^W$$

$$W_u = \sum_{i_u} \frac{A_{i_u}^W}{A_P^W} W_{i_u} + \frac{D_u^W}{A_P^W} (p_U - p_D) + S_p^W$$

(A3.12)

where  $i_e$  implies all the nodes surrounding  $e$  etc,  $S_p^{U,V,W}$  are source terms and

$$D_e^U = (\Delta \eta, \Delta z)_e \quad D_w^U = (\Delta \eta, \Delta z)_w$$

$$D_n^V = (\Delta \xi, \Delta z)_n \quad D_s^V = (\Delta \xi, \Delta z)_s$$

$$D_d^W = (\Delta \eta, \Delta \xi)_d \quad D_u^W = (\Delta \eta, \Delta \xi)_u$$

But

$$U = U^* + \delta u$$

$$V = V^* + \delta v$$

$$W = \bar{W}^* + \delta w \quad (A3.13)$$

Perturbation analysis on the set of equations (A3.12) gives:

$$\delta u_e = \sum_{i_e} \frac{A_{i_e}^U}{A_P^U} \delta u_{i_e} + D_e'^U (p_P' - p_E')$$

$$\delta u_w = \sum_{i_w} \frac{A_{i_w}^U}{A_P^U} \delta u_{i_w} + D_w'^U (p_W' - p_P')$$

$$\delta v_n = \sum_{i_n} \frac{A_{i_n}^V}{A_P^V} \delta v_{i_n} + D_n'^V (p_P' - p_N')$$

$$\delta v_s = \sum_{i_s} \frac{A_{i_s}^V}{A_P^V} \delta v_{i_s} + D_s'^V (p_S' - p_P')$$

$$\delta w_d = \sum_{i_d} \frac{A_{i_d}^W}{A_P^W} \delta w_{i_d} + D_d'^W (p_P' - p_D')$$

$$\delta w_u = \sum_{i_u} \frac{A_{i_u}^W}{A_P^W} \delta w_{i_u} + D_u'^W (p_U' - p_P')$$

(A3.14)

where  $p_P' = p_P - p_P^*$

(A3.13) and (A3.14) give:

$$\begin{aligned}
 U_e &= U_e^* + \left[ \sum_{i_e} \frac{A_{i_e}^U}{A_P^U} \delta u_{i_e} + D_e^U (p_P' - p_E') \right] \\
 U_w &= U_w^* + \left[ \sum_{i_w} \frac{A_{i_w}^U}{A_P^U} \delta u_{i_w} + D_w^U (p_W' - p_P') \right] \\
 V_n &= V_n^* + \left[ \sum_{i_n} \frac{A_{i_n}^V}{A_P^V} \delta v_{i_n} + D_n^V (p_P' - p_N') \right] \\
 V_s &= V_s^* + \left[ \sum_{i_s} \frac{A_{i_s}^V}{A_P^V} \delta v_{i_s} + D_s^V (p_S' - p_P') \right] \\
 W_d &= W_d^* + \left[ \sum_{i_d} \frac{A_{i_d}^W}{A_P^W} \delta w_{i_d} + D_d^W (p_P' - p_D') \right] \\
 W_u &= W_u^* + \left[ \sum_{i_u} \frac{A_{i_u}^W}{A_P^W} \delta w_{i_u} + D_u^W (p_U' - p_P') \right]
 \end{aligned}
 \tag{A3.15}$$

Substituting (A3.15) in (A3.11) we get the full pressure-correction equation:

$$\begin{aligned}
 &(\rho U^* \Delta \eta \Delta z)_e - (\rho U^* \Delta \eta \Delta z)_w \\
 &+ (\rho V^* \Delta \xi \Delta z)_n - (\rho V^* \Delta \xi \Delta z)_s
 \end{aligned}$$

$$\begin{aligned}
& + (\rho W^* \Delta \eta \Delta \xi)_d - (\rho W^* \Delta \eta \Delta \xi)_u \\
& + (\rho \Delta \eta \Delta z)_e \left[ \sum_{i_e} \frac{A_{i_e}^U}{A_P^U} \delta u_{i_e} + D_e'^U (p_P' - p_E') \right] \\
& - (\rho \Delta \eta \Delta z)_w \left[ \sum_{i_w} \frac{A_{i_w}^U}{A_P^U} \delta u_{i_w} + D_w'^U (p_W' - p_P') \right] \\
& + (\rho \Delta \xi \Delta z)_n \left[ \sum_{i_n} \frac{A_{i_n}^V}{A_P^V} \delta v_{i_n} + D_n'^V (p_P' - p_N') \right] \\
& - (\rho \Delta \xi \Delta z)_s \left[ \sum_{i_s} \frac{A_{i_s}^V}{A_P^V} \delta v_{i_s} + D_s'^V (p_S' - p_P') \right] \\
& + (\rho \Delta \eta \Delta \xi)_d \left[ \sum_{i_d} \frac{A_{i_d}^W}{A_P^W} \delta w_{i_d} + D_d'^W (p_P' - p_D') \right] \\
& - (\rho \Delta \eta \Delta \xi)_u \left[ \sum_{i_u} \frac{A_{i_u}^W}{A_P^W} \delta w_{i_u} + D_u'^W (p_U' - p_P') \right]
\end{aligned}$$

= 0

(A3.16)



Equation (A3.16) gives:

$$\begin{aligned}
 A_P^P p_P' &= \sum_{\substack{i=E,W \\ N,S \\ D,U}} A_i^P p_i' \\
 &- [ (\rho U^* \Delta \eta \Delta z)_e - (\rho U^* \Delta \eta \Delta z)_w \\
 &+ (\rho V^* \Delta \xi \Delta z)_n - (\rho V^* \Delta \xi \Delta z)_s \\
 &+ (\rho W^* \Delta \eta \Delta \xi)_d - (\rho W^* \Delta \eta \Delta \xi)_n ] \\
 &- (\rho \Delta \eta \Delta z)_e \sum_{i_e} \frac{A_{i_e}^U}{A_P^U} \delta u_{i_e} + (\rho \Delta \eta \Delta z)_w \sum_{i_w} \frac{A_{i_w}^U}{A_P^U} \delta u_{i_w} \\
 &- (\rho \Delta \xi \Delta z)_n \sum_{i_n} \frac{A_{i_n}^V}{A_P^V} \delta v_{i_n} + (\rho \Delta \xi \Delta z)_s \sum_{i_s} \frac{A_{i_s}^V}{A_P^V} \delta v_{i_s} \\
 &- (\rho \Delta \eta \Delta \xi)_d \sum_{i_d} \frac{A_{i_d}^W}{A_P^W} \delta w_{i_d} + (\rho \Delta \eta \Delta \xi)_u \sum_{i_u} \frac{A_{i_u}^W}{A_P^W} \delta w_{i_u}
 \end{aligned}
 \tag{A3.17}$$

where

$$A_E^P = (\rho \Delta \eta \Delta z)_e D_e'^U$$

$$A_W^P = (\rho \Delta \eta \Delta z)_w D_w'^U$$

$$A_N^P = (\rho \Delta \xi \Delta z)_n D_n'^V$$

$$A_S^P = (\rho \Delta \xi \Delta z)_s D_s'^V$$

$$A_D^P = (\rho \Delta \eta \Delta \xi)_d D_d'^W$$

$$A_U^P = (\rho \Delta \eta \Delta \xi)_u D_u'^W$$

$$A_P^P = \sum_i A_i^P$$

Subtracting the old "predictive" pressure-correction equation from (A3.17)

we get the final "correcting" pressure-correction equation:

$$\begin{aligned} \bar{A}_P^P p_{2P}' &= A_i^P p_{2i}' \\ &+ (\rho \Delta \eta \Delta z)_w \sum_{i_w} \frac{A_{i_w}^U}{A_P^U} \delta u_{i_w} - (\rho \Delta \eta \Delta z)_e \sum_{i_e} \frac{A_{i_e}^U}{A_P^U} \delta u_{i_e} \\ &+ (\rho \Delta \xi \Delta z)_s \sum_{i_s} \frac{A_{i_s}^V}{A_P^V} \delta v_{i_s} - (\rho \Delta \xi \Delta z)_n \sum_{i_n} \frac{A_{i_n}^V}{A_P^V} \delta v_{i_n} \\ &+ (\rho \Delta \eta \Delta \xi)_u \sum_{i_u} \frac{A_{i_u}^W}{A_P^W} \delta w_{i_u} - (\rho \Delta \eta \Delta \xi)_d \sum_{i_d} \frac{A_{i_d}^W}{A_P^W} \delta w_{i_d} \end{aligned} \quad (A3.18)$$

while the old "predictive" pressure-correction equation has the form:

$$\begin{aligned} A_P^P p_{1P}' &= \sum_i A_i^P p_{1i}' \\ &- [(\rho U^* \Delta \eta \Delta z)_w^e + (\rho V^* \Delta \xi \Delta z)_s^n + (\rho W^* \Delta \eta \Delta \xi)_u^d] \end{aligned} \quad (A3.19)$$

Equations (A3.19) and (A3.18) represent equations (A3.6) and (A3.10) respectively.

We can now write the full, exact pressure-correction equation:

$$\begin{aligned}
 A_P^P P_P' &= \left( A_E^P P_E' + A_W^P P_W' + A_N^P P_N' + A_S^P P_S' + A_D^P P_D' + A_U^P P_U' \right) \\
 &- \left\{ (\rho \Delta \eta \Delta z)_e U_e^* - (\rho \Delta \eta \Delta z)_w U_w^* \right. \\
 &\quad + (\rho \Delta \xi \Delta z)_n V_n^* - (\rho \Delta \xi \Delta z)_s V_s^* \\
 &\quad \left. + (\rho \Delta \eta \Delta \xi)_d W_d^* - (\rho \Delta \eta \Delta \xi)_u W_u^* \right\} \\
 &- (\rho \Delta \eta \Delta z)_e \left[ \frac{A_E^U}{A_P^U} \delta u_{Ee} + \frac{A_W^U}{A_P^U} \delta u_{We} + \frac{A_N^U}{A_P^U} \delta u_{Ne} \right. \\
 &\quad \left. + \frac{A_S^U}{A_P^U} \delta u_{Se} + \frac{A_D^U}{A_P^U} \delta u_{De} + \frac{A_U^U}{A_P^U} \delta u_{Ue} \right] \\
 &- (\rho \Delta \eta \Delta z)_w \left[ \frac{A_E^U}{A_P^U} \delta u_{Ew} + \frac{A_W^U}{A_P^U} \delta u_{Ww} + \frac{A_N^U}{A_P^U} \delta u_{Nw} \right. \\
 &\quad \left. + \frac{A_S^U}{A_P^U} \delta u_{Sw} + \frac{A_D^U}{A_P^U} \delta u_{Dw} + \frac{A_U^U}{A_P^U} \delta u_{Uw} \right] \\
 &+ (\rho \Delta \xi \Delta z)_n \left[ \frac{A_E^V}{A_P^V} \delta v_{En} + \frac{A_W^V}{A_P^V} \delta v_{Wn} + \frac{A_N^V}{A_P^V} \delta v_{Nn} \right. \\
 &\quad \left. + \frac{A_S^V}{A_P^V} \delta v_{Sn} + \frac{A_D^V}{A_P^V} \delta v_{Dn} + \frac{A_U^V}{A_P^V} \delta v_{Un} \right]
 \end{aligned}$$

$$\begin{aligned}
& - (\rho \Delta \xi \Delta z)_s \left[ \frac{A_E^V}{A_P^V} \delta v_{Es} + \frac{A_W^V}{A_P^V} \delta v_{Ws} + \frac{A_N^V}{A_P^V} \delta v_{Ns} \right. \\
& \quad \left. + \frac{A_S^V}{A_P^V} \delta v_{Ss} + \frac{A_D^V}{A_P^V} \delta v_{Ds} + \frac{A_U^V}{A_P^V} \delta v_{Us} \right] \\
& + (\rho \Delta \xi \Delta \eta)_d \left[ \frac{A_E^W}{A_P^W} \delta w_{Ed} + \frac{A_W^W}{A_P^W} \delta w_{Wd} + \frac{A_N^W}{A_P^W} \delta w_{Nd} \right. \\
& \quad \left. + \frac{A_S^W}{A_P^W} \delta w_{Sd} + \frac{A_D^W}{A_P^W} \delta w_{Dd} + \frac{A_U^W}{A_P^W} \delta w_{Ud} \right] \\
& - (\rho \Delta \xi \Delta \eta)_u \left[ \frac{A_E^W}{A_P^W} \delta w_{Eu} + \frac{A_W^W}{A_P^W} \delta w_{Wu} + \frac{A_N^W}{A_P^W} \delta w_{Nu} \right. \\
& \quad \left. + \frac{A_S^W}{A_P^W} \delta w_{Su} + \frac{A_D^W}{A_P^W} \delta w_{Du} + \frac{A_U^W}{A_P^W} \delta w_{Uu} \right] \Bigg\} \quad (A3.20)
\end{aligned}$$

where  $p' = p'_1 + p'_2$  and  $A_{lm}^\phi$  means the coefficient for velocity  $\phi$  (U, V, W) at node  $l$  (E, W, N, S, D, U, P) surrounding node  $m$  (e or w for U, n or s

for  $V$  and  $d$  or  $u$  for  $W$ ). For fully-developed flows, the two last terms of (A3.20) are absent as are likewise the coefficients referring to downstream and upstream positions (see Figures 1a and 1b).

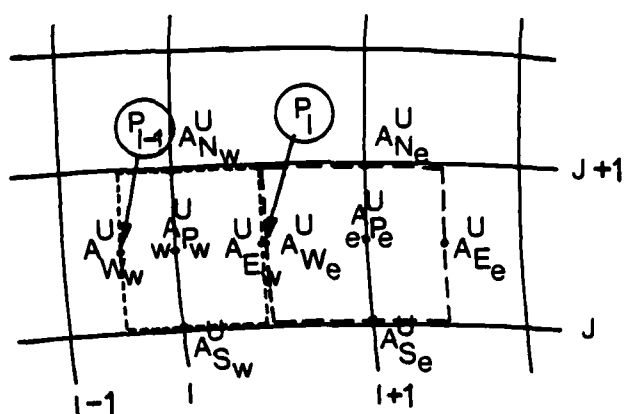


Fig 1-a Control volumes and coefficients  
U-velocity

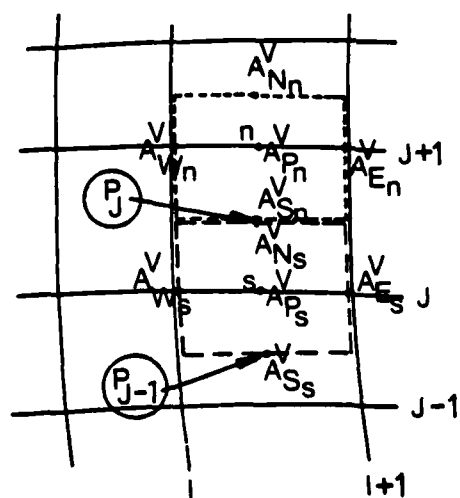


Fig 1-b Control volumes and coefficients  
V-velocity

APPENDIX 4

Derivation of the Equations for  $c_{\mu}$  and  $Pr_t$   
for the ASM Turbulence Model  
including Density Fluctuation Effects

As has been shown in Section 4.1.4 of Chapter 4, the Reynolds stresses and heat fluxes (when an algebraic stress model including density fluctuation effects is used) are calculated from equations (4.11) and (4.13) presented also below:

$$\frac{\overline{u_i u_j} - \frac{2}{3} \delta_{ij} k}{k} = \phi \frac{P_{ij}^* - \frac{2}{3} \delta_{ij} P^*}{\epsilon} \quad (A4.1)$$

$$\text{and} \quad -\overline{u_i \theta'} = \phi_T \frac{k}{\epsilon} \overline{u_i u_k} \frac{\partial \theta}{\partial x_k} - \phi_T' \frac{k}{\epsilon} P_{i\theta}^* \quad (A4.2)$$

$$\text{where} \quad \phi = (1 - c_2)/c_1$$

$$\phi_T = 1/c_{1T}$$

$$\phi_T' = \phi_T(1 - c_{2T})$$

$$c_1 = 2.2 ; \quad c_2 = 0.55 ; \quad c_{1T} = 3.2 ; \quad c_{2T} = 0.5$$

$$P^* = P + G ; \quad P_{ij}^* = P_{ij} + G_{ij} ; \quad P_{i\theta}^* = P_{i\theta} + G_{i\theta}$$

The production of turbulence energy ( $P^*$ ), the production of  $\overline{u_i u_j}$  ( $P_{ij}^*$ ) and the production of  $\overline{u_i \theta'}$  ( $P_{i\theta}^*$ ) (with buoyant effects taken into account) for the flow through a spirally fluted tube but only for the part of the solution domain where the fluid is in solid body rotation and a polar

grid is used (axisymmetric flow) have the form:

$$\begin{aligned} p^* &= -\bar{v}\bar{w} \frac{\partial w}{\partial r} + g_r \frac{\bar{\rho}'v}{\rho} \\ &= -\bar{v}\bar{w} \frac{\partial w}{\partial r} - \frac{g_r \alpha}{T} \bar{v}\bar{\theta}, \end{aligned}$$

$$\begin{aligned} p_{rr}^* &= \bar{u}\bar{v} \frac{U}{r} + 2g_r \frac{\bar{\rho}'v}{\rho} \\ &= \bar{u}\bar{v} \frac{U}{r} - 2g_r \frac{\alpha}{T} \bar{v}\bar{\theta}, \end{aligned}$$

$$p_{zz}^* = -\bar{v}\bar{w} 2 \frac{\partial w}{\partial r}$$

$$\begin{aligned} p_{\xi r}^* &= \bar{u}^2 \frac{U}{r} - \bar{v}^2 \frac{\partial U}{\partial r} + g_r \frac{\bar{\rho}'u}{\rho} \\ &= \bar{u}^2 \frac{U}{r} - \bar{v}^2 \frac{\partial U}{\partial r} - g_r \frac{\alpha}{T} \bar{u}\bar{\theta}, \end{aligned}$$

$$\begin{aligned} p_{rz}^* &= -\bar{v}^2 \frac{\partial w}{\partial r} + \bar{u}\bar{w} \frac{U}{r} + g_r \frac{\bar{\rho}'w}{\rho} \\ &= -\bar{v}^2 \frac{\partial w}{\partial r} + \bar{u}\bar{w} \frac{U}{r} - g_r \frac{\alpha}{T} \bar{w}\bar{\theta}, \end{aligned}$$

$$p_{\xi\theta}^* = -\bar{v}\bar{\theta}, \frac{\partial U}{\partial r}$$

$$\begin{aligned} p_{r\theta}^* &= \bar{u}\bar{\theta}, \frac{U}{r} + g_r \frac{\bar{\rho}'\theta}{\rho} \\ &= \bar{u}\bar{\theta}, \frac{U}{r} - g_r \frac{\alpha}{T} \bar{\theta}^2 \end{aligned}$$

$$p_{z\theta}^* = -\bar{v}\bar{\theta}, \frac{\partial w}{\partial r}$$

(A4.3)



where  $g_r = \frac{1}{r} \left( U^2 + \frac{2}{3} k \right)$ ,  $a = -\frac{T}{\rho} \left( \frac{\partial \rho}{\partial T} \right)_p$

while  $P_{\xi\xi}^*$  and  $P_{\xi z}^*$  have been ignored since they are less important than the other production terms. Moreover, the terms  $P_{rr}^*$ ,  $P_{\xi r}^*$ ,  $P_{rz}^*$  can be simplified further and assume the forms:

$$\begin{aligned} P_{rr}^* &= -2g_r \frac{\alpha}{T} \bar{v}\theta', \\ P_{\xi r}^* &= \frac{g_r \alpha}{T} \bar{u}\theta', \\ P_{rz}^* &= -\bar{v}^2 \frac{\partial W}{\partial r} - \frac{g_r \alpha}{T} \bar{w}\theta', \end{aligned} \quad (A4.4)$$

Equation (A4.1) yields:

$$\begin{aligned} \bar{u}^2 &= \frac{2}{3} k + k \frac{\phi}{\epsilon} \left( P_{\xi\xi}^* - \frac{2}{3} P^* \right) \\ &= \frac{2}{3} k - \frac{2}{3} k \frac{\phi}{\epsilon} P^* \\ \bar{v}^2 &= \frac{2}{3} k + k \frac{\phi}{\epsilon} \left( P_{rr}^* - \frac{2}{3} P^* \right) \\ \bar{w}^2 &= \frac{2}{3} k + k \frac{\phi}{\epsilon} \left( P_{zz}^* - \frac{2}{3} P^* \right) \\ \bar{u}\bar{v} &= k \phi \frac{P_{\xi r}^*}{\epsilon} \\ \bar{u}\bar{w} &= k \phi \frac{P_{\xi z}^*}{\epsilon} = 0 \\ \bar{v}\bar{w} &= k \phi \frac{P_{rz}^*}{\epsilon} \end{aligned} \quad (A4.5)$$

while equation (A4.2) gives:

$$\begin{aligned}
 -\bar{u}\theta' &= \phi_T \frac{k}{\varepsilon} \bar{u}\bar{v} \frac{\partial\theta}{\partial r} - \phi_T' \frac{k}{\varepsilon} P_{\xi\theta}^* \\
 -\bar{v}\theta' &= \phi_T \frac{k}{\varepsilon} \bar{v}^2 \frac{\partial\theta}{\partial r} - \phi_T' \frac{k}{\varepsilon} P_{r\theta}^* \\
 -\bar{w}\theta' &= \phi_T \frac{k}{\varepsilon} \bar{w}\bar{v} \frac{\partial\theta}{\partial r} - \phi_T' \frac{k}{\varepsilon} P_{z\theta}^*
 \end{aligned} \tag{A4.6}$$

So, from the last of equations (A4.5) after substituting  $P_{rz}^*$  and  $\bar{w}\theta'$  we can have:

$$\begin{aligned}
 \bar{w} &= -\frac{\phi_T \bar{v}^2}{k} \left( \frac{k^2}{\varepsilon} \right) \frac{\partial W}{\partial r} + \frac{\phi}{k} \left( \frac{k^2}{\varepsilon} \right) \frac{\alpha g r}{T} \left[ \phi_T \frac{k}{\varepsilon} \bar{w}\bar{v} \frac{\partial\theta}{\partial r} - \right. \\
 &\quad \left. - \phi_T' \frac{k}{\varepsilon} P_{z\theta}^* \right]
 \end{aligned} \tag{A4.7}$$

Substituting the equation of  $P_{z\theta}^*$ , then the equation of  $\bar{v}\theta'$  into (A4.7) and finally the equation of  $P_{r\theta}^*$  into the resultant equation (taking into account from reference [69] that  $\theta'^2 = -c_T' \frac{k}{\varepsilon} \bar{v}\theta' \frac{\partial\theta}{\partial r}$ ) we get:

$$\begin{aligned}
 \bar{w} &= \frac{\partial W}{\partial r} \frac{k^2}{\varepsilon} \left\{ \frac{\left( -\frac{\phi}{k} (1 + \phi_T \phi_T' A) - \frac{\phi \phi_T \phi_T'^2 A^2 c_T'}{k(1 - A c_T' \phi_T')} \right) \bar{v}^2}{(1 - \phi \phi_T A)} + \right. \\
 &\quad \left. + \frac{\left( \frac{\phi \phi_T'^2 A}{k \partial\theta/\partial r} + \frac{\phi \phi_T'^3 A^2 c_T'}{k(1 - \phi_T' c_T' A) \partial\theta/\partial r} \right) \frac{U}{r} \frac{\bar{w}}{\bar{u}\theta'}}{(1 - \phi \phi_T A)} \right\}
 \end{aligned} \tag{A4.8}$$

where 
$$A = \frac{\alpha g_r}{T} \left( \frac{k}{\epsilon} \right)^2 \frac{\partial \theta}{\partial r} \quad (A4.9)$$

Substituting into (A4.8) the expression for  $\overline{u\theta'}$  after some calculations in order to express  $\overline{u\theta'}$  in terms of  $\overline{v^2}$  we get:

$$\overline{v\omega} = \frac{\partial \omega}{\partial r} \frac{k^2}{\epsilon} \frac{\overline{v^2}}{k} B \quad (A4.10)$$

where

$$B = \frac{\phi}{(1 - \phi_T \phi A)} + \frac{\phi \phi_T \phi_T' A}{\left[ (1 - \phi_T \phi A) (1 - \phi_T' c_T' A) + \phi_T'^2 \left( \frac{k}{\epsilon} \right)^2 \frac{U}{r} \frac{\partial U}{\partial r} \right]} \quad (A4.11)$$

From equation (A4.10) one can yield:

$$c_\mu = \frac{\overline{v^2}}{k} B \quad (A4.12)$$

where

$$\frac{\overline{v^2}}{k} = \frac{2}{3} \left( 1 - \frac{\phi}{\epsilon} P^* \right) - \frac{\phi}{\epsilon} \frac{2\alpha g_r}{T} \overline{v\theta'} \quad (A4.13)$$

Analogous procedure has been followed in order to calculate the turbulent Prandtl number.

From the equation of  $\overline{v\theta'}$  after substituting the expression of  $P_r^* \theta$  we get:

$$-\overline{v\theta'} (1 - \phi_T' c_T' A) = \phi_T \frac{k}{\epsilon} \frac{\partial \theta}{\partial r} \overline{v^2} - \phi_T' \frac{k}{\epsilon} \frac{U}{r} \overline{u\theta'} \quad (A4.14)$$

Substituting the expression of  $\overline{u\theta'}$  (function of  $\overline{v\theta'}$ ) into (A4.14) the following equation is formed:

$$-\bar{v}\theta' = \frac{\partial \theta}{\partial r} \frac{k^2}{\epsilon} \Delta \quad (\text{A4.15})$$

where

$$\Delta = \frac{\Gamma \frac{2}{3} \left( 1 - \frac{\phi_P^*}{\epsilon} \right)}{(1 - 2A\Gamma)} \quad (\text{A4.16})$$

and

$$\Gamma = \frac{\phi_T (1 - \phi_T \phi_A)}{\left[ (1 - \phi_T' c_T' A) (1 - \phi_T \phi_A) + \phi_T'^2 \left( \frac{k}{\epsilon} \right)^2 \frac{U}{r} \frac{\partial U}{\partial r} \right]} \quad (\text{A4.17})$$

So, from equations (A4.10) and (A4.15) it is clear that:

$$\bar{p}_{r_t} = \frac{B \frac{\bar{v}^2}{k}}{\Delta} = \frac{c_\mu (1 - 2A\Gamma)}{\Gamma \frac{2}{3} (1 - \phi_P^*/\epsilon)} \quad (\text{A4.18})$$

## APPENDIX 5

### The Computer Program for Solving the Dynamic and Temperature Fields in a Spirally Fluted Tube

#### Introductory Remarks

In this appendix, the computer code for calculating the dynamic and temperature fields in a spirally fluted tube is presented. The program has been developed from the original curvilinear TEACH code written at Imperial College by Antonoupoulos, Gosman and Issa [86] devised for the solution of steady two-dimensional turbulent (or laminar) elliptic flows. The programming language is FORTRAN IV. The present appendix is divided into two main sections. The first section presents the flow chart with a description of the most important sub-routines, while in the second one the listing of the computer code with a glossary of FORTRAN symbols are given.

#### 5.1 User's Guide

The computer program includes the main routine, CONTRO, and 13 sub-routines (INIT, RADCUR, PROPS, CALCU, CALCV, CALCW, CALCP, CALCT, CALCTE, CALCED, LISOLV, PROMOD, PRINT). The complete flow chart of the program is given below, while a broad description of the computer procedure, based on the flow chart, is discussed prior to outlining the structure of the most important of the sub-routines. Moreover, in the present section, several special features introduced into the computer code for handling this particular flow are discussed, such as: the use of cubic splines for interpolating viscosity near the walls, use of the parabolic sublayer treatment

(PSL), addition of extra nodes for calculating the temperature field, etc.

#### 5.1.1 General Structure

As its name suggests, CONTRO is the main routine responsible for the overall control of the program's work-flow by calling sequentially the rest of the sub-routines. Initially, in CONTRO turbulence constants, fluid properties, control parameters for termination tests and monitoring (i.e. SORMAX, MAXIT, IMON, JMON) are initialized after the main geometric quantities, such as control volume dimensions, solution domain characteristics (i.e.  $R_a$ ,  $h$ ,  $R_b$ ,  $n$ ,  $\phi$ ) are read in as data.

The first sub-routine called by CONTRO is INIT where the geometric interpolation coefficients are calculated while all dependent variables and other important arrays are set to zero.

Next, sub-routine RADCUR is called. In this, quantities related to the co-ordinates' curvature are calculated while a special treatment for the boundaries is introduced by calling section MODRAD of sub-routine PROMOD. PROMOD is the sub-routine which introduces the appropriate modifications for handling the boundaries by means of individual sections, playing the role of independent sub-routines, with entry points defined as MOD- (implying MODifications) followed by some symbol declaring their use (for example, -RAD for the boundary modifications for the radii, -U for the U-momentum equation, etc).

Next, the initial dynamic and temperature fields are set which can also be the results from a previous run if the integer named JOB has a

value different from one.

Called next is sub-routine PROPS. Here, the viscosity is calculated for the whole solution domain. Depending on whether the laminar or the turbulent regime is solved the viscosity is set either to a constant value or it is calculated from the appropriate equations for each turbulence model used. In the case of turbulent flows, special attention is given to the near-wall region since even the finest grids adopted are not fine enough for interpolating the viscosity in this region if the same treatment used for the rest of the solution domain, is applied. Thus, a cubic spline interpolation is used for a number of cell-rows attached to the wall. This is necessary because of the very non-linear variation of effective viscosity in the wall-adjacent sublayer.

CONTRO then calls PRINT which gives an output of the initial dynamic field, while at that point both the marching and the iteration loops begin. Parameter NITER gives how many times the iterative procedure has been performed (which may not exceed the pre-set value of MAXIT). During the marching procedure, CONTRO calls, in a fixed sequence, CALCU, CALCV, CALCW, CALCP. However, because the parabolic sublayer treatment has been adopted, a parameter JTS is defined which gives the number of cell-rows attached to the wall where neither CALCV nor CALCP is called. Instead, the V-velocity is calculated from continuity applied to the scalar cells while the variation of static pressure is neglected. Sub-routines CALCU and CALCW are solved over the whole solution domain while CALCP is called twice since the PISO algorithm (see Appendix 3) has been adopted. A detailed description of sub-routines  $CALC\phi$  ( $\phi = U, V, W, k, \epsilon, T$ ) and CALCP can be found in the

following section. Just before and after the pressure-correction equation is solved, CONTRO calls MODVEL which, being one of the PROMOD sections, updates the boundary velocities.

Depending on whether both the turbulence models (mixing-length hypothesis plus  $k$ - $\epsilon$  Boussinesq viscosity model) are used in different parts of the solution domain (IBOTH = 1) or just one of these is adopted (IBOTH  $\neq$  1), CONTRO sets or not the boundary conditions for the turbulence energy  $k$  and its dissipation  $\epsilon$  at  $J = JG$  (the matching interface between the two models). The value of  $JG$  has been fixed at the beginning of CONTRO.

Depending on whether the simplified algebraic-stress model, including density fluctuation ("buoyancy") effects, is used (NASM = 1) or not (NASM = 0), sub-routine CALCT is either called or bypassed.

Depending on whether the  $k$ - $\epsilon$  Boussinesq viscosity model is used (IBOTH  $\neq$  0) or not (IBOTH = 0), sub-routines CALCTE and CALCED for the solution of the discretized equations for  $k$  and  $\epsilon$  are either called or ignored.

Next, CONTRO calls sub-routine PROPS where, as has been described above, the calculation of viscosity takes place, while an intermediate output is issued, via sub-routine PRINT, which includes the summed residuals calculated in sub-routines CALC $\phi$ , the computed variables at some position defined by the I and J values (IMON, JMON) as well as the velocity, pressure (and  $k$ ,  $\epsilon$ ,  $\theta$ ) fields if the number of iterations performed is an exact multiple of INDPRI.



AD-A150 774

FLUID MECHANICS AND HEAT TRANSFER SPIRALLY FLUTED  
TUBING(U) GA TECHNOLOGIES INC SAN DIEGO CA

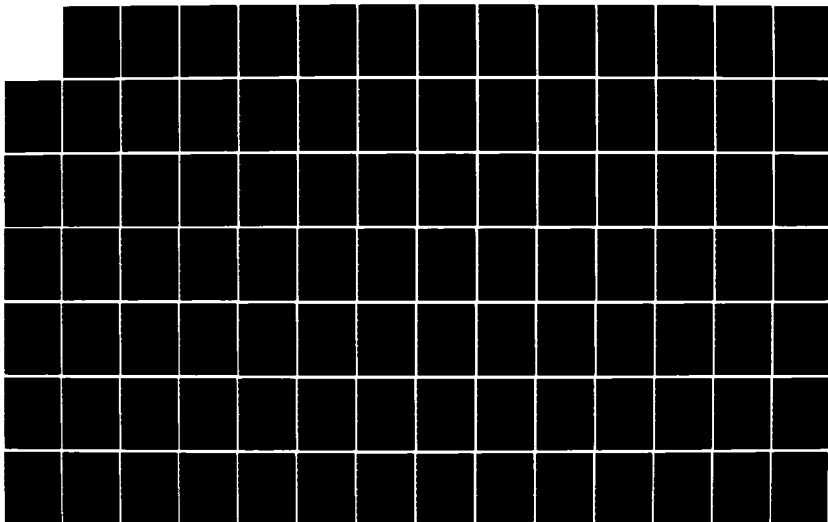
J S YAMPOLSKY ET AL. DEC 84 GA-A17833 N00014-82-C-0721

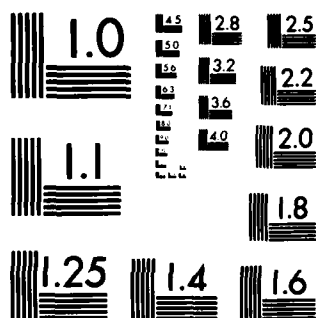
F/G 20/4

7/8

UNCLASSIFIED

NL





MICROCOPY RESOLUTION TEST CHART  
NATIONAL BUREAU OF STANDARDS-1963-A

At that point, termination tests for the iteration procedure start. If the number of iterations are greater than MAXIT or the maximum of the residual sums calculated in CALC $\phi$  and CALCP (SORCE1) is lower than a control value SORMAX (usually assigned the value  $10^{-3}$ ), the iteration procedure stops. If the simplified ASM including density fluctuation effects is applied (NASM = 1), the parameter SORCE2 (instead of SORCE 1) is tested against SORMAX with the only difference that SORCE2 includes also the residual sum of the temperature. Otherwise, the dynamic field is solved first and stored prior to solving the temperature equation. In this case, the whole iterative procedure is repeated only for CALCT, terminated when the residual sum calculated in CALCT is again smaller than SORMAX or the number of iterations exceed MAXIT. Moreover, a special treatment is adopted for the near-wall region by introducing two extra nodes in the first row of cells attached to the wall since it is very important for the grid to be highly refined in this region, for the calculation of the temperature field, when high Prandtl number fluids at high Reynolds numbers are used.

As soon as the iteration procedure is completed, a final output is issued via sub-routine PRINT. Thereafter, important flow parameters, such as friction factors, local Nusselt numbers, flow rates, etc, are calculated and the program is terminated.

#### 5.1.2 Details

In this section a detailed description is provided of the most important sub-routines, all of which have been subjected to significant changes and additions although their names have been kept the same as the

corresponding routines in the original TEACH program.

The finite difference equations (see equation (2.38)) for  $\phi \equiv U, V, W, \theta, k, \epsilon$  are solved in sub-routines  $CALC\phi$  called by CONTRO in a fixed sequence during an iterative procedure described in Section 5.1.1 of the present appendix. The general structure of all the sub-routines  $CALC\phi$  is given below.

#### 5.1.2a CALC $\phi$

All these sub-routines may be divided into four chapters where the following operations take place:

In chapter 1 the finite-difference coefficients and source terms are calculated using equations (2.39). Within double DO-loops (the outer one sweeping the solution domain in the  $\xi$ -direction and the inner one in the  $\eta$ -direction) the convective fluxes are calculated first, followed by the diffusion terms and finally by the source terms. In the first chapter no special treatment is performed for the cells adjacent to the boundaries.

In chapter 2(problem modification) PROMOD, is called in order to modify the finite-difference coefficients for the inclusion of boundary conditions or special source terms. It includes several chapters, one for each dependent variable, each with its own entry point. So, every sub-routine  $CALC\phi$  actually calls the corresponding chapter  $MOD\phi$  of PROMOD in order to incorporate the modifications.

In chapter 3, the coefficients  $A_p^\phi$  and residual sources  $RESOR\phi$  are calculated while the under-relaxation treatment is introduced which modifies

the above coefficients  $A_p^\phi$  and the source terms  $SU^\phi$  in order to avoid instability of the computational procedure. However, use of improper under-relaxation factors can cause instability, so the choice of the best values is one of the most important requirements for improving convergence of the solution procedure. Details about this treatment can be found in Section 2.5a of Chapter 2 as well as in Gosman et al [91].

Finally, in chapter 4, the solution of the finite-difference equations is performed over the whole solution domain (both the two-dimensional and one-dimensional regions). Sub-routine LISOLV is called repeatedly and it is there that the solution actually takes place following the line-by-line procedure described in Section 2.5c of Chapter 2. The integer NSWP $\phi$  defines how many times sub-routine LISOLV will be called from CALC $\phi$ , affecting the accuracy of the solution of the linearized equations and consequently the stability of the solution procedure. Improper choice of NSWP $\phi$  can cause instability, mainly in the solution of the pressure-correction equation since for every iteration of the computational procedure the starting pressure correction ( $p'$ ) field is zero.

Sub-routine CALCP, although it solves an equation of the general form given by (2.38), presents some special features which are reported below.

#### 5.1.2b CALCP

Sub-routine CALCP is called twice (see algorithm PISO in Appendix 3) during an iteration of the procedure described in Section 5.1.1 of the present appendix. It can be divided into five chapters facilitating its

understanding while its function is the solution of the pressure-correction ( $p'$ ) field. On the first call, the parameter INUMB takes the value zero while on the second call it takes the value 1 regulating the choice of the source term. Thus, if INUMB = 0, the source term I (see equation (2.45) of Chapter 2) is chosen, while if INUMB = 1, the source term II. So, two equations of the general form given by equation (2.38) of Chapter 2 are created, solved during the double call of sub-routine CALCP by CONTRO.

In chapter 1, the coefficients  $A_E^P$ ,  $A_W^P$ ,  $A_N^P$ ,  $A_S^P$  (see equation (2.46) of Chapter 2) are calculated over the two-dimensional region of the solution domain. Depending on the value of INUMB, the appropriate source term (I or II of equation (2.45)) is calculated. If INUMB is zero, the mass residual (RESORM) is also calculated.

In chapter 2, sub-routine PROMOD is called in order to incorporate modifications of the boundary cells, while in chapter 3 the calculation of the coefficient  $A_P^P$  takes place. The solution of the finite-difference equations is performed in chapter 4 by calling repeatedly sub-routine LISOLV. All these operations, from chapter 2 to chapter 4, are independent of the value of INUMB.

In chapter 5, the calculation of the pressure correction, with provision for under-relaxation, is performed, while if INUMB = 0 (first call of CALCP) the calculation of velocity corrections (given by equations (2.47) of Chapter 2) also takes place, these being used in the evaluation of term II during the second call of CALCP (INUMB = 1).

Chapter 5, at the end of sub-routine CALCP, distinguishes this particular sub-routine from the other CALC $\phi$  sub-routines. Moreover, another interesting characteristic of CALCP is the fact that there is no need for a calculation of the residual sources for the  $p'$ -equation; instead the absolute mass sources are summed and stored (RESORM).

### 5.1.2c LISOLV

All the additions introduced into the computer code in order to solve the one-dimensional (core) region of the solution domain are included in sub-routine LISOLV. Sub-routine LISOLV is called by sub-routines CALC $\phi$  ( $\phi \equiv U, V, W, k, \epsilon, \theta$ ) and CALCP. In order to control the choice of the finite-difference coefficients for the solution of the one-dimensional region, a parameter has been introduced into the computer code called INDEX whose value is specific to a particular meaning of  $\phi$  (INDEX = 1 for CALCU, 2 for CALCW, 3 for CALCTE, 4 for CALCED and 5 for CALCT). Only the solutions of the V-velocity and  $p'$  pressure correction do not extend up to the tube-axis. Thus, if the variable INDEX takes the value 1 then, all the coefficients used in the one-dimensional region are related to U-velocity, i.e.

$$A_N^U = r_n \mu e_n$$

$$A_S^U = r_s \mu e_s$$

$$SU^U = - \left( \frac{dU}{dr} \frac{d\mu_s}{dr} \right)_p$$

$$SP^U = - \left( \frac{\mu_e}{r^2} \right)_p$$

and

$$AP^U = r_n \mu_{en} + r_s \mu_{es} + \left( \frac{\mu_e}{r^2} \right)_p$$

(derived in Section 4.2.2b of Chapter 4). Sub-routine LISOLV is divided into three chapters.

In chapter 1, all the modifications needed for the extension of the calculations to the tube axis are introduced. Since the describing equations in this region are solved on one radial line, nodal points are located in the one-dimensional extension of the solution domain. Also, the under-relaxation factors (URF1(N) where N takes the values 1 for U, 2 for W, 3 for k, 4 for  $\epsilon$ , 5 for  $\theta$  and 6 for viscosity) for the core region are initialized.

In chapter 2, the finite-difference equations, described by equation (4.51) for the one-dimensional region and by equation (2.38) for the two-dimensional region, are solved at the same time, using the line-by-line iteration procedure (presented in 2.5c of Chapter 2) along the  $\eta$ -lines, sweeping in  $\xi$ -direction.

In chapter 3, the finite-difference equations, described by equation (2.38) of Chapter 2, for the two-dimensional region only, are solved using the line-by-line iteration procedure (modified to include the cyclic boundary conditions, also described in Section 2.5c of Chapter 2) along the  $\xi$ -lines, sweeping in  $\eta$ -direction. Finally, the values of  $\phi$  or  $p'$  calculated in LISOLV are returned to CALC $\phi$  or CALCP.



### 5.1.2d PROPS

Sub-routine PROPS is called by CONTRO for calculating the turbulent viscosity  $\mu_t$  as well as the thermal conductivity  $\Gamma_t$  for the whole solution domain. Sub-routine PROPS is divided into five chapters:

In chapter 1, the turbulent viscosity for the two-dimensional region is calculated: (a) for the near-wall region from equation (4.1) if the mixing-length hypothesis is used; (b) for the rest of the solution domain from equation (4.3) with  $c_\mu$  calculated either from equations (4.15c) and (4.18) if one of the forms of the simplified algebraic-stress model (described in Section 4.1.4 of Chapter 4) is applied or assigned the value 0.09 if the k- $\epsilon$  Boussinesq viscosity is used.

Chapter 2 sets the values of the turbulent viscosity at the boundaries of the 2-D region. Also, the cubic spline interpolation treatment mentioned in the general description of the computer code is applied for calculating the turbulent viscosity at the control volume faces for a number of cell rows adjacent to the tube wall.

In chapter 3, the calculation of thermal conductivity  $\Gamma_t$  ( $= \mu_t / Pr_t$ ) for the 2-D region takes place: (a) for the near-wall region from equation (4.2) if the mixing-length hypothesis is applied; (b) for the rest of the solution domain, either from equation (4.20) if the simplified algebraic-stress model, including density fluctuation effects, is used, or from equation (4.8) if the k- $\epsilon$  Boussinesq viscosity model is applied.

Chapter 4 sets the boundary values of the thermal conductivity  $\Gamma_t$

for the 2-D region of the solution domain.

Finally, in chapter 5, the turbulent viscosity is calculated for the 1-D region of the solution domain. These values are stored and used in every call of LISOLV during an iteration of the procedure shown in the flow chart.

### 5.2.1 Glossary of FORTRAN Symbols

AH	-	Rib height, h
AN(I,J)	-	Coefficient of combined convective/diffusive flux through north-face of control volume
AS(I,J)	-	Coefficient of combined convective/diffusive flux through south-face of control volume
AE(I,J)	-	Coefficient of combined convective/diffusive flux through east-face of control volume
AW(I,J)	-	Coefficient of combined convective/diffusive flux through west-face of control volume
AU(I,J)	-	Coefficient of combined convective/diffusive flux through upstream-face of control volume
AD(I,J)	-	Coefficient of combined convective/diffusive flux through downstream-face of control volume
AP(I,J)	-	Sum of coefficients of combined convective/diffusive fluxes through the faces of the control volume
AREAXY(I,J)	-	Area of control volume
AKC1, AKC2, AKF, AKCT1, AKCT2, AKCTD, AKFT, AKFTD	}	Constants of simplified ASM model with density fluctuation effects

ANUSS	=	Nusselt number
ANUSSE(I)	=	Local Nusselt number
CE(I)	=	Coefficient of convective flux through east-face of control volume
CD(I,J)	=	Coefficient of convective flux through downstream-face of control volume
CU	=	Coefficient of convective flux through upstream-face of control volume
CN	=	Coefficient of convective flux through north-face of control volume
CS	=	Coefficient of convective flux through south-face of control volume
CW	=	Coefficient of convective flux through west-face of control volume
CCE(I)	=	Source term calculated at east-face of control volume
CCW	=	Source term calculated at west-face of control volume
CCD(I,J)	=	Source term calculated at downstream-face of control volume
CCU	=	Source term calculated at upstream-face of control volume
CCN	=	Source term calculated at north face of control volume
CCS	=	Source term calculated at south face of control volume
CMU	=	Constant of turbulence model (= 0.09)
CDT	=	Constant of turbulence model (= 1.0)

C1M	=	Constant of turbulence model (= 1.44)
C2M	=	Constant of turbulence model (= 1.92)
CAPPA	=	Von Karman constant
CPW	=	$C_p$
CMUA(I,J)	=	Variable $c_\mu$ in the two-dimensional region
CMUR(J)	=	Variable $c_\mu$ in the one-dimensional region
DU(I,J)	=	Coefficient of velocity-correction term for U-velocity
DV(I,J)	=	Coefficient of velocity-correction term for V-velocity
DW(I,J)	=	Coefficient of velocity-correction term for W-velocity
DEN(I,J)	=	Density, $\rho$
DXC(I,J)	=	Length of north or south face of the control volume
DYC(I,J)	=	Length of west or east face of the control volume
DENSIT	=	Density, $\rho$
DPDZ	=	$dp/dz$
DXIDF(I,J)	=	$\partial \xi / \partial \theta$
DETADF(I,J)	=	$\partial \eta / \partial \theta$
DRDXI(I,J)	=	$\partial r / \partial \xi$
DRDETA(I,J)	=	$\partial r / \partial \eta$
DXDY(I,J)	=	co-ordinate curvature = $\frac{1}{h_\xi} \frac{\partial h_\xi}{\partial \eta}$
DYDX(I,J)	=	co-ordinate curvature = $\frac{1}{h_\eta} \frac{\partial h_\eta}{\partial \xi}$
DIE	=	coefficient of diffusive flux through east-face of control volume

DIN	-	Coefficient of diffusive flux through north-face of control volume
ED(I,J)	-	Energy dissipation rate, $\epsilon$
ELOG	-	Constant of P-function for heat transfer at walls
FID(J <sup>*</sup> ,1)	-	U
FID(J <sup>*</sup> ,2)	-	W
FID(J <sup>*</sup> ,3)	-	k
FID(J <sup>*</sup> ,4)	-	$\epsilon$
FID(J <sup>*</sup> ,5)	-	$\Theta$
FLOWTOT	-	Total mass-flow rate through tube
FIAXIS	-	Spiral angle, $\Phi$
GREAT	-	A very large value ( $10^{30}$ )
GENN(I,J)	-	Generation of turbulence energy k
HYDDIA	-	Hydraulic diameter, $D_h$
HEDU	-	Heading "U-velocity"
HEDV	-	Heading "V-velocity"
HEDW	-	Heading "W-velocity"
HEDP	-	Heading "P-pressure"
HEDT	-	Heading "T-temperature"
HEDK	-	Heading "k-energy"
HEDD	-	Heading " $\epsilon$ -dissipation"
HEDMU	-	Heading "MU-viscosity"
I	-	Index for dependent variables and co-ordinates (constant $\xi$ )
IT	-	I-index of maximum dimension of dependent variables
INDEX	-	Integer controlling the choice of finite-difference coefficients used in sub-routine LISOLV for the one-dimensional region of the solution domain

IPREF	=	I-index of location where pressure is fixed
IBOTH	=	Integer controlling the choice of turbulence model
INCALU	=	Logical parameter for solution of U-equation
INCALV	=	Logical parameter for solution of V-equation
INCALW	=	Logical parameter for solution of W-equation
INCALP	=	Logical parameter for solution of p'-equation
INCALT	=	Logical parameter for solution of $\Theta$ -equation
INCALK	=	Logical parameter for solution of k-equation
INCALD	=	Logical parameter for solution of $\epsilon$ -equation
INPRO	=	Logical parameter for calculation of viscosity
J	=	Index for dependent variables and co-ordinates (constant $\eta$ )
JT	=	J-index of maximum dimension of dependent variables
JPREF	=	J-index of location where pressure is fixed
JTS	=	Number of row-cells where the PSL treatment is applied
JG	=	Number of row-cells in the two-dimensional region where the $k\sim\epsilon$ Boussinesq viscosity model is applied
$J^*$	=	$J + N1D$
MAXIT	=	Maximum number of iterations to be completed if iteration sequence is not stopped by test on value of SORCE
MAXIT1	=	Number of iterations after which only the temperature equation is solved
N1D	=	Maximum value of nodal points in the one-dimensional region of the solution domain
NI	=	Maximum value of I-index

NJ	=	Maximum value of J-index
NIM1	=	NI - 1
NJM1	=	NJ - 1
NSWPU	=	Number of calls of LISOLV for U-equation
NSWPV	=	Number of calls of LISOLV for V-equation
NSWPP	=	Number of calls of LISOLV for p'-equation
NSWPT	=	Number of calls of LISOLV for $\theta$ -equation
NSWPK	=	Number of calls of LISOLV for k-equation
NSWPD	=	Number of calls of LISOLV for $\epsilon$ -equation
NITER	=	Number of iterations completed
P(I,J)	=	Pressure, p
PP(I,J)	=	Pressure correction, p'
PRANDT	=	Turbulent Prandtl number
PRTE	=	Constant of turbulence model in k-equation ( $\sigma_k$ )
PRED	=	Constant of turbulence model in $\epsilon$ -equation ( $\sigma_\epsilon$ )
PIH	=	$2\pi/H$ , H = spiral pitch
PI	=	$\pi$
PRANDL	=	Laminar Prandtl number
QFLUX	=	Heat flux per unit area of tube surface
RDIM	=	Dimension of tube diameter ( $2R_p$ )
RESORU	=	Sum of residual sources within calculation domain for U-equation
RESORV	=	Sum of residual sources within calculation domain for V-equation
RESORM	=	Sum of mass sources within calculation domain
RESORW	=	Sum of residual sources within calculation domain for W-equation

RESORT	-	Sum of residual sources within calculation domain for $\Theta$ -equation
RESORK	-	Sum of residual sources within calculation domain for k-equation
RESORD	-	Sum of residual sources within calculation domain for $\epsilon$ -equation
RESU(I,J)	-	Residual sources for U-equation
RESV(I,J)	-	Residual sources for V-equation
RESW(I,J)	-	Residual sources for W-equation
RESM(I,J)	-	Mass sources calculated in CALCP
RAB	-	$R_a$
RBB	-	$R_b$
RID(J <sup>*</sup> )	-	Radii at I = 2 from the tube axis up to the wall
RA	-	Inner radius $R_a$
RB	-	Mean radius of the fluted surface $R_b$
SU(I,J)	-	Coefficient of linearized source treatment
SP(I,J)	-	Coefficient of linearized source treatment
SMALL	-	A very small value ( $10^{-30}$ )
SWET	-	Perimeter of the cross-stream plane
T(I,J)	-	Temperature $\Theta$ ( $= T - T_{ref}$ )
TE(I,J)	-	Turbulence energy, k
TIN	-	Initial value of temperature
TWALL	-	Temperature at the wall
TAUXS(I)	-	$\xi$ -direction shear stress at south wall-boundary of the solution domain
TAUXN(I)	-	$\xi$ -direction shear stress at north wall-boundary of the solution domain
TAUZS(I)	-	z-direction shear stress at south wall-boundary of the solution domain



TAUZN(I)	=	z-direction shear stress at north wall-boundary of the solution domain
THETA	=	$2\pi/n$ , $n$ = number of flutes
URFU	=	Under-relaxation factor for U-velocity
URFV	=	Under-relaxation factor for V-velocity
URFW	=	Under-relaxation factor for W-velocity
URFP	=	Under-relaxation factor for pressure
URFT	=	Under-relaxation factor for temperature
URFVIS	=	Under-relaxation factor for viscosity
URFK	=	Under-relaxation factor for turbulence energy
URFD	=	Under-relaxation factor for energy dissipation
URF1(1)	=	URFU
URF1(2)	=	URFW
URF1(3)	=	URFK
URF1(4)	=	URFD
URF1(5)	=	URFT
URF1(6)	=	URFVIS
U(I,J)	=	Component of mean velocity in $\xi$ -direction
UU(I,J)	=	Corrections for U-velocity
V(I,J)	=	Component of mean velocity in $\eta$ -direction
VIS(I,J)	=	Effective viscosity $\mu_e = \mu + \mu_t$
VISCOS	=	Laminar viscosity $\mu$
VV(I,J)	=	Velocity corrections for V-velocity
VIS1D(J)	=	Viscosity in 1-D region
W(I,J)	=	Component of mean velocity in axial direction
WFE(I,J)	=	Geometric interpolation coefficient in $\xi$ -direction
WFN(I,J)	=	Geometric interpolation coefficient in $\eta$ -direction
WMEAN	=	Mean value of W-velocity

YPLUSS(I)        =    Local Reynolds number based on friction  
                         velocity and distance from south wall-boundary  
                         of the solution domain

YPLUSN(I)        =    Local Reynolds number based on friction  
                         velocity and distance from north wall-boundary  
                         of the solution domain

## 5-2-2 Listing of the computer code

```

      PROGRAM MAIN(INPUT,OUTPUT,TAPE5=INPUT,TAPE6=OUTPUT,TAPE22,TAPE11,
1        TAPE55,TAPE99)
      C      SUBROUTINE CONTR0
      C*****
      C*
      C* A COMPUTER CODE FOR THE CALCULATION OF TURBULENT TWO-
      C* DIMENSIONAL FLOWS THROUGH A SPIRALLY FLUTED TUBE
      C* DEVELOPED BY A.PAPPA (BASED ON THE TEACH CODE BY ANTO-
      C* NIOPOULOS, GOSMAN, ISSA) IN THE MECHANICAL ENGRG.
      C* DEPT. OF MECH. ENGRG. PLUG. PO BOX 28, MANCHESTER
      C* M60 10D, ENGLAND
      C*****
      C
      C CHAPTER 0 0 0 0 0 0 0 0 PRELIMINARIES 0 0 0 0 0 0 0 0
      C
      C DIMENSION HEDU(6),HEDV(6),HEDW(6),HEDP(6),HEDT(6)
      C          ,HEDK(6),HEDD(6),HEDIII(6)
      C DIMENSION PSI(25,25)
      C COMMON
      C
      C RESORU,URFU,RESORV,URFV,RESORW,RESOPW,URFW,
      C URFV,RESORT,URFT,RESORK,URFK,RESOPD,URFD,
      C RESU(25,25),RESV(25,25),RESW(25,25),RESM(25,25),
      C DU(25,25),DV(25,25),DW(25,25),U(25,25),V(25,25),
      C U(25,25),P(25,25),T(25,25),TE(25,25),FD(25,25),
      C PP(25,25),DEFU(25,25),VIS(25,25),AN(25,25),AS(25,25),
      C AF(25,25),AW(25,25),AU(25,25),AD(25,25),CF(25),CD(25,25),
      C CCE(25),CCD(25,25),AP(25,25),SH(25,25),SP(25,25),FXC(25,25),
      C DYC(25,25),D7C(4),WFE(25,25),WFN(25,25),WFD(4),
      C APFAXY(25,25),F1D(50,5),N1D,WMEAN,INDEX,HYDDIA,PAR,R1D(50),
      C VELIN,TIN,TWALL,FLOWIN,GREAT,
      C UREVIS,VISCOS,DENSIT,PRANDT,
      C PRTE,PRFD,CMU,CNT,C1H,C2H,CAPPA,FLOG,ALANDA,
      C USUPU,NSUPV,NSUPW,NSUPD,NSWPT,
      C JSUPK,JSUPD,
      C IPREF,JIPREF,KIPREF,INDCOS
      C COMMON TAUXS(25),TAUXN(25),TAUYS(25),TAUYN(25),
      C YPLUSS(25),YPLUSSN(25)
      C IT,JT,N1,N2,NIM1,NIM2
      C SVET,FLOWTOT,CPH,REFLUX,FLOWT
      C K1,K2
      C RA,RR,THETA,AN,DPD7,FLQUAX,DYIDE(25,25),DETADE(25,25),PIH
      C DDDXT(25,25),DDDETA(25,25),HTRH(25,25)
      C PI,WTN,FLOWW
      C SMALL,SUMS,SUPD,TNIMP,DXY(25,25),DYDX(25,25)
      C LEVEL 2,III
      C COMMON/RLK2/III(25,25),VV(25,25),AMU(25,25),ASII(25,25),
      C AFU(25,25),AWU(25,25),AUU(25,25),AUU(25,25),
      C ANV(25,25),ASV(25,25),AEV(25,25),AWV(25,25),
      C COIT(25,10),VRU(25),JTS,
      C ADV(25,25),AIV(25,25),AA(25)
      C JC,THOTH,TER(25,2),FDR(25,2),PRDDN(50),GENN(25,25)
      C PRANDI,GHT(25,25),AMISS
      C PRDD(25,25),AK7(25,25),AKD(25,25),AKA(25,25),RVT(25,25),AKF
      C AKET,AKETD,AKCTD,F1P(25),F1K7(25),F1KD(25),F1KA(25),F1RVT(25)
      C NOIMP,CVIA(25,25),CMUR(25)
      C NOIMP2
      C APV(25,25),APV(25,25),PR(25,25),ANGL(25,25)

```

```

1      ,KASH,KASH
1      ,VISV(25,25),VA(25,25),VH(25,25),VC(25,25)
1      ,PSC(5),IMEG,MAXIT2
1      ,PRS(75,25),RPH,UTTER,MAXIT
1      ,TLENSC,VISID(50),XMLL(25,25)
      DIMENSION AMISSF(25)
      LOGICAL INCALH,INCALV,INCALP,INCALT,INPRO
1      ,TNCALK,INCALD
      GPAT=1.0E30
      SMALL=1.0E-30
      PT=4.0*ATAN(1.)
      UTTER=.1
      IT=25
      JT=25
      NSWP1=X
      NSWPV=2
      NSWPW=10
      NSWPP=2
      NSWPT=20
      NSWPK=2
      NSWPD=2
-----HEADINGS-----
      READ(5,010) HEDH,HEDV,HEDL,HEDP,HEDT,HEDK,HEDD,HEDM
1      010 FORMAT(6A4)
C
CHAPTER 1 1 1 1 1 PARAMETERS AND CONTROL INDICES 1 1 1 1 1 1
C
      NT=20
      NI=20
      N10=20
      J2=1
      N1=1
      N101=N1-1
      N102=N1-1
      N103=N1-2
      N104=N1-2
      RDIM=0.015
-----GEOMETRY (GRID SPACING)-----
      READ(11) DXC,DYC,DXIDF,DETADE,DPDVI,DRDETA,HTHR,RP,ANGL
1      ,RH,RA,AM,IFLUT,FTAXIS,JG,XMLI
      DO 7119 J=1,NI
      DO 7119 I=1,NJ
      DXC(I,J)=DXC(I,J)*RDIM
      DYC(I,J)=DYC(I,J)*RDIM
      DXIDF(I,J)=DXIDF(I,J)*RDIM*(-1.)
      DETADE(I,J)=DETADE(I,J)*RDIM
      DPDVI(I,J)=DPDVI(I,J)/RDIM
      DRDETA(I,J)=DRDETA(I,J)/RDIM
      RP(I,J)=RP(I,J)*RDIM
      XMLI(I,J)=XMLI(I,J)*RDIM
7119 CONTINUE
      RH=RH*RDIM
      RA=RA*RDIM
      AM=AM*RDIM
      WAW=RA
      JG=1.0
      IROTH=1

```

```

      THETA=2.*PI/FLOAT(NFLUT)
      IF(IHOTH.EQ.0) JG=2
      IF(IHOTH.EQ.2) JG=NJ
      RRR=RR
      DO 12 J=2,NJM1
      DO 12 I=2,NHM1
12    APFAXY(I,J)=.25*(DXC(I,J+1)+DXC(I,J))* (DYC(I,J)+DYC(I+1,J))
      DZC(1)=1.
      XTOT=0.
      DO 44R2 J=1,NJ
      ANGL(1,J)=ANGL(NJM1,J)
      ANGL(NI,J)=ANGL(2,J)
      RR(1,J)=RR(NI,J)
44R2  W0(NI,J)=RR(2,J)
      DO 3721 I=1,NJ
      ANGL(I,1)=ANGL(I,2)
3721  W0(I,1)=W0
      PTH=-TAN(FIAXIS)/RH
      DO 100 I=2,NIM1
      100  XTOT=XTOT+DYC(I,2)
      YTOT=0.
      DO 110 J=2,NJM1
      110  YTOT=YTOT+DYC(2,J)
      ZTOT=0.
      ZTOT=ZTOT+DZC(1)
C-----LOGICAL PARAMETERS CONTROLLING THE CALL OF SUBROUTINES-----
      INCALU=.TRUE.
      INCALV=.TRUE.
      INCALW=.TRUE.
      INCALP=.TRUE.
      INCALT=.FALSE.
      IMPRO=.TRUE.
      IF(IHOTH.EQ.0) GO TO 4455
      INCALK=.TRUE.
      INCALD=.TRUE.
      GO TO 4466
4455  CONTINUE
      INCALV=.FALSE.
      INCALD=.FALSE.
4466  CONTINUE
C-----FLUID PROPERTIES-----
      VISCOS=1.E-3
      DENSITY=1100
      PRANDT=.9
      CPW=1005.7
      THCOND=1.420
      PRANDL=0.718
C-----THERMAL ENCE CONSTANTS-----
      AKC1=.2
      AKC2=.55
      AKF=(1.-AKC2)/AKC1
      AKCT1=3.2
      AKCT2=.5
      AKCTD=1.6
      AKFT=1./AKCT1
      AKFTD=AKFT*(1.-AKCT2)
      COT=1.0

```

```

CMH=.09
C1M=1.44
C2M=1.92
CAPPA=.4187
FLOG=.793
PDEF=CAPPA**2/(C2M-C1M)/CMU**5
PPTF=1.
ALAMDA=.005

```

```

*****
C*      IF(MASH.EQ.0) NO ASM IS USED *
C*      IF(MASH.EQ.1) BUOYANCY ASM OF GIBSON AND LAUNDER *
C*      IF(MASH.EQ.2) ASM WITH SWIRL EFFECT *
C*      IF(MASH.EQ.1) TEMPERATURE SOLVED SIMULTANEOUSLY WITH *
C*      MOMENTUM EQUATIONS (BUOYANCY ASM) *
C*      IF(MASH.EQ.0) TEMPERATURE SOLVED AFTER MOMENTUM EQUIL. *
C*      FULLY CONVERGED AND DYNAMIC FIELD STOPED *
*****

```

```

KASM=2
NASH=0

```

```

-----BOUNDARY VALUES-----

```

```

VFITN=0.1
DPD7=-1000.
UTN=1.55
INDEX=0
THPRIN=0.0
TEIN=0.001*WIN**2
FOIN=DENSIT*CMU*TEIN**2/(1U.*VISCOS)
TYN=300.0
HUMPR=1000
THAI=400.0
CPU=4181.3
THCOND=.507
DEFLUX=500.

```

```

-----PRESSURE CALCULATION-----

```

```

PREF=0.0
IPREF=2
JPREF=2
KPREF=2

```

```

-----PROGRAM CONTROL AND MONITOR-----

```

```

MAXIT=2200
SOPMAX=1.0E-3
MAXIT2=5
IMON=3
JMON=3
KMON=2
INDPRJ=MAXIT
IIMIN=0
IEMSC=0
HUMPR=1

```

```

-----HINDER-RELAXATION FACTORS-----

```

```

HDFU=.7
HDFV=.7
HDFW=.8
HDFD=.5
HDFE=1.0
HDFV=.6
HDFD=.6

```

```

      HRFVIS=.7
C
CHAPTER 2 2 2 2 2 2 INITIAL OPERATIONS 2 2 2 2 2 2 2 2 2
C
C-----CALCULATE GEOMETRICAL QUANTITIES AND SET VARIABLES TO ZERO
      CALL INIT
      CALL PARCUR
      DO 4547 I=1,NI
      DO 4547 J=1,NJ
        DXC(1,J)=DXC(NIM1,J)
        DYC(1,J)=DYC(NIM1,J)
        DXIDF(1,J)=DXIDF(I,J)
        DETADF(1,J)=DETADF(I,J)
        AREAXY(1,J)=AREAXY(NIM1,J)
        AREAXY(NIM1,J)=AREAXY(2,J)
        WFM(1,J)=WFM(NIM1,J)
        DXIDF(1,J)=DXIDF(NIM1,J)
        DETADF(1,J)=DETADF(NIM1,J)
        DETADF(NIM1,J)=DETADF(2,J)
        DXIDF(NIM1,J)=DXIDF(2,J)
        DYC(NIM1,J)=DYC(2,J)
        DYC(I,NJ)=DYC(I,NJ+1)
        DXIDF(I,1)=DXIDF(I,2)
        DETADF(I,1)=DETADF(I,2)
        DRDXT(1,J)=DRDXT(NIM1,J)
        DRDXT(2,J)=0.0
        DRDXT(NIM1,J)=0.0
        DRDXT(I,1)=DRDXT(I,2)
        DRDFTA(1,J)=DRDFTA(NIM1,J)
        DRDFTA(NIM1,J)=DRDFTA(2,J)
        DRDFTA(I,1)=DRDFTA(I,2)
        HTHR(1,J)=HTHR(NIM1,J)
        HTHR(NIM1,J)=HTHR(2,J)
        HTHR(I,1)=HTHR(I,2)
        DYC(I,1)=DXC(I,2)
        DYC(I,1)=DYC(I,2)
4547 CONTINUE
        DRDXT(2,1)=DRDXT(2,2)
        DRDFTA(2,1)=DRDFTA(2,2)
        HTHR(2,1)=HTHR(2,2)
        DETADF(2,1)=DETADF(2,2)
        DXIDF(2,1)=DXIDF(2,2)
        DO 3113 J=2,NJ+1
          T=2
          WFF1=DXC(I-1,J)/(DXC(I,J)+DXC(I-1,J))
          WFF2=DXC(I-1,J+1)/(DXC(I,J+1)+DXC(I-1,J+1))
          WFF(I,J)=.5*(WFF1+WFF2)
3113 WFF(NIM1,J)=WFF(2,J)
          WFF(2,NJ)=DYC(1,NJ)/(DXC(1,NJ)+DXC(2,NJ))
          WFF(NIM1,NJ)=WFF(2,NJ)
        DO 3562 J=2,NIM1
          WFF(I,1)=DXC(I-1,1)/(DXC(I-1,1)+DYC(I,1))
          WFF(I,1)=WFF(2,1)
        DO 641 JJ=1,NJ
          JJ=JJ+1-JJ
          DXC(1,J)=DXC(NIM1,J)
641 WOTTF(6,501) (DYC(I,J),I=1,NI)

```

```

WRITE(6,502)
DO 642 JJ=1,NJ
  J=JJ+1-JJ
  DYC(1,J)=DYC(NIM1,J)
642 WRITE(6,501) (DYC(I,J),I=1,NI)
  WRITE(6,502)
501 FORMAT(5X,(1UF10.3,/))
502 FORMAT(1H0,8U(1H-))
DO 643 JJ=1,NJ
  J=JJ+1-JJ
643 WRITE(6,501) (AREAXY(I,J),I=1,NI)
  WRITE(6,502)
DO 721 JJ=1,NJ
  J=JJ+1-JJ
721 WRITE(6,501) (PPDXI(I,J),I=1,NI)
  WRITE(6,502)
DO 722 JJ=1,NJ
  J=JJ+1-JJ
722 WRITE(6,501) (PPDETA(I,J),I=1,NI)
  WRITE(6,502)
DO 723 JJ=1,NJ
  J=JJ+1-JJ
723 WRITE(6,501) (HTHR(I,J),I=1,NI)
  WRITE(6,502)
DO 746 JJ=1,NJ
  J=JJ+1-JJ
746 WRITE(6,501) (DETADF(I,J),I=1,NI)
  WRITE(6,502)
DO 782 JJ=1,NJ
  J=JJ+1-JJ
782 WRITE(6,501) (DXIDF(I,J),I=1,NI)
  WRITE(6,502)
DO 785 JJ=1,NJ
  J=JJ+1-JJ
785 WRITE(6,501) (ANGL(I,J),I=1,NI)
  DO 787 JJ=1,NJ
    J=JJ+1-JJ
787 WRITE(6,501) (RR(I,J),I=1,NI)
  WRITE(6,502)
DO 791 JJ=1,NJ
  J=JJ+1-JJ
791 WRITE(6,501) (WFE(I,J),I=1,NI)
  WRITE(6,502)
DO 799 JJ=1,NJ
  J=JJ+1-JJ
799 WRITE(6,501) (WFH(I,J),I=1,NI)
-----INITIATE VARIABLE FIELDS-----
DO 422 I=1,NI
DO 422 J=1,NJ
  DENS(I,J)=DENSIT
  VTS(I,J)=VISCOS
422 CONTINUE
DO 7811 I=1,NI
  TAUYS(I)=0.
  TAUXX(I)=0.
  TAUYS(I)=0.
  TAUXX(I)=0.

```



```

      YBLUSS(T)=0.
7811 YBLUSS(T)=0.
      P(JDREF,JPREF)=PREF
      JOR=1
      IF (JOR.EQ.1) GO TO 211
      READ(22) U,V,W,P,VIS,MITER,FID,VISID,T,TE,ED,SNORK,SNORD,VISV
      REUTJD 22
      GO TO 215
211 CONTINUE
      DO 200 I=1,M1
      DO 200 J=1,MJ1
      TE(T,L(T,J)) RPS(I,J)=.25*(RR(T,J)+RR(T+1,J)+RR(T,J+1)+RR(T+1,
1J+1))
      IF (T.EQ.1) RRS(1T,J)=RRS(2,J)
      U(I,J)=UIN*(1.-RRS(1,J)**2/PRR**2)*2.
      W(I,J)=.1*TAN(FIAXIS)*W(I,J)
      V(I,J)=.1*U(I,J)
      V(I,1)=0.
      V(T,2)=0.
      W(T,MJ)=0.
      U(T,MJ)=0.
      V(T,MJ)=0.
200 CONTINUE
      DO 225 I=1,M1
      DO 225 J=1,MJ
      TE(T,J)=TEIN
      ED(T,J)=EDIN
225 T(I,J)=TIN
      DO 226 I=1,M1
226 T(I,MJ)=TMAT1
      NINEJ=JJ+N1D
      DO 2251 J=1,NINEJ
      TE(J,GF.(N1D+3)) GO TO 2252
      FID(J,1)=U(2,3)*FLOAT(J-1)/FLOAT(N1D+2)
      R=FLOAT(J-1)/FLOAT(N1D+2)*(RA+.5*NYC(2,2))
      FID(J,2)=2.*WTR*(1.-R*R/RP**2)
      FID(J,3)=TEIN
      FID(J,4)=EDIN
      FID(J,5)=TIN
      VISID(J)=VISCS
      GO TO 2251
2252 CONTINUE
      FID(J,1)=U(2,J-N1D)
      FID(J,2)=W(2,J-N1D)
      FID(J,3)=T(2,J-N1D)
      FID(J,4)=ED(2,J-N1D)
      FID(J,5)=T(2,J-N1D)
      VISID(J)=VISCS
2251 CONTINUE
      CALL PROPS
215 CONTINUE
-----INFLOW CALCULATION-----
      FLOWIN=0.0
      AREFAT=0.
      DO 800 J=2,MJ1
      AREFAT=AREFAT+.5*(DEF(1,J)+DEN(2,J))*NYC(2,J)*D7C(1)
      FLOWIN=FLOWIN+DEF(1,J)*NYC(2,J)*D7C(1)*U(2,J)

```

```

800 CONTINUE
C-----AXIAL FLOW CALCULATION-----
TAREA=0.
DO 2472 I=2,NIM1
DO 2472 J=2,NJM1
TARF6=TAREA+ARFAXY(I,J)
2472 CONTINUE
FLOWAX=PI*RR*RB*WIN*DENSI/LOAT(NFLUT)
C-----RESIDUAL SOURCE NORMALISING VALUES-----
SNORU=FLOWAX*WIN
SNORV=SNORU
SNORW=SNORU
SNORM=FLOWAX
SNORT=QFLUX*2.*PI*RB*DZC(1)/CPW
TF(IQB,NE.1) GO TO 2572
SNORK=FLOWAX*TEIN
SNORD=FLOWAX*EDIN
2572 CONTINUE
C-----PROBLEM HEADING-----
WRITE(6,220)
270 FORMAT(///1H0,120(1H*)///)
WRITE(6,230) WIN
230 FORMAT(///1H0,15X,*INLET FLUID VELOCITY*,T60,1H=,3X,1PE11.3)
WS=4.*YTOT*ZTOT
WP=4.*(YTOT+ZTOT)
SWET=0.
DO 2311 I=2,NIM1
SWET=SWET+DXC(I,NJ)
2311 CONTINUE
HYDDIA=4.*(TAREA*2.*PI/THETA+PI*RA*RA)/(SWET*2.*PI/THETA)
RE=DENSI*HYDDIA*WIN/VISCOS
WRITE(6,240) RE
240 FORMAT(1H0,15X,*REYNOLDS NUMBER*,T60,1H=,3X,1PE11.3)
WRITE(6,250) PRANDT
250 FORMAT(1H0,15X,*PRANDT NUMBER*,T60,1H=,3X,1PE11.3)
WRITE(6,270) VISCOS
270 FORMAT(1H0,15X,*FLUID VISCOSITY*,T60,1H=,3X,1PE11.3)
WRITE(6,280) DENSI
280 FORMAT(1H0,15X,*FLUID DENSITY*,T60,1H=,3X,1PE11.3///)
WRITE(6,290) QFLUX,TIN
290 FORMAT(1H0,15X,*TEMPERATURE BOUNDARY CONDITIONS ARE*/
11H,25X,*WALL HEAT FLUX = *,1PE11.3/
11H,25X,*INLET TEMPERATURE = *,1PE11.3//)
WRITE(6,291) (BR,RA,AM,NFLUT,FIAXIS)
291 FORMAT(15H DUCT GEOMETRY,/,4H RR=E10.3,/,4H RA=E10.3,
/,4H AM=E10.3,/,7H NFLUT=,110,/,8H FIAXIS=E10.3)
WRITE(6,220)
C-----INITIAL OUTPUT-----
IF(INCALI) CALL PRINT(2,1,NI,NJ,IT,JT,XU,Y,U,HEDU)
IF(INCALV) CALL PRINT(1,2,NI,NJ,IT,JT,X,YV,V,HEDV)
IF(INCALW) CALL PRINT(1,1,NI,NJ,IT,JT,X,Y,W,HEDW)
IF(INCALP) CALL PRINT(1,1,NI,NJ,IT,JT,X,Y,P,HEDP)
IF(INCALT) CALL PRINT(1,1,NI,NJ,IT,JT,X,Y,T,HEDT)
NI=NJ
IF(TROTH,EQ.1) NJ=JG
IF(INCALK) CALL PRINT(1,1,NI,NJ,IT,JT,X,Y,TE,HEDK)

```

```

      IF(TNCALD) CALL PRINT(1,1,NT,NJ,IT,IT,X,Y,ED,HEDD)
      NJ=NJL
      IF(JIPRO) CALL PRINT(1,1,NT,NJ,IT,IT,X,Y,VIS,HEDMU)
C
CHAPTER 3 3 3 3 3 3 3 ITERATION LOOP 3 3 3 3 3 3 3 3
C
      WRITE(6,310) IMON,JMON
      NITER1=NITER+300
      MAXIT1=1900
C-----BEGINNING OF THE ITERATION LOOP-----
      300 NITER=NITER+1
      IF(KAS1.EQ.2) NOUMR2=NITER1
      IF(KAS1.EQ.1) NOUMR2=NITER1
      IF(KAS1.EQ.0) NOUMR2=1
      NOUMR=NOUMR2+1
      IF(NITER.GE.MAXIT1) INCALT=.TRUE.
      IF(NAS1.EQ.0.AND.NITER.GT.MAXIT1) GO TO 4195
      IF(THOT.FU.0) GO TO 2233
      IF(MOD(NITER,40).NE.0) GO TO 2233
      SNORD=0.0
      SNORK=0.0
      JGM1=JG-1
      DO 2244 I=2,NJM1
      DO 2244 J=2,JGM1
      SNORD=SNORD+C1F*CMU*GENN(I,J)+DEN(I,J)*TE(I,J)/VIS(I,J)
      2244 SNORK=SNORK+GENN(I,J)
      2233 CONTINUE
C-----UPDATE MAIN DEPENDENT VARIABLES-----
      DO 212 J=1,NJM1
      H(NT,J)=H(2,J)
      H(1,J)=H(NIM1,J)
      212 CONTINUE
      DO 210 J=1,NJM1
      V(NT,J)=V(2,J)
      210 V(1,J)=V(NIM1,J)
      DO 2121 J=1,NJ
      U(1,J)=U(NIM1,J)
      W(NT,J)=W(2,J)
      2121 CONTINUE
      DO 2651 J=1,NJ
      T(1,J)=T(NIM1,J)
      T(NT,J)=T(2,J)
      2651 CONTINUE
C-----BEGINNING OF THE MARCHING LOOP-----
      INDEX=1
      JTS=4
      IF(TNCALD) CALL CALCU
C***** PSI PROCEDURE *****
C*****
C-----CALCULATION OF V-VELOCITY FROM CONTINUITY FOR J>NJMT-----
      NJMT=NJ-JTS
      DO 3901 J=2,NIM1
      DO 3901 JJ=NJMT,NJM1
      J=NJ-JJ+NJ-(JTS+1)
      CONT(I,J)=DENSIT*H(I,J)+DYC(I,J)*DZC(1)-DENSIT*H(I+1,J)+DYC(I+1,J)
      1*WZC(1)-PIH*.5*(DXIDF(I+1,J)+DXIDF(I+1,J+1))*DENSIT*(W(I,J)*(1.
      1-WFF(I+1,J))+W(I+1,J)*WFF(I+1,J)+DYC(I+1,J)*DZC(1)+PIH*.5*(

```

```

1DVIDF(I,J)+DXIDF(I,J+1))*DENSIT*(W(I,J)*WFF(I,J)+W(I-1,J)*(1.-
1UFF(I,J))*DYC(I,J)*DZC(1)-PIH*.5*(DETADF(I,J+1)+DETADF(J+1,J+1))
1*DENSIT*(W(I,J+1)*WFN(I,J+1)+W(I,J)*(1.-WFN(I,J+1))*DXC(I,J+1)
1*DZC(1)+PIH*.5*(DETADF(I,J)+DETADF(J+1,J))*DENSIT*(W(I,J)*WFN(I,
1,J)+W(I,J-1)*(1.-WFN(I,J))*DXC(I,J)*DZC(1)
V(I,J)=(DENSIT*V(I,J+1)*DXC(I,J+1)-CONT(I,J))/(DENSIT*DXC(I,J))
3901 CONTINUE
DO 3902 J=NJMT,NJ
V(1,J)=V(NJM1,J)
3902 V(NT,J)=V(2,J)
DO 3903 I=1,NJ
3903 VPI(I)=V(I,NJMT)
-----CALCULATION OF V-VELOCITY FROM V-MOMENTUM EQU. FOR J<NJMT-----
NJI=NJ
NJI=(JTS-1)
NJI1=NJI-JTS
INDEX=0
IF(TJCALV) CALL CALCV
NJI=NJI
NJI1=NJI-1
NJI2=NJI-2
NJI14=NJI+N10
NJI15=NJI+N10-1
INDEX=2
IF(TJCALW) CALL CALCW
CALL MODVFL
DO 3383 J=2,NJM1
DV(NT,J)=DV(2,J)
3383 DV(1,J)=DV(NJM1,J)
DO 3768 J=3,NJM1
DV(NT,J)=DV(2,J)
3768 DV(1,J)=DV(NJM1,J)
DO 3366 I=1,NJ
DV(T,2)=DV(T,3)
3366 DV(I,NJ)=DV(I,NJM1)
CALL MODVEL
NJI=NJ
NJI=(JTS-1)
NJI1=NJI-JTS
SUMS=0.0
INDEX=0
IF(TJCALP) CALL CALCP
INIMH=1
SUMS=0.0
IF(TJCALP) CALL CALCP
INIMH=0
NJI=NJI
NJI1=NJI-1
NJI2=NJI-2
NJMS=NJI-(JTS-1)
NJNT=NJI-JTS
NJI14=NJI+N10
NJI15=NJI+N10-1
DO 4189 I=1,NJ
DO 4189 J=NJMS,NJ
P(I,J)=P(I,NJMT)
4189 CONTINUE

```

```

C*****
      CALL MODVEL
      FLOWTOT=0
      N1D1=N1D+1
      DO 97R2 J=2,N1D1
        IF(J.EQ.N1D1) FLOWTOT=FLOWTOT+DENSIT*2.*PI*R1D(J)*F1D(J,2)*
        1.5*(R1D(J+1)-R1D(J-1))
        IF(J.EQ.N1D1) F1DW=.75*F1D(J,2)+.25*F1D(J-1,2)
        IF(J.EQ.N1D1) FLOWTOT=FLOWTOT+DENSIT*2.*PI*F1DW*
        1.25*(3.*R1D(J)+R1D(J-1))*(R1D(J)-R1D(J-1))*5
      97R2 CONTINUE
      FLOWTOT=FLOWTOT+PI*(.5*R1D(2))*2*F1D(1,2)*DENSIT+
      1FLOWN*FLOAT(NFLUT)
      R471 CONTINUE
      UMEAN=FLOWTOT/(TAPEA*FLOAT(NFLUT)+PI*RA**2)/DENSIT
      FLOWT=FLOWTOT/FLOAT(NFLUT)
C-----CALCULATION OF BOUNDARY VALUES FOR TURBULENT ENERGY AND ENERGY
C DISSIPATION JUST OUTSIDE THE MIXING LENGTH HYPOTHESIS REGION-----
      IF(THOTH.EQ.1) GO TO 3720
      DO 3719 I=2,NIN1
        DO 3719 J=1,2
          IF(N.EQ.1) J=JG-1
          IF(N.EQ.2) J=JG
          A01=.25*(DRDXI(I,J)+DRDXI(I+1,J)+DRDXI(I,J+1)+DRDXI(I+1,J+1))
          A02=.25*(DRDETA(I,J)+DRDETA(I+1,J)+DRDETA(I,J+1)+DRDETA(I+1,J+1))
          A01=.25*(DXIDF(I,J)+DXIDF(I+1,J)+DXIDF(I,J+1)+DXIDF(I+1,J+1))+PIH
          A02=.25*PIH*(DETADE(I,J)+DETADE(I+1,J)+DETADE(I,J+1)+DETADE(I+1
          1,J+1))
          AM1=DXDY(I,J)
          AM2=DYDX(I,J)
          AM3=.25*(WTHR(I,J)+WTHR(I+1,J)+WTHR(I,J+1)+WTHR(I+1,J+1))
          DYFW=.5*(DXC(I,J)+DXC(I,J+1))
          DIIDXP=(U(I+1,J)-U(I,J))/DXEW
          VP=.5*(V(I,J)+V(I,J+1))
          DYDYP=DXDY(I,J)
          TERM1=DIIDXP+VP*DXDYP
          DYIS=.5*(DYC(I,J)+DYC(I+1,J))
          DVNDYP=(V(I,J+1)-V(I,J))/DYNS
          UP=.5*(U(I,J)+U(I+1,J))
          DVDXP=DYDX(I,J)
          TERM2=DVNDYP+UP*DYDXP
          DIIDP=U(I)
          VFF=.5*(V(I+1,J+1)+V(I+1,J))
          VP=VFF*WFF(I+1,J)+VP*(1.-WFF(I+1,J))
          VUH=.5*(V(I-1,J+1)+V(I-1,J))
          VU=VU*WFF(I,J)+VUH*(1.-WFF(I,J))
          DVDXP=(VP-VU)/DXEW
          UHH=.5*(U(I+1,J+1)+U(I+1,J))
          UP=UHH*WFF(I,J+1)+UP*(1.-WFF(I,J+1))
          USS=.5*(U(I+1,J-1)+U(I+1,J-1))
          US=UP*WFF(I,J)+USS*(1.-WFF(I,J))
          DVNDYP=(UH-USS)/DYNS
          TERM4=DVDXP+DIIDYP-VP*DYDXP-UP*DYDYP
          UP=.5*(U(I,J)+U(I,J))
          UFF=.5*(U(I+1,J)+U(I+1,J))
          UUH=.5*(U(I-1,J)+U(I-1,J))
          UE=UFF*WFF(I+1,J)+UP*(1.-WFF(I+1,J))

```

```

      WM=WP*WFF(I,J)+WUU*(1.-WFF(I,J))
      DWDXP=(WE-WU)/DXEW
      UUU=.5*(U(I+1,J)+U(I,J))
      UDD=.5*(U(I+1,J)+U(I,J))
      UN=UDD*WFD(1)+UP*(1.-WFD(1))
      IF(PIH.EQ.0.0) GO TO 3652
      DUDDZP=0.0
      TERM5=DWDXP+AH3*DUDDZP+AK1*DUUXP+AK2*DUUYD+(-AK2*AH2+AK1*AH1-
1AH3*AH3*AP2/AK1)*VP
3652 CONTINUE
      IF(PIH.EQ.0.0) TERM5=DWDXP
      VDD=.5*(V(I,J+1)+V(I,J))
      VUU=.5*(V(I,J+1)+V(I,J))
      VN=VDD*WFD(1)+VP*(1.-WFD(1))
      VU=VU*WFD(1)+VUU*(1.-WFD(1))
      DVDZP=(VD-VU)/DZC(1)
      WUU=.5*(W(I,J+1)+W(I,J+1))
      USS=.5*(W(I,J-1)+W(I,J-1))
      UN=UUN*WFN(I,J+1)+UP*(1.-WFN(I,J+1))
      US=UP*WFN(I,J)+USS*(1.-WFN(I,J))
      DUDYP=(UN-US)/DYNS
      IF(PIH.EQ.0.0) GO TO 3642
      DVDZP=0.0
      TERM6=DUDYP+AH3*DVDZP+AK1*DUDXP+AK2*DUDYP+(-AK1*AH1+AK2*AH2
1+AH3*AP2*AH3/AK1)*UP
3642 CONTINUE
      IF(PIH.EQ.0.0) TERM6=DUDYP
      TERM3=AK1*DUUXP+AK2*DUDYP
      FDN(I,J)=(2.*(TERM1**2+TERM2**2+TERM3**2)+TERM4**2+TERM5**2+
1TERM6**2)*(VTS(I,J)-VISCOS)/DENSIT
      TER(I,J)=SUPT(EDH(I,J))*(VTS(I,J)-VISCOS)/(DENSIT*CMH)
3710 CONTINUE
      DO 3819 N=1,2
      FDN(1,N)=FDN(NIM1,N)
      FDN(2,N)=FDN(2,N)
      TER(1,N)=TER(NIM1,N)
      TER(2,N)=TER(2,N)
3819 CONTINUE
      JGM1=JG-1
      DO 3919 I=1,N1
      TE(I,JG)=TER(I,2)
      ED(I,JG)=FDP(I,2)
      TE(I,JGM1)=TER(I,1)
      ED(I,JGM1)=FDP(I,1)
3919 CONTINUE
3720 CONTINUE
4105 CONTINUE
*****
C*      INTRODUCTION OF 2 EXTRA NODES IN THE FIRST ROW OF      *
C*      CELLS ADJACENT TO THE WALL FOR THE TEMPERATURE EQU.    *
*****
      IF(MAS.EQ.1) GO TO 4366
      IF(MITER.EQ.(MAXIT1+1)) GO TO 4111
      GO TO 4366
4111 CONTINUE
      NJF1=NJ-1
      NJF2=NJ-2

```

```

NIFR=NJ-3
JOLD=NJ
JCAP=2
IJ=NJ+JCAP
IJM1=NJ-1
JIP1=NJ+1
DO 4477 I=1,NJ
  T(I,NJ)=T(I,JOLD)
DO 4477 J=JOLD,NJM1
  U(I,J)=U(I,NJF1)*.5*(NJ-J)**2/FLOAT(JCAP+1)
  U(I,NJ)=0.0
  V(I,J)=V(I,NJF1)/FLOAT(JCAP+1)*.25*(NJ-J)*(1.+(NJ-J))
  V(I,NJ)=0.0
  W(I,J)=W(I,NJF1)/FLOAT(JCAP+1)*.5*(NJ-J)**2
  W(I,NJ)=0.0
  T(I,J)=T(I,NJF1)/FLOAT(JCAP+1)*.5*(NJ-J)**2
  JM1=J-1
  GMT(I,JM1)=VISCOS/PRANDL+(GMT(I,NJF2)-VISCOS/PRANDL)/FLOAT(
1 JCAP+1)*.25*(NJ-J)*(1.+(NJ-J))
  GMT(I,NJ)=VISCOS/PRANDL
  GMT(I,NJM1)=VISCOS/PRANDL
  VTS(I,J)=VISCOS+(VTS(I,NJF1)-VISCOS)/FLOAT(JCAP+1)*.5*(NJ-J)**2
  VTS(I,NJ)=VISCOS
  DEN(I,J)=DENSIT
  DEN(I,NJ)=DENSIT
  IF(J.EQ.JOLD) DYC(I,J)=DYC(I,NJF1)*2./6.
  IF(J.EQ.NJM1) DYC(I,J)=DYC(I,NJF1)*1./6.
4477 DYC(I,NJ)=0.0
DO 3911 I=1,NJ
  J=NJF1
  U(I,NJF1)=U(I,NJF1)+(U(I,NJF2)-U(I,NJF1))*1.5/6.*DYC(I,NJF1)
1 /(.5*(DYC(I,NJF1)+DYC(I,NJF2)))
  W(I,NJF1)=W(I,NJF1)+(W(I,NJF2)-W(I,NJF1))*1.5/6.*DYC(I,NJF1)
1 /(.5*(DYC(I,NJF1)+DYC(I,NJF2)))
  DYC(I,NJF1)=DYC(I,NJF1)/2.
  T(I,NJF1)=T(I,NJF1)*.5*(NJ-J)**2/FLOAT(JCAP+1)
  VTS(I,NJF1)=VISCOS+(VTS(I,NJF1)-VISCOS)/FLOAT(JCAP+1)*.5*(NJ-J)
1 **2
3911 CONTINUE
DO 4488 I=1,NJ
  DYC(I,NJ)=DYC(I,JOLD)
DO 4488 J=JOLD,NJM1
  DYC(I,J)=DYC(I,NJ)+(DYC(I,NJF1)-DYC(I,NJ))*25*(NJ-J)*(1.+
1 (NJ-J))/FLOAT(JCAP+1)
4488 CONTINUE
DO 4499 I=1,NJ
  DYIDE(I,NJ)=DYIDE(I,JOLD)
  DETADF(I,NJ)=DETADF(I,JOLD)
DO 4499 J=JOLD,NJM1
  APEAXY(I,J)=DYC(I,J)*DYC(I,J)
  APEAXY(I,NJF1)=DYC(I,NJF1)*DYC(I,NJF1)
  APEAXY(I,NJ)=0.0
  DYIDE(I,J)=DYIDE(I,NJ)+(DYIDE(I,NJF1)-DYIDE(I,NJ))/FLOAT(JCAP
1 +1)*.25*(NJ-J)*(1.+(NJ-J))
  DETADF(I,J)=DETADF(I,NJ)+(DETADF(I,NJF1)-DETADF(I,NJ))/FLOAT(
1 JCAP+1)*.25*(NJ-J)*(1.+(NJ-J))
  P(I,J)=P(I,NJF1)

```

```

4409 P(I,NJ)=P(I,NJF1)
DO 4411 J=NJF1,NJM1
DO 4411 I=2,NIM1
WFF1=DYC(I-1,J)/(DYC(I,J)+DYC(I-1,J))
WFF2=DYC(I-1,J+1)/(DYC(I,J+1)+DYC(I-1,J+1))
4411 WFF(I,J)=.5*(WFF1+WFF2)
DO 4422 I=2,NIM1
4422 WFF(I,NJ)=DYC(I-1,NJ)/(DYC(I-1,NJ)+DYC(I,NJ))
DO 4433 J=NJF1,NJ
WFE(1,J)=WFF(NJM1,J)
4433 WFE(NT,J)=WFE(2,J)
DO 4444 I=2,NIM1
WFM(I,NJ)=1.
DO 4444 J=NJF1,NJM1
WFM1=DYC(I+1,J-1)/(DYC(I+1,J)+DYC(I+1,J-1))
WFM2=DYC(I,J-1)/(DYC(I,J)+DYC(I,J-1))
4444 WFM(I,J)=.5*(WFM1+WFM2)
DO 1411 J=NJF1,NJ
WFM(1,J)=WFM(NJM1,J)
1411 WFM(NT,J)=WFM(2,J)
4366 CONTINUE
INDEX=5
IF (INCALT) CALL CALCT
IF (KASH.EQ.2.AND.NITER.GT.MAXIT1) GO TO 4196
NJJ=NJ
IF (IROTH.EQ.1) NJ=JG
INDEX=3
IF (INCALK) CALL CALCTE
INDEX=4
IF (INCALD) CALL CALCFD
IF (IROTH.EQ.1) NJ=NJJ
IF (IROTH.EQ.1) NJM1=NJJ-1
IF (IROTH.EQ.1) NJM2=NJJ-2
IF (IROTH.EQ.1) NJMFW=NJJ+N1D
IF (IROTH.EQ.1) NJMFW1=NJJ+N1D-1
4196 CONTINUE
IF (INCALT) GO TO 1739
GO TO 1738
1739 CONTINUE
DO 1734 I=2,NIM1
T(I,NJ)=T(I,NJM1)+QFLUX/THCOND*(.5*DYC(I,NJM1))
1734 CONTINUE
DO 9876 I=1,NT
DO 9876 J=1,NJ
T(I,1)=F1D(N1D+1,5)
T(I,2)=F1D(N1D+2,5)
T(1,J)=T(NIM1,J)
9876 T(NJ,J)=T(2,J)
IF (KASH.EQ.0.AND.NITER.GT.MAXIT1) GO TO 4197
1738 CONTINUE
DO 2914 I=1,NJ
DO 2914 J=1,NJ
IF (INDEX.EQ.0) GO TO 3586
H(I,1)=F1D(N1D+1,1)
J(I,1)=F1D(N1D+1,2)
T(I,1)=F1D(N1D+1,5)
H(I,2)=F1D(N1D+2,1)

```



```

      U(I,2)=F1D(N1D+2,2)
      T(I,2)=F1D(N1D+2,5)
      TE(I,1)=F1D(N1D+1,3)
      ED(I,1)=F1D(N1D+1,4)
      GO TO 3585
3586 DTST=RA+.5*DYC(I,2)
      U(I,1)=U(I,2)*RA/DIST
      W(I,1)=W(I,2)*((RR-RA)/(RP-DIST))*(.1/.7)
      TE(I,1)=TE(I,2)
      ED(I,1)=ED(I,2)
3585 CONTINUE
      U(1,J)=U(NIM1,J)
      U(NT,J)=U(2,J)
      W(1,J)=W(NIM1,J)
      W(NT,J)=W(2,J)
      T(1,J)=T(NIM1,J)
      T(NT,J)=T(2,J)
      TE(1,J)=TE(NIM1,J)
      TE(NT,J)=TE(2,J)
      ED(1,J)=ED(NIM1,J)
      ED(NT,J)=ED(2,J)
      TE(1,NJ)=0.0
      ED(1,NJ)=0.0
2914 CONTINUE
      ILEMSC=1
      IF(IUPRO) CALL PROPS
C-----INTERMEDIATE OUTPUT-----
      RESOPU=RESOPU/SNORU
      RESORV=RESOPV/SNORV
      RESOPW=RESOPW/SNORW
      RESORM=RESORM/SNORM
      RESORT=RESORT/SNORT
      RESORK=RESORK/SNORK
      RESORD=RESORD/SNORD
      DO 2317 I=1,NJ
      DO 2317 J=1,NJ
      RESV(I,J)=RESV(I,J)/SNORV
      RESW(I,J)=RESW(I,J)/SNORW
      RESM(I,J)=RESM(I,J)/SNORM
2317 RESU(I,J)=RESU(I,J)/SNOPU
      WRITE(55) U,V,W
      RETURN 55
      WRITE(22) U,V,W,P,VIS,NITER,F1D,VIS1D,T,TE,ED,SNORK,SNOPD,VISV
      RETURN 22
      WRITE(99) GEUN,PRODD
      RETURN 99
      WRITE(6,311) NITER,RESORU,RESORV,RESOPW,RESORM,RESORT,
1 RESORK,RESORD,
1 U(IMON,JMON),V(IMON,JMON),W(IMON,JMON)
1 P(IMON,JMON),TE(IMON,JMON)
      GO TO 4198
4197 CONTINUE
      RESORT=RESORT/SNORT
      WRITE(6,666) NITER,RESORT,T(IMON,JMON),T(2,NJ)
666 FORMAT(1H,I5,3X,1P1F9.2,3X,1P2E10.2)
4198 CONTINUE
      IF(MOD(NITER,INDPRI).NE.0) GO TO 301

```

```

WRITE(6,3301) NITER
3301 FORMAT(1H,14)
IF(INCALU) CALL PRINT(2,1,NT,NJ,IT,IT,X,Y,U,HEDU)
IF(INCALV) CALL PRINT(1,2,NT,NJ,IT,IT,X,Y,V,HEDV)
IF(INCALW) CALL PRINT(1,1,NT,NJ,IT,IT,X,Y,W,HEDW)
IF(INCALP) CALL PRINT(1,1,NT,NJ,IT,IT,X,Y,P,HEDP)
IF(INCAIT) CALL PRINT(1,1,NT,NJ,IT,IT,X,Y,T,HEDT)
J1=J1
IF(ITHH.EQ.1) NJ=JG
IF(INCALK) CALL PRINT(1,1,NT,NJ,IT,IT,X,Y,TF,HEDK)
IF(INCALD) CALL PRINT(1,1,NT,NJ,IT,IT,X,Y,FD,HEDD)
J1=J1
IF(INPRO) CALL PRINT(1,1,NT,NJ,IT,IT,X,Y,VIS,HEDMU)
WRITE(6,310) IMON,IMUN
301 CONTINUE

```

-----TERMINATION TESTS-----

```

IF(MASK.EQ.0.AND.NITER.GT.MAXIT1) GO TO 331
SORCE=AMAX1(RESORU,RESOPV,RESORM,RESORW,RESORP,RESORD)
IF(NITER.EQ.MAXIT) GO TO 302
IF(SORCE.LE.SORMAX) MAXIT1=NITER
GO TO 300
331 CONTINUE
IF(NITER.EQ.MAXIT) GO TO 302
SORMAX=1.EF-5
IF(RESORP.GT.SORMAX) GO TO 300
302 CONTINUE

```

CHAPTER 4 4 4 4 4 4 FINAL OPERATIONS AND OUTPUT 4 4 4 4 4 4

```

IF(INCALU) CALL PRINT(2,1,NT,NJ,IT,IT,X,Y,U,HEDU)
IF(INCALV) CALL PRINT(1,2,NT,NJ,IT,IT,X,Y,V,HEDV)
IF(INCALW) CALL PRINT(1,1,NT,NJ,IT,IT,X,Y,W,HEDW)
IF(INCALP) CALL PRINT(1,1,NT,NJ,IT,IT,X,Y,P,HEDP)
IF(INCAIT) GO TO 114
GO TO 113
114 CONTINUE
IF(INCAIT) CALL PRINT(1,1,NT,NJ,IT,IT,X,Y,T,HEDT)
113 CONTINUE
J1=J1
IF(ITHH.EQ.1) NJ=JG
IF(INCALK) CALL PRINT(1,1,NT,NJ,IT,IT,X,Y,TF,HEDK)
IF(INCALD) CALL PRINT(1,1,NT,NJ,IT,IT,X,Y,FD,HEDD)
J1=J1
IF(INPRO) CALL PRINT(1,1,NT,NJ,IT,IT,X,Y,VIS,HEDMU)
IF(INDEX.EQ.0) GO TO 222
NINEW=NJ+N10
DO 539 I=1,5
IF(I.EQ.3.AND.IPOTH.EQ.1) NINEW=JG+N10
IF(I.EQ.4.AND.IPOTH.EQ.1) NINEW=JG+N10
IF(I.EQ.5) NINEW=NJ+N10
WRITE(6,503) (I,(F10(I,1),J=1,NINEW))
539 CONTINUE
N103=N10+3
WRITE(6,545) (VIS10(I),J=1,N103)
545 FORMAT(1H,1P1(F10,2)
500 FORMAT(15,(/5,10F10,4))
FINNY=0

```

```

FLOWTOT=0.
NJNEW1=N1D+NJM1
DO 9544 I=2,NJM1
DO 9545 J=2,NJNEW1
- IF (Y.EQ.2.AND.J.LT.(N1D+2)) GO TO 1546
IF (J.LT.(N1D+2)) GO TO 9545
JJ=J-N1D
FLUX=FLUX+DEN(I,JJ)*W(I,JJ)*T(I,JJ)*AREAXY(I,JJ)
1*FLOAT(NFLUT)
FLOWTOT=FLOWTOT+DEN(I,JJ)*W(I,JJ)*AREAXY(I,JJ)*FLOAT
1(NFLUT)
GO TO 9545
1546 CONTINUE
IF (J.NE.N1D1) FLOWTOT=FLOWTOT+DENSIT*F1D(J,2)*2.*PI*R1D(J)*
1.5*(R1D(J+1)-R1D(J-1))
IF (J.EQ.N1D1) F1DW=.75*F1D(J,2)+.25*F1D(J-1,2)
IF (J.EQ.N1D1) F1DT=.75*F1D(J,5)+.25*F1D(J-1,5)
IF (J.EQ.N1D1) FLOWTOT=FLOWTOT+DENSIT*F1DW*2.*PI*
1*.5*(R1D(J)-R1D(J-1))+.5*(R1D(J)+R1D(J-1))
IF (J.NE.N1D1) FLUX=FLUX+DENSIT*F1D(J,2)*F1D(J,5)*2.*PI*R1D(J)
1*.5*(R1D(J+1)-R1D(J-1))
IF (J.EQ.N1D1) FLUX=FLUX+DENSIT*F1DW*F1DT*2.*PI*
1(R1D(J)-R1D(J-1))+.5*(R1D(J)+R1D(J-1))
9545 CONTINUE
9546 CONTINUE
FLUX=FLUX+PI*(.5*R1D(2))*2*F1D(1,2)*F1D(1,5)*DENSIT
FLOWTOT=FLOWTOT+PI*(.5*R1D(2))*2*F1D(1,2)*DENSIT
THULK=FLUX/FLOWTOT
DO 5634 I=2,NJM1
DT=T(I,NJ)-THULK
ANUSSE(I)=DEFLUX*SWET*FLOAT(NFLUT)/(THCOND*DT*PI)
5634 CONTINUE
ANUSS=0.0
DO 5635 I=2,NJM1
5635 ANUSS=ANUSS+ANUSSE(I)+DXC(I,NJ)
ANUSS=ANUSS/SWET
2222 CONTINUE
REY=DENSIT*WMEAN*HYDDTA/VISCOS
FRE=-DPDZ/(.5*DENSIT*WMEAN**2)*HYDDTA
WRITE(6,637) DPDZ,FRE,WMEAN
SWET=SWET*FLOAT(NFLUT)
TOTA=TARFA*FLOAT(NFLUT)+PI*PA*RA
WRITE(6,1637) TOTA,HYDDTA,SWET,REY
1637 FORMAT(6H TOTA=,F10.3,8H HYDDTA=,F10.3,6H SWET=,F10.3
1,5H REY=,F10.3)
637 FORMAT(5X,25HTOTAL PRESSURE DROP=,F10.3/5X,
125HERICTION FACTOR=,F10.3,15H MEAN VELOCITY=,F10.3)
WRITE(6,8956) (THULK,(ANUSSE(I),I=2,NJM1))
8956 FORMAT(/,5X,7H THULK=,F10.3//,5X,10H ANUSSELT=,/,5X,(10F10.3))
WRITE(6,8876) ANUSS
8876 FORMAT(/,5X,8HANUSSELT=,F10.3)
WRITE(6,683)
683 FORMAT(/5X,28HSTREAM FUNCTION DISTRIBUTION/)
DO 141 I=1,NJM1
141 PSI(I,1)=0.
DO 142 I=2,NJM1
DO 142 I=1,NJM1

```

```

142   PSI(I,J)=PSI(I,J-1)+H(I+1,J)*NYC(I+1,J)
      DO 122 JJ=2,NJ
      J=JJ-JJ+1
122   WRITE(6,125) (PSI(I,J),I=1,NIM1)
125   FORMAT(5X,12E10.4)
      WRITE(6,570)
570   FORMAT(/5X,12HTAUXS VALUES)
      WRITE(6,571) (TAUXS(I),I=1,N1)
571   FORMAT(10E12.4)
      WRITE(6,572)
572   FORMAT(/5X,12HTAUXN VALUES)
      WRITE(6,571) (TAUXN(I),I=1,N1)
      WRITE(6,573)
573   FORMAT(/5X,12HTAU7S VALUES)
      WRITE(6,571) (TAU7S(I),I=1,N1)
      WRITE(6,574)
574   FORMAT(/5X,12HTAU7N VALUES)
      WRITE(6,571) (TAU7N(I),I=1,N1)
      WRITE(6,575)
575   FORMAT(/5X,13HYPLUS VALUES)
      WRITE(6,571) (YPLUS(I),I=1,NT)
      WRITE(6,576)
576   FORMAT(/5X,13HYPLUSN VALUES)
      WRITE(6,571) (YPLUSN(I),I=1,NT)
C-----FORMAT STATEMENTS-----
310   FORMAT(1H0,7HITER ,1H1,17(1H-),29HABSOLUTE RESIDUAL SOURCE SUMS,
      117(1H-),1H1,6X,1H1,2(1H-),34HFIELD VALUES AT MONITORING LOCATION(,
      1T2,1H,,1T2,1H),3H--1,,7X,3HNO,,5X,4HMMOM,5X,4HVMOM,5X,4HWMOM
      1,5X,4HMASS,5X,4HENER,5X,4HPKE,,5X,4HDTSC,16X,1H1,9X,1HVV,9X,1HVV,
      19V,1HP,9X,2HTE/)
311   FORMAT(1H,15,3X,1P7E9.2,1CX,1P5F10.2)
      STOP
      END

```

## SUBROUTINE INIT

COMMON

```

1      RESORU,URFU,RESORV,URFV,RESORM,RESORW,URFW,
1      URFK,RESORT,URFT,RESORK,URFK,RESORD,URFD,
1      RFSU(25,25),RFSV(25,25),RFSW(25,25),RFSM(25,25),
1      DU(25,25),DV(25,25),DW(25,25),U(25,25),V(25,25),
1      J(25,25),P(25,25),T(25,25),TE(25,25),ED(25,25),
1      PP(25,25),DFH(25,25),VIS(25,25),AN(25,25),AS(25,25),
1      AF(25,25),AU(25,25),AH(25,25),AD(25,25),CF(25),CD(25,25),
1      CCE(25),CCU(25,25),AP(25,25),SU(25,25),SP(25,25),DXC(25,25),
1      DYC(25,25),DZC(4),WFE(25,25),WFN(25,25),WFD(4),
1      ARFAXY(25,25),FID(50,5),U1D,WMEAN,INDEX,HYDDIA,PAF,P1D(50),
1      VFLIN,TJN,TWALL,FLOWIN,GRFAT,
1      IIRFVIS,VISCOS,DENSIT,PRAUNT,
1      PRTE,PRFD,CMU,CPT,C11,C21,CAPPA,ELOG,ALAMPA,
1      NSWPII,NSWPIV,NSWPIW,NSWPP,NSWPT,
1      NSWPK,NSWPD,
1      IPREF,JPREF,KPREF,INDCOS
COMMON TAUXS(25),TAUXM(25),TAUZE(25),TAUZN(25),
1      YPLUSS(25),YPLUSN(25)
1      TT,JT,N1,NJ,NIM1,NJM1
1      SWFT,FLOWTOT,CPW,QFLUX,FLOWT
1      N1,N2
1      PA,RE,THETA,AH,DPDZ,FLOWAX,DXIDE(25,25),DETADE(25,25),PIH
1      DRDXT(25,25),DRDETA(25,25),HTRP(25,25)
1      PT,UTN,FLOWU
1      SHALL,SIMS,SHIN,TNIMP,DXY(25,25),DYDX(25,25)
LEVEL 2,III
COMMON RLK2/III(25,25),VV(25,25),AMU(25,25),ASU(25,25),
1      AFU(25,25),AWU(25,25),ADU(25,25),AHU(25,25),
1      ANV(25,25),ASV(25,25),AFV(25,25),AWV(25,25),
1      CONT(25,10),VBN(25),JTS,
1      ADV(25,25),AHV(25,25),AA(25)
1      JG,IROTH,TER(25,2),EDB(25,2),PRODN(50),GENN(25,25)
1      PRANDI,GIT(25,25),AMHIS
1      PRDN(25,25),AK7(25,25),AKD(25,25),AKA(25,25),RVT(25,25),AKF
1      AKFT,AKFTD,AKCTD,F1P(25),F1VZ(25),F1KD(25),F1VA(25),F1RVT(25)
1      NOIMP,CMUA(25,25),CMUR(25)
1      NOIMR2
1      APII(25,25),APV(25,25),RR(25,25),ANGL(25,25)
1      KASII,HASH
1      VISV(25,25),VA(25,25),VH(25,25),VC(25,25)
1      PSC(5),IMEG,MAYIT2
1      PRS(25,25),PRE,NTTFR,NAXIT
1      TIFNSC,VIS1D(50),XPLL(25,25)

```

C  
CHAPTER 1 1 1 1 1 CALCULATE GEOMETRICAL QUANTITIES 1 1 1 1 1  
C

```

C-----WEIGHTING AT H-LOCATIONS-----
DO 501 J=2,NJM1
DO 501 J=3,NIM1
WFF1=DXC(I-1,J)/(DXC(I,J)+DYC(I-1,J))
WFF2=DXC(I-1,J+1)/(DXC(I,J+1)+DYC(I-1,J+1))
501 WFF(I,J)=.5*(WFF1+WFF2)
DO 571 I=3,NIM1
571 WFE(I,NJ)=DYC(I-1,NJ)/(DXC(I-1,NJ)+DXC(I,NJ))
C-----WEIGHTING AT V-LOCATIONS-----

```

```

      DO 631 I=1,NJ
      DO 631 J=1,NJ
631  WFN(I,J)=0.0
      DO 511 I=2,NIM1
      WFN(I,NJ)=1.0
      WFN(I,2)=0.0
      DO 511 J=3,NJM1
      WFN1=DYC(I+1,J-1)/(DYC(I+1,J)+DYC(I+1,J-1))
      WFN2=DYC(I,J-1)/(DYC(I,J)+DYC(I,J-1))
511  WFN(I,J)=.5*(WFN1+WFN2)
      DO 897 J=2,NJ
      WFN(1,J)=WFN(NIM1,J)
897  WFN(NJ,J)=WFN(2,J)
C    WEIGHTING AT 4-LOCATIONS
      WFD(1)=1.0
C
C
C    CHAPTER 2 2 2 2 2 SET VARIABLES EQUAL TO ZERO 2 2 2 2 2
C
      RESORH=0.0
      RESORV=0.0
      RESORW=0.0
      RESORX=0.0
      RESORT=0.0
      RESORK=0.0
      RESORD=0.0
      DO 710 I=1,NJ
      DO 710 J=1,NJ
      SH(I,J)=0.0
      SP(I,J)=0.0
      RESH(I,J)=0.0
      RESV(I,J)=0.0
      RESW(I,J)=0.0
      RESX(I,J)=0.0
      R(I,J)=0.0
      V(I,J)=0.0
      W(I,J)=0.0
      P(I,J)=0.0
      TF(I,J)=0.0
      EP(I,J)=0.0
      PP(I,J)=0.0
      III(I,J)=0.0
      VV(I,J)=0.0
      AMH(I,J)=0.0
      ASH(I,J)=0.0
      ADH(I,J)=0.0
      AHH(I,J)=0.0
      AFH(I,J)=0.0
      AMV(I,J)=0.0
      ASV(I,J)=0.0
      ADV(I,J)=0.0
      AMV(I,J)=0.0
      ASV(I,J)=0.0
      AFV(I,J)=0.0
      AMV(I,J)=0.0
      ASV(I,J)=0.0
      AFV(I,J)=0.0
      AMV(I,J)=0.0
      ASV(I,J)=0.0
      AFV(I,J)=0.0

```

```

T(I,J)=0.0
DU(I,J)=0.0
DV(I,J)=0.0
DW(I,J)=0.0
PDD(I,J)=0.0
AK7(I,J)=0.09
AKD(I,J)=0.1
AKA(I,J)=0.0
RVT(I,J)=0.0
CMIA(I,J)=0.09
DEN(I,J)=0.0
VIS(I,J)=0.0
VTSV(I,J)=VTSFOS
VA(I,J)=0.0
VD(I,J)=0.0
VF(I,J)=0.0
700 CONTINUE
N103="10+3
DO 717 J=1,N103
F1P(J)=0.0
F1K7(J)=0.09
F1KD(J)=0.1
F1KA(J)=0.0
F1RVT(J)=0.0
CMIA(J)=0.09
707 CONTINUE
PFTIIR"
END

```

SUBROUTINE PADCUR  
COMMON

```

1      RESORII,UREII,RESORV,URFV,RESORM,RESORW,UPFW,
1      URFP,RESORT,URFT,RESORP,UPFK,RESOPD,URFD,
1      RESII(25,25),RESV(25,25),RESW(25,25),RESM(25,25),
1      DU(25,25),DV(25,25),DW(25,25),U(25,25),V(25,25),
1      W(25,25),P(25,25),T(25,25),TE(25,25),FD(25,25),
1      PP(25,25),DEN(25,25),VIS(25,25),AN(25,25),AS(25,25),
1      AF(25,25),AW(25,25),AU(25,25),AD(25,25),CE(25),CD(25,25),
1      CCE(25),CCD(25,25),AP(25,25),SU(25,25),SP(25,25),DXC(25,25),
1      DYC(25,25),D7C(4),WFE(25,25),WFN(25,25),WFD(4),
1      AREAXY(25,25),F1D(50,5),N1D,WMEAN,INDEX,HYDDIA,PAR,P1D(50),
1      VFLII,TJN,TWALL,FLOWIN,GREAT,
1      URFVIS,VISCOS,DENSIT,PRANDT,
1      PRTE,PRFD,CMII,CDT,C1M,C2M,CAPPA,ELOG,ALAMDA,
1      NSWPII,NSWPIV,NSWPIW,NSWPP,NSWPT,
1      NSWPK,NSWPD,
1      IPREF,JPREF,KPREF,INDCOS
COMMON TAUXS(25),TAUXN(25),TAUYS(25),TAUYN(25),
1      YPLUSS(25),YPLUSN(25)
1      IT,JT,N1,NJ,NIM1,NJM1
1      SWET,FLOWTOT,CPW,QFLUX,FLOWT
1      N1,N2
1      RA,RP,THETA,AR,DPDZ,FLOWAX,DXIDF(25,25),DETADF(25,25),PIH
1      DRDXI(25,25),DPDETA(25,25),HTHR(25,25)
1      PI,NTN,FLOWW
1      SHALI,SUMS,SUMD,TNIMP,DXDY(25,25),DYDX(25,25)
1      LEVEL 2,III
COMMON PLK2/III(25,25),VV(25,25),ANII(25,25),ASII(25,25),
1      AEII(25,25),AWII(25,25),ADII(25,25),AUII(25,25),
1      ANIV(25,25),ASV(25,25),AFV(25,25),AWV(25,25),
1      CONT(25,10),VPN(25),JTS,
1      ADV(25,25),AIV(25,25),AA(25)
1      JG,IBOTH,TEP(25,2),FDR(25,2),PRODD(50),GFENN(25,25)
1      PRANDI,GHT(25,25),AMISS
1      PRODD(25,25),AK7(25,25),AKD(25,25),AKA(25,25),RVT(25,25),AKF
1      AKFT,AKFTD,AKCTD,F1P(25),F1P7(25),F1KD(25),F1KA(25),F1RVT(25)
1      PCHHP,CHHA(25,25),C1UR(25)
1      NOIMR2
1      APII(25,25),APV(25,25),PR(25,25),ANGI(25,25)
1      KASH,NASH
1      VISV(25,25),VA(25,25),VB(25,25),VC(25,25)
1      PSC(5),IMFG,MAXIT2
1      PDS(25,25),KBU,NTTER,MAXIT
1      TLFHSC,VISID(50),XPLI(25,25)
C-----CALCULATION OF RADII OF CURVATURE OF COORDINATE LINES-----
DO 50 I=2,NJM1
DO 50 J=2,NJM1
DXDY(I,J)=(DXC(T,J+1)-DXC(I,J))/(.5*(DYC(T,J)+DYC(I+1,J)))
C/(.5*(DXC(I,J)+DXC(T,J+1)))
DYDX(I,J)=(DYC(T+1,J)-DYC(I,J))/(.5*(DXC(T,J)+DXC(I,J+1)))
C/(.5*(DYC(I,J)+DYC(T+1,J)))
CONTINUE
50 DO 60 J=2,NJM1
I=1
DYDY(T,J)=DXDY(NJM1,J)
I=NT

```



```

      DYDX(I,J)=DXDY(2,J)
60) CONTINUE
      DO 70 I=2,NTM1
        J=1
        DYDX(I,J)=DYDX(I,J+1)
        J=NJ
70) DYDX(I,J)=DYDX(I,J-1)
      CALL MODRAD
      RETURN
      END

      SUBROUTINE PROPS
C
CHAPTER 0 0 0 0 0 0 0 0 PRELIMINARIES 0 0 0 0 0 0 0
C
      COMMON
1      HRSORH,HREFH,RESORV,HREFV,RESORM,RESOPW,HREFV,
1      HREFP,RESORT,HREFT,RESORK,HREFK,RESORD,HREFD,
1      RESU(25,25),RESV(25,25),RESW(25,25),RESM(25,25),
1      DU(25,25),DV(25,25),DW(25,25),U(25,25),V(25,25),
1      W(25,25),P(25,25),T(25,25),TE(25,25),FD(25,25),
1      PP(25,25),UEN(25,25),VIS(25,25),AN(25,25),AS(25,25),
1      AF(25,25),AW(25,25),AH(25,25),AD(25,25),CF(25),CD(25,25),
1      CCF(25),CCD(25,25),AP(25,25),SU(25,25),SP(25,25),DXC(25,25),
1      DYC(25,25),D7C(4),WFE(25,25),WFH(25,25),WFD(4),
1      ARFAXY(25,25),F1D(50,5),H1D,WMEAN,INDEX,HYDRIA,RAP,R1D(50),
1      VFLIN,TIN,TWALL,FLOWIN,GREAT,
1      HREFVIS,VISCOS,DENSIT,PRANDT,
1      PRTE,PREO,CMU,COT,C1H,C2H,CAPPA,ELOG,ALAMDA,
1      NSWPU,NSWPUV,NSWPUW,NSWPP,NSWPT,
1      NSWPK,NSWPD,
1      IPREF,JREF,KREF,INDCOS
      COMMON TAUXS(25),TAUXM(25),TAUYS(25),TAUYM(25),
1      YPLUSS(25),YPLUSN(25),
1      IT,JT,N1,N2,NIM1,NJM1
1      ,SWET,FLOWTOT,CPW,REFLUX,FLOUT
1      ,N1,N2
1      ,RA,RR,THETA,AA,DPUT,FLOWAX,DXIDE(25,25),DETANF(25,25),PIH
1      ,DRDXI(25,25),DRDETA(25,25),MTHP(25,25)
1      ,PI,WTH,FLOWW
1      ,SIAL,SUMS,SIMP,INIMP,DXDY(25,25),DYDX(25,25)
      LEVEL 2,III
      COMMON R1K2/III(25,25),VV(25,25),ANU(25,25),ASU(25,25),
1      AFU(25,25),AWU(25,25),ADU(25,25),AUU(25,25),
1      ANV(25,25),ASV(25,25),AFV(25,25),AWV(25,25),
1      COUT(25,10),VHL(25),JTS,
1      ADV(25,25),AIV(25,25),AA(25)
1      ,JG,INTH,TEP(25,2),EDP(25,2),PRDN(50),GENN(25,25)
1      ,PRANDI,GHT(25,25),AMUSS
1      ,PRDU(25,25),AKZ(25,25),AKD(25,25),AKA(25,25),PVT(25,25),AKF
1      ,AKET,AKETO,AKETO,F1P(25),F1VZ(25),F1KD(25),F1KA(25),F1RVT(25)
1      ,NOIMP,CENH(25,25),CHHR(25)
1      ,NOIMP?
1      ,ADU(25,25),APV(25,25),PR(25,25),ANGL(25,25)
1      ,KASH,NASH
1      ,VISV(25,25),VA(25,25),VB(25,25),VC(25,25)
1      ,RSC(5),IMER,MAYIT2
1      ,HRS(25,25),RRR,HITER,MAYIT
1      ,LEHSC,VISID(50),XPLI(25,25)
C*****
C*      CALCULATION OF EFFECTIVE VISCOSITY AND THERMAL
C*      DIFFUSIVITY FOR THE 2-D REGION OF THE SOLUTION
C*      DOMAIN
C*****
CHAPTER 1 1 1 1 1 1 1 TURBULENT VISCOSITY 1 1 1 1 1 1
C
C-----CALCULATION OF EFFECTIVE VISCOSITY FROM MIXING LENGTH HYPOTHESIS-----

```

```

NYW=.11*(PB-AH)
EYCHAT=VISCOS/PRANDT
JGP1=JG+1
JGM1=JG-1
IF(JHOTH.EQ.2) GO TO 1238
IF(IROTH.EQ.0) JGS=2
IF(IROTH.EQ.1) JGS=JGM1
DO 100 I=2,NIM1
DO 100 J=JGS,NJM1
VTSOLD=VTS(I,J)
WN=W(I,J)*(1.-WFN(I,J+1))+W(I,J+1)*WFN(I,J+1)
WS=W(I,J)*WFN(I,J)+W(I,J-1)*(1.-WFN(I,J))
DWDYV=(WN-WS)/(.5*(DYC(I,J)+DYC(I+1,J)))
RLV=.25*(XMLL(I,J)+XMLL(I+1,J)+XMLL(I,J+1)+XMLL(I+1,J+1))
IF(TIFHSC.EQ.C) GO TO 3225
RLV=RLV*.4187*(1.-EXP(-RLV*SQRT(DENSIT)*SQRT(ABS(TAUZN(I)))/VISCOS
1/2*...))
3225 CONTINUE
VTS(I,J)=DEN(I,J)*RLV*RLV*ABS(DWDYV)+VISCOS
C-----UNDER= RELAX VISCOSITY -----
70 VTS(I,J)=URFVTS*VTS(I,J)+(1.-URFVTS)*VTSOLD
100 CONTINUE
1238 CONTINUE
C-----CALCULATION OF EFFECTIVE VISCOSITY FROM K-E MODEL OR SIMPLIFIED
C ASH MODEL-----
IF(IROTH.EQ.0) GO TO 1037
JGL2=JG-2
IF(IROTH.EQ.1) JGL=JGM2
IF(IROTH.EQ.2) JGL=NJM1
DO 111 I=2,NIM1
DO 111 J=2,JGL
VTSOLD=VTS(I,J)
IF(NITER.LT.NCUMR2) GO TO 4873
IF(KASH.EQ.C) GO TOY 4873
IF(KASH.EQ.2) GO TO 4878
IF(PRANDL.EQ.C.70R) AKFC=C.0001
IF(PRANDL.EQ.C.703) AKPC=0.0001
AKA(I,J)=AKPC*(TF(I,J)/(ED(I,J)+SMALL))**2*DXYDY(I,J)*(2./3.*TF(I,
1,J)
1+ (.5*(U(I,J)+U(I+1,J))**2)*(T(I,J+1)-T(I,J-1))/(DYC(I,J)+DYC(I+1,
1,J))
AKDDYD=(.25*(U(I,J)+U(I,J+1)+U(I+1,J)+U(I+1,J+1))-.25*(U(I,J)+
1U(I+1,J)+U(I,J-1)+U(I+1,J-1)))/(.5*(DYC(I,J)+DYC(I+1,J)))
PRDD(I,J)=GFHN(T,J)/APFAXY(T,J)/DEN(I,J)
AKC=AKFT*(1.-AKFT*AKF+AKA(I,J))/(1.-AKFTD*AKCTD*AKA(I,J))*(1.-
1AKFT*AKF*
1AKA(I,J))+AKFTD**2*(TF(I,J)/(ED(I,J)+SMALL))**2*DXYDY(I,J)*.5*(
1U(I,J)+U(I+1,J))*AKDDYD)
AKD(I,J)=AKC*2./3.*(1.-AKF/(ED(I,J)+SMALL)*PRDD(I,J))/(1.-2.*
1AKA(I,J)
1*AKC*AKF/(ED(I,J)+SMALL))
RVT(I,J)=-AKD(I,J)*TF(I,J)**2/(ED(I,J)+SMALL)*(T(I,J+1)-T(I,
1,J-1))/(DYC(I,J)+DYC(I+1,J))
AKH=AKF*(1.-AKFT*AKFTD*AKA(I,J))/(1.-AKF*AKFT*AKA(I,J))+(AKF*AKFT
1*AKFTD**2
1*AKA(I,J)**2*AKCTD*(1.-AKFT*AKF*AKA(I,J))-AKF*AKFT*AKFTD**3*AKA(I,
1,J)*DXYD(

```

```

1(I,J)*.5*(U(I,J)+U(I+1,J))*AKDUDY*(TE(I,J)/(FD(I,J)+SMALL))*2)/(1.
1-AKF*AKFT*AKA(I,J))/((1.-AKFT*AKF*AKA(I,J))*(1.-AKFTD*AKCTD*AKA(
1(I,J))+AKFTD
1**2*(TE(I,J)/(ED(I,J)+SMALL))*2*DXDY(I,J)*.5*(U(I,J)+U(I+1,J))*
1AKDUDY)
AKZ(I,J)=AKF*(2./3.*(1.-AKF/(FD(I,J)+SMALL)*PRDD(I,1))-AKF/(ED(I,J)
1)+
1SMALL)*2.*AKRC*DXDY(I,J)*(2./3.*TE(I,J)+.5*(U(I,J)+U(I+1,J)))*2
1)*RVT(I,J))
IF(J.LT.(JG-4)) CMHA(I,J)=AKZ(I,J)
IF(J.GE.(JG-4)) CMHA(I,J)=U.00
GO TO 4R73
4R78 CONTINUE
AKDUDY=(.25*(U(I,J)+U(I,J+1)+U(I+1,J)+U(I+1,J+1))-.25*(U(I,J)+
1U(I+1,J)+U(I,J-1)+U(I+1,J-1)))/(.5*(DYC(I,J)+DYC(I+1,J)))
RKDUDY=.5*(U(I,J)+U(I+1,J))*DXDY(I,J)
IF(J.GE.(JG-4)) CMUA(I,J)=U.00
AK7(I,J)=2./3.*(1.-.7/3)*.7/3./(1.+1.7/9.*RKDUDY*(TE(I,J)/
1FD(I,J))*2*(BKDUDY+.7*AKDUDY))
IF(J.LT.(JG-4)) CMUA(I,J)=AK7(I,J)
4R73 CONTINUE
IF(KASH.EQ.0) CMH=U.00
IF(KASH.EQ.0) CMUA(I,J)=U.00
IF(MITER.LT.NOUN*2) VTS(I,J)=CMH
1*DEN(I,J)*TE(I,J)**2/(FD(I,J)+SMALL)+VISCOS
IF(MITER.GE.NOUN*2) VTS(I,J)=CMUA(I,J)
1*DEN(I,J)*TE(I,J)**2/(FD(I,J)+SMALL)+VISCOS
VTS(I,J)=URFVIS*VTS(I,J)+(1.-URFVIS)*VISOLD
111 CONTINUE
1037 CONTINUE
C
CHAPTER 2 2 2 2 VISCOSITIES AT BOUNDARIES 2 2 2 2 2 2 2
C
DO 150 I=2,NIP1
J=1
VTS(1,J)=VIS(I,J+1)
J=NJ
VTS(I,J)=VISCOS
150 CONTINUE
DO 170 J=1,NJ
VTS(1,J)=VIS(NIP1,J)
VTS(JI,J)=VIS(2,J)
170 CONTINUE
C-----CUBIC SPLINE INTERPOLATION FOR NEAR WALL REGION-----
JSTR=NJ/2+1
UJJ=(UJ-JSTR-1)/2
DO 335 J=2,NIP1
DO 335 JJ=1,NJJ
TJ=2*JJ-1
J=NJ-IJ
RJV=.5*(RR(T,NJ)+RR(I+1,NJ))-0.25*(RR(I,J)+RR(I+1,J)+RR(I+1,J+1)
1+RR(I,J+1))
IF(J.LT.NJH1) RJVP1=.5*(RR(T,NJ)+RR(I+1,NJ))-0.25*(RR(I,J+1)
1+RR(I+1,J+1)+RR(I+1,J+2)+RR(I,J+2))
IF(J.EQ.NJH1) RJVP1=0.0
RJVP1=.5*(RR(T,NJ)+RR(I+1,NJ))-0.25*(RR(T,J)+RR(I+1,J)+RR(T,J-1)+
1RR(I+1,J-1))

```

```

VC(I,JJ)=VIS(I,J-1)/(PJV-RJVM1)/(RJVP1-RJVM1)+VIS(I,J+1)/(RJVP1-
1RJVP1)/(RJVP1-RJVM1)-VIS(I,J)/(RJVP1-RJVP1)/(PJV-RJVM1)
VA(I,JJ)=VC(I,JJ)*RJVP1+VIS(I,J)*RJVP1/(RJVP1-RJVP1)-VIS(I,J+1)
1*PJVP1/(RJVP1-RJVP1)
VP(I,JJ)=VC(I,JJ)*(RJVP1-RJVP1)+(VTS(I,J+1)-VIS(I,J))/(RJVP1-RJVP1)
IF(J.LT.NJM1) RJVN=.5*(RR(I,NJ)+RR(I+1,NJ))-0.5*(RR(I,J+1)+
1RR(I+1,J+1))
IF(J.EQ.NJM1) RJVN=(.5*(RR(I,NJ)+RR(I+1,NJ))-0.25*(RR(I,IJ)+
1RR(I+1,NJ)+RR(I,NJM1)+RR(I+1,NJM1)))/2.
RJVNS=.5*(RR(I,NJ)+RR(I+1,NJ))-0.5*(RR(I,J)+RR(I+1,J))
VISV(I,J)=VA(I,JJ)+VB(I,JJ)*RJVN+VC(I,JJ)*RJVN+RJVNS
VISV(I,J-1)=VA(I,JJ)+VB(I,JJ)*RJVS+VC(I,JJ)*RJVS+RJVNS
3355 CONTINUE
NJTM=NJ-2*NJJ
NJTM=NJTM-1
DO 3791 I=2,NIM1
DO 3791 J=2,NJTM
3791 VISV(I,J)=VIS(I,J)*(1.-WFN(I,J+1))+VIS(I,J+1)*WFN(I,J+1)
DO 3366 I=2,NIM1
VISV(I,NJ)=VIS(I,NJ)
3366 VISV(I,1)=VIS(I,1)
DO 3377 J=1,NJ
VISV(1,J)=VISV(NIM1,J)
3377 VISV(NI,J)=VISV(2,J)
DO 3898 I=1,NJ
DO 3898 J=1,NJ
3898 IF(VISV(I,J).LT.VISCOS) VISV(I,J)=VISCOS

```

C  
CHAPTER 3 3 3 3 CALCULATION OF TURBULENT PRANDL NUMBER 3 3 3 3  
C

```

DO 3322 I=2,NIM1
DO 3322 J=1,NJM1
C-----INSERT CEDECIS DISTRIBUTION OF PRANDT-----
RLV=.5*(XMLL(I,J)+XMLL(I+1,J))
RLVV=RLV/(RB+AH)
IF(PRANDL.GE.0.02.AND.PRANDL.LE.0.3) BDPL=476.2*(PRANDL**2)
1-188.1*PRANDL+38.57
IF(PRANDL.GT.0.3.AND.PRANDL.LT.7.) BDPL=0.102*(PRANDL**2)
1+9.08*PRANDL+22.4
IF(PRANDL.GE.7.) BDPL=5.16*PRANDL+58.9
IF(TAU7N(I).NE.0.0) PRANDT=.4187*(1.-EXP(-RLV/(76.*VISCOS/DENSIT*
1ARS(TAU7N(I))/DENSIT)**
1(-0.5))))/.44/(1.-EXP(-PLV/(BDPL/SQRT(PRANDL)*VISCOS/DENSIT*
1ARS(TAU7N(I))/DENSIT)**(-0.5))))
IF(TAU7N(I).EQ.0.0) PRANDT=0.9
IF(KASM.EQ.0) GO TO 7968
IF(KASM.EQ.?) GO TO 7968
IF(MITER.LT.NOUMR?) GO TO 7968
IF(J.LT.(JG-4)) PRANDT=AK7(I,J)/(AKD(I,J)+SMALL)
7968 CONTINUE
GMT(I,J)=VISCOS/PRANDT+(VISV(I,J)-VISCOS)/PRANDT
3322 CONTINUE

```

C  
CHAPTER 4 4 4 4 BOUNDARY VALUES FOR THERMAL DIFFUSIVITY 4 4 4 4  
C

```

DO 1019 J=1,NJM1
GMT(1,J)=GMT(NIM1,J)
1019 GMT(NI,J)=GMT(2,J)
DO 1020 I=1,NI

```

```

1020 GMT(I,N1)=VISCOS/PRANDL
IF(TLENSC.EQ.0) GO TO 9191
C*****
C*          CALCULATION OF EFFECTIVE VISCOSITY FOR THE
C*          1-D REGION (CORE REGION) OF THE SOLUTION
C*          DOMAIN
C*****
C
CHAPTER 5 5 5 CALCULATION OF EFFECTIVE VISCOSITY FOR THE 1-D REGION
C
C-----LOCATION OF POINTS IN ONE DIMENSIONAL EXTENSION-----
R1D(N1D+4)=PA+.5*DYC(2,4)+DYC(2,3)+DYC(2,2)
R1D(N1D+3)=PA+.5*DYC(2,3)+DYC(2,2)
R1D(N1D+2)=PA+.5*DYC(2,2)
R1D(N1D+1)=PA
R1D(1)=0.0
DO 432 J=2,N1D
R1D(J)=R1D(J-1)+R1D(N1D+1)/FLOAT(N1D)
432 CONTINUE
HREF1(6)=HREFVIS
HJNEW=NJ+N1D
N1D2=N1D+2
N1D3=N1D+3
F1D(1,1)=0.0
DO 543 II=1,5
F1D(1,II)=F1D(2,II)
543 CONTINUE
IF(JNOTH.EQ.1) GO TO 768
DO 654 II=1,5
F1D(NJNEW,II)=0.0
654 CONTINUE
768 CONTINUE
DO 987 J=2,N1D2
IF(NITER.EQ.1) VIS1OLD=VISCOS
IF(NITER.GT.1) VIS1OLD=VF1D(J)
IF(JNOTH.NE.0) GO TO 3993
DWDYV=(F1D(J+1,2)-F1D(J-1,2))/(P1D(J+1)-R1D(J-1))
DIV=RP(2,NJ)-R1D(J)
IF(TLENSC.EQ.0) GO TO 418
RLV=.4187*RLV*(1.-EXP(-RLV*SQRT(DENSIT)*SQRT(ABS(TAUZA(1))))/
1 VISCOS/20.))
IF(DIV.GT.RYW) RLV=RYW
418 CONTINUE
VF1D(J)=DENSIT*RLV*RLV*ARS(DWDYV)+VISCOS
GO TO 3992
3993 CONTINUE
IF(NITER.LT.1000000) GO TO 1985
IF(KASH.EQ.2) GO TO 3981
IF(KASH.EQ.0) GO TO 1985
IF(PRANDL.EQ.0.708) AKBC=0.0001
IF(PRANDL.EQ.0.703) AKPC=0.0001
F1KA(J)=AKBC*(F1D(J,3)/(F1D(J,4)+SMALL))**2/R1D(J)*(2./3.*F1D(J,
1 3)
1+F1D(J,1)**2)*(F1D(J+1,5)-F1D(J-1,5))/(P1D(J+1)-R1D(J-1))
F1KBY=(F1D(J+1,1)-F1D(J-1,1))/(P1D(J+1)-R1D(J-1))
F1K(J)=PHODD(J)/DENSIT
F1KF=AKFT*(1.-AKFT*AKF*F1KA(J))/((1.-AKFTD*AKCTD*F1KA(J))*(1.-

```

```

1AKFT*AKF*
1F1KA(J)+AKFTD**2*(F1D(J,3)/(F1D(J,4)+SMALL))**2/R1D(J)*F1D(J,1)*
1FDUDY)
F1KD(J)=F1KC*2./3.*(1.-AKF/(F1D(J,4)+SMALL)*F1P(J))/(1.-2.*F1KA(
1J)
1*F1KC*AKF/(F1D(J,4)+SMALL))
F1WVT(J)=-F1KD(J)*F1D(J,3)**2/(F1D(J,4)+SMALL)*(F1D(J+1,5)-F1D(
1J-1,5))/(P1D(J+1)-R1D(J-1))
F1KP=AKF*(1.+AKFT*AKFTD*F1KA(J))/(1.-AKF*AKFT*F1KA(J))+(AKF*AKFT*
1AKFTD**2
1*F1KA(J)**2*AKCTD*(1.-AKFT*AKF*F1KA(J))-AKF*AKFT*AKFTD**3*F1KA(J)
1/P1D(
1J)*F1D(J,1)*FDUDY*(F1D(J,3)/(F1D(J,4)+SMALL))**2)/(1.-AKFT*AKF*
1F1KA
1(J))/(1.-AKFT*AKF*F1KA(J))*(1.-AKFTD*AKCTD*F1KA(J))+AKFTD**2*(
1F1D(J,3)
1/(F1D(J,4)+SMALL))**2/R1D(J)*F1D(J,1)*FDUDY)
F1K7(J)=F1KP*(2./3.*(1.-AKF/(F1D(J,4)+SMALL)*F1P(J))-AKF/(F1D(J,
14)+
1SMALL)*2.*AKCTD/R1D(J)*(2./3.*F1D(J,3)+F1D(J,1)**2)*F1PVT(J))
CMUR(J)=F1K7(J)
GO TO 1985
3981 CONTINUE
FDUDY=(F1D(J+1,1)-F1D(J-1,1))/(P1D(J+1)-R1D(J-1))
GDUDY=F1D(J,1)/R1D(J)
F1K7(J)=2./3.*(1.-7/3.)*7/3./(1.+1.7/9.*GDUDY*(F1D(J,3)/
1F1D(J,4))**2*(GDUDY+.7*FDUDY))
CMUR(J)=F1K7(J)
1985 CONTINUE
IF(KASH_FG_N) CMUR=0.0
IF(KASH_FG_N) CMUR(J)=0.09
IF(NITF_LT_NUMR2) VTS1D(J)=CMUR*DENSIT*F1D(J,3)*F1D(J,3)
1/(F1D(J,4)+SMALL)+VTSFOS
IF(NITF_GF_NUMR2) VTS1D(J)=CMUR(J)*DENSIT*F1D(J,3)*F1D(J,3)
1/(F1D(J,4)+SMALL)+VTSFOS
3992 CONTINUE
VTS1D(J)=HREF(6)*VTS1D(J)+(1.-HREF(6))*VTS1OLD
IF(J_FG_2) VTS1D(J-1)=VTS1D(J)
987 CONTINUE
VTS1D(J1D3)=VIS(2,3)
9101 CONTINUE
RETURN
END

```

## SUBROUTINE CALCII

```

C
CHAPTER 0 0 0 0 0 0 0 0 PRELIMINARIES 0 0 0 0 0 0 0
C
COMMON
1 RESORII,URFII,RESORV,URFV,RESORW,URFW,
1 UREFP,RESOPT,UREFT,RESORP,UREP,RESORD,UREF,
1 RESII(25,25),RESV(25,25),RESW(25,25),RESM(25,25),
1 DI(25,25),DV(25,25),DW(25,25),U(25,25),V(25,25),
1 W(25,25),P(25,25),T(25,25),TE(25,25),FD(25,25),
1 PP(25,25),DEII(25,25),VIS(25,25),AM(25,25),AS(25,25),
1 AF(25,25),AW(25,25),AI(25,25),AD(25,25),CF(25),CD(25,25),
1 CCE(25),CCD(25,25),AP(25,25),SI(25,25),SP(25,25),DXC(25,25),
1 DYC(25,25),D7C(4),WFE(25,25),WFN(25,25),WFD(4),
1 AREAXY(25,25),FID(50,5),IID,WMEAN,INDEX,HYDDIA,RAH,PIID(SII),
1 VELII,TII,TWII,FLOWIN,GREAT,
1 UREFVIS,VISCOS,DENSIT,PRAINDT,
1 PRTE,PRED,CMU,COT,C1H,C2H,CAPPA,FIOR,ALAMDA,
1 NSUPII,NSUPV,NSUPW,NSUPD,NSUPPT,
1 NSUPK,LSUPD,
1 IPREF,JPREF,KPREF,INDCOS
COMMON TAIIXS(25),TAIIXN(25),TAIIS(25),TAIIZM(25),
1 YPIIIS(25),YPIISN(25)
1 IT,JT,NI,NJ,NIM1,NJM1
1 ,SWET,FLOWTOT,CPW,REFLUX,FLOWT
1 ,N1,N2
1 ,RA,RP,THETA,AP,DPD7,FLOWAX,DXIDF(25,25),DETADF(25,25),DIH
1 ,DPDXT(25,25),DPDFTA(25,25),HTHR(25,25)
1 ,PI,WTH,FLOWW
1 ,SMALL,SIMS,SIMP,TNIMP,DYDY(25,25),DYDX(25,25)
LEVEL 2,III
COMMON/PLK2/III(25,25),VV(25,25),ANU(25,25),ASII(25,25),
1 AFII(25,25),AWII(25,25),ADII(25,25),AIII(25,25),
1 APV(25,25),ASV(25,25),AEV(25,25),AWV(25,25),
1 CONT(25,10),VRK(25),JTS,
1 ADV(25,25),AIV(25,25),AA(25)
1 ,JG,INOTH,TER(25,2),FDP(25,2),PRODD(50),GENN(25,25)
1 ,PRANDL,GIT(25,25),AMISS
1 ,PRDD(25,25),AK7(25,25),AKD(25,25),AKA(25,25),RVT(25,25),AKF
1 ,AKET,AKETD,AKCTD,F1P(25),F1P7(25),F1KH(25),F1KA(25),F1PVT(25)
1 ,HOMIP,CMIA(25,25),CHIR(25)
1 ,HOMR2
1 ,APU(25,25),APV(25,25),PR(25,25),ANGI(25,25)
1 ,VASII,HASM
1 ,VISV(25,25),VA(25,25),VB(25,25),VC(25,25)
1 ,PSC(5),IMEG,MAYIT2
1 ,PNS(25,25),PRE,NTTER,MAXIT
1 ,IFISC,VISID(50),XYLL(25,25)

```

```

C
CHAPTER 1 1 1 1 1 1 ASSEMBLY OF COEFFICIENTS 1 1 1 1 1 1 1
C

```

```

UTM2=NI-2
RESORII=0.0
DO 49 I=2,NTI:1
DO 49 J=2,NJH1
DYDY(1,I)=DYDY(NIM1,J)
DYDY(1,J)=DYDY(NIM1,J)

```

```

DYD=.25*(DXC(I,J)+DXC(I-1,J)+DXC(I,J+1)+DYC(I-1,J+1))
AREADU=.5*(ARFAXY(I,J)+ARFAXY(I-1,J))
GDE=UFN(I,J)*W(I,J)
GDW=DFN(I-1,J)*W(I-1,J)
CD(I,J)=U*.5*(GDE+GDW)*AREADU
VISO=.5*(VIS(I,J)+VIS(I-1,J))
DID=VISO*ARFADU/.5*D7C(1)
AD(I,J)=AMAY1(WFN(1)*CD(I,J),-(1.-WFD(1))*CD(I,J),DID)
1=WFD(1)*CD(I,J)
ADU(I,J)=AD(I,J)
DMDXD=(W(I,J)-W(I-1,J))/DYD
CCD(I,J)=ARFADU*DMDXD*VISO
CCD(I,J)=0.0
49 CONTINUE
DO 5, I J=2,NJH1
DXIDF(1,J)=DXIDF(NIM1,J)
DFTADF(1,J)=DFTADF(NIM1,J)
I=1
DXEPI=.5*(DYC(I,J)+DXC(I,J+1))
DYE=.5*(DYC(I,J)+DYC(I+1,J))
APFAEW=DYE*D7C(1)
GE=DFN(I,J)+.5*(U(I,J)+U(I+1,J))
CE(J)=GE*ARFAEW
VTSF=VIS(I,J)
DTF=VISE*ARFAEW/DXEPI
C1=.25*(DXIDF(I,J)+DXIDF(I+1,J)+DXIDF(I+1,J+1)+DXIDF(I,J+1))
C2=DFN(I,J)*W(I,J)*APFAEW
CE(J)=CE(J)+C1*PIH*C2
C3=.25*(DXIDF(I,J)+DXIDF(I+1,J)+DXIDF(I+1,J+1)+DXIDF(I,J+1))
C3=DIE*PIH*C2
DTF=DIE+C1*C3*PIH
DYD=.25*(DXC(I,J)+DXC(I,J+1)+DXC(I+1,J)+DYC(I+1,J+1))
DYDD=.25*(DYC(I,J)+DYC(I,J+1)+DYC(I+1,J)+DYC(NIM2,I+1))
AE(I,J)=AMAY1(DIE*.5*CE(J),-.5*CE(J),-.5*CE(J))
AE(I,J)=AE(I,J)
DIDXF=(U(I+1,J)-U(I,J))/DXEPI
VF=.5*(V(I,J+1)+V(I,J))
CCF(J)=VISE*(DIDXF+2.*VF*DXDY(I,J))*APFAEW
A1=C1
A2=.25*(DFTADF(I,J)+DFTADF(I,J+1)+DFTADF(I+1,J)+DFTADF(I+1,J+1))
DYJ=DYE+.25*(DYC(I+1,J+1)+DYC(I,J+1)+DYC(I,J-1)+DYC(I+1,J-1))
IF(J.EQ.2) DYN=DYE+.25*(DYC(I+1,J+1)+DYC(I,J+1))
IF(J.EQ.NJH1) DYN=DYE+.25*(DYC(I,J-1)+DYC(I+1,J-1))
DIDETA=(.5*(U(I+1,J+1)+U(I,J+1))-.5*(U(I+1,J-1)+U(I,J-1)))
1)/DYN
CCE(J)=CCF(J)+A1*A2*PIH*PIH*DIDETA*VISE*APFAEW
DMDXJ=(W(I+1,J)-W(NIM2,J))/(DXEPI+.25*(DXC(I+1,J)+DYC(NIM2,I+1))
1+DXC(I+1,J+1)+DYC(NIM2,I+1)))
CCF(J)=CCF(J)+A1*VISE*APFAEW*PIH*DMDXJ
R1=.25*(DRDYI(I+1,J)+DRDYJ(I+1,J+1)+DRDYI(I,J)+DRDYJ(I,J+1))
R2=.25*(DRDFTA(I+1,J)+DRDFTA(I+1,J+1)+DRDFTA(I,J)+DRDFTA(I,J+1))
CCF(J)=CCF(J)-PIH*PIH*A1*A2*VTSF*ARFAEW*VF*DRDY(I,J)
CCF(J)=CCF(J)+PIH*PIH*A1*A1*VTSF*ARFAEW*VF*DRDY(I,J)
HTRP=.25*(HTHR(I,J)+HTHR(I+1,J)+HTHR(I,J+1)+HTHR(I+1,J+1))
CCF(J)=CCF(J)-VTSF*ARFAEW*VF*R2*HTRP*HTRP
5) CONTINUE
DO 1, I I=2,NIH1

```



```

J=1
DYN=.5*(DXC(I,J+1)+DXC(I-1,J+1))
APFAD=DYN*DZC(1)
GME=DFN(I,J)*V(I,J+1)
GMW=DFN(I-1,J)*V(I-1,J+1)
CN=.5*(GME+GMW)*AREAN
VTSN=.5*(VIS(I,J)+VIS(I-1,J))
IF(TINDEX.EQ.0) DIN=0.0
IF(TINDEX.EQ.1) DIN=VTSN*AREAN/(.5*DYC(I,J+1))
C1=DFTANF(I,J+1)
C2=.5*(DEN(I,J)*W(I,J)+DEN(I-1,J)*W(I-1,J))*AREAN
CN=CN+C1*PIH*C2
C2=DFTADF(I,J+1)
C3=DIN*C2*PIH
DTJ=(C1*PIH*C2*PTH*VISH*ARFAN/(.5*DYC(I,J+1))
IF(TINDEX.EQ.1) DIN=(C1*PIH*C2*PTH+.5)*VTSN*AREAN/(.5*DYC(I,J+1))
WFUN=.5*(WFN(I,J+1)+WFN(I-1,J+1))
AM(I,J)=AMAX1(WFUN*CN,(1.-WFUN)*CN,DIN)-WFUN*CN
AM(I-1,J)=AM(I,J)
DVDXN=(V(I,J+1)-V(I-1,J+1))/DXH
DYDXN=.5*(DYDX(I,J)+DYDX(I-1,J))
VN=V(I,J+1)*WFF(I,J)+V(I-1,J+1)*(1.-WFF(I,J))
DYDYN=.5*(DYDY(I,J)+DYDY(I-1,J))
IN=II(I,J)
IF(TINDEX.EQ.0) CN=0.0
IF(TINDEX.EQ.1) CN=VTSN*AREAN*(DVDXN-VN*DYDXN-UN*DXDYN)
A1=DFTANF(I,J+1)
DMDXI=(W(I,J)-W(I-1,J))/DXH
CCJ=CCN+PTH*A1*VISH*DMDXI*AREAN
A2=DXJDF(I,J+1)
DUDYI=(U(I+1,J)-U(I-1,J))/(DXC(I,J+1)+DXC(I-1,J+1))
CCN=CCN+A1*A2*PIH*PIH*DUDYI*VISH*AREAN
D1=DYDXN
D2=DXDYN
CCJ=CCJ+PIH*PIH*A1*A1*VTSN*AREAN*VN*B1
CCJ=CCJ+PIH*PIH*A1*A2*VTSN*AREAN*VN*B2
CCN=CCN+A1*VISH*AREAN*VN*HTR(I,J+1)*HTR(I,J+1)*DRDETA(I,J+1)/A2
DUDETA=(U(I,J+1)-U(I,J))/(.5*DYC(I,J+1))
DO 101 J=2,NJM1
C-----COMPUTE AREAS AND VOLUME-----
DYN=.5*(DXC(I,J+1)+DXC(I-1,J+1))
DYF=.5*(DYC(I,J)+DYC(I+1,J))
DYD=.25*(DXC(I,J)+DXC(I-1,J)+DXC(I,J+1)+DXC(I-1,J+1))
AREAN=DYN*DZC(1)
APFAD=DYE*DZC(1)
APFADI=.5*(AREAXY(I,J)+AREAXY(I-1,J))
C-----CALCULATE CONVECTION COEFFICIENTS-----
GF=DEN(I,J)*.5*(U(I,J)+U(I+1,J))
GNF=(DEN(I,J)*(1.-WFD(1))+DEN(I,J)*WFD(1))*V(I,J)
GNW=(DEN(I-1,J)*(1.-WFD(1))+DEN(I-1,J)*WFD(1))*
1W(I-1,J)
GNF=(DEN(I,J)*(1.-WFN(I,J+1))+DEN(I,J+1)*WFN(I,J+1))*V(I,J+1)
C)
GNW=(DEN(I-1,J)*(1.-WFN(I-1,J+1))+DEN(I-1,J+1)*
1WFN(I-1,J+1))*V(I-1,J+1)
CW=CF(J)
CE(J)=GF*APFAD

```

```

CS=CN
CH=0.5*(GNE+GNW)*ARFAN
CI=CD(I,J)
CD(I,J)=0.5*(GDF+GDW)*AREADI
-----CALCULATE DIFFUSION COEFFICIENTS-----
IF (J.LT.NJM1) VTSN=VTSV(I,J)*DXC(I-1,J+1)/(DXC(I-1,J+1)+DXC(I,
1J+1))+VTSV(I-1,J)*DXC(I,J+1)/(DXC(I-1,J+1)+DXC(I,J+1))
IF (J.EQ.NJM1) VISH=VISCOS
VISDF=VIS(I,J)*(1.-WFD(1))+VIS(I,J)*WFD(1)
VTSNW=VIS(I-1,J)*(1.-WFD(1))+VIS(I-1,J)*WFD(1)
VTSN=.5*(VISDF+VTSNW)
VTSF=VIS(I,J)
D7DP=.5*DZC(1)
R1 D7DP=D7DP+.5*DZC(1)
R2 DTD=VTSN*AREADI/D7DP
DYNP=.5*DYC(I,J)
IF (J.EQ.NJM1) GO TO R4
R3 DYNP=DYNP+.5*DYC(I,J+1)
R4 DTJ=VISH*ARFAN/DYNP
DXEP=.5*(DYC(I,J)+DYC(I,J+1))
DTF=VTSF*ARFAN/DXEP
C1=.25*(DXIDF(I,J)+DXIDF(I+1,J)+DXIDF(I,J+1)+DXIDF(I+1,J+1))
C2=DEF(I,J)*W(I,J)*ARFAN
CF(J)=CF(J)+C1*PIH*C2
C3=.25*(DYIDF(I,J)+DYIDF(I+1,J)+DYIDF(I,J+1)+DYIDF(I+1,J+1))
C3=DTF*PIH*C2
DTF=DTF+C1*C3*PIH
C1=DETADF(I,J+1)
C2=(DEF(I,J)*W(I,J)*(1.-WFN(I,J+1))+DEF(I,J+1)*W(I,J+1)*WFN(I,
1J+1))*ARFAN
C3=(DEF(I-1,J)*W(I-1,J)*(1.-WFN(I-1,J+1))+DEF(I-1,J+1)*W(I-1,
1J+1)*WFN(I-1,J+1))*ARFAN
CH=CH+C1*PIH*.5*(C2+C3)
C2=DETADF(I,J+1)
C3=DTJ*C2*PIH
DTJ=DTJ+C1*PIH*C3
-----CALCULATE MASS SOURCE FOR USE IN STABILISATION PROCEDURE-----
SMP=CD(I,J)-CH+CH-CS+CF(J)-CW
CP=AMAX1(0.0,SMP)
CD=CP
-----ASSEMBLE MAIN COEFFICIENTS-----
DTF=AMAX1(DTF,.5*CF(I),.5*CF(J))
AF(I,J)=DIE-.5*CF(J)
AW(I,J)=AE(I-1,J)+CW
WFIN=1.
IF (J.EQ.NJM1) GO TO 114
WFIN=DYC(I,J)/(DYC(I,J)+DYC(I,J+1))
114 CONTINUE
AH(I,J)=AMAX1(WFIN*CN,(1.-WFIN)*CN,DTJ)-WFIN*CN
AS(I,J)=AH(I,J)+CS
AI(I,J)=AD(I,J)+CI
DI(I,J)=DYC(I,J)*DZC(1)
AD(I,J)=AMAX1(WFD(1)*CD(I,J),(1.-WFD(1))*CD(I,J),DTD)
1-WFD(1)*CD(I,J)
SI(I,J)=CP*II(I,J)+PI(I,J)*(P(I-1,J)-P(I,J))
SP(I,J)=-CP
-----COMPLETE ASSEMBLY OF SOURCE TERMS-----

```

```

CFW=CCE(J)
CFS=CCN
CFH=CCD(T,J)
DIIDYE=(U(I+1,J)-U(I,J))/DXEPII
DYDYF=DXDY(T,J)
VF=.5*(V(I,J+1)+V(I,J))
CCE(J)=VISE*APEAEW*(DIIDYE+2.*VE*DXDYE)
A1=.25*(DXIDF(I,J)+DXIDF(I+1,J)+DYIDF(I+1,J+1)+DXIDF(I,J+1))
A2=.25*(DFTADF(I+1,J)+DFTADF(I,J)+DFTADF(I,J+1)+DFTADF(I+1,J+1))
DYN=DYF+.25*(DYC(I+1,J+1)+DYC(I,J+1)+DYC(I,J-1)+DYC(I+1,J-1))
IF(J.EQ.2) DYN=DYF+.25*(DYC(I+1,J+1)+DYC(I,J+1))
IF(J.EQ.NJM1) DYN=DYF+.25*(DYC(I,J-1)+DYC(I+1,J-1))
DIIDETA=(.5*(U(I+1,J+1)+U(I,J+1))-.5*(U(I+1,J-1)+U(I,J-1)))/DYN
CCE(J)=CCE(J)+A1*A2*PTH*PTH*DIIDETA*VISE*APEAEW
DWDXI=(U(I+1,J)-U(I-1,J))/(DXEPII+.25*(DXC(I+1,J)+DXC(I+1,J+1)+DXC(I-1,J)+DXC(I-1,J+1)))
CCE(J)=CCE(J)+A1*PIH*VISE*DWDXI*AREAEW
R1=.25*(DRDYI(I,J)+DRDYI(I+1,J)+DRDYI(I,J+1)+DRDYI(I+1,J+1))
R2=.25*(DRDETA(I,J)+DRDETA(I+1,J)+DRDETA(I,J+1)+DRDETA(I+1,J+1))
CCE(J)=CCE(J)-PTH*PIH*A1*A2*VISE*DYDX(I,J)*AREAEW*VF
CCE(J)=CCE(J)+PTH*PTH*A1*A1*VISE*DXDY(I,J)*AREAEW*VF
HTRHP=.25*(HTR(I,J)+HTR(I+1,J)+HTR(I,J+1)+HTR(I+1,J+1))
CCE(J)=CCE(J)-VISE*AREAEW*VF*R2+HTRHP*HTRHP
DWDYN=(V(I,J+1)-V(I-1,J+1))/DYN
DYDXNE=DYDX(I,J)*(1.-WFN(I,J+1))+DYDX(I,J+1)*WFN(I,J+1)
DYDXIW=DYDX(I-1,J)*(1.-WFN(I-1,J+1))+DYDX(I-1,J+1)*WFN(I-1,J+1)
WFEW=DXC(I-1,J+1)/(DXC(I-1,J+1)+DXC(I,J+1))
DYDXNE=DYDXNE*WFEW+DYDXIW*(1.-WFEW)
DYDXIW=DYDX(I,J)*(1.-WFN(I,J+1))+DXDY(I,J+1)*WFN(I,J+1)
DXDYIW=DYDX(I-1,J)*(1.-WFN(I-1,J+1))+DXDY(I-1,J+1)*WFN(I-1,J+1)
DYDXIW=DYDXIW*WFEW+DXDYIW*(1.-WFEW)
WFEV=DXC(I-1,J+1)/(DXC(I-1,J+1)+DXC(I,J+1))
VN=V(I,J+1)*WFEV+V(I-1,J+1)*(1.-WFEV)
WFIW=U(I,J+1)+WFIW+U(I,J)*(1.-WFIW)
IF(J.EQ.2) WFIW=0.0
IF(T.GT.2.AND.J.GT.2) WFIW=.5*(WFN(I,J)+WFN(I-1,J))
IF(T.EQ.2.AND.J.GT.2) WFIW=DYC(I,J-1)/(DYC(I,J)+DYC(I,J-1))
WFIW=U(I,J)*WFIW+U(I,J-1)*(1.-WFIW)
CFH=VTSN*AREAN*(DWDYN-VN*DYDXN-WN*DXDYN)
A1=DETADF(I,J+1)
WFE=J(I,J)*(1.-WFN(I,J+1))+W(I+1,J)*WFN(I,J+1)
WFW=J(I-1,J)*(1.-WFN(I-1,J+1))+W(I-1,J+1)*WFN(I-1,J+1)
DWDXI=(WFE-WFW)/DYN
IF(J.EQ.NJM1) DWDXI=(W(I,J+1)-W(I-1,J+1))/DYN
CFH=CCN+PIH*A1*VSN*DWDXI*AREAN
A2=DXIDF(I,J+1)
WFINE=DYC(I+1,J)/(DYC(I+1,J)+DYC(I+1,J+1))
WFINE=DYC(I-1,J)/(DYC(I-1,J)+DYC(I-1,J+1))
WFIW=J(I+1,J)*(1.-WFINE)+U(I+1,J+1)*WFINE
WFIW=J(I-1,J)*(1.-WFIW)+U(I-1,J+1)*WFIW
DIIDXI=(WFE-WFIW)/(DXC(I,J+1)+DXC(I-1,J+1))
CFH=CCN+A1*A2*PTH*PTH*DIIDXI*VTSN*AREAN
R1=DYDXN
R2=DXDYN
CFH=CCN-PIH*PIH*A1*A1*VSN*AREAN*VN*R1

```

```

CCU=CCU+PIH*PIH*A1*A2*VISN*AREAN*VN*B2
CCU=CCU-A1*VISN*AREAN*VN*WTHR(I,J+1)*WTHR(I,J+1)*DRNETA(I,J+1)/A2
DIIDFTAN=(U(I,J+1)-U(I,J))/(.5*(DYC(I,J)+DYC(I,J+1)))
DWDYD=(W(I,J)-W(I-1,J))/DYD
CCD(I,J)=VISD*AREADII*DWDYD
CCD(I,J)=C.D
SU(I,J)=SU(I,J)+CCD(I,J)-CCU+CCF(I)-CCW+CCN-CCS
VISP=VIS(I,J)*WFE(I,J)+VIS(I-1,J)*(1.-WFE(I,J))
DFNP=.5*(DEN(I,J)+DEN(I-1,J))
DYDYP=DYD(I,J)*WFE(I,J)+DYD(I-1,J)*(1.-WFE(I,J))
DYDYP=DYD(I,J)*WFE(I,J)+DYD(I-1,J)*(1.-WFE(I,J))
VW=.5*(V(I-1,J+1)+V(I-1,J))
DWDYP=(VE-VW)/DYD
DIIDYP=(IIN-IC)/DYC(I,J)
VP=VE*WFE(I,J)+VW*(1.-WFE(I,J))
IIP=II(I,J)
VOL=.5*(APEAXY(I,J)+APEAXY(I-1,J))*DZC(1)
SI(I,J)=SI(I,J)+VISP*(DWDYP+DIIDYP-VP*DYDYP)*VOL
SP(I,J)=SP(I,J)-VISP*DYDYP*DYDYP*VOL
WFEV=DYC(I-1,J)/(DYC(I-1,J)+DYC(I,J))
VS=V(I,J)*WFEV+V(I-1,J)*(1.-WFEV)
DWDYP=(VW-VS)/DYC(I,J)
SI(I,J)=SI(I,J)-2.*VISP*DWDYP*DYDYP*VOL
SP(I,J)=SP(I,J)-2.*VISP*DYDYP*DYDYP*VOL
SI(I,J)=SI(I,J)+DFNP*VP*VP*DYDYP*VOL
SORCE=-DFNP*VP*DYDYP*VOL
SP1=AMIN1(SORCE,0)
SU1=SORCE-SP1
SU(I,J)=SU(I,J)+SU1*U(I,J)
SP(I,J)=SP(I,J)+SP1
IF(PIH.EQ.0.0) GO TO 3274
HTRP=.5*(HTRP(I,J)+HTRP(I,J+1))
A5=.5*(DXIDF(I,J)+DXIDF(I,J+1))
A1=.5*(DRDXT(I,J)+DRDXT(I,J+1))
A6=.5*(DETADF(I,J)+DETADF(I,J+1))
R2=.5*(DRDETA(I,J)+DRDETA(I,J+1))
WP=W(I,J)*WFE(I,J)+W(I-1,J)*(1.-WFE(I,J))
SP(I,J)=SP(I,J)-(-HTRP*HTRP*R2/(PIH*A5)+PIH*A5*DYDYP-PIH*A6+
1DYDYP)*(PIH*A5*DYDYP-PIH*A6+DYDYP-HTRP*HTRP*R2/(PIH*A5))*VISP+
1VOL
DWDYP=.5*(U(I+1,J)-U(I-1,J))/(.25*(DYC(I,J)+DYC(I,J+1)+DYC(
1I-1,J)+DYC(I-1,J+1)))
DWDYP=(U(I,J)-U(I-1,J))/(.25*(DYC(I,J)+DYC(I,J+1)+DYC(I-1,J)+
1DYC(I-1,J+1)))
WFEN=DYC(I-1,J+1)/(DYC(I-1,J+1)+DYC(I,J+1))
WN=WFE*WFEN+WN*(1.-WFEN)
WFE=V(I,J)*WFN(I,J)+W(I-1,J)*(1.-WFN(I,J))
WSW=W(I-1,J)*WFN(I-1,J)+W(I-1,J-1)*(1.-WFN(I-1,J))
WFE=DXC(I-1,J)/(DXC(I-1,J)+DXC(I,J))
VS=USE*WFE+WSW*(1.-WFE)
DWDYP=(WN-VS)/DYC(I,J)
SI(I,J)=SI(I,J)-(-HTRP*HTRP*R2/(PIH*A5)+PIH*A5*DYDYP-PIH*A6+
1DYDYP)*VOL*(DFNP*
1VP*VP-VISP*(DWDYP+PIH*A5*DYDYP+PIH*A6*DYDYP))
3274 CONTINUE
101 CONTINUE
100 CONTINUE

```

C  
CHAPTER 2 2 2 2 2 2 2 PROBLEM MODIFICATIONS 2 2 2 2 2 2 2

C  
CALL MODII

C  
CHAPTER 3 FINAL COEFF. ASSEMBLY AND RESIDUAL SOURCE CALCULATION 3 3

C  
DO 300 I=2,NIM1  
DO 301 J=2,NJM1  
AP(I,J)=AD(I,J)+AU(I,I)+AN(I,J)+AS(I,J)  
1+AF(I,J)+AW(I,J)-SP(I,J)  
DU(I,J)=DU(I,J)/AP(I,I)  
RESOR=AF(I,J)\*U(I+1,J)+AW(I,J)\*U(I-1,J)+  
1AN(I,J)\*U(I,J+1)+AS(I,J)\*U(I,J-1)+  
1AD(I,J)\*U(I,J)+AU(I,J)\*U(I,J)-  
1AP(I,J)\*U(I,J)+SU(I,J)  
RESU(I,J)=RESOR  
VOL=.5\*(AREAXY(I,J)+APEAXY(I-1,J))\*DZC(1)  
SORVOL=GREAT\*VOL  
IF(-SP(I,J).GT.0.5\*SOPVOL) RESOP=RESOR/SOPVOL  
IF(-SP(I,J).GT.0.5\*SOPVOL) RESU(I,J)=RESU(I,J)/SOPVOL  
IF(J.EQ.2.AND.NITER.GE.MAXIT2) GO TO 4810  
RESORU=RESORU+ABS(RESOR)  
4810 CONTINUE  
RESU(I,J)=RESU(I,J)/VOL  
C-----UNDER-RELAXATION  
AP(I,J)=AP(I,J)/URFU  
SU(I,J)=SU(I,J)+(1.-URFU)\*AP(I,I)\*U(I,J)  
DU(I,J)=DU(I,J)\*URFU  
301 CONTINUE  
300 CONTINUE  
DO 343 I=2,NIM1  
DO 343 J=2,NJM1  
AN(I,J)=AN(I,J)  
ASU(I,J)=AS(I,J)  
AFU(I,J)=AF(I,J)  
AWU(I,J)=AW(I,J)  
ADU(I,J)=AD(I,J)  
AUU(I,J)=AU(I,J)  
343 ADU(I,J)=AP(I,J)

C  
CHAPTER 4 4 4 SOLUTION OF DIFFERENCE EQUATION 4 4 4 4 4 4 4

C  
IF(NITER.GE.MAXIT2) RSC(INDEX)=0.0  
IF(NITER.GE.MAXIT2) IMEG=0  
IF(NITER.LT.MAXIT2) IMEG=1  
DO 400 N=1,NSLPU  
IF(N.GT.1.AND.NITER.GE.MAXIT2) IMEG=1  
400 CALL IISOLV(2,2,NI,NJ,IT,IT,U)  
IF(NITER.GE.MAXIT2) RESORU=RESORU+RSC(INDEX)  
RETURN  
END

## SUBROUTINE CALCV

```

C
CHAPTER 0 0 0 0 0 0 0 0 PRELIMINARIES 0 0 0 0 0 0 0
C
COMMON
1 RESORH,URFU,RESORV,URFV,RESORM,RESOPW,URFW,
1 URFK,RESORT,URFT,RESORK,URFK,RESORD,URFD,
1 RESH(25,25),HFSW(25,25),RESW(25,25),RESM(25,25),
1 DH(25,25),DV(25,25),DW(25,25),U(25,25),V(25,25),
1 W(25,25),P(25,25),T(25,25),TE(25,25),ED(25,25),
1 PP(25,25),DEFN(25,25),VIS(25,25),AN(25,25),AS(25,25),
1 AF(25,25),AW(25,25),AH(25,25),AD(25,25),CE(25),CD(25,25),
1 CCE(25),CCD(25,25),AP(25,25),SH(25,25),SP(25,25),DXC(25,25),
1 DYC(25,25),D7C(4),WFE(25,25),WFN(25,25),WFD(4),
1 ARFAXY(25,25),F1D(50,5),N1D,WMEAN,INDEX,HYDDIA,RAF,P1D(50),
1 VELIN,TJN,TWALL,FLOWIN,GFAT,
1 HPEVIS,VISCOS,DENSIT,PRANDT,
1 PRTE,PREC,CPI,CPII,CPII,CAPPA,FI,OG,ALAMDA,
1 NSJPU,NSWPV,NSUPW,NSUPP,NSWPT,
1 NSJPK,NSWPD,
1 IPREF,JPREF,KPREF,INDCUS
COMMON TAUSS(25),TAUXN(25),TAUZE(25),TAUZI(25),
1 YPLUSS(25),YPLUSN(25)
1 JT,JT,NI,NI,NIM1,NJM1
1 SWET,FLOWTOT,CPW,REFLUX,FLOWT
1 N1,N2
1 PA,RP,THETA,AM,DPD7,FLOWAX,DXINF(25,25),DETANF(25,25),PIH
1 DNDXI(25,25),DPOETA(25,25),HTHP(25,25)
1 PI,HTN,FLOWW
1 SMALL,SUMS,SUMK,INIMP,DXDY(25,25),DYDX(25,25)
LEVEL 2,III
COMMON PLK2/III(25,25),VV(25,25),AMH(25,25),ASH(25,25),
1 AEH(25,25),AWH(25,25),ADH(25,25),AHH(25,25),
1 AHV(25,25),ASV(25,25),AEV(25,25),AWV(25,25),
1 CONT(25,10),VRN(25),JTS,
1 ADV(25,25),AHV(25,25),AA(25)
1 JG,IROTH,TEP(25,2),FUR(25,2),PRODD(50),GENN(25,25)
1 PPANDI,GIT(25,25),AMHSE
1 PHDD(25,25),AKZ(25,25),AKD(25,25),AKA(25,25),RVT(25,25),AKF
1 AKFT,AKFTD,AKCTD,F1P(25),F1VZ(25),F1KD(25),F1KA(25),F1RVT(25)
1 NQIMP,CNHA(25,25),CNHP(25)
1 NQIMP2
1 APH(25,25),APV(25,25),APW(25,25),ANGL(25,25)
1 PASI,PASM
1 VISV(25,25),VA(25,25),VB(25,25),VC(25,25)
1 PSC(5),IMER,MAYIT2
1 RPS(25,25),RBB,HTTFR,MAXIT
1 TLENSC,VISID(50),XMLL(25,25)
C
CHAPTER 1 1 1 1 1 1 ASSEMBLY OF COEFFICIENTS 1 1 1 1 1 1 1
C
RESORV=0.0
DO 49 I=2,NIM1
DO 49 J=3,NJM1
DYD=.25*(DYC(I,J)+DYC(I,J-1)+DYC(I+1,J)+DYC(I+1,J-1))
ARFADH=.5*(ARFAXY(I,J)+ARFAXY(I,J-1))
GDH=DEFN(I,J)*b(I,J)

```

```

GPS=DEN(I,J-1)*W(I,J-1)
CD(I,J)=0.5*(GDM+GDS)*APEADII
VISD=.5*(VIS(I,J)+VIS(I,J-1))
DYN=VISD*ARFADU/(.5*DYC(1))
AD(I,J)=AMAX1(WFD(1)*CD(I,J),-(1.-WFD(1))*CD(I,J),DYN)
1=WFD(1)*CD(I,J)
ADV(I,J)=AD(I,J)
DMDYN=(W(I,J)-W(I,J-1))/DYD
CCD(I,J)=VISD*APEADII*DMDYN
CCD(I,J)=0.0
49 CONTINUE
DO 50 J=3,N,J-1
I=1
DVE=.5*(DYC(I+1,J)+DYC(I+1,J-1))
APEAFW=DYF*DZC(1)
GEN=.5*(DFN(I,J)+DFN(I+1,J))*H(I+1,J)
GES=.5*(DFN(I,J-1)+DFN(I+1,J-1))*H(I+1,J-1)
CF(J)=0.5*(GEN+GES)*APEAFW
VTSF=VISV(I,J-1)*DXC(I+1,J)/(DXC(I,J)+DYC(I+1,J))+VISV(I+1,J-1)
1=DXC(I,J)/(DXC(I,J)+DYC(I+1,J))
DTE=VTSF*ARFAEW/(.5*(DXC(I,J)+DYC(I+1,J)))
WF=(.5*(W(I,J)+W(I,J-1))+.5*(W(I+1,J)+W(I+1,J-1)))*.5
DENM=.25*(DFN(I,J)+DEN(I,J-1)+DFN(I+1,J)+DEN(I+1,J-1))
C1=.25*(DXIDF(I+1,J+1)+DXIDF(I+1,J-1)+2.*DXIDF(I+1,J))
C2=C1*PIH*DENM*WE*ARFAEW
CF(J)=CF(J)+C2
C3=C1
C4=PIE*C1*PIH*C3*PIH
DYF=DJF+C4
WFVF=.5*(WFF(I+1,J)+WFF(I+1,J-1))
AF(I,J)=AMAX1(WFVF*CF(J),-(1.-WFVF)*CF(J),DTE)-WFVF*CF(J)
AFV(I,J)=AF(I,J)
DIDDYE=(H(I+1,J)-U(I+1,J-1))/DYE
DYDXIF=DYDX(I,J)*(1.-WFF(I+1,J))+DYDX(I+1,J)*WFF(I+1,J)
DYDXSE=DYDX(I,J-1)*(1.-WFF(I+1,J-1))+DYDX(I+1,J-1)*WFF(I+1,J-1)
DYDYF=.5*(DYDXAF+DYDXSE)
DYDYIF=DYDY(I,J)*(1.-WFF(I+1,J))+DYDY(I+1,J)*WFF(I+1,J)
DYDYSE=DYDY(I,J-1)*(1.-WFF(I+1,J-1))+DYDY(I+1,J-1)*WFF(I+1,J-1)
DYDYF=.5*(DYDYIE+DYDYSE)
VF=V(I+1,J)*WFVF+V(I,J)*(1.-WFVF)
IF=.5*(H(I+1,J)+U(I+1,J-1))
CFE(J)=VTSF*ARFAEW*(DIDDYE-VF*DYDXF-IF*DYDYF)
A1=C1
WNE=U(I+1,J)*WFF(I+1,J)+U(I,J)*(1.-WFF(I+1,J))
WSE=U(I+1,J-1)*WFF(I+1,J-1)+U(I,J-1)*(1.-WFF(I+1,J-1))
DWDETA=(WNE-WSE)/DYE
CCF(J)=CCF(J)+A1*PIH*VISE*DWDETA*ARFAEW
WFVNF=.5*(WFF(I+1,J)+WFF(I+1,J+1))
IF(J,GT,3) WFVSF=.5*(WFF(I+1,J-1)+WFF(I+1,J-2))
IF(J,EG,3) WFVSF=WFF(I+1,J)
V1=V(I+1,J+1)*WFVNF+V(I,J+1)*(1.-WFVNF)
V2=V(I+1,J-1)*WFVSF+V(I,J-1)*(1.-WFVSF)
DYDYF=(V1-V2)/(DYC(I+1,J)+DYC(I+1,J-1))
H1=.25*(DETADF(I+1,J+1)+DETADF(I+1,J-1)+2.*DETADF(I+1,J))
H2=.25*(DPDETA(I+1,J+1)+DPDETA(I+1,J-1)+2.*DPDETA(I+1,J))
CFE(J)=CCF(J)+PIH*A1*VISE*ARFAEW*(PIH*B1*DYDYF-PIH*
1A1*DYDYF*H1+PIH*H2*H2+DYDYF)

```

```

CCE(J)=CCE(J)+VISE*ARFAEW*UF*HTHR(I+1,J)*HTHR(I+1,J)*P2
DVDYE=(V(I+1,J)-V(I,J))/(.5*(DXC(I+1,J)+DXC(I,J)))
500 CONTINUE
DO 1000 I=2,NIM1
  J=2
  DYN=.5*(DXC(I,J)+DXC(I,J+1))
  APEAN=DXN*DZC(1)
  GN=DEH(I,J)*.5*(V(I,J+1)+V(I,J))
  CN=GN*APEAN
  VTSN=VIS(I,J)
  DYNPV=.5*(DYC(I,J)+DYC(I+1,J))
  DIN=VTSN*ARFAN/DYNPV
  C1=.25*(DETADF(I,J)+DETADF(I+1,I)+DETADF(I,J+1)+DETADF(I+1,J+1))
  C2=DEH(I,J)*W(I,J)*ARFAN
  CN=CN+C1*PIH*C2
  C3=.25*(DETADF(I,J)+DETADF(I+1,I)+DETADF(I,J+1)+DETADF(I+1,J+1))
  C3=C1*PIH+C2*PIH*DIN
  DTJ=DJN+C3
  DTJ=AMAX1(DTJ,-.5*CN,.5*CN)
  AN(I,J)=DIN*.5*CN
  ANV(I,2)=AN(I,J)
  DVDYN=(V(I,J+1)-V(I,J))/DYNPV
  UN=.5*(U(I,J)+U(I+1,J))
  DYDXH=DYDX(I,J)
  CN=VTSN*ARFAN*(DVDYN+2*.5*UN*DYDXH)
  DWDYH=(.5*(U(I,J+1)+U(I,J))-U(I,J-1))/DYNPV
  A4=.25*(DETADF(I,J)+DETADF(I+1,I)+DETADF(I,J+1)+DETADF(I+1,J+1))
  CFN=CN+A4*PIH*VTSN*APEAN*DWDYH
  VNE1=V(I+1,I)*WFF(I+1,J-1)+V(I,J)*(1.-WFE(I+1,J-1))
  WFEH=DXC(I,J+1)/(DXC(I,J-1)+DXC(I+1,J+1))
  VNE2=V(I+1,J+1)*WFFN+V(I,J+1)*(1.-WFEH)
  VNE=.5*(VNE1+VNE2)
  VNW1=V(I,J)*WFE(I,J-1)+V(I-1,I)*(1.-WFE(I,J-1))
  WFFN=DXC(I-1,J+1)/(DXC(I-1,J+1)+DXC(I,J+1))
  VNW2=V(I-1,J+1)*(1.-WFFN)+V(I,J+1)*WFFN
  VNW=.5*(VNW1+VNW2)
  DVDYN=(VNE-VNW)/DXH
  A7=.25*(DXIDF(I,J)+DXIDF(I+1,J)+DXIDF(I,J+1)+DXIDF(I+1,J+1))
  AR=.25*(DETADF(I,J)+DETADF(I+1,J)+DETADF(I,J+1)+DETADF(I+1,J+1))
  R1=.25*(DRDXI(I,J)+DRDXI(I+1,J)+DRDXI(I,J+1)+DRDXI(I+1,J+1))
  R2=.25*(DRDETA(I,J)+DRDETA(I+1,J)+DRDETA(I,J+1)+DRDETA(I+1,J+1))
  CFN=CN+PIH*AR*VTSN*APEAN*(PIH*A7*DVDYN-PTH*A7*UN*DYDY(I,J)+PTH*
  1AR*UN*DYDX(I,J))
  HTHRP=.25*(HTHR(I,J)+HTHR(I+1,J)+HTHR(I,J+1)+HTHR(I+1,J+1))
  CFN=CFN+VTSN*ARFAN*UN*P2*A8/A7*HTHRP*HTHRP
  DO 1001 J=3,NJM1
    C-----COMPUTE ARFAS AND VOLUME-----
    DYN=.5*(DXC(I,J)+DXC(I,J+1))
    DYF=.5*(DYC(I+1,J)+DYC(I+1,J-1))
    DYD=.25*(DYC(I,J)+DYC(I,J-1)+DYC(I+1,J)+DYC(I+1,J-1))
    APEAN=DXN*DZC(1)
    APEAW=DYE*DZC(1)
    APEANI=.5*(ARFAXY(I,J)+ARFAXY(I,J-1))
    C-----CALCULATE CONVECTION COEFFICIENTS-----
    GN=DEH(I,J)*.5*(V(I,J)+V(I,J+1))
    GFW=(DEH(I,J)*(1.-WFD(1))+DEH(I,J)*WFD(1))*W(I,J)
    GNS=(DEH(I,J-1)*(1.-WFD(1))+DEH(I,J-1)*WFD(1))*

```



```

1W(I,J-1)
WF(I,J)=(DEN(I,J)*(1.-WFE(I+1,J))+DEN(I+1,J)*WFF(I+1,J))*U(I+1,J)
C)
GES=(DEN(I,J-1)*(1.-WFE(I+1,J-1))+DEN(I+1,J-1)*
1WFF(I+1,J-1))*U(I+1,J-1)
CS=CU
CN=CN*AREAN
CU=CF(J)
CF(J)=0.5*(GEN+GES)*AREAFW
CU=CU(I,J)
CD(I,J)=0.5*(GDN+GDS)*AREADU
C-----CALCULATE DIFFUSION COEFFICIENTS-----
VTSF=VTSV(I,J-1)*DXC(I+1,J)/(DXC(I,J)+DXC(I+1,J))+VTSV(I+1,J-1)+
1DYC(I,J)/(DYC(I,J)+DYC(I+1,J))
VTSN=VTS(I,J)*(1.-WFD(1))+VTS(I+1,J)*WFD(1)
VTSDS=VTS(I,J-1)*(1.-WFD(1))+VTS(I+1,J-1)*WFD(1)
VTSN=.5*(VTSN+VTSDS)
VTSN=VTS(I,J)
DZDP=.5*DZC(1)
R1 DZDP=DZDP+.5*DZC(1)
R2 DTD=VTSN*AREADU/DZDP
DYNPV=.5*(DYC(I,J)+DYC(I+1,J))
DTN=VTSN*AREAN/DYNPV
DYEP=.5*DXC(I,J)
R3 DYEP=DXEP+.5*DXC(I+1,J)
DTE=VTSF*AREAFW/DYEP
WFE=W(I,J)*(1.-WFE(I+1,J))+W(I+1,J)*WFF(I+1,J)
WFE=W(I,J-1)*(1.-WFE(I+1,J-1))+W(I+1,J-1)*WFF(I+1,J-1)
WE=.5*(WFE+WFE)
C1=.25*(DYINF(I+1,J+1)+DXIDF(I+1,J-1)+2.*DXIDF(I+1,J))
DENW=.25*(DEN(I,J)+DEN(I,J-1)+DEN(I+1,J)+DEN(I+1,J-1))
C2=C1*PIH*DEFM*WE*AREAFW
CE(J)=CF(J)+C2
C3=C1
C4=0.1F*C1*PIH*C3*PIH
DTE=DTE+C4
C1=.25*(DETADF(I,J)+DETADF(I+1,J)+DETADF(I,J+1)+DETADF(I+1,J+1))
C2=DEF(I,J)*W(I,J)*AREAN
CN=CU+(C1*PIH*C2)
C2=.25*(DETADF(I,J)+DETADF(I+1,J)+DETADF(I,J+1)+DETADF(I+1,J+1))
C3=C1*PIH*C2*PIH*DTN
DTH=DTN+C3
C-----CALCULATE MASS SOURCE FOR USE IN STABILISATION PROCEDURE-----
SMP=CD(I,J)-CU+CN-CS+CF(J)-CW
CP=AMAX1(0.,CP)
CD(I)=CP
C-----ASSEMBLE MAIN COEFFICIENTS-----
DTJ=AMAX1(DIN,.5*CN,.5*CN)
AN(I,J)=0.1U+.5*CN
AS(I,J)=AN(I,J-1)+CS
WFVF=DXC(I,J)/(DXC(I,J)+DXC(I+1,J))
AF(I,J)=AMAX1(WFVF*CE(J),-(1.-WFVF)*CF(J),DIE)-WFVF*CF(J)
AW(I,J)=AE(I-1,J)+CW
AH(I,J)=AD(I,J)+CU
AD(I,J)=AMAX1(WFD(1)*CD(I,J),-(1.-WFD(1))*CD(I,J),DTD)
1-WFD(1)*CD(I,J)
UV(I,J)=DXC(I,J)*DZC(1)

```

```

SH(I,J)=CP0*V(I,J)+DV(I,J)*(P(I,J-1)-P(I,J))
SP(I,J)=-CP
C-----COMPLETE ASSEMBLY OF SOURCE TERMS-----
VOL=.5*(AREAXY(I,J)+AREAXY(I,J-1))*DZC(1)
CFW=CCE(J)
CCS=CCN
CPI=CCD(I,J)
DWDVD=(W(I,J)-W(I,J-1))/DVD
CCD(I,J)=VISC*APFADH*DWDVD
CCD(I,J)=0.0
DUDYE=(U(I+1,J)-U(I+1,J-1))/DYE
DYDXJF=DYDX(I,J)*(1.-WFE(I+1,J))+DYDX(I+1,J)*WFE(I+1,J)
DYDXSF=DYDX(I,J-1)*(1.-WFE(I+1,J-1))+DYDX(I+1,J-1)*WFE(I+1,J-1)
DYDXF=.5*(DYDXJF+DYDXSF)
DYDYJF=DYDY(I,J)*(1.-WFE(I+1,J))+DYDY(I+1,J)*WFE(I+1,J)
DYDYSF=DYDY(I,J-1)*(1.-WFE(I+1,J-1))+DYDY(I+1,J-1)*WFE(I+1,J-1)
DYDYF=.5*(DYDYJF+DYDYSF)
VF=V(I+1,J)+WFVF+V(I,J)*(1.-WFVF)
WFVW=.5*(WFE(I,J)+WFE(I,J-1))
VW=V(I,J)+WFVW+V(I-1,J)*(1.-WFVW)
WF=.5*(U(I+1,J)+U(I+1,J-1))
HW=.5*(U(I,J)+U(I,J-1))
CCE(J)=VISC*AREAEW*(DUDYE-VF*DYDXF-HF*DYDYF)
A1=.25*(DXIDF(I+1,J+1)+DXIDF(I+1,J-1)+2.*DXIDF(I+1,J))
DWDFTA=(WNE-WSE)/DYF
CCE(J)=CCE(J)+A1*PIH*VISC*DWDFTA*ARFAEW
WFV11=.5*(WFE(I+1,J)+WFE(I+1,J+1))
WFV12=.5*(WFE(I+1,J-1)+WFE(I+1,J-2))
IF(J.EQ.3) WFV12=WFE(I+1,1)
V13=V(I,J+1)*(1.-WFV11)+V(I+1,J+1)*WFV11
V14=V(I,J-1)*(1.-WFV12)+V(I+1,J-1)*WFV12
DWDYF=(V13-V14)/(DYC(I+1,J)+DYC(I+1,J-1))
R1=.25*(DETADF(I+1,J+1)+DETADF(I+1,J-1)+2.*DETADF(I+1,J))
R2=.25*(DPRDTA(I+1,J+1)+DPRDTA(I+1,J-1)+2.*DPRDTA(I+1,J))
CCE(J)=CCE(J)+PIH*A1*UF*DYDXF+PIH*R1*HF*DYDYF
1*DYDYF=PIH*A1*UF*DYDXF+PIH*R1*HF*DYDYF
CCE(J)=CCE(J)+VISC*APFAEW*UF*HTHR(I+1,J)*HTHR(I+1,J)*F2
DWDYE=(V(I+1,J)-V(I,J))/(.5*(DXC(I+1,J)+DXC(I,J)))
DWDYH=(V(I,J+1)-V(I,J))/DYNPV
HN=.5*(U(I+1,J)+U(I,J))
HE=.5*(U(I+1,J-1)+U(I,J-1))
DYDXH=DYDX(I,J)
CFN=VISC*APFAN*(DWDYH+2.*HN*DYDXH)
WFV21=.5*(WFE(I,J)+WFE(I,J+1))
V15=V(I,J+1)+WFV21+V(I-1,J+1)*(1.-WFV21)
DWDYH=(.5*(V13+VF)-.5*(V15+VW))/(.5*(DXC(I,J)+DXC(I,J+1)))
A7=.25*(DXIDF(I,J)+DXIDF(I+1,J)+DXIDF(I,J+1)+DXIDF(I+1,J+1))
A9=.25*(DETADF(I,J)+DETADF(I+1,J)+DETADF(I,J+1)+DETADF(I+1,J+1))
R1=.25*(DPRDY(I,J)+DPRXT(I+1,J)+DPRDY(I,J+1)+DPRXT(I+1,J+1))
R2=.25*(DPRDTA(I,J)+DPRDTA(I+1,J)+DPRDTA(I,J+1)+DPRDTA(I+1,J+1))
CFN=CFN+PIH*AP*VISC*APFAN*(PIH*A7*DWDYH-PIH*A7*HN*DYDY(I,J)+
1*PIH*AP*HN*DYDY(I,J))
HTHR2=.25*(HTHR(I,J)+HTHR(I+1,J)+HTHR(I,J+1)+HTHR(I+1,J+1))
CCE(J)=CCE(J)+VISC*APFAN*HN*R2*HTHR*HTHR*A8/A7
DWDH=.25*(DYC(I,J)+DYC(I+1,J)+DYC(I,J+1)+DYC(I+1,J+1))
DWDYH=(W(I,J+1)-W(I,J-1))/(DYD+DYD)
A4=.25*(DETADF(I,J)+DETADF(I+1,J)+DETADF(I,J+1)+DETADF(I+1,J+1))

```

```

CCN=CCN+A4*PIH*VISN*AP*EAN*DKDYH
SH(T,J)=SH(T,J)+CCD(I,J)-CCU+CCF(I)-CCW+CCN-CCS
SH1=SH(T,J)
DUDXP=(VF-VH)/DXC(I,J)
DIUDVP=(IH-IIS)/DYD
IP=.5*(IH+IIS)
VTSP=VIS(I,J)*WFN(I,J)+VIS(I,J-1)*(1-WFN(I,J))
VP=V(I,J)
DYDYP=.5*(DYDY(T,J)+DYDY(T,J-1))
DYDXP=.5*(DYDX(T,J)+DYDX(T,J-1))
SH(T,J)=SH(T,J)+VTSP*(DUDYP+DIUDVP-IP*DXDYP)*DYDXP*VOL
SP(T,J)=SP(T,J)-VIS*DYDXP*DYDXP*VOL
DIUDXP=(IF-IH)/DXC(I,J)
SH(I,J)=SH(I,J)-2*VIS*DIUDXP*DYDYP*VOL
SP(I,J)=SP(I,J)-2*VIS*DXDYP*DYDYP*VOL
DENP=.5*(DEN(I,J)+DEN(I,J-1))
SH(I,J)=SH(I,J)+DENP*IP*(IP*DXDYP*VOL
SORCF=-DENP*IP*DYDXP*VOL
SP1=AMIN1(SORCF,0)
SH1=SORCF-SP1
SH(T,J)=SH(T,J)+SH1*V(I,J)
SP(T,J)=SP(T,J)+SP1
IF(PIH-EG(0,0) GO TO 3275
WUJ=W(I,J)*WFE(T,J)+W(I-1,J)*(1-WFE(T,J))
WSW=W(I,J-1)*WFE(T,J-1)+W(I-1,J-1)*(1-WFE(T,J-1))
W13=.5*(WUJ+WSW)
DUDXP=(WE-W13)/DXC(I,J)
R1P=.5*(DRDXI(I,J)+DRDXI(I+1,J))
R2P=.5*(DRDETA(T,J)+DRDETA(T+1,J))
HTHRP=.5*(HTHR(T,J)+HTHR(T+1,J))
R5=.5*(DXIDF(I,J)+DXIDF(I+1,J))
R4=.5*(DETADE(I,J)+DETADE(I+1,J))
VP=.5*(V(I,J)+V(I,J-1))
DUDYP=(V(I,J)-V(I,J-1))/DYD
DIUDXP=(IF-IH)/DXC(I,J)
DUDYP=.5*(V(I,J+1)-V(I,J-1))/DYD
SP(I,J)=SP(I,J)-(HTHRP*HTHRP*P2P/(PIH*R5)-PIH*R5*DXDYP+FIH*P6*
1DYDXP)*V(ISP+VOL*(PIH*P6*DYDYP-PIH*R5*DXDYP+HTHRP*HTHRP*P2P/(PIH*
1R5))
SH(I,J)=SH(I,J)-(HTHRP*HTHRP*P2P/(PIH*R5)-PIH*R5*DXDYP+FIH*P6*
1DYDXP)*VOL*(DENP*
1JP*IP-VTSP*(DUDYP+PIH*R5*DUDXP+PIH*P6*DIUDVP))

```

3275 CONTINUE

101 CONTINUE

103 CONTINUE

C  
CHAPTER 2 2 2 2 2 2 2 PROFILE MODIFICATIONS 2 2 2 2 2 2

C  
CALL MINDV

E  
CHAPTER 3 FINAL COEFF. ASSEMBLY AND RESIDUAL SOURCE CALCULATION 3 3

C  
DO 3110 J=2,NJM1  
DO 3111 J=3,NJM1  
AP(T,J)=AP(T,J)+AH(I,J)+AI(I,J)+AS(T,J)  
1+AF(I,J)+AM(I,J)-SH(I,J)  
DV(T,J)=DV(T,J)/AP(T,J)

```

      RESOR=AF(I,J)*V(I+1,J)+AW(I,J)*V(I-1,J)+
      1AN(I,J)*V(I,J+1)+AS(I,J)*V(I,J-1)+
      1AD(I,J)*V(I,J)+AU(I,J)*V(I,J)-
      1AP(I,J)*V(I,J)+SU(I,J)
      RESV(I,J)=RESOR
      VOL=.5*(AREAXY(I,J)+APFAXY(I,J-1))*DZC(1)
      SORVOL=GREAT*VOL
      IF(-SP(I,J).GT.0.5*SOPVOL) RESOR=RESOR/SOPVOL
      IF(-SP(I,J).GT.0.5*SOPVOL) RESV(I,J)=RESV(I,J)/SORVOL
      RESORV=RESORV+APS(RESOR)
      RESV(I,J)=RESV(I,J)/VOL
C-----UNDER-RELAXATION
      AP(I,J)=AP(I,J)/URFV
      SU(I,J)=SU(I,J)+(1.-URFV)*AP(I,J)*V(I,J)
      DV(I,J)=DV(I,J)*URFV
301 CONTINUE
300 CONTINUE
      DO 387 I=2,NJM1
      DO 387 J=3,NJM1
      ANV(I,J)=AN(I,J)
      ASV(I,J)=AS(I,J)
      AFV(I,J)=AF(I,J)
      AWV(I,J)=AW(I,J)
      ADV(I,J)=AU(I,J)
      APV(I,J)=AP(I,J)
387 APV(I,J)=AP(I,J)
C
CHAPTER 4 4 4 SOLUTION OF DIFFERENCE EQUATION 4 4 4 4 4 4
C
      DO 400 N=1,NISWV
400 CALL LISOLV(2,3,NJ,NJ,IT,IT,V)
      RETURN
      END

```

## SUBROUTINE CALCW

```

C
CHAPTER 0 0 0 0 0 0 0 PRELIMINARIES 0 0 0 0 0 0 0
C
COMMON
1 RESORU,UREF,RESORV,UREV,RESORW,RESOPW,UREW,
1 UREF,RESORT,UREF,RESORK,UREK,RESORD,URED,
1 RESU(25,25),RESV(25,25),RESW(25,25),RESM(25,25),
1 DU(25,25),DV(25,25),DW(25,25),U(25,25),V(25,25),
1 W(25,25),P(25,25),T(25,25),TE(25,25),EU(25,25),
1 PP(25,25),DEF(25,25),VIS(25,25),AN(25,25),AS(25,25),
1 AF(25,25),AW(25,25),AU(25,25),AD(25,25),CE(25),CO(25,25),
1 CCF(25),CCD(25,25),AP(25,25),SU(25,25),SP(25,25),DXC(25,25),
1 DYC(25,25),DZC(4),WFE(25,25),WFN(25,25),WFD(4),
1 ARFAXY(25,25),FID(50,5),NID,WMEAN,INDEX,HYDRA,PAP,PID(50),
1 VFI,UTJA,TWALL,FLOWIN,GREAT,
1 UREFVIS,VISCOS,DEHSIT,PRANT,
1 PRTE,PRFD,CMH,COT,C1H,C2H,CAPPA,FILOG,ALAMPA,
1 NSWP, NSWPV, NSWPW, NSWPP,NSWPT,
1 NSWPK,NSWPD,
1 JPRFF,JPRFF,KPRFF,INDCOS
COMMON TAUXS(25),TAUXN(25),TAUZE(25),TAUZN(25),
1 YPIUSS(25),YPIUSH(25)
1 IT,JT,PI,NJ,NIM1,NJM1
1 SHET,FLOWTOT,CPW,RELUY,FLOWT
1 N1,U7
1 PA,RR,THETA,ADP07,FLOWAX,DXINF(25,25),DETADF(25,25),PIH
1 DRDXT(25,25),DRDFTA(25,25),HTHR(25,25)
1 PI,WIN,FLOWW
1 SIALI,SUMS,SIMP,INIMP,DXDY(25,25),DYDX(25,25)
LEVEL 2,III
COMMON/PLK2/III(25,25),VV(25,25),AII(25,25),ASII(25,25),
1 AFI(25,25),AFI(25,25),ADU(25,25),AIII(25,25),
1 ADV(25,25),ASV(25,25),AFV(25,25),AWV(25,25),
1 CONT(25,10),VRK(25),JTS,
1 ADV(25,25),AIV(25,25),AA(25)
1 JG,THOTH,TFE(25,2),FDR(25,2),PRDD(50),GENN(25,25)
1 HPANDI,GHT(25,25),AMIES
1 PRDD(25,25),AKZ(25,25),AKD(25,25),AKA(25,25),RVT(25,25),AKF
1 AKET,AKETD,AKCTD,F1P(25),F1KZ(25),F1KA(25),F1RVT(25)
1 NOMIP,CMHA(25,25),CMHP(25)
1 NOMIP2
1 APII(25,25),APV(25,25),RR(25,25),ANGL(25,25)
1 KASII,NASM
1 VISV(25,25),VA(25,25),VB(25,25),VC(25,25)
1 RSC(5),IMEG,MAXIT2
1 PRS(25,25),RRH,NTFER,MAXIT
1 TLENSC,VTSID(50),XMLL(25,25)
CHAPTER 1 1 1 1 1 1 ASSEMBLY OF COEFFICIENTS 1 1 1 1 1 1 1
C
RESORU=0.0
DO 49 I=2,NJM1
DO 49 J=2,NJM1
ARFADU=ARFAXY(I,J)
GD=DEF(I,J)+.5*(U(I,J)+U(J,J))
CO(I,J)=GD*ARFADU
VTSID=VTS(I,J)

```

```

DTD=VISO*ARFADU/DZC(1)
DTD=AMAX1(DTD,-.5*CD(T,J),-.5*CD(I,J))
AD(I,J)=UID= .5*CD(I,J)
UWDZD=0.
CD(I,J)=VISO*AREADII*UWDZD
CD(I,J)=0.0
49 CONTINUE
D74=.5*(DZC(1)+DZC(1))
DO 50 J=2,NJM1
I=1
APEAFW=DYC(I+1,J)*D74
GF0=DEF(I,J)*U(I+1,J)
GF1=DEF(I,J)*U(T+1,J)
CF(J)=0.5*(GF0+GF1)*APEAEW
C1=.5*(DXIDF(I+1,J)+DYIDF(I+1,J+1))
C2=.5*(DEF(T,J)*W(I,J)+DEF(I+1,J)*W(I+1,J))*APEAEW
CF(J)=CF(J)+C1*PIH*C2
VTSE=.5*(VIS(T,J)+VIS(I,J))
DYNN=.25*(DYC(I,J)+DXC(T,J+1)+DYC(I+1,J)+DXC(I+1,J+1))
DTE=VISE*ARFAFW/DYNN
C2=.5*(DXIDF(I+1,J)+DYIDF(I+1,J+1))
C3=C1*PIH*C2*PIH*DIET.
DTE=DTE+C3
AF(I,J)=AMAX1(WFE(I+1,J)*CF(J),-(1.-WFE(I+1,J))*CF(J),DTE)
1=WFE(T+1,J)*CF(J)
DIID7E=0.
CFE(J)=VISE+APEAEW*DIID7E
A1=.5*(DETADF(I+1,J)+DETADF(I+1,J+1))
DIIM=.5*(U(I+1,J+1)-U(I+1,J-1))
IF(J.EQ.NJM1) DYNN=DYC(T+1,J)
DYNN=DYC(T+1,J)
IF(J.EQ.NJM1) DIIM=U(I+1,NJ)=.5*(U(I+1,J)+U(T+1,J-1))
IF(J.EQ.2) DIIM=.5*(U(T+1,J+1)+U(I+1,J))-U(I+1,1)
CFE(J)=CFE(J)+A1*PIH*VISE*DIIM/DYNN*ARFAFW
A2=.5*(DXIDF(I+1,J)+DYIDF(I+1,J+1))
DIIDXI=.5*(U(I+2,J)-U(T,J))/DYNN
CFE(J)=CFE(J)+PIH*A2*DIIDXI*ARFAFW*VTSE
A1=.5*(DXIDF(I+1,J)+DYIDF(I+1,J+1))
A2=.5*(DETADF(I+1,J)+DETADF(I+1,J+1))
W1=U(I+1,J+1)*WFE(T+1,J+1)+W(I,J+1)*(1.-WFE(T+1,J+1))
W2=U(T+1,J-1)*WFE(T+1,J-1)+W(I,J-1)*(1.-WFE(I+1,J-1))
DWDFTA=(WN-WS)/(DYC(I+1,J)+.5*(DYC(I+1,J+1)+DYC(I+1,J-1)))
IF(J.EQ.NJM1) DWDFTA=(WN-WS)/(DYC(I+1,J)+.5*DYC(I+1,J-1))
IF(J.EQ.2) DWDFTA=(WN-WS)/(DYC(T+1,J)+.5*DYC(I+1,J+1))
CFE(J)=CFE(J)+A1*PIH*VISE*DWDFTA*PIH*ARFAFW*A2*2.
R1=.5*(DWDXT(T+1,J)+DWDXT(I+1,J+1))
R2=.5*(DWDFTA(I+1,J)+DWDFTA(I+1,J+1))
VE=.25*(V(I,J)+V(T,J+1)+V(I+1,J)+V(T+1,J+1))
DYDXF=.5*(DYDX(T,J)+DYDX(T+1,J))
DYDYE=.5*(DYDY(T,J)+DYDY(T+1,J))
CFE(J)=CFE(J)-PIH*A2*DYDXF*VE*VTSE*ARFAFW+PIH*A1*VE*DYDYE*VTSE*
1APEAFW
HTHRE=.5*(HTHP(T+1,J)+HTHP(I+1,J+1))
IF(PIH.EQ.U) GO TO 3276
CFE(J)=CFE(J)-HTHRE*HTHRE*R2*VE*VTSE*ARFAFW/(PIH*A1)
DWDXI=(U(I+1,J)-U(T,J))/DYNN
3276 CONTINUE

```

```

50 CONTINUE
DO 100 I=2,NIM1
J=1
AREAN=DYC(I,J+1)*DZW
GND=DEN(I,J)*V(I,J+1)
GNU=DEN(I,J)*V(I,J+1)
CN=C1.5*(GND+GNU)*AREAN
C1=.5*(DETADF(I,J+1)+DETADF(I+1,J+1))
C2=DFN(I,J)*W(I,J)*AREAN
CN=C1+C1*PIH*C2
VISH=.5*(VIS(I,J)+VIS(I,J+1))
DTI=VISH*AREAN/(.25*(DYC(I,J+1)+DYC(I+1,J+1)))
IF (INDEX(FQU), DIN)=0
C1=.5*(DETADF(I+1,J+1)+DETADF(I,J+1))
C2=.5*(DETADF(I+1,J+1)+DETADF(I,J+1))
C3=C1*C2*PIH*PIH*DIN*2
DTI=C1*C2*PIH*PIH*2*.5*VISH*AREAN/(.25*(DYC(I,J+1)+DYC(I+1,J+1)))
1 +DTI
AN(I,J)=AMAY1*(WFN(I,J+1)*C1)-(1-WFN(I,J+1))*CN/DIN-WFN(I,J+1)*CN
DND7,J=1
CCH=1.0
A1=.5*(DETADF(I+1,J+1)+DETADF(I,J+1))
A2=.5*(DXIDF(I,J+1)+DXIDF(I+1,J+1))
WFEF2=DYC(I,J+1)/(DYC(I,J+1)+DYC(I+1,J+1))
WFEW2=DYC(I-1,J+1)/(DYC(I-1,J+1)+DYC(I,J+1))
WF2=W(I+1,J)*WFEF2+W(I,J)*(1-WFEF2)
WU2=W(I-1,J)*(1-WFEW2)+W(I,J)*WFEW2
DNDX1=(WE2-WU2)/DYC(I,J+1)
CCH=(CCH+A1*PIH*A2*PIH*DNDX1*AREAN*VISH)*2
A2=.5*(DETADF(I,J+1)+DETADF(I+1,J+1))
DYJN=.25*(DYC(I,J)+DYC(I,J+1)+DYC(I+1,J)+DYC(I+1,J+1))
DNDETA=0.0
A3=.5*(DXIDF(I,J+1)+DXIDF(I+1,J+1))
P1=.5*(DNDX1(I,J+1)+DNDX1(I+1,J+1))
R2=.5*(DNDETA(I,J+1)+DNDETA(I+1,J+1))
HN=.5*(H(I,J)+H(I+1,J))
WF2=V(I+1,J+1)*WFEF2+V(I,J+1)*(1-WFEF2)
WU2=V(I-1,J+1)*(1-WFEW2)+V(I,J+1)*WFEW2
DNDY1=(WF2-WU2)/DYC(I,J+1)
HTHR1=.5*(HTHR(I,J+1)+HTHR(I+1,J+1))
DYH=.25*(DYC(I,J+1)+DYC(I+1,J+1))
DNDY1=(W(I,J+1)-W(I,J))/DYH
DO 101 J=2,NJM1
C-----COMPUTE AREAS AND VOLUME-----
AREAN=DYC(I,J+1)*DZW
AREAEW=DYC(I+1,J)*DZW
AREADH=AREAXY(I,J)
C-----CALCULATE CONVECTION COEFFICIENTS-----
GND=.5*DEN(I,J)*(W(I,J)+W(I,J+1))
GNU=(DEN(I,J)*(1-WFE(I+1,J))+DEN(I+1,J)*WFE(I+1,J))*H(I+1,J)
G)
GH=(DEN(I,J)*(1-WFE(I+1,J))+DEN(I+1,J)*
1*WFE(I+1,J))*U(I+1,J)
GND=(DEN(I,J)*(1-WFE(I,J+1))+DEN(I+1,J)*WFE(I,J+1))
C*V(I,J+1)
GNU=(DEN(I,J)*(1-WFE(I,J+1))+DEN(I+1,J)*
C*WFE(I,J+1))*V(I,J+1)

```

```

CII=CU(I,J)
CD(I,J)=GD*AREADII
CS=CF(J)
CN=0.5*(GND+GNI)*AREAN
CH=CF(J)
CF(J)=0.5*(GED+GEI)*ARFAEW
C1=.5*(DETADF(I,J+1)+DETADF(I+1,J+1))
C2=(DFN(I,J)*W(I,J)*(1.-WFI(I,J+1))+DFN(I,J+1)*W(I,J+1)*WFI(I,
1J+1))*AREAN
CN=CI+C1*PIH*C2
C1=.5*(DXIDF(I+1,J)+DXIDF(I+1,J+1))
C2=(DEF(I,J)*W(I,J)*(1.-WFE(I+1,J))+DEF(I+1,J)*W(I+1,J)*
1WFF(I+1,J))*ARFAEW
CF(J)=CF(J)+C1*PIH*C2
C-----CALCULATE DIFFUSION COEFFICIENTS-----
A1=.5*(DETADF(I+1,J)+DETADF(I+1,J+1))
IF(J.LT.NJ1) VTSN=VISV(I,J)
IF(J.EQ.NJ1) VTSN=VISCOS
IF(J.LT.NJ1) VTSNE=VTSV(I,J)*DYC(I+1,J+1)/(DXC(I+1,J+1)+DYC(I,
1J+1))+VTSV(I+1,J)*DYC(I,J+1)/(DYC(I+1,J+1)+DYC(I,J+1))
IF(J.EQ.NJ1) VTSNE=VTSV(I,J)*DYC(I+1,J)/(DXC(I+1,J)+DYC(I,J))+VTSV(I+1,J-1)
1*DYC(I,J)/(DYC(I+1,J)+DYC(I,J))
VISE=.5*(VTSN+VTSNE)
VTSN=VIS(I,J)
DID=VTSN*AREADII/DYC(1)
DYNP=.25*(DYC(I,J)+DYC(I+1,J))
IF(J.EQ.NJ1) GO TO R2
R1 DYIP=DYNP+.25*(DYC(I,J+1)+DYC(I+1,J+1))
R2 DTH=VTSN*AREAN/DYNP
DYEP=.25*(DYC(I,J)+DYC(I+1,J))
R3 DYEP=DYEP+.25*(DYC(I+1,J)+DYC(I+1,J+1))
DTE=VISE*ARFAEW/DYEP
DTJ1=DTH
DTE1=DTE
C1=.5*(DXIDF(I+1,J)+DXIDF(I+1,J+1))
C2=.5*(DXIDF(I+1,J)+DXIDF(I+1,J+1))
C3=(C1*PIH*C2*FIH*DIE)*?
DTE=DTE+C3
C1=.5*(DETADF(I+1,J+1)+DETADF(I+1,J+1))
C2=.5*(DETADF(I+1,J+1)+DETADF(I+1,J+1))
C3=C1*C2*PIH*PIH*DIN*?
DTH=DTH+C3
DTE2=DTE
DTH2=DTH
C-----CALCULATE MASS SOURCE FOR USE IN STABILISATION PROCEDURE-----
SMP=CD(I,J)-CI+CI-CS+CF(J)-CW
CP=AMAX1(C,C,SMP)
CD=CP
C-----ASSEMBLE MAIN COEFFICIENTS-----
DID=AMAX1(DID,.5*CD(I,J)+.5*CD(I,J))
AI(I,J)=AD(I,J)+CI
AD(I,J)=DID+.5*CD(I,J)
AN(I,J)=AMAX1(WFI(I,J+1)*CN, (1.-WFI(I,J+1))*CN,DIN)-WFI(I,J+1)*CN
AS(I,J)=AN(I,J-1)+CS
AF(I,J)=AMAX1(WFE(I+1,J)*CE(J), (1.-WFE(I+1,J))*CE(J),DTE)
1-WFF(I+1,J)*CF(J)

```



```

AP(I,J)=AF(I-1,J)+CW
DW(I,J)=AREADII
SI(I,J)=CPO*W(I,J)=.5*AREADII*(D7C(1)+D2C(1))*DPDZ
SP(I,J)=-CP
C-----COMPLETE ASSEMBLY OF SOURCE TERMS-----
CCN=CCD(I,J)
CCS=CCN
CCW=CCE(J)
DWD7D=0.
CCD(I,J)=VISD*AREADII*DWD7D
CCD(I,J)=0.
DUD7E=0.
CCE(J)=VISE*APEAEW*DUD7E
A1=.5*(DETADF(I+1,J)+DETADF(I+1,J+1))
WFN1=DYC(I+1,J)/(DYC(I+1,J)+DYC(I+1,J+1))
WFN2=DYC(I+1,J-1)/(DYC(I+1,J-1)+DYC(I+1,J))
IINF=I(I+1,J+1)*WFN1+I(I+1,J)*(1.-WFN1)
IUSE=I(I+1,J-1)*(1.-WFN2)+I(I+1,J)*WFN2
DIIM=IINF-IUSE
IF(J.FQ.NJ1) DIIM=I(I+1,NJ)-IUSE
IF(J.FQ.2) DIIM=IINF-I(I+1,1)
DVINN=DYC(I+1,J)
CCE(J)=CCF(J)+A1*PIH*VISE*DIIM/DVINN*ARFAFW
A1=.5*(DXIDF(I+1,J)+DYIDF(I+1,J+1))
A2=.5*(DETADF(I+1,J)+DETADF(I+1,J+1))
WNE=W(I+1,J+1)*WFE(I+1,J+1)+W(I+1,J)*(1.-WFE(I+1,J+1))
WSE=W(I+1,J-1)*WFE(I+1,J-1)+W(I+1,J)*(1.-WFE(I+1,J-1))
DWDETA=(WNE-WSE)/(DYC(I+1,J)+.5*(DYC(I+1,J+1)+DYC(I+1,J-1)))
IF(J.FQ.NJ1) DWDETA=(WNE-WSE)/(DYC(I+1,J)+.5*DYC(I+1,J-1))
IF(J.FQ.2) DWDETA=(WNE-WSE)/(DYC(I+1,J)+.5*DYC(I+1,J+1))
CCE(J)=CCF(J)+2.*A1*PIH*VISE*DWDETA*PIH*APEAEW*A2
A2=.5*(DXIDF(I+1,J)+DYIDF(I+1,J+1))
DVINN=.25*(DYC(I+1,J)+DXC(I+1,J)+DYC(I+1,J+1)+DXC(I+1,J+1))
IF(T.LT.NI1) DIIDX=.5*(U(I+2,J)-U(I,J))/DXNN
IF(T.FQ.NI1) DIIDX=.5*(U(3,J)-U(I,J))/DXNN
CCF(J)=CCF(J)+PIH*A2*DIIDX*ARFAFW*VISE
C1=.5*(DETADF(I+1,J)+DETADF(I+1,J+1))
C2=.5*(DXIDF(I+1,J)+DYIDF(I+1,J+1))
R1F=.5*(DPDYI(I+1,J)+DPDYI(T+1,J+1))
R2F=.5*(DRDFTA(I+1,J)+DRDFTA(T+1,J+1))
DYDYF=DYDY(T+1,J)*WFE(I+1,J)+DYDY(I,J)*(1.-WFE(I+1,J))
DYDYF=DYDY(I+1,J)*WFE(I+1,J)+DYDY(T,J)*(1.-WFE(I+1,J))
WFE3U=DYC(I+1,J)/(DXC(I+1,J)+DXC(I+1,J+1))
WFE31=DYC(I+1,J)/(DXC(I+1,J)+DXC(I+1,J))
VWF=V(I+1,J+1)*WFE3U+V(I+1,J)*(1.-WFE3U)
VWF=V(I+1,J)*WFE31+V(I,J)*(1.-WFE31)
VF=.5*(VWF+VSE)
IF=I(I+1,J)
CCF(J)=CCF(J)-(PIH*C1*DYDYF+VF-PIH*C2*DYDYF+VF)*VISE*
1ARFAFW
HTRPE=.5*(HTRP(T+1,J)+HTRP(T+1,J+1))
IF(PIH.FQ.0.0) GO TO 3277
CCF(J)=CCE(J)-HTRPE*HTRPE*R2F*VF*VISE*APEAEW/(PIH*C2)
3277 CONTINUE
DYF=.25*(DXC(T,J)+DXC(I+1,J+1)+DXC(I+1,J)+DXC(I+1,J+1))
DWDXTF=(U(I+1,J)-W(I,J))/DXF
DUD7D=J.

```



```

SORVOL=GREAT*VCI
IF(-SP(I,J).GT.0.5*SOPVOL) RESOP=RESOP/SOPVOL
IF(-SP(I,J).GT.0.5*SOPVOL) RESW(I,J)=RESW(I,J)/SOPVOL
IF(J.EQ.2.AND.NITER.GE.MAXIT2) GO TO 4809
RESOPW=RESOPW+ABS(RESOP)
4800 CONTINUE
RESV(I,J)=RESW(I,J)/VOL
C-----IMDEF=RELAXATION
AP(I,J)=AP(I,J)/UPFW
SU(I,J)=SU(I,J)+(1.-UPFW)*AP(I,J)*W(I,J)
DW(I,J)=DW(I,J)*UPFW
301 CONTINUE
300 CONTINUE
C
CHAPTER 4 4 4 SOLUTION OF DIFFERENCE EQUATION 4 4 4 4 4 4
C
IF(NITER.GE.MAXIT2) RSC(INDEX)=0.0
IF(NITER.GE.MAXIT2) IMEG=0
IF(NITER.LT.MAXIT2) IMEG=1
DO 400 N=1,NSLPH
IF(N.GT.1.AND.NITER.GE.MAXIT2) IMEG=1
400 CALL EISOLV(2,2,NI,NJ,IT,JT,W)
IF(NITER.GE.MAXIT2) RESOPW=RESOPW+RSC(INDEX)
RETURN
END

```

## SUBROUTINE CALCP

C  
CHAPTER 0 0 0 0 0 0 0 0 PRELIMINARIES 0 0 0 0 0 0 0  
C

## COMMON

```

1 RESORU,UREF,RESORV,UREV,RESORM,RESORU,UPFW,
1 UREF,PESOPT,UPFT,RESOPK,UPFK,RESORD,URFD,
1 RESU(25,25),RESV(25,25),RESW(25,25),RESM(25,25),
1 DU(25,25),DV(25,25),DW(25,25),U(25,25),V(25,25),
1 W(25,25),P(25,25),T(25,25),TE(25,25),ED(25,25),
1 PP(25,25),DEN(25,25),VIS(25,25),AP(25,25),AS(25,25),
1 AF(25,25),AW(25,25),AU(25,25),AD(25,25),CF(25),CD(25,25),
1 CCE(25),CCD(25,25),AP(25,25),SU(25,25),SP(25,25),DXC(25,25),
1 OYC(25,25),DZC(4),WFE(25,25),WFN(25,25),WFD(4),
1 APFAXV(25,25),F1D(50,5),N1D,WMEAN,INDEX,HYDRIA,RAP,R1D(50),
1 VFLIN,TIN,TWAIL,FLOWIN,GREAT,
1 UREVIS,VISCOS,DENSIT,PRAINT,
1 PRTE,PRED,CMU,CNT,C1M,C2M,CAPPA,EI OG,ALAKDA,
1 NSUPU,NSUPV,NSUPW,NSWPP,NSWPT,
1 NSWPK,NSWPD,
1 IPREF,JPREF,KPREF,INDCOS
COMMON TAUXS(25),TAUXN(25),TAUYS(25),TAUYN(25),
1 YPLUSS(25),YPLUSN(25)
1 IT,JT,N1,NJ,NIM1,NJM1
1 SWET,FLOWTOT,CPW,CFLUX,FLOWT
1 N1,N2
1 PA,RP,THETA,AR,DRD7,FLOWAX,DXIDF(25,25),DETANF(25,25),PIW
1 DRDXT(25,25),DRDETA(25,25),HTHP(25,25)
1 PI,HTH,FLOWW
1 SHALI,SHMS,SHHD,INIMP,DXDY(25,25),DYDX(25,25)
LEVEL 2,III
COMMON/RLK2/BU(25,25),VV(25,25),AWU(25,25),ASU(25,25),
1 AFU(25,25),AWU(25,25),ADU(25,25),AUU(25,25),
1 ARV(25,25),ASV(25,25),AFV(25,25),AWV(25,25),
1 CONT(25,10),VPA(25),JTS,
1 ADV(25,25),AUV(25,25),AA(25)
1 JF,THOTH,TER(25,2),FDR(25,2),PRODD(50),GENH(25,25)
1 PRANDL,GHT(25,25),ANUS
1 PRODD(25,25),AKZ(25,25),AKD(25,25),AKA(25,25),RVT(25,25),AKF
1 AKFT,AKFTD,AKCTD,F1P(25),F1KZ(25),F1KD(25),F1KA(25),F1RVT(25)
1 NQIMP,CNHA(25,25),CHUR(25)
1 NQIMP2
1 APII(25,25),APV(25,25),RR(25,25),ANGL(25,25)
1 KASH,NASM
1 VISV(25,25),VA(25,25),VB(25,25),VC(25,25)
1 RSC(5),IMEG,MAYIT2
1 RRS(25,25),PPH,HTTER,MAYIT
1 TLFNSC,VISID(50),XPLL(25,25)

```

C  
CHAPTER 1 1 1 1 1 1 ASSEMBLY OF COEFFICIENTS 1 1 1 1 1 1 1  
C

```

DO 10 I=1,NJ
DO 10 J=1,NJ
10 PR(T,J)=0.
RESORM=0.0
DO 49 I=2,NJM1
DO 49 J=2,NJM1

```

```

AHEADII=AREAXY(I,J)
DENN=DEN(I,J)
CN(I,J)=DENN*W(I,J)*AHEADII
AN(I,J)=DENN*AREFADII*DU(I,J)
49 CONTINUE
DO 511 J=2,NJN1
  I=1
  APEAFU=DYC(I+1,J)*DZC(1)
  DENF=DEN(I,J)
  CF(J)=DENF*II(I+1,J)*APEAFU
  AF(I,J)=DENF*ARFAEW*DI(I+1,J)
511 CONTINUE
DO 1111 I=2,NIN1
  J=1
  APEAN=DYC(I,J+1)*DZC(1)
  DENF=DEN(I,J)
  CN=DENF*V(I,J+1)*ARFAN
  AN(I,J)=DENF*ARFAN*DV(I,J+1)
DO 111 J=2,NJN1
C-----COMPUTE AREAS AND VOLUME-----
APEAN=DYC(I,J+1)*DZC(1)
APEAFU=DYC(I+1,J)*DZC(1)
AREFADII=AREAXY(I,J)
C-----CALCULATE COEFFICIENTS-----
DENF=DEN(I,J)*(1.-WFN(I,J+1))+DEN(I,J+1)*WFN(I,J+1)
DENF=DEN(I,J)*(1.-WFE(I+1,J))+DEN(I+1,J)*WFE(I+1,J)
DENN=DEN(I,J)*(1.-WFD(1))+DEN(I,J)*WFD(1)
AN(I,J)=DENN*ARFAN*DV(I,J+1)
AS(I,J)=AT(I,J-1)
AF(I,J)=DENF*ARFAEW*DI(I+1,J)
AU(I,J)=AF(I-1,J)
AI(I,J)=AD(I,J)
AN(I,J)=DENN*AREFADII*DU(I,J)
C-----CALCULATE SOURCE TERMS-----
IF(THIMP_FU_1) GO TO 1946
CS=CU
CN=DENF*V(I,J+1)*ARFAN
CU=CE(J)
F(I)=DENF*II(I+1,J)*APEAFU
II=FD(I,J)
CN(I,J)=DENF*V(I,J)*AHEADII
SPP=CN-CS+CF(J)-CU+FD(I,J)-CU
SP(I,J)=II-U
SI(I,J)=SPP
C-----EXTRA TERMS DUE TO SPIRALLING-----
A1=.5*(DXIDF(I+1,I)+DXIDF(I+1,J+1))
A2=.5*(DXIDF(I,J)+DXIDF(I,J+1))
A3=.5*(DETADF(I,J+1)+DETADF(I+1,J+1))
A4=.5*(DETADF(I,J)+DETADF(I+1,J))
C3=(DEN(I+1,J)*V(I+1,I)*WFE(I+1,J)+DEN(I,J)*W(I,J)*(1.-WFE(I+1,
1J)))*DYC(I+1,J)*DZC(1)
C4=(DEN(I-1,J)*II(I-1,I)*(1.-WFE(I,J))+DEN(I,J)*W(I,I)*WFE(I,J))*
1DYC(I,J)*DZC(1)
C5=(DEN(I,J+1)*W(I,J+1)*WFN(I,J+1)+DEN(I,I)*W(I,J)*(1.-WFN(I,I+1)
1))*DXC(I,J+1)*DZC(1)
C6=(DEN(I,J-1)*W(I,J-1)*(1.-WFN(I,J))+DEN(I,J)*W(I,I)*WFN(I,J))*
1DYC(I,J)*DZC(1)

```

```

SOURCE=A1*PIH*C3-A2*PIH*C4+A3*PIH*C5-A4*PIH*C6
SH(I,J)=SH(I,J)-SOURCE
SUMS=SUMS+SH(I,J)
GO TO 1947
1946 CONTINUE
IF (T.LT.NIM1) AA(T)=DEFN*AREAFW*(AEU(I+1,J)*UU(I+2,J)+AWU
1(I+1,J)*UU(I,J)+AHU(I+1,J)*UU(I+1,J+1)+ASU(I+1,J)*UU
1(I+1,J-1)+ADU(I+1,J)*UU(I+1,J)+AHU(I+1,J)*UU(I+1,J
1))/ (APH(I+1,J)+SMALL)
IF (T.EQ.NIM1) AA(T)=DEFN*AREAFW*(AEU(2,J)*UU(3,J)+AWU(2,J)*
1UU(1,J)+AHU(2,J)*UU(2,J+1)+ASU(2,J)*UU(2,J-1)+ADU(2,J)
1*UU(2,J)+AHU(2,J)*UU(2,J))/ (APH(2,J)+SMALL)
HR=-5*(DEN(I,J)+DEN(I-1,J))*DVC(I,J)*DZC(1)*(AEU(I,J)*UU
1(I+1,J)+AWU(I,J)*UU(I-1,J)+AHU(I,J)*UU(I,J+1)+ASU(
1I,J)*UU(I,J-1)+ADU(I,J)*UU(I,J)+AHU(I,J)*UU(I,J))
1/(APH(I,J)+SMALL)
CC=DEFN*AREAN*(AEV(I,J+1)*VV(I+1,J+1)+AVV(
1I,J+1)*VV(I-1,J+1)+AHV(I,J+1)*VV(I,J+2)+ASV(I,J+1)*
1VV(I,J)+ADV(I,J+1)*VV(I,J+1)+AHV(I,J+1)*VV(I,J+1))
1/(APV(I,J+1)+SMALL)
IF (J.EQ.2) DD=0
IF (J.GT.2) DD=-5*(DEN(I,J)+DEN(I,J-1))*DXC(I,J)*DZC(1)*(
1AEV(I,J)*VV(I+1,J)+AHV(I,J)*VV(I-1,J)+AVV(I,J)*VV(
1I,J+1)+ASV(I,J)*VV(I,J-1)+ADV(I,J)*VV(I,J)+AHV(I,J)
1)*VV(I,J))/ (APV(I,J)+SMALL)
SH(I,J)=-(AA(T)-HR+CC-DD)
SHAD=SHAD+SH(I,J)
SP(I,J)=0.0
GO TO 1944
1947 CONTINUE
RESM(I,J)=SH(I,J)
RESM(T,J)=RESM(T,J)/AREAFX(T,J)
RESORM=RESORM+ABS(SH(T,J))
1944 CONTINUE
101 CONTINUE
100 CONTINUE
C
CHAPTER 2 2 2 2 2 2 2 PROBLEM MODIFICATIONS 2 2 2 2 2 2
C
CALL MODP
C
CHAPTER 3 3 3 3 3 FINAL COEFFICIENT ASSEMBLY 3 3 3 3 3 3
C
DO 300 T=2,NIM1
DO 301 J=2,NJM1
301 AP(I,J)=AP(I,J)+AS(T,J)+AF(I,J)+AW(I,J)+AD(T,J)+AH(T,J)
1=SP(I,J)
300 CONTINUE
C
CHAPTER 4 4 4 4 4 SOLUTION OF DIFFERENCE EQUATIONS 4 4 4 4 4
C
DO 400 N=1,NSWPP
400 CALL LISOLV(2,2,NIM1,NJM1,IT,JT,PP)
90 CONTINUE
DO 2018 J=2,NJM1
PP(1,J)=PP(NIM1,J)
2018 PP(NT,J)=PP(2,J)

```

```

      DO 2817 I=2,NIM1
2817 PP(I,1)=PP(I,2)
C
CHAPTER 5 5 5 5 CORRECT VELOCITIES AND PPESSURE 5 5 5 5 5
C
      DO 500 I=2,NIM1
      DO 501 J=2,NJM1
C-----CORRECTION OF THE VFLOCITIES-----
      IF (JUMP.EQ.1) GO TO 1949
      U(I,J)=U(I,J)+DU(I,J)*(PP(I-1,J)-PP(I,J))
      IF (J.NE.2) V(I,J)=V(I,J)+DV(I,J)*(PP(I,J-1)-PP(I,J))
501 CONTINUE
500 CONTINUE
504 CONTINUE
      DO 2013 I=2,NIM1
      DO 2013 J=2,NJM1
      UU(I,J)=UU(I,J)*(PP(I-1,J)-PP(I,J))
2013 IF (J.NE.2) VV(I,J)=VV(I,J)*(PP(I,J-1)-PP(I,J))
      DO 2014 J=2,NJM1
      UU(1,J)=UU(NIM1,J)
2014 UU(NI,J)=UU(2,J)
      DO 2016 I=2,NIM1
      UU(I,1)=UU(I,2)
      UU(I,NJ)=0.0
      VV(I,1)=0.0
      VV(I,2)=0.0
2016 VV(I,NJ)=0.0
      DO 2019 J=2,NJM1
      VV(1,J)=VV(NIM1,J)
2019 VV(NI,J)=VV(2,J)
      UU(1,1)=UU(NIM1,1)
      UU(1,NJ)=0.0
      UU(NI,1)=UU(2,1)
2018 UU(NI,NJ)=0.0
      VV(1,1)=VV(NIM1,1)
      VV(1,NJ)=0.0
      VV(NI,1)=VV(2,1)
2020 VV(NI,NJ)=0.0
1949 CONTINUE
C-----PRESSURES(WITH PROVISION FOR UNDER-RELAXATION)-----
      PPREF=PP(2,2)
      DO 502 I=2,NIM1
      DO 502 J=2,NJM1
      P(I,J)=P(I,J)+UPFP*(PP(I,J)-PPREF)
      P(1,J)=P(NIM1,J)
      P(NI,J)=P(2,J)
      P(I,1)=P(I,2)
      P(I,NJ)=P(I,NJM1)
502 CONTINUE
      P(NI,1)=P(2,2)
      P(NI,NJ)=P(2,NJM1)
      P(1,1)=P(NIM1,2)
      PPREF=PP(2,2)
      RETURN
      END

```

## SUBROUTINE CALCT

C  
CHAPTER 0 0 0 0 0 0 0 PRELIMINARIES 0 0 0 0 0 0  
C

## COMMON

```

1 RESORU,URFU,RESORV,URFV,RESORM,RESORW,URFW,
1 URFP,RESOPT,URFT,RESOPK,URFK,RESOPD,URFD,
1 RESU(25,25),RESV(25,25),RESW(25,25),RESM(25,25),
1 DU(25,25),DV(25,25),DW(25,25),U(25,25),V(25,25),
1 W(25,25),D(25,25),T(25,25),TE(25,25),ED(25,25),
1 HP(25,25),UFH(25,25),VIS(25,25),AN(25,25),AS(25,25),
1 AF(25,25),AV(25,25),AU(25,25),AD(25,25),CE(25),CD(25,25),
1 CCE(25),CCD(25,25),AP(25,25),SU(25,25),SP(25,25),DXC(25,25),
1 DYC(25,25),DYC(4),WFE(25,25),WFH(25,25),WFD(4),
1 APFAXY(25,25),FID(50,5),HID,WMEAN,INDEX,HYDRIA,PAF,RID(50),
1 VELIN,TJN,TWALL,FLWIN,GRFAT,
1 URFVIS,VISCOS,DENSIT,PRAHT,
1 PRTE,PRED,CMU,CNT,C1H,C2H,CAPPA,ELOG,ALANDA,
1 NSWPI,NSWPIV,NSWPIW,NSWPP,NSWPT,
1 NSWPK,NSWPD,
1 IPREF,JPREF,KPREF,INDCOS
COMMON TAUXS(25),TAUXN(25),TAUZY(25),TAUZN(25),
1 YPLUSS(25),YPLUSN(25)
1 TT,JT,NI,NJ,NIM1,NJM1
1 SVET,FLOWTOT,CPW,QFLUX,FLOWT
1 NI,NJ
1 RA,RR,THETA,AN,DPD7,FLWAX,DXINF(25,25),DETADF(25,25),PIH
1 DRDXT(25,25),DPDFTA(25,25),HTHR(25,25)
1 PI,WIN,FLOWN
1 SMALL,SUMS,SUMD,INUMR,DXDY(25,25),DYDX(25,25)
LEVEL 2,III
COMMON/RLK2/UU(25,25),VV(25,25),ANU(25,25),ASU(25,25),
1 AFU(25,25),AWU(25,25),ADU(25,25),AUU(25,25),
1 ANV(25,25),ASV(25,25),AFV(25,25),AWV(25,25),
1 COT(25,10),VRN(25),JTS,
1 ADV(25,25),AIV(25,25),AA(25)
1 JG,THOTH,TER(25,2),FDR(25,2),PRDD(50),GENN(25,25)
1 PRANDL,GIT(25,25),ANUSS
1 FMDU(25,25),AK7(25,25),AKD(25,25),AKA(25,25),RVT(25,25),AKF
1 AKFT,AKFTD,AKCTD,F1P(25),F1K2(25),F1K0(25),F1KA(25),F1RVT(25)
1 NOLUP,CMHA(25,25),CMUR(25)
1 NOLUP2
1 APH(25,25),APV(25,25),PR(25,25),ANGL(25,25)
1 KASH,NASK
1 VISV(25,25),VA(25,25),VH(25,25),VC(25,25)
1 RSC(5),IMEG,MAXIT2
1 PRS(25,25),PRB,NITER,MAXIT
1 TLFHSC,VTSID(50),XPLL(25,25)

```

C  
CHAPTER 1 1 1 1 1 1 ASSEMBLY OF COEFFICIENTS 1 1 1 1 1 1  
C

```

RESORT=0.0
DO 49 J=2,NJM1
DO 49 J=2,NJM1
AREADU=AREAXY(1,J)
GD=DFN(J,J)*W(J,J)
CD(I,J)=GD*AREADU

```



```

      GAMN=GNT(I,J)
      DID=GAMN*AREADU/(.5*D7C(1))
      AN(I,J)=AMAX1(WFD(1)*CD(I,J),-(1.-WFD(1))*CD(I,J),DID)
      1=WFD(1)*CD(I,J)
49  CONTINUE
      DO 50 J=2,NJM1
      I=1
      ARFAW=DYC(I+1,J)*D7C(1)
      GF=DFN(I,J)*U(I+1,J)
      CF(J)=GF*ARFAW
      C1=.5*(DXIDF(I+1,J)+DXIDF(I+1,J+1))
      C2=DFN(I,J)*W(I,J)*(1.-WFE(I+1,J))+DEN(I+1,J)*W(I+1,J)*WFE(I+1,J)
      CF(J)=CF(J)+C1*PIH*C2+APEAEU
      GME=.25*(GMT(I,J)+GMT(I+1,J)+GMT(I,J-1)+GMT(I+1,J-1))
      DTF=GME*ARFAW/(.25*(DYC(I+1,J)+DXC(I+1,J+1)+DXC(I,J)+DXC(I,J+1)
      1))
      DTE=DTE*(1.+PIH*PIH*C1*C1)
      AF(I,J)=AMAX1(WFE(I+1,J)*CE(J),-(1.-WFE(I+1,J))*CE(J),DTE)
      1=WFE(I+1,J)*CE(J)
      DTXIF=(1+(I+1,J)-T(I,J))/(.25*(DXC(I+1,J)+DXC(I+1,J+1)+DXC(I,J)+
      1DYC(I,J+1)))
      TH=.25*(T(I,J)+T(I+1,J)+T(I,J+1)+T(I+1,J+1))
      IF(J.EQ.NJM1) TH=.5*(T(I,NJ)+T(I+1,NJ))
      TS=.25*(T(I,J)+T(I+1,J)+T(I,J-1)+T(I+1,J-1))
      IF(J.EQ.2) TS=.5*(T(I,1)+T(I+1,1))
      DTDETAE=(TH-TS)/DYC(I+1,J)
      C3=.5*(DETANF(I+1,J)+DETANF(I+1,J+1))
      CCE(J)=PIH*PIH*C1*C3*GAME*APEAEU*DTDETAE
      CCE(J)=CCE(J)+PIH*C1*GAME*APEAEU*QFLUX*SWET/CPW/FLOWT
50  CONTINUE
      DO 100 I=2,NIM1
      J=1
      ARFAN=DXC(I,J+1)*D7C(1)
      GM=DFN(I,J)*V(I,J+1)
      CM=GM*ARFAN
      C1=.5*(DETANF(I,J+1)+DETANF(I+1,J+1))
      C2=DFN(I,J)*W(I,J)*ARFAN
      CM=CM+C1*PIH*C2
      GAMN=GMT(I,J)
      DIN=GAMN*AREAN/(.25*(DYC(I,J+1)+DYC(I+1,J+1)))
      DTN=DTN*(1.+PIH*PIH*C1*C1)
      AN(I,J)=AMAX1(WFN(I,J+1)*CN,-(1.-WFN(I,J+1))*CN,DIN)-WFN(I,J+1)*CN
      C4=.5*(DXIDF(I,J+1)+DXIDF(I+1,J+1))
      DTXIN=(T(I+1,J)-T(I,J))/(DXC(I,J+1)+.5*(DXC(I-1,J+1)+DXC(I+1,
      1J+1)))
      CCN=PIH*PIH*C1*C4*GAMN*AREAN*DTXIN
      CCN=CCN+PIH*C1*GAMN*ARFAN*QFLUX*SWET/CPW/FLOWT
      DO 101 J=2,NJM1
C----- COMPUTE AREAS AND VOLUME-----
      AREAN=DXC(I,J+1)*D7C(1)
      APEAEU=DYC(I+1,J)*D7C(1)
      AREADU=AREAYY(I,J)
C----- CALCULATE CONVECTION COEFFICIENTS-----
      GN=(DFN(I,J)*(1.-WFN(I,J+1))+DEN(I,J+1)+WFN(I,J+1))*V(I,J+1)
      GF=(DFN(I,J)*(1.-WFE(I+1,J))+DEN(I+1,J)*WFE(I+1,J))*U(I+1,J)
      GD=(DFN(I,J)*(1.-WFD(1))+DEN(I,J)*WFD(1))*W(I,J)
      GS=GM

```

```

CN=GI*AREAU
C11=.5*(DETADF(I,J+1)+DETADF(I+1,J+1))
C2=DFN(I,J)*W(I,J)*(1.-WFN(I,J+1))+DEN(I,J+1)*W(I,J+1)*WFN(I,J+1)
CN=CN+C11*PIH+C2*AREAN
C4=CE(J)
CF(J)=GF*ARFAFW
C12=.5*(DXIDF(I+1,J)+DXIDF(I+1,J+1))
C7=DFN(I,J)*W(I,J)*(1.-WFF(I+1,J))+DEN(I+1,J)*W(I+1,J)*WFF(I+1,J)
CF(I)=CF(J)+C12*PIH+C7*ARFAFW
CU=CD(I,J)
CD(I,J)=GD*ARFADU
C-----CALCULATE DIFFUSION COEFFICIENTS-----
IF(J.LT.NJH1) GAMN=GMT(I,J)
IF(J.EQ.NJH1) GAMN=GMT(I,NJ)
IF(J.LT.NJH1) GAMNE=GMT(I,J)*DXC(I+1,J+1)/(DXC(I+1,J+1)+DXC(I,J+1))+GMT(I+1,J)*DXC(I,J+1)/(DXC(I+1,J+1)+DXC(I,J+1))
IF(J.EQ.NJH1) GAMNE=GMT(I,NJ)
IF(J.NE.2) GAMSE=GMT(I,J-1)*DXC(I+1,J)/(DXC(I+1,J)+DXC(I+1,J+1))+GMT(I+1,J-1)*DXC(I,J)/(DXC(I+1,J)+DXC(I+1,J+1))
IF(J.EQ.2) GAMSE=.5*(GMT(I,1)+GMT(I+1,1))
GAME=.5*(GAMNE+GAMSE)
IF(J.LT.NJH1) GAND=.5*(GMT(I,J)+GMT(I,J-1))
NJH2=NJ-2
IF(J.EQ.NJH1) GAND=.5*(GMT(I,NJ)+GMT(I,NJH2))
DYNP=.25*(DYC(I,J)+DYC(I+1,J))
IF(J.EQ.NJH1) GO TO R2
R1 DYNP=DYNP+.25*(DYC(I+1,J)+DYC(I+1,J+1))
R2 DTJ=GAMN*AREAN/DYNP
DTJ=DTJ*(1.+PIH*PIH*C11*C11)
DYEP=.25*(DYC(I,J)+DYC(I,J+1))
R3 DYEP=DYEP+.25*(DYC(I+1,J)+DYC(I+1,J+1))
R4 DJE=GAMF*ARFAFW/DYEP
DTE=DTE*(1.+PIH*PIH*C12*C12)
D7DP=.5*D7C(1)
R5 D7DP=D7DP+.5*D7C(1)
R6 DTJ=GAND*ARFADU/D7DP
C-----CALCULATE MASS SOURCE FOR USE IN STABILISATION PROCEDURE-----
SMP=CN-CS+CF(J)-CW+CD(I,J)-CU
CP=MAX1(0.,CP,SMP)
CD=CP
C-----ASSEMBLE MATR. COEFFICIENTS-----
AN(I,J)=AMAX1(WFN(I,J+1)*CN,-(1.-WFN(I,J+1))*CN,DTN)-WFN(I,J+1)*CN
AS(I,J)=AN(I,J-1)+CS
AF(I,J)=AMAX1(WFF(I+1,J)*CE(J),-(1.-WFF(I+1,J))*CE(J),DIF)
1-WFF(I+1,J)*CE(J)
AU(I,J)=AF(I,J)+CW
AU(I,J)=AU(I,J)+CU
AD(I,J)=AMAX1(WFD(1)*CD(I,J),-(1.-WFD(1))*CD(I,J),D7D)
1-WFD(1)*CD(I,J)
SU(I,J)=CPU*T(I,J)
VOL=ARFAXY(I,J)*D7C(1)
SU(I,J)=SU(I,J)-(DEN(I,J)*U(I,J)*QFLUX*SWET/FLOWT)*VOL*NZC(1)
1/CPW
SP(I,J)=-CP
CCS=CCN
CCW=CCF(J)
UTDXIF=(T(I+1,J)-T(I,J))/DXEP

```

```

C13=.5*(DETADF(I+1,J)+DETADF(I+1,J+1))
IF(J.EQ.NJM1) GO TO 3583
TN1=T(I,J)*(1.-WFF(I+1,J))+T(I+1,J)*WFE(I+1,J)
TN2=T(I,J+1)*(1.-WFF(I+1,J+1))+T(I+1,J+1)*WFE(I+1,J+1)
WFNT=DYC(I+1,J)/(DYC(I+1,J)+DYC(I+1,J+1))
TN=TN1*(1.-WFNT)+TN2*WFNT
GO TO 3683
3583 CONTINUE
TN=T(I,NJ)*(1.-WFF(I+1,NJ))+T(I+1,NJ)*WFE(I+1,NJ)
3683 CONTINUE
IF(J.EQ.2) GO TO 3795
TS1=T(I,J)*(1.-WFF(I+1,J))+T(I+1,J)*WFE(I+1,J)
TS2=T(I,J-1)*(1.-WFF(I+1,J-1))+T(I+1,J-1)*WFE(I+1,J-1)
WFST=DYC(I+1,J-1)/(DYC(I+1,J-1)+DYC(I+1,J))
TS=TS1*WFST+TS2*(1.-WFST)
GO TO 3796
3795 CONTINUE
TS=T(I,1)*(1.-WFE(I+1,1))+T(I+1,1)*WFF(I+1,1)
3796 CONTINUE
DTUFTAE=(TN-TS)/DYC(I+1,J)
CCE(J)=PIH*PIH*C12*(C13*GAME*ARFAEW*DTDETAF
CCE(J)=CCE(J)+PIH*C12*GAME*ARFAEW*QFLHX*SWET/CPW/FLOWT
C14=.5*(DXIDF(I,J+1)+DXIDF(I+1,J+1))
IF(J.EQ.NJM1) GO TO 4455
TN3=T(I,J)*WFE(I,J)+T(I-1,J)*(1.-WFF(I,J))
TN4=T(I,J+1)*WFE(I,J+1)+T(I-1,J+1)*(1.-WFF(I,J+1))
WFHW=DYC(I,J)/(DYC(I,J)+DYC(I,J+1))
TNW=TN3*(1.-WFHW)+TN4*WFHW
GO TO 4466
4455 CONTINUE
TNW=T(I,NJ)*WFE(I,NJ)+T(I-1,NJ)*(1.-WFE(I,NJ))
4466 CONTINUE
DTDXIN=(TN-TNW)/DYC(I,J+1)
CCN=PIH*PIH*C11*C14*GAMH*ARFAN*DTDXIN
CCJ=CCN+PIH*C11*GAMH*ARFAN*QFLHX*SWET/CPW/FLOWT
SU(I,J)=SU(I,J)+CCE(J)-CCW+CCN-CCS
101 CONTINUE
100 CONTINUE
C
CHAPTER 2 2 2 2 2 2 PROBLEM MODIFICATIONS 2 2 2 2 2 2
C
CALL MODT
C
CHAPTER 3 FINAL COEFFICIENT ASSEMBLY AND RESIDUAL SOURCE CALCULATION 3
C
DO 300 J=2,NJM1
DO 301 J=2,NJM1
AP(I,J)=AN(I,J)+AS(I,J)+AF(I,J)+AW(I,J)+AD(I,J)+AU(I,J)-SP(I,J)
RESOR=AN(I,J)*T(I,J+1)+AS(I,J)*T(I,J-1)+AF(I,J)*T(I+1,J)
1 +AW(I,J)*T(I-1,J)+AD(I,J)*T(I,J)+AU(I,J)*T(I,J)
1 -AP(I,J)*T(I,J)+SU(I,J)
VOL=AREAXY(I,J)*D7C(1)
SORVOL=GREAT*VOL
IF(-SP(I,J).GT.0.5*SURVOL) RESOR=RESOR/SORVOL
IF(J.EQ.2.AND.NITER.GE.MAXIT2) GO TO 4808
RESORT=RESORT+APS(RESOR)
4808 CONTINUE

```

```

C-----UNDER-RELAXATION
      AP(I,J)=AP(I,J)/URFT
      SU(I,J)=SU(I,J)+(1.-URFT)*AP(I,J)*T(I,J)
301 CONTINUE
300 CONTINUE
C
CHAPTER 4 4 4 4 4 SOLUTION OF DIFFERENCE EQUATIONS 4 4 4 4 4
C
      IF(NITER.GE.MAXIT2) RSC(INDEX)=0.0
      IF(NITER.GE.MAXIT2) IMFG=0
      IF(NITER.LT.MAXIT2) IMFG=1
      DO 400 N=1,NSUPT
      IF(N.GT.1.AND.NITER.GE.MAXIT2) IMFG=1
400 CALL LISOLV(2,2,NI,NJ,IT,JT,T)
      IF(NITER.GE.MAXIT2) RESORT=RESORT+RSC(INDEX)
      RETURN
      END

```

## SUBROUTINE CALCTE

```

C
CHAPTER 0 0 0 0 0 0 0 PRELIMINARIES 0 0 0 0 0 0
C
COMMON
1 RESORII,URFU,RESORV,URFV,RESORM,RESOPW,URFW,
1 URFP,RESOPT,URFT,RESORK,URFK,RESORD,URFD,
1 RESII(25,25),RESV(25,25),RESW(25,25),RESM(25,25),
1 DII(25,25),DV(25,25),DU(25,25),U(25,25),V(25,25),
1 W(25,25),P(25,25),T(25,25),TE(25,25),FD(25,25),
1 PP(25,25),DEF(25,25),VIS(25,25),AN(25,25),AS(25,25),
1 AF(25,25),AW(25,25),AH(25,25),AD(25,25),CE(25),CD(25,25),
1 CCE(25),CCD(25,25),AP(25,25),SH(25,25),SP(25,25),DXC(25,25),
1 DYC(25,25),D7C(4),WFE(25,25),WFN(25,25),WFD(4),
1 AREAXY(25,25),F1D(50,5),N1D,WMEAN,INDEX,HYDDIA,RAP,R1D(50),
1 VELIN,TIN,TWALL,FLOWIN,GREAT,
1 HREFVIS,VISCOS,DEFENSIT,PRANDT,
1 PRTE,PRED,CMII,CHT,C1II,C2II,CAPPA,ELOG,ALANDA,
1 NSWPII,NSWPIV,NSWPIJ,NSWPIP,NSWPT,
1 NSWPK,NSWPD,
1 IPREF,JPREF,KPREF,INDCOS
COMMON TAUXX(25),TAUXN(25),TAUZZ(25),TAUZN(25),
1 YPLUSS(25),YPLUSN(25)
1 ,IT,JT,N1,IIJ,NIM1,NJM1
1 ,SWET,FLOWTOT,CPW,DFLUX,FLOWT
1 ,N1,N2
1 ,RA,RP,THETA,AH,DPDZ,FLOWAX,DXIDF(25,25),DETADF(25,25),PIH
1 ,DRDXI(25,25),DRDFTA(25,25),HTHP(25,25)
1 ,PI,WTH,FLOWW
1 ,SITALL,SUMS,SHMM,TIIMR,DXDY(25,25),DYDX(25,25)
1 LEVEL 2,III
COMMON/PLK2/UU(25,25),VV(25,25),ANU(25,25),ASH(25,25),
1 AFH(25,25),AWH(25,25),ADU(25,25),AUH(25,25),
1 ANV(25,25),ASV(25,25),AFV(25,25),AWV(25,25),
1 COMT(25,10),VPH(25),JTS,
1 ADV(25,25),AHV(25,25),AA(25)
1 ,JG,INOTH,TER(25,2),FDR(25,2),PRODD(50),GENN(25,25)
1 ,PRANDL,CHT(25,25),AMUSS
1 ,PRDD(25,25),AK7(25,25),AKD(25,25),AKA(25,25),RVT(25,25),AKF
1 ,AKET,AKETD,AKCTD,F1P(25),F1VZ(25),F1KD(25),F1KA(25),F1RVT(25)
1 ,NOIMP,CFIIA(25,25),CHIR(25)
1 ,NOIMH2
1 ,APU(25,25),APV(25,25),RR(25,25),ANGL(25,25)
1 ,KASH,NASH
1 ,VISV(25,25),VA(25,25),VB(25,25),VC(25,25)
1 ,PSC(5),IMEF,MAYIT2
1 ,PRS(25,25),RRD,HTFR,MAXTT
1 ,TIEHSC,VTS1D(50),XMLL(25,25)
1 DTIEUSION GEN(25,25)
----- NOTE TEMPORARY USE OF PP-ARRAY -----
EQUIVALENCE (PP(1,1),GEN(1,1))

C
CHAPTER 1 1 1 1 1 1 ASSEMBLY OF COEFFICIENTS 1 1 1 1 1 1
C
RESORK=0.
JGM1=JG-1

```

```

DO 500 J=2,JGM1
  I=1
  ARFAFW=DYC(I+1,J)*D7C(1)
  GF=DEF(I,J)*U(I+1,J)
  AK1=.5*PIH*(DXIDF(I+1,J)+DXIDF(I+1,J+1))
  AK2=.5*PIH*(DETADF(I+1,J)+DETADF(I+1,J+1))
  GF=GF+DEF(I,J)*(WFE(I+1,J)*W(I+1,J)+(1.-WFE(I+1,J))*W(I,J)
1)*AK1
  DYE=DYC(I+1,J)+.5*(DYC(I+1,J+1)+DYC(I+1,J-1))
  IF(J.FO.2) DYE=DYC(I+1,J)+.5*DYC(I+1,J+1)
  DEFYF=((WFE(I+1,J+1)*TE(I+1,J+1)+(1.-WFE(I+1,J)
1J+1))
1*TE(I,J+1)-(WFE(I+1,J-1)*TE(I+1,J-1)+(1.-WFE(I+1,J-1))*TE(I,J-
1)))/DYE
  GAIF=.5*(VIS(I,J)+VIS(I+1,J))/POTE
  CFF(I)=GAME*AK1*AK2*DFDYE*ARFAEW
  CF(I)=GF*ARFAEW
  DTF=GAME*ARFAEW/(.25*(DXC(I+1,J)+DXC(I+1,J+1)+DXC(I,J)+DXC(I,
1J+1)))
  DIE=DTE*(1.+AK1*AK1)
  AF(I,J)=AMAX1(WFE(I+1,J)*CF(I),(1.-WFE(I+1,J))*CF(I),DIE)
  I=WFE(I+1,J)*CF(I)
500 CONTINUE
DO 1000 T=2,TJM1
  J=1
  AREAN=DYC(I,J+1)*D2C(1)
  GN=DEF(I,J)*V(I,J+1)
  AK1=.5*(DXIDF(I,J+1)+DXIDF(I+1,J+1))*PIH
  AK2=.5*PIH*(DETADF(I,J+1)+DETADF(I+1,J+1))
  GN=GN+DEF(I,J)*(WFE(I,J+1)*W(I,J+1)+(1.-WFE(I,J+1))*W(I,J)
1)*AK2
  DYJ=DYC(I,J+1)+.5*(DYC(I+1,J+1)+DYC(I-1,J+1))
  DFDXJ=(TE(I+1,J)-TE(I-1,J))/DXH
  GAJN=VIS(I,J)/FOTE
  CFJ=GAJN*AK1*AK2*ARFAN*DFDXN
  CN=GF*AREAN
  DTN=GAJN*AREAN/(.25*(DYC(I,J+1)+DYC(I+1,J+1)))
  DTN=DTN*(1.+AK2*AK2)
  AN(I,J)=AMAX1(WFE(I,J+1)*CN,(1.-WFE(I,J+1))*CN,DTN)-WFE(I,J+1)*CN
DO 1001 J=2,JGM1
C-----COMPUTE AREAS AND VOLUME-----
  ARFAJ=DYC(I,J+1)*D7C(1)
  ARFAFW=DYC(I+1,J)*D7C(1)
  ARFAUJ=ARFAYY(I,J)
C-----CALCULATE CONVECTION COEFFICIENTS-----
  GN=(DEF(I,J)*(1.-WFE(T,J+1))+DEF(T,J+1)*WFE(I,J+1))*V(I,J+1)
  GF=(DEF(I,J)*(1.-WFE(T+1,J))+DEF(T+1,J)*WFE(I+1,J))*H(I+1,J)
  AK1=.5*PIH*(DXIDF(I+1,J)+DXIDF(I+1,J+1))
  GN=GN+(DEF(I,J)*W(I,J)*(1.-WFE(I,J+1))+DEF(I,J+1)
1*W(T,J+1)*WFE(T,J+1))*AK1
  GF=GF+(DEF(I,J)*W(I,J)*(1.-WFE(I+1,J))+
1DEF(T+1,J)*W(I+1,J)*WFE(T+1,J))*AK1
  GN=(DEF(I,J)*(1.-WFE(1))+DEF(T,J)*WFE(1))*W(I,J)
  CS=CF
  CN=GF*AREAN
  CU=CF(I)

```

```

CF(J)=GE*ARFAFL
CI=0.0
C-----CALCULATE DIFFUSION COEFFICIENTS-----
GAMN=VISV(I,J)/PRTE
GAME=(VIS(I,J)*(1.-WFE(I+1,J))+VIS(I+1,J)*WFE(I+1,J))/PRTE
GAND=(VTS(I,J)*(1.-WFH(1))+VTS(I,J)*WFH(1))/PRTE
DYNP=.25*(DYC(I,J)+DYC(I+1,J))
R1 DYNP=DYNP+.25*(DYC(I,J+1)+DYC(I+1,J+1))
R2 DTN=GAMN*ARFAN/DYNP
DIN=DIN*(1.+AK2*AK2)
DYEP=.25*(DXC(I,J)+DXC(I,J+1))
R3 DYEP=DYEP+.25*(DXC(I+1,J)+DXC(I+1,J+1))
R4 DTE=GAME*ARFAEW/DYEP
DIE=DIE*(1.+AK1*AK1)
D7DP=.5*D7C(1)
R5 D7DP=D7DP+.5*D7C(1)
R6 DTD=GAND*ARFADU/D7DP
C-----CALCULATE MASS SOURCE FOR USE IN STABILISATION PROCEDURE-----
SKP=CF-CS+CF(J)-CW
CP=AMAX1(0.0,SKP)
CP0=CP
CCW=CF(J)
DYE=DYC(I+1,J)+.5*(DYC(I+1,J+1)+DYC(I+1,J-1))
TF(J,EQ.2) DYE=DYC(I+1,J)+.5*DYC(I+1,J+1)
DEFDYE=((WFE(I+1,J+1)*TE(I+1,J+1)+(1.-WFE(I+1,
1 J+1))*TE(I,J+1))-(WFE(I+1,J-1)*TE(I+1,J-1)+(1.-
2 WFE(I+1,J-1))*TE(I,J-1)))/DYE
AK3=.5*PIH*(DETADF(I+1,J)+DETADF(I+1,J+1))
CCE(J)=GAME*AK1*AK3*DEFDYE*ARAEW
CCN=CCW
DXN=DXC(I,J+1)+.5*(DXC(I+1,J+1)+DXC(I-1,J+1))
DEFDXN=((WFH(I+1,J+1)*TE(I+1,J+1)+(1.-WFH(I+1,J+1))*TE(I+1,J
1 ))-(WFH(I-1,J+1)*TE(I-1,J+1)+(1.-WFH(I-1,J+1))*TE(I-1,J)))/DXN
AK4=.5*PIH*(DXIDF(I,J+1)+DXIDF(I+1,J+1))
CCI=GAMN*AK4*AK2*ARFAN*DEFDXN
C-----ASSEMBLE MAIN COEFFICIENTS-----
AN(I,J)=AMAX1(WFH(I,J+1)*CN,=(1.-WFH(I,J+1))*CN,DIN)-WFH(I,J+1)*CN
AS(I,J)=AN(I,J-1)+CS
AF(I,J)=AMAX1(WFE(I+1,J)*CE(J),=(1.-WFE(I+1,J))*CF(J),DTE)
1-WFE(I+1,J)*CE(J)
AU(I,J)=AF(I-1,J)+CW
AI(I,J)=CI
SI(I,J)=CP0*TE(I,J)
SP(I,J)=-CP
SU(I,J)=SU(I,J)+CCN-CCS+CCE(J)-CCW
AR1=.25*(DRDXT(I,J)+DRDXT(I+1,J)+DRDXT(I,J+1)+DRDXT(I+1,J+1))
AR2=.25*(DRDETA(I,J)+DRDETA(I+1,J)+DRDETA(I,J+1)+DRDETA(I+1,J+1))
AR3=.25*(DXIDF(I,J)+DXIDF(I+1,J)+DXIDF(I,J+1)+DXIDF(I+1,J+1))
AK2=.25*PIH*(DETADF(I,J)+DETADF(I+1,J)+DETADF(I,J+1)+DETADF(I+1,
1 J+1))
AH1=DXDY(I,J)
AH2=DYDX(I,J)
AH3=.25*(HTHR(I,J)+HTHR(I+1,J)+HTHR(I,J+1)+HTHR(I+1,J+1))
DYEW=.5*(DXC(I,J)+DXC(I,J+1))
DIIDXP=(U(I+1,J)-U(I,J))/DYEW
V0=.5*(V(I,J)+V(I,J+1))

```

```

DYDYP=DXDY(I,J)
TERM1=DUOXP+VP*DXDYP
DYNS=.5*(DYC(I,J)+DYC(I+1,J))
DVDYP=(V(I,J+1)-V(I,J))/DYNS
IIP=.5*(U(I,J)+U(I+1,J))
DYDXP=UDYDX(I,J)
TFHM7=UDVDYP+IIP*DYDXP
DWDZP=0.
VEE=.5*(V(I+1,J+1)+V(I+1,J))
VF=VEE*UFF(I+1,J)+VP*(1.-UFF(I+1,J))
VWE=.5*(V(I-1,J+1)+V(I-1,J))
VM=VP*WFF(I,J)+VWE*(1.-WFF(I,J))
DVDXP=(VE-VM)/DXEW
IIN=.5*(U(I+1,J+1)+U(I,J+1))
IN=IIN*UFN(I,J+1)+IIP*(1.-UFN(I,J+1))
ISS=.5*(U(I+1,J-1)+U(I,J-1))
IS=IIP*JFN(I,J)+ISS*(1.-JFN(I,J))
DIIDYP=(IIN-ISS)/DYNS
TFHM4=DVDXP+DIIDYP-VP*DYDXP-IIP*DYDYP
WP=.5*(W(I,J+1)+W(I,J))
WFF=.5*(W(I+1,J)+W(I+1,J))
WWE=.5*(W(I-1,J)+W(I-1,J))
WF=WEE*WFF(I+1,J)+WP*(1.-WFF(I+1,J))
WW=VP*WFF(I,J)+WWE*(1.-WFF(I,J))
DWDXP=(WE-WW)/DXEW
IIII=.5*(U(I+1,J)+U(I,J))
IID=.5*(U(I+1,J)+U(I,J))
IIR=IID*WFD(1)+IIP*(1.-WFD(1))
IF(PIH.EQ.0.0) GO TO 3896
DUDZP=0.
TFHM5=DWDXP+AH3*DIIDZP+AK1*DIIDXP+AK2*DIIDYP+(-AK2*AH2+AK1*AH1-
1AH3*AH3*AR2/AK1)*VP
3896 CONTINUE
IF(PIH.EQ.0.0) TERM5=DWDXP
VND=.5*(V(I,J+1)+V(I,J))
VIII=.5*(V(I,J+1)+V(I,J))
VN=VND*WFD(1)+VP*(1.-WFD(1))
VII=VP*WFD(1)+VIII*(1.-WFD(1))
DVD7P=(VN-VII)/D7C(1)
WNI=.5*(W(I,J+1)+W(I,J+1))
WSE=.5*(W(I,J-1)+W(I,J-1))
WN=IIN*WFN(I,J+1)+WP*(1.-WFN(I,J+1))
US=VP*WFN(I,J)+WSE*(1.-WFN(I,J))
UDYYP=(WN-US)/DYNS
IF(PIH.EQ.0.0) GO TO 3897
DVD7P=0.
TFHM6=UDYYP+AH3*DVD7P+AK1*DVDXP+AK2*DVDYP+(-AK1*AH1+AK2*AH2+
1AH3*AR2*AH3/AK1)*IIP
3897 CONTINUE
IF(PIH.EQ.0.0) TERM6=UDYYP
TFHM3=AK1*DWDXP+AK2*DWYYP
C-----GENERATION TERM -----
GFU(I,J)=(2.*(TERM1**2+TERM2**2+TERM3**2)+TERM4**2+TERM5**2
1+TERM6**2)*DEN(I,J)*CMUTF(I,J)*TF(I,J)/(FD(I,J)+SMALL)
IF(KASH.NE.1.AND.NITER.GE.NOUMK) GO TO 5022
IF(NITER.LT.NOUMK) GO TO 5721
IF(PHANDL.EQ.C.708) AWHC=0.0001

```



```

IF (PRANDL.EQ.7.03) AKRC=0.0001
GEN(I,J)=(2.*(TERM1**2+TERM2**2+TERM3**2)+TERM4**2+TERM5**2+
1TERM6**2)*DEN(I,J)*CMUA(I,J)*TE(I,J)*TF(I,J)/(ED(I,J)+SMALL)
GEN(I,J)=GEN(I,J)-AKRC*DEN(I,J)*DXDY(I,J)*(2./3.*TE(I,J)+.5*(
1II(I,J)+II(I+1,J))**2)*RVT(I,J)
5721 CONTINUE
GO TO 5923
5922 CONTINUE
GEN(I,J)=(2.*(TERM1**2+TERM2**2+TERM3**2)+TERM4**2+TERM5**2
1+TERM6**2)*DEN(I,J)*CMUA(I,J)*TE(I,J)*TE(I,J)/(ED(I,J)+
1SMALL)
5923 CONTINUE
VOL=AREADU*D7C(1)
SH(I,J)=SH(I,J)+GEN(I,J)*VOL
IF (NITER.LT.NOUMH) SP(I,J)=SP(I,J)-CMU
1*CDT*DEN(I,J)**2*TE(I,J)*VOL/VIS(I,J)
IF (NITER.GE.NOUMH) SP(I,J)=SP(I,J)-CMUA(I,J)
1*CDT*DEN(I,J)**2*TE(I,J)*VOL/VIS(I,J)
C
101 CONTINUE
100 CONTINUE
C
CHAPTER 2 2 2 2 2 2 PROBLEM MODIFICATIONS 2 2 2 2 2
C
CALL MORTE
C
CHAPTER 3 FINAL COEFFICIENT ASSEMBLY AND RESIDUAL SOURCE CALCULATION 3
C
DO 300 I=2,NIM1
DO 301 J=2,NJM1
AP(I,J)=AM(I,J)+AS(I,J)+AF(I,J)+AW(I,J)+AD(I,J)+AU(I,J)-SP(I,J)
RESOR=AM(I,J)*TE(I,J+1)+AS(I,J)*TE(I,J-1)+AF(I,J)*TE(I+1,J)
1+AW(I,J)*TE(I-1,J)+AD(I,J)*TE(I,J)+AU(I,J)*TE(I,J)
1-AP(I,J)*TE(I,J)+SH(I,J)
VOL=AREAXY(I,J)*D7C(1)
SORVOL=GREAT*VOL
IF (-SP(I,J).GT.0.5*SORVOL) PESUP=RESOR/SORVOL
IF (J.EQ.2.AND.NITER.GE.MAXIT2) GO TO 4807
RESORK=RESUPK+ARS(RESOR)
4807 CONTINUE
C-----INDEX=RELAXATION
AP(I,J)=AP(I,J)/HREF
SH(I,J)=SH(I,J)+(1.-URFK)*AP(I,J)*TE(I,J)
GEN(I,J)=GEN(I,J)*VOL
301 CONTINUE
300 CONTINUE
C
CHAPTER 4 4 4 4 4 SOLUTION OF DIFFERENCE EQUATIONS 4 4 4 4 4
C
IF (NITER.GE.MAXIT2) RSC(INDEX)=0.0
IF (NITER.GE.MAXIT2) IMEG=0
IF (NITER.LT.MAXIT2) IMEG=1
DO 400 N=1,NSHPK
IF (N.GT.1.AND.NITER.GE.MAXIT2) IMEG=1
400 CALL LISOLV(2,2,NJ,NJ,IT,JT,TF)
IF (NITER.GE.MAXIT2) RESORK=RESUPK+RSC(INDEX)
RETURN

```

## SUBROUTINE CALCED

C  
CHAPTER 0 0 0 0 0 0 0 PRELIMINARIES 0 0 0 0 0 0  
C

## COMMON

```

1 RESORII,IRFII,RESORV,IRFV,RESORN,RESOPW,IRFV,
1 IIRFP,RESOPT,IIRFT,RESORK,IIRFK,RESORD,IRFD,
1 RESU(25,25),RESV(25,25),RESW(25,25),RFSM(25,25),
1 DU(25,25),DV(25,25),DW(25,25),U(25,25),V(25,25),
1 W(25,25),P(25,25),T(25,25),TE(25,25),FD(25,25),
1 PP(25,25),DEN(25,25),VIS(25,25),AN(25,25),AS(25,25),
1 AF(25,25),AW(25,25),AU(25,25),AD(25,25),CF(25),CD(25,25),
1 CCE(25),CCD(25,25),AP(25,25),SU(25,25),SP(25,25),DXC(25,25),
1 DYC(25,25),D7C(4),WFE(25,25),WFH(25,25),WFD(4),
1 APFAXY(25,25),F1D(50,5),N10,WMEAN,INDEX,HYDRIA,RAP,R1D(50),
1 VELTH,TIN,THALL,FLOWIN,GRFAT,
1 IIRFVIS,VISCOS,DENSIT,PRANDT,
1 PRTE,PRED,CMII,CHT,C1H,C2H,CAPPA,EI OG,ALAMDA,
1 NSWPII,NSWPIV,NSWPIW,NSWPP,NSWPT,
1 NSWPK,NSWPD,
1 IPRFF,JPRFF,KPRFF,INDCOS
COMMON TAUXS(25),TAUXN(25),TAUYS(25),TAUYN(25),
1 YPLUSS(25),YPLUSN(25)
1 JT,JT,NI,NJ,NIM1,NJM1
1 SWFT,FLOWTOT,CPW,REFLUX,FLOWT
1 N1,N2
1 PA,RR,THETA,AN,DPD7,FLOWAX,DXIDF(25,25),DETADF(25,25),PIH
1 DRDXT(25,25),DRDETA(25,25),HTHP(25,25)
1 PI,WTN,FLOW
1 SMALL,SUMS,SUMD,INUMR,DXDY(25,25),DYDX(25,25)
LEVEL 2,III
COMMON/RLK2/III(25,25),VV(25,25),ANU(25,25),ASII(25,25),
1 AFII(25,25),AWII(25,25),AHII(25,25),AIII(25,25),
1 AIV(25,25),ASV(25,25),AFV(25,25),AHV(25,25),
1 CONT(25,10),VRN(25),JTS,
1 ADV(25,25),AIV(25,25),AA(25)
1 JG,IUOTH,TER(25,2),FDR(25,2),PRODD(50),GENN(25,25)
1 PRANDL,GHT(25,25),ANISS
1 PRDU(25,25),AK7(25,25),AKD(25,25),AKA(25,25),RVT(25,25),AKF
1 AKET,AKETD,AKCTD,F1P(25),F1K2(25),F1K3(25),F1KA(25),F1RVT(25)
1 NOIMP,CMIIA(25,25),CMIR(25)
1 NOIMR2
1 APII(25,25),APV(25,25),PR(25,25),ANGL(25,25)
1 KASH,HASM
1 VISV(25,25),VA(25,25),VB(25,25),VC(25,25)
1 RSC(5),IMFG,MAXIT2
1 RPS(25,25),HRE,NITER,MAXIT
1 TIENSC,VISID(50),XPLI(25,25)

```

DIMENSION GEN(25,25)

C----- NOTE TEMPORARY USE OF PR-ARRAY -----  
EQUIVALENCE (PR(1,1),GEN(1,1))

C  
CHAPTER 1 1 1 1 1 1 ASSEMBLY OF COEFFICIENTS 1 1 1 1 1 1  
C

RESORD=0  
JGM1=JG-1

```

DO 50 J=2,JGM1
I=1
APEAFW=DYC(T+1,J)*D7C(1)
GF=DFN(I,J)*U(I+1,J)
AK1=.5*PIH*(DXIDF(I+1,J)+DXIDF(T+1,J+1))
AK2=.5*PIH*(DETAUF(I+1,J)+DETAUF(T+1,J+1))
GF=GF+DFN(I,J)*(WFF(I+1,J)*W(T+1,J)+(1.-WFF(I+1,J))*W(I,J
1))*AK1
DYE=DYC(I+1,J)+.5*(DYC(I+1,J+1)+DYC(I+1,J-1))
TF(J,FO,2) DYE=DYC(I+1,J)+.5*DYC(I+1,J+1)
DFDYE=((WFF(I+1,J+1)*FD(I+1,J+1)+(1.-WFF(I+1,
1J+1))
1*FD(I,J+1))-(WFF(I+1,J-1)*ED(I+1,J-1)+(1.-WFF(I+1,J-1))*ED(I,J-
1)))/DYE
GAME=.5*(VIS(I,J)+VIS(I+1,J))/PRED
GAME=GAME-VISCOS/PRED+VISCOS
CF(J)=GAME*AK1*AK2*DFDYE*APEAFW
CF(J)=GF*ARFAEW
DTE=GAME*ARFAEW/ (.25*(DXC(I+1,J)+DXC(I+1,I+1)+DXC(I,J)+DXC(I,J+1)
1))
DYE=DIE*(1.+AK1*AK1)
AF(I,J)=AMAX1(WFF(I+1,J)*CF(J),-(1.-WFF(I+1,J))*CF(J),DIE)
1-WFF(I+1,J)*CF(J)
50 CONTINUE
DO 100 I=2,NIM1
J=1
APEAN=DXC(I,J+1)*D7C(1)
GN=DFN(I,J)*V(I,J+1)
AK1=.5*(DXIDF(I,J+1)+DXIDF(I+1,J+1))*PIH
AK2=.5*PIH*(DETAUF(I,I+1)+DETAUF(T+1,J+1))
GN=GN+DFN(I,J)*(WFN(I,J+1)*W(T,J+1)+(1.-WFN(I,J+1))*W(I,J
1))*AK2
DYN=DXC(I,J+1)+.5*(DXC(T+1,J+1)+DXC(I-1,J+1))
DFDXN=(ED(I+1,J)-ED(I-1,J))/DXN
GAMN=VIS(I,J)/PRED
GAMN=GAMN-VISCOS/PRED+VISCOS
CN=GAMN*AK1*AK2*APEAN*DFDXN
CN=GN*AREAN
DIN=GAMN*APEAN/ (.25*(DYC(I,J+1)+DYC(T+1,I+1)))
DIN=DIN*(1.+AK2*AK2)
AN(I,J)=AMAX1(WFN(I,J+1)*CN,-(1.-WFN(I,J+1))*CN,DIN)-WFN(I,J+1)*CN
DO 101 J=2,JGM1
C-----COMPUTE AREAS AND VOLUME-----
APEAN=DXC(I,J+1)*D7C(1)
APEAFW=DYC(I+1,I)*D7C(1)
APEADU=AKEAXY(I,J)
C-----CALCULATE CONVECTION COEFFICIENTS-----
GN=(DFN(I,J)*(1.-WFN(T,J+1))+DEN(I,J+1)*WFN(I,J+1))*V(I,J+1)
GF=(DFN(I,J)*(1.-WFF(T+1,J))+DEN(I+1,J)*WFF(I+1,J))*U(I+1,J)
AK2=.5*PIH*(DETAUF(I,J+1)+DETAUF(I+1,J+1))
AK1=.5*PIH*(DXIDF(I+1,J)+DXIDF(I+1,J+1))
CN=GN+(DEN(I,J)*W(T,I)*(1.-WFN(I,J+1))+DEN(I,J+1)
1*W(I,J+1)*WFN(T,J+1))*AK2
GF=GF+(DEN(I,J)*W(T,I)*(1.-WFF(I+1,J))+
1*DEN(I+1,J)*W(I+1,J)*WFF(T+1,J))*AK1
GN=(DFN(I,J)*(1.-WFN(1))+DEN(T,I)*WFD(1))*W(I,J)
CS=CN

```

```

CN=GN*AREAN
CW=CF(J)
CF(J)=GF*AREAFW
CU=0.0
C-----CALCULATE DIFFUSION COEFFICIENTS-----
GAMN=VISV(I,J)/PRED
GAME=(VIS(I,J)*(1.-WFE(I+1,J))+VIS(I+1,J)*WFE(I+1,J))/PRED
GAMN=GAMN-VISCOS/PRED+VISCOS
GAME=GAME-VISCOS/PRED+VISCOS
GAMD=(VIS(I,J)*(1.-WFN(1))+VIS(I,J)*WFN(1))/PRED
DYNP=.25*(DYC(I,J)+DYC(I+1,J))
R1 DYNP=DYNP+.75*(DYC(I,J+1)+DYC(I+1,J+1))
R2 DIN=GAMN*AREAN/DYNP
DIN=DIN*(1.+AK2*AK2)
DYEP=.25*(DYC(I,J)+DXC(I,J+1))
R3 DYEP=DXEP+.75*(DXC(I+1,J)+DXC(I+1,J+1))
R4 DIE=GAME*AREAFW/DYEP
DIE=DIE*(1.+AK1*AK1)
D7DP=.5*D7C(1)
R5 D7DP=D7DP+.5*D7C(1)
R6 DID=GAMD*AREAFW/D7DP
C-----CALCULATE MASS SOURCE FOR USE IN STABILISATION PROCEDURE-----
SMP=CN-CS+CF(J)-CW
CP=AMAX1(0.0,SMP)
CPO=CP
CCW=CCF(J)
DYE=DYC(J+1,J)+.5*(DYC(I+1,J+1)+DYC(I+1,J-1))
TF(I,ENL7) DYE=DYC(I+1,J)+.5*DYC(I+1,J+1)
DFDYE=((WFE(I+1,J+1)*FD(I+1,J+1)+(1.-WFE(I+1,
1 J+1))*ED(I+1,J+1))-(WFE(I+1,J-1)*FD(I+1,J-1)+(1.-
2 WFE(I+1,J-1))*ED(I+1,J-1)))/DYE
AK3=.5*PIH*(DETADF(I+1,J)+DETADF(I+1,J+1))
CCF(J)=GAME*AK1*AK3*DFDYE*AREAFW
CCS=CCN
DXN=DXC(I,J+1)+.5*(DYC(I+1,J+1)+DXC(I-1,J+1))
DFDXN=((WFN(I+1,J+1)*ED(I+1,J+1)+(1.-WFN(I+1,J+1))*ED(I+1,J
1 ))-
1 (WFN(I-1,J+1)*ED(I-1,J+1)+(1.-WFN(I-1,J+1))*ED(I-1,J))) / DXN
AK4=.5*PIH*(DXIDF(I,J+1)+DXIDF(I+1,J+1))
CCN=GAMN*AK4*AK2*AREAN*DFDXN
C-----ASSEMBLE MAIN COEFFICIENTS-----
AN(T,J)=AMAX1(WFN(I,J+1)*CN,(1.-WFN(T,J+1))*CN/DIN)-WFN(T,J+1)*CN
AS(T,J)=AN(T,J-1)+CS
AF(T,J)=AMAX1(WFE(I+1,J)*CF(J),(1.-WFE(I+1,J))*CF(J),DIE)
1-WFE(T+1,J)*CF(J)
AM(T,J)=AE(T-1,J)+CW
AU(T,J)=CU
SU(T,J)=CPO*ED(T,J)
SP(T,J)=-CP
SU(T,J)=SU(I,J)+CCN-CCS+CCF(J)-CCW
C-----COMPLETE ASSEMBLY OF SOURCE TERMS-----
VOL=AREAFW*H7C(1)
IF(NITER_LT_HOUMR) SU(I,J)=SU(I,J)+CMU
1*CF1M*GEN(I,J)*VOL*DEN(I,J)*TE(I,J)/VIS(I,J)
IF(NITER_GE_HOUMR) SU(I,J)=SU(I,J)+CMHA(I,J)
1*CF1M*GEN(I,J)*VOL*DEN(I,J)*TE(I,J)/VIS(I,J)
SP(T,J)=SP(T,J)-C2M*DEN(I,J)*FD(I,J)*VOL/TE(I,J)

```

```

C
  101 CONTINUE
  100 CONTINUE
C
CHAPTER 2 2 2 2 2 2 PROBLEM MODIFICATIONS 2 2 2 2 2
C
  CALL MODER
C
CHAPTER 3 FINAL COEFFICIENT ASSEMBLY AND RESIDUAL SOURCE CALCULATION 3
C
  DO 300 I=2,NIM1
  DO 301 J=2,JGM1
    AP(I,J)=AH(I,J)+AS(I,J)+AF(I,J)+AW(I,J)+AN(I,J)+AU(I,J)-SP(I,J)
    RESOR=AH(I,J)*ED(I,J+1)+AS(I,J)*ED(I,J-1)+AF(I,J)*ED(I+1,J)
    1 +AW(I,J)*ED(I-1,J)+AN(I,J)*ED(I,J)+AU(I,J)*ED(I,J)
    1 -AP(I,J)*ED(I,J)+SU(I,J)
    VOL=APFAXY(I,J)*D7C(1)
    SORVOL=GHEAT*VOL
    IF(-SP(I,J).GT.C.5*SOPVOL) RESOR=RESOR/SORVOL
    IF(J.EQ.2.AND.NITER.GE.MAXIT2) GO TO 4806
    RESORD=RESORD+ARS(RESOR)
  4806 CONTINUE
C-----UNDER-RELAXATION
    AP(I,J)=AP(I,J)/URFD
    SU(I,J)=SU(I,J)+(1.-URFD)*AP(I,J)*ED(I,J)
  301 CONTINUE
  300 CONTINUE
C
CHAPTER 4 4 4 4 4 SOLUTION OF DIFFERENCE EQUATIONS 4 4 4 4 4
C
    IF(NITER.GE.MAXIT2) HSC(INDEX)=0.0
    IF(NITER.GE.MAXIT2) IMEG=0
    IF(NITER.LT.MAXIT2) IMEG=1
    DO 400 N=1,NSWPD
    IF(N.GT.1.AND.NITER.GE.MAXIT2) IMEG=1
  400 CALL LISOLV(2,2,NI,NJ,IT,JT,ED)
    IF(NITER.GE.MAXIT2) RESORD=RESORD+RSC(INDEX)
  RETURN
  END

```

SUBROUTINE LISOLV(ISTART,JSTART,NI,NJ,IT,JT,PHI)

C CHAPTER 0 0 0 0 0 0 0 0 PRELIMINARIES 0 0 0 0 0 0 0  
C

      DIMENSION PHI(IT,JT),A(50),P(50),C(50),D(50),URF1(6)

      COMMON

```

1      RESORII,URFII,RESORV,URFV,RESORM,RESOPW,URFW,
1      URFP,RESOPT,URFT,RESORK,URFK,RESORD,URFD,
1      RESII(25,25),RESV(25,25),RESW(25,25),RESM(25,25),
1      DII(25,25),DVI(25,25),DW(25,25),II(25,25),V(25,25),
1      W(25,25),P(25,25),T(25,25),TE(25,25),FD(25,25),
1      PD(25,25),DEN(25,25),VIS(25,25),AN(25,25),AS(25,25),
1      AE(25,25),AW(25,25),AI(25,25),AD(25,25),CE(25),CD(25,25),
1      CCE(25),CCD(25,25),AP(25,25),SI(25,25),SP(25,25),DXC(25,25),
1      DYC(25,25),DZC(4),WFE(25,25),WFN(25,25),WFD(4),
1      AREAXY(25,25),FID(50,5),HID,WMEAN,INDEX,HYDDIA,PAE,PID(50),
1      VELTH,TIN,TWALL,FLOWIN,GFAT,
1      IIPFVIS,VISCOS,DENSIT,PRAINDT,
1      PRTE,PRFD,CMU,COT,C1H,C2H,CAPPA,ELOG,ALAMDA,
1      NSUPII,NSUPV,NSUPW,NSUPP,NSUPT,
1      NSWPK,NSWPD,
1      IPREF,JIPREF,KIPREF,INDCOS
1      COMMON TAUXS(25),TAUXN(25),TAUZS(25),TAUZN(25),
1      YPIUSS(25),YPLUSN(25)
1      TUUM(6)
1      SWET,FLOWTOT,CPW,REFLUX,FLOWT
1      N1,N2
1      RA,HR,THETA,AN,DPD7,FLOWAX,DXIDF(25,25),DETADE(25,25),PIH
1      ,DPDXT(25,25),DPDFTA(25,25),HTHP(25,25)
1      ,PI,UTH,FLOWW
1      ,SMALL,SUMS,SIMN,INIIMP,DXDY(25,25),PYDX(25,25)
1      LEVEL 2,III
1      COMMON/PLK2/III(25,25),VV(25,25),ANU(25,25),ASII(25,25),
1      AFII(25,25),AWII(25,25),ADII(25,25),AUII(25,25),
1      AIV(25,25),ASV(25,25),AFV(25,25),AWV(25,25),
1      COT(25,10),VRH(25),JTS,
1      ADV(25,25),AIV(25,25),AA(25)
1      ,JG,IBOTH,TER(25,2),FDR(25,2),PRODD(50),REHN(25,25)
1      ,PRANDL,GIT(25,25),ANUSS
1      ,PRDD(25,25),AK7(25,25),AKD(25,25),AKA(25,25),RVT(25,25),AKF
1      ,AKFT,AKFTD,AKCTD,F1P(25),F1KZ(25),F1KH(25),F1KA(25),F1RVT(25)
1      ,NOIIMP,CMIIA(25,25),CIIR(25)
1      ,JOUIMP2
1      ,APII(25,25),APV(25,25),PR(25,25),ANRL(25,25)
1      ,KASH,NASH
1      ,VISV(25,25),VA(25,25),VH(25,25),VC(25,25)
1      ,RSC(5),IMEG,MAXIT2
1      ,PRS(25,25),RPB,HITER,MAXIT
1      ,ILENSC,VISID(50),XPLI(25,25)

```

C-----UNDER RELAXATION FACTORS FOR THE 1-D REGION-----

```

1      IIPF1(1)=IIPFII
1      IIPF1(2)=IIPFW
1      IIPF1(3)=IIPFK
1      IIPF1(4)=IIPFD
1      IIPF1(5)=IIPFT
1      IIPF1(6)=IIPFVIS
1      NIHI=NI-1

```

```

      NJM1=NJ-1
      NIM2=NJ-2
      NJM2=NJ-2
      JSTM1=JSTART-1
      ISTM1=ISTART-1
      A(JSTM1)=0.
      (***** SOLUTION FROM THE TUBE-AXIS TO THE TUBE-WALL *****
      *
      ***** COMMENCE W-F SWEEPS-----
      I=ISTART
      ITART=ISTART
      JSTART=JSTART
      IF (INDEX.EQ.0) GO TO 411
      NJNEW=NJ+N1D
      N1D2=N1D+2
      DO 421 J=N1D2,NJNEW
      F1D(J,INDEX)=PHI(2,J-N1D)
      421 CONTINUE
      NJNEW1=NJNEW-1
      -----LOCATION OF POINTS IN ONE DIMENSIONAL EXTENSION-----
      R1D(N1D+4)=PA+.5*DYC(2,4)+DYC(2,3)+DYC(2,2)
      R1D(N1D+3)=PA+.5*DYC(2,3)+DYC(2,2)
      R1D(N1D+2)=PA+.5*DYC(2,2)
      R1D(N1D+1)=PA
      R1D(1)=0.
      DO 412 J=2,N1D
      R1D(J)=R1D(J-1)+R1D(N1D+1)/FLOAT(N1D)
      412 CONTINUE
      -----COMMENCE S-H TRAVERSE-----
      F1D(1,INDEX)=F1D(2,INDEX)
      F1D(1,1)=0.
      IF (THOTH.EQ.1) GO TO 4699
      F1D(NJNEW,INDEX)=0.
      4699 CONTINUE
      C(JSTM1)=F1D(JSTM1,INDEX)
      N1D3=N1D+3
      DO 411 J=JSTART,NJNEW1
      IF (J.GE.N1D3) GO TO 403
      IF (INDEX.EQ.1) PRVAR=1.
      IF (INDEX.EQ.2) PRVAR=1.
      IF (INDEX.EQ.3) PRVAR=PRTE
      IF (INDEX.EQ.4) PRVAR=PRFD
      IF (KASM.EQ.2) GO TO 4284
      IF (NITER.LT.NOUMR2.AND.INDEX.EQ.5) PRVAR=.9
      IF (NITER.GE.NOUMR2.AND.INDEX.EQ.5) PRVAR=F1KZ(J)/(F1KD(J)+SMALL)
      GO TO 4285
      4284 IF (INDEX.EQ.5) PRVAR=.9
      4285 CONTINUE
      A(J)=.5*(VIS1D(J)+VIS1D(J+1))*(.5*(R1D(J)+R1D(J+1))
      1/R1D(J)
      1/(R1D(J+1)-R1D(J))
      1/PRVAR
      R(J)=.5*(VIS1D(J)+VIS1D(J+1))*(.5*(R1D(J)+R1D(J+1))
      1/R1D(J)
      1/(R1D(J)-R1D(J-1))
      1/PRVAR

```

```

      IF(INDEX.EQ.4) A(J)=A(J)*PRVAR/(.5*(VIS1D(J)+VIS1D(J+1)))*(.5*
1(VIS1D(J)+VIS1D(J+1))/PRVAR-VTSCOS/PRVAR+VISCOS)
      IF(INDEX.EQ.4) R(J)=R(J)*PRVAR/(.5*(VIS1D(J)+VIS1D(J+1)))*(.5*
1(VIS1D(J)+VIS1D(J+1))/PRVAR-VTSCOS/PRVAR+VISCOS)
      IF(INDEX.EQ.5) A(J)=A(J)*PRVAR/(.5*(VIS1D(J)+VIS1D(J+1)))*(.5*
1(VIS1D(J)+VIS1D(J+1))/PRVAR-VTSCOS/PRVAR+VISCOS/PRANDL)
      IF(INDEX.EQ.5) R(J)=R(J)*PRVAR/(.5*(VIS1D(J)+VIS1D(J+1)))*(.5*(
1VIS1D(J)+VIS1D(J+1))/PRVAR-VTSCOS/PRVAR+VISCOS/PRANDL)
      IF(J.EQ.2) R(J)=0.
      D(J)=A(J)+H(J)
      IF(INDEX.EQ.1) D(J)=D(J)+VIS1D(J)/R1D(J)/P1D(J)*.5*(R1D(J+1)-
1R1D(J-1))
      IF(INDEX.EQ.1) C(J)=VIS1D(J)/R1D(J)*.5*(F1D(J+1,1)-F1D(J-1,1)
1)-(.25*(VIS1D(J+1)+VIS1D(J))*(P1D(J+1)+R1D(J))*(F1D(J+1,1)+F1D(
2J,1))/(P1D(J+1)+R1D(J))-.25*(VIS1D(J)+VIS1D(J-1))
2*(R1D(J)+R1D(J-1))*(F1D(J,1)+F1D(J-1,1))/(R1D(J)+P1D(J-1)))/
3R1D(J)
      IF(INDEX.EQ.2) C(J)=-.5*(R1D(J+1)-R1D(J-1))*DPDZ
      IF(INDEX.EQ.3) PRODD(J)=(ABS(F1D(J+1,2)-F1D(J-1,2)))/(P1D(J+1)-
1R1D(J-1))*2*DENSIT*CMH*F1D(J,3)**2/(F1D(J,4)+SMALL)
      IF(NITER.LT.NOUMR) GO TO 73R2
      IF(PRANDL.EQ.0.70R) AYBC=0.0001
      IF(PRANDL.EQ.0.70R) AKPC=0.0001
      IF(INDEX.EQ.3) PRODD(J)=(ABS(F1D(J+1,2)-F1D(J-1,2)))/(P1D(J+1)-
1R1D(J-1))*2*DENSIT*CMH*F1D(J,3)**2/(F1D(J,4)+SMALL)
      IF(KASH.EQ.7) GO TO 73R7
      IF(INDEX.EQ.3) PRODD(J)=PRODD(J)-AKPC*DENSIT/R1D(J)*(2./3.*F1D(J,
13)+F1D(J,1)**2)*F1RVT(J)
73R2 CONTINUE
      IF(INDEX.EQ.3) C(J)=PRODD(J)*.5*(P1D(J+1)-R1D(J-1))
      IF(NITER.LT.NOUMR.AND.INDEX.EQ.3) D(J)=D(J)+CMH
1*DENSIT*DENSIT*CDT*F1D(J,INDEX)/VIS1D(J)*.5*(P1D(J+1)-R1D(J-1))
      IF(NITER.GE.NOUMR.AND.INDEX.EQ.3) D(J)=D(J)+CMH*F1D(J,INDEX)
1*DENSIT*DENSIT*CDT*F1D(J,INDEX)/VIS1D(J)*.5*(P1D(J+1)-R1D(J-1))
      IF(NITER.LT.NOUMR.AND.INDEX.EQ.4) C(J)=CMH
1*F1D(J,INDEX)/VIS1D(J)*.5*(P1D(J+1)-R1D(J-1))*DENSIT*F1D(J,INDEX
1-1)
      IF(NITER.GE.NOUMR.AND.INDEX.EQ.4) C(J)=CMH*F1D(J,INDEX)
1*F1D(J,INDEX)/VIS1D(J)*.5*(P1D(J+1)-R1D(J-1))*DENSIT*F1D(J,INDEX
1-1)
      IF(INDEX.EQ.4) D(J)=D(J)+C2F*DENSIT*F1D(J,INDEX)/(F1D(J,INDEX-1)
1+SMALL)*.5*(R1D(J+1)-R1D(J-1))
      IF(INDEX.EQ.5) C(J)=-DENSIT*F1D(J,2)/(FLOWT*CPW)*SWET
1*OFIIX*.5*(P1D(J+1)-R1D(J-1))*D7C(1)
      IF(TEMP.EQ.1) GO TO 19R9
      CATI=C(J)+A(J)*F1D(J+1,INDEX)+B(J)*F1D(J-1,INDEX)-D(J)*F1D(J,
1INDEX)
      RSC(INDEX)=RSC(INDEX)+ABS(CATI)
19R9 CONTINUE
      D(J)=D(J)/UPF1(INDEX)
      C(J)=C(J)+(1.-URF1(INDEX))*D(J)*F1D(J,INDEX)
      GO TO 409
404 CONTINUE
C-----ASSEMBLE TDMA COEFFICIENTS-----
      A(J)=1./(R1D(J+1)-R1D(J))*VIS1D(N1D)*R1D(N1D)
      R(J)=1./(R1D(J)-R1D(J-1))*VIS1D(N1D)*R1D(N1D)
      D(J)=A(J)+H(J)

```



```

      IF(J.EQ.2) R(J)=0.
      C(J)=0.
      GO TO 409
403  CONTINUE
      JJ=J-N1D
      PHI(1,JJ)=PHI(NIM1,JJ)
      PHI(N1,JJ)=PHI(2,JJ)
      A(J)=AN(I,JJ)
      B(J)=AS(I,JJ)
      C(J)=AF(I,JJ)*PHI(I+1,JJ)+AW(I,JJ)*PHI(I-1,JJ)
      +SH(I,JJ)+AD(I,JJ)*PHI(I,JJ)+AU(I,JJ)*PHI(I,JJ)
      D(J)=AP(I,JJ)
409  CONTINUE
      TERM=1./(D(J)-B(J)*A(J-1))
      A(J)=A(J)*TERM
401  C(J)=(C(J)+R(J)*C(J-1))*TERM
C-----OBTAIN NEW PHI'S-----
      DO 415 JJ=JSTART,NJNEW1
      JJ=NJNEW+JSTM1-JJ
      F1D(J,INDEX)=A(J)*F1D(J+1,INDEX)+C(J)
      IF(J.GE.(N1D+1)) PHI(T,J-N1D)=F1D(J,INDEX)
415  CONTINUE
411  CONTINUE
      IF(INDEX.NE.5) LL=1
      IF(INDEX.EQ.1) LL=4
      IF(INDEX.EQ.2) LL=4
      IF(INDEX.EQ.3) LL=2
      IF(INDEX.EQ.4) LL=2
      IF(INDEX.EQ.5) LL=4
      DO 7987 L=1,LL
C-----COMMENCE W-F SWEEP-----
      DO 100 I=ISTART,NIM1
      C(JSTM1)=PHI(T,JSTM1)
C-----COMMENCE S-W TRAVERSE-----
      DO 101 J=JSTART,NJM1
      PHI(1,J)=PHI(N1F1,J)
      PHI(N1,J)=PHI(2,J)
C-----ASSEMBLE TDEA COEFFICIENTS-----
      A(J)=AN(I,J)
      B(J)=AS(I,J)
      C(J)=AF(I,J)*PHI(I+1,J)+AW(I,J)*PHI(I-1,J)+
      +AD(I,J)*PHI(I,J)+AU(I,J)*PHI(I,J)+
      +SH(I,J)
      D(J)=AP(I,J)
C-----FOR I GREATER THAN ISTART SPECIFIED VALUE AT S BOUNDARY-----
      IF(INDEX.NE.0.AND.J.EQ.JSTART) C(J)=C(J)+GREAT*F1D(N1D
      +JSTART,INDEX)
      IF(INDEX.NE.0.AND.J.EQ.ISTART) D(J)=GREAT
      TERM=1./(D(J)-B(J)*A(J-1))
      A(J)=A(J)*TERM
      101 C(J)=(C(J)+R(J)*C(J-1))*TERM
C-----OBTAIN NEW PHI'S-----
      DO 102 JJ=JSTART,NJM1
      JJ=NJ+JSTM1-JJ
      102 PHI(I,J)=A(J)*PHI(I,J+1)+C(J)
      100 CONTINUE
C*****

```

```

C*          INTRODUCTION OF SPECIAL TREATMENT FOR CYCLIC          *
C*          BOUNDARY CONDITONS                                     *
C*****
      A(ISTM1)=0.0
      IF(INDEX_NE.0) JTART=JSTART+1
C-----COMMENCE N-S SWEEP-----
      DO 200 J=JTART,NJM1
        C(ISTM1)=PHI(ISTM1,J)
C-----COMMENCE W-F TRAVERSE-----
      DO 201 I=2,NIM1
        A(I)=AE(I,J)
        H(I)=AH(I,J)
        C(I)=AN(I,J)*PHI(I,J+1)+AS(I,J)*PHI(I,J-1)+
        1AN(I,J)*PHI(I,J)+AH(I,J)*PHI(I,J)+
        1SH(I,J)
        D(I)=AP(I,J)
        IF(I.EQ.2) GO TO 307
        TERM=1./(D(I)-H(I)*A(I-1))
        C(I)=(C(I)+P(I)*C(I-1))*TERM
        H(I)=H(I)*H(I-1)*TERM
        GO TO 201
307   TERM=1./D(I)
        C(I)=C(I)*TERM
        H(I)=P(I)*TERM
201   A(I)=A(I)*TERM
        B(NIM2)=A(NIM2)+B(NIM2)
        DO 302 II=3,NIM2
          I=NIM2+2-II
          C(I)=A(I)*C(I+1)+C(I)
302   H(I)=A(I)*B(I+1)+P(I)
        PHINM1=(C(NIM1)+A(NIM1)*C(2))/(1.-B(NIM1)-A(NIM1)*B(2))
C-----OBTAIN NEW PHI'S-----
      DO 303 I=2,NIM2
303   PHI(I,J)=P(I)*PHINM1+C(I)
        PHI(NIM1,J)=PHINM1
      200 CONTINUE
      7987 CONTINUE
      RETURN
      END

```

## SUBROUTINE PROLOG

CHAPTER 0 0 0 0 0 0 0 PRELIMINARIES 0 0 0 0 0 0 0 0

## COMMON

```

1 RESORII,URFU,RESORV,URFV,RESORM,PESOPW,URFW,
1 IIRFP,RESOPT,IIRFT,RESORK,IIRFK,PESOPD,URFD,
1 RESII(25,25),RESV(25,25),RESW(25,25),RESM(25,25),
1 DII(25,25),DV(25,25),DW(25,25),U(25,25),V(25,25),
1 W(25,25),P(25,25),T(25,25),TE(25,25),ED(25,25),
1 PP(25,25),DEFI(25,25),VIS(25,25),AN(25,25),AS(25,25),
1 AF(25,25),AW(25,25),AI(25,25),AD(25,25),CF(25),CD(25,25),
1 CCE(25),CCD(25,25),AP(25,25),SII(25,25),SP(25,25),DXC(25,25),
1 DYC(25,25),D7C(4),WFE(25,25),WFN(25,25),WFO(4),
1 APEAXY(25,25),FID(50,5),NID,WMEAN,INDEX,HYDDIA,RAF,RID(50),
1 VFLIN,TIN,TUALL,FLOWIN,GRFAT,
1 IIRFVIS,VISCOS,DENSIT,PRANDT,
1 PRTE,PRFD,CMU,COT,C1H,C2H,CAPPA,ELOG,ALAMDA,
1 NSWPII,NSWPIV,NSWPIW,NSWPP,NSWPT,
1 NSWPK,NSWPD,
1 IPREF,JREF,KREF,INDCOS

```

## COMMON TAUXS(25),TAUXM(25),TAUZY(25),TAUZN(25),

```

1 YPLUS(25),YPLUSH(25)
1 IT,JT,NI,NJ,NIM1,NJH1
1 SWFT,FLOWTOT,CPW,CFLOW,FLOWT
1 N1,N2
1 RA,RR,THETA,AH,DPDZ,FLOWAX,DXIDF(25,25),DETADF(25,25),PIH
1 DRDXT(25,25),DRDETA(25,25),MTHR(25,25)
1 PI,WTN,FLOWW
1 SMALL,SUMS,SIIMD,INIIMP,DXDY(25,25),DYDX(25,25)

```

## LEVEL 2,III

## COMMON/RLK2/OU(25,25),VV(25,25),ANU(25,25),ASII(25,25),

```

1 AFII(25,25),AWII(25,25),ADU(25,25),AUII(25,25),
1 ANV(25,25),ASV(25,25),AEV(25,25),AWV(25,25),
1 CONT(25,10),VRH(25),JTS,
1 ADV(25,25),AUV(25,25),AA(25)
1 JG,IBOTH,TER(25,2),EDR(25,2),PRODD(50),GENN(25,25)
1 PRANDL,GHT(25,25),AMISS
1 PRDU(25,25),AK7(25,25),AKD(25,25),AKA(25,25),RVT(25,25),AKF
1 AKFT,AKFTD,AKFTD,F1P(25),F1VZ(25),F1KD(25),F1KA(25),F1RVT(25)
1 NOUIMP,CHIA(25,25),CHUR(25)
1 NOUMR?
1 APU(25,25),APV(25,25),RR(25,25),ANGL(25,25)
1 KASH,NASH
1 VISV(25,25),VA(25,25),VB(25,25),VC(25,25)
1 RSC(5),IMER,NAVIT2
1 RPS(25,25),HRE,NITER,MAXIT
1 TLENSC,VISID(50),XPLL(25,25)

```

## DIMENSION GEN(25,25)

## EQUIVALENCE (PP(1,1),GEN(1,1))

```

-----
CT      IMPORTANT NOTICE. ARRAYS TAU..ETC. AND YPLUS..ETC. SHODD   I
CT      BE ADDED OR REMOVED AS NECESSARY DEPENDING ON THE PRESENCE  I
CT      OF WALLS IN EACH PROBLEM                                     I
-----
CHAPTER 1 1 1 1 1 1 1 1 1 PROPERTIES 1 1 1 1 1 1 1 1 1

```

```

C      ENTRY MODPRO
C-----NO MODIFICATIONS FOR THIS PROBLEM
      RETURN

C
CHAPTER 2 2 2 2 2 2 2 2 11 MOMENTUM 2 2 2 2 2 2 2 2
C
      ENTRY MODII
      CMU25=CMU1*.25
C-----N-BOUNDARY-----
      DO 200 I=2,NJM1
      IF (T.GE.N1) GO TO 202
201  AN(I,NJM1)=0.
      GO TO 203
202  AN(I,NJM1)=0.
      YP=.5*DYC(I,NJM1)
      SORTK=SQRT(WFF(T,NJM1)*TE(I,NJM1)+(1.-WFF(I,NJM1))*TE(I-1,NJM1
1))
      DENII=WFF(I,NJM1)*DEN(T,NJM1)+(1.-WFF(I,NJM1))*DEN(I-1,NJM1)
      YPLIISA=WFF(T,NJM1)*YPLIISN(I)+(1.-WFF(I,NJM1))*YPLIISN(I-1)
      IF (YPLIISA.LE.11.63) GO TO 208
      TMULT=DENII*CMU25*SORTK*CAPPA/ALOG(ELOR*YPLIISA)
      TMII T=TMULT*(1.+PTH*PTH*DETADF(T,NJ)*DETADF(I,NJ))
      GO TO 209
208  TMULT=1./YP*(1.+PTH*PTH*DETADF(T,NJ)*DETADF(I,NJ))
      1*(VISV(T,NJM1)*DXC(I-1,NJ)/(DXC(I-1,NJ)+DXC(I,NJ))+
2VISV(T-1,NJM1)*DXC(T,NJ)/(DXC(I-1,NJ)+DXC(I,NJ)))
209  TAUYN(I)=-TMII T*U(I,NJM1)
      TERM=TMULT*.5*(DXC(T,NJ)+DXC(I-1,NJ))*D7C(1)
      SP(I,NJM1)=CP(I,NJM1)-TERM
203  CONTINUE
200  CONTINUE
      TAUYN(1)=TAUYN(NJM1)
      TAUYN(N1)=TAUYN(2)
C-----S-BOUNDARY-----
      DO 210 I=2,NJM1
      IF (T.GE.N2) GO TO 212
211  CONTINUE
      YP=.5*DYC(I,2)
      SORTK=SQRT(WFF(T,2)*TE(I,2)+(1.-WFF(I,2))*TE(I-1,2))
      DENII=WFF(I,2)*DEN(I,2)+(1.-WFF(I,2))*DEN(I-1,2)
      YPLIISA=WFF(T,2)*YPLIISN(I)+(1.-WFF(I,2))*YPLIISN(I-1)
      IF (YPLIISA.LE.11.63) GO TO 218
      TMULT=DENII*CMU25*SORTK*CAPPA/ALOG(ELOR*YPLIISA)
      GO TO 219
218  TMII T=VISCOS/YP
219  TAUYS(I)=-TMULT*U(I,2)
215  TERM=TMULT*.5*(DXC(I,2)+DXC(I-1,2))*D7C(1)
216  SP(I,2)=SP(I,2)-TERM
      AS(T,2)=0.
      GO TO 210
212  CONTINUE
210  CONTINUE
      TAUYS(2)=TAUYS(3)
      TAUYS(NJ)=TAUYS(NJM1)
      DO 231 J=1,NJ
      DO 231 J=1,NJ

```

```

      AH(I,J)=0.
231 AD(I,J)=0.
      RETURN
C
CHAPTER 3 3 3 3 3 3 3 3 V MOMENTUM 3 3 3 3 3 3 3 3
C
      ENTRY MODV
      DO 330 I=1,N1
      DO 330 J=1,NJ
      AH(I,J)=0.
330 AD(I,J)=0.
      RETURN
C
CHAPTER 4 4 4 4 4 4 4 4 W MOMENTUM 4 4 4 4 4 4 4 4
C
      ENTRY MODW
      CMU25=CMU11*.25
C-----S-BOUNDARY-----
      DO 420 I=2,NJM1
      IF(I.GE.N2) GO TO 402
401 CONTINUE
      YP=.25*(DYC(I,2)+DYC(I+1,2))
      SORTK=SQRT(WFD(1)*TE(I,2)+(1.-WFD(1))*TE(I,2))
      DENW=WFD(1)*DEN(I,2)+(1.-WFD(1))*DEN(I,2)
      YPLIISA=WFD(1)*YPLIIS(I)+(1.-WFD(1))*YPLIIS(I)
      IF (YPLIISA.LE.11.63) GO TO 408
      TMULT=DENW*CMU25*SORTK*CAPPA/ALOG(ELOG*YPLIISA)
      GO TO 405
408 TMULT=VTS COS/YP
405 TAU7S(I)=-TMULT*W(I,2)
      TERM=TMULT*.5*(D7C(1)+D7C(1))*DXC(I,2)
      SP(I,2)=SP(I,2)-TERM
      AS(I,2)=0.
      GO TO 420
402 CONTINUE
      IF(INDEX.NE.U) GO TO 420
      SU(I,2)=SU(I,2)-DPD7*(RA+.25*(DYC(I,2)+DYC(I+1,2)))*D7C(1)*
      1DXC(I,2)*.5
420 CONTINUE
C-----W-BOUNDARY-----
      DO 425 I=2,NJM1
      IF(I.LE.N1) GO TO 412
411 CONTINUE
      YP=.25*(DYC(I,NJM1)+DYC(I+1,NJM1))
      SORTK=SQRT(WFD(1)*TE(I,NJM1)+(1.-WFD(1))*TE(I,NJM1))
      DENW=WFD(1)*DEN(I,NJM1)+(1.-WFD(1))*DEN(I,NJM1)
      YPLIISA=WFD(1)*YPLIIS(I)+(1.-WFD(1))*YPLIIS(I)
      IF (YPLIISA.LE.11.63) GO TO 418
      TMULT=DENW*CMU25*SORTK*CAPPA/ALOG(ELOG*YPLIISA)
      TMULT=TMULT*(1.+PIH*PTH*.5*(DETADF(I,NJ)+DETADF(I+1,NJ)))*(DETADF(
      1I,NJ)+DETADF(I+1,NJ)))
      GO TO 415
418 TMULT=1./YP*(1.+PIH*PTH*.5*(DETADF(I,NJ)+DETADF(I+1,NJ)))*(
      1DETADF(I,NJ)+DETADF(I+1,NJ)))
      1*VISV(I,NJM1)
415 TAU7N(I)=-TMULT*W(I,NJM1)
      TERM=TMULT*.5*(D7C(1)+D7C(1))*DXC(I,NJ)

```

```

      SP(I,NJM1)=SP(I,NJM1)-TERM
      AN(I,NJM1)=0.
      GO TO 425
412  AM(I,NJM1)=0.
425  CONTINUE
      TAU7N(1)=TAU7N(NIM1)
      TAU7N(NT)=TAU7N(2)
430  DO 431 I=2,NIM1
      DO 431 J=2,NJM1
      AN(I,J)=0.0
431  AH(I,J)=0.
440  CONTINUE
      RETURN
C
CHAPTER 5 5 5 5 VELOCITY UPDATING 5 5 5 5 5 5 5 5 5
C
      ENTRY MODVEL
      DO 1551 J=2,NJM1
      H(NT,J)=H(2,J)
      H(1,J)=H(NIM1,J)
1551  CONTINUE
      DO 3451 J=3,NJ
      V(1,J)=V(NIM1,J)
      V(NT,J)=V(2,J)
3451  CONTINUE
      FLOWW=0.
      TAREADW=0.
      DO 5661 I=2,NIM1
      DO 5661 J=2,NJM1
      FLOWW=FLOWW+DEN(I,J)*U(I,J)*AREAXY(I,J)
      TAREADW=TAREADW+AREAXY(I,J)*DEN(I,J)*DW(I,J)
5661  CONTINUE
      DO 3463 J=1,NJ
      W(1,J)=W(NIM1,J)
      W(NT,J)=W(2,J)
3463  CONTINUE
      DO 560 I=1,NJ
      H(T,NJ)=0.
      W(T,NJ)=0.
      V(T,NJ)=0.
      V(I,1)=0.
560  CONTINUE
      RETURN
C
CHAPTER 6 6 6 6 6 6 PRESSURE CORRECTION 6 6 6 6 6 6 6 6 6
C
      ENTRY MODP
      DO 380 I=1,NJ
      DO 389 J=1,NJ
      AH(I,J)=0.
389  AN(I,J)=0.
      RETURN
C
CHAPTER 7 7 7 7 7 7 7 THERMAL ENERGY 7 7 7 7 7 7 7 7 7
C
      ENTRY MODT
      DO 3694 I=2,NIM1

```

```

      DO 3698 J=1,NJ
      AH(T,J)=0.0
3698 AD(T,J)=0.0
C-----N-BOUNDARY-----
      J=NIJ1
      DO 1931 J=2,NIJ1
      SH(T,NJM1)=SU(I,NJM1)+QFLUX*D7C(1)*DXC(J,NJ)/CPW
      AN(T,NJM1)=0.
C-----S-BOUNDARY-----
      IF(INDX.NE.0) GO TO 1931
      SH(I,2)=SH(I,2)-QFLUX*D7C(1)*DXC(I,2)/CPW*(FLOWT-FLOWW)/FLOWT
      1*SWFT/(HA*THETA)
      AS(I,2)=0.
1931 CONTINUE
      SH(2,3)=GREAT*G.0
      SP(2,3)=-GREAT
      RETURN
C
CHAPTER 8 8 8 8 8 8 8 TURBULENCE K.E. 8 8 8 8 8 8 8
C
      ENTRY MODTE
      CMU25=CMU**25
C-----S-BOUNDARY-----
      DO 820 I=2,NIJ1
      IF(T.GE.N2) GO TO 819
811 YP=.25*(DYC(I,2)+DYC(I+1,2))
      DENP=DEN(I,2)
      SORTK=SQRT(TF(I,2))
      VOL=APFAXY(I,2)*D7C(1)
      GENCOU=.5*(ABS(TAUXS(I+1)*U(I+1,2))+ABS(TAUXS(I)*U(I,2))
      1+ABS(TAUXS(I)*W(I,2))+ABS(TAUXS(I)*W(I,2)))
      1 /YP
      J=2
      UP=.5*(U(I+1,J)+U(I,J))
      US=.5*(U(I+1,J-1)+U(I,J-1))
      UNN=.5*(U(I+1,J+1)+U(I,J+1))
      UN=UNN*UFN(I,J+1)+UP*(1.-UFN(I,J+1))
      DUDY=(UN-US)/(2.*YP)
      WP=.5*(W(I,J)+W(I,J))
      WS=.5*(W(I,J-1)+W(I,J-1))
      WNN=.5*(W(I,J+1)+W(I,J+1))
      WN=WNN*UFN(I,J+1)+WP*(1.-UFN(I,J+1))
      DUDY=(WN-WS)/(2.*YP)
      SH(I,J)=SH(I,J)-GEN(I,J)*VOL
      GEN(I,J)=GEN(I,J)-(DUDY**2+DWDY**2)*VIS(I,J)+GENCOU
      SH(I,J)=SU(I,J)+GEN(I,J)*VOL
      YPLUSS(T)=DENP*SORTK*CMU25*YP/VISCOS
      IF(YPLUSS(T).LE.11.03) GO TO 802
      DITERM=DEN(I,2)*CMU/CMU25*SORTK*ALOG(FLAG*YPLUSS(T))
      1/(CAPPA*YP)
      GO TO 803
802 CONTINUE
      DITERM=DEN(I,2)*CMU/CMU25*SORTK*YPLUSS(T)/YP
811 CONTINUE
      O.DTERM=-(CDT*CMU*DEN(I,2)**2*TF(I,2)*VOL/VIS(I,2))
      SP(I,2)=SP(I,2)-O.DTERM-DITERM*VOL
      GO TO 820

```

```

R19 CONTINUE
IF (INDEX_NE_0) GO TO R20
AS(I,2)=0.0
R20 CONTINUE
C-----H-BOUNDARY-----
DO R40 I=2,NIM1
IF (TROTHER_0.2) GO TO R21
IF (T_GT_N1) GO TO R39
R21 YP=.25*(DYC(I,NJM1)+DYC(I+1,NJM1))
DFUP=DFH(I,NJM1)
SORTK=SOR(TF(I,NJM1))
VOL=AREAXY(T,NJM1)*DZC(1)
GENCOU=.5*(ABS(TAUXN(T+1)*U(I+1,NJM1))+ABS(TAUXN(I)*
1 U(I,NJM1))+ABS(TAUXN(I)*W(I,NJM1))+ABS(TAUXN(I)*
1 U(T,NJM1)))/YP
J=NJM1
UH=.5*(U(I+1,J+1)+U(I,J+1))
UP=.5*(U(I+1,J)+U(I,J))
USS=.5*(U(I+1,J-1)+U(I,J-1))
US=UP*WEN(I,J)+USS*(1.-WEN(I,J))
DUDY=(UH-US)/(2.*YP)
WP=.5*(U(I,J)+U(I,J))
UN=.5*(U(I,J+1)+U(I,J+1))
WS=.5*(U(I,J-1)+U(I,J-1))
WS=WP*WEN(I,J)+WS*(1.-WEN(I,J))
DUDY=(UN-WS)/(2.*YP)
SU(I,J)=SU(I,J)-GEN(I,J)*VOL
GEN(I,J)=GEN(I,J)-(DUDY**2+DUDY**2)*VIS(I,J)+GENCOU
SU(I,J)=SU(I,J)+GEN(I,J)*VOL
YPLIUSN(I)=DFUP*SORTK*CMU25*YP/VISCOS
IF (YPLIUSN(I).LE.11.63) GO TO R22
DIFERM=DFH(I,NJM1)*CMU/ CMU25*SORTK*ALOG(FLAG*YPLIUSN(I))
1 / (CAPP*YP)
GO TO R23
R22 CONTINUE
DIFERM=DFH(I,NJM1)*CMU/CMU25*SORTK*YPLIUSN(I)/YP
R23 CONTINUE
OLDTRM=(COT*CMU*DFH(I,NJM1)**2*TE(I,NJM1)*VOL/VIS(I,NJM1)
SP(I,NJM1)=SP(I,NJM1)-OLDTRM-DIFERM*VOL
GO TO R40
R39 JGM1=JG-1
SU(I,JGM1)=GREAT*TER(T,1)
SP(I,JGM1)=GREAT
R40 CONTINUE
R45 DO R46 I=2,NIM1
DO R46 J=2,NJM1
AU(I,J)=0.0
AI(I,J)=0.0
R46 CONTINUE
RETURN
C
CHAPTER 0 0 0 0 0 0 0 DISSIPATION 0 0 0 0 0 0 0 0 0
C
ENTPY MODFD
CMU25=CMU**75
C-----S-BOUNDARY-----
DO R40 I=2,NIM1

```



```

      IF(I.GF.N2) GO TO 912
911  YP=.25*(DYC(I,2)+DYC(I+1,2))
      TERM=CMI75/ (CAPPA*YP)
      VOL=ARFAXY(I,2)*DZC(1)
      SH(I,2)=GREAT*TERM*TE(I,2)**1.5*VOL
      SP(I,2)=-GREAT*VOL
      GO TO 910
912  CONTINUE
      IF(INDEX.NE.0) GO TO 910
      AS(I,2)=0.0
910  CONTINUE
C-----N-BOUNDARY-----
      DO 920 I=2,NIM1
      IF(THOTH.EQ.2) GO TO 921
      IF(I.GT.N1) GO TO 922
921  YP=.25*(DYC(I,NJM1)+DYC(I+1,NJM1))
      TERM=CMI75/ (CAPPA*YP)
      VOL=ARFAXY(I,NJM1)*DZC(1)
      SH(I,NJM1)=GREAT*TERM*TE(I,NJM1)**1.5*VOL
      SP(I,NJM1)=-GREAT*VOL
      GO TO 920
922  CONTINUE
      JGM1=JG-1
      SH(I,JGM1)=GREAT*FDR(I,1)
      SP(I,JGM1)=-GREAT
920  CONTINUE
925  DO 926 I=2,NIM1
      DO 926 J=2,NJM1
      AN(I,J)=0.0
      AH(I,J)=0.
926  CONTINUE
      RETURN
C
CHAPTER 10 10 10 10 10 RADII OF CURVATURE 10 10 10 10 10 10
C
      ENTRY MODRAD
C-----SPECIFY RADII OF CURVATURE OF ROUNDAPIES-----
C-----S-BOUNDARY-----
      DO 1000 I=1,N1
      J=1
      1000  DYDY(I,J)=1./RA
C-----N-BOUNDARY-----
      J=NJ
      DO 1001 I=2,NIM1
      1001  DYDY(I,J)=1./(.5*(RR(I,J)+RR(I+1,J)))
      DYDY(N1,NJ)=DYDY(2,NJ)
      DYDY(1,NJ)=DYDY(NIM1,NJ)
      DO 1010 J=2,NJM1
C-----V-BOUNDARY-----
      DYDX(1,J)=DYDX(NIM1,J)
C-----E-BOUNDARY-----
      DYDX(N1,J)=DYDX(2,J)
      1010  CONTINUE
      DYDX(1,1)=DYDX(NIM1,1)
      DYDX(N1,1)=DYDX(2,1)
      DYDX(1,NJ)=DYDX(NIM1,NJ)
      DYDX(N1,NJ)=DYDX(2,NJ)

```

RETURN  
END

```

SUBROUTINE PRINT(ISTART,JSTART,NI,NJ,IT,JT,X,Y,
1PMI,HEAD)
DIMENSIONPHI(IT,JT),HEAD(6),STOPE(50)
DIMENSION F(7),F4(11)
DATA F/4H(1H ,4H ,A00,4HI3, ,4H11I ,4H10, ,4H7X, ,
14HA6) /
DATA F4/4H 1I ,4H 2I ,4H 3I ,4H 4I ,4H 5I ,4H 6I ,
1 ,4H 7I ,4H 8I ,4H 9I ,4H10I ,4H11I /
DATA HI,HY/4H I = ,4H Y = /
WRITE(6,110)HEAD
ISKIP=1
JSKIP=1
ISTA=ISTART-12
100 CONTINUE
ISTA=ISTA+12
IFND=ISTA+11
IFND=MIN0(NI,IFND)
F(4)=F4(IFND-ISTA)
WRITE(6,F) HI,(I,I=ISTA,IFND,ISKIP)
WRITE(6,112)
DO 101 JJ=JSTART,NJ,JSKIP
J=JSTART+NJ-JJ
DO 120 I=ISTA,IFND
A=PHI(I,J)
IF(AHS(A).LT.1.E-20) A=0.0
120 STORE(I)=A
101 WRITE(6,113) J,(STORE(I),I=ISTA,IFND,ISKIP)
-----
IF(IFND.IT.NI)GO TO 100
200 CONTINUE
RETURN
110 FORMAT(1H0,///,20(2H*-),7X,6A6,7X,20(2H*-)/)
111 FORMAT(1H0,6H I = ,I3,11I10,7X,* Y = *)
112 FORMAT(3H JJ)
113 FORMAT(1H ,I3,1P12F10.2,0PF7.3)
END

```

AD-A150 774

FLUID MECHANICS AND HEAT TRANSFER SPIRALLY FLUTED  
TUBING(U) GA TECHNOLOGIES INC SAN DIEGO CA  
J S YAMPOLSKY ET AL. DEC 84 GA-A17833 N00014-82-C-0721

010

UNCLASSIFIED

F/G 20/4

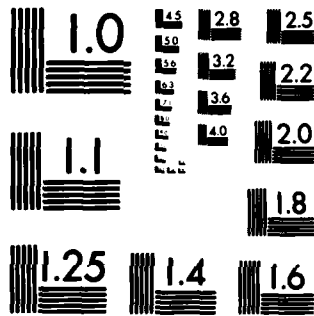
NL



END

FORMED

DTIC



MICROCOPY RESOLUTION TEST CHART  
NATIONAL BUREAU OF STANDARDS-1963-A

### References

1. Yampolsky, J.S. "Spiral fluted tubing". Summary report. Publication of General Atomic Company, (October 1979), GA-A15524.
2. Bergles, A.E. "Augmentation of forced-convection heat transfer". Turbulent Forced Convection in Channels and Bundles, edited by S. Kakaç and D.B. Spalding, Vol.2 (1979), Hemisphere Publishing Co.
3. Joshi, S.D. and Bergles, A.E. "Survey and evaluation of passive heat transfer augmentation techniques for laminar flow". Journal of Mechanical Engineers, Vol.1 (1980), pp.105-124.
4. Bergles, A.E. and Webb, R.L. "Bibliography on augmentation of convective heat and mass transfer". Previews Heat and Mass Transfer 4, (1978), No.4, pp.89-106.
5. Bergles, A.E. "Classification of augmentation techniques". Previews Heat and Mass Transfer 4, (1979). No.2.
6. Joule, J.P. Phil. Trans. Roy. Soc. London, Vol.151 (1861), pp.133-160.
7. Whitham, J.M. Street Railway Journal, Vol.12 (1896), p.374.
8. Royds, R. "Heat transmission by radiation, conduction and convection". Constable and Company, London, pp.191-201.
9. White, A. "Flow of a fluid in an axially rotating pipe". Journal of Mech. Engin. Science, Vol.6, No.1 (1964), pp.47-52.
10. Harvey, P.H., Nandapurkar, S.S. and Holland, F.A. "Friction factors for a tube rotating about its own axis". The Canadian Journal of Chemical Engineering, Vol.49 (1971).
11. Murakani, M. and Kikuyama, K. "Turbulent flow in axially rotating pipes". Journal of Fluids Engineering, Vol.102 (1980), pp.97-103.
12. Nagib, H.M., Lavan, Z., Fejer, A.A. and Wolf, L. "Stability of pipe flow with superposed solid-body rotation". The Physics of Fluids, Vol.14, No.4 (1971), pp.766-768.
13. Cannon, J.N. and Kays, W.M. "Heat transfer to a fluid flowing inside a pipe rotating about its longitudinal axis". Journal of Heat Transfer, (1969), pp.135-139.
14. McElhiney, J.E. and Preckshot, G.W. "Heat transfer in the entrance length of a horizontal rotating tube". Int. J. Heat and Mass Transfer, Vol.20 (1977), pp.847-854.

15. Meri, Y., Fukada, T. and Nakayama, W. "Convective heat transfer in a rotating radial circular pipe" (2nd report), Int. J. Heat and Mass Transfer, Vol.14 (1971), p.1807.
16. Miyazaki, H. "Combined free and forced convective heat transfer and fluid flow in a rotating curved circular tube". Int. J. Heat and Mass Transfer, Vol.14, pp.1295-1309.
17. Skiadraessis, D. and Spalding, D.B. Paper presented at the Sixth Int. Heat Transfer Conference, Toronto (1978).
18. Porter, J.E. and Poulter, R. Heat Trans., Vol. II (1970), Paper FC3.7, Elsevier.
19. Savkar, S.D. Physics of Fluids, Vol.14 (1971), pp.2670-2679.
20. Newton, D.C. and Allen, P.H.G. Letters in Heat and Mass Transfer, Vol.4 (1977), pp. 9-16.
21. Kudirka, A.A. ASME Paper No.65-HT-47 (1965).
22. Tauscher, W.A., Sparrow, E.M. and Lloyd, J.R. "Int. J. Heat and Mass Transfer, Vol.13 (1970), pp.681-688.
23. Kinney, R.B. "Fully developed frictional and heat transfer characteristics of laminar flow in porous tubes". Int. J. Heat and Mass Transfer, Vol.11 (1968), pp.1393-1401.
24. Kinney, R.B. and Sparrow, E.M. J. Heat Transfer, Vol.92 (1970), pp.117-125.
25. Nikuradse, J. "Laws for flow in rough pipes". VDI-Forschungsheft 361, Series B, 4 (1933), NACA-TM1292 (1950).
26. Cope, W.F. "The friction and heat transmission coefficients of rough pipes". Proc. Inst. Mech. Engrs. 145, (1941), pp.99-105.
27. Nunner, W. "Heat transfer and pressure drop in rough tubes". VDI-Forschungsheft 455, Series B, 22 (1956), pp.5-39, AERE Lib/Trans 786 (1958).
28. Schlichting, H. "Boundary layer theory". McGraw-Hill, New York (1955).
29. Dipprey, D.F. and Sabersky, R.H. "Heat and momentum transfer in smooth and rough tubes at various Prandtl numbers". Int. J. Heat and Mass Transfer, Vol.6 (1963), pp.329-353.
30. Owen, P.R. and Thomson, W.R. "Heat transfer across rough surfaces". J. Fluid Mech., Vol.15 (1963), pp.321-334.
31. Martinelli, R.C. "Heat transfer to molten metals". Trans. ASME, J. Heat Transfer, Vol.69 (1947), p. 947.

32. Galin, N.M. "Heat transfer with turbulent gas flow over rough walls". Teploenergetika, Vol.14, No.5 (1967), pp.86-93.
33. Burck, E. "The influence of Pr number on heat transfer and pressure drop of artificially roughened channels". Augmentation of Convective Heat and Mass Transfer, Winter Annual Meeting, ASME (1970).
34. Smith, J.W. and Gowen, R.A. "Heat transfer efficiency in rough pipes at high Prandtl number". AIChE. Journal, Vol.11, No.5 (1965), pp.941-943.
35. Kolar, V. "Heat transfer in turbulent flow of fluids through smooth and rough tubes". Int. J. Heat and Mass Transfer, Vol.8 (1965), pp.639-653.
36. Skupinski, E. "Heat transfer and pressure drop from artificially roughened walls". Diss. T.H. Aachen (1961).
37. Gee, D.L. and Webb, R.L. "Forced convection heat transfer in helically rib-roughened tubes". J. Heat and Mass Transfer, Vol.23 (1980), pp.1127-1136.
38. Smith, J.W., Gowen, R.A. and Charles, M.E. "Turbulent heat transfer and temperature profiles in a rifled pipe". Chemical Engineering Science, Vol.23 (1968), pp.751-758.
39. White, L. and Wilkie, D. "The heat transfer and pressure loss characteristics of some multi-start ribbed surfaces". Augmentation of Convective Heat and Mass Transfer, Bergles and Webb (eds.), ASME, New York (1970), pp.55-62.
40. Marnier, W.J. and Bergles, A.E. "Augmentation of tubeside laminar flow heat transfer by means of twisted tape inserts, static-mixers and internally finned tubes". Paper presented at Sixth Int. Heat Transfer Conference, Toronto (1978).
41. Bergles, A.E. "Laminar flow heat transfer in horizontal tubes under normal and augmented conditions". Heat Transfer Laboratory Report HTL-11, ISU-ERI-Ames-77179, Iowa State University, Ames (1975).
42. Watkinson, A.P., Milette, D.L. and Kubanek, G.R. "Heat transfer and pressure drop of internally finned tubes in laminar oil flow". Am. Soc. Mech. Engrs. Paper No. 75-HT-41 (1975).
43. Kubanek, G.R., Watkinson, A.P. and Milette, D.L. "Heat transfer and pressure drop of internally finned tubes in turbulent airflow". Trans. ASHRAE, Vol.81, Part 1 (1975), pp.330-347.
44. Watkinson, A.P., Milette, D.L. and Tarassoff, P. "Turbulent heat transfer and pressure drop in internally finned tubes". AIChE Symposium Series No.131, Vol.69 (1973), pp.94-103.
45. Kumar, P. and Judd, R.L. "Heat transfer with coiled wire turbulence promoters". Canadian Journal of Chemical Engrg., Vol.48 (1970), pp.378-383.

46. Hong, S.W. and Bergles, A.E. "Augmentation of laminar flow heat transfer in tubes by means of twisted-tape inserts". J. of Heat Transfer (May 1976), pp.251-256.
47. Lopina, R.F. and Bergles, A.E. "Heat transfer and pressure drop in tape-generated swirl flow of single-phase water". Trans. ASME, J. of Heat Transfer (August 1969), pp.434-441.
48. Bergles, A.E., Lee, R.A. and Mimic, B.B. "Heat transfer in rough tubes with tape generated swirl flow". J. of Heat Transfer, Vol.91 (1969), pp.443-445.
49. Van Rooyen, R.S. and Kröger, D.G. Paper presented at Sixth Int. Heat Transfer Conference, Toronto (1978).
50. Kryukov, Y.V. and Buykov, G.P. Heat Transf., Soviet Res., Vol.5, No.1 (1973), pp.26-28.
51. Koch Engineering Company, Inc., Bulletin KSM-2.
52. Chen, S.J. Kenics Corporation Bulletin KTEK-2, KTEK-3 (1972).
53. Kidd, G.J. Jr. "The heat transfer and pressure-drop characteristics of gas flow inside spirally corrugated tubes". J. of Heat Transfer (August 1970), pp.513-519.
54. Lawson, C.G., Kadl, R.J. and McDonald, R.E. "Enhanced heat-transfer tubes for horizontal condensers with possible applications in Nuclear power plant design". Trans. of the ANS, Vol.9, No.2 (Oct.-Nov. 1966), pp.565-566.
55. Yorkshire Imperial Alloys Heat Exchanger Tubes : Design Data for Horizontal Roped Tubes in Steam Condensers. Technical Memorandum.
56. Silberman, E. "Turbulence in helically corrugated pipe flow". J. of the Engineering Mechanics Division (August 1980), pp.699-717.
57. Laufer, J. "The structure of turbulence in fully developed pipe flow". Report 1174, National Advisory Committee for Aeronautics (1954).
58. Silberman, E. "Effect of helix angle on flow in corrugated pipes". J. of the Hydraulics Division, Proceed. Amer. Society of Civil Eng. (1970), pp.2253-2263).
59. LaRue, J.C., Libby, P.A. and Yampolsky, J.S. "Fluid mechanics and heat transfer. Spirally fluted tubing". Progress Report GA-A1654L (August 1981).
60. Yampolsky, J.S. and Pavlics, P. "Tubing for augmented heat transfer". Progress Report GA-A17109 (August 1983).
61. Mizushima, T. "Buoyancy effect on any diffusivities in thermally stratified flow in an open channel". Proceedings of the Sixth Int. Heat Transfer Conference, Vol.1 (1979), pp.91-96.
62. Hu, M.H. and Chang, Y.P. "Optimization of finned tubes for heat transfer in laminar flow". Trans. ASME, J. of Heat Transfer (August 1973), pp.332-338.

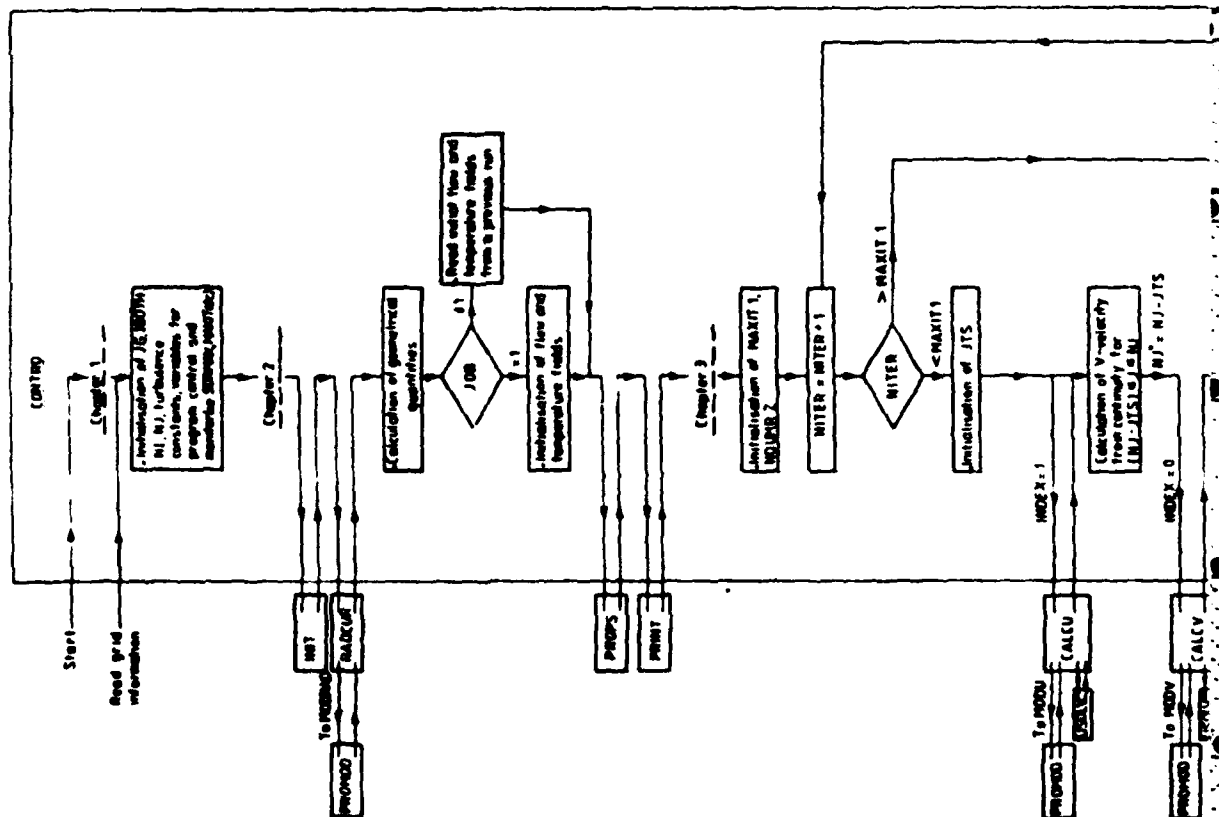


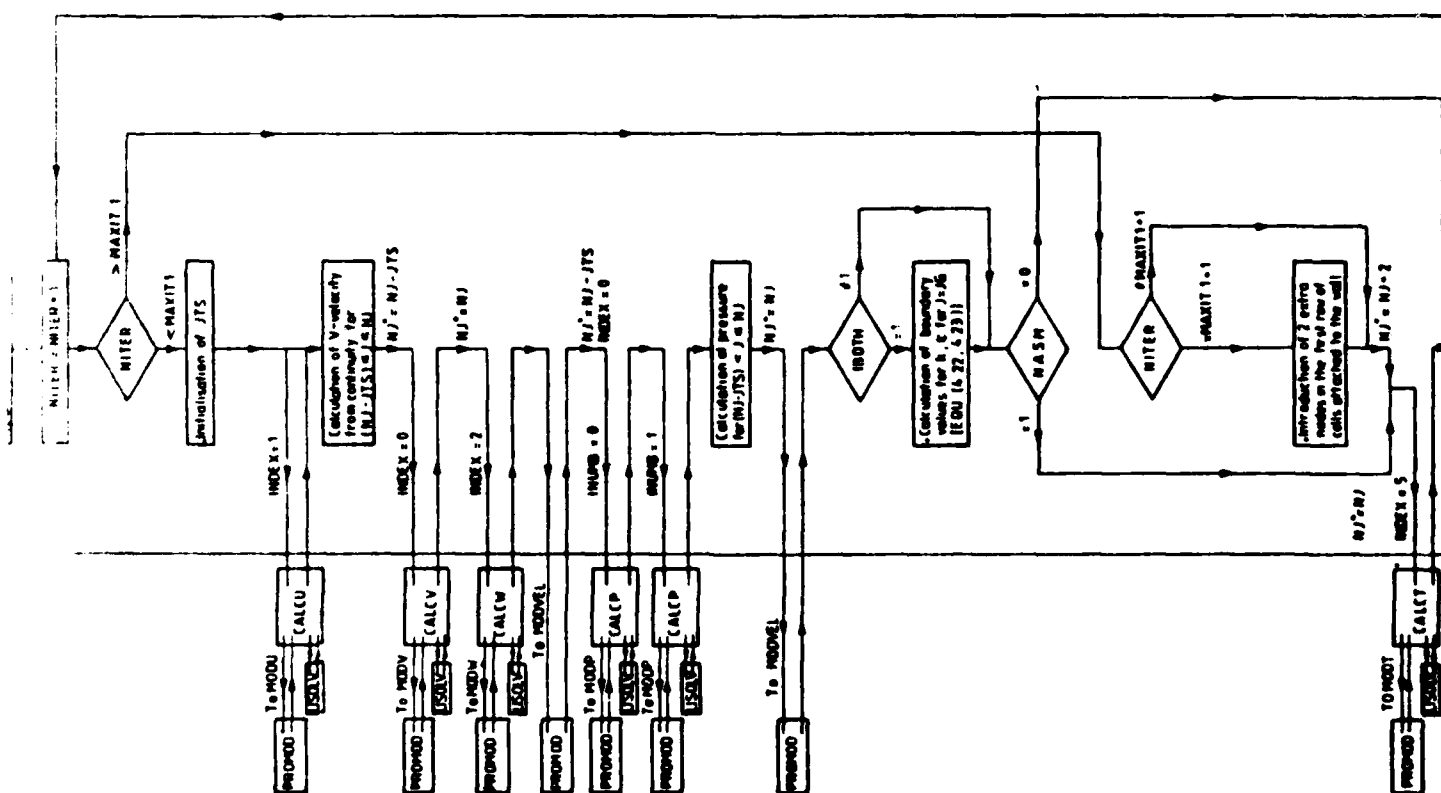
63. Masliyah, J.H. and Nandakumar, K. "Fully developed viscous flows in internally finned tubes". The Chemical Eng. Journal, Vol.10 (1975), pp.113-120.
64. Masliyah, J.H. and Nandakumar, K. "Heat transfer in internally finned tubes". Trans. ASME, J. of Heat Transfer (May 1976), pp.257-261.
65. Patankar, S.V., Ivanovic, M. and Sparrow, E.M. "Analysis of turbulent flow and heat transfer in internally finned tubes and annuli". Trans. ASME, J. of Heat Transfer (February 1979), Vol.101, pp.29-37.
66. Date, A.W. and Singham, J.R. "Numerical prediction of friction and heat transfer coefficients of fully developed laminar flow in tubes containing twisted tapes". ASME Paper 72-HT-17 (1972).
67. Date, A.W. "Prediction of fully developed flow in a tube containing a twisted tape". Int. J. of Heat and Mass Transfer 17 (1974), pp.845-859.
68. Launder, B.E. and Jones, W.P. "The prediction of laminarization with a two-equation model of turbulence". Int. J. Heat and Mass Transfer, Vol.15(2) (1972), pp.301-314.
69. Gibson, M.M. and Launder, B.E. "On the calculation of horizontal, turbulent, free shear flows under gravitational influence". Trans. ASME, J. of Heat Transfer (February 1976), pp.81-87.
70. Masliyah, J.H. and Nandakumar, K. "Steady laminar flow through twisted pipes". Fluid Flow in Square Tubes. Trans. ASME, J. of Heat Transfer, Vol.103 (November 1981), pp.785-790.
71. Masliyah, J.H. and Nandakumar, K. "Steady laminar flow through twisted pipes". Heat Transfer in Square Tubes. Trans. ASME, J. of Heat Transfer, Vol.103 (November 1981), pp.791-796.
72. Spalding, D.B. "A novel finite difference formulation for differential expressions involving both first and second derivatives". Int. J. Numerical Methods in Engrg., Vol.4 (1972), pp.551-559.
73. Raithby, G.D. and Torrance, K.E. "Upstream-weighted differencing schemes and their application to elliptic problems involving fluid flow". Computers and Fluids, Vol.2 (1974), pp.191-206.
74. Raithby, G.D. "Skew-upstream differencing scheme for problems involving fluid flow". Computer Methods in Applied Mechanics and Engrg., Vol.9 (1976).
75. Bergles, A.E., Nelson, R.M. and Webb, R.L. "Assessment, development and coordination of technology base studies in enhanced heat transfer". Quarterly Progress Report 5 on DOE Grant No. DE-FG07-81ID12222, Iowa State University (December 1982).
76. Junkan, G.H. and Webb, R.L. "Energy conservation via heat transfer enhancement". HTL-30, ISU-ERI-Ames-83158, CDO-4649-16, idem.

77. Bergles, A.E., Blumenkrantz, A.R. and Taborek, J. "Performance evaluation criteria for enhanced heat transfer surfaces". J. of Heat Transfer (1974), Japan Soc. of Mechanical Engrs., Vol.2, pp.239-243.
78. Shah, R.K. Paper presented at Sixth Int. Heat Transfer Conference, Toronto (1978).
79. Issa, R. "Solution of implicitly discretized fluid flow equations by operator splitting". Imperial College, Mech. Eng. Dept. Rep. FS/82/15 (1982).
80. Gosman, A.D., Issa, R. and Watkins, P. "Application of a new implicit algorithm for compressible and incompressible recirculating flows". Imperial College, Mech. Eng. Dept. Rep. FS/83/3 (1983).
81. Patankar, S.V. and Spalding, D.B. "A calculation procedure for heat, mass and momentum transfer in three-dimensional parabolic flows". Int. J. Heat and Mass Transfer 15, 1787 (1972).
82. LaRue, J.C. Personal communication (1983).
83. Barba, A., Bergeles, G., Demirdzic, I, Gosman, A.D. and Launder, B.E. "The computation of flow in spirally fluted tubes". AIChE Symposium Series No.225, 79, 100 (1983).
84. Barba, A., Bergeles, G., Gosman, A.D. and Launder, B.E. "The prediction of convective heat transfer in viscous flow through spirally fluted tubes". ASME Paper No. 83-WA/HT-37 (1983).
85. Barba, A., Gosman, A.D. and Launder, B.E. "The prediction of heat transfer performance in spirally fluted tubes: The turbulent flow regime". Presented at the 1st UK National Heat Transfer Conference, Leeds, July 3rd - 5th (1984).
86. Antonopoulos, K., Gosman, A.D. and Issa, R. "A prediction method for laminar and turbulent flow in tube assemblies". Proc. 6th Int. Conf. on Numerical Methods in Fluid Dynamics, Vol.1 (June 1978), p.355-362, Tbilisi, USSR.
87. Patankar, S.V. "Numerical heat transfer and fluid flow". Hemisphere Publishing Corp. Mc-Graw-Hill Book Co.
88. Leonard, B.P. "A survey of finite differences of opinion on numerical muddling of the incomprehensible defective confusion equation". Finite Element Methods in Convection Dominated Flows, Applied Mechanics Division, ASME Winter Annual Meeting, New York (December 1979).
89. Leonard, B.P. "A stable and accurate convective modelling procedure based on quadratic upstream interpolation". Comput. Maths. Appl. Mech. Engrg., 19 (1979), pp.59-98.
90. Han., T., Humphrey, J.A.C. and Launder, B.E. "A comparison of hybrid and quadratic upstream differencing in high Reynolds number elliptic flows". Comput. Maths. Appl. Mech. Engrg. 29 (1981), pp.81-95.

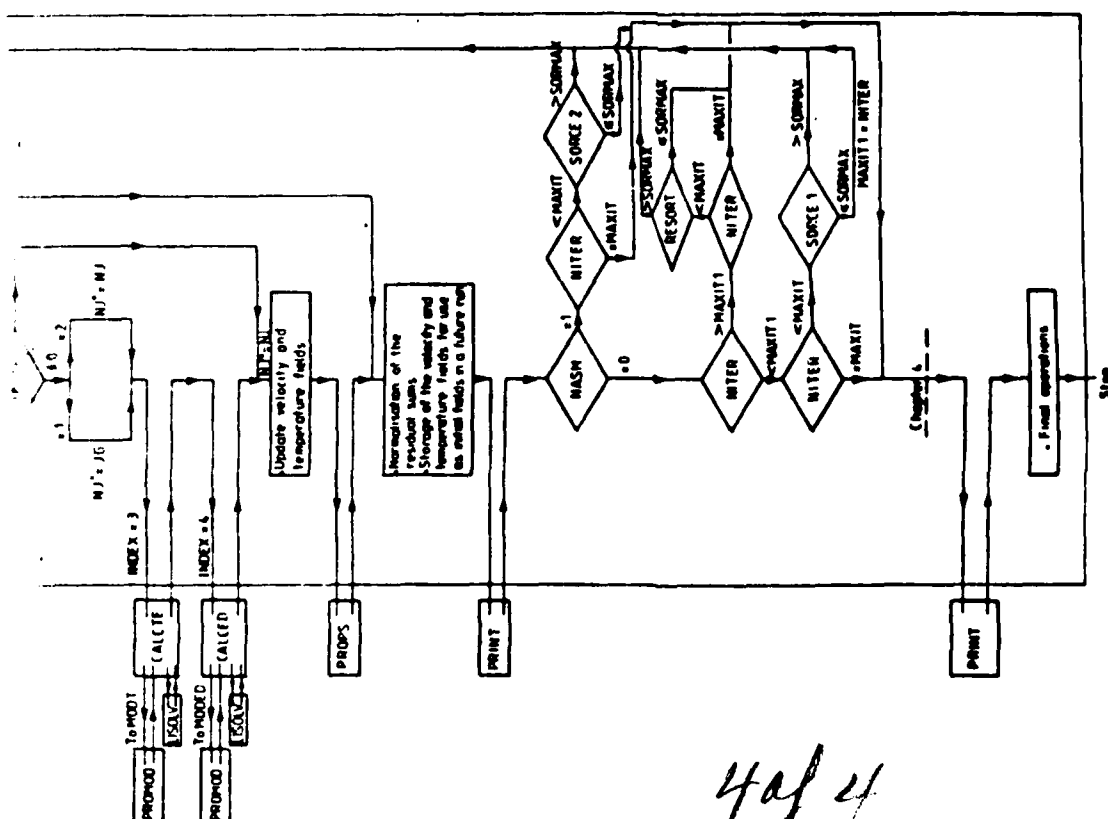
91. Gosman, A.D. and Ideriah, F.J.K. "TEACH-T: A general computer program for two-dimensional, turbulent, recirculating flows". Imperial College, London, Mech. Eng. Dept. (June 1976).
92. Launder, B.E. "A generalized algebraic-stress transport hypothesis". AIAAJ 20, 436 (1982).
93. Launder, B.E., Reece, G.J. and Rodi, W. "Progress in the development of a Reynolds-stress turbulence closure". J. Fluid Mech., Vol.68, Part 3 (1975), pp.537-566.
94. Reilly, D.J. "An experimental investigation of enhanced heat transfer on horizontal condenser tubes". M.S. Thesis, Naval Postgraduate School (1978).
95. Cebeci, T. "A model for eddy conductivity and turbulent Prandtl number". Journal of Heat Transfer, (May 1973), pp.227-234.
96. Patankar, S.V. "Wall-shear-stress and heat-flux laws for turbulent boundary layer with a pressure gradient: Use of Van Driest's eddy-viscosity hypothesis". Imperial College, TWF/TN/14 (May 1966).
97. Kays, W.M. "Convective heat and mass transfer". McGraw-Hill Publ. (1979).
98. Launder, B.E. "Heat and mass transport". Topics in Applied Physics, Vol.12, Springer-Verlag (1978).
99. Reynolds, A.J. "The prediction of turbulent Prandtl and Schmidt numbers". Int. J. Heat and Mass Transfer, Vol.18 (1975), pp. 1055-1069.
100. Launder, B.E. and Spalding, D.B. "The numerical calculation of turbulent flow". Comp. Math. Appl. Mech. Engrg., 3, 269 (1974).
101. Launder, B.E. Personal communication.
102. Younis, B.A. "On modelling the effects of streamline curvature on turbulent shear flows". PhD Thesis, Mech. Eng. Dept., Imperial College (March 1984).
103. Launder, B.E. "On the effects of gravitational field on the turbulent transport of heat and momentum". J. Fluid Mech., Vol.67 (1975).
104. Launder, B.E. "Quasi-buoyant effects in stratified swirling turbulent flow". Personal communication (1982).
105. Iacovides, H. and Launder, B.E. "PSL - An economical approach to the numerical analysis of near-wall elliptic flows".(1983)
106. Launder, B.E. "Numerical computation of convective heat transfer in complex turbulent flows: Time to abandon wall functions?" (1984).

107. Launder, B.E. "Turbulence transport models for numerical computation of complex turbulent flows". MSc Lecture Notes (1977).
108. Patel, V.C. and Head, M.R. "Some observations of skin friction and velocity profiles in fully developed pipe and channel flows". J. Fluid Mech., 38, 181 (1969).
109. Demirdzic, I. "Equations of turbulent flow in a straight spirally-fluted duct". Personal communication.
110. Jones, W.P. and Launder, B.E. "The prediction of laminarization with a two-equation model of turbulence". Int. J. Heat and Mass Transfer, Vol.15 (1972), pp.301-314.
111. Jones, W.P. and Launder, B.E. "On the prediction of laminarescent turbulent boundary layers". ASME Paper 69-HT-13 (1969).
112. Durst, F. and Rastogi, A.K. "Calculations of turbulent boundary layer flows with drag reducing polymer additives". The Physics of Fluids, Vol.20, No.12 (1977), pp.1975-1985.
113. Azzola, J. and Humphrey, J.A.C. "Developing turbulent flow in a 180° curved pipe and its downstream tangent". 2nd Inter. Symposium of Applications of Laser Anemometry to Fluid Mechanics (1984).











**END**

**FILMED**

**4-85**

**DTIC**